Jan Awrejcewicz *Editor*

Dynamical Systems in Applications

Łódź, Poland December 11–14, 2017

Springer

Springer Proceedings in Mathematics & Statistics

Volume 249

Springer Proceedings in Mathematics & Statistics

This book series features volumes composed of selected contributions from workshops and conferences in all areas of current research in mathematics and statistics, including operation research and optimization. In addition to an overall evaluation of the interest, scientific quality, and timeliness of each proposal at the hands of the publisher, individual contributions are all refereed to the high quality standards of leading journals in the field. Thus, this series provides the research community with well-edited, authoritative reports on developments in the most exciting areas of mathematical and statistical research today.

More information about this series at http://www.springer.com/series/10533

Jan Awrejcewicz
Editor

Dynamical Systems in Applications

Łódź, Poland December 11–14, 2017

Springer

Editor
Jan Awrejcewicz
Department of Automation,
   Biomechanics and Mechatronics
Łódź University of Technology
Łódź, Poland

Preface

The International Conference "Dynamical Systems: Theory and Applications" (DSTA), held on December 11–14, 2017 in Łódź (Poland), was the 14th edition of a conference series with over a 25-year history. This scientific meeting organized by the Department of Automation, Biomechanics and Mechatronics of the Lodz University of Technology gathers numerous outstanding researchers and engineers from different fields of science, who deal with widely understood problems of dynamics met in daily life. This book collects only a small, carefully selected part of the topics covered by the participants of the latest edition of DSTA Conference. This volume covers a very wide spectrum of topics, varying from purely mathematical to purely engineering approaches that were presented by both experienced and ambitious young researchers. All of the chapters ranging from purely theoretical to application-oriented studies are connected by the common factor—dynamical systems.

The main aim of this volume is not only to provide the reader with an overview of the recent developments in the field of dynamical systems but also to help them in finding answers to their own problems and inspire them for further research.

In Chapter "Gait Transitions in Artificial Non-standard Snake-Like Locomotion Systems Using Adaptive Control", Behn and Kräml presented a nonstandard mechanical model of a snake-like robot. They investigated most advantageous gait patterns for a 10-link prototype proposed by them. In addition, they used numerical simulations to obtain a gait transition algorithm that is able to autonomously change velocity and the number of resting mass points.

Breńkacz et al. (Chapter "The Experimental Determination of Bearings Dynamic Coefficients in a Wide Range of Rotational Speeds, Taking into Account the Resonance and Hydrodynamic Instability") presented their results of the experimental determination of bearings dynamic coefficients. They described the outcomes of computations for both stably operating machines and for a broad range of rotational speeds, taking into account the resonance and hydrodynamic instability.

In Chapter "Analysis of Rail Vibration Signal Time and Frequency Structures Generated by Different Mechanisms", Burdzik focused on the identification of the excitation characteristics for a rail vibration structure. He analyzed the frequency

forms of vibrations with respect to a possibility to separate them into signals of longitudinal, transverse, and vertical vibrations.

Chmielewski et al. (Chapter "Model Based Research on Ice Engine Powered by Alternative Fuels") presented theoretical and analytical dependencies describing the heat generation in the cylinder of the 2 DOF dynamic model in a piston-crankshaft system with the ICE engine powered by an alternative fuels.

In Chapter "Experimental Evaluation of Mathematical and Artificial Neural Network Modeling of Energy Storage System", Chmielewski et al. (2) proposed a recurrent artificial neural network structure as a model of an energy storage system. Their approach allows one to forecast the properties of electromechanical energy storage systems and it can be used for prediction and control in battery management systems.

Csukas and Duma (Chapter "Finite Element Analysis of a Configuration of Optomechatronic Choppers with Rotational Shafts") applied the finite element analysis to investigate the fundamental issues of the optomechatronic choppers with rotational shafts. They obtained some preliminary results allowing for optimization of such devices for specific application.

In Chapter "Charpy Impact Testing Machine in Modeling of Vehicle Frontal Crash with Street Lights", Danek and Pawlak presented interesting numerical results obtained while studying the possibility of applying a Charpy impact testing machine as an alternative method for real crash tests.

Dutkiewicz (Chapter "Interaction of Bridge Cables and Wake Behind in the Vortex Induced Vibrations") investigated an influence of the vortex induced vibrations on the interaction of the circular section of the bridge cables.

In Chapter "Steady-State Behaviour of the Jeffcott Rotor Comparing Various Analytical Approaches to the Solution of the Reynolds Equation for Plain Journal Bearing", Dyk et al. focused on the behavior of the Jeffcott rotor supported by HD journal bearings. They studied rotor's steady-state responses and compared results for various analytical approaches with the solution of the Reynolds equation.

Falborski et al. (Chapter "Numerical Investigation on Dynamic Performance of a Multi-storey Steel Structure Model and Comparison with Experimental Results") presented a numerical evaluation of the dynamic response of a two-storey steel structure model considered as a 2-DOF system with lumped parameters determined by free vibration tests.

Chapter "Accumulation of the Energy in Mechanical Resonance" is devoted to energy accumulation on mechanical resonance and its use in impact working machines and in machines with the crankshaft systems, as studied by Fiebig.

In Chapter "Application of Time-Frequency Methods for Assessment of Gas Metal Arc Welding Condition", Górka and Jamrozik proposed a method for the evaluation of material joining stability in the gas metal arc welding process. Their research yielded a reliable analytical method to distinguish correct and incorrect joint by using the intrinsic mode function obtained from the empirical mode decomposition.

In Chapter "A 3-Link Model of a Human for Simulating a Fall in Forward Direction", Grzelczyk et al. proposed a novel 3-link biomechanical model of a human for simulating a forward fall. Parameters of the model were obtained based on the 3D scanned human body model created in Inventor, while model's kinematics was obtained from the experimental observation with a motion capture system.

In Chapter "Reflectance and Transmittance of Cholesteric Liquid Crystal Sandwiched Between Polarizers", Grzelczyk and Awrejcewicz calculated the reflection and transmission coefficients of the light incident on the cholesteric liquid crystal sandwiched within two isotropic media and optical polarizers. Application of the exact 4×4 matrix method allowed them to take into account both the effect of refraction and multiple reflections at the interfaces of dielectric discontinuities.

Chapter "Analysis of Nonlinear Dynamic Behavior of a Rotating Electrical Machine Rotor-Bearing System Using Optimal Auxiliary Functions Method" is focused on the dynamical analysis of a rotating electrical machine. For this purpose, Herisanu and Marinca applied the optimal auxiliary function method that allowed them to solve the problem of the parametrically excited system supported by nonlinear bearings and unbalanced by the rotor force.

Jarzębowska et al. (Chapter "Development of a Computational Based Reference Dynamics Model of a Flexible Link Manipulator") described the development of a new derivation method for a flexible link manipulator allowing for the generation of dynamic equations without formulating additional material constraints.

In Chapter "Optimization of Geometry of Cavitational Tunnel Using CFD Method", Jasionowski and Kostrzewa presented the application of the computational fluid dynamics software for numerical optimization of the geometry of a cavitation tunnel allowing to determine an optimal shape of counter-barricade in terms of receiving largest low-pressure that induces the cavitation phenomenon.

Steel multilayer welding was the subject of the study by Kik et al. (Chapter "Application of Numerical Simulations on 10GN2MFA Steel Multilayer Welding"). The applied numerical simulations allowed for optimization of the welding process with respect to re-structural changes, stresses, and hardness distribution in the heat affected zone.

Komorski et al. (Chapter "Application of Time-Frequency Analysis of Acoustic Signal to Detecting Flat Places on the Rolling Surface of a Tram Wheel") applied the time-frequency analysis of an acoustic signal for detection of the imperfections of the rolling surface of tram wheels. Their research yielded a method for monitoring and diagnosing wheel flat places as well as increasing safety and reliability of the public transport.

In Chapter "Development of a Prototype Dynamic Weighing System for Single Bucket Excavator", Kosiara et al. presented the prototype of the dynamic weighing system for a single bucket excavator, developed at the Wrocław University of Science and Technology. A comparison of the numerical and experimental results indicates high accuracy of the developed system in weighing of the transported payload.

Kralikova et al. (Chapter "Design of Illumination and Lighting Visualization by Simulation Methods") proposed a simulation method to design internal artificial illumination and lighting visualization that can be applied for the improvement of the occupational safety and to create flexible spaces that are adapting themselves according to the type of the activity carried out.

In Chapter "Optimal Design of Multibody Systems Using the Adjoint Method", Maciąg et al. investigated the possibility of application of the proposed computational algorithm using the adjoint method to obtain optimal design of a multibody system.

Mirosław and Zawadzki (Chapter "Non-linear Modelling of Human Body Dynamic") presented a nonlinear method of modeling of static and dynamic loads of human body parts during movement. Their model describes a human body as a chain composing of three types of elements—bones, elastic tendons, and muscles.

In Chapter "Dynamics of a Portable Module Handling System", Mitoraj and Szczotka described a model of a light module handling system developed for inspection, maintenance, and repair services typically conducted for the seabed-located oil and gas production facilities.

Palechor et al. (Chapter "Dynamic Analysis of a Beam with Additional Auxiliary Mass Spatial Via Spectral Element Method") proposed a new spectral element with auxiliary mass while dealing with the wave propagation in structures during the spectral analysis.

Pałczyński (Chapter "Influence of Air Temperature on Dynamic Properties of Pipes Supplied with Pulsating Flow") presented the results of an investigation of an influence of air temperature on dynamic properties of pipes supplied with pulsating flow.

Kinetic energy recuperation system for city buses was modeled by Pałczyński and Łagodziński (Chapter "Model of Kinetic Energy Recuperation System for City Buses"). Based on real driving cycles of buses, the authors were able to model the flywheel supported in an active magnetic bearing, two reverse electric motors, the high ratio gears, and the control system.

Saków et al. (Chapter "Signal Prediction in Bilateral Teleoperation with Force-Feedback") focused their research on the development of the sensor-less and self-sensing control scheme for a bilateral teleportation system with a force-feedback based on the prediction of input of a nonlinear inverse model by prediction blocks.

An analysis of a nonideal rotor mechanism with a limited power source and the study of effectiveness of the method of direct separation of motions to study complex nonlinear mechanical system with 3 DOFs were presented by Shahlaei-Far and Balthazar in Chapter "Method of Direct Separation of Motions Applied to a Non-ideal Electromechanical Pendulum System".

In Chapter "Problem of Dynamics of an Elastic Rod with Decreasing Function of Elastic-Plastic External Resistance", Shatskyi and Perepichka described application of the model of elastic-plastic resistance with decreasing relation between sheer stress and jump of displacement on the lateral surface to study the problem of

wave propagation and shock perturbation in a semi-infinite elastic rod interacting with the medium.

Shatskyi et al. (Chapter "Hysteretic Properties of Shell Dampers") described their achievements in the analytical modeling of four variants for hysteric energy dissipation in the system of shells with deformable filler at the expense of dry friction.

Chapter "Modal Analysis of the Vehicle Model" by Svoboda et al. deals with the numerical solution of modal analysis of a simple vehicle model taking into account the vertical oscillation of the symmetrical and asymmetrical loading and different kinematic excitations.

Skujrat and Kosiara (Chapter "Directional Stability Control of Body Steer Wheeled Articulated Vehicles") proposed and tested a new mathematical algorithm for the estimation of stability control of a body steer wheeled articulated vehicles.

In Chapter "Influence of the Mechanical Properties of Pantograph Structural Parts on Its Interaction with a Catenary", Szlachetka et al. applied Reyleigh's method to calculate the first natural frequency of transversal vibrations of clamped-free bars with variable cross section and the shape of a solid and hallow curvilinear truncated cone.

Urbanowicz and Firkowski (Chapter "Modelling Water Hammer with Quasi-Steady and Unsteady Friction in Viscoelastic Pipelines") focused on the mathematical modeling of the water hammer in viscoelastic pipelines, taking into account the retarded deformation of the pipe wall as well as quasi-steady and unsteady friction in viscoelastic conduits.

The concept of the developed autonomous vibration damper in passive suspension system of a vehicle was presented by Warczek et al. in Chapter "The Concept of Autonomous Damper in Vehicle Suspension".

Chapter "Validation of the Numerical Model of Impuls I Electric Multiple Unit Driver's Cab" by Wątroba et al. presents validation of the numerical model of the electric multiple unit driver's cab by a comparison of the numerical simulation with a real-life model.

Wojnicz et al. (Chapter "Approach for Determination of Functioning of Lower Limb Muscles") focused on the approach for determination of activity of the chosen lower limb muscles that are essential for gait performance. For this purpose, they applied the planar multibody model and electromyography (EMG) signals.

In Chapter "Modeling and Control of Motion Systems for an Electro-Hydraulic Tripod Manipulator", Wos and Dindorf presented the theoretical and experimental based modeling resulting in the prototype of a spatial 3-DOF electro-hydraulic parallel manipulator consisting of a stationary base and a mobile platform.

Zarodnyuk and Cherkasov (Chapter "Support Reaction in the Brachistochrone Problem in a Resistant Medium") considered the problem of the horizontal coordinate's maximization problem as well as related the brachistochrone problem for particle moving in the vertical plane under the influence of gravity and viscous drag being proportional to the velocity movement.

In Chapter "Free Vibration of Cantilever Bars Having a Shape of Solid and Hollow Curvilinear Truncated Cone", Szlachetka et al. addressed the dynamic interaction in the pantograph of a rail vehicle. The authors analyzed the influence of mechanical properties of pantograph's structural parts on its interaction with the catenary, taking into account friction forces, suspension springs, and aerodynamic effects.

Zelei et al. (Chapter "Four-Bar Mechanism Substitution for Balance Board Experiments: A Parametric Study") presented the parametric study aimed at finding a substitution for a rolling balance board that would exhibit approximately the same kinematic behavior as the balance board in the relevant tilt angle region.

Chapter "Numerical and Experimental Modal Analysis of Laminated Glass Beams" by Zemanová et al. deals with the numerical and experimental modal analysis of a multilayer structure made of glass planes bonded to an interlayer foil. For this purpose, the finite element discretization and the Newton method were used to solve the problem of the frequency and temperature sensitivity.

In Chapter "Methods of Simulation Investigations of Non-linear Vibrations in the Steering System of a Motorcycle", Żardecki and Dębowski introduced a novel method for modeling and simulation of nonlinear vibrations with shimmy phenomena of the steering mechanism of a motorcycle.

I greatly appreciate the help of the Springer Editor, Elizabeth Leow, in publishing the chapters recommended by the Scientific Committee of the DSTA 2017 Conference after a standard peer review procedure. Also, I would like to express my gratitude to reviewers for their help and professional support during the book preparation.

Łódź, Poland   Jan Awrejcewicz
June 2018

Contents

Gait Transitions in Artificial Non-standard Snake-Like Locomotion Systems Using Adaptive Control

Carsten Behn and Jonas Kräml

Abstract This chapter contributes to the modeling, analysis and control of terrestrial artificial locomotion systems. Inspired by previous models, we set up an unconventional model for a snake-like locomotion systems in form of a chain of visco-elastically interconnected mass points in a plane with passive joints, but – in contrast to literature – active links (time-varying link-length) and rotatable skids to change the movement direction and to avoid obstacles. We investigate this model in a dynamical way and focus on controlling these link lengths to achieve a global movement, steered by the skids. From dynamics, the actuator forces have to adjust the prescribed link length for the locomotion. Since it is impossible to determine the necessary actuator forces a-priori, we apply an adaptive lambda-tracking controller to enable the system to adjust these force outputs on-line on its own. Prescribed motion patterns, i.e. specific gaits, are required to guarantee a controlled movement that differ in the number of resting mass points, the load of actuators and spikes, and the lateral forces of the skids. In contrast to literature, the investigated system of n = 10 mass points exhibit a large variety of possible gaits. To determine the most advantageous gaits, numerical investigations are performed and a weighting function offers a decision of best possible gaits. Using these gaits, a gait transition algorithm, which autonomously changes velocity and number of resting mass points depending on the spike, actuator and lateral skid force load, is presented and tested in numerical simulations.

Keywords Snake-like locomotion system · Uncertain system · Path following · Adaptive control · Gait transition

---

C. Behn (✉)
Department of Engineering and Natural Sciences, Merseburg University
of Applied Sciences, Eberhard-Leibnitz-Straße 2, 06217 Merseburg, Germany
e-mail: carsten.behn@hs-merseburg.de

J. Kräml
Department of Mechanical Engineering, Technische Universität Ilmenau,
Max-Planck-Ring 12, 98693 Ilmenau, Germany
e-mail: jonas.kraeml@tu-ilmenau.de

1 Introduction

Earthworms and snakes serve as a biological inspiration for terrestrial robotic loco-
motion systems [16]. Most of the works within this field are inspired by the remark-
able works of Miller (since 1987, important works e.g. [7, 8]) and Shigeo Hirose
[4]. In recent years, most research focussed on fabrication, navigation and con-
trol/measurement problems, see [6, 9, 15] from a technical point of view with minor
analytical investigations. This is our starting point, to present some modeling and
analytical investigations on snake-like systems. For this, we introduce a non-standard
mechanical model of a snake-like robots in Sect. 2 in order to extend some models
and ideas from worm-like locomotion systems in [13]. Moreover, almost all pro-
totypes use active joints to achieve a special kind of snake locomotion (serpentine
movement) [3]. Hence, contrary to literature, we model a snake-like locomotion
system using passive joints, active links, spikes and rotatable skids to change the
movement direction and to avoid obstacles. To achieve movement, special gaits have
to be generated in Sect. 3 and are adaptively tracked in dynamics Sect. 4. Because of
an uncertain environment, the snake has to adjust its locomotion pattern, i.e., has to
perform a gait shift in Sect. 5. Finally, all theoretic items are tested in simulations in
Sect. 6.

2 Kinematic Model

The kinematic model is presented in Fig. 1. It contains several mass points m_i which
are connected by links with lengths r_j (hereafter named l_j). The unit vector $\vec{e}_{i,i-1}$
points from element m_i to element m_{i-1}. Each mass element is equipped with rotat-
able and spikes skids by the angle Γ_i preventing backward displacements. The angle
Θ_j describes the angle between the x-axis and the link l_j, introducing $\gamma_j := \Gamma_j - \Theta_j$.
Each mass element has a skid-fixed coordinate system with $\vec{e}_i$ in tangential and $\vec{g}_i$ in
the normal direction, Eq. (1).

$$\vec{e}_i = \cos(\Gamma_i)\vec{e}_x + \sin(\Gamma)\vec{e}_y, \qquad \vec{g}_i = -\sin(\Gamma_i)\vec{e}_x + \cos(\Gamma)\vec{e}_y \qquad (1)$$

The positions $\vec{x}_i$ of the mass elements m_i are here (in inertial system):

$$\vec{r}_i = x_i \vec{e}_x + y_i \vec{e}_y \qquad (2)$$

We assume the spiked skids to be *ideal*, i.e., preventing a backwards movement of
the mass element in the skid direction, and a movement laterally to the skid direction,
which is hereafter named as *no side-slip* condition. Therefore, it yields Eq. (3):

$$v_{t,i} = \dot{\vec{r}}_i \cdot \vec{e}_i \geq 0, \qquad v_{n,i} = \dot{\vec{r}}_i \cdot \vec{g}_i = 0 \qquad (3)$$
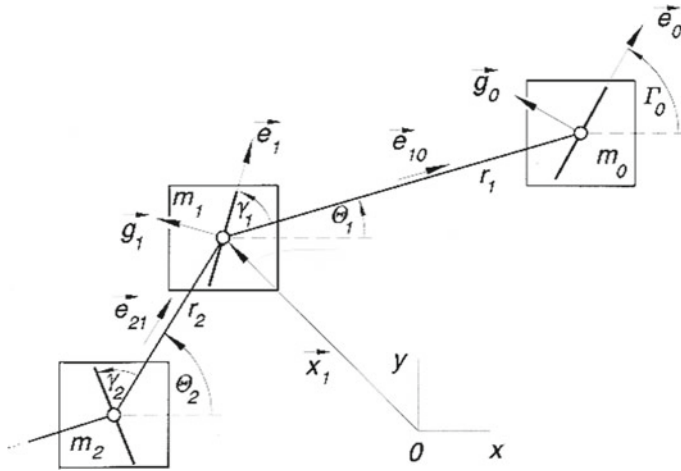
Fig. 1 Mass-point model of a snake from [11]

The *input variables* of the model are the link lengths $l_j(t)$ and the skid angles $\Gamma_i(x_i, y_i)$ which are prescribed as functions of the position $\vec{r}_i$ of mass element m_i. According to [11], the kinematic model is (with the special case $\Gamma_0 = \Theta_1 + \gamma_0$):

$$
\left.
\begin{aligned}
& \Gamma_i = \Theta_i + \gamma_i \\
& \dot{x}_i = v_i \cos(\Gamma_i) \\
& \dot{y}_i = v_i \sin(\Gamma_i) \\
\text{backward:} \quad & v_i = \frac{v_{i-1}\cos(\gamma_{i-1}+\Theta_{i-1}-\Theta_i)-\dot{l}_i}{\cos(\gamma_i)} \\
\text{- special case:} \quad & v_1 = \frac{v_0\cos(\Gamma_0-\Theta_1)-\dot{l}_1}{\cos(\gamma_1)} \\
\text{forward:} \quad & v_i = \frac{v_{i+1}\cos(\gamma_{i+1})+\dot{l}_i}{\cos(\gamma_i+\Theta_i-\Theta_{i+1})} \\
\text{- special case:} \quad & v_0 = \frac{v_1\cos(\gamma_1)+\dot{l}_1}{\cos(\Gamma_0-\Theta_1)} \\
\text{generally:} \quad & \dot{\Theta}_i = \frac{v_{i-1}\sin(\gamma_{i-1}+\Theta_{i-1}-\Theta_i)-v_i\sin(\gamma_i)}{l_i(t)}
\end{aligned}
\right\}
\tag{4}
$$

Rotatable skids allow for a plane movement. Their angle Γ_i referring to the inertial system is a system input for tracking *predefined* paths. For this, the skid angle of the head segment Γ_0 is defined as a function of the position and the rearward skid angles. There are several (testing) paths possible, e.g., U-turn, lane change or sinusoid. According to [3], we focus on 4 different types of skid adjusting mechanisms for the rearwards mass elements:

tractrix/exact following/swerve backwards/swerve forwards.

These 4 different skid adjusting mechanisms describe the way in which a mass element m_i follows the predecessor m_{i-1} and the head segment m_0, resp. This may be useful, when traversing an obstacle in order to allow a larger curve radius for rearwards segments.

3 Gaits

To allow a movement of the snake model, the distances between the mass points have to be shortened and lengthened. To guarantee forward movement, at least one mass element has to move forward and at least one has to rest. There are several motion patterns conceivably, so-called *gaits*. As shown in [12], gaits have to be designed systematically: At first, gaits differ in the number of active spikes $a \in \{1, \ldots, n\}$ (i.e., resting mass elements). Furthermore, there is a periodic sequence of active spikes $\mathbf{A}(t)$, e.g., for a system with $N = 4$ mass points and $a = 2$ a possible sequence is $\mathbf{A}(t) = \{0, 1\} \to \{1, 2\} \to \{2, 3\} \to \{3, 0\}$, while $\mathbf{A}(t) = \{0, 1\} \to \{2, 3\} \to \{1, 2\} \to \{3, 0\}$ is not recommended (no traveling wave). With this knowledge, it can be deduced whether a distance $l_j(t)$ has to be shortened or lengthened at a certain time. Following the recommendation from [12], the sequence of active spike should move to left or to the right, like a worm does. Thus, admissible gaits can be described explicitly by the start sequence $\mathbf{A}_0$ of the resting mass points and the direction dir of the wave of active spikes ("*l*" for *left* or "*r*" for *right*).
The reference distance functions are built w.r.t. [12]. The time intervals are defined as:

$$ t \in \left[p\frac{T}{N}, (p+1)\frac{T}{N} \right], \quad p \in \mathbf{N}_0. $$

To guarantee a smooth movement of the system, i.e., there are no jerks to the mass points, approximations like $\sin^2(\cdot)$-functions are used for the link lengths, while $\tau = t - p\frac{T}{N}$:

$$ l_j(\tau) = l_{0*} + \varepsilon l_0 N f \tau - \frac{1}{2\pi}\varepsilon l_0 \sin\left(2\pi f N \tau\right), \text{ with } \dot{l}_j(\tau) = \varepsilon l_0 2 N f \sin^2\left(\pi f N \tau\right) \tag{5} $$

- $|\varepsilon| \in (0; 1)$ is the relative factor of the maximum distance change,
- f is the frequency of the $\mathbf{A}(t)$-sequence with its periodic time $T = \frac{1}{f}$, chosen in simulation to avoid a rigid-body-movement of the whole system,
- $l_0 > 0$ is the initial distance,
- l_{0*} is the distance at the beginning of the time interval ($\tau = 0$), depending on the previous interval either l_0, $l_0(1 + \varepsilon)$ or $l_0(1 - \varepsilon)$, [10].

Further investigations in [5] – considering one-dimensional, worm-like locomotion and generation of optimal gaits – have determined the most advantageous gaits regarding the loads of spikes and actuators for a system with $N = 10$ mass elements. Hence, these gaits are used for the considerations here and are listed in Table 1.

Table 1 Most advantageous gaits for $N = 10$

a	Gait
1	$A_0 = \{1\},\, dir = r$
2	$A_0 = \{2, 3\},\, dir = r$
3	$A_0 = \{0, 1, 2\},\, dir = r$
4	$A_0 = \{6, 7, 8, 9\},\, dir = l$
5	$A_0 = \{2, 3, 4, 5, 6\},\, dir = l$
6	$A_0 = \{5, 6, 7, 8, 9, 0\},\, dir = l$
7	$A_0 = \{2, 3, 4, 5, 6, 7, 8\},\, dir = l$
8	$A_0 = \{1, 2, 3, 4, 5, 6, 7, 8\},\, dir = l$
9	$A_0 = \{1, 2, 3, 4, 5, 6, 7, 8, 9\},\, dir = l$

4 Dynamic Model

To allow the system to shorten and lengthen its links between the mass elements, viscoelastic actuators are assumed between the segments in the following dynamic model. The applied forces are exemplarily given to element i, see Fig. 2. The linear *spring forces* $F_{c,i}$ and $F_{c,i+1}$ are obtained from the distances between the neighboring mass elements:

$$\vec{F}_{c,i} = c_i \cdot \left(\|(\vec{r}_{i-1} - \vec{r}_i)\| - l_{0,i} \right) \vec{e}_{i,i-1}$$
$$\vec{F}_{c,i+1} = -c_{i+1} \cdot \left(\|(\vec{r}_i - \vec{r}_{i+1})\| - l_{0,i+1} \right) \vec{e}_{i+1,i} \tag{6}$$
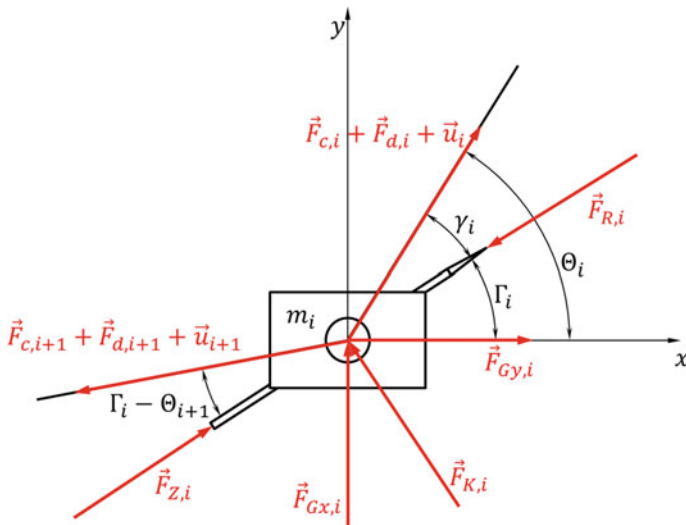
Fig. 2 Mass element with forces

The linear *damper forces* $F_{d,i}$ and $F_{d,i+1}$ are determined (under the assumption of the *no side-slip* condition, i.e., the normal velocity component $v_{n,i} = 0$) using $v_{t,i}$ as the velocity of the mass element m_i in the skid direction ($\vec{e}_i$ direction):

$$\begin{aligned}
\vec{F}_{d,i} &= d_i \cdot \left[v_{t,i-1} \cdot \cos(\Gamma_{i-1} - \Theta_i) - v_{t,i} \cdot \cos(\gamma_i) \right] \vec{e}_{i,i-1} \\
\vec{F}_{d,i+1} &= -d_{i+1} \cdot \left[v_{t,i} \cdot \cos(\Gamma_i - \Theta_{i+1}) - v_{t,i+1} \cdot \cos(\gamma_{i+1}) \right] \vec{e}_{i+1,i}
\end{aligned} \tag{7}$$

The *weight forces* $\vec{F}_{Gx,i}$ and $\vec{F}_{Gy,i}$ are calculated in dependence on the slope angles α_x and α_y (rotation of the plane around x- respectively y-axis):

$$\vec{F}_{Gx,i} = -m_i g \sin(\alpha_x)\vec{e}_x \quad \text{and} \quad \vec{F}_{Gy,i} = -m_i g \sin(\alpha_y)\vec{e}_y \tag{8}$$

According to [3], Stokes's *friction forces* are assumed in the skid direction:

$$\vec{F}_{R,i} = -k_{St} v_{t,i} \vec{e}_i \tag{9}$$

According to [13], the *ideal spikes* (spike force F_Z) have to fulfill:

$$\dot{x}_i \geq 0, \qquad F_{Z,i} \geq 0 \quad \text{with complementary-slackness condition} \quad \dot{x}_i \cdot F_{Z,i} = 0 \,. \tag{10}$$

This condition is fulfilled using Eq. (11), where $\vec{F}_i$ is the sum of all applied forces.

$$\vec{F}_{Z,i}(v_{t,i}, \vec{F}_i) = \left[-\frac{1}{2}[1 - \text{sign}(v_{t,i})][1 - \text{sign}(\vec{F}_i \cdot \vec{e}_i)]\vec{F}_i \cdot \vec{e}_i \right] \vec{e}_i \tag{11}$$

Because the skids are considered to be **ideal** –fulfilling the *no side-slip* condition– the skid forces are, taking the inertial fraction into account:

$$\vec{F}_{K,i} = \left(m_i v_{t,i} \dot{\Gamma}_i - \vec{F}_i \cdot \vec{g}_i \right) \vec{g}_i \tag{12}$$

Applied actuators shall generate a movement of the system and serve as inputs to control the distances between the segments. To track a prescribed motion pattern/gait in an uncertain environment, an adaptive λ-tracking controller is used which generates the necessary *actuator forces* on its own. Introducing on the error $e_j(t)$:

- $l_j(t) := x_{j-1}(t) - x_j(t)$, the distance between neighboring mass points (outputs);
- $l_{ref,j}(t)$, the predefined reference distance functions of Eq. (5);
- $e_j(t) := l_j(t) - l_{ref,j}(t)$, error of the output;

we apply the controller Eq. (13), see [1, 2]. It contains regular PD-feedback, which adapts the gain of P- and D- elements depending on the 2-norm of the error $\|\mathbf{e}(t)\|$. The controller's goal is to track a reference function of the outputs and to keep the error within a certain tolerated accuracy λ:

$$\mathbf{e}(t) := \mathbf{l}(t) - \mathbf{l}_{ref}(t)$$

$$\mathbf{u}(t) = k(t)\,\mathbf{e}(t) + k(t)\,\kappa\,\dot{\mathbf{e}}(t) = k(t) \cdot (\mathbf{e}(t) + \kappa\,\dot{\mathbf{e}}(t))$$

$$\dot{k}(t) = \begin{cases} \gamma \cdot (\|\mathbf{e}(t)\| - \lambda)^2, & \|\mathbf{e}(t)\| \geq \lambda + 1 \\ \gamma \cdot (\|\mathbf{e}(t)\| - \lambda)^{0.5}, & \lambda + 1 > \|\mathbf{e}(t)\| \geq \lambda \\ 0, & (\|\mathbf{e}(t)\| < \lambda) \wedge (t - t_E < t_d) \\ -\sigma k(t), & (\|\mathbf{e}(t)\| < \lambda) \wedge (t - t_E \geq t_d) \end{cases} \tag{13}$$

with $\gamma > 1$, $\kappa > 0$, $\sigma > 0$, $t_d \geq 0$, $\lambda \geq 0$, $k_0 > 0$, determined in [5]. Remark: *It is obvious that the proposed controller is based on output derivative. This is sometimes quite hard to arrange, see [14] for a way out.*

With this relation, Newton's second law can be applied to get the equations of motion. At first, the following relationships between the skid-fixed and the inertial coordinate system are needed:

$$\vec{e}_i = \cos(\Gamma_i)\vec{e}_x + \sin(\Gamma_i)\vec{e}_y \quad \text{and} \quad \vec{g}_i = -\sin(\Gamma_i)\vec{e}_x + \cos(\Gamma_i)\vec{e}_y \tag{14}$$

Furthermore, by differentiating, we get:

$$\dot{\vec{r}}_i = v_{t,i}\vec{e}_i + v_{n,i}\vec{g}_i \quad \text{and} \quad \ddot{\vec{r}}_i = \left(\dot{v}_{t,i} - v_{n,i}\dot{\Gamma}_i\right)\vec{e}_i + \left(\dot{v}_{n,i} + v_{t,i}\dot{\Gamma}_i\right)\vec{g}_i \tag{15}$$

Summarizing, the differential equation for element m_i in skid coordinates is:

In skid direction $\vec{e}_i$:

$$\left.\begin{aligned} m_0 \left(\dot{v}_{t,0} - v_{n,0}\dot{\Gamma}_0\right) &= \left(-F_{c,1} - F_{d,1} - u_1\right)\cos(\Gamma_0 - \Theta_1) + F_{Z,0} + F_{R,0} \\ &\quad + F_{Gx,0}\cos(\Gamma_0) + F_{Gy,0}\sin(\Gamma_0) \\ m_i \left(\dot{v}_{t,i} - v_{n,i}\dot{\Gamma}_i\right) &= \left(-F_{c,i+1} - F_{d,i+1} - u_{i+1}\right)\cos(\Gamma_i - \Theta_{i+1}) + F_{Z,i} + F_{R,i} \\ &\quad + \left(F_{c,i} + F_{d,i} + u_i\right)\cos(\gamma_i) + F_{Gx,i}\cos(\Gamma_i) + F_{Gy,i}\sin(\Gamma_i) \\ m_n \left(\dot{v}_{t,n} - v_{n,n}\dot{\Gamma}_n\right) &= \left(F_{c,n} + F_{d,n} + u_n\right)\cos(\gamma_n) + F_{Z,n} + F_{R,n} \\ &\quad + F_{Gx,n}\cos(\Gamma_n) + F_{Gy,n}\sin(\Gamma_n) \end{aligned}\right\} \tag{16}$$

Normal to skid direction $\vec{g}_i$:

$$\left.\begin{aligned} m_0 \left(\dot{v}_{n,0} + v_{t,0}\dot{\Gamma}_0\right) &= \left(+F_{c,1} + F_{d,1} + u_1\right)\sin(\Gamma_0 - \Theta_1) + F_{K,0} \\ &\quad - F_{Gx,0}\sin(\Gamma_0) + F_{Gy,0}\cos(\Gamma_0) \\ m_i \left(\dot{v}_{n,i} + v_{t,i}\dot{\Gamma}_i\right) &= \left(+F_{c,i+1} + F_{d,i+1} + u_{i+1}\right)\sin(\Gamma_i - \Theta_{i+1}) - F_{Gx,i}\sin(\Gamma_i) \\ &\quad + \left(-F_{c,i} - F_{d,i} - u_i\right)\sin(\gamma_i) + F_{K,i} + F_{Gy,i}\cos(\Gamma_i) \\ m_n \left(\dot{v}_{n,n} + v_{t,n}\dot{\Gamma}_n\right) &= \left(-F_{c,n} - F_{d,n} - u_n\right)\sin(\gamma_n) + F_{K,n} \\ &\quad - F_{Gx,n}\sin(\Gamma_n) + F_{Gy,n}\cos(\Gamma_n) \end{aligned}\right\} \tag{17}$$

5 Gait Transition

In Sect. 3, most advantageous gaits are presented, which have to be autonomously selected to be the best for actual situation. Thinking of an uncertain environment (changing slope, malfunction of actuators, failing of spikes), a *gait transition* becomes important, because changes result in different loads of (the remaining) actuators, spikes and skids. Hence, the system has to be enabled to react to such changes in switching its gait and frequency on its own. <u>Remark:</u> *Analogous example of driving a car – increasing the frequency can be compared to accelerating while gait changing is similar to gear shifting.*

The frequency shall only be changed after concluding a single period, i.e., when a part of the sequence $\mathbf{A}(t)$ is finished. Changing the frequency has a large influence on the loads of actuators and spikes. To adjust the frequency, a P-feedback is used. It is possible to weight the load of actuators, spikes and skids against each other using factors w_u, w_{Fz} and w_{Fk}:

$$
f_1 = \frac{w_{Fz} f_0 (1 + k_{p,Fz}(F_{z,soll} - F_{z,ist})) + w_u f_0 (1 + k_{p,u}(u_{soll} - u_{ist}))}{w_{Fz} + w_u + w_{Fk}}
$$
$$
+ \frac{w_{Fk} f_0 (1 + k_{p,Fk}(F_{k,soll} - F_{k,ist}))}{w_{Fz} + w_u + w_{Fk}} \tag{18}
$$

with $k_{p,u}$, $k_{p,Fz}$ and $k_{p,Fk}$ as gain parameters for actuators, spikes and skids, f_0 as the previous frequency and f_1 as the newly adjusted frequency. The set points u_{set}, $F_{z,set}$ and $F_{k,set}$ are predefined, while the actual values are within a single period:

$$
F_{z,act} = \max \left\{ F_{z,0}, F_{z,1}, \ldots, F_{z,9} \right\}, \ F_{k,act} = \max \left\{ F_{k,0}, F_{k,1}, \ldots, F_{k,9} \right\}
$$
$$
\bar{u}_j = \frac{1}{T_e} \int_{t-T_e}^{t} u_j(\tau) \, d\tau, \qquad\qquad u_{act} = \max \left\{ \bar{u}_1, \bar{u}_2, \ldots, \bar{u}_9 \right\} \tag{19}
$$

The value for the frequency has to be limited to f_{max}. Otherwise, there would occur rigid-body-movement, if the frequency exceeded f_{max}, according to [13]. During the period of existence of such rigid-body motion, it is uncontrollable in this time-interval. This maximum frequency f_{max}, from a kinematical theory according to [13], is given by:

$$
f_{max}(a) = \sqrt{\frac{g \sin(\alpha)}{2\pi \varepsilon l_0 N(N-a)}} \tag{20}
$$

After finishing a total period T, i.e., when the sequence of active spikes would start again, the system changes the number of active spikes a. The model upshifts (decrease the number of active spikes a), if the maximum frequency f_{max} of a gait is reached. It downshifts (increases the number of active spikes a), if the current reference velocity Eq. (21) is also reachable with the next slower gait without exceeding the maximum

frequency of the slower gait [13]:

$$\bar{v}_{ref}(a, f) = (N - a)\varepsilon l_0 f \tag{21}$$

This downshift frequency f_{min} is:

$$\bar{v}_{min,a} = \bar{v}_{max,a+1} \quad \Leftrightarrow \quad f_{min} = \frac{N - (a + 1)}{N - a} f_{max,a+1} \tag{22}$$

After shifting the gait, the frequency has to be adapted to guarantee the same velocity before and after a gait transition. The analogy to car driving is the adaption of the engine speed while shifting. The frequency after the transition is:

$$\bar{v}_{new} = \bar{v}_{old} \quad \Leftrightarrow \quad f_{new} = \frac{N - a_{old}}{N - a_{new}} f_{old} \tag{23}$$

In Fig. 3, the algorithm of frequency control and gait transition is shown, which is executed after the end of the first single period.
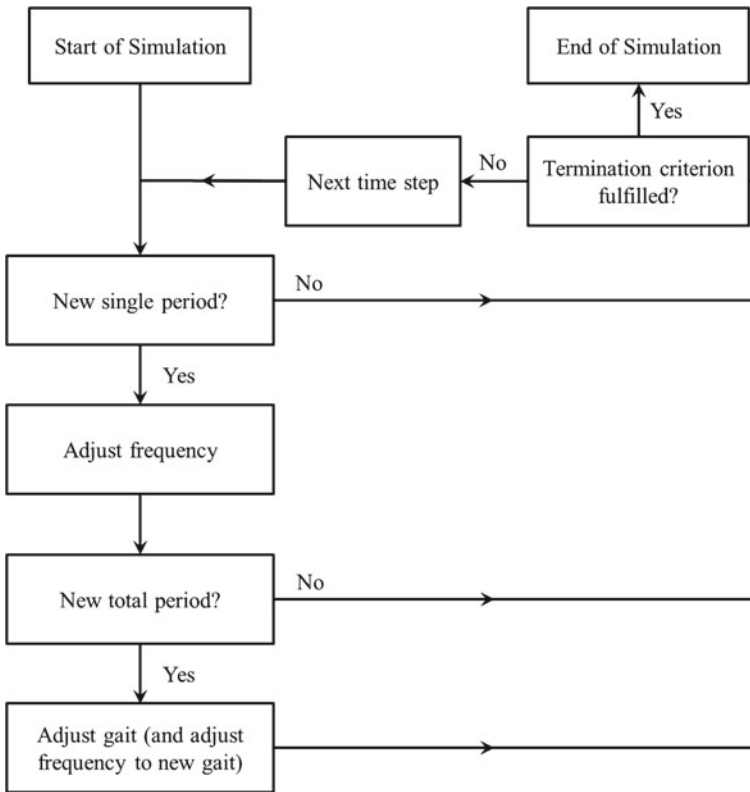
Fig. 3 Algorithm of frequency control and gait transition
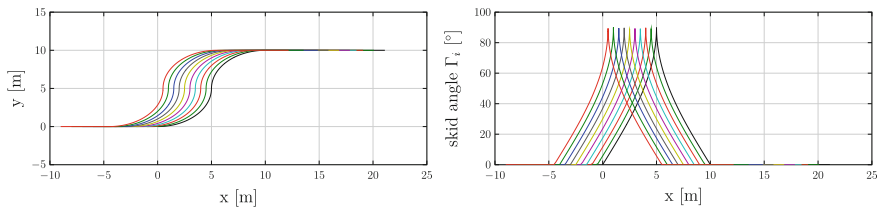
Fig. 4 Model movement (left), and skid angles Γ_i (right)
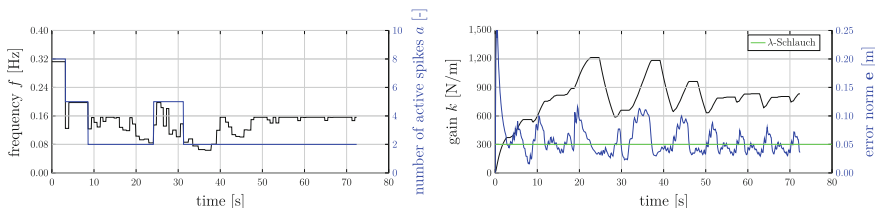
Fig. 5 Frequency and number of active spikes (left), gain and error norm (left)
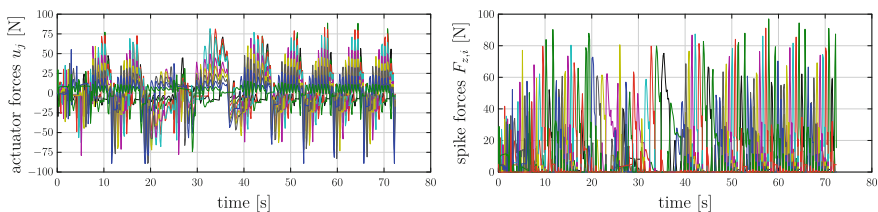
Fig. 6 Actuator forces (left), and spike forces (right)

6 Simulation

To demonstrate the functionality of the model, the results of a simulation are shown in Figs. 4, 5 and 6. The model performs a lane change while the rearwards mass elements swerve backwards. In Fig. 5(left) can be seen that the frequency and number of active spikes are adjusted depending on the loads of actuators, spikes and skids, see Fig. 6. Furthermore, the working principle of the adaptive λ-tracking PD-controller is shown in Fig. 5(right).

7 Conclusion and Outlook

The presented snake-like model consisting of 10 mass points is able to move two-dimensionally by shortening and lengthening its links between each mass point. This is achieved by using viscoelastic actuators which are controlled by an adap-

tive λ-tracking PD-controller. To allow lateral movement, spikes respectively skids are mounted at each mass points which are considered as ideal. They inhibit backward movement (spikes) and side-slip (skids) of the mass points. The model is able to adjust the gait and its frequency depending on the loads of actuators, spikes and skids. The gathered knowledge from previous investigations considering one-dimensional worm-like locomotion is transferred to this model, e.g., most advantageous gaits, limitation of actuator forces and using only three different gaits in order to reduce the number of gait shifting. The model is able to use different types of skid adjusting mechanisms, such as tractrix, exact following, swerve backwards and swerve forwards, as well as different curve paths, e.g., U-turns, lane changes and sinusoid.

To conclude the presented work, an example of application is presented hereafter. The model shall move through an environment with obstacles while using different types of skid adjusting mechanisms and curve paths (future work is obviously addressed to path planning). As shown in Fig. 7(left), the model is able to move even through narrow spaces. It adjusts its frequency and gait, see Fig. 8(left). Furthermore, the described adaptive λ-tracking PD-controller for the actuators works reliably, as one can clearly see in Fig. 8(right). The system loads are presented in Fig. 9.
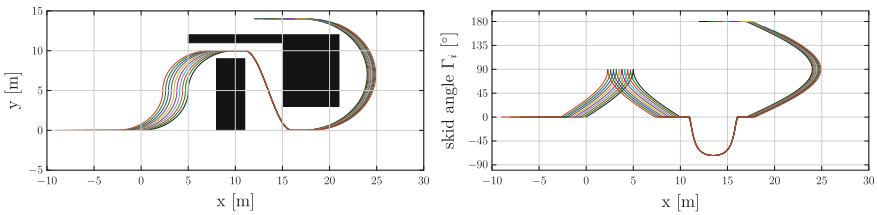
Fig. 7 Model movement (left), and skid angle Γ_i (right)
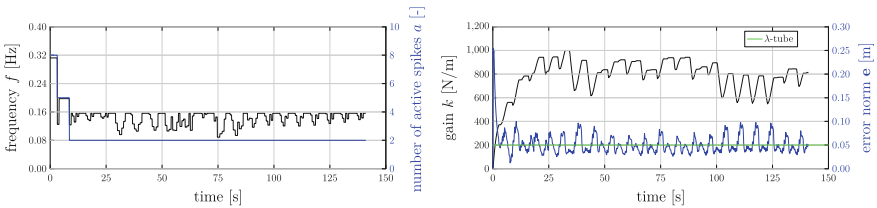
Fig. 8 Frequency and number of active spikes (left), gain and error norm (right)
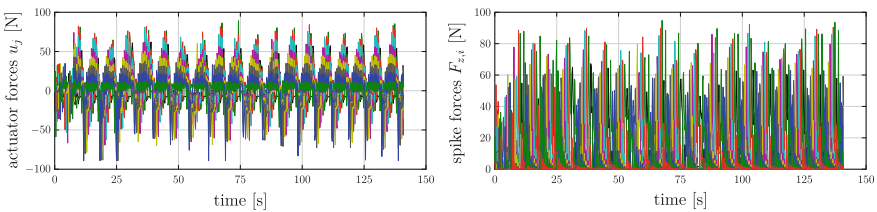
Fig. 9 Actuator forces (left), and spike forces (right)

References

1. Behn, C.: Mathematical modeling and control of biologically inspired uncertain motion systems with adaptive features. Habilitation, Technische Universität Ilmenau, Germany (2013)
2. Behn, C., Loepelmann, P.: Adaptive versus fuzzy control of uncertain mechanical systems. Int. J. Appl. Mech. (IJAM) **4** (2012)
3. Behn, C., Heinz, L., Krüger, M.: Kinematic and dynamic description of non-standard snake-like locomotion systems. Mechatronics **37**, 1–11 (2016)
4. Hirose, S.: Biologically inspired robots: snake-like locomotors and manipulators. Oxford University Press, Oxford (1993)
5. Kräml, J., Behn, C.: Gait transition in artificial locomotion systems using adaptive control. In: Proceedings of the 13th International Conference on Informatics in Control, Automation and Robotics, July 29–31, pp. 119–129. SciTePress (2016). https://doi.org/10.5220/0006003001190129
6. Lu, Z., Fenga, D., Xie, Y., et al.: Study on the motion control of snake-likerobots on land and in water. Perspect. Sci. **7**, 101–108 (2016)
7. Miller, G.S.P.: The motion dynamics of snakes and worms. Comput. Graph. **22**(4), 169–178 (1988)
8. Miller, G.S.P.: Snake robots for search and rescue. In: Ayers, J., et al. (eds.) Neurotechnology for Biomimetic Robots, vol. 13, pp. 271–284. MIT Press, Cambridge, MA (2002)
9. Pfotzer, L., Klemm, S., Roennau, A., et al.: Autonomous navigation for reconfigurable snake-like robots in challenging, unknown environments. Robot. Auton. Syst. **89**, 123–135 (2017)
10. Schwebke, S., Behn, C.: Worm-like robotic systems: generation, analysis and shift of gaits using adaptive control. Artif. Intell. Res. **2**, 12–35 (2013)
11. Steigenberger, J.: On a class of biomorphic motion systems. Preprint No. M 99/12. Institute of Mathematics, Technische Universität Ilmenau, Germany (1999)
12. Steigenberger, J., Behn, C.: Gait generation considering dynamics for artificial segmented worms. Robot. Auton. Syst. **59**(7), 555–562 (2011)
13. Steigenberger, J., Behn, C.: Worm-Like Locomotion Systems: An Intermediate Theoretical Approach. Oldenbourg, Munich (2012)
14. Ye, X.: Universal λ-tracking for nonlinearly-perturbed systems without restrictions on the relative degree. Automatica **35**, 109–119 (1999)
15. Yildirim, S., Yasar, E.: Development of an obstacle-avoidance algorithm for snake-like robots. Measurement **73**, 68–73 (2015)
16. Zimmermann, K., Zeidis, I., Behn, C.: Mechanics of Terrestrial Locomotion-with a Focus on Non-pedal Motion Systems. Springer, Berlin (2009)

The Experimental Determination of Bearings Dynamic Coefficients in a Wide Range of Rotational Speeds, Taking into Account the Resonance and Hydrodynamic Instability

Łukasz Breńkacz, Grzegorz Żywica, Marta Drosińska-Komor and Natalia Szewczuk-Krypa

Abstract Methods for the experimental determination of dynamic coefficients are commonly used for the analysis of various types of bearings, including hydrodynamic, aerodynamic and foil bearings. There are currently several algorithms that allow estimating bearing dynamic coefficients. Such algorithms usually use various excitation techniques applied to rotor–bearings systems. So far only a small number of scientific publications show how calculated dynamic coefficients of bearings change as speed rises. In the literature, there are no computation results that demonstrate changes in these coefficients either in a broad range of speeds (that would cover resonant speeds) or at speeds at which a phenomenon of hydrodynamic instability can be observed. This article fills the literature gap in question. For calculation purposes, the impulse response method based on an in-house algorithm (with a linear approximation using the least squares method) was applied. On its basis, the stiffness, damping and mass coefficients of a rotor–bearings system were calculated. It turns out that some of the obtained values of damping coefficients are negative at the resonant speed. Moreover, if the values are calculated at a speed at which the

Ł. Breńkacz (✉) · G. Żywica
The Department of Turbine Dynamics and Diagnostics, Institute of Fluid Flow Machinery,
Polish Academy of Sciences, Fiszera 14, 80-231 Gdańsk, Poland
e-mail: lukasz.brenkacz@imp.gda.pl

G. Żywica
e-mail: grzegorz.zywica@imp.gda.pl

M. Drosińska-Komor · N. Szewczuk-Krypa
Faculty of Ocean Engineering and Ship Technology, Gdańsk University
of Technology, G. Narutowicza 11/12, 80-233 Gdańsk, Poland
e-mail: mardrosi@pg.edu.pl

N. Szewczuk-Krypa
e-mail: natszew1@pg.edu.pl

hydrodynamic instability phenomenon is present they are accompanied by considerably higher standard deviations. On the basis of our computation results and the literature review, capabilities and limitations of the method used for the experimental identification of dynamic coefficients of hydrodynamic bearings were discussed.

Keywords Bearing dynamic coefficients · Experimental research · Nonlinear coefficients · Impact excitation · Hydrodynamic bearing

1   Introduction

Hydrodynamic radial bearings are commonly used in supporting rotors of power turbines because they allow a long-term operation at very low vibration levels bearings. The literature is rich in articles on the determination of bearings' dynamic coefficients. A review of the articles on this subject is contained in the article [1]. This review also demonstrates how big the measurement errors are. The various approaches to the bearing identification problem are discussed, including the different force excitation methods of incremental loading, sinusoidal, pseudorandom, impulse, known/additional unbalance, and non-contact excitation. Also bearing excitation and rotor excitation approaches are discussed. Data processing methods in the time and frequency domains are presented. Methods of evaluating the effects of measurement uncertainty on overall bearing coefficient confidence levels are reviewed. In this review, the relative strengths and weaknesses of bearing identification methods are presented, and developments and trends in improving bearing measurements are documented. A strong side of this article is the fact that it provides the calculation results of dynamic coefficients of hydrodynamic bearings as a function of the rotational speed. As it turns out, error values generated during calculations vary greatly in a wide range of rotational speeds that covers resonant speeds and higher speeds.

Rotordynamic coefficients of a controllable floating ring bearing (FRB) were measured and described in the article [2]. Controllability of the bearing was achieved by using a magnetorheological fluid (MRF) as a lubricant along with the external magnetic field. Magnetic field induced field-dependent viscosity of the MRF changes dynamic coefficients (stiffness, damping, etc.) of the bearing, and vibration amplitudes of the rotor were suppressed by the enhanced stiffness and/or damping. The rotating floating ring in the FRB separates the MRF into two lubricant films. Since the ring rotates slower than the shaft, shear rate in the outer film is lower compared to the inner film, pertaining controllability by limiting the so-called shear-thinning effect of the MRF. A test rig is built to measure and identify the rotordynamic coefficients of the MRF lubricated FRB. Coefficients of the bearing with various magnetic field strength are compared. Results show enhancements of dynamic properties of the bearing with external magnetic field, demonstrating the viability of this type of smart bearings in rotor control or behaviour alteration applications.

The requirement of bearing coefficients identification based on flexible rotor-bearing systems has stimulated the investigation of bearing forces over the years,

whereby in industry high-speed balancing machines and flexible rotor-bearing test rigs can be used to measure the dynamic force coefficients of bearings [3]. However, the actual rotor vibration at the bearing nodes cannot be measured or simply calculated by the data acquired from a single measurement station outside of the bearing. To solve this problem, a double-section interpolation-iteration method to identify the dynamic coefficients has been developed which uses previously identified coefficients to predict new vibration vectors from a finite element model and then updates the vibration vectors at the bearings to recalculate the coefficients. Moreover, the experimental work, in which an active magnetic bearing was used to excite a flexible test rig supported by tilting pad bearings, was also carried out to validate the method, with the vibration shape predicted by the identified results matching the test data very well and the first forward mode parameters also matching the results from sine-swept identification.

The method for the determination of bearing dynamic coefficients applied by the authors of this article operates in the frequency domain. Its first version was presented by Nordmann and Schoellhorn [4]. The basic algorithm was extended by adding the possibility to compute sixteen stiffness and damping coefficients [5].

In the article [6], an in-house algorithm was used to obtain the dynamic coefficients of bearings. It is a modified version of the algorithm for the computation of stiffness and damping coefficients introduced by Qiu and Tieu. The modification was done in such a manner that it also allows calculating eight mass coefficients. The determination of stiffness, damping and mass coefficients by means of a single algorithm permits verification of the results already in a preliminary stage of an experimental investigation. The identified dynamic coefficients of a bearing can be verified on the basis of mass coefficients since a shaft mass is usually known in advance. This approach allows identifying all dynamical parameters of a rotor—bearings system by means of an experimental research [7]. Some issues connected with the identification of bearing dynamic coefficients and bearing modelling are presented in publications [8–10].

2 Basic Technical Characteristics of the Test Rig

The description of the test rig and research apparatus used during the research can be found in the papers [11, 12]. Figure 1 shows a photo of the test rig, while Fig. 2 contains a diagram illustrating its most important components along with their dimensions. The length of the test rig is 1.25 m, and its width and height are 0.36 and 0.65 m, respectively. The axes of the coordinate system used during the experimental investigation are shown in the top left-hand corner of Fig. 2. The test rig rests on a 13 mm thick steel plate with two channel bars attached to it. The channel bars are equipped with rubber feet (allowing for height adjustment and leveling of the plate). The rotor shaft is supported by two bearings. The system is driven by a three-phase motor with a maximum speed of 3450 rpm. The motor rotations were adjusted by means of a frequency inverter with a capacity of 1.5 kW. The motor is mounted to
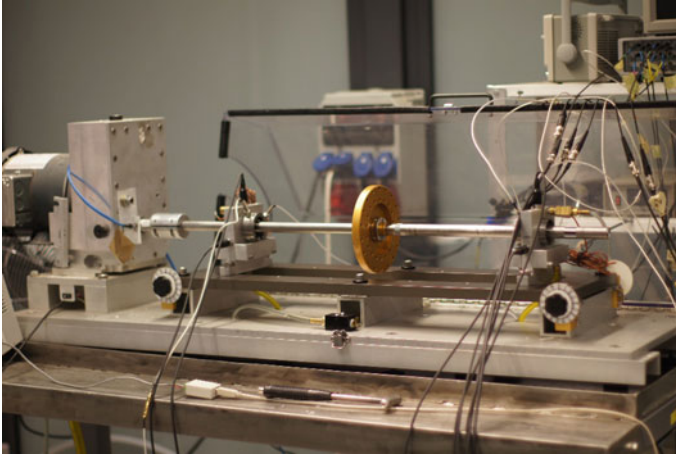
Fig. 1 Photo of the test rig
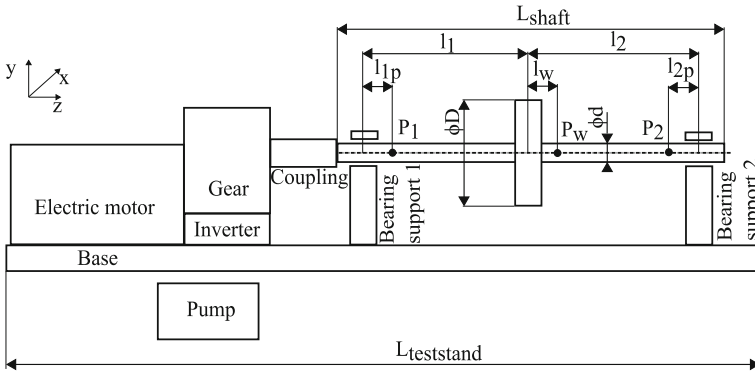
Fig. 2 Diagram of the test rig

a gear that increases the speed with a gear ratio 3.5:1. The presence of the inverter allows varying the motor speed up to 12,000 rpm. The gear is connected to the rotor shaft by means of a permanent coupling. The coupling diameter is 50 mm and its length is 60 mm. The oil lubricated bearing system is equipped with a pump. During experimental tests, the oil pressure was 0.16 MPa.

The tested rotor has a length of 920 mm. The distance between the coupling and the first bearing support is 170 mm. The rotor was mounted in two bearing supports. The distance between the supports is 580 mm. The rotor disc is equidistant to each bearing support. The rotor diameter is 19.02 mm and the rotor disc diameter is 152.4 mm. Excitations were applied to the shaft using an impact hammer at the point that is shifted 30 mm from the rotor disc's midpoint. For safety reasons, the rotor—bearings system was equipped with a lockable casing made of hard transparent plastic.

The rotor is supported by two hydrodynamic bearings with the same geometries. The radial bearing clearance is 76 µm and the bearing length is 12.6 mm. Every bearing has two supply ports located horizontally on both sides of the shaft. The supply ports have a diameter of 2.54 mm. The oil supply pressure was 0.16 MPa. The viscosity grade of the lubricating oil is consistent with the recommendations stated in ISO 13.

It should be stressed that dynamics of the rotating system is affected not only by the coupling and bearings but also by the whole supporting structure [13]. There are also some elements that have an impact on vibrations of the entire system since they influence vibration trajectories of the bearing journals [14].

3   Calculation Procedure

The movement of a point can be described using Eq. (1). After some transformations described in [6] it was possible to obtain the equation that can be used for calculating bearing dynamic coefficients (2), where ω denotes frequency.

$$m \cdot \ddot{x} + c \cdot \dot{x} + k \cdot x = f(t) \tag{1}$$

$$\begin{bmatrix} k_{xx} - m_{xx}\omega^2 + c_{xx} j\omega \; k_{xy} - m_{xy}\omega^2 + c_{xy} j\omega \\ k_{yx} - m_{yx}\omega^2 + c_{yx} j\omega \; k_{yy} - m_{yy}\omega^2 + c_{yy} j\omega \end{bmatrix} \cdot \begin{bmatrix} 1 \; 0 \; -\omega^2 \; 0 \; j\omega \; 0 \\ 0 \; 1 \; 0 \; -\omega^2 \; 0 \; j\omega \end{bmatrix}$$

$$= \begin{bmatrix} k_{xx} \; k_{xy} \\ k_{yx} \; k_{yy} \\ m_{xx} \; m_{xy} \\ m_{yx} \; m_{yy} \\ c_{xx} \; c_{xy} \\ c_{yx} \; c_{yy} \end{bmatrix} \tag{2}$$

During the experimental research that served for the determination of stiffness, damping and mass coefficients, forty-second periods of the rotor operation were registered. In each measurement, the rotor was excited in the Y direction a dozen or so times (using an impact hammer). Then the whole operation was repeated, but this time the rotor was excited in the direction perpendicular to its axis of rotation, namely, the X direction. For the calculation purposes, there was a need to obtain the signal fragments recorded from the time the excitation is applied and lasting until the rotor returns to its normal operating cycle. For each rotational speed tested, 10 signal fragments in the X and Y directions were chosen. The calculations were carried out for 11 rotational speeds in the range 2250–6000 rpm, making a total of 220 sets of measurement series. During each measurement series, four eddy current sensors served for measuring rotor vibrations. They recorded displacements in two mutually perpendicular directions, near each bearing support. In the calculation process, 220

signals recorded after the excitations were used and also the reference signals (registered with no excitations present). A proper preparation of data needed to compute the bearings' dynamic coefficients was very time-consuming.

During the preparation of data, for each signal registered after the excitation took place, its corresponding reference signal had to be subtracted from it. This was done for both bearings in one computational step. For each rotational speed tested, 10 sets of stiffness, damping and mass coefficients were determined. And then four sets that had the highest standard deviation values were rejected. On the basis of the remaining six sets, mean values and standard deviations of stiffness and damping coefficients were computed for each rotational speed.

4   Measurement Results

In order to obtain the complete set of data needed to compute the bearings' dynamic coefficients for one rotational speed, it was necessary to conduct the analysis in two stages. In the first stage, the rotor was excited in the Y direction using an impact hammer. In the second stage of the analysis, the rotor operated at the same speed and the impact hammer applied a force perpendicular to the Y direction, namely, the force acting in the X direction.

The determination of stiffness, damping and mass coefficients was performed simultaneously for two bearings. Bearing no. 1 is situated near the coupling that connects the rotor shaft with the drive motor's shaft, and bearing no. 2 is mounted on the opposite side of the test rig. Excitation forces were applied using an impact hammer that hit the shaft near the rotor disk located between the bearing supports. As it turns out, the coupling has a significant impact on the experimental results. In order to obtain reliable values of bearings' dynamic coefficients, this impact should be minimised in some way.

The plots illustrating the values of stiffness, damping and mass coefficients obtained for bearing no. 2 (situated far away from the coupling that heavily influences the rotor operation) are shown in Fig. 3. We can divide the results into two parts. Let the first part denote the results obtained for speeds in the range of 2250 to 3750 rpm and the second part the results obtained for speeds higher than 3750 rpm. This division can be defined on the basis of the size of vibration trajectories of the rotor. It can be observed that in the first speed range the vibration amplitudes are small. In the second speed range, the amplitudes are significantly higher than in the first range; moreover, a resonance occurs there. Looking at the plot that shows values of the stiffness coefficients of the hydrodynamic bearings, the same division can be applied. Let us note that the values obtained for speeds higher than 3750 rpm are characterised by higher standard deviations.

Let us also say a few words about graphs that demonstrate vibration spectra. It can be observed that the 1X component dominates on all graphs obtained for the bearing no. 2 and for speeds lower than 2750 rpm. For higher speeds, the 1/2X component is dominant. This is a clear indication of the hydrodynamic instability
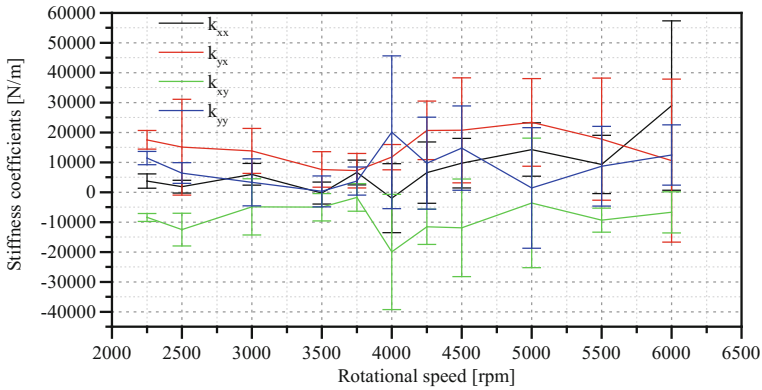
Fig. 3 The experimentally determined stiffness coefficients of bearing no. 2 versus rotational speed
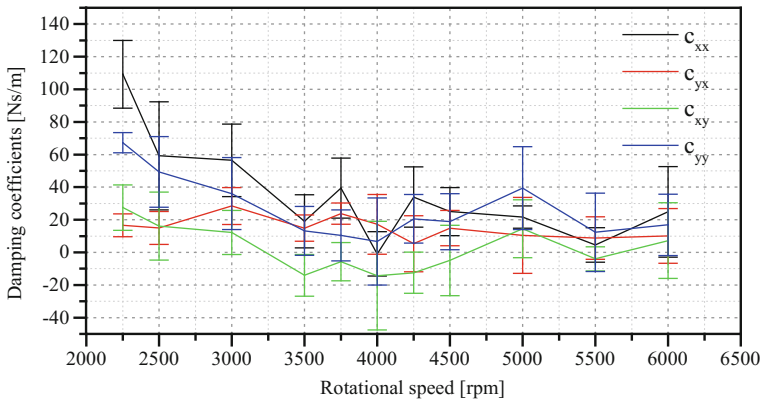
Fig. 4 The experimentally determined damping coefficients of bearing no. 2 versus rotational speed

and nonlinear properties of the bearings' lubrication film. The phenomenon of the hydrodynamic instability may be caused by many reasons, such as an inappropriate geometry of the bearing (e.g. not carefully selected radial clearance or the skewed bush), an improper oil pressure, a change in the viscosity of the oil brought about by a change in its temperature or a whippy rotor.

Figure 4 presents values of the damping coefficients versus rotational speed. As can be seen, the damping coefficients decrease (coming close to zero) as the rotational speed increases. For a speed close to 4000 rpm, the c_{xy} coefficient takes a value lower than zero. It means that the vibrations that occurred after the excitation force was applied are not damped but they their amplitude rises.

Figure 5 shows values of the mass coefficients of bearing no. 2 versus rotational speed. It is interesting to note that if we draw the curves representing m_{2XX} and m_{2YY} coefficients using the linear interpolation (in the form of a polynomial function of a low degree), one curve increases and the other one decreases. Moreover, they intersect
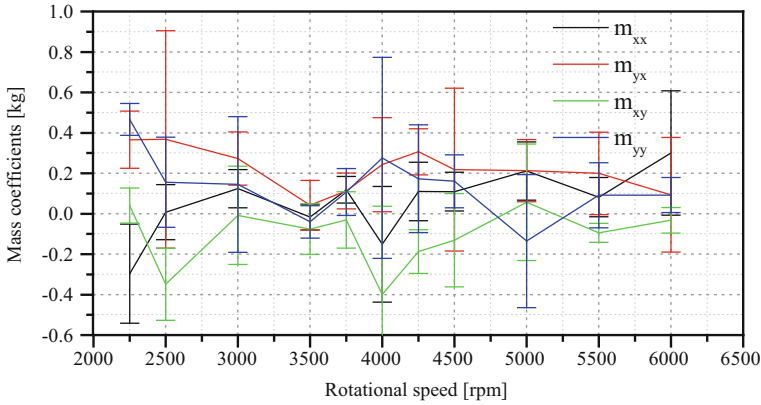
Fig. 5 The experimentally determined mass coefficients of bearing no. 2 versus rotational speed

and pass through zero at the speed at which the resonance occurs. The shaft mass calculated on the basis of the mass coefficients obtained at a speed of 2250 rpm can be described by the following formula:

$$m_{2xx} + m_{2yy} + m_{2xy} + m_{2yx} = (0.3 \pm 0.25) + (0.47 \pm 0.08) + (0.04 \pm 0.09)$$
$$+ (0.37 \pm 0.14) = 1.18 \pm 0.56 \text{ kg} \quad (3)$$

Comparing this value with a half of the mass of the shaft (i.e. 2.35 kg), it turns out that we get a result that is about two times lower than the real mass of the shaft.

At some rotational speeds, damping coefficients have values lower than zero, and this observation can be related to the resonance phenomenon. Figure 6 presents a signal registered at the second bearing during the operation at a speed of 4000 rpm after the excitation applied in the Y direction. It can be seen that the vibration amplitude increases from 0 to over 30 µm during a period of 300 ms. It means that the operation of the rotor is far from a stable operation and can even lead to a serious damage to the fluid-flow machine.

5 Verification of the Obtained Results

In order to verify the experimental results, a verification method proposed by Qiu and Tieu was used [5]. A model of the system that consists of a mass point with one degree of freedom, damping coefficients and stiffness coefficients was developed (using the Abaqus 6.14-2 software). The value of the force used during the experimental research and also the experimentally determined stiffness and damping coefficients were incorporated into the model. The model served to calculate the displacement of the mass point to which the impulse force was applied. The calculated displacement
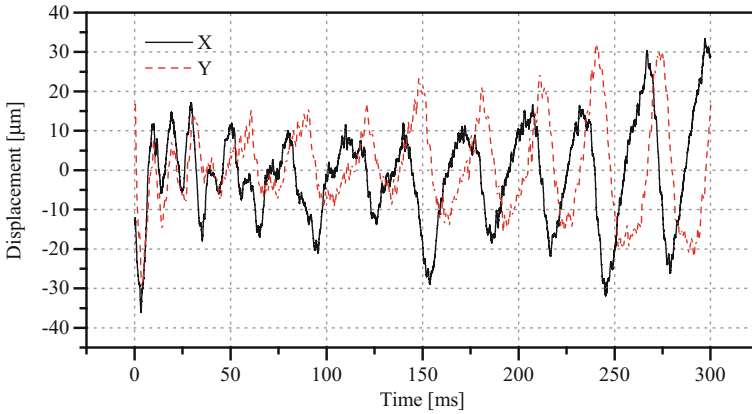
Fig. 6 Vibration amplitude registered at bearing no. 2 during the operation at a speed of 4000 rpm after an excitation was applied in the Y direction (using an impact hammer) versus time

Fig. 7 Schematic diagram of the model that consists of a concentrated mass, damping coefficients and stiffness coefficients
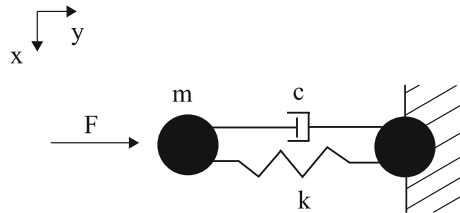
was then compared with the system response measured during the experimental research.

The model, created using the Abaqus, consists of two points lying on a straight line. The first point has all degrees of freedom removed and the second point has only one degree of freedom, namely, the displacement in the Y direction. The mass of the second point is 2.35 kg, which equals to a half of the mass of the rotor (measured during the experimental research). An element, characterised by elastic and damping properties, has been inserted between the two points in question. The values of stiffness and damping have been measured experimentally and they are 8700 Nm and 51 Nm/s, respectively. A schematic diagram representing the created model is demonstrated in Fig. 7.

The value of the excitation force that was incorporated into the model corresponds to a half of the value of the force measured during the experimental research. The values of this force (in Newtons) for the subsequent time steps are as follows: F = [0, 0, 11, 59, 49, 44, 10, 0] N.

The time step during the numerical analysis was consistent with the sampling frequency in the experimental research. The duration of the excitation force was approximately 0.1 ms (the same as during experimental research). The movement of the rotor was calculated for a time of 1 s.
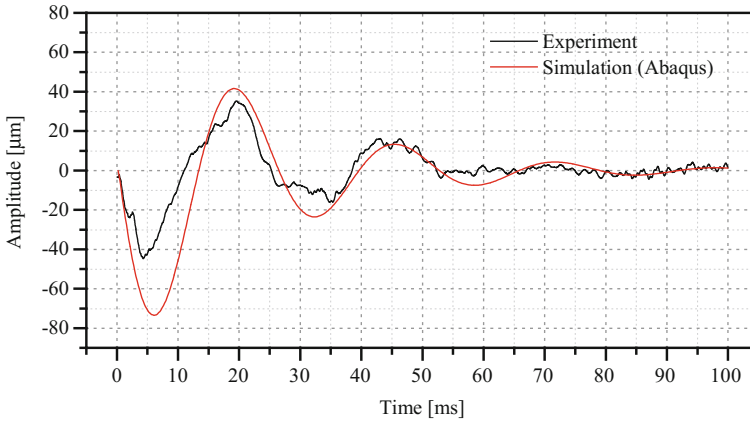
Fig. 8 The dynamic response of a real rotor and of its numerical model (into which the experimentally determined damping and stiffness coefficients were incorporated), presented as a function of time

The displacement of the point that has one degree of freedom is shown in 0The red line represents the results obtained using the model presented in this chapter of the article and the vibration amplitude measured during experimental tests is drawn using a black line. The results presented in Fig. 8 show that the stiffness and damping coefficients computed on the basis of the experimental research describe well the measured signals. Differences between experimentally and numerically obtained results can be explained by the presence of nonlinear damping in the system. Such a time-dependent damping is quite difficult to estimate as it has been proved in the paper [15].

6   Summary and Conclusions

On the basis of the research results, one can say that the values of the computed stiffness, damping and mass coefficients change in an expected manner in the whole speed range. The stiffness coefficients obtained for the lowest test speed (2250 rpm) are approximately 20,000 N/m. The highest stiffnesses bearing no. 2 were observed for coefficients: k_{xy} and k_{yx}. The values k_{xx} and k_{yy} are about twice lower. All stiffness coefficients decrease smoothly up to a speed of 3750 rpm and then rise around the resonant speed. The standard deviation values increase as the rotational speed of the rotor rises, which means that the calculated values are less repetitive.

The damping coefficients for bearing no. 2 take the highest values for low rotational speeds and they decrease as the speed increases. The value of c_{xx} coefficient oscillates around 110 Ns/m and the value of c_{yy} coefficient is about 65 Ns/m. The cross-coupled damping coefficients have values between 20 and 30 Ns/m. Almost

all obtained values of damping coefficients are higher than zero. Only around the resonant speed, c_{xy} coefficient is well below zero.

The mass coefficients computed for bearing no. 2 take the following values: m_{yy} and m_{yx}—approx. 0.4 kg, m_{xx} and m_{xy}—approx. -0.4 kg. It is interesting to note that if we draw the curves representing m_{xx} and m_{yy} coefficients using the linear interpolation (in the form of a polynomial function of a low degree), the values of these coefficients change from positive values (at low speeds) to approximately the same but negative values, at highest tested speeds. These curves pass through zero around the resonant speed. This is consistent with the fact that the ellipses representing the motion of the shaft rotate by some angle around the rotation axis of the shaft after passing through the resonant speed.

This article describes the computations of dynamic coefficients of hydrodynamic bearings carried out not only for a stably-operating machine but also for a broad range of rotational speeds. It turns out that the results obtained are less accurate at speeds at which higher vibration amplitudes are observed, which is reflected by increased standard deviation values. The method presented herein should be used only for analysing stably-operating rotating systems (i.e. systems that are characterised by small vibration amplitudes). Though the method allows computing dynamic coefficients of hydrodynamic bearings, damping coefficients obtained using impulse excitations can take negative values—this is due to an increased vibration amplitude after the excitation and the insufficient damping capability. The presented analysis is associated with an increased risk of obtaining inaccurate results and hence should be performed with a great caution. During passing through the resonant speed, mass coefficients can change from positive values to negative values (and vice versa).

References

1. Tiwari, R., Lees, A.W., Friswell, M.I.: Identification of dynamic bearing parameters: a review. Shock Vib. Dig. **36**, 99–124 (2004)
2. Wang, X., Li, H., Meng, G.: Rotordynamic coefficients of a controllable magnetorheological fluid lubricated floating ring bearing. Tribol. Int. **114**, 1–14 (2017)
3. Li, Q., Wang, W., Weaver, B., Wood, H.: Model-based interpolation-iteration method for bearing coefficients identification of operating flexible rotor-bearing system. Int. J. Mech. Sci. **131–132**, 471–479 (2017)
4. Nordmann, R., Schoellhorn, K.: Identification of stiffness and damping coefficients of journal bearings by means of the impact method. In: 2nd International Conference on Vibrations in Rotating Machinery, pp. 231–238 (1980)
5. Qiu, Z.L., Tieu, A.K.: Identification of sixteen force coefficients of two journal bearings from impulse responses. Wear **212**, 206–212 (1997)
6. Breńkacz, Ł.: Identification of stiffness, damping and mass coefficients of rotor-bearing system using impulse response method. J. Vibroeng. **17**, 2272–2282 (2015)

7. Breńkacz, Ł., Żywica, G.: The sensitivity analysis of the method for identification of bearing dynamic coefficients. In: Awrejcewicz, J. (ed.) Dynamical Systems: Modelling: Łódź Poland, December 7–10, 2015, pp. 81–96. Springer International Publishing, Cham (2016)

8. Kudra, G., Awrejcewicz, J.: Application and experimental validation of new computational models of friction forces and rolling resistance. Acta Mech. **226**, 2831–2848 (2015)

9. Awrejcewicz, J., Dzyubak, L.P.: Chaos caused by hysteresis and saturation phenomenon in 2-DOF vibrations of the rotor supported by the magneto-hydrodynamic bearing. Int. J. Bifurc. Chaos. **21**, 2801 (2011)

10. Kaźmierczak, M., Kudra, G., Awrejcewicz, J., Wasilewski, G.: Mathematical modelling, numerical simulations and experimental verification of bifurcation dynamics of a pendulum driven by a dc motor. Eur. J. Phys. **36** (2015)

11. Breńkacz, Ł., Żywica, G.: An experimental investigation conducted in order to determine bearing dynamic coefficients of two hydrodynamic bearings using impulse responses. Trans. Inst. Fluid-Flow Mach. **133**, 39–54 (2016)

12. Breńkacz, Ł., Żywica, G., Drosińska-Komor, M.: The experimental identification of the dynamic coefficients of two hydrodynamic journal bearings operating at constant rotational speed and under nonlinear conditions. Polish Marit. Res. **24**, 108–115 (2017)

13. Bagiński, P., Żywica, G.: Analysis of dynamic compliance of the supporting structure for the prototype of organic Rankine cycle micro-turbine with a capacity of 100 kWe. J. Vibroeng. **18**, 3153–3163 (2016)

14. Jin, J., Wang, Z., Cao, L.: Numerical analysis on the influence of the twisted blade on the aerodynamic performance of turbine. Pol. Marit. Res. **23**, 86–90 (2016)

15. Olejnik, P., Awrejcewicz, J.: Coupled oscillators in identification of nonlinear damping of a real parametric pendulum. Mech. Syst. Signal Process. **98**, 91–107 (2018)

Analysis of Rail Vibration Signal Time and Frequency Structures Generated by Different Mechanisms

Rafał Burdzik

Abstract Rail vibration signals are complex data represent different phenomena occurred by the wheel-rail contact or others excitations in railway infrastructure. Such signals can be considered as source of interesting information or unwanted degradation or annoying effect. Thus proper analysis of rail vibration signals are important task for the engineering research. The paper presents results of the pre-liminary analysis of rail vibration signal time and frequency structures generated by different mechanisms. The research assumption was to generate vibrations in the railway rail as a result of various dynamic interactions, which arise as a result of exploitation of the railway infrastructure and vehicle traffic, including the passage of the car through the railway crossing. The aim of the research was to compare the amplitude and frequency of vibration signals and to analyze the possibilities of determination of distinguishing features from different sources signals of vibrations as forced mechanisms. In order to analyze the propagation properties of the vibra-tion wave during the experiments, signals were recorded in 3 perpendicular axes, as carriers of information about longitudinal, transverse and vertical waves. As a result of the conducted research, data sets were collected as orthogonal vibration signals generated by rail vehicle passage and the car passage, by switching of the point mechanism and as a result of single impulse of force, as an example of repair work on the tracks. Further research will be conducted towards statistical analysis of the collected data sets and the use of dedicated signal processing methods.

Keywords Rail vibration · Wave propagation · Vibration excitation of rail track

R. Burdzik (✉)
Faculty of Transport, Silesian University of Technology, Krasińskiego 8, 40-019
Katowice, Poland
e-mail: rafal.burdzik@polsl.pl

1 Introduction

Signal processing methods are mostly focused on determination of information carried by the raw signals. Thus it is required to employed proper mathematical and statistical methods and techniques. Due to different nature and properties of the signals there are many methods dedicated for defined types of the signals. Therefore first stage of each analysis should be observation and classification of the signal. When engineering surveys are analyzed, always pay attention to the importance of results in relation to the correctness of the system operation or its safety. Dynamical phenomena occurred by the wheel-rail contact or railway vehicle whole-body movement are extremely important for the railway safety and reliability [1–3]. For the purposes of safety securing and increase of reliability of railway system many activities are employed [4, 5]. Thus it can be pointed that vibration research should be considered in term of safety. With the increase of train speed, axle load and volume of traffic, the vibration of the vehicle and track coupling system will be intensified, the safe operation of trains will be reduced and the dynamic forces acting on the track structure will be increased significantly. As a result, fatigue and damage of components of the track structure will emerge, and settlement of the rail will occur under repeated action of dynamic loads [6–8]. Other group of railway vibration research is focused on external influence of railway vibration. The emission of vibration includes the vehicle-track-soil interaction, the vehicle and track irregularities, and the dynamic axle loads [9]. The rail provides the contact between the train wheel and the track. Vibrations generated by trains are propagating from the rail to the ballast go through the sleepers [10]. The profile irregularity of a railway line is one of the essential vibration sources for vehicles and track. With a high number of trains, the properties of the track amplify the excitation [11].

The paper presents results of the preliminary analysis of rail vibration signal time and frequency structures generated by different mechanisms. Rail vibration signals are complex data collections represent dynamical responds for different excitations. Depending on sampling frequency and time of registration it can be big data collections. It required proper mathematical algorithms for the analysis. The properties of the signal also can be different (random, stationary, non-stationary), thus the application of statistical methods can be limited. Therefore the first stage on the analysis is to analyse time and frequency structures of the signals.

2 Research Methodology

The research assumption was to generate vibrations in the railway rail as a result of various dynamic interactions, which arise as a result of exploitation of the railway infrastructure and vehicle traffic, including the passage of the car through the rail-way crossing. The aim of the investigations was to record vibration signals generated by typical dynamical excitation which occurred in infrastructure environment
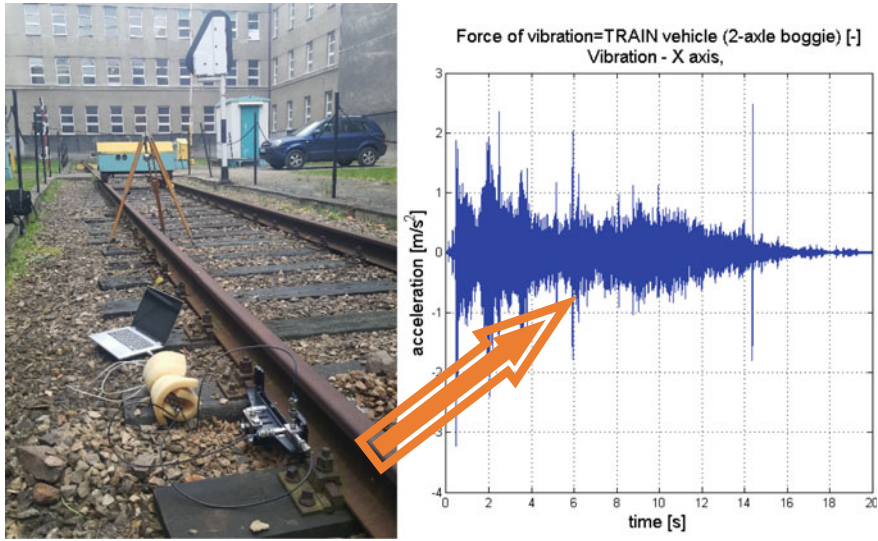
Fig. 1 The scheme of the experimental setup (test track with typical equipment)

of railway system. Some results of the preliminary research have been presented in [12]. To ensure repeatability of measurements it was decided to choose the same path of the propagation for different excitation [13]. Vibration sensors were placed on the rail (Fig. 1) by the special certified holder. It allows to applied this research methodology for the in situ research. The measurement system consists of three one axis acceleration sensors, data acquisition unit and notebook. Research methodology and mobile measurement system with sensor's holder allow to conduct similar research on the real rail track under the rail vehicle passage (in situ conditions).

In order to analyze the propagation properties of the vibration wave during the experiments, signals were recorded in 3 perpendicular axes, as carriers of information about longitudinal, transverse and vertical waves. Velocity of propagation of a particular type of waves is determined by the equations:

$$v_l = \sqrt{\frac{E(1-v)}{(1+v)(1-2v)\rho}} \tag{1}$$

$$v_t = \sqrt{\frac{E}{2(1+v)\rho}} \tag{2}$$

$$v_s = 0.96v_t \tag{3}$$

where,

v_l longitudinal waves,
v_t transverse waves,

v_s surface (vertical) waves,
E Young's modulus,
v Poisson's ratio,
ρ density.

The aim of the research was to compare vibration signals and to analyze the possibilities of determination of distinguishing features from different sources signals of vibrations as forced mechanisms. Experiments were conducted on the experimental test track with typical equipment, such as crossing signalling devices and point mechanisms. The track used was composed of two rails lying on wood sleepers joined by rail pads. It was decided to conduct preliminary research under controlled condition for evaluation of research methodology and to verified dynamical responds of rail under the operation of typical devices in typical traffic condition. The experimental test track allowed to repeat measuring cycles.

The scope of the research included measurement of the rail vibration generate by the single force impulse, switching of the point mechanism, train passing on the track and car passing through the crossing level. For the realization of planned scope different research methods needed to be employed. The main purpose of single research method was to simulate the typical, real dynamical excitation occurred in railway system. The set of four chosen excitation types have been depicted in Fig. 2.
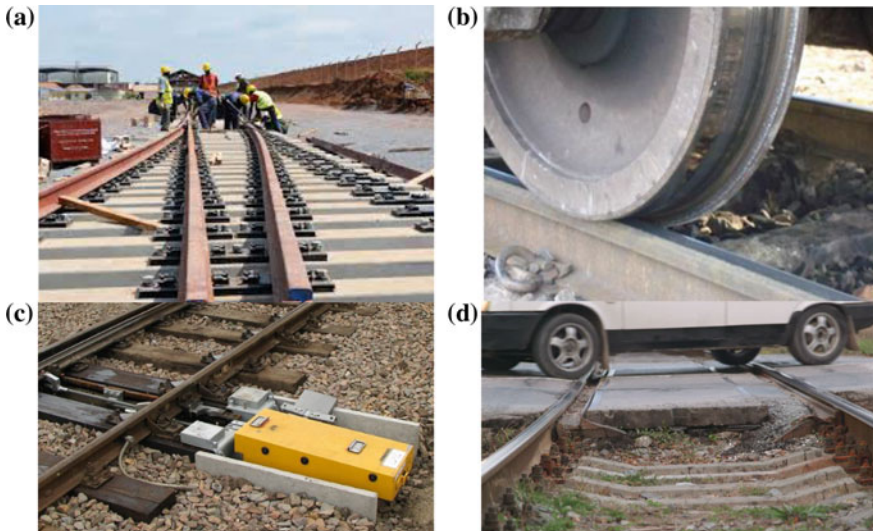
Fig. 2 The set of tested types of vibration excitation of rail track: **a** single force impulse, **b** train passing on the track, **c** switching of the point mechanism, **d** car passing through the crossing level

3   Research Results

The consideration of problem of waves propagation based on the theory of surface waves propagation. Propagation of vibration theory is described by the Rayleigh surface waves or by Love's waves when the elastic layer rests on the stiffer centre [14]. Rail vibration are propagating in solid but non constant structure because of different types of rail jointing methods [15]. Thus the waves propagation properties are different than studied in ground vibration. However based on the difference in the propagation of waves, depending on whether the vibration was transverse or longitudinal during the research the vibration acceleration was recorded in three orthogonal axes: longitudinal, transverse and vertical.

For the purpose of analysis of rail vibration structure the comparative waveforms of vibration registered for the different excitation source have been presented. As the example of the comparative analysis the vertical vibration has been depicted in Fig. 3.

Presented waveforms of the vibration are different but it could be difficult to describe time domain estimator based just on the amplitude values. Thus it was decided to conduct the comparative analysis of the vibration spectrum, which allows to identify the frequency components of the vibration. A signal is represented in the domain of frequency by application of the discrete Fourier transform. In the sphere of signal processing, it is mainly used to transform the $f(t)$ function, being continuous in the domain of time, into the $F(\omega)$ function, continuous in the domain of frequency, as result we obtain spectrum of the signal. The Fourier transform can be express as formula:

$$F(\omega) = \int\limits_{-\infty}^{\infty} f(t) \cdot e^{-i2\,\pi\omega t} d(t) \tag{4}$$

The results as the comparative analysis of frequency structure of the longitudinal, transverse and vertical vibration have been depicted in Figs. 4, 5 and 6.

The frequency structure of the longitudinal and transverse vibration are similar in the frequency domain but the amplitude of the specific frequency components are different. Also it is interesting that vibration registered during switch of point mechanism and bogie passing (train simulator) have similar frequency structure, which weren't visible based on the analysis of waveforms. The single force response signal induces higher frequencies vibration (around 1 kH) and car passing rail vibration are low frequencies.

The frequency structure of the vertical vibration are much more similar in the frequency domain for all studied cases. For all signals the most dominant frequencies are below 500 Hz.

Based on the analysis of the results it can be assumed that it could be possible to separate the vibration properties of signals arising from different sources (generation mechanism). The main frequencies for the dominant components of the signals have
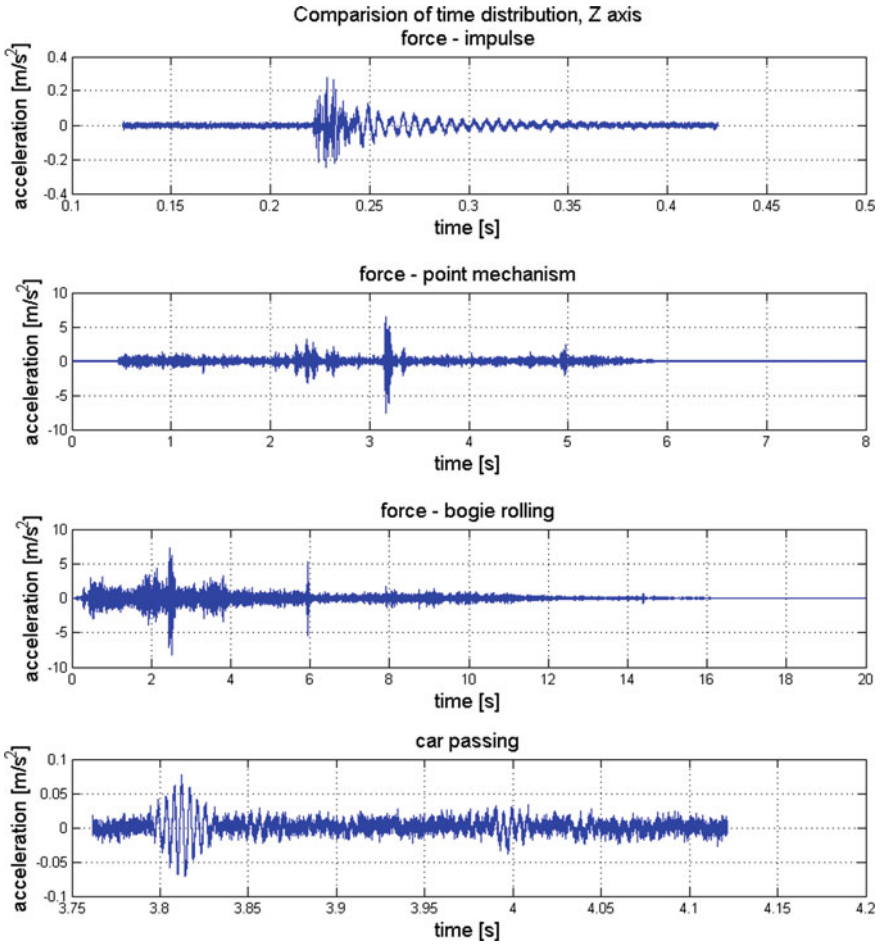
Fig. 3 Waveforms of vibration generate by different mechanism: single force impulse, point mechanism, rail vehicle passing, car passing

been collected and depicted in Table 1. This table shows differences in dominant frequency components of the vibration signal generated by tested excitation mechanisms. It can be result of dynamics of the excitation but at the same moments it can be correlated with different properties. Due to nature of these signals more advanced signal processing methods should be employed. Time-frequency representation of the signal will allow to observe distribution of the signal in time and frequency domain simultaneously.
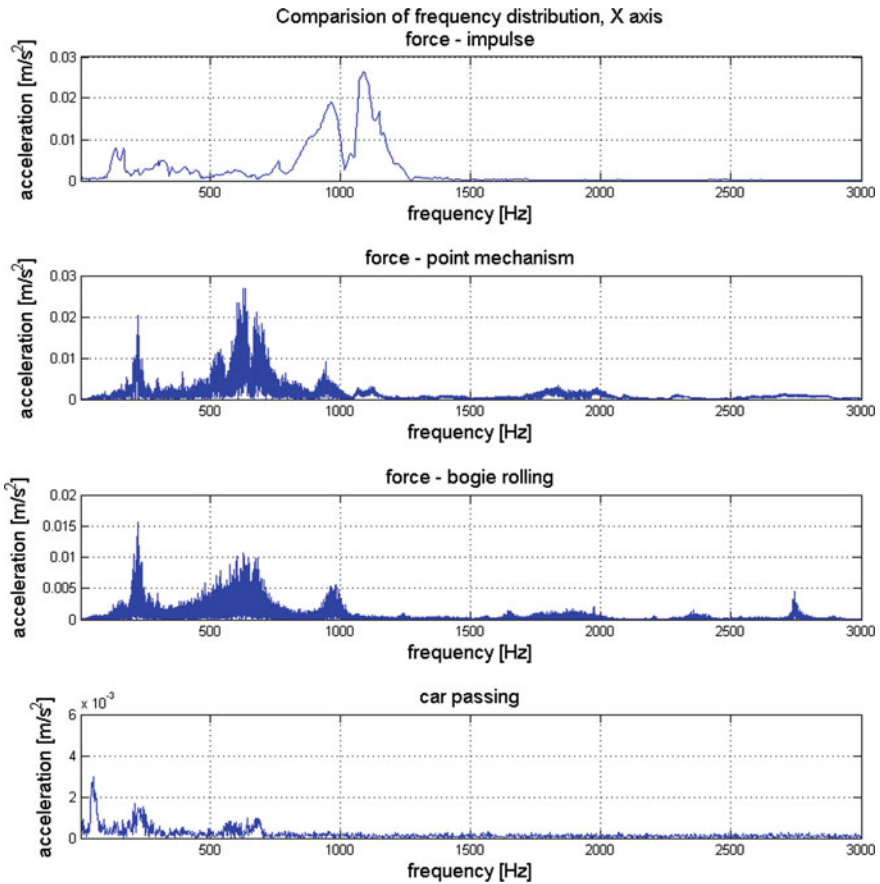
Fig. 4 Frequency structure of longitudinal vibration generate by different mechanism: single force impulse, point mechanism, rail vehicle passing, car passing

4 Conclusions

General analysis of the signal structure is first stage for development of proper complex analysis of the research results. Distribution of values in time and frequency domains show general mathematical and statistical properties of collected data. Also such analysis can be useful for interpretation due to the functional and safety conditions of engineering system of measured signals. Research on vibration in railway transport system is an important area of investigation, especially for the civil and mechanical engineering disciplines. From the large number of publications in these scope the presented paper is focused on analysis of rail track propagation of vibration occurred by the multiple sources, as vehicle movement and typical devices functionality.
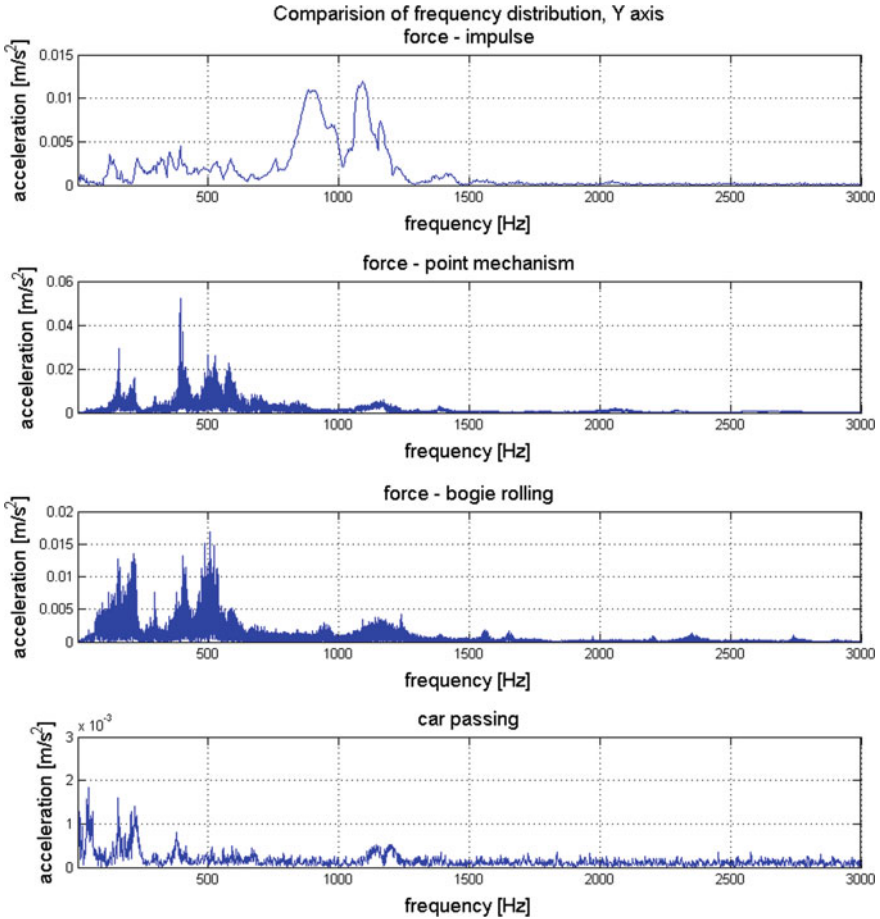
Fig. 5 Frequency structure of transverse vibration generate by different mechanism: single force impulse, point mechanism, rail vehicle passing, car passing

The results were collected during numerous experiments with different vibration excitation mechanical sources. The structures of vibration were presented as frequency distribution of the signal separately for the longitudinal, transverse and vertical vibration. The result shows some similarities for longitudinal and transverse vibration structure and different dominant frequency components for the vertical vibration.

As the preliminary conclusion it can be assumed that differences in spectrums of vibration for analyzed excitation characteristics could be useful for the recognition and identification of the vibration source. For the purpose of identification of source components further investigation will be conducted.
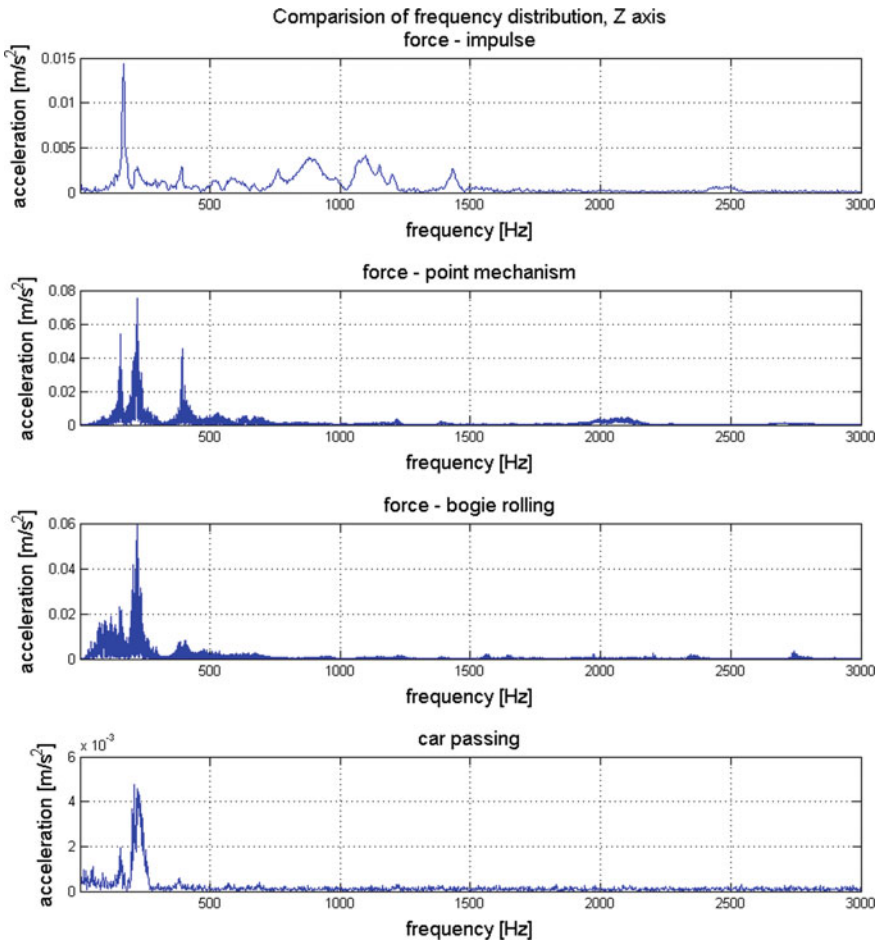
Fig. 6 Frequency structure of vertical vibration generate by different mechanism: single force impulse, point mechanism, rail vehicle passing, car passing

Table 1 Main frequencies identified during research

Axis	Source			
	Single force impulse (Hz)	Point mechanism (Hz)	Rail vehicle passing (Hz)	Car passing (Hz)
X	ca. 960, ca. 1080	ca. 220, ca. 630, ca. 940	ca. 220, ca. 630, ca. 960, ca. 2740	ca. 50, ca. 210, ca. 680
Y	ca. 900, ca. 1090	ca. 155, ca. 390, ca. 530, ca. 570	ca. 220, ca. 405, ca. 510, ca. 1160	ca. 40, ca. 150, ca. 220, ca. 380
Z	ca. 170, ca. 880, ca. 1100	ca. 155, ca. 220, ca. 390	ca. 95, ca. 155, ca. 220, ca. 400	ca. 50, ca. 155, ca. 210

References

1. Burdzik, R., Nowak, B., Młyńczak, J., Deuszkiewicz, P.: Analysis of the detection and crossing signaling system in safety terms. Diagnostyka **17**(4), 65–72 (2016)
2. Siergiejczyk, M., Paś, J., Rosiński, A.: Issue of reliability–exploitation evaluation of electronic transport systems used in the railway environment with consideration of electromagnetic interference. IET Intel. Transport Syst. **10**(1), 587–593 (2016)
3. Siergiejczyk, M., Rosiński, A.: The concept of monitoring a teletransmission track of the highway emergency response system. Diagnostyka **16**(4), 49–54 (2015)
4. Mikołajczak, P., Napiórkowski, J.: Analysing the reliability of working parts operating in abrasive soil pulp taking into consideration confounding factors. Eksploatacja i Niezawodnosc—-Maintenance Reliab. **18**(4), 544–551 (2014)
5. Napiorkowski, J., Mikolajczak, P., Legutko, S., Krolczyk, J.B.: Developing wear model of construction materials in abrasive soil pulp employing discriminant analysis. Tehnički vjesnik/Technical Gazette **24**(Suppl. 1), 15–20 (2017)
6. Lei, X., Noda, N.A.: Analyses of dynamic response of vehicle and track coupling system with random irregularity of track vertical profile. J. Sound Vib. **258**(1), 147–165 (2002)
7. Ling, L., et al.: A 3D model for coupling dynamics analysis of high-speed train/track system. J. Zhejiang Univ. Sci. A **15**(12), 964–983 (2014)
8. Bąkowski, H., Posmyk, A., Krawczyk, J.: Tribological properties of rail steel in straight moderately loaded sections of railway tracks. Arch. Metall. Mater. **56**(3), 813–822 (2011)
9. Auersch, L.: Theoretical and experimental excitation force spectra for railway induced ground vibration: vehicle-track-soil interaction, irregularities and soil measurements. Veh. Syst. Dyn. **48**, 235–261 (2010)
10. Krylov, V.: Spectra of low frequency ground vibrations generated by high speed trains on layered ground. J. Low Freq. Noise Vib. Active Control **16**(4), 257–270 (1997)
11. Picoux, B., Le Houedec, D.: Diagnosis and prediction of vibration from railway trains. Soil Dyn. Earthq. Eng. **25**, 905–921 (2005)
12. Burdzik, R., Nowak, B.: Identification of the vibration environment of railway infrastructure. Procedia Eng. **187**, 556–561 (2017)
13. Dabrowski, Z., Zawisza, M.: Investigations of the vibroacoustic signals sensitivity to mechanical defects not recognised by the OBD system in diesel engines. Solid State Phenom. **180**, 194–199 (2012)
14. Bednarz, J.: Experimental verification of the developed soil model describing the propagation of vibration wave in the ground. J. KONES **19**, 31–39 (2012)
15. Sładkowski, A., Bizoń, K.: The use of semi-automatic technique of finite elements mesh generation for solutions of some railway transport problems. Mechanics **23**(2), 190–196 (2017)

Model Based Research on ICE Engine Powered by Alternative Fuels

Adrian Chmielewski, Robert Gumiński, Tomasz Mydłowski, Artur Małecki and Krzysztof Bogdziński

Abstract The paper presents 2 DOF dynamic model of the piston-crankshaft system of HONDA NHX 110. The piston-crankshaft system was combined with pressure curve, which was obtained from the experimental research, measured in the cylinder during the execution of the working cycle of ICE engine. In the article the theoretical and analytical dependencies, which described heat generation in the cylinder, have been presented. Based on research results obtained from the experiment and simulation model the value of angular displacement, velocity and acceleration value of flywheel and shaft have been illustrated. Moreover piston displacement, velocity and acceleration has been showed. In the paper, the research results and simulation results at different angles of the ignition advance of ICE engine powered by compressed natural gas—CNG have been analyzed and compared.

Keywords 2 DOF dynamic model · ICE engine · Alternative fuels
Piston-crankshaft system

A. Chmielewski (✉) · R. Gumiński · T. Mydłowski · A. Małecki · K. Bogdziński
Faculty of Automotive and Construction Machinery Engineering, Institute of Vehicles, Warsaw
University of Technology, Narbutta 84, 02–524 Warsaw, Poland
e-mail: a.chmielewski@mechatronika.net.pl

R. Gumiński
e-mail: rgumin@simr.pw.edu.pl

T. Mydłowski
e-mail: mydlowski@mechatronika.net.pl

A. Małecki
e-mail: a.malecki85@gmail.com

K. Bogdziński
e-mail: k.bogdzinski@mechatronika.net.pl

1   Introduction

Nowadays more and more attention is given to distributed energy generation systems [1, 2], which include: renewable energy sources or cogeneration systems [3–6]. Some of them including internal combustion engines (ICE) powered by alternative fuels (e.g. biogas) [7, 8]. Especially important from economic stand point are low power output engines.

The structure of the following work is as follows: in Sect. 2 a research stand for conducting pressure change measurements inside the combustion chamber of a CNG powered ICE was presented. In Sect. 3 presents an analytical description of piston and crankshaft system and description of heat exchange in combustion chamber. Results of the research were used in a model simulation (model of the piston and crankshaft mechanism of low power output Honda NHX internal combustion engine powered by CNG with 2 degrees of freedom was used). Analytical dependencies of the model are presented in Sect. 3. In Sect. 4 the simulation model and simulation results are presented. Section 5 contains the main conclusions and limitations of usage of simulation models for describing thermodynamic processes.

2   Test Stand Description

The engine test stand, presented in Fig. 1, consisted of the Honda NHX 110 4 stroke internal combustion engine, an electric machine, the programmable engine management unit ECU MASTER EMU, the measurement track and control system. The engine was equipped with the trifunctional catalytic converter. The receiver of the generated torque was a brushless electric motor with permanent magnets, working as an electric generator. The power receiving circuit consisted of a 3-phase rectifying bridge (maximum voltage: 400 V, maximum current: 300 A), a transistor module, a resistor module (0.05 Ω), a brushless electric motor with permanent magnets (resistance: 0.0004 Ω, input voltage: 30–70 V, rotational speed: 150 rpm per 1 V of voltage input, maximum rotational speed 10,500 rpm, current draw with no load: 13 A at 20 V voltage input). Control over the transistor module was performed by a custom microprocessor control module, described in detail in [6, 9–11]. A toothed belt transmission (ratio i = 1.42) was used to transfer the torque from engine crankshaft to the electric generator. Torque was measured with a Zemic L6N load cell sensor (accuracy class: C3). Engine crankshaft angle was registered with a single-turn digital absolute encoder with 14 bit precision. The SSI standard communication protocol was used for data transmission from the encoder, at a rate of 44.9 kHz, which resulted in accuracy of 0.5° CA (crankshaft angle) at 3800 rpm (1° CA at 7600 rpm respectively). Detailed description of the test stand was provided in [8, 9].

Fig. 1 The scheme of the test stand
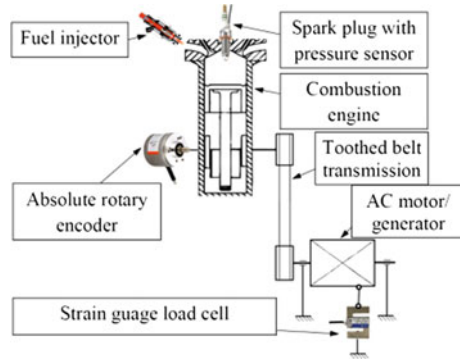
Fig. 2 Open indicator graphs for ICE powered by CNG
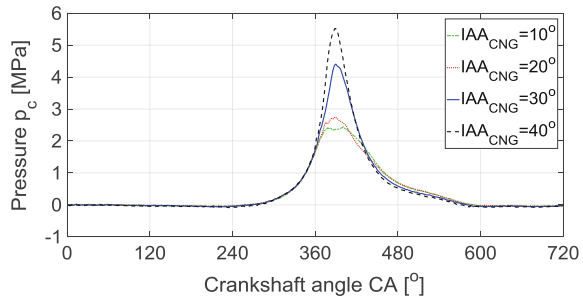
2.1 Research Results—Indicator Pressure Graphs

In the following section, open indicator graphs obtained from experimental research are presented (Fig. 2). Results for ICE powered by CNG.

Analysis of Fig. 2 shows that with the increase of ignition advance angle, the maximum pressure in the combustion chamber increases (for ignition advance angle from ranging from 0 to 720 CA). The obtained results of pressure change were used as source data for the piston and crankshaft assembly with 2 degrees of freedom model of Honda NHX 110 engine, presented in Sect. 2.

3 Analytical Background

3.1 Analytical Description of 2DOF Crankshaft Assembly

In the following section the analytical dependencies of the crankshaft assembly with 2 degrees of freedom were presented. A geometry model was presented in Fig. 3. The model assumes a static reduction of crankshaft masses. Similar assumptions were made in [12–16]. The analyzed physical model has 2 degrees of freedom. The fragment of the crankshaft connecting the flywheel with the crank has rigidity k.
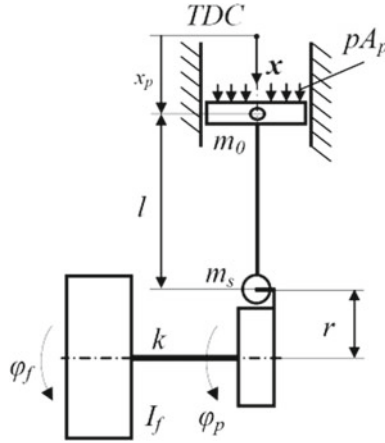
Fig. 3 Diagram of the crankshaft assembly with 2 DOF
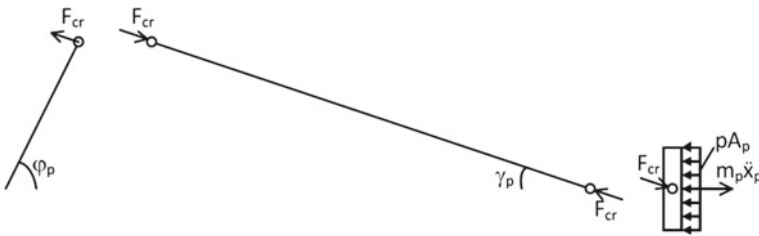
Fig. 4 Diagram presenting the distribution of force and angles in analyzed system

In Fig. 4 a diagram of the crankshaft assembly with indication of forces and torque was presented.

Based on analysis of Figs. 3 and 4, the equation for the moments of inertia of crankshaft's crank can be written:

$$F_{cr}r\sin(\varphi_p + \gamma_p) - I_p\ddot{\varphi}_p - k(\varphi_p - \varphi_f) = 0 \tag{1}$$

and the dependence for sum of moments of the flywheel can be written:

$$I_f\ddot{\varphi}_f - k(\varphi_p - \varphi_f) = 0 \tag{2}$$

The sum of projected forces on x axis for the piston (based on Figs. 3 and 4) is:

$$F_{cr}\cos\gamma_p + m_p\ddot{x}_p - pA_p = 0 \tag{3}$$

From analysis of Fig. 4, knowing that:

$$\frac{l}{\sin \varphi_p} = \frac{r}{\sin \gamma_p} \tag{4}$$

Using the law of sines, the dependencies between γ_p and φ_p can be determined:

$$\cos \gamma_p = \sqrt{1 - \frac{r^2}{l^2} \sin^2 \varphi_p} = \sqrt{1 - \lambda^2 \sin^2 \varphi_p} \tag{5}$$

Fitting the dependencies (2–5) into dependency (1) results in equation for angular acceleration of the piston:

$$\ddot{\varphi}_p = \frac{r\left(pA_p - m_p\ddot{x}_p\right)}{I_p} \frac{\left(\sin \varphi_p \sqrt{1 - \lambda^2 \sin^2 \varphi_p} + \lambda \sin \varphi_p \cos \varphi_p\right)}{\sqrt{1 - \lambda^2 \sin^2 \varphi_p}} - \frac{k}{I_p}(\varphi_p - \varphi_f) \tag{6}$$

From geometrical and trigonometric dependencies the final unknown value can be determined from Eq. (6), linear displacement of piston x_p:

$$x_p = r + l - r \cos \varphi_p - l \cos \gamma_p \tag{7}$$

After transformations, knowing that $\lambda = r/l$:

$$x_p = r\left\{(1 - \cos \varphi_p) + \frac{l}{r}(1 - \sqrt{1 - \frac{r^2}{l^2} \sin^2 \varphi_p})\right\}$$
$$= r\left\{(1 - \cos \varphi_p) + \frac{1}{\lambda}(1 - \sqrt{1 - \lambda^2 \sin^2 \varphi_p})\right\} \tag{8}$$

The result is:

$$x_p = r\left\{(1 - \cos \varphi_p) + \frac{\lambda}{4}(1 - \cos 2\varphi_p)\right\} \tag{9}$$

Differentiating the dependency (9) results in dependency for the speed of the piston:

$$\dot{x}_p = \frac{dx_p}{dt} = r\dot{\varphi}_p\left\{\sin \varphi_p + \frac{\lambda}{2} \sin 2\varphi_p\right\} \tag{10}$$

Differentiating for the second time (8) results in dependency for acceleration of the piston:

$$\ddot{x}_p = \frac{d^2x_{p0}}{dt^2} = r\left[\ddot{\varphi}_p\left(\sin \varphi_p + \frac{\lambda}{2} \sin 2\varphi_p\right) + \dot{\varphi}_p^2\left(\cos \varphi_p + \lambda \cos 2\varphi_p\right)\right] \tag{11}$$

Transforming and differentiating the dependency (2) twice results in the equation for angular acceleration of the flywheel:

$$\ddot{\varphi}_f = \frac{k}{I_f}(\varphi_p - \varphi_f) \tag{12}$$

In Eq. (3) one unknown value, p, is present. The value can be determined from the thermodynamic domain, which was analyzed in Sect. 3.2.

3.2 Analytical Dependencies of Thermodynamic Domain

In order to determine the pressure changes inside the combustion chamber with the use of the first law of thermodynamics, using the zero-dimensional model, it can be written that in accordance with the law of conservation of energy (for low power output engine) [17–23]:

$$\begin{aligned}
\frac{dQ_h}{d\varphi} &= \frac{c_v}{R}\left(p\frac{dV}{d\varphi} + V_c\frac{dp}{d\varphi}\right) + p\frac{dV_c}{d\varphi} + \frac{dQ_{hetr}}{d\varphi} \\
&= \frac{1}{n-1}\left(p\frac{dV_c}{d\varphi} + V_c\frac{dp}{d\varphi}\right) + p\frac{dV_c}{d\varphi} + \frac{dQ_{hetr}}{d\varphi}
\end{aligned} \tag{13}$$

Transforming the dependency (13), $dp/d\varphi$ can be determined:

$$\frac{dp}{d\varphi} = \frac{n-1}{V_c}\left(\frac{dQ_h}{d\varphi} - \frac{dQ_{hetr}}{d\varphi}\right) - \frac{n}{V_c}p\frac{dV_c}{d\varphi} \tag{14}$$

where: n—the ratio of specific heat (−), $n = 1.338\text{-}6 \times 10^{-5}T_{gas} + 10^{-8}T_{gas}^2$, $T_{gas} = pV/m_{air}R$, T_{gas}—the temperature of the flowing gas (K), m_{air}—the mass of the air in the cylinder (kg), R—the individual gas constant (J/kgK).

The rate of heat transfer Q_{hert}/dt from the flowing gas to the combustion chamber wall is dominated by the forced convection [18, 19], so the following can be calculated:

$$\begin{aligned}
\frac{dQ_{hert}}{dt} &= hA(T_{gas} - T_{spt}) = \overbrace{St\varsigma c_p v}^{h}\, A\left(\frac{pV_c}{m_{air}R} - T_{spt}\right) \\
&= St\varsigma\,\overbrace{\frac{R}{1-\frac{1}{n}}}^{c_p}\, vA\left(\frac{pV_c}{m_{air}R} - T_{spt}\right) \\
&= 0.715\exp(-0.14(\dot{x}_{p\,mean}))\varsigma\frac{R}{1-\frac{1}{n}}vA\left(\frac{pV_c}{m_{air}R} - T_{spt}\right) \tag{15}
\end{aligned}$$

where: c_p—specific heat (J/kgK), St—the Stanton number (–), v—turbulent gas fluctuating velocity (m/s), $v = 0.5$ $(\dot{x}_{p\,mean})$, T_{spt}—measured temperature of the spark plug (K).

The heat flux in combustion chamber can be calculated by solving the partial differential equation which contains two boundary conditions:

$$\frac{\partial T}{\partial t} = \alpha \frac{\partial T^2}{\partial^2 x} \left| \begin{array}{l} T(0, t) = T_{win}(t) \; for \; x = 0 \\ T(a, t) = T_{wot}(t) \; for \; x = a \end{array} \right. \tag{16}$$

where: T_{win}—instantaneous temperature inside of the cylinder wall (K), T_{wot}—the steady state temperature of the cylinder of the surface of the outside wall at distance a from the inside wall surface (K), α—thermal conductivity, $\alpha = k/\zeta c$, k—thermal conductivity (W/mK), c—the specific heat (J/kgK), ζ—gas density (kg/m^3).

T_{win} can be calculated as follows [19]:

$$T_{win} = T_{wmean} + \sum_{n=1}^{M} (A_n \cos(n\omega t) + B_n \sin(n\omega t)) \tag{17}$$

where: T_{wmean}—time averaged value of T_{win}, $\omega = \dot{\varphi}_p$—the angular frequency of the temperature variation—the half of the engine angular velocity for the four-stroke engine, M—harmonic number (–).

We can write the following solution of (17):

$$T(x, t) = T_{wmean} - (T_{wmean} - T_{wot}) + \sum_{n=1}^{\infty} (\exp(-c_n x)) E_n(x, t)$$

$$= T_{wmean} - (T_{wmean} - T_{wot})$$

$$+ \sum_{n=1}^{\infty} (\exp(-c_n x)) \overbrace{A_n \cos(n\dot{\varphi}t - c_n x) + B_n \sin(n\dot{\varphi}t - c_n x)}^{E_n(x,t)}$$

$$= T_{wmean} - (T_{wmean} - T_{wot})$$

$$+ \sum_{n=1}^{\infty} (\exp(-c_n x)) \overbrace{\frac{2}{\tau} \int_0^{\tau} T_w(t) \cos(\dot{\varphi}nt)dt}^{A_n} \cos(n\dot{\varphi}t - \overbrace{\sqrt{\frac{n\dot{\varphi}}{2\alpha}}}^{c_n} x)$$

$$+ \overbrace{\frac{2}{\tau} \int_0^{\tau} T_w(t) \cos(\dot{\varphi}nt)dt}^{B_n} \sin(n\dot{\varphi}t - \overbrace{\sqrt{\frac{n\dot{\varphi}}{2\alpha}}}^{c_n} x) \tag{18}$$

The heat flux at the cylinder (for $x=0$) can be expressed by using Furier's law as follows:

$$q(t) = -k \left. \frac{\partial T}{\partial x} \right|_{x=0} = \frac{k}{a}(T_{wmean} - T_{wot}) + k \sum_{n=1}^{M} c_n \{([A_n + B_n] \cos(n\dot{\varphi}t)$$

$$+ ([B_n - A_n] \sin(n\dot{\varphi}t)\} \tag{19}$$

The useful formula for small scale engine proposed by Wu-Chen-Hiseh-Ke [18, 19] allows to calculate T_{spt} with use of intake manifold pressure p_{imp}, based on experimental research:

$$T_{spt} = b_{spt1}\omega + b_{spt2}\omega^2 + b_{spt3}p_{imp} + b_{spt4}p_{imp}\omega + b_{spt5}p_{imp}^2 + b_{spt6}\varepsilon \tag{20}$$

where: b_{spi}—coefficients, described in detail in [18, 19] (–), ε—compression ratio (–).

Similarly, we can determine the Stanton number, based on experimental data [18, 19]:

$$St = \psi \varepsilon S^2 \left(b \left(10^5 V_c(\varphi) \right)^2 + \exp((l\dot{x}_{mean}^2)) \right) \tag{21}$$

where: $\psi\epsilon < 5.9; 6 >$, $l\epsilon < -0.01; -0.015 >$– coefficients, S—stroke (m), $S = 2r$.

The V_c volume we can calculate to input x_p from (8), we can write as follows:

$$V_c = V_{ch} + Ax_p = \frac{V_{sc}}{\varepsilon - 1} + \frac{\pi d^2}{4} \underbrace{r \left\{ (1 - \cos \varphi_p) + \frac{1}{\lambda}(1 - \sqrt{1 - \lambda^2 \sin^2 \varphi_p}) \right\}}_{x_p}$$

$$= \frac{\overbrace{\dfrac{\pi d^2}{4} S|_{S=2r}}^{V_{sc}}}{\varepsilon - 1} + \frac{\pi d^2}{4} r \left\{ (1 - \cos \varphi_p) + \frac{1}{\lambda}(1 - \sqrt{1 - \lambda^2 \sin^2 \varphi_p}) \right\} \tag{22}$$

The last unknown parameter in (13) and (14) dQ_h. The heat release rate connected with the crank angle can be obtained from the rate of mass fraction calculated as follows:

$$\frac{dQ_h}{d\varphi_p} = w_1 \frac{w_2 + 1}{\varphi_{d0}} \left(\frac{\varphi_{deg} - \varphi_0}{\varphi_{d0}} \right)^{w_2} \exp\left\{ -w_1 \left(\frac{\varphi_{deg} - \varphi_0}{\varphi_{d0}} \right)^{w_2+1} \right\} g_f W_u \tag{23}$$

where: $w_1 = 5$, $w_2 = 2$ according to [18, 19], W_u—the fuel caloric value (MJ/kg), g_f—the fuel mass injected into the cylinder (kg/s), φ_{d0}—the total combustion expressed in crank angle—CA (deg), φ_0—the start of combustion expressed in crank angle—CA (deg), $\varphi_0 = IAA + 25.5p_{\text{in manifold}} - 0.0605\dot{\varphi}_p - 0.2801 p_{\text{in manifold}}\dot{\varphi}_p + 6.88 \times 10^{-4}\dot{\varphi}_p^2$, $p_{inmanifold}$—intake manifold pressure (MPa). The φ_{deg} can be expressed as follows:
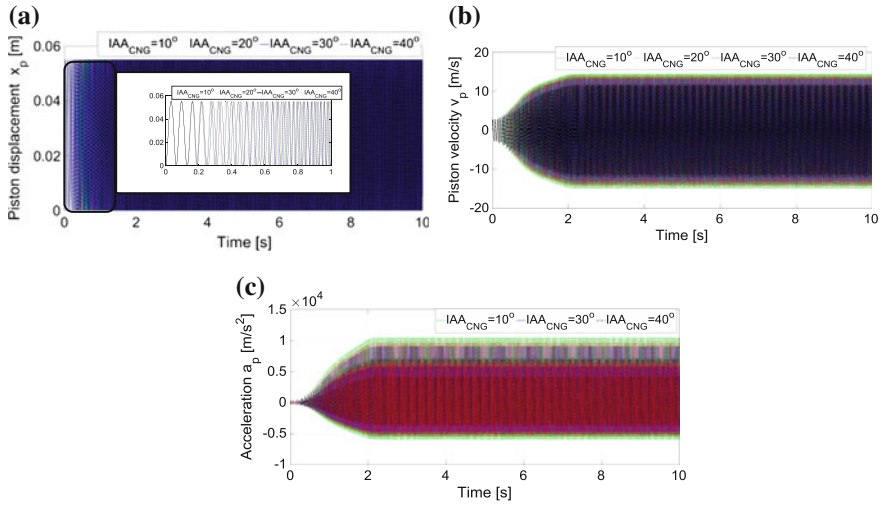
Fig. 5 Parameters of piston of engine fueled by CNG: **a** piston displacement x_p, **b** piston velocity v_p, **c** piston acceleration a_p

$$\varphi_{\deg}[\text{deg}] = \varphi_p[\text{rad}]\frac{180°}{\pi} \tag{24}$$

4 Simulation Model and Simulation Results

A simulation model was prepared based on dependencies (1–12). Changes of pressure were determined and implemented into the model based on analysis of research results presented in Fig. 2, respectively for CNG. Analytical description of pressure changes was presented with use of dependency (13–24).

Figure 5 presents respectively: linear displacement (Fig. 5a), piston velocity (Fig. 5b) and acceleration of the piston (Fig. 5c) of engine fueled by CNG. It presents the results of the simulations for the following main parameters: $k = 9150$ N/m, $l = 0.091$ m, $r = 0.0275$ m, $m_f = 2.851$ kg, $m_p = 0.22$ kg, $r_f = 0.11$ m. Change in rotational speed (Fig. 5a) is caused by change in frequency, the assembly accelerates (up to 2 s), which is shown by the increasing density of displacements. After approximately 2 s (for $IAA_{CNG} = 10$ up to 40 before TDC—Top Dead Centre) the assembly reaches the constant amplitude. If the ignition advance angle IAA_{CNG} increases (which increases the pressure in the cylinder as well) then piston velocity and piston acceleration amplitude decrease. Similar results for the acceleration, velocity, and displacement values have been obtained for the model with 3DOF in the works [12–14]. From a practical point of view, selecting the appropriate inertia of the flywheel I_f is crucial.

Figure 6 presents angular displacement (Fig. 6a), angular velocity (Fig. 6b) and angular acceleration (Fig. 6c) of shaft in engine fueled by CNG. For $IAA_{CNG} = 10$

(a)

(b)

(c)
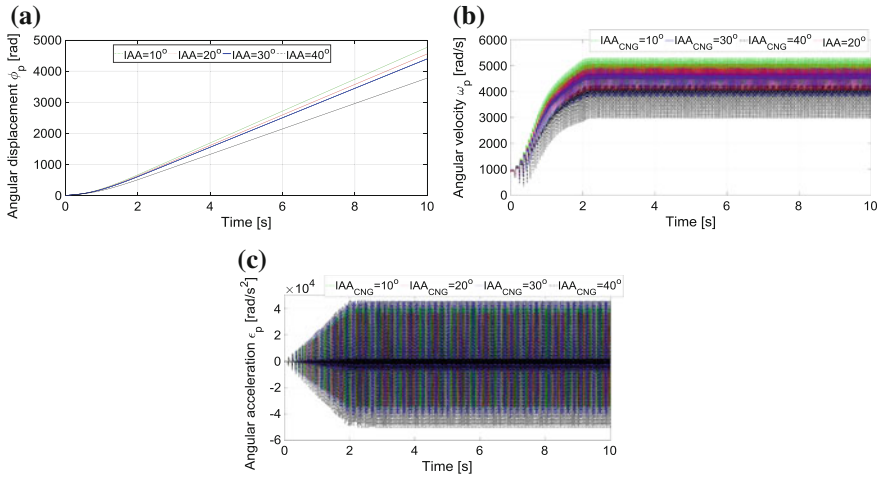
Fig. 6 Parameters of shaft of engine fueled by CNG: **a** angular displacement φ_p, **b** angular velocity ω_p, **c** angular acceleration ε_p

the assembly start up time is the shortest, at 1.95 s, $\omega_{pIAAA\_CNG=10}$=4990 rad/s (Fig. 6b). Angular accelerations in steady state don't exceed 4.2×10^4rad/s^2 and -5×10^4rad/s^2 for all ignition advance angles.

Figure 7 presents angular displacement (Fig. 7a), speed (Fig. 7b) and acceleration (Fig. 7c) of flywheel of engine fueled by CNG. Greatest increase in angular displacement can be observed in the first second after assembly start up, which accelerates (angular accelerations for all ignition advance angles increase). The highest values of angular accelerations appear for ignition advance angle IAA_{CNG}=40 . This is a result of increased pressure inside the combustion chamber, for IAA_{CNG}=40 p_{max}=5.2 MPa (Fig. 2).As a consequence, greater forces affect the flywheel (visible higher amplitudes of angular speed changes—Fig. 7b).

5 Conclusions

In the article, a model of the piston and crankshaft assembly with 2 degrees of freedom is presented. The model was paired with a chart of indicated pressure changes inside the combustion chamber, acquired from experimental research. To describe the changes of pressure inside the combustion chamber, a zero-dimensional analytical model using the law of conservation of energy was used.

Presented simulations show, that for all ignition advance angles the angular accelerations in steady state do not exceed 4.2×10^4rad/s^2 and -5×10^4rad/s^2.

The greatest increase in angular displacement can be observed in the first second after assembly start up, as it is accelerating (angular accelerations for all ignition

(a)

(b)

(c)
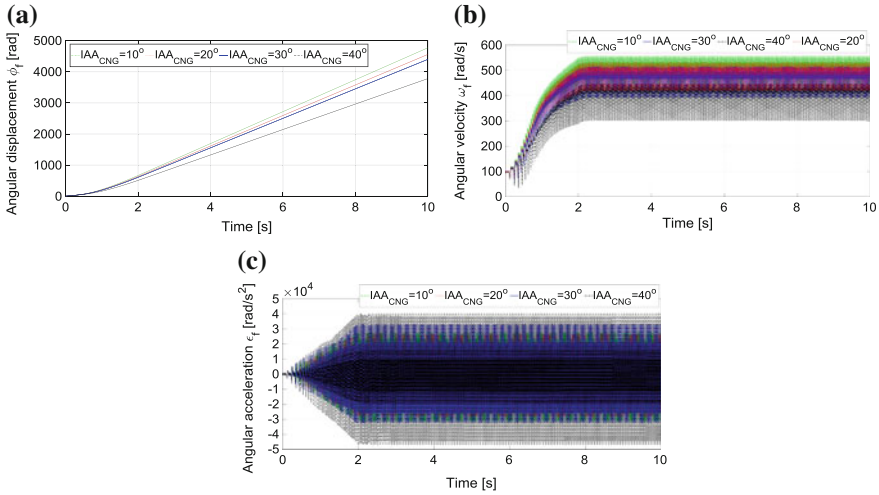
Fig. 7 Parameters of flywheel of engine fueled by CNG: **a** angular displacement φ_f, **b** angular velocity ω_f, **c** angular acceleration ε_f

advance angles increase). The highest values of angular accelerations (Fig. 7c) appear for ignition advance angle $IAA_{CNG} = 40$. This is a result of increased pressure inside the combustion chamber, for $IAA_{CNG} = 40$ $p_{max} = 5.2$ MPa.

The analysis presented in this work and the proposition of merging a piston and crankshaft assembly model with 2 degrees of freedom with a thermodynamic model that takes into account the combustion processes opens up new possibilities of modeling combined systems (mechanical domain—thermodynamic domain).

Below are presented the mechanical equations coupled with equations governing the pressure change.

$$\ddot{\varphi}_p = \frac{r(pA_p - m_p\ddot{x}_p)}{I_p} \frac{\left(\sin\varphi_p\sqrt{1 - \lambda^2\sin^2\varphi_p} + \lambda\sin\varphi_p\cos\varphi_p\right)}{\sqrt{1 - \lambda^2\sin^2\varphi_p}} - \frac{k}{I_p}(\varphi_p - \varphi_f)$$

$$\ddot{\varphi}_f = \frac{k}{I_f}(\varphi_p - \varphi_f)$$

$$\ddot{x}_p = \frac{d^2 x_{p0}}{dt^2} = r\left[\ddot{\varphi}_p\left(\sin\varphi + \frac{\lambda}{2}\sin 2\varphi_p\right) + \dot{\varphi}_p^2(\cos\varphi_p + \lambda\cos 2\varphi_p)\right]$$

$$\frac{dp}{d\varphi_p} = \frac{n-1}{V_c}\left(\frac{dQ_h}{d\varphi_p} - \frac{dQ_{hetr}}{d\varphi_p}\right) - \frac{n}{V_c}p\frac{dV_c}{d\varphi_p} \rightarrow p\,(by\ numerical\ solution\ we\ can\ find\ p)$$

$$\frac{dQ_h}{d\varphi_p} = w_1\frac{w_2+1}{\varphi_{d0}}\left(\frac{\varphi_{\deg} - \varphi_0}{\varphi_{d0}}\right)^{w_2}\exp\left\{-w_1\left(\frac{\varphi_{\deg} - \varphi_0}{\varphi_{d0}}\right)^{w_2+1}\right\}g_f W_u;\ \varphi_{\deg}[\deg] = \varphi[rad]\frac{180^o}{\pi}$$

$$\varphi_0 = IAA + 25.5 p_{\text{in manifold}} - 0.0605\dot{\varphi}_p - 0.2801 p_{\text{in manifold}}\dot{\varphi}_p + 6.88 \times 10^{-4}\dot{\varphi}_p^2$$

$$\frac{dQ_h}{d\varphi_p} = \frac{c_v}{R}\left(p\frac{dV_c}{d\varphi_p} + V_c\frac{dp}{d\varphi_p}\right) + p\frac{dV_c}{d\varphi_p} + \frac{dQ_{hetr}}{d\varphi_p} \rightarrow \frac{dp}{d\varphi_p}$$

$$\frac{dQ_{hert}}{dt} = hA(T_{gas} - T_{spt}) = \overbrace{St\varsigma c_p v}^{h} A\left(\frac{pV_c}{m_{air}R} - T_{spt}\right) = St\varsigma\overbrace{\frac{R}{1 - \frac{1}{n}}}^{c_p} vA\left(\frac{pV_c}{m_{air}R} - T_{spt}\right) =$$

$$0.715\exp(-0.14(\dot{x}_{p\,mean}))\varsigma\frac{R}{1 - \frac{1}{n}}vA\left(\frac{pV_c}{m_{air}R} - T_{spt}\right)$$

$$V_c = \overbrace{\frac{\frac{\pi d^2}{4}S|_{S=2r}}{\varepsilon - 1}}^{V_{sc}} + \frac{\pi d^2}{4}\overbrace{r\left\{(1 - \cos\varphi_p) + \frac{1}{\lambda}(1 - \sqrt{1 - \lambda^2\sin^2\varphi_p})\right\}}^{x_p} = V_{sc} + \frac{\pi d^2}{4}x_p$$

$$\frac{dV_c}{d\varphi_p} = \frac{\pi d^2}{4}\overbrace{r\dot{\varphi}_p\left\{\sin\varphi_p + \frac{\lambda}{2}\sin 2\varphi_p\right\}}^{\dot{x}_p}\frac{\pi d^2}{4}$$

References

1. Chmielewski, A., Gumiński, R., Mączak, J., Radkowski, S., Szulim, P.: Aspects of balanced development of RES and distributed micro–cogeneration use in Poland: case study of a mCHP with Stirling engine. Renew. Sustain. Energy Rev. **60**, 930–952 (2016)
2. Milewski, J., Szabłowski, Ł., Kuta, J.: Control strategy for an internal combustion engine fuelled by natural gas operating in distributed generation. Energy Procedia **14**, 1478–1483 (2012)
3. Szabłowski, Ł., Milewski, J., Kuta, J., Badyda, K.: Control strategy of a natural gas fuelled piston engine working in distributed generation system. Rynek Energii **3**, 33–40 (2011)
4. Chmielewski, A., Gontarz, S., Gumiński, R., Mączak, J., Szulim, P.: Research study of the micro cogeneration system with automatic loading unit. In: Szewczyk, R., Zieliński, C., Kaliczyńska, M. (eds.) Challenges in Automation, Robotics and Measurement Techniques. Advances in Intelligent Systems and Computing, vol. 440, pp. 375–386. Springer, Cham (2016)
5. Nunes de Faria, M.M., Vargas Machuca Bueno, J.P., Elmas Alami Ayad, S.M.M., Pereira Belchior, C.R.: Thermodynamic simulation model for predicting the performance of spark ignition engines using biogas as fuel. Energy Conversion and Management (2017) (in print)

6. Mydłowski, T., Nader, S., Biskup, K., Jasiński, M.: Wykorzystanie urządzenia ECU Master EMU do sterowania silnikami z zapłonem iskrowym (Using the ECU Master EMU device to control spark ignition combustion engines). Zeszyty Naukowe Instytutu Pojazdów **86**, 125–129 (2011) (in Polish)

7. Małecki, A., Mydłowski, T., Dybała, J.: Badania wpływu zanieczyszczeń biopaliw na sprawność silnika ZI (Research on the impact of biofuels pollutants on the SI engine efficiency). Zeszyty Naukowe Instytutu Pojazdów **99**, 89–97 (2014) (in Polish)

8. Chmielewski, A., Gumiński, R., Mydłowski, T., Małecki, A., Bogdziński, K.: Research study of HONDA NHX 110 powered by an alternative fuel. In: IOP Conference Series: Earth and Environmental Science (EES), Second International Conference on the Sustainable Energy and Environmental Development, SEED 2017 Cracow (in Print)

9. Małecki, A., Mydłowski, T., Dybała, J.: Stanowisko hamowniane do badań silników spalinowych o małych mocach (The engine dynamometer to test internal combustion engines with low power). Zeszyty Naukowe Instytutu Pojazdów **96**, 55–66 (2013) (in Polish)

10. Dybała, J., Mydłowski, T., Małecki, A., Bogdziński, K.: Dynamometer and test stand for low power internal combustion engine. Combust. Engines **162**, 996–1000 (2015)

11. Małecki, A., Mydłowski, T., Radkowski, S.: Przegląd uniwersalnych sterowników do silników ZI (Review of programmable electronic fuel injection controllers). Zeszyty Naukowe Instytutu Pojazdów **93**, 93–101 (2013)

12. Chmielewski, A., Gumiński, R., Radkowski, S.: Chosen properties of a dynamic model of crankshaft assembly with three degrees of freedom. In: 20th International Conference on Methods and Models in Automation and Robotics 978-1-4799-8701-6/15/$31.00 ©2015 IEEE, pp. 1038–1041 (2015)

13. Chmielewski, A., Gumiński, R., Mączak, J.: Selected properties of the dynamic model of the piston-crankshaft assembly in Stirling engine combined with the thermodynamic submodel. Int. J. Struct. Stab. Dyn. **17**, 1740009 (25 pages) (2017)

14. Chmielewski, A., Gumiński, R., Mączak J., Selected properties of the adiabatic model of the stirling engine combined with the model of the piston-crankshaft system. In: 21st International Conference on Methods and Models in Automation and Robotics (MMAR), 978-1-5090-1866-6/16/$31.00 ©2016 IEEE, pp. 543–548 (2016)

15. Awrejcewicz, J., Kudra, G.: The triple pendulum with barriers and the Piston—connecting rod—cranckshaft model. J. Theor. Appl. Mech. **1**(45), 15–23 (2007)

16. Kudra, G., Awrejcewicz, J.: Modeling and numerical investigation of non-linear dynamics of a mono-cylinder combustion engine. IN: Proceedings of DETC'03 ASME 2003 Design Engineering Technical Conferences and Computers and Information in Engineering Conference, Chicago, Illinois, USA, pp. 1–9 (2003)

17. Pham, P.X., Vo, D.Q., Jazar, R.N.: Development of fuel metering techniques for spark ignition engines. Fuel **206**, 701–715 (2017)

18. Wu, Y.Y., Chen, B.-C., Hsieh, F.C.: Heat transfer model for small-scale air-cooled spark-ignition four-stroke engines. Int. J. Heat Mass Transf. **49**, 3895–3905 (2006)

19. Wu, Y.Y., Chen, B.C., Hsieh, F.C., Ke, C.T.: Heat transfer model for small-scale spark-ignition engines. Int. J. Heat Mass Transf. **52**, 1875–1886 (2009)

20. Morrone, P., Algieri, A., Bova, S.: Development of a lumped model for the characterization of the intake phase in spark-ignition internal combustion engines. Energy Procedia **101**, 590–597 (2016)

21. Nunes, M.M., Vargas Machuca Bueno, J.P., ElmassalamiAyad, S.M.M., Belchior, C.R.P.: Thermodynamic simulation model for predicting the performance of spark ignition engines using biogas fuel. Energy Convers. Manage. **149**, 1096–1108 (2017)

22. Chaudhari, A.J., Sahoo, N., Kulkarni, V.: Simulation models for spark ignition engine: a comparative performance study. Energy Procedia **54**, 330–341 (2014)

23. Chen, B.C., Wu, Y.Y., Hsieh, F.C.: Estimation of engine rotational dynamics using Kalman filter based on a kinematic model. IEEE Trans. Veh. Technol. **8**(59), 3728–3735 (2010)

Experimental Evaluation of Mathematical and Artificial Neural Network Modeling of Energy Storage System

Adrian Chmielewski, Jakub Możaryn, Robert Gumiński, Krzysztof Bogdziński and Przemysław Szulim

Abstract This article presents an experimental evaluation based on a mathematical model and an artificial neural network (ANN) model of an energy storage system. Because of a nonlinear description of charging/discharging dynamics in subsequent cycles and a coupling of the terminal voltage and temperatures of a battery, the recurrent artificial neural network structure (R-ANN) is proposed. Both models, analytical and R-ANN were employed to predict a behavior of the VRLA AGM battery. A training and testing data were gathered at the laboratory stand in different working conditions. As a result, we present the analysis of differences between proposed modeling approaches.

Keywords Recurrent artificial neural network · Energy storage · Experimental evaluation · VRLA AGM battery

A. Chmielewski (✉) · R. Gumiński · K. Bogdziński · P. Szulim
Faculty of Automotive and Construction Machinery Engineering, Institute of Vehicles,
Warsaw University of Technology, Narbutta 84, 02–524 Warsaw, Poland
e-mail: a.chmielewski@mechatronika.net.pl

R. Gumiński
e-mail: rgumin@simr.pw.edu.pl

K. Bogdziński
e-mail: k.bogdzinski@mechatronika.net.pl

P. Szulim
e-mail: p.szulim@mechatronika.net.pl

J. Możaryn
Faculty of Mechatronics, Institute of Automatic Control and Robotics,
Warsaw University of Technology, Św A. Boboli 8, 02-525 Warsaw, Poland
e-mail: j.mozaryn@mchtr.pw.edu.pl

1 Introduction

To improve algorithms for prediction and control in Battery Management Systems (BMS) for distributed systems it is essential to know the operating curves of typical electrochemical batteries, which can be supported by mathematical models. This approach plays important role in hybrid systems [1–4]. Research of a dynamic operation of an electrochemical battery [5] in a specific load cycle supported by a mathematical model (e.g. energy balance model, neural network model, ARMA model, fuzzy model [6]) can give answers to different questions regarding the operation of batteries [7–11] in technical facilities. It should be also emphasized, that the energy storage modeling gets recently an increasing interest connected with new developments in the field of electric vehicles [12, 13] or polygeneration systems [14–16].

Charging/discharging dynamics of an energy storage system is highly nonlinear, especially during a rapid discharging phase. Therefore, to simplify an identification procedure we propose to use artificial neural networks (ANN). They have some important advantages over standard linear identification methods i.e. an approximation of multivariable nonlinear functions, an easy adaptation of model parameters and a very rapid calculation of model equations. In contrary to energy-balance models, designing ANN does not require an exact knowledge of model functions, and physical parameters that describe the model, but only values of model variables (cause-effect relationships).

In energy storage systems usefulness of ANNs for identification were proposed mostly in the form of feed-forward models and recurrent models [17–21]. In particular, interesting for our research are Simple Recurrent Neural Networks (SRNNs)—where connections between units form a directed cycle. Such networks exhibit dynamic temporal behavior, a property that can be utilized for the prediction of the State of Charge (SoC) of the energy storage system in subsequent charge/discharge cycles. With properly chosen battery data, system parameters and operating conditions, recurrent ANN model can be used in prediction to some extent a battery performance under a wide variety of operating conditions.

The article is organized as follows. In Sect. 2 a test stand of electrochemical energy storage systems (VRLA AGM battery) is described. Section 3 presents an analytical model of the electrochemical battery. Then, in Sect. 4, recurrent ANN (R-ANN) model of energy storage system is presented. In Sect. 5 analytical and R-ANN models are subsequently validated and compared against experimental results. Finally, in Sect. 6, concluding remarks are given.

2 Test Stand with the Energy Storage System

To conduct an experimental research, the test stand has been prepared, complete with a data acquisition module, a load control unit and a software application for
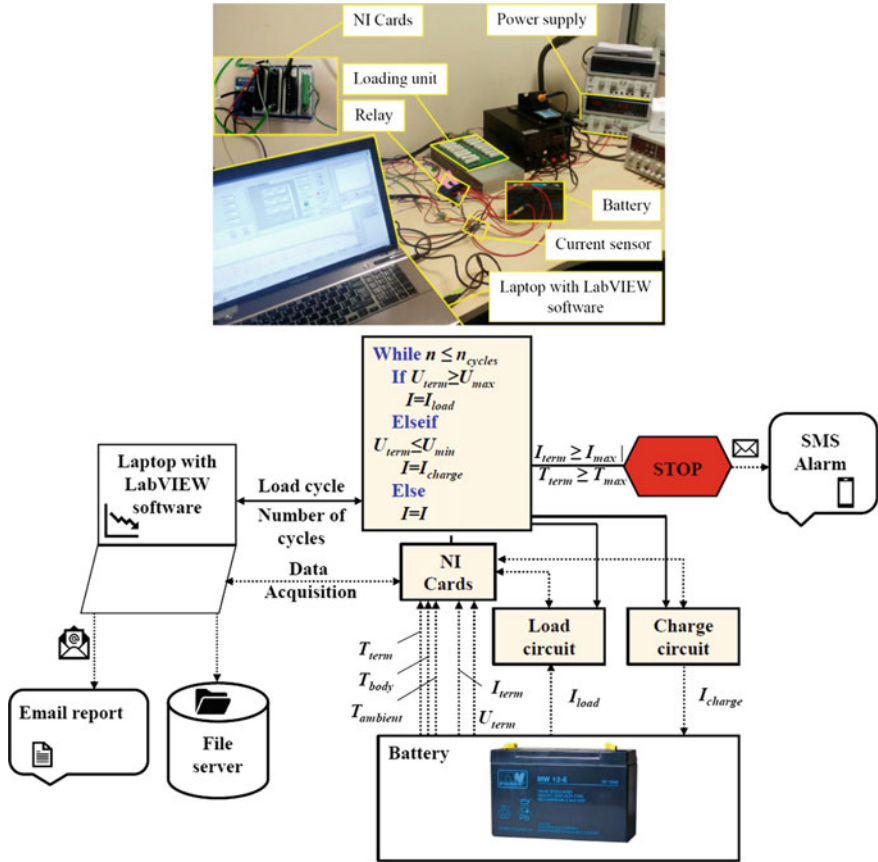
Fig. 1 The test stand

long duration tests (for a detailed description see [22]). The measurement circuit of the test stand (Fig. 1) consists of: a PC class computer, a modular data acquisition chassis (National Instruments hardware), a programmable laboratory power supply, a loading control unit (load circuit connects the battery to a controllable load power unit—the individual controllable current source which was prepared by authors) and the control application which has been written in LabVIEW 2016. The application allows for acquisition of the following parameters of the battery: voltage measured at the terminals of the battery, value of a charging/discharging current and a direction of current flow, an ambient temperature, temperatures at battery terminals and a battery body. All signals can be sampled up to the rate of 100 Hz.
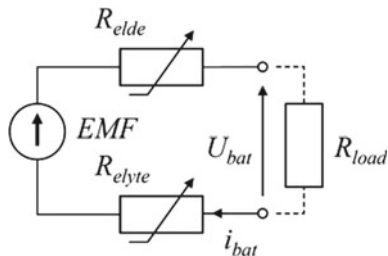
3 Mathematical Model of the Electrochemical Energy Storage System

Figure 2 presents a physical model of the battery and takes into account previous experimental research where the iteration-approximation method has been employed [22–24].

Based on the analysis of the Fig. 2, the internal resistance R_i of the battery can be calculated as:

$$R_i(i_{bat}, T, Q) = R_{elde}(T, Q) + R_{elyte} + bEMF(i_{bat}, T, Q)I_n^{-1}, \qquad (1)$$

where: R_{elde}, R_{eleyte}—electrodes and electrolyte resistance, respectively, $bEMF(i_{bat}, T, Q)I_n^{-1}$—ratio which defines the relative change of the electromotive force of the polarization during the flow of the nominal current I_n versus EMF for the nominal capacity of Q_n, R_{load}—resistance of the external load ($R_{load} = U_{load}/I_{load}$).

In this article the experimental data has been employed to determine R_i:

$$R_i = (U_m - U_{m+1})/(I_{m+1} - I_m) \qquad (2)$$

where: $U_m > U_{m+1}$ and $I_{m+1} > I_m$.

The family of U_m, U_{m+1} characteristics was determined during the experimental research described in [23–27]. Once R_i was determined, while transforming the below Eq. (9), it became possible to calculate the EMF, for charging (+) and discharging (−) respectively:

$$EMF = U_{term} \mp i_{bat}((U_m - U_{m+1})/(I_{m+1} - I_m)) \qquad (3)$$

The internal resistance of the battery R_i was determined using the iteration-and-approximation method [25] and subsequently it was used in the simulation model in order to account for the change of the battery's resistance depending on the change of its SOC. The properties of the electrochemical battery were defined by using the Peukert's equation, described in detail in [23–25].

The following relation has been used for the purpose of mathematical modeling of a battery's effective capacity:

$$Q_{Bat}(i_{bat}, t, T) = c_T(T)\eta(i_{bat}, T)Q_n \pm \int_0^t i_{bat}(t)dt \qquad (4)$$

Knowing that the battery's state of charge is the ratio of its effective capacity to nominal capacity, one can write:

$$SOC = \frac{Q_{Bat}}{Q_n} = \frac{w_T(T)\eta(i_{bat}, T)Q_{nom} - \int_0^t i_{bat}(t)dt}{Q_n}$$

$$= \overbrace{w_T(T)\eta(i_{bat}, T)|_{\substack{i_{bat} \cong I_n \\ T \cong T_n}}}^{\cong 1} - \frac{1}{Q_{nom}}\int_0^t i_{bat}(t)dt = 1 - \frac{1}{Q_{nom}}\int_0^t i_{bat}(t)dt \quad (5)$$

The EMF electromotive force, which depends on the SoC, can be expressed in the following form:

$$EMF(SOC) = EMF_{\min} + \Delta U_{term} \cdot SOC$$
$$= EMF_{\min} + (EMF_{\max} - EMF_{\min}) \cdot SOC \qquad (6)$$

Values of $EMF_{\min}$ and $EMF_{\max}$ have been determined on the basis of experiments [23, 26, 28].

4 Design of the Artificial Neural Network Model of the Energy Storage System

In the ANN modeling there was studied the dependence of the voltage (U_{term}) of the battery terminals as a function of the charging/discharging current load (I_{term}), the ambient temperature ($T_{ambient}$), the battery body temperature (T_{body}) and the temperature at battery terminals (T_{term}). Datasets were gathered at laboratory test stand described in Chap. 2.

Because of a nonlinear description of charging/discharging dynamics in specific cycles and the coupling of the terminal voltage and temperatures of a battery, the recurrent artificial neural network structure (R-ANN) of Jordan type was chosen, where context units are fed from the output layer [29, 30]. The proposed R-ANN has 1 hidden layer of n nonlinear neurons described by a sigmoidal activation function:
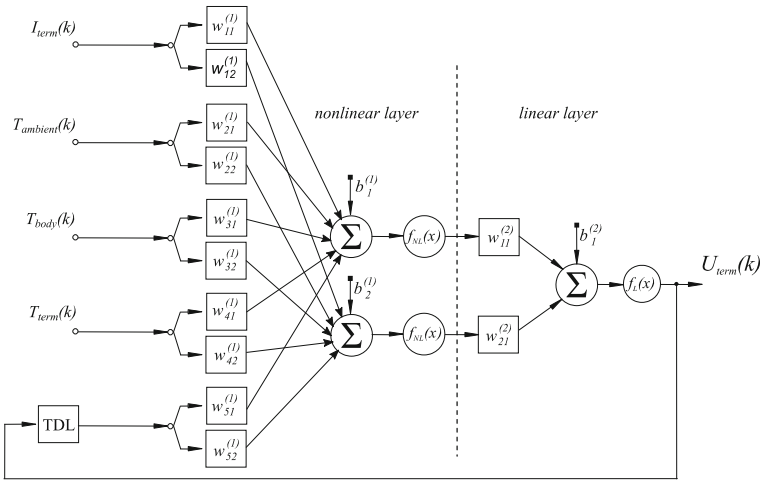
Fig. 3 RNN structure with two neurons in hidden layer, and 1 neuron in output layer

$$
\begin{aligned}
y_{(j)NL}^{(1)}(k) &= f_{(j)NL}^{(1)}(x_{(j)NL}^{(1)}, k) = \tan sig(x_{(j)NL}^{(1)}, k) \\
&= \frac{2}{1 + e^{-2x_{(j)NL}^{(1)}(k)}} - 1, \ f_{(j)NL}^{(1)} \in [-1, 1]
\end{aligned} \tag{7}
$$

and a linear output layer, with 1 neuron described by a linear activation function:

$$
y_L^{(2)}(k) = f_L^{(2)}(x_L^{(2)}, k) = x_L^{(2)}(k), \ f_L^{(2)} \in R \tag{8}
$$

where:

$$
x_{(n)NL}^{(1)}(k) = b_{(n)}^{(1)} + w_{p+1n}^{(1)}y_L^{(2)}(k-1) + \sum_{i=1}^{p} w_{in}^{(1)}x_i(k) \tag{9}
$$

$$
x_{(n)L}^{(2)}(k) = b_{(n)}^{(2)} + \sum_{i=1}^{n} w_{i1}^{(2)}y_{(i)NL}^{(1)}(k) \tag{10}
$$

P—the number of neuron inputs in nonlinear hidden layer, $w_{ij}^{(m)}$—the weight of the i-th input to j-th neuron in layer m, x_i—the i-th input to the network, $b_{(n)}^{(m)}$- the threshold offset of the n-th neuron in layer m.

The exemplary 2-layer R-ANN neural network structure used to model energy storage system, described by (7)–(10) is presented in Fig. 3.
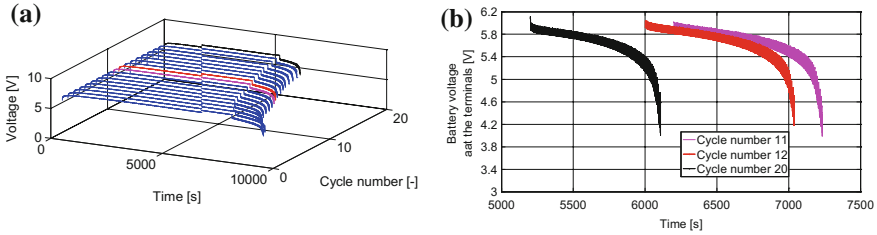
Fig. 4 **a** 20 consecutive cycles in the experiment, **b** cycles chosen for preparation and validation of analytical and ANN models

5 Evaluation of the Analytical and ANN Models of Energy Storage System

5.1 Experimental Datasets

The experiment was prepared on a 6 V 12 Ah valve regulated sealed lead-acid type rechargeable battery (VRLA). The battery charge cycle process was set to 2.1 A and was carried out until a maximum voltage of 6.6 V was reached, after which the battery was switched to load circuit. The load cycle selected for the experiment was a repeating draw of 8, 12 and 16 A, each load of 3 s duration, respectively. The load cycle was carried out until a minimal voltage of 4 V of the battery.

There were chosen 3 datasets (Fig. 4a), based on the performed experiments. Figure 4b) shows selected datasets during discharging for validation analytical and R-ANN models.

First, to calculate coefficients of models of the discharge dynamics of VRLA AGM battery, the dataset from the experiment 11 was used. Then, the datasets from experiments 12 and 20 were chosen to check the generalization and prediction properties of models.

Preliminary analysis showed, that within the datasets concerned, variables are correlated to a very small extent. Moreover, the lag time was significantly larger than the sampling of signals measured at the laboratory stand. Therefore there were selected every 30th measurement sample as a data for training of R-ANN model. It still ensured adequate coverage of the measurement range for both training data and testing data, and greatly reduced the R-ANN training time.

5.2 Evaluation of Analytical Model of Energy Storage System

Based on Eqs. (1–6) the analytical model has been created and simulated. The dynamic cycle has been implemented in the simulation model (the same as in the case of the conducted experiment—Fig. 5a). Figure 5b presents the curve of the
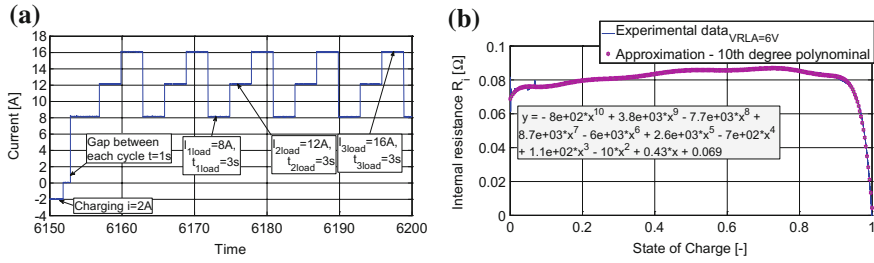
Fig. 5 **a** Load cycle from experimental research, **b** internal resistance of the battery from experimental research—implemented in simulation

internal resistance of the VRLA AGM battery. The change of internal resistance was described by 10-degree polynomial. The approximated general equation has been implemented to simulate a battery.

5.3 Evaluation of R-ANN Model of Energy Storage System

During an evaluation, there was investigated the efficiency of R-ANN models trained in a batch mode using backpropagation and Lavenberg-Marquardt algorithms [29–32]. For each R-ANN all weights and biases were initialized using Nguyen-Widrow initialization procedure [31].

Let us denote error of the battery voltage estimation as follows

$$e(k) = y_i(k) - y_{NNi}(k) \tag{11}$$

where: $y_i(k)$—modeled signal (voltage of the battery terminals), $y_{NNi}(k)$—R-ANN output, k—sample number.

The performance function of R-ANN was chosen as a mean squared error:

$$MSE = \frac{1}{N} \sum_{k=1}^{N} [e(k)]^2 \tag{12}$$

where: N—the number of data samples.

During R-ANN training the following stop conditions were chosen: $epochs < 500$ or $MSE = 0.001$.

The quality of R-ANN model of the energy storage system was evaluated using (13) and following indices [31–33]:

- average absolute error [V]:

$$e_{av} = \frac{1}{N} \sum_{k=1}^{N} |e(k)| \tag{13}$$

- maximum absolute error [V]:

$$e_{\max} = \max_{N} |e(k)| \tag{14}$$

There were trained and tested R-ANNs with 2, 3, 5, and 10 neurons in hidden layer, with the estimated number of weights equal to 15, 22, 36 and 71 respectively. This is in compliance with the required number of samples in training set, that should be at least two times bigger than the estimated number of weights [31].

The main problem during the analysis of results is a big number of estimated signals and gathered data. This makes the evaluation of the repeatability of obtained models problematic. Therefore, we propose to use aggregate statistical indicators for the set of models with similar structures [33]:

- Estimation of the expected value of maximal relative average error of the voltage approximation:

$$m_{sav} = \frac{1}{L} \sum_{j=1}^{L} \left| \frac{\sum_{k=1}^{N} e^j(k)}{\sum_{k=1}^{N} y(k)} \right| \tag{15}$$

- Estimation of the expected value of maximal relative average absolute error of the voltage approximation:

$$m_{sava} = \frac{1}{L} \sum_{j=1}^{L} \frac{\sum_{k=1}^{N} |e^j(k)|}{\sum_{k=1}^{N} |y(k)|} \tag{16}$$

where: L—the number of neural models with the same structure, $e^j(k)$—the error (11) calculated for j-th model.

Quality index (15) allows estimating the relative steady error for the set of neural models, whereas index (16) allows estimating the relative absolute error for the set neural models, and is a measure of dispersion of relative error around the average value. The presented criterions can be used for general comparison of different ANN models [32–34].
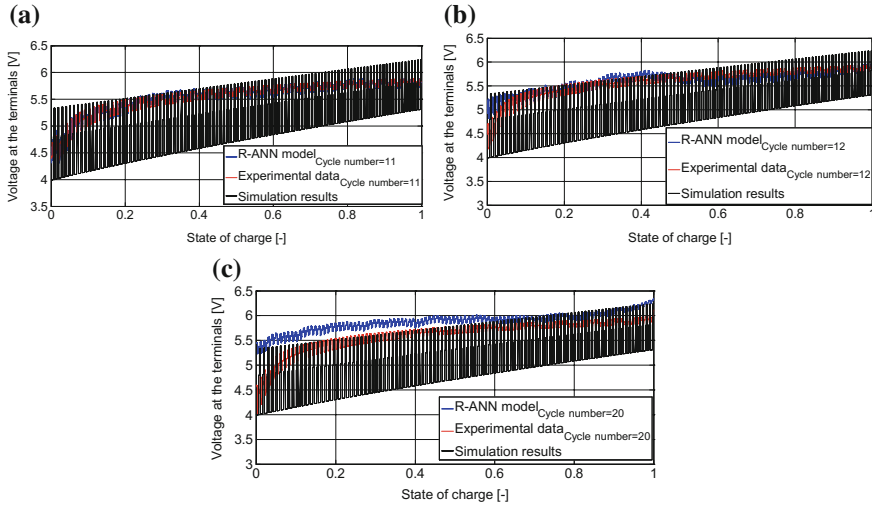
Fig. 6 Comparison of voltage curves for experimental research, R-ANNs model and analytical model for: **a** 11th cycle—approximation, **b** 12th cycle—prediction, **c** 20th cycle—prediction

5.4 Comparison of Analytical and R-ANN Models of Energy Storage System

Figure 6 presents comparison results for R-ANN, simulation model, and experimental research, for 11th (approximation), 12th (prediction), 20th (prediction) cycles. For analytical model, in all cases, the maximum error does not exceed 19.5% between the simulation results for the analytical model and the experimental data.

In Table 1 there are gathered quality indices (13)–(15) and aggregated quality indices[1] (6)–(7) for R-ANNs before and after training with different parameters identifying dynamical models of considered energy storage system.[2]

Results show, that training of R-ANNs using Lavenberg-Marquardt method gives good results for the training data. For all identified in this research R-ANNs an average absolute error decreases around 250 times (1–3% of error in relation to modeled output) and a maximum absolute error decreases around 25 times (5–10% of modeled output). Observed results show, that the values of quality indices (28)–(30) don't differ significantly as the number of neurons in hidden layer grow.

The testing data was predicted with less accuracy than training data. As it can be seen in Table 1 for prediction of data from 12th cycle (next cycle) an average absolute error improves only around 75 times (10% in relation to modeled output) and

---

[1]Aggregated quality indexes we calculated for L = 20

[2]To simplify the description, network structure was represented as #*mnn-method-#epochs* where: #*mnn-* number of neurons in nonlinear hidden layer, *method-* training method acronym, #*epochs-* number of training epochs (e.g. 2-LM-500 is R-ANN with 2 neurons in hidden layer, trained with Levenberg-Marquardt algorithm in 500 epochs).

Table 1 Quality indices for R-ANNs of energy storage system

R-ANN structure	Data set	Training time	MSE	e_{av}	e_{max}	m_{sav}	m_{sava}
R-ANN without training	Train, experiment 11	–	26.4356	5.0597	7.5876	4.98004	4.53681
	Test, experiment 12		57.1378	7.5512	8.1141	1.32033	9.84298
	Test, experiment 20		50.8929	7.1285	7.4127	4.76109	4.76109
2-LM-500	Train, experiment 11	~9 s	0.0012	0.0200	0.2655	1.5×10^{-7}	0.00550
	Test, experiment 12		0.0229	0.1120	0.7079	0.00882	0.01320
	Test, experiment 20		0.1737	0.3483	1.5946	0.07133	0.07133
3-LM-500	Train, experiment 11	~12 s	0.0009	0.0215	0.3664	49.5×10^{-7}	0.00537
	Test, experiment 12		0.0209	0.0939	0.7888	0.00124	0.00391
	Test, experiment 20		0.1117	0.2676	1.3613	0.05595	0.05595
5-LM-500	Train, experiment 11	~19 s	0.0010	0.0243	0.3475	2510×10^{-7}	0.00601
	Test, experiment 12		0.0195	0.0993	0.7791	0.02704	0.03594
	Test, experiment 20		0.0669	0.2129	0.8102	0.06559	0.07487
10-LM-500	Train, experiment 11	~45 s	0.0007	0.0200	0.3105	402.9×10^{-7}	0.00297
	Test, experiment 12		0.0182	0.0948	0.7213	0.01124	0.01754
	Test, experiment 20		0.1053	0.3001	0.7721	0.03857	0.03857

maximum absolute error improves around 10 times (15–25% in relation to modeled output). For prediction of data from 20th cycle (9 cycles ahead) an average absolute error improves only around 25 times (around 20% in relation to modeled output) and maximum absolute error improves around 10 times (15–25% in relation to modeled output). Also aggregated quality indexes show that the precision of SoC forecasting with R-ANN models and their repeatability decrease as the number of predicted cycles increase.

Obtained results (Fig. 6 and Table 1) show significant differences between the analytical model and R-ANN model. For 11th and 12th cycle, approximation and prediction errors for R-ANN models were smaller almost 7–10 times than for the analytical model. For the 20th cycle results were similar for both models.

6 Conclusions

The article presents the possibility of predicting State of Charge (SOC) of the electrical energy storage system in subsequent charging/discharging cycles. The study was conducted with electrolytic battery (VRLA AGM type) in a dynamic cycle. Three datasets were selected for calculation of parameters and verification of analytical

and R-ANN models. For the analytical model the maximum error did not exceed 19.5%—for approximated and predicted cycle. The results for proposed R-ANN model were better than for the calculated analytical model for 2 subsequent cycles. However, prediction errors significantly increased where there were more cycles. Hence, for the presented research, SoC forecasting using proposed R-ANN can't exceed few (1–2) cycles ahead.

In order to properly correct the model, reduce the maximum error between the signals estimated with analytical or R-ANN model and the experimental results, it is necessary to take into account the changes of the electrical energy storage system properties in subsequent cycles (charging/discharging). On the basis of performance studies of several dozen or several hundred cycles, by obtaining a set of cycle time points, an attempt can be made to determine the general form of the polynomial of such changes. Then it can be implemented in the analytical or R-ANN model in the form of additional feedback.

The presented approach opens up new possibilities for the modeling and the forecasting the properties of electrochemical energy storage systems and is important in the practical application of such mathematical models (analytical, energy-based models or artificial neural networks), especially in BMS for distributed polygeneration systems and electric vehicles.

References

1. Micallef, A., Apap, M., Spiteri-Staines, C., Guerrero, J.M.: Mitigation of harmonics in grid-connected and islanded microgrids via virtual admittances and impedances. IEEE Trans. Smart Grid **2**(8), 651–661 (2015)
2. Chia, Y.Y., Lee, L.H., Shafiabady, N., Isa, D.: A load predictive energy management system for supercapacitor-battery hybrid energy storage system in solar application using the support vector machine. Appl. Energy **137**, 588–602 (2015)
3. Kalogirou, S.A., Mellit, A.: Artificial intelligence techniques for photovoltaic applications: a review. Prog. Energy Combust. Sci. **34**, 574–632 (2008)
4. Koohi-Kamali, S., Rahim, N.A., Mokhlis, H., Tyagi, V.V.: Photovoltaic electricity generator dynamic modeling methods for smart grid applications: a review. Renew. Sustain. Energy Rev. **57**, 131–172 (2016)
5. Kularatna, N.: Energy storage devices—a general overview. Energy Storage Devices Electron. Syst. 1–28 (2015)
6. Shun-Hung, T., Yu-Wen, C.: A novel identification method for Takagi-Sugeno fuzzy model. Fuzzy Sets Syst. **338**, 117–135 (2018)
7. Lai, Y., Du, S., Ai, L., Ai, L., Cheng, Y., Tang, Y., Jia, M.: Insight into heat generation of lithium ion batteries based on the electrochemical-thermal model at high discharge rates. Int. J. Hydrogen Energy **40**, 13039–13049 (2015)
8. Li, J., Cheng, Y., Jia, M., Tang, Y., Lin, Y., Zhian, Z., Liu, Y.: An electrochemical-thermal model based on dynamic responses for lithium iron phosphate battery. J. Power Sour. **255**, 130–143 (2014)
9. Saito, Y., Shikano, M., Kobayashi, H.: Heat generation behavior during charging and discharging of lithium-ion batteries after long-time storage. J. Power Sour. **244**, 294–299 (2013)
10. Li, J., Wang, L., Lyu, C., Wang, H., Liu, X.: New method for parameter estimation of an electrochemical-thermal coupling model for $LiCoO_2$ battery. J. Power Sour. **307**, 220–230 (2016)

11. Gu, W.B., Wang, C.Y.: Thermal-electrochemical modeling of battery systems. J. Electrochem. Soc. **147**, 2910–2922 (2000)

12. Chmielewski, A., Szulim, P., Gregorczyk, M., Gumiński, R., Mydłowski, T., Mączak, J.: Model of an electric vehicle powered by a PV cell—a case study. In: 22nd International Conference on Methods and Models in Automation & Robotics, Międzyzdroje, 1009–1014, (2017). DOI: https://doi.org/10.1109/mmar.2017.8046968

13. Szumanowski, A., Chang, Y., Piórkowski, P.: Analysis of different control strategies and operating modes of compact hybrid planetary transmission drive. In: IEEE Vehicle Power and Propulsion Conference, Chicago, 673–680 (2005)

14. Collazos, A., Maréchal, F., Gähler, C.: Predictive optimal management method for the control of polygeneration systems. Comput. Chem. Eng. **33**(10), 1584–1592 (2009). https://doi.org/10.1016/j.compchemeng.2009.05.009

15. Chaoui, H., Ibe-Ekeocha, Chinemerem, C., Gualous H.: Aging prediction and state of charge estimation of a LiFePO4 battery using input time-delayed neural networks. Electr. Power Syst. Res. **146**, 189–197 (2017)

16. Chmielewski, A., Gumiński, R., Mączak, J., Radkowski, S., Szulim, P.: Aspects of balanced development of RES and distributed micro cogeneration use in Poland: case study of a μCHP with Stirling engine. Renew. Sustain. Energy Rev. **60**, 930–952 (2016)

17. Lee, J., Kang, M.J., Park, G.L.: Battery consumption modeling for electric vehicles based on artificial neural networks. In: Computational Science and Its Applications—ICCSA 2014: 14th International Conference, Guimarães, Portugal, Proceedings, Part IV,, Springer International Publishing, 733–742 (2014) https://doi.org/10.1007/978-3-319-09147-1_53

18. Swan, D., Arikara, M., Patton, A.: Battery Modeling for Electric Vehicle Applications Using Neural Networks. SAE Technical Paper 931009, 1993, https://doi.org/10.4271/931009

19. O'Gorman, C.C., Ingersoll, D., Jungst, R.G., Paez, T.L.: Artificial neural network simulation of battery performance. In: Proceedings of the Thirty-First Hawaii International Conference on System Sciences, Kohala Coast, HI, vol. 5, 115–121 (1998) https://doi.org/10.1109/hicss.1998.648303

20. Abolhassani, M.N., Gharib, N., Moqtader, H., Hejabi, M., Amiri, M., Torabi, F., Mosahebi, A.: Prediction of state-of-charge effects on lead-acid battery characteristics using neural network parameter modifier. J. Power Sour. **158**(2), 932–935 (2006). https://doi.org/10.1016/j.jpowsour.2005.11.023

21. Ala, A.H.: Kalman filters versus neural networks in battery state of charge estimation: a comparative study. Int. J. Mod. Nonlinear Theory Appl. **3**, 199–209 (2014). https://doi.org/10.4236/ijmnta.2014.35022

22. Chmielewski, A., Bogdziński, K., Szulim, P., Mydłowski, T.: Test stand for operational research of Energy storage: description and preliminary research. Zeszyty Naukowe Instytutu Pojazdów—Proc. Inst. Veh. **113** (4), 33–39 (2017)

23. Chmielewski, A., Mączak, J., Szulim, P.: Experimental research and simulation model of electrochemical energy stores. Automation 2017, 15–17 March, Warsaw, Springer. Advances in Intelligent Systems and Computing, **550**, 236–246 (2017)

24. Szumanowski, A., Chang, Y., Piórkowski, P.: Method of battery adjustment for hybrid drive by modeling and simulation. IEEE, 681–687 (2005)

25. Szumanowski, A., Chang, Y.: Battery management system based on battery nonlinear dynamics modeling. IEEE Trans. Veh. Technol. **57**(3), 1425–1432 (2008)

26. Chmielewski, A., Mączak, J., Szulim P.: Experimental research of electrochemical energy storage. In: International Conference Automation 2017, Warsaw, Springer. Advances in Intelligent Systems and Computing, **550**, 227–235 (2017)

27. Zhoujian, A., Li, J., Liting, W., Chao, D., Qi, P.: Investigation on lithium-ion battery electrochemical and thermal characteristic based on electrochemical-thermal coupled model. Appl. Therm. Eng. **137**, 792–807 (2018)

28. Szumanowski, A.: Hybrid Electric Power Train Engineering and technology: Modeling, Control and Simulation. IGI Global Disseminator of knowledge, USA (2013)

29. Hagan, M.T., Demuth, H.B., Beale, M.H.: Neural Network Design. PWS Publishing, Boston (1996)
30. Hagan, M.T., Menhaj, M.: Training feed-forward networks with the Marquardt algorithm. IEEE Trans. Neural Netw. **5**(6), 989–993 (1994)
31. Nguyen, D., Widrow, B.: Improving the learning speed of 2-layer neural networks by choosing initial values of the adaptive weights. Proc. Int. Joint Conf Neural Netw. **3**, 21–26 (1990)
32. Osowski, S.: Neural Networks for Information Processing. OWPW, Warsaw (1994). (in Polish)
33. Możaryn J., Kurek J.E.: Relative error indices for comparison of neural models of different robots. In: Jablonski, R., Brezina, T. (eds.) Recent Advances In Mechatronics. Springer, 233–238 (2010) https://doi.org/10.1007/978-3-642-05022-0_40
34. Jordan, M.I.: Serial order: a parallel distributed processing approach. Adv. Psychol. **121**, 471–495 (1997)

Finite Element Analysis of a Configuration of Optomechatronic Choppers with Rotational Shafts

Eduard-Sebastian Csukas and Virgil-Florin Duma

Abstract We have introduced and patented a novel type of choppers with rotational shafts which can be operated at much higher speeds than classical choppers with rotational disks or with oscillatory elements. The aim of this preliminary study is to perform a Finite Element Analysis (FEA) using ANSYS of the fundamental issues of choppers with shafts, i.e. their structural stability and deformations—for their maximum possible rotational speed, of 120 krpm. The main steps of the FEA are pointed out. While different possible materials can be explored with regard to the maximum speed that the choppers are operated at, steel is considered in this study. The multi-parametric analysis is approached taking into account geometrical parameters of the device: radius and axial dimension of the shaft, shape, dimensions, and number of slits. The performances of the choppers with regard to their deformations and the highest possible rotational speed can be obtained from the analysis. Due to space limitations, preliminary results of this analysis for a one-slit shaft and the corresponding rules-of-thumb that can be extracted from it are briefly presented.

Keywords Optomechatronic devices · Optical choppers · Rotational shafts
Laser impulses · Finite element analysis (FEA) · Multi-parametric analysis

1 Introduction

Choppers are one of the most used optomechatronic devices for laser systems and applications [1], which include radiometers [2, 3], telescopes [4], lidars [5], laser manufacturing [6], X-rays [7], spectral [8, 9] or biomedical systems [10]. Choppers are used to generate controlled laser impulses [6], to attenuate light bundles [2, 3] or to analyze laser beams [11]. They have different types of moving parts, rotational or oscillatory, in macro- or micro-configurations, the latter built as Micro-Electro-Mechanical Systems (MEMS) [12, 13].

E.-S. Csukas · V.-F. Duma (✉)
"Aurel Vlaicu" University of Arad, Arad, Romania
e-mail: duma.virgil@osamember.org

The most common configuration of choppers, in a macro-device construct, is with rotational disks with windows with linear margins [14, 15], used both for generating laser impulses and for light attenuation, as an alternative to other such devices [16]. Besides these classical choppers, other devices have been proposed, also with rotational disks, but with windows with non-linear margins, semi-circular, outward or inward [17–19]; also with circular holes [20]. They are able to produce laser impulses with different shapes than classical devices [17].

However, all choppers with rotational disks have limited chop frequencies, due to their limited rotational speeds, even if the number of windows is increased—from the common disk with 2 windows up to even 100. In order to solve this issue, we have introduced—patent pending [20]—different configurations of choppers with fast rotational shafts that can reach nowadays spinning speeds of 60 krpm [21], and, with motors currently in development, even up to 120 krpm. On the other hand, due to these high speeds, issues can appear regarding the structural integrity and the deformations of such choppers; these aspects thus have to be studied with Finite Element Analysis (EA) [22]; this is the aim of the present study.

In the following, one of the configurations of the novel chopper with rotational shafts is presented in Sect. 2. Section 3 presents elements of the FEA for this most convenient variant of such devices, i.e. with cylindrical shafts with a single slit. In Sect. 3 the structural integrity and the deformations of such choppers are also pointed out, while Sect. 4 concludes the study.

2 Choppers with Rotational Cylindrical Shafts

The device is presented in Fig. 1. The axis of the laser beam is positioned perpendicular to the axis of the shaft.

During the rotational movement of the shaft the input laser beam is chopped by it and generates an output accordingly with the requirements of the application.

We have introduced different configurations of such choppers, with various shapes of the shafts (cylindrical, spherical, or conical); each can be done with longitudinal slits—as in Fig. 1—or with cylindrical holes that go through the axis of the shaft [21]. Advantages of these types of choppers with regard to choppers with disks [14, 15, 17–20] include: (a) easier and more precise mechanical tooling of the shafts; (b) the possibility to choose the proper material shaft based on its speed; (b) high performance mechanical strength; (c) interchangeable shafts during life time cycles.

3 FEA of Choppers with Rotational Shafts

For choppers with cylindrical rotational shafts in Fig. 1 we used the static-structural simulation load, in order to determine the strength of the shaft during functioning at the maximum rotational speed of 120 krpm. The main scope is to obtain the optimal

Fig. 1 Optomechatronic chopper with rotational cylindrical shaft. Notations: 1. rotational shaft (cylindrical); 2. first margin of the front slit; 3. incident laser beam; 4. Emergent (chopped) laser beam; 5. second margin of the front slit; 6. bottom part of the shaft; 7. cage; 8. rear slit
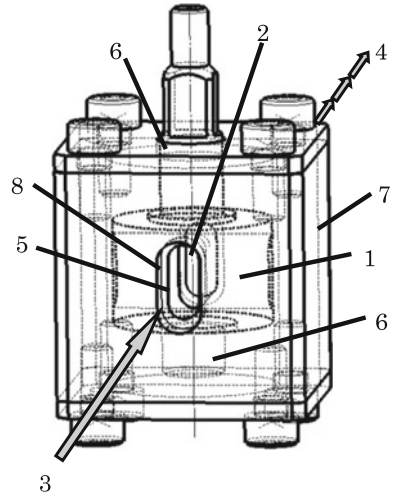
Fig. 2 Structure of a static-structural parametric simulation: cylindrical shaft with a slit
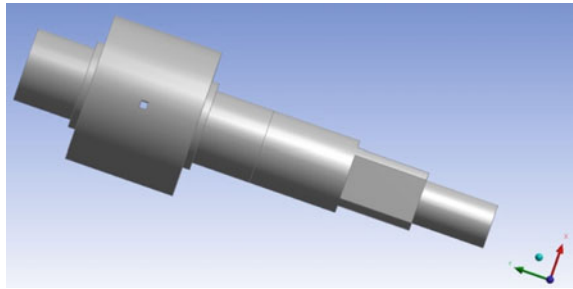
configurations of the chopper shaft taking into account the material properties; in this respect the shaft could be made from Composite Materials, Aluminum Alloys, Steel, and Beryllium. Besides rotational speed, the geometrical configurations and dimensions of the shaft have to be considered in this optimization process.

The case considered in this study is represented by a shaft with a square slit with a width from 1 to 5 mm (Fig. 2); other geometrical parameters are: diameter and length of the shaft, as well as the distance between its bearings. From these parameters we create a tight connection between them, obtaining 35 parameterized load cases (Fig. 3).

In this direction, for this geometry of the slit more cases with 2–5 across section slits were created. From such a study we can extract data regarding how to choose and use a chopper configuration for a specific application. To complete the FEA, it is suitable to use the indirect method to determine the stiffness matrix of a two-dimensional (2D) or a three-dimensional (3D) element.

To use this method it is necessary to follow the steps detailed below [22]:
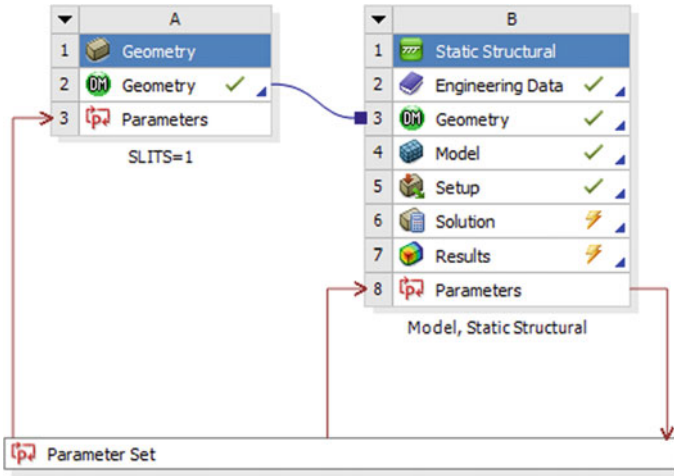
Fig. 3 Structure of a static-structural parametric simulation

(a) The elements displacements are defined; they refer to any point of an element, and are based on the formula:

$$\{U\} = \begin{Bmatrix} u(x, y, z) \\ v(x, y, z) \\ w(x, y, z) \end{Bmatrix} = [f(x, y, z)] \cdot \{a\} \tag{1}$$

where: $\{U\}$—displacement matrix of any point on element (3×1); $\{f(x, y, z)\}$—variable matrix of displacement field $(3 \times n)$; $\{a\}$—generalized coordinates matrix $(n \times 1)$.

(b) The computation of nodal displacements $\{U_e\}$, taking into account the general coordinates $\{a\}$ and geometrical characteristics $\{A\}$ of the elements:

$$\{U_e\} = [A] \cdot \{a\}, \tag{2}$$

where: $\{U_e\}$—unknown nodal displacement matrix of finite elements; $\{A\}$—geometrical characteristics of an element.

(c) Taking into account the nodal displacement, the general coordinates computation have the relation: $\{a\} = [A]^{-1} \cdot 1e\{U_e\}$. Thus, the displacement of one point which belongs to one element is:

$$\{U\} = [f(x, y, z)] \cdot [A]^{-1} \cdot \{U_e\}$$
$$\Rightarrow \{U\} = [N] \cdot \{U_e\} \quad \text{where} \quad [N] = [f(x, y, z)] \cdot [A]^{-1} \tag{3}$$

represents the displacement interpolation matrix on elements domain.

(d) Specific deformations dependence of the $\{U_e\}$ computation:

Using Eq. (1) and also the specific deformation and displacements, we obtain:

$$\{\varepsilon\}/[f(x, y, z)]'[A]^{-1} \cdot \{U_e\}$$

Note that:

$$[f(x, y, z)]'[A]^{-1} = [B] \Rightarrow \{\varepsilon\} = [B] \cdot \{U_e\} \tag{4}$$

We can obtain the matrix $[f(x, y, z)]'$ by difference the matrix $[f(x, y, z)]$ related with x, y, z taking into account the calculated deformation.

(e) The tension computation $\{\sigma\}$, by taking into account the nodal displacements $\{U_e\}$: Hooke's law is valid in this case: $\{\sigma\} = [D] \cdot \{\varepsilon\}$, where: $[D]$—material stiffness matrix. From Eq. (4) we obtain:

$$\{\sigma\} = [D] \cdot [B] \cdot \{U_e\} \tag{5}$$

(f) The relation between nodal forces and element displacements:

$$\{\delta U\}^T \cdot \{F_e\} = \int_V \{\delta_\varepsilon\}^T \cdot \{\sigma\} \cdot dV. \tag{6}$$

From Eq. (4) we obtain:

$$\{\delta_\varepsilon\} = [B] \cdot \{\delta U_e\},$$

where:

$$\{\delta_\varepsilon\}^T = \{\delta U_\varepsilon\}^T \cdot [B]^T \tag{7}$$

Replacing Eqs. (5) and (7) in Eq. (4), we obtain:

$$\{\delta U_\varepsilon\}^T \cdot \{F_\varepsilon\} = \int_V \{\delta U_\varepsilon\}^T \cdot [B]^T \cdot [D] \cdot [B] \cdot \{U_\varepsilon\} \tag{8}$$

$$\Rightarrow \{F_\varepsilon\} = \left\{ \int_V [B]^T \cdot [D] \cdot [B] \cdot dV \right\} \tag{9}$$

$$\text{Note that}: [K_\varepsilon] = \int_V [B]^T \cdot [D] \cdot [B] \cdot dV, \tag{10}$$

Total Deformation - [mm]
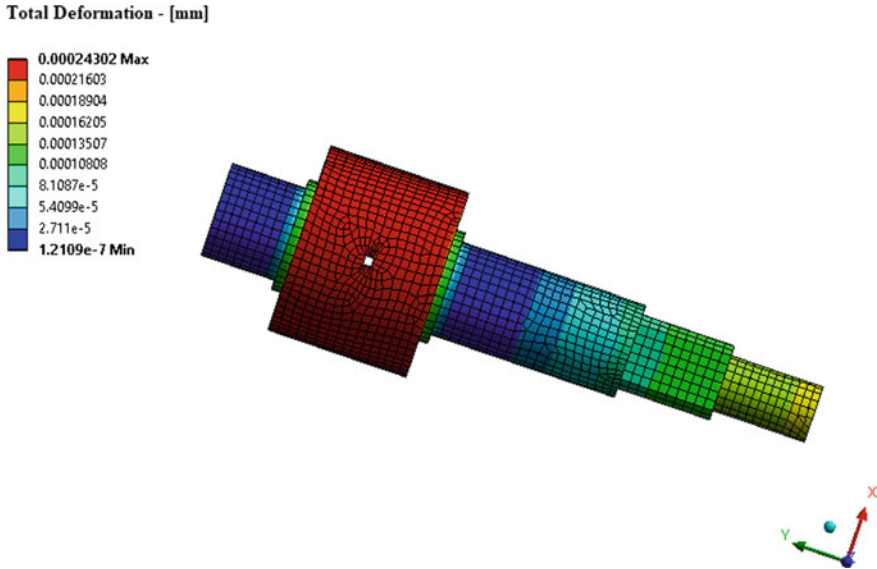
Fig. 4 Total deformations of the shaft

therefore the equation above becomes:

$$\{F_\varepsilon\} = [K_\varepsilon] \cdot \{U_\varepsilon\} \tag{11}$$

where: $\{F_\varepsilon\}$—nodal forces column vector applied on an element; $\{K_\varepsilon\}$—stiffness matrix of an element; $\{U_\varepsilon\}$—nodal displacements column vector applied on an element. This mathematical approach shows, through the final Eq. (11), how the FEA provides the forces applied on the system and obtains the deformations that appear in each node of interest. The generated forces which appear in simulations are given by the boundary conditions of the system.

With ANSYS WB, the tool used for this investigation, with a static–structural simulation we can extract various results based on this analysis. Table 1 was thus generated by combining the defined parameters (shaft diameter, slit position, and width of the slit), as well as the boundary conditions of the analysis.

The following aspects have been obtained from the analysis: the directional and total displacements [mm]—the latter in Fig. 4, the Equivalent (von Mises) Stress [MPa]—Fig. 5, and the Equivalent Elastic and Plastic Strain [mm/mm]. The case of a shaft with only one slit has been considered in this example.

One can see from Fig. 4 that the maximum reached deformation of the shaft at maximum rotational speed considered is smaller than 1 μm for the 20 mm diameter shaft, which represents the best technological precision that one can reach, therefore the functionality of the device (i.e., the shape of the transmitted laser impulse [15, 17, 20]) is not affected for this dimension of the device. From Table 1 these deformations

Table 1 Shaft with one slit—for an OL 55 material of the chopper shaft

Design point	Square slits B × H (B = H)(mm)	Shaft diameter (mm)	Directional deformation maximum (mm)	Total deforma-tion maximum (mm)	Equivalent stress maximum (MPa)	Equivalent plastic strain maximum (mm/mm)
Input			Output			
1	1	20	8.58E−05	0.000244	17.473	0
2	1	40	0.387	19.952	0	0
3	1	60	−0.109	0.009735	196.46	0.00010184
4	1	80	0.00243	0.017783	219.23	0.0010602
5	1	100	0.0125	0.26522	308.27	0.054656
8	2	20	9.55E−05	0.000267	19.218	0
10	2	60	0.007755	0.00761	205.91	9.84E−06
11	2	80	0.01221	0.01814	225.36	0.0011049
12	2	100	0.01278	0.2878	330.06	0.06656
13	2	120	0.02188	2.2107	747.44	0.29614
15	3	20	0.0010978	0.000311	19.854	0
17	3	60	−0.4049	0.0157	203.59	0.00011939
18	3	80	0.02746	0.018859	227.68	0.013311
19	3	100	0.012377	0.3283	370.99	0.098398
20	3	120	0.022346	2.3498	769.98	0.33401
21	3	140	0.039507	6.5844	1308.5	0.7148
22	4	20	0.00013489	0.000389	21.015	0
24	4	60	−0.014011	0.00828	212.11	0.00016402
25	4	80	0.015702	0.0203	226.73	0.002481
26	4	100	0.013541	0.4064	412.57	0.11931
29	5	20	0.0001886	0.000522	23.544	0
30	5	40	0.01494	0.005093	112.83	0
31	5	60	0.5087	0.017295	220.02	0.0002325
32	5	80	0.028053	0.024566	228.68	0.0049086
33	5	100	0.013749	0.53717	465.08	0.14736
34	5	120	0.024248	2.963	944.77	0.40377

increase with the shaft diameter, therefore one must limit the rotational speed to (much) smaller values, depending on the tolerances to the shape and to the duration of the laser impulses.

From Fig. 5 the structural integrity of the device is fine for the same small diameter of 20 mm, but from Table 1 the same kind of remark as above can be done: as the diameter increases, the speed has to be smaller (while also taking into account the width of the slits).

Equivalent von Mises Stress - [MPa]
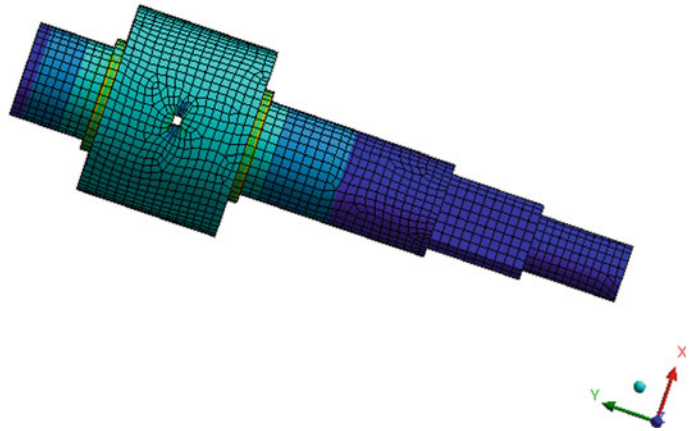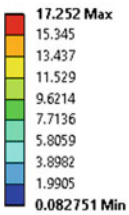
Fig. 5 Equivalent von Mises stresses of the shaft

4 Conclusions

We reported a FEA of optomechanical choppers with rotational shafts that, to our knowledge, we have proposed (patent pending) [20] and developed, as a configuration capable to reach much higher chop (therefore light impulses) frequencies of laser beams. Elements of the FEA have been provided and some preliminary results have been extracted from it in order to offer a tool to optimize such devices for specific applications.

The case of a chopper shaft with one slit was considered, and the deformations, as well as the stresses in the structure were obtained, in a multi-parametric approach (considering the geometry of the device, as well as its rotational speed). The former may affect the functionality of the device, while the latter gives its structural integrity. It was found that the rotational speed has to be limited to lower values, as the diameter of the shaft is increased and as the slits are larger. For the smallest diameter considered (20 mm), however, the device can be driven even at the maximum speed of 120 krpm.

Future work comprises a detailed study of these aspects (with a higher number of slits), as well as other materials or shaft configurations.

References

1. Bass, M., (ed.): Handbook of Optics. McGraw-Hill Inc., New York (2010)
2. He, Y., et al.: Modulate chopper technique used in pyroelectric uncooled focal plane thermal imager. Proc. SPIE **4919**, 283–288 (2002)
3. Rodriguez-Arteaga, H., Cardenas-Garcia, D.: Gray-Body radiation using a blackbody source and an optical chopper. Int. J. Thermophys. **36**(8), 1757–1765 (2015)
4. Lemke, D., et al.: Optical chopper for the HIRDLS instrument. Proc. SPIE **3437**, 125–136 (1998)
5. McDermid, I.S., Beyerle, G., Haner, D.A., Leblanc, T.: Redesign and improved performance of the tropospheric ozone lidar at the jet propulsion laboratory table mountain facility. Appl. Opt. **41**, 7550–7555 (2002)
6. Wan, D.-P., Liu, H.-B., Wang, Y.-M., Hu, D.-J., Gui, Z.-X.: CO_2 laser beam modulating for surface texturing machining. Opt. Laser Tech. **40**, 309–314 (2008)
7. Osawa, H., Ohkochi, T., Fujisawa, M., Kimura, S., Kinoshita, T.: Development of optical choppers for time-resolved measurements at soft X-ray synchrotron radiation beamlines. J. Synchrotron Radiat. **24**, 560–565 (2017)
8. Gondal, M.A., Yamani, Z.H.: Highly sensitive electronically modulated photoacoustic spectrometer for ozone detection. Appl. Opt. **46**, 7083–7090 (2007)
9. Makoui, A., Killinger, D.K.: Transient fluorescence spectroscopy of terbium doped dipicolinic acid: a fluorescence lifetime measurement technique. JOSA B **26**, 691–698 (2009)
10. Cucu, R.G., Podoleanu, AGh, Rogers, J.A., Pedro, J., Rosen, R.B.: Combined confocal/en face T-scan-based ultrahigh-resolution optical coherence tomography in vivo retinal imaging. Opt. Lett. **31**(11), 1684–1686 (2006)
11. Dávila-Pintle, J.A., Reynoso-Lara, E., Bravo-García, Y.E.: Chopper z-scan technique for elliptic Gaussian beams. Opt. Express **24**, 21105–21112 (2016)
12. Syms, R.R.A., Zou, H., Stagg, J., Veladi, H.: Sliding-blade MEMS iris and variable optical attenuator. J. Micromech. Microeng. **14**(12), 1700 (2004)
13. Tsuchiya, T., Kogita, Y., Taniyama, A., Hirai, Y., Sugano, K., Tabata, O.: Time-resolved micro-raman stress spectroscopy for single-crystal silicon resonators using a mems optical chopper. J. Microelectromech. Syst. **25**(1), 188–196 (2016)
14. Benjamin, K., Armitage, A., South, R.: Harmonic errors associated with the use of choppers in optical experiments. Measurement **39**, 764–770 (2006)
15. Duma, V.-F.: Theoretical approach on optical choppers for top-hat light beam distributions. J. Opt. A: Pure Appl. Opt. **10**, 064008 (2008)
16. Duma, V.-F., Nicolov, M.: Neutral density filters with Risley prisms: analysis and design. Appl. Opt. **48**, 2678–2685 (2009)
17. Duma, V.-F.: Optical choppers with circular-shaped windows: modulation functions. Commun. Nonlinear Sci. Numer. Simul. **16**, 2218–2224 (2011)
18. Duma, V.-F.: Prototypes and modulation functions of classical and novel configurations of optical chopper wheels. Lat. Am. J. Solids Struct. **10**(1), 5–18 (2013)
19. Matchko, R.M., Gerhart, G.R.: High-speed imaging chopper polarimetry. Opt. Eng. **47**(1), 016001 (2008)
20. Duma, V.-F., Demian, D.: Optical modulator, has solid rotating shaft with some through slots of well-defined profiles. Romanian Patent request RO129610-A0 (2014)
21. Yun, S.H., Boudoux, C., Tearney, G.J., Bouma, B.E.: High-speed wavelength-swept semiconductor laser with a polygon-scanner-based wavelength filter. Opt. Letters **28**, 1981–1983 (2003)
22. Faur, N.: Elemente Finite Fundamente. Editura Politehnica, Timișoara (2002)

Charpy Impact Testing Machine
in Modeling of Vehicle Frontal Crash
with Street Lights

Wojciech Danek and Mariusz Pawlak

Abstract Real tests of a crash of a vehicle with lighting column are an expensive but necessary part of norm EN-126767:2008. During the design process of lighting columns, it is necessary to provide some modifications to receive sufficient safety class. To not repeat the experiments and to reduce the costs, numerical simulations are carried out, and when finally good results are received, a real crash test of a vehicle with real size streetlight can be performed. However, a truly challenging problem is the validation of the numerical models without experiments and making a good conclusion based on them. To investigate if something else than a real car crash experiments can be used, a small model of a Charpy Impact testing machine was created. The pendulum mass, the location of striking edge and radius of the striking edge can be altered in the model. The location of the mass center of the obstacle with which the crash is to be observed is also important. Experimental results from the testing machine were collected and compared with results from numerical simulations and conclusions were drawn.

Keywords Lighting column · Crash tests · Numerical simulations
High speed camera

1 Introduction

A modern trend for design elements included in road infrastructure is assurance of maximum safety for drivers and passengers. For this purpose, each newly designed infrastructural element is subject to a series of numerical analyses [2–5, 19, 21–24] whose purposes are to determine properties of the element during the impact by the

W. Danek · M. Pawlak (✉)
Faculty of Mechanical Engineering, Silesian University of Technology, ul. Konarskiego 18a,
44-100 Gliwice, Poland
e-mail: mariusz.pawlak@polsl.pl

W. Danek
e-mail: wojciech.danek@polsl.pl

vehicle. As a result, the effect of the passive safety of passengers is determined. The results of the numerical simulations must be verified by experimental studies. Cost of experimental studies is very high, thus many companies try to find an alternative method of the numerical model verification. For this purpose, a similar device to the Charpy hammer is proposed. This device makes it possible to perform a crash test for a model with smaller dimensions and to determine the influence of changes in lighting column parameters on the values of passive safety coefficients specified in the EN 12767 standard. Based on the results of collision tests on the Charpy hammer, it is possible to verify the numerical model of real size.

2 Passive Safety

Supporting road equipment structures like lighting columns can, during a collision, constitute a threat to drivers and passengers. Therefore, when this element of road equipment is designed, the increase of passive safety for drivers and passengers should be sought. For this purpose, European standard EN 12767 distinguishes three categories of passive safety [8]:

- High energy absorbing (HE),
- Low energy absorbing (LE),
- Non-energy absorbing (NE) (Fig. 1).

Constructions qualified as HE class are intended to significantly reduce the car's velocity and to reduce the risk of crashes with another car or with other elements of road infrastructure. Lighting columns that qualify within two classes (NE, LE) are intended to reduce the car's velocity with low risk of significant damage to health.

All street lights used on the roads should be passively safe or additional safety barriers should be applied [7–12].

In order to determine which class of passive safety a particular construction can be qualified to, there are two types of coefficients: Acceleration Severity Index (ASI) and Theoretical Head Impact Velocity (THIV). ASI allows determination of a nuisance motion of the vehicle for people sitting near selected measuring points (usually the center of gravity). It is considered a determinant of accident severity to passengers in the vehicle upon impact with an obstacle. It is determined from the dependence shown below [10]:

$$ASI(t) = \left[\left(\bar{a}x/\hat{a}x \right)^2 + \left(\bar{a}y/\hat{a}y \right)^2 + \left(\bar{a}z/\hat{a}z \right)^2 \right]^{1/2} \tag{1}$$

where:
a_x, a_y, a_z—components of acceleration of the chosen point P of the vehicle from the movable averaged time interval $\delta = 50$ ms,
a_x, a_y, a_z—limit value of acceleration along X, Y, Z axes of the vehicle.

For passengers using seat belts, limit values of acceleration are equal to:

- $x = 12$ g,

Fig. 1 Level of energy absorption according to EN 12767 [8]

HE

LE

NE
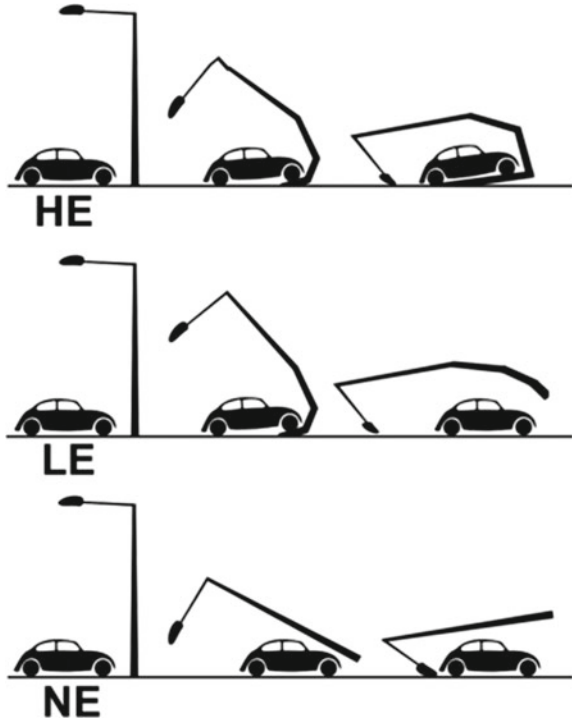
- $y = 9$ g,
- $z = 10$ g,

where

$$g = 9.81 \text{ m/s}^2$$

Theoretical Head Impact Velocity is the velocity of the head during an impact with a surface inside the vehicle and is determined from the dependence shown below [10]:

$$THIV = \left[V_x^2(T) + V_y^2(T) \right]^{1/2} \tag{2}$$

where:
$V_x(T)$, $V_y(T)$—velocity of the theoretical head at the time of impact on the surface inside the vehicle.

Values of these two coefficients are determined for different velocities depending on the road where this obstacle is located. These two coefficients are to measure the safety of passengers in a car to ensure that during crash the negative influence on the health of people is minimised. Costs of eventual recovery for patients after road accidents are high and the process is time-consuming [6].

Table 1 Maximum values of passive safety coefficients for different classes

Energy absorption level		Vehicle user safety level			
		Standard low impact speed test		Speed class test (50, 70, 100 [km/h]) at impact	
		Maximum values		Maximum values	
		ASI	THIV (km/h)	ASI	THIV (km/h)
HE	1	1	27	1.4	44
	2	1	27	1.2	33
	3	1	27	1.0	27
LE	1	1	27	1.4	44
	2	1	27	1.2	33
	3	1	27	1.0	27
NE	1	1	27	1.2	33
	2	1	27	1.0	27
	3	0.6	11	0.6	11
	4	Without requirements	Without requirements		

The values of the passive safety coefficients for assigning a structure to a passive safety class are shown in Table 1.

3 Tests on Modified Charpy Impact Testing Machine

Experimental studies have been carried out on a device construction of which is based on the Charpy hammer. This device was created as a master thesis at the Institute of Theoretical and Applied Mechanics at the Silesian University of Technology (Fig. 2).

In order to determine the kinematic parameters and the ASI passive safety factor during the impact, a high-speed Phantom v. 9.1 camera was used to record a collision with an appropriate number of frames (3500 fps). TEMA Automotive software was used to analyze the recorded collision films. The diagram of the test bench is shown in Fig. 3.

The test plan was defined to determine the effect of the impact velocity and the position of the centre of gravity of the lighting column on the value of the ASI passive safety factor. The impact of the vehicle's centre of gravity on the ASI value was described in the article [23, 24], therefore it was decided to assess the impact of the change of the column centre of gravity on the ASI value. The impact velocity was changed by changing the angle of the hammer arm's inclination, while the centre of gravity was changed by adding a load on the upper part of the column under analysis. One mass is 0.035 kg and two masses are 0.07 kg. The whole test plan is shown in Table 2.
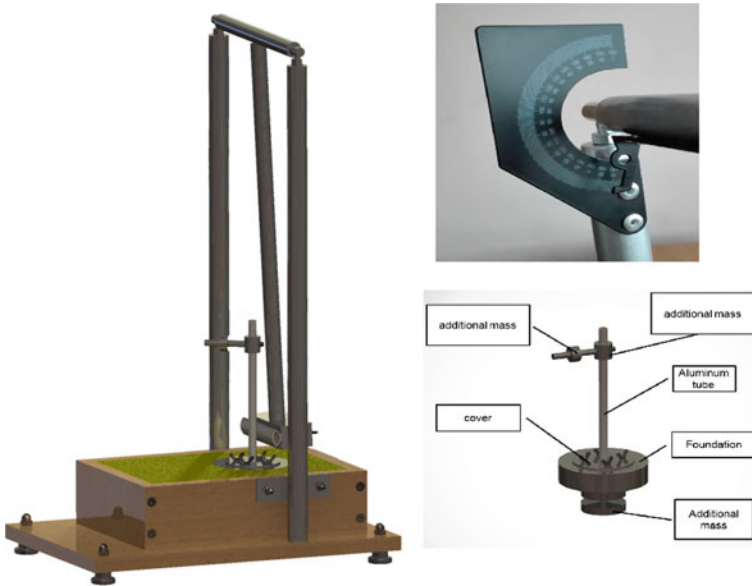
Fig. 2 View of Charpy impact testing machine
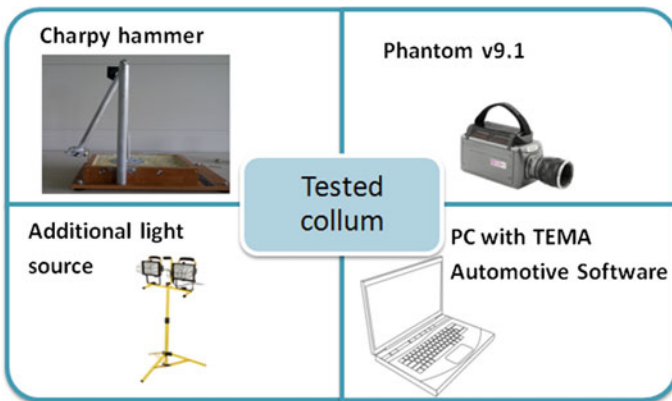
Fig. 3 Test stand

A picture of the measuring device with selected points allowing to determine the kinematic values is shown in Fig. 4. Results obtained from the analysis of collision films are presented in Figs. 5, 6, 7 and 8.

The description of the measuring points is as follows:

- Point 1—A point at the end of the hammer arm,
- Point 2 and Point 3—Reference points for determining the film scale,
- Point 4—A point at the end of the analysed column.

Table 2 Test plan

No.	Inclination angle (°)	Additional mass
Test 1	170	Without additional mass
Test 2	130	Without additional mass
Test 3	90	Without additional mass
Test 4	170	With one additional mass
Test 5	130	With one additional mass
Test 6	90	With one additional mass
Test 7	170	With two additional mass
Test 8	130	With two additional mass
Test 9	90	With two additional mass
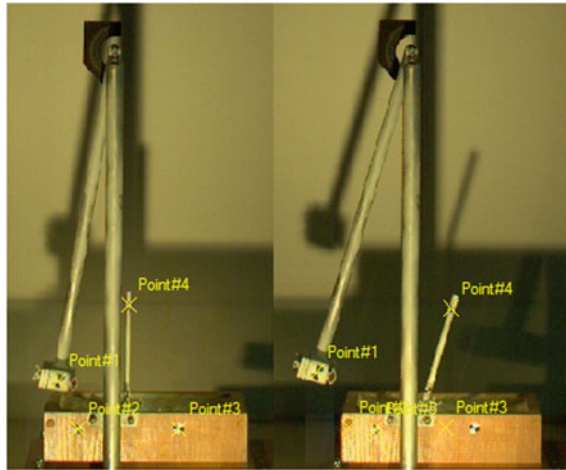
Fig. 4 Scheme of the test stand with markers before and after the impact
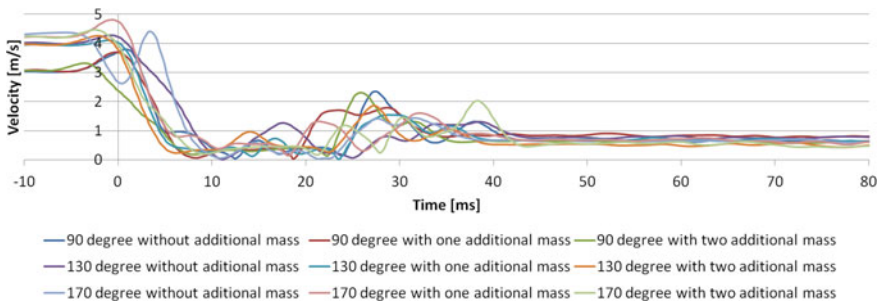
Fig. 5 Velocities of point 1 during the impact

Figure 5 shows the velocities obtained during impact for point 1 which one is the point at the end of the hammer arm for all analysed cases.

Figures 6 and 7 show displacements and velocities of point 4 for all analysed cases.

On the basis of the displacements of point 4 shown in Fig. 6, it can be stated that when additional mass is added, the maximum column deflection decreases. This is especially noticeable at higher impact speeds.

Based on the speed results from point 1 shown in Fig. 5, an equivalent of ASI passive safety factor has been determined. The graph of this coefficient in the time domain is shown in Fig. 8.

On the basis of the graph shown in Fig. 8, it can be concluded that with an additional mass causing the centre of gravity to change position, the value of the ASI passive safety coefficient is reduced. Below are presented aluminum tubes and broken bumpers after tests (Fig. 9).
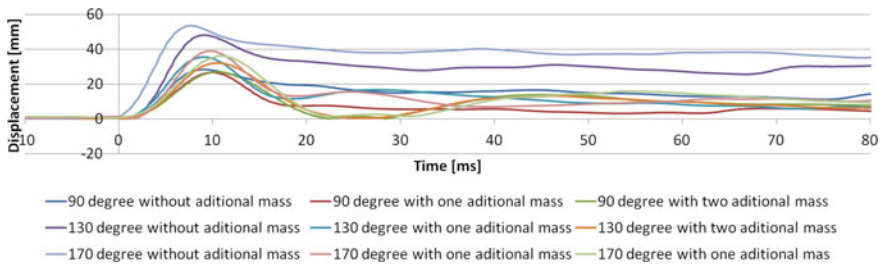
Fig. 6 Displacement of point 4 during the impact
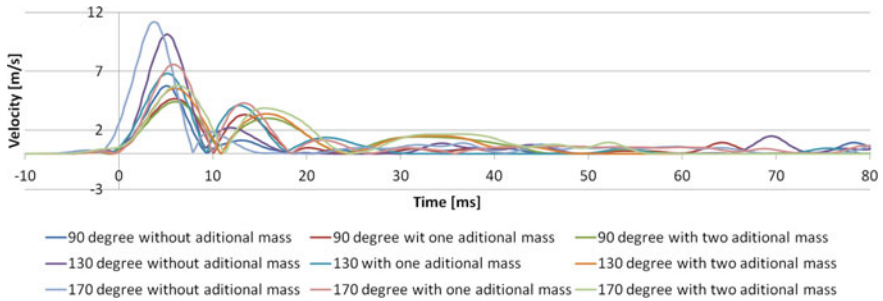
Fig. 7 Velocities of point 4 during the impact
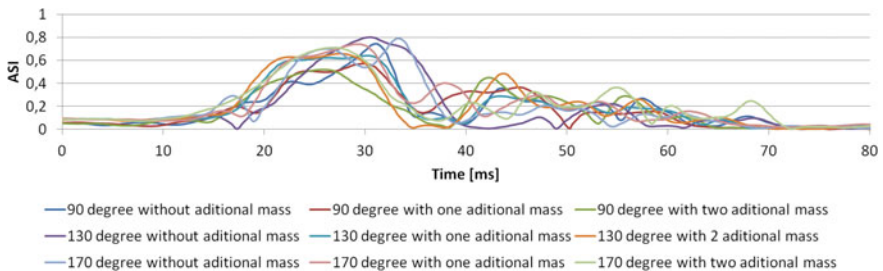
Fig. 8 Equivalent of ASI coefficient during the impact

Fig. 9 View of aluminum
tubes after tests on Charpy
hammer with various angle
of inclination and masses

4 Numerical Analysis of a Crash with Street Lights

A numerical model of street light was prepared in LS Prepost, a preprocessor for LS
Dyna [15, 16, 18], engineering software very often used in the automotive industry
[20–22]. More information about method implemented in the software can be found
in the literature [1, 17, 18]. The foundation was made of concrete, the soil was
implemented in LS Dyna as *MAT_SOIL_AND_FOAM [13, 14]. According to the
Charpy tests, the mass on the top of aluminum tube generated additional stiffness
and had a high influence on displacement, velocities and equivalent ASI coefficient
during impact on Impact Testing Machine. In publications [23–25], conclusions on
the influence of vehicle center of mass on ASI factor and rigid body movement
of street light with foundation during a crash test were presented. A next step was
to apply numerical simulations of car impact with a street light [3–5], to estimate
if additional mass on the top can have an influence on safety factors. Below is
presented a model of a street light with foundation, soil, and car. Numbers from 1 to
6 mark displacements of a street light with different additional masses (from 1 up to
50 kg). Presented results are from the crash test at a speed of 35 km/h (Fig. 10).

The influence of the mass is not so significant as it was on Charpy test because
the real light column is slender and an additional mass was limited to a mass of
streetlight (max 50 kg).
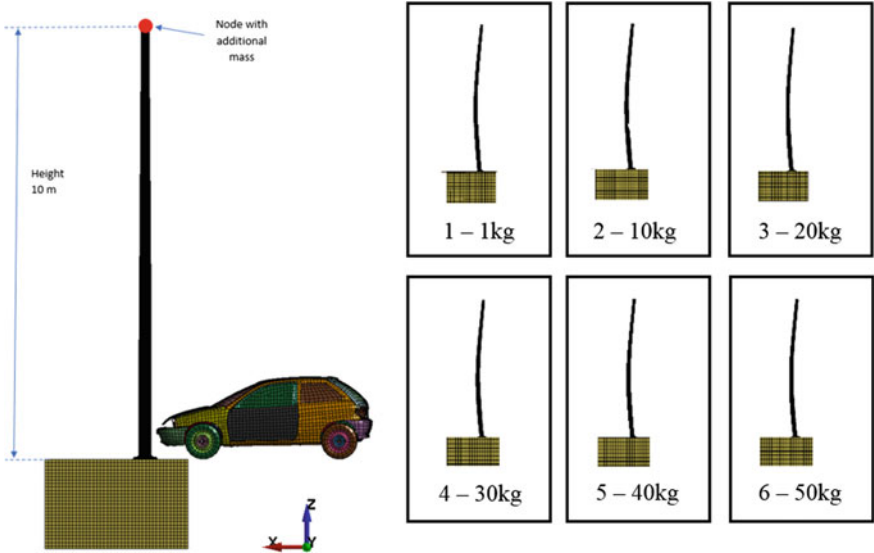
Fig. 10 Street light column with vehicle on the left, on the right displacement plots of column with additional mass 1, 10, 20, 30, 40 and 50 kg
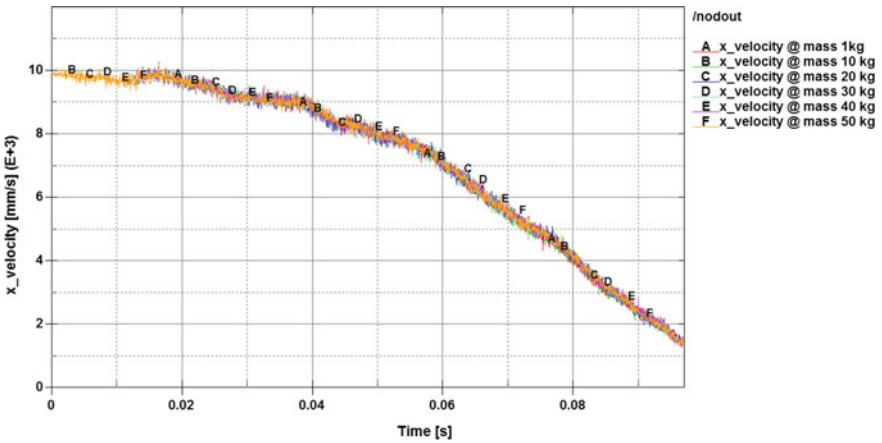
Fig. 11 Velocity curves of vehicle center of mass along X axis

Velocity curves for x direction generated from accelerometer node located at the vehicle center of mass are presented in Figs. 11, 12 and 13.
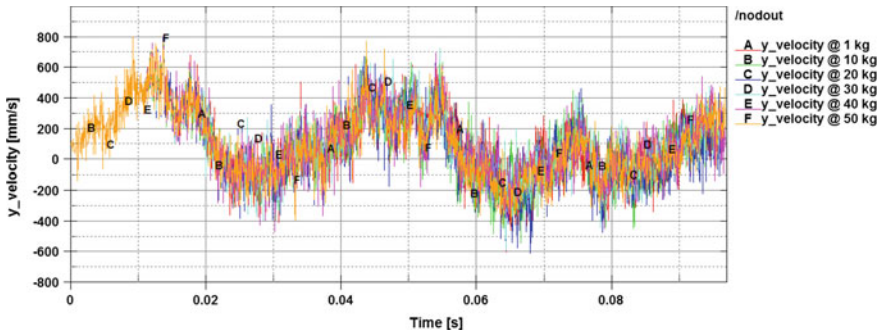
Fig. 12 Velocity curves of vehicle center of mass along Y axis
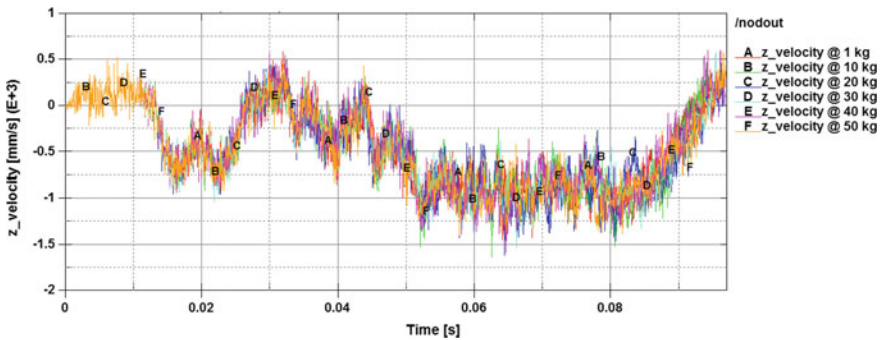
Fig. 13 Velocity curves of vehicle center of mass along Z axis

5 Conclusions

Results from a numerical model, which was based on a real object, differ when compared with experimental tests from the Charpy Impact Testing Machine. It is impossible to receive the same correlation between them because kinematic conditions are varied. It can be presumed that applying two times higher mass on the top of the light column would make a difference in velocity curves, but for safety reason, it would not be possible to apply in reality. However, it remains to be investigated if there is the influence of foundation on safety factors, the mass is high comparing to the column, and location of the mass center can have an impact on ASI coefficient.

References

1. Belytschko, T., Liu, W.K., Moran, B.: Nonlinear Finite Elements for Continua and Structures. Wiley, New York (2001)
2. Borovkov, A., Klyavin, O., Michailov, A., Kemppinen, M., Kajatsalo, M.: Finite element modeling and analysis of crash safe composite lighting columns, contact-impact problem. In: 9th International LS-DYNA Users Conference, Manchester, pp. 11–20 (2013)
3. Danek, W., Mężyk, A., Świtoński E., Gąsiorek D.: Wyznaczanie współczynników bezpieczeństwa biernego przy zderzeniu pojazdu ze słupem oświetleniowym na podstawie symulacji numerycznej. In: Techniki komputerowe w inżynierii. XIV Konferencja naukowo-techniczna. TKI 2016, Teresin, pp. 1–2 (2016)
4. Danek, W., Gąsiorek, D.: Symulacja numeryczna zderzenia pojazdu z aluminiowym, wykopywanym słupem oświetleniowym. In: 56. Sympozjon Modelowanie w Mechanice, Ustroń, p. 60 (2016)
5. Danek, W., Gąsiorek, D.: Numerical simulation of car crash with lighting columns mounted in the ground. In: 4th International Conference Mechatronics: Ideas for Industrial Applications, Wisła, pp. 40–41 (2017)
6. Duda, S., Gąsiorek, D., Gembalczyk, G., Kciuk, S., Mężyk, A.: Mechatronic device for locomotor training. Acta Mech. et automatica **10**(4), 310–315 (2016)
7. Eppinger, R. et al.: Development of improved injury criteria for the assessment of advanced automotive restraint systems−II. National Highway Traffic Safety Administration (1999)
8. European Committee for Standardization, EN 12767 Passive safety of support structures for road equipment −Requirements and test methods. Draft proposal of revised EN 12767. 2005-06-02. 30p. 28
9. European Committee for Standardization, SFS-EN- 40-3-3 Lighting Columns–Part 3-3: Design and Verification–Verification by Calculation, Finnish Standards Association, Helsinki, 2004 (73 p. ICS 93.080.40)
10. European Committee for Standardization, SFS-EN 40-3-1 Lighting Columns, Part 3-1: Design and Verification–Specification for Characteristic Loads, Edita Oyj, Helsinki, 2000 (32 p. ICS 91.160.20)
11. European Committee for Standardization, SFS-EN 1317-1 Road Restraint Systems, Part 1: Terminology and General Criteria for Test Methods, Edita Oyj, Helsinki, 1998 (30 p. ICS 01.040.93; 13.200; 93.080.30)
12. European Committee for Standardization, SFS-EN 1317-2 Road Restraint Systems, Part 2: Performance Classes, Impact Test Acceptance Criteria and Test Methods for Safety Barriers, Edita Oyj, Helsinki, 1998 (15 p. ICS 13.200;93.080.30)
13. European Committee for Standardization, SFS-EN 1317-3 Road Restraint Systems, Part 3: Performance Classes, Impact Test Acceptance Criteria and Test Methods for Crash Cushions, Edita Oyj, Helsinki, 2001 (19 p. ICS 13.200;93.080.30)
14. Fasanella, E.L., Jackson, K.E., Kellas, S.: Soft soil impact testing and simulation of aerospace structures. In: The 10th LS-DYNA Users Conference, Dearborn, pp. 29–42 (2008)
15. Fasanella, E.L., Jackson, K.E.: Developing Soil Models for Dynamic Impact Simulations. NASA Langley Research Center, Hampton, NASA Technical Reports Server (2009)
16. Hallquist, J.O.: LS-DYNA Keyword User's Manual; Version 971. Livermore Software Technology Company, Livermore (2006)
17. Hallquist, J.O.: LS-DYNA Theory Manual, Version 971. Livermore Software Technology Company, Livermore (2006)
18. Hallquist, J.O.: Recent developments in LS-DYNA. In: German LS-DYNA Forum, Bamberg (2011)
19. Hiermaier, S.J.: A Structures Under Crash and Impact, Continuum Mechanics Discretization and Experimental Characterization. Springer, Berlin (2008)
20. Kiczko, A., Niezgoda, T., Nowak, J., Dziewulski, P.: Numerical implementation of car impact into the modified road barrier. J. Kones Powertrain Transp. **17**, 189–196 (2010)

21. Kosaka, I.: Improvement of energy absorption for the side member using topography optimization. In: 11th International LS-DYNA Users Conference, Dearborn, pp. 25–30 (2010)
22. Mitchell, G., Tolnai, M., Gokani, V., Picon, R., Yang, S., Klinger, R.E., Williamson, E.B.: Design of retrofit vehicular barriers using mechanical anchors. CTR Technical Report (2006)
23. Pawlak, M.: Comparison of acceleration severity index of vehicle impacting with permanent road equipment support structures. In: 13th Conference on Dynamical Systems Theory and Application. DSTA, Łódź, p. 236 (2015)
24. Pawlak, M.: The acceleration severity index in the impact of a vehicle against permanent road equipment support structures. Mech. Res. Commun. **77**, 21–28 (2016)
25. Zukas, J.A.: High Velocity Impact Dynamics. Wiley, New York (1990)

Interaction of Bridge Cables and Wake Behind in the Vortex Induced Vibrations

Maciej Dutkiewicz

Abstract In the paper the interaction of wake and the cable with passive damper is analyzed. Vortex induced vibrations (VIV) are caused by vortex shedding, located behind the cable. On the basis of formulation of the fluid forces applied to the cable in the direction of lift, it is described the coupled model where force is resulting from the coupling of cable and wake. The system of dynamical motion equations, corresponding to the coupled model, is supplemented by the equation representing the oscillating lift force acting on the vibrating cable. This equation models the near wake dynamics describing the fluctuating nature of vortex shedding. The numerical simulations are performed for the circular section of the cable. The vertical vibrations, perpendicular to the wind directions, are analyzed. In the first part of the paper the analysis of lift equation is performed for different variation of damping coefficients to fit the curve that fulfilled the fluid equations. The behavior of lift coefficient in time domain and velocity in location domain are presented. Then, for the chosen parameters of oscillating equation coming from the first part of numerical research, the dynamical behavior of the system: cable with and without damper and wake is performed. The displacements and velocities of vibrating cable with and without damper as well as the dynamical response of the wake in time domain are presented. Dimensionless amplitude of motion of the cable and the damper for different damping coefficient of the damper and amplitudes of derivatives of displacement are presented.

Keywords Vortex induced vibrations · Vortex shedding · Air flow · Drag
Lift force · Vibration model · Stress Reynolds tensor · Turbulence kinetic energy
Energy dissipation

M. Dutkiewicz (✉)
Department of Building Construction, Faculty of Civil and Environmental Engineering and Architecture, University of Science and Technology in Bydgoszcz, Al. Prof. S. Kaliskiego 7, 85-796 Bydgoszcz, Poland
e-mail: macdut@utp.edu.pl

1 Introduction

There are many cases of vibrations caused by vortex shedding. Designing of slender structures under the wind load and due to vortices is a very important issue. These constructions are e.g.: tall building, chimneys, cable bridges or overhead transmission lines. The problems of vortex induced vibrations (VIV) are often analyzed with use of computational fluid dynamics, analytical models and experiments. Studies are performed for crossflow and in line vibrations. Important research on vortex induced vibrations was conducted by Blevins [1], McCroskey [2], Sarpkaya [3], Bearman [4]. These works deal with vibrations of the circular cylinder and vortex-induced or forced excitations, under two-dimensional conditions. The analysis of wake shedding behind the object was the subject of many previous works, and the first ones concerned the single oscillator [5, 6]. In these works the force acting on the structure from the fluid is modeled by a nonlinear, self-excited oscillator. In this model the system is described by coupled ordinary differential equations. Important results regarding coupling of structure in VIV were received by Facchinetti et al. [7]. In this work the model dynamics of the structure of one degree of freedom with the wake is investigated and discussed with regard to the choice of the coupling terms and the values of model parameters. As the vortex induced vibrations can occur in line of wind flow this subject was analyzed in the works of King [8], Griffin and Ramberg [9], Curie and Turnbull [10] and Naudascher [11]. Interesting analysis based on experiments are included in the papers of Sarpkaya [12], Maull and Milliner [13], Bernam and Graham [14]. Sarpkaya was the first who made the experiments in the U-tube tunnel, Maull and Milliner discussed the sinusoidal flow past a circular cylinder and measured forces normal and transverse to the flow direction as a function of time and movement of vortices in the flow has been established. Bernam and Graham presented flow visualisation studies to aid the discussion of the different modes of vortex shedding which occur and the relationship between the vortex shedding and the forces induced on the bodies. In recent years the methods based on computer fluid dynamics (CFD) led to huge number of studies also in the field of vortex induced vibrations. Important work is that of Utsunomiya [15] who used the surface-singularity method. Important part of researches concern the nonlinear dynamical behaviour. The nonlinearity of the systems describe the chaotic zones of motions [16, 17] and bifurcational dynamics that reflect the real cases in nature [18].

The VIV of bridge cable equipped with the damper is the subject of the paper. The article is divided into five parts, introduction, mathematical formulation of the flow and vortex induced vibrations models, numerical analysis and results, discussion and conclusions.

2 Mathematical Formulation

The analyzed bridge cable is modeled as rigid cylinder that is spring-supported and equipped with the damper as well as immersed in a uniform incompressible undisturbed air flow. The rigid cylinder of mass m_1, diameter D, and length L is assumed to be exposed to a flow of velocity v. The cylinder is assumed to be mounted at both ends with two elastic springs of total stiffness k_{1y} and, damping coefficient b_{1y} and with passive damper of mass m_{2y}, total stiffness k_{2y}, damping coefficient b_{2y}. The coordinates axis is located at the center of the cylinder at its stationary position.

2.1 Formulation of the Structural and Vortex Induced Model

The external lift force acting on the cylinder is $F(t)$ (Fig. 1).

The motion of the cylinders m_1 and m_2 in the lift direction is defined as:

$$m_1\ddot{y}_1 + (b_{1y} + b_{2y})\dot{y}_1 - b_{2y}\dot{y}_2 + (k_1 + k_2)y_1 - k_2y_2 = F, \tag{1}$$

$$m_2\ddot{y}_2 - b_{2y}\dot{y}_1 + b_{2y}\dot{y}_2 - k_2y_1 + k_2y_2 = 0, \tag{2}$$

$$F = \frac{1}{2}\rho V^2 DLC_L, \tag{3}$$

Modified oscillator equation was taken on the basis of formula proposed by Hartlen and Curie [19]:

$$\ddot{C}_L - \alpha\omega_0\dot{C}_L + \frac{\gamma}{\omega_0}\left(\dot{C}_L\right)^5 + \omega_0^2 C_L = b\dot{y}_1, \tag{4}$$

Fig. 1 Vortex induced vibration model
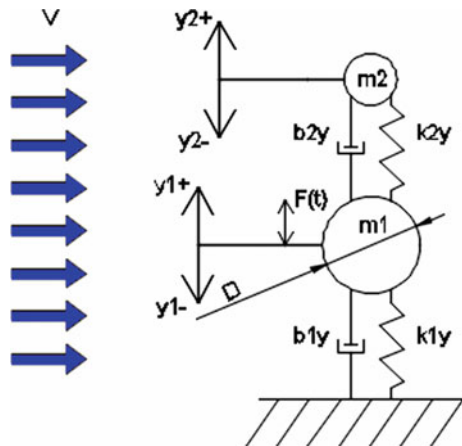
where C_L is the lift coefficient, α, γ, b—damping coefficients, $\omega_0 = \frac{f_s}{f_n} = \frac{SV}{f_n D}$, f_s—vortex shedding frequency, $\omega_n = 2\pi f_n$—natural frequency of the cylinder.

2.2 Fluid Model

In the analyzed problem, the equations of motion of the air flow around the cylinder take the following form [20]:

$$\frac{D\bar{v}_i}{Dt} = \bar{f}_i - \frac{1}{\rho}\frac{\partial \bar{\rho}}{\partial x_i} + \frac{1}{\rho}\frac{\partial}{\partial x_j}\left(\bar{\tau}_{ij} + \tau_{ij}^*\right), \tag{5}$$

where $\bar{\tau}_{ij} = \mu\left(\frac{\partial \bar{v}_i}{\partial x_j} + \frac{\partial \bar{v}_j}{\partial x_i}\right)$.

Additional continuity equations describing mean and fluctuating components are:

$$\frac{\partial \bar{v}_i}{\partial x_i} = 0, \quad \frac{\partial v_i'}{\partial x_i'} = 0, \tag{6}$$

To solve the above equations, the additional stress Reynolds tensor is adopted in the following form:

$$\tau_{ij}^* = \mu_t(\bar{v}_{i,j} + \bar{v}_{j,i}) - \frac{2}{3}\bar{\rho}k\delta_{ij}, \quad \mu_t = \frac{\rho c_\mu k^2}{\varepsilon}, \tag{7}$$

The $k - \varepsilon$ dependences are formulated in additional transport equations:

$$\frac{\partial}{\partial t}(\bar{\rho}k) + (\bar{\rho}k\bar{v}_i)_{,i} = \left(\bar{\tau}_{ij}\bar{v}_j\right)_{,i} - \bar{\rho}\varepsilon + \left(\mu_k k_{,i}\right)_{,i}, \tag{8}$$

$$\frac{\partial}{\partial t}(\bar{\rho}\varepsilon) + (\bar{\rho}\varepsilon\bar{v}_i)_{,i} = c_{\varepsilon 1}\left(\bar{\tau}_{ij}\bar{v}_j\right)_{,i} - c_{\varepsilon 2}\bar{\rho}\frac{\varepsilon^2}{k} + \left(\mu_\varepsilon \varepsilon_{,i}\right)_{,i}, \tag{9}$$

where: k—turbulence kinetic energy; ε—turbulence kinetic energy dissipation; $\mu_{k(\varepsilon)} = \mu + \frac{\mu_t}{\sigma_{k(\varepsilon)}}$ with the following assumption: $c_\mu = 0.09$, $c_{\varepsilon 1} = 1.45$, $c_{\varepsilon 2} = 1.92$, $\sigma_k = 1.00$, $\sigma_\varepsilon = 1.30$.

3 Analysis of Lift Equation

The motivation of oscillator equation analysis was to fulfill the equation of Navier-Stokes equations presented in the fluid model [Eqs. (5–9)] and conditions referring to interacted of the system built of cable with damper and wake. The oscillator equation that fulfilled the fluid model has the following form:
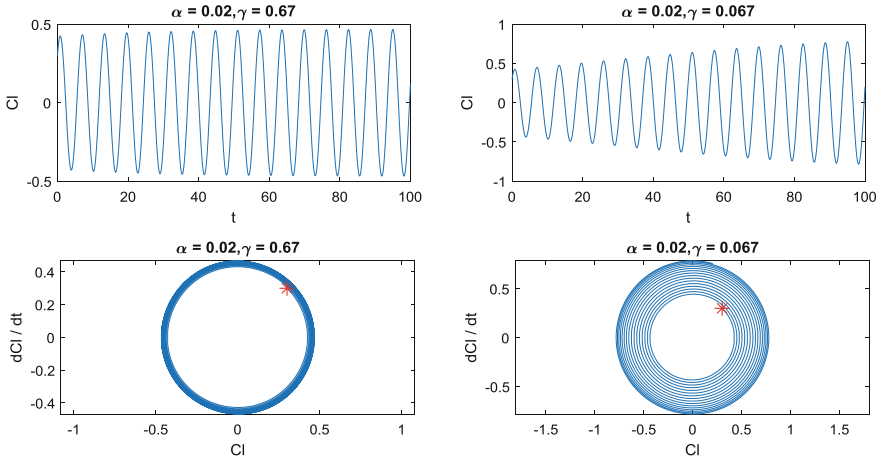
Fig. 2 Lift force coefficient Cl for different parameters of damping in time domain and dCl/dt in Cl domain in means of Eq. 10

$$\ddot{C}_L - \alpha\omega_0\dot{C}_L + \frac{\gamma}{\omega_0}\left(\dot{C}_L\right)^5 + \omega_0^2 C_L = 0, \tag{10}$$

Figure 2 presents coefficients Cl and dCl/dt for different parameters of α and γ in Eq. (10). For further analysis, the equations with parameters $\alpha = 0.02$, $\gamma = 0.67$ is taken into consideration.

4 Analysis and Discussion of System Vibrations

In this section the analysis of system Eqs. (1–4), describing the interference of cable with damper and wake behind is presented.

4.1 Analysis of Lift

Figure 3 presents coefficients Cl and dCl/dt for different parameters of α, γ related to Eq. (4) and for the second case related to Eq. (11):

$$\ddot{C}_L - \alpha\omega_0\dot{C}_L + \frac{\gamma}{\omega_0}\left(\dot{C}_L\right)^5 + \omega_0^2 C_L = b(\dot{y}_1 + \dot{y}_2), \tag{11}$$

where b is the coefficient tuned via model according to [16], equal to 0.4. Amplitudes of Cl and dCl/dt are bigger when taking into consideration Eq. (11) then from Eq. (4).

Cl accord.eq.4 ver time, α=0.02, γ=0.67,

dCl/dt accord.eq.4 ver time, α=0.02, γ=0.67

Cl accord.eq.11 ver time, α=0.02, γ=0.67

dCl/dt accord.eq.11 ver time, α=0.02, γ=0.67

Cl(accord.eq.4) ver time, α=0.02, γ=0.67, without damper

dCl/dt(accord.eq.4) ver time, α=0.02, γ=0.67, without damper
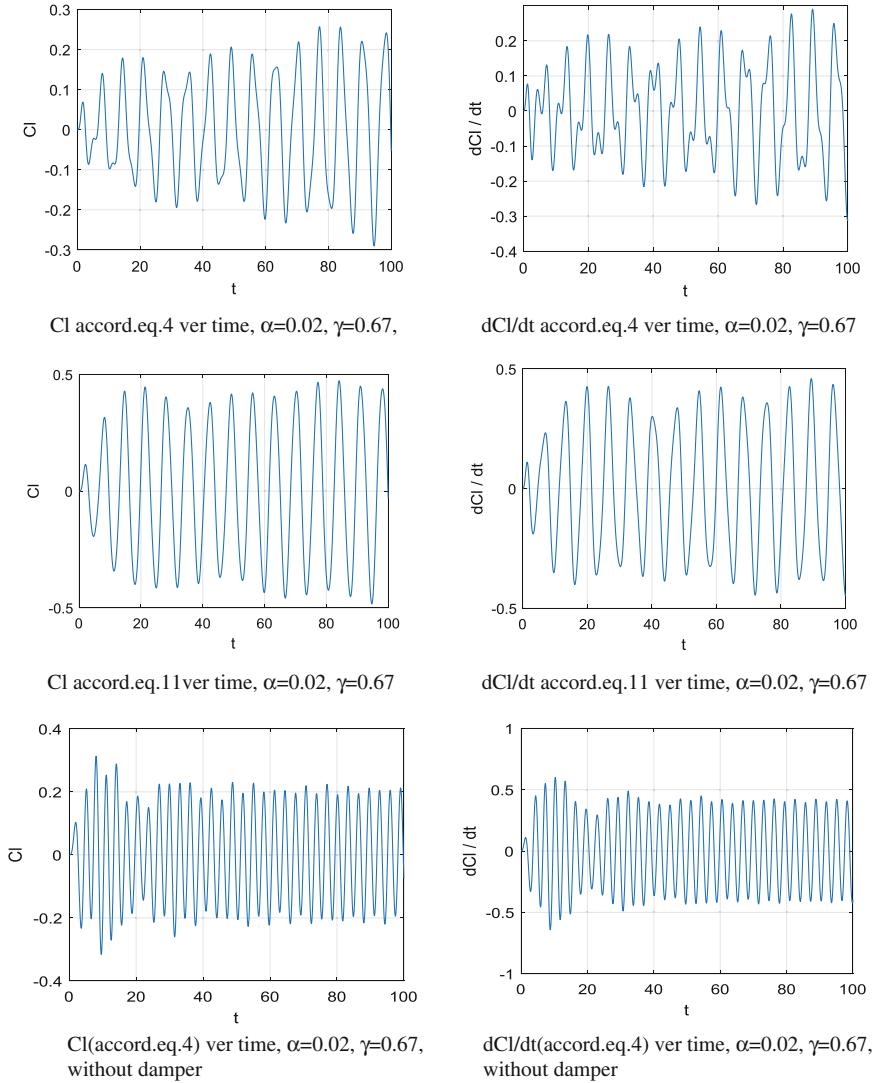
Fig. 3 Lift force coefficient Cl and dCl/dt for different parameters of damping in time domain

Amplitudes of Cl calculated according to Eq. (4) are 29% smaller then amplitudes calculated for the system without damper.

Figure 4 presents amplitude Cl for variation of the coefficients γ, where there is no interference according to Eq. (10), and case with interference in the meaning of system Eqs. (1–4).

According to Figs. 4, lift Cl decrease with the increase of γ for ($\alpha = 0.02$, $\gamma = 0.67$).
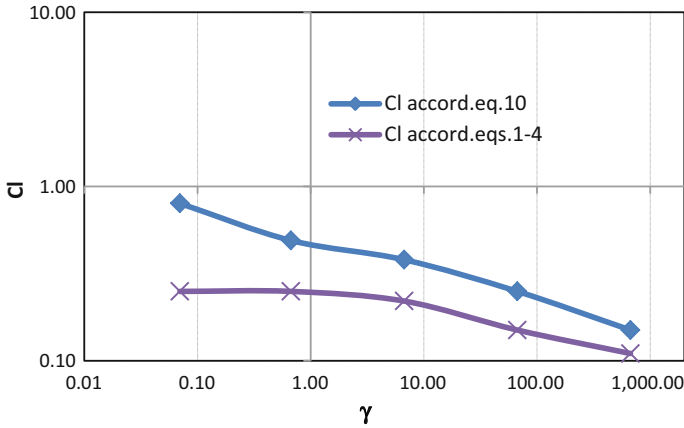
Fig. 4 Amplitude Cl for variation of the coefficients γ, according to Eq. (10) and according to system Eqs. (1–4)

4.2 Analysis of Cable with Damper Vibrations

Figure 5 presents displacements y1 and velocity dy1/dt of the cable for stiffness ratio k1/k2 and damping ratio b1/b2. The results show that amplitudes of cable with damper are 55% smaller then amplitudes of cable without damper.

Figure 6 presents the phase portraits of cable's displacements with and without damper. System with damper has the following parameters: m1/m2 = 10, k1y/k2y = 2, b1y/b2y = 2, α = 0.02, γ = 0.67.

Figure 7 shows the dependence of amplitudes of cable (y1) and damper (y2) for different damping coefficient b2y/b1y. Each curve decrease with increase of damping coefficient b2y/b1y.

On the Fig. 8 the dimensionless cable's amplitudes of motion for different damping ratio b1y/b2y for reduced flow velocity is presented. The displacement amplitude increases up to maximum value of 1.50 for b1y/b2y = 0.2, and displacement amplitude increases up to maximum value of 0.55 for b1y/b2y = 0.18.

5 Conclusions

In the paper the interaction of cable with damper and wake is investigated. The vertical vibrations, perpendicular to the wind directions, are analyzed. The equation expressing the lift force, that models the near wake dynamics describing the fluctuating nature of vortex shedding is presented. This wake oscillator interacts with the two degree-of-freedom structure oscillator of cable with damper. The analyzed for the circular section of the cable is performed.

y1ver time, m1/m2=10, k1y/k2y=2,
b1y/b2y=2, α=0.02, γ=0.67

dy1/dt ver time, m1/m2=10,
k1y/k2y=2, b1y/b2y=2, α=0.02, γ=0.67

y1ver time, α=0.02, γ=0.67, without
damper

dy1/dtver time, α=0.02, γ=0.67, without
damper
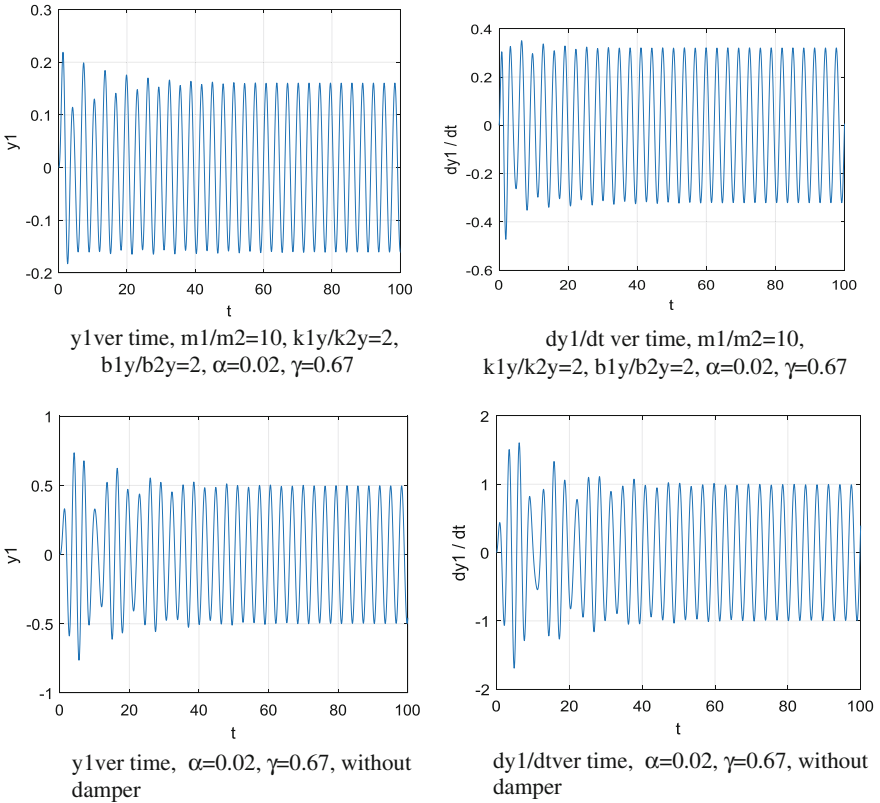
Fig. 5 Displacements of cable (y1) with and without damper, velocity of cable (dy1/dt) with and without damper in time domain for coefficient of stiffness (k1y/k2y) and damping (b1y/b2y)

System with damper: m1/m2=10,k1y/k2y=2,
b1y/b2y=2, α=0.02, γ=0.67

System without damper,α=0.02, γ=0.67
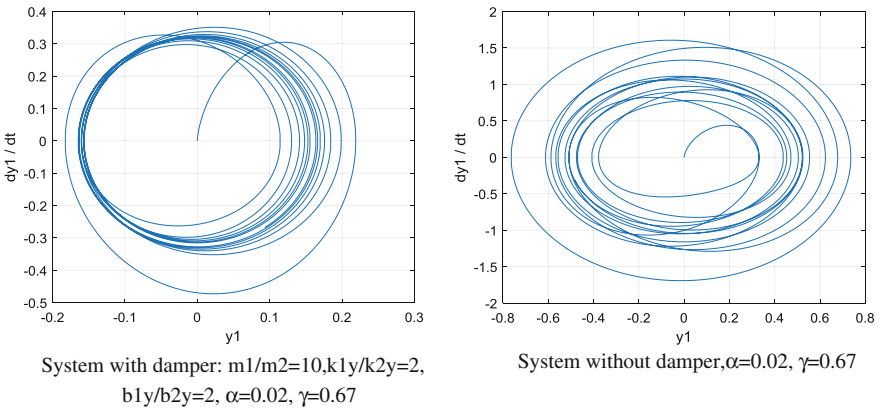
Fig. 6 Phase portraits of cable's displacements with and without damper
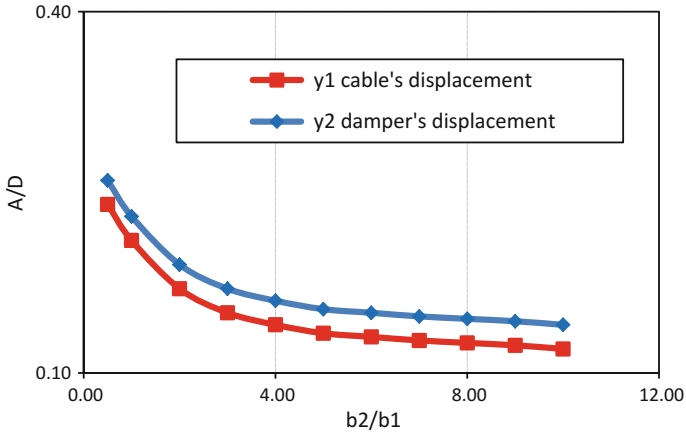
Fig. 7 Dimensionless amplitude of motion for damping variation of the damper and for different damping coefficient of the damper
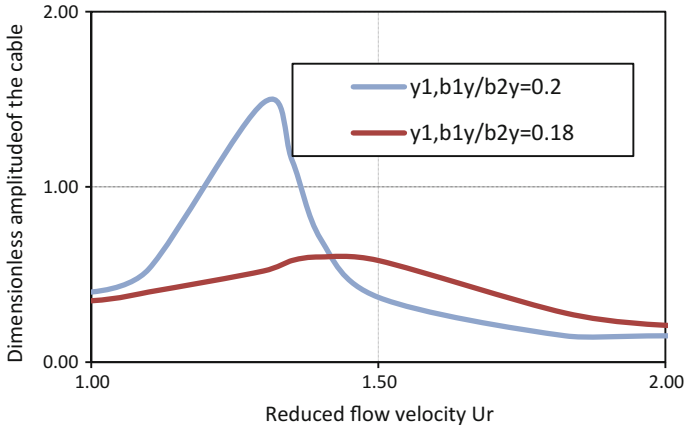
Fig. 8 Dimensionless cable's amplitudes (y1) and velocity (dy1/dt) of motion for reduced flow velocity Vr for different damping coefficients b1y/b2y

The model is investigated numerically and discussed with respect to the choice of the coupling terms and the values of model parameters.

The behavior of lift coefficient in time domain for different parameters of damping and velocity in Cl domain is presented as the result of searching and fixing suitable parameters of oscillating equation for fulfilling the fluid flow equations. Amplitudes of lift coefficient for variation of parameters γ of oscillating equation are presented.

In the study, the dynamical displacements and velocities of the cable with and without damper in time domain are drawn and dimensionless amplitudes of motion of the cable with damper for different relations of spring and damping parameters of the system are performed.

References

1. Blevins, R.D.: Flow-Induced Vibration. van Nostrand Reinhold, New York (1977)
2. McCroskey, W.J.: Some current research in unsteady fluid dynamics. J. Fluids Eng. **99**, 8–38 (1977)
3. Sarpkaya, T.: Vortex-induced oscillations. A selective review. J. Appl. Mech. **46**, 241–258 (1979)
4. Bearman, P.W., Luo, S.C.: Investigation of the aerodynamic instability of a square-section cylinder by forced oscillation. J. Fluids Struct. **2**, 161–176 (1988)
5. Bearman, P.W.: Vortex shedding from oscillating bluff bodies. Ann Rev Fluid Mech. **16**, 195–222 (1984)
6. Bishop, R.E.D., Hassan, A.Y.: The lift and drag forces on a circular cylinder oscillating in a flowing fluid. Proc. Roy. Soc. Lond. **A277**, 51–75 (1964)
7. Facchinetti, M.L., de Langre, E., Biolley, F.: Coupling of structure and wake oscillators in vortex-induced vibrations. J. Fluids Struct. **19**, 123–140 (2004)
8. King, R., Prosser, M.J., Johns, D.J.: On vortex excitation of model piles in water. J. Sound Vib. **29**, 169–188 (1973)
9. Griffin, O.M., Ramberg, S.E.: Vortex shedding from a cylinder vibrating in line with an incident uniform flow. J. Fluid Mech. **75**, 257–271 (1976)
10. Currie, I.G., Turnbull, D.H.: Streamwise oscillations of cylinders near the critical Reynolds number. J. Fluids Struct. **1**, 185–196 (1987)
11. Naudascher, E.: Flow-induced streamwise vibrations of structures. J. Fluids Struct. **1**, 265–298 (1987)
12. Sarpkaya, T.: Past progress and outstanding problems in time-dependent flows about ocean structures. In: Proceedings of the International Symposium on Separated Flow Marine Structures, Trondheim, pp. 1–36 (1985)
13. Maull, D.J., Milliner, M.G.: Sinusoidal flow past a circular cylinder. Coastal Eng. **2**, 149–168 (1978)
14. Bearman, P.W., Graham, J.M.R.: Hydrodynamic forces on cylindrical bodies in oscillating flow. In: Proceedings 2nd International Conference on BOSS, London, pp. 309–322 (1979)
15. Utsunomiya, H., Nagao, F., Uenovama, H.: Study of flows around rectangular cylinders by finite vortex sheets. J. Wind Eng. **37**, 271–280 (1988)
16. Awrejcewicz, J., Kudra, G., Wasilewski, G.: Chaotic zones in triple pendulum dynamics observed experimentally and numerically. Appl. Mech. Mater. **9**, 1–17 (2008)
17. Awrejcewicz, J., Kudra, G.: Experimental and numerical investigation of chaotic regions in the triple physical pendulum. Nonlinear Dyn. **50**, 755–766 (2007)
18. Awrejcewicz, J., Kudra, G.: Mathematical modelling and simulation of the bifurcational wobblestone dynamics. Discontinuity, Nonlinearity, Complex. **3**(2), 123–132 (2014)
19. Hartlen, R.T., Curie, I.G.: Lift oscillator model for vortex induced vibrations. ASCE J. Eng. Mech. **96**, 577–591 (1970)
20. Hunt, B.: Fluid Mechanics for Civil Engineers. Christchurch, New Zealand (1995)

Steady-State Behaviour of the Rigid Jeffcott Rotor Comparing Various Analytical Approaches to the Solution of the Reynolds Equation for Plain Journal Bearing

Štěpán Dyk, Miroslav Byrtus and Luboš Smolík

Abstract A planar 2 DOF model of an unbalanced rigid disc on a massless rigid shaft (rigid Jeffcott rotor) is extended considering nonlinear forces in plain journal bearings. To express the fluid-film forces in the journal bearings, several approximate analytical solutions of the Reynolds equation are used, including widely used approximations for infinitely long and infinitely short journal bearing and a method using correction polynomial functions to extend the area of aspect ratios. The differences in steady-state response of such a rotor are studied. The influence of the approximate solution type, eccentricity ratio and aspect ratio is analysed. The aim is to find out the more effective approach to journal bearing description which could be further used in detailed dynamical analyses of both stable and unstable dynamic behaviour along with nonlinear phenomena like bifurcations and transitions to chaotic motions.

Keywords Rigid Jeffcott rotor · Steady-state response · Reynolds equation Analytical solution · Plain journal bearings

1 Introduction

The *Jeffcott rotor* [1], also known as the *Laval rotor* [2], is one of the most-simplified mathematical models of rotor. It was used as the first-approximation in simulations of rotor behaviour. Although the 2 DOF model could be perceived as an oversimplification, its simplicity enables to easily include various complex phenomena and to

Š. Dyk (✉) · M. Byrtus · L. Smolík
NTIS, Faculty of Applied Sciences, Technická 8, 301 00 Pilsen, Czech Republic
e-mail: sdyk@ntis.zcu.cz

M. Byrtus
e-mail: mbyrtus@ntis.zcu.cz

L. Smolík
e-mail: carlist@ntis.zcu.cz

95

make a fundamental analyses of their influence on the rotor behaviour. The modifications of Jeffcott rotor are widely used to show various rotordynamics phenomena such as influence of rotor clearances and rotor-stator contacts [3], effects of seals [4], parametric vibration caused by cracked shaft [5] and a number of other phenomena.

One of the most studied subjects is the influence of a hydrodynamic lubrication in journal bearings on the dynamics of the rotor. A partial differential equation which describes the pressure distribution of thin viscous films in journal bearings was derived at the end of 19th century by Reynolds [6]. An analytical solution of the Reynolds equation for the finite length journal bearing has been found only lately [7]. However, the approximate analytical solutions could be highly useful as well, considering their relative simplicity and closed-form expression that can be easily used in wide class of engineering applications. There are two well-known and widely used approximations for the solution of pressure distribution in journal bearing: infinitely long journal bearing approximation (ILJB) for aspect ratios[1] $L/D \gg 1$ and infinitely short journal bearing approximation (ISJB) for aspect ratios $L/D \ll 1$. In case of ILJB [8], the pressure gradient in the circumferential direction is much larger than in the axial direction and in case of ISJB [9, 10] the pressure gradient in the circumferential direction is much smaller than in the axial direction. In both cases, the Reynolds partial equation is reduced to an ordinary differential equation, whose solution in closed form can be found. However, the solution is limited by the appropriate assumptions and it does not hold for aspect ratios $L/D \to 1$.

There are some approaches such as perturbation method that extends the interval of aspect ratios where the solution holds. The method and the solution are discussed in [11] for the Reynolds equation without squeeze-term and it has been subsequently extended for full Reynolds equation [12]. However, even if using these methods, the analytical solution for aspect ratios $L/D \in \langle 0.5; 2 \rangle$ does not hold as the assumptions are not satisfied. One of the possible ways to obtain an analytical closed-form expression for the solution of Reynolds equation with $L/D \to 1$ is a usage of correction functions [13]. The multiplicative polynomial functions are used to fit the approximate solution (ISJB, ILJB) to the referential (numerically obtained) pressure distribution in the bearing.

There are several another approaches for solving the Reynolds equation. Hydrodynamic lubrication in systems with Hertzian contacts is often computed employing Grubin's approximation [14]. Another analytical methods are focused for the special cases of finite journal bearings such as a porous bearing [15], which employs analytical solution for the infinitely long porous bearing and Warner's correction factors [16], a journal bearing in a turbulent flow regime [17], or a tilting pad bearing [18].

Relatively small number of authors employ analytical methods for a stability analysis of finite length journal bearings. Various perturbation methods [19, 20] and spectral element methods [21] are the most widely used techniques for such analysis.

---

[1]The aspect ratio is formulated for axial length L of the bearing and journal diameter D.

2 Jeffcott Rotor with Hydrodynamic Journal Bearing Forces

Based on the scheme depicted in the Fig. 1, the mathematical model of Jeffcott rotor can be formulated. In the original Jeffcott model, the elastic forces of flexible shaft or elastic forces in the bearing were considered. However, the phenomena occuring in the journal bearings are more complex and the bearing forces can be represented more precisely using an approximate solution of Reynolds equation which describes a pressure distribution in the bearing and which can be transformed to the force acting to the journal.

As shown in the Fig. 1, a position of the geometric centre C of journal is described in the non-rotating space by the horizontal displacement x and vertical displacement y. The angular speed of the rotor is ω, mass of the rotor is m and its static unbalance is ΔmE. In central position, the radial clearance between the journal and a bearing is c.

The mathematical model of the Jeffcott rotor in journal bearings can be formulated in the matrix form

$$
\begin{bmatrix} m & 0 \\ 0 & m \end{bmatrix} \begin{bmatrix} \ddot{x} \\ \ddot{y} \end{bmatrix} = \begin{bmatrix} 0 \\ -mg \end{bmatrix} + \Delta mE\omega^2 \begin{bmatrix} \cos \omega t \\ \sin \omega t \end{bmatrix} +
$$
$$
+ \begin{bmatrix} F_{rad}^{(X)}(e, \dot{e}, \dot{\Phi}, \omega) \cos \Phi - F_{tan}^{(X)}(e, \dot{e}, \dot{\Phi}, \omega) \sin \Phi \\ F_{rad}^{(X)}(e, \dot{e}, \dot{\Phi}, \omega) \sin \Phi + F_{tan}^{(X)}(e, \dot{e}, \dot{\Phi}, \omega) \cos \Phi \end{bmatrix},
$$

$$(1)$$
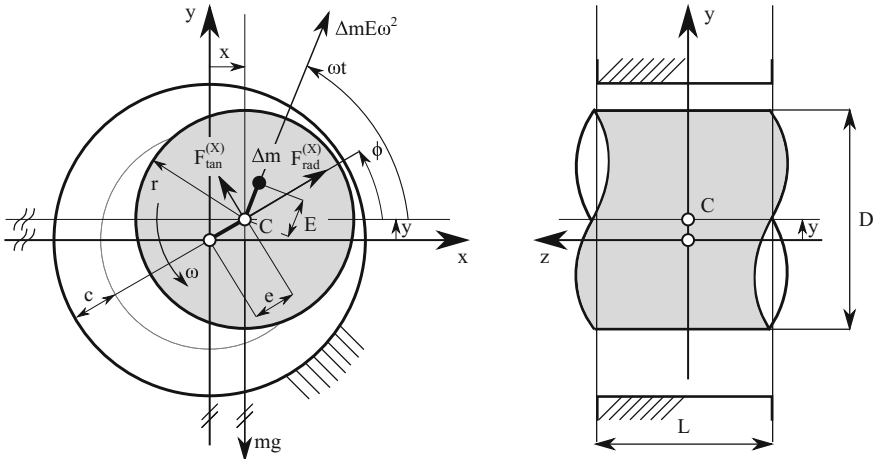
Fig. 1 The schematic of the considered Jeffcott rotor

where indices $X = IL, IS, IL_{cor}, IS_{cor}$ correspond to the infinitely long, infinitely short, corrected infinitely long and corrected infinitely short journal bearing, respectively.

The eccentricity e and relative eccentricity ε are defined in the form

$$e(t) = \sqrt{x(t)^2 + y(t)^2}, \qquad \varepsilon(t) = \frac{e(t)}{c}. \tag{2}$$

The derivatives of excentricity and relative excentricity are

$$\dot{e}(t) = \frac{de(t)}{dt} = \frac{x(t)\dot{x}(t) + y(t)\dot{y}(t)}{e(t)}, \qquad \dot{\varepsilon}(t) = \frac{d\varepsilon(t)}{dt} = \frac{1}{c}\frac{de(t)}{dt} = \frac{\dot{e}(t)}{c}. \tag{3}$$

The goniometric functions of the angle Φ are obviously

$$\cos \Phi = \frac{x}{e}, \qquad \sin \Phi = \frac{y}{e}, \tag{4}$$

and the angle Φ can be directly expressed in the form

$$\Phi = \text{arctg2}\left(\frac{y}{x}\right) = \begin{cases} \text{arctg}\left(\frac{y}{x}\right) & x > 0 \wedge y > 0, \\ \text{arctg}\left(\frac{y}{x}\right) + \pi & x < 0, \\ \text{arctg}\left(\frac{y}{x}\right) + 2\pi & x > 0 \wedge y < 0. \end{cases} \tag{5}$$

The derivative $\dot{\Phi}$ of angle Φ is

$$\dot{\Phi} = \frac{x(t)\dot{y}(t) - y(t)\dot{x}(t)}{x(t)^2 + y(t)^2}. \tag{6}$$

Formulas for forces in HD journal bearings introduced in [8] (IL) and [9, 10] (IS) have been summarized in [13]. Corresponding to the directions indicated in the Fig. 1 (the influence of oil film on the shaft), the forces can be expressed as

$$F_{rad}^{(IL)} = -6\mu RL \left(\frac{R}{c}\right)^2 \left[|\omega - 2\dot{\Phi}|\frac{2\varepsilon^2}{(2+\varepsilon^2)(1-\varepsilon^2)} + \frac{\pi\dot{\varepsilon}}{(1-\varepsilon^2)^{3/2}}\right], \tag{7}$$

$$F_{tan}^{(IL)} = 6\mu RL \left(\frac{R}{c}\right)^2 \left[(\omega - 2\dot{\Phi})\frac{\pi\varepsilon}{(2+\varepsilon^2)(1-\varepsilon^2)^{1/2}} + \frac{4\dot{\varepsilon}}{(1+\varepsilon)(1-\varepsilon^2)}\right], \tag{8}$$

$$F_{rad}^{(IS)} = -\mu RL \left(\frac{L}{c}\right)^2 \left[|\omega - 2\dot{\Phi}|\frac{\varepsilon^2}{(1-\varepsilon^2)^2} + \frac{\pi(1+2\varepsilon^2)\dot{\varepsilon}}{2(1-\varepsilon^2)^{5/2}}\right], \tag{9}$$

$$F_{tan}^{(IS)} = \mu RL \left(\frac{L}{c}\right)^2 \left[(\omega - 2\dot{\Phi})\frac{\pi\varepsilon}{4(1-\varepsilon^2)^{3/2}} + \frac{2\varepsilon\dot{\varepsilon}}{(1-\varepsilon^2)^2}\right]. \tag{10}$$

The IL-based and IS-based forces corrected for the finite journal bearing have been published in [13]. They are considered in the form

$$F_{rad}^{(IL_{cor})} = C_{rad}^{(IL_{cor})} (L/D, \varepsilon) F_{rad}^{(IL)}, \qquad F_{tan}^{(IL_{cor})} = C_{tan}^{(IL_{cor})} (L/D, \varepsilon) F_{tan}^{(IL)}, \qquad (11)$$

$$F_{rad}^{(IS_{cor})} = C_{rad}^{(IS_{cor})} (L/D, \varepsilon) F_{rad}^{(IS)}, \qquad F_{tan}^{(IS_{cor})} = C_{tan}^{(IS_{cor})} (L/D, \varepsilon) F_{tan}^{(IS)}, \qquad (12)$$

where $C_Y^{(X)} (L/D, \varepsilon)$ are correction polynomials defined for $X = IL, IS$ and $Y = rad, tan$.

3 Application and Results

To find a numerical solution for the system (1), the set of second order ODEs can be rewritten in state-space. Mathematical model (1) can be formally rewritten as

$$M\ddot{q} = \underbrace{f_G + f_e(t) + f_o^{(X)}(q, \dot{q}, \omega, t)}_{f^{(X)}(q, \dot{q}, \omega, t)}, \qquad X = IS, IL, IS_{cor}, IL_{cor}, \qquad (13)$$

where $q = [x, y]^T$ is vector of generalized coordinates and M is mass matrix. At the right hand side, a vector of gravitation forces f_G, vector of unbalance forces $f_e(t)$ and vector of oil-film forces $f_o^{(X)}(q, \dot{q}, \omega, t)$ are defined. The model can be written in the state-space with state vector $u = [q^T, \dot{q}^T]^T$ as

$$\dot{u} = \begin{bmatrix} \dot{q} \\ \ddot{q} \end{bmatrix} = \begin{bmatrix} \dot{q} \\ M^{-1} f^{(X)}(q, \dot{q}, \omega, t) \end{bmatrix}, \qquad X = IS, IL, IS_{cor}, IL_{cor}. \qquad (14)$$

The set of first order Eq. (14) is solved using the Runge-Kutta method with adaptive time step. The simulation is performed for $t \in \langle 0, 1.5 \rangle$ [s] and the time interval $t_{ss} \in \langle 1, 1.5 \rangle$ [s] of steady-state behaviour is subjected to the subsequent analyses. Particular parameters of the Jeffcott rotor used in the analyses are shown in the Table 1. For the comparison of results, numerical simulations in *AVL Excite* software have been performed. Herein, the model is created using a multibody approach and the Reynolds equation is solved using finite element method.

Two different types of analyses were performed to investigate the dynamical behaviour of the system: *unbalance response analysis* of the Jeffcott rotor and the *analysis of whirl instability* caused by the fluid-film of HD bearings. In the Figs. 2, 3 and 4, an unbalance response of the Jeffcott rotor is shown via orbits of the centre of journal for chosen rotational speeds. The aspect ratio $\eta = 1$ is considered for finite length bearing (Fig. 3) and for limit values of the approximate solutions $\eta = 0.5$, $\eta = 2$ for IS and IL journal bearing (Figs. 2 and 4, respectively). Qualitative and quantitative change of the orbits occurs with increasing speed of the rotor. However, orbits of the rotor also differ for the different HD bearings models at the same

Table 1 Parameters of the Jeffcott rotor in HD journal bearings [13]

Parameter	Value
Radial clearance	$c = 0.9 \times 10^{-3}$ m
Unbalance	$\Delta m = 0.01$ kg
Unbalance eccentricity	$E = 0.01$ m
Rotor mass	$m = 3$ kg
Rotor RPM	$n = \langle 500; 2900 \rangle$ RPM
Dynamic viscosity	$\mu = 0.07$ Pa·s
Bearing diameter	$D = 47.37 \times 10^{-3}$ m
Bearing axial length	$L = \eta D, \eta \in \langle 0, 5; 2 \rangle$
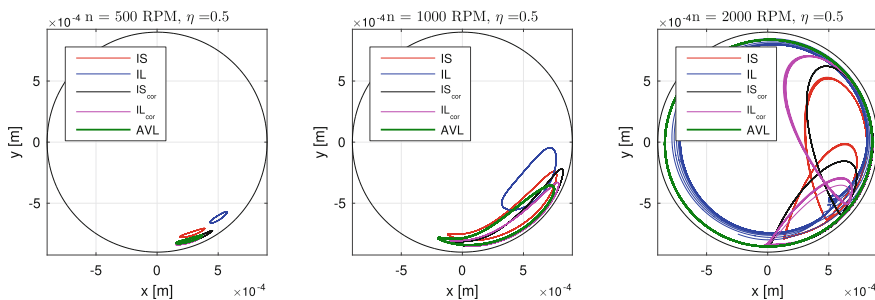
Fig. 2 Orbits of the Jeffcott rotor with all the considered hydrodynamic forces for aspect ratio $\eta = \frac{L}{D} = 0.5$
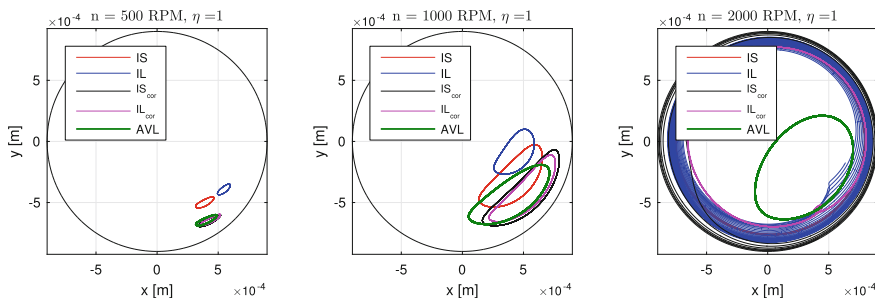
Fig. 3 Orbits of the Jeffcott rotor with all the considered hydrodynamic forces for aspect ratio $\eta = \frac{L}{D} = 1$

speeds. The IS_{cor} and IL_{cor} solutions are relatively close, particularly at lower speeds. As expected, the approximate solution IS is closer to the both corrected solutions for $\eta = 0.5$ and IL is closer to the both corrected solution for $\eta = 2$.

The analysis of the oil-film whirl instability is induced even in case of perfectly balanced rotor ($\Delta mE = 0$). The motion of Jeffcott rotor with parameters shown in the Table 1 has been simulated for all the considered HD forces in journal bearings and
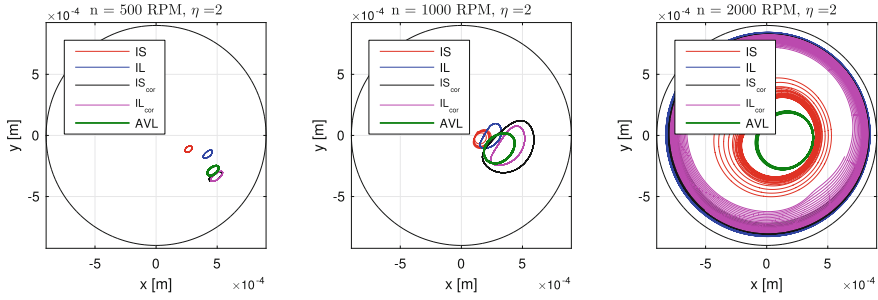
Fig. 4 Orbits of the Jeffcott rotor with all the considered hydrodynamic forces for aspect ratio $\eta = \frac{L}{D} = 2$
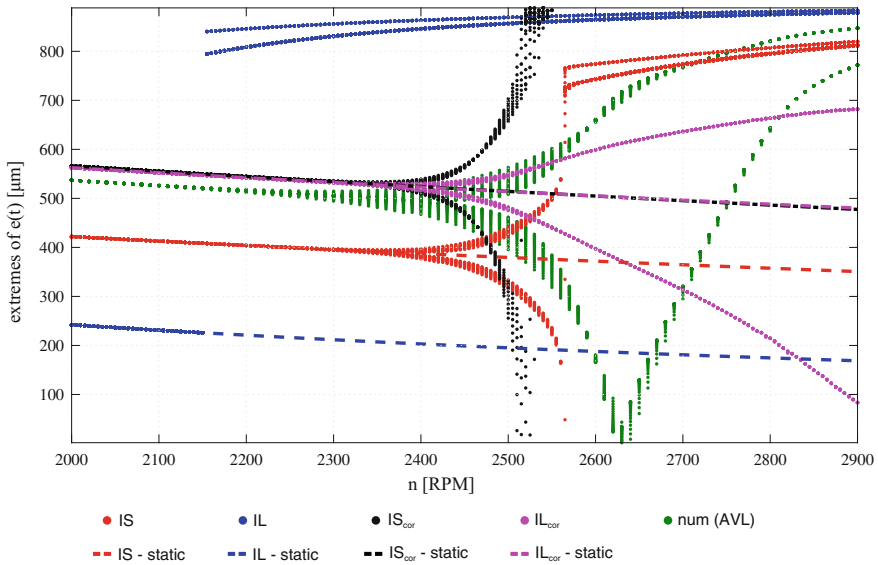
Fig. 5 Bifurcation of eccentricities of the Jeffcott rotor with all the considered hydrodynamic forces for $\eta = \frac{L}{D} = 1$. Solution obtained by the static analysis is depicted by the dashed line

for the rotational speeds $\omega = \pi n/30$, $n = \langle 2000, 2900 \rangle$ RPM. To depict the whirl instability, bifurcation diagram Fig. 5 was used. The extremes of the eccentricities $e(t_{ss})$ are evaluated at all the considered rotational speeds. It enables to distinguish the areas with fixed point attractor (single point at the particular speed) and areas of the limit-cycle attractor (two or more different points at the particular speed).

The diagram in Fig. 5 shows almost identical extremes of eccentricities for both corrected models IS_{cor} and IL_{cor} in the area of fixed point attractor and the bifurcation occurs at the pretty close rotational speeds. However, the behaviour of both models differs in the area of limit cycle attractor. The amplitudes of IS based model grow more

rapidly and it even does not converge to the limit cycle for larger values of rotational speeds. The location of a bifurcation point differs for IS and IL approximations.

An additional information of the bifurcation analyses can be obtained using static analysis. This follows from (13) with omitted dynamical forces: inertial forces $M\ddot{q}$ and centrifugal forces $f_e(t)$. All the terms in formulas of oil-film forces (7)–(12) that are dependent on $\dot{\varepsilon}$ also equals zero in the static case. The problem can be formulated in the form of set of nonlinear algebraic equations

$$f_G + f_o(q, \omega) = 0 \tag{15}$$

which is solved using Trust-Region Dogleg Method. For the chosen rotational speed ω of the rotor, a static solution q_{static} is find which satisfies (15). Corresponding eccentricities [transformed using (2)] are depicted in the bifurcation diagram by the dashed line.

Obviously, for the stable area before bifurcation of the dynamical solution a static solution directly corresponds to the dynamical solution (without unbalance). However, in the area after bifurcation point, the static solution corresponds to unstable dynamical solution.

4   Conclusions

The paper focuses on the behaviour of Jeffcott rotor supported by HD journal bearings. To describe bearing forces, various approximate analytical solutions of Reynolds equation for plain journal bearings are used. The differences in the rotor behaviour are demonstrated using the unbalance response and the analysis of the whirl instability. The unbalance response analysis shows the similar behaviour of the corrected IL and IS models, particularly at lower speeds. Both of these two models come to the IL or IS approximations with the aspect ratio coming close to the corresponding limit state (IS or IL).

The analysis of whirl instability shows the different location of Hopf bifurcation for all the considered forces. Qualitatively different behaviour in the limit-cycle area is observed. The dynamical steady-state computations are supplemented by the static analysis of the system via numerical solution of set of nonlinear algebraic equations. This shows the possible unstable equilibria in the area of limit-cycle attractor of the Jeffcott rotor.

To provide a comparison, multibody simulation-based computations have been performed in AVL Excite where the Reynolds equation is solved using the finite element method. The comparison shows satisfactory agreement particularly for the corrected IL and IS based approximations in wide range of aspect ratios $\eta = \frac{L}{D} \in \{0.5; 1; 2\}$ in case of unbalance response. The agreement of the bifurcation point for corrected IS and IL models with numerical model have been provided for the case of $\eta = 1$.

References

1. Jeffcott, H.H.: XXVII. The lateral vibration of loaded shafts in the neighbourhood of a whirling speed. The effect of want of balance. Phil. Mag. **37**(219), 304–314 (1919)
2. Gasch, R.: Dynamic behaviour of the laval rotor with a transverse crack. Mech. Syst. Signal Process. **22**(4), 790–804 (2008). (Special Issue: Crack Effects in Rotordynamics)
3. Vlajic, N., Champneys, A.R., Balachandran, B.: Nonlinear dynamics of a Jeffcott rotor with torsional deformations and rotor-stator contact. Int. J. Non-Linear Mech. **92**, 102–110 (2017)
4. Li, W., Yang, Y., Sheng, D., Chen, J.: A novel nonlinear model of rotor/bearing/seal system and numerical analysis. Mech. Mach. Theory **46**(5), 618–631 (2011)
5. Ishida, Y.: Cracked rotors: industrial machine case histories and nonlinear effects shown by simple Jeffcott rotor. Mech. Syst. Signal Process. **22**(4), 805–817 (2008). (Special Issue: Crack Effects in Rotordynamics)
6. Reynolds, O.: On the theory of lubrication and its application to Mr. Beauchamp tower's experiments, including an experimental determination of the viscosity of olive oil. Philos. Trans. R. Soc. Lond. **177**, 157–234 (1886)
7. Sfyris, D., Chasalevris, A.: An exact analytical solution of the reynolds equation for the finite journal bearing lubrication. Tribol. Int. **55**, 46–58 (2012)
8. Sommerfeld, A.: Zur hydrodynamischen theorie der schmiermittelreibung. Z. Math. Phys. **50**(1–2), 97–155 (1904)
9. Ocvirk, F.: Short-bearing approximation for full journal bearings. Technical Report, Cornell University, 10 (1952)
10. Buckholz, R., Hwang, B.: The accuracy of short bearing theory for newtonian lubricants. J. Tribol. **108**(1), 73–79 (1986)
11. Vignolo, G.G., Barilá, D.O., Quinzani, L.: Approximate analytical solution to reynolds equation for finite length journal bearings. Tribol. Int. **44**(1), 10891099 (2011)
12. Gong, R.-Z., Li, D.-Y., Wnag, H.-J., Han, L., Quin, D.: Analytical solution of reynolds equation under dynamic conditions. J. Eng. Tribol. **230**(4), 416–427 (2016)
13. Bastani, Y., de Queiroz, M.: A new analytic approximation for the hydrodynamic forces in finite-length journal bearings. J. Tribol. **132**(1), 014502–01–014502–9 (2010)
14. Vichard, J.P.: Transient effects in the lubrication of Hertzian contacts. J. Mech. Eng. Sci. **13**(3), 173–189 (1971)
15. D'Agostino, V., Senatore, A.: Analytical solution for two-dimensional reynolds equation for porous journal bearings. Industr. Lubr. Tribol. **58**(2), 110–117 (2006)
16. Warner, P.C.: Static and dynamic properties of partial journal bearings. J. Basic Eng. **85**(2), 247–257 (1963)
17. Zhang, Y., Hei, D., Liu, C., Guo, B., Lu, Y., Müller, N.: An approximate solution of oil film forces of turbulent finite length journal bearing. Tribol. Int. **74**(1), 110–120 (2014)
18. Okabe, E.P.: Analytical model of a tilting pad bearing including turbulence and fluid inertia effects. Tribol. Int. **114**, 245–256 (2017)
19. Brancati, R., Rocca, E., Russo, R.: Non-linear stability analysis of a rigid rotor on tilting pad journal bearings. Tribol. Int. **29**(7), 571–578 (1996)
20. Jang, G.H., Yoon, J.W.: Stability analysis of a hydrodynamic journal bearing with rotating herringbone grooves. J. Tribol. **125**, 291–300 (2003)
21. Chen, C.-Y., Yen, R.-H., Chang, C.-C.: Spectral element analysis of herringbone-grooved journal bearings with groove-ridge discontinuity. Int. J. Numer. Meth. Fluids **66**(9), 1116–1131 (2011)

Numerical Investigation on Dynamic Performance of a Multi-storey Steel Structure Model and Comparison with Experimental Results

Tomasz Falborski, Barbara Sołtysik and Robert Jankowski

Abstract Shaking table testing is the most commonly adopted method to simulate earthquake forces. This approach allows us to analyze the dynamic performance and provides a valuable insight into the dynamics of building structures, which helps to improve their future safety and reliability. The present study aims to conduct a numerical evaluation of dynamic response of a multi-storey steel structure model, which was previously examined during an extensive shaking table investigation. The experimental model was subjected to a number of different earthquake ground motions and a mining tremor. In order to perform this numerical research, the analyzed two-storey steel structure model was considered as a 2-DOF system with lumped parameters, which were determined by conducting free vibration tests. The results obtained demonstrate that not only seismic excitations but also mining tremors may considerably deteriorate structural behaviour by inducting strong structural vibrations. The time-acceleration history plots computed for the multi-storey structure model idealized as a 2-DOF system are consistent with those recorded during the previously conducted shaking table investigation, which confirms high accuracy in assuming lumped parameters to characterize the analyzed two-storey steel structure model.

Keywords Structural dynamics · Earthquake excitations
Multi-degree-of-freedom system · Differential equation of motion

T. Falborski (✉) · B. Sołtysik · R. Jankowski
Faculty of Civil and Environmental Engineering,
Gdansk University of Technology, 11/12 Narutowicza St., 80-233 Gdansk, Poland
e-mail: tomfalbo@pg.gda.pl

B. Sołtysik
e-mail: barwiech@pg.gda.pl

R. Jankowski
e-mail: jankowr@pg.gda.pl

1   Introduction

Earthquakes are identified among the most severe and unpredictable dynamic excitations, which building structures can be exposed to. Strong ground motions may cause a lot of damage in a wide variety of ways and, therefore, have become an issue of major concern of both professional and research communities (see, for example, [1–11]). Earthquakes produce large-magnitude forces of short duration that must be resisted by a structure without causing collapse and preferably without significant damage to the structural members. For that reason, ground motions resulting from earthquakes present unique challenge to the design of structures and became an issue of major concern in many seismically active regions.

Shaking table testing is the most commonly adopted approach to simulate earthquake forces. It allows us to analyze the seismic performance and provides a valuable insight into the dynamics of building structures, which helps to improve their future safety and reliability. Therefore, the present study aims to conduct a numerical evaluation of dynamic response of a two-storey steel structure model, which was previously examined during an extensive shaking table investigation. The experimental model was subjected to a number of different earthquake ground motions and one mining tremor as an example of so-called mining-induced seismicity (see, for example, [12]). In order to perform this numerical research, the analyzed two-storey steel structure model was considered as a two-degree-of-freedom (2-DOF) system with lumped parameters, which were determined by conducting free vibration tests.

2   Experimental Model and Shaking Table Investigation

In order to conduct the experimental investigation, a two-storey steel structure model was firstly prepared, as indicated in Fig. 1. It was built using two welded steel frames and three concrete plates. The welded steel frames were constructed using the rectangular hollow section elements (RHS $15 \times 15 \times 1.5$ mm). The columns were arranged in a rectangular pattern with spacing of 0.465 m in the longitudinal direction and 0.556 m in the transverse one. Additional diagonal bracing was used in the sidewall planes to counteract transverse and torsional vibrations. Concrete plates ($50 \times 50 \times 7$ cm) were used to simulate the weight of floors and a foundation slab. The two-storey structure model was 2.30 m high and weighs nearly 150 kg. The seismic response of the experimental model under a number of dynamic excitations, including earthquake ground motions and a strong mining tremor (see [13]), was extensively studied during a comprehensive shaking table investigation carried out with the use of a middle-sized shaking table located at Gdansk University of Technology, Poland. The more detailed results obtained from the shaking table study for both single- and two-storey steel structure models have already been presented in previous publications (see [14]).

Fig. 1 Two-storey
experimental model mounted
on the middle-sized shaking
table

Fig. 2 Experimental model
as a two-degree-of-freedom
system
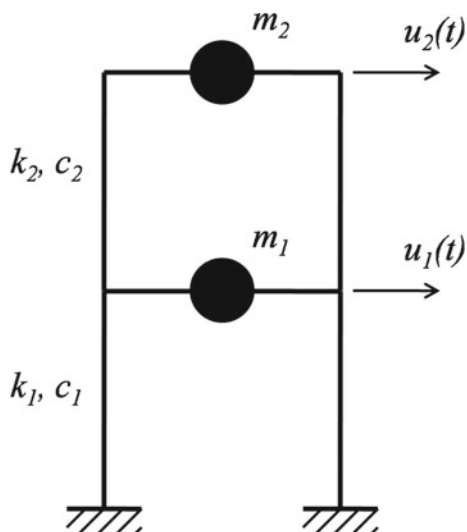
3 Numerical Analysis

In order to perform the numerical evaluation of dynamic response of the experimentally examined two-storey steel structure model, lumped-mass system has been applied (Fig. 2). The experimental model was idealized as a 2-DOF system, for which the dynamic equation of motion is given by (see, for example, [15, 16]):

$$M \cdot \ddot{u}(t) + C \cdot \dot{u}(t) + K \cdot u(t) = -MI \cdot \ddot{u}_g(t) \tag{1}$$

in which M, C, and K denotes mass, damping, and stiffness matrices, respectively, $u(t)$, $\dot{u}(t)$, and $\ddot{u}(t)$ the displacement, velocity, and acceleration of the structure model, respectively, $\ddot{u}_g(t)$ the ground acceleration, and I is the influence coefficient matrix, having 1 for elements corresponding to degrees of freedom in the direction of the applied ground motion and 0 for the other degrees of freedom. Matrices M, C, K, $u(t)$, $\dot{u}(t)$, $\ddot{u}(t)$, and I are defined as follows:

$$M = \begin{bmatrix} m_1 & 0 \\ 0 & m_2 \end{bmatrix} \tag{2}$$

$$C = \begin{bmatrix} c_1 + c_2 & -c_2 \\ -c_2 & c_2 \end{bmatrix} \tag{3}$$

$$K = \begin{bmatrix} k_1 + k_2 & -k_2 \\ -k_2 & k_2 \end{bmatrix} \tag{4}$$

$$\ddot{u}(t) = \begin{Bmatrix} \ddot{u}_1(t) \\ \ddot{u}_2(t) \end{Bmatrix} \tag{5}$$

$$\dot{u}(t) = \begin{Bmatrix} \dot{u}_1(t) \\ \dot{u}_2(t) \end{Bmatrix} \tag{6}$$

$$u(t) = \begin{Bmatrix} u_1(t) \\ u_2(t) \end{Bmatrix} \tag{7}$$

$$I = \begin{Bmatrix} 1 \\ 1 \end{Bmatrix} \tag{8}$$

The 2-DOF system was characterized by the following parameters:

$$m_1 = m_2 = 47.56\,\text{kg} \tag{9}$$

$$k_1 = k_2 = \omega^2 m = 20,571\,\frac{\text{N}}{\text{m}} \tag{10}$$

$$c_1 = c_2 = 2m\omega\xi = 10.48\,\frac{\text{kg}}{\text{s}} \tag{11}$$

where m_1 and m_2 denote lumped masses concentrated at the mid-height and the roof level, k_1 and k_2 the values of lateral stiffness, c_1 and c_2 the values of viscous damping. The natural circular frequency ω and the damping ratio ξ were previously determined by conducting free vibration tests.

In order to solve the second-order differential equation of motion (Eq. 1), the unconditionally stable Newmark's average acceleration method was applied (see [17]), as it is the most frequently used integration procedure in the case of seismic analyses of structures. The 2-DOF system considered in the present study was

subjected to the same dynamic excitations, which were previously applied to the experimental model during the shaking table investigation (see [13]).

The acceleration time histories computed for the 2-DOF system under various seismic excitations are presented in Figs. 3, 4, 5, 6 and 7. The comparison of the results obtained from the numerical analysis using lumped-mass model and the shaking table investigation are briefly reported in Table 1.
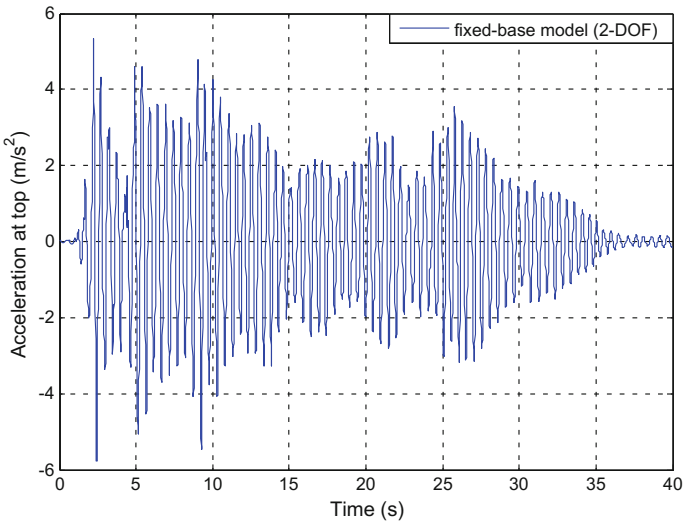
Fig. 3 Computed time-acceleration history for the 1940 El Centro earthquake
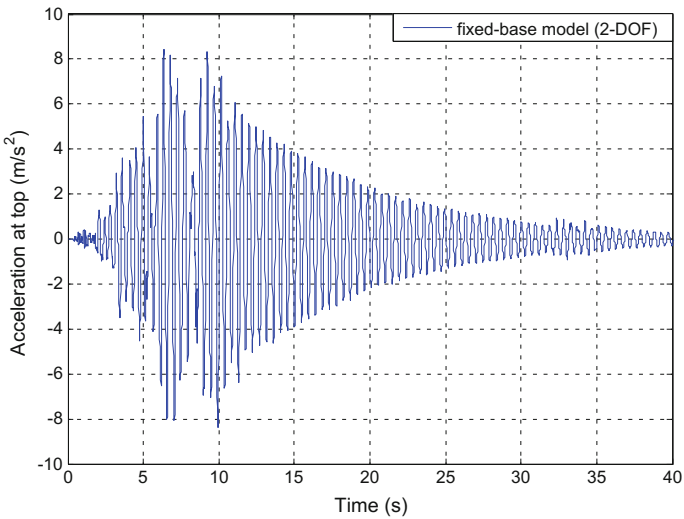
Fig. 4 Computed time-acceleration history for the 1971 San Fernando earthquake
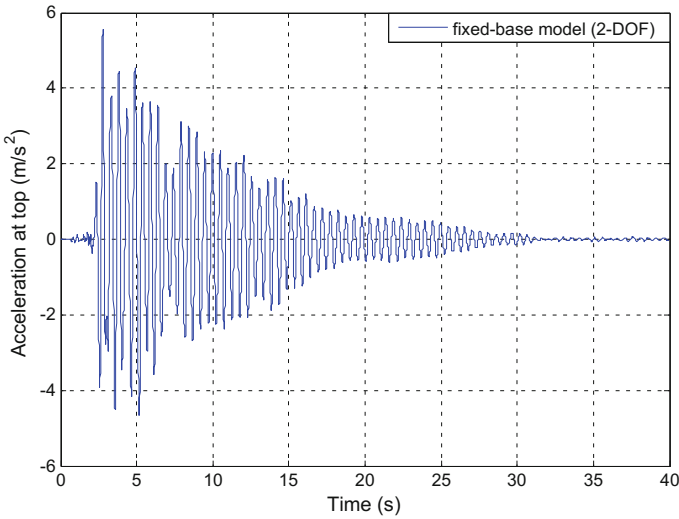
Fig. 5 Computed time-acceleration history for the 1989 Loma Prieta earthquake
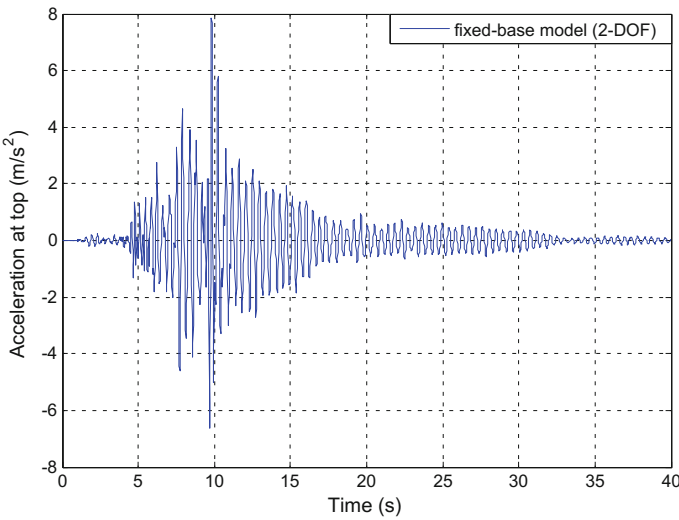
Fig. 6 Computed time-acceleration history for the 1994 Northridge earthquake

4 Final Summary and Conclusions

The present research was designed to perform a numerical evaluation of dynamic response of a two-storey steel structure model, which was previously examined during an extensive shaking table investigation. The analyzed structure model was idealized as a 2-DOF system and subjected to a number of different dynamic excitations. In
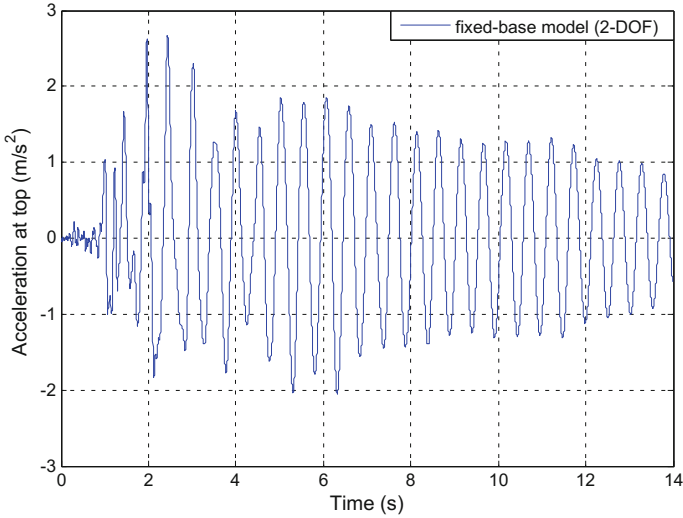
Fig. 7 Computed time-acceleration history for the 2002 Polkowice mining tremor

order to solve the second-order differential equation of motion, Newmark's average acceleration method was adopted.

As expected, the results obtained showed that strong dynamic excitations may considerably deteriorate structural safety by inducting structural vibrations. The time-acceleration history plots computed for the two-storey structure model idealized as a 2-DOF system are consistent with those recorded during the previously conducted shaking table investigation. Close inspection of Table 1 explicitly demonstrates that the peak values of the lateral accelerations at the top of the structure model from both experimental and numerical studies are almost the same which confirms high accuracy in assuming lumped parameters to characterize the analyzed two-storey structure. These parameters will be employed in further numerical research, which will cover the evaluation of dynamic response of both fixed-base and base-isolated structures including soil-structure interaction effects.

The results clearly show that not only seismic excitations but also mining tremors may considerably deteriorate structural behaviour by inducting strong structural vibrations.

Table 1 Comparison of numerical and experimental results

Dynamic excitation	Peak acceleration at the top of the two-storey steel structure model (m/s^2)	
	Lumped-mass numerical analysis	Shaking table investigation
El Centro earthquake, 18.05.1940 (NS component, PGA = 3.070 m/s^2)	5.77	5.98
San Fernando earthquake, 9.02.1971 (Pacoima Dam station, N74°E component, PGA = 5.688 m/s^2)	8.45	8.41
Loma Prieta earthquake, 17.10.1989 (Corralitos station, NS component, PGA = 3.158 m/s^2)	5.54	5.49
Northridge earthquake, 17.01.1994 (Santa Monica station, EW component, PGA = 4.332 m/s^2)	7.85	7.68
Polkowice mining tremor, 20.02.2002 (NS component, PGA = 1.634 m/s^2)	2.67	2.67

Where PGA denotes the *Peak Ground Acceleration*

References

1. Chen, W.F., Scawthorn, C.: Earthquake Engineering Handbook. CRC Press, Boca Raton (2003)
2. Wasti, S.T., Ozcebe, G.: Seismic Assessment and Rehabilitation of Existing Buildings. Kluwer Academic Publishers, Dordrecht (2003)
3. Jankowski, R., Mahmoud, S.: Earthquake-Induced Structural Pounding. Springer, Switzerland (2015)
4. Ebrahimian, M., Todorovska, M.I., Falborski, T.: Wave method for structural health monitoring: testing using full-scale shake table experiment data. J. Struct. Eng. **143**(4), https://doi.org/10.1061/(asce)st.1943-541x.0001712 (2016)
5. Jankowski, R.: Pounding between superstructure segments in multi-supported elevated bridge with three-span continuous deck under 3D non-uniform earthquake excitation. J. Earthq. Tsunami, **9**, Paper No. 1550012 (2015)
6. Jankowski, R., Mahmoud, S.: Linking of adjacent three-storey buildings for mitigation of structural pounding during earthquakes. Bull. Earthq. Eng. **14**, 3075–3097 (2016)
7. Naderpour, H., Barros, R.C., Khatami, S.M., Jankowski, R.: Numerical study on pounding between two adjacent buildings under earthquake excitation. Shock Vibr., Paper No. 1504783 (2016)
8. Sołtysik, B., Falborski, T., Jankowski, R.: Investigation on damage-involved structural response of colliding steel structures during ground motions. Key Eng. Mater. **713**, 26–29 (2016)
9. Falborski, T., Sołtysik, B., Jankowski, R.: Mathematical modelling of a seismic isolation system to protect structures during damaging earthquakes. Key Eng. Mater. **713**, 220–223 (2016)
10. Falborski, T., Jankowski, R., Kwiecień, A.: Experimental study on polymer mass used to repair damaged structures. Key Eng. Mater. **488**, 347–350 (2012)

11. Falborski, T., Jankowski, R.: Behaviour of asymmetric structure with base isolation made of polymeric bearings. In: Geotechnical, Geological and Earthquake Engineering Vol. 40: Seismic Behaviour and Design of Irregular and Complex Civil Structures II, 333–341 (2016)
12. Zembaty, Z.: Rockburst induced ground motion—a comparative study. Soil Dyn. Earthq. Eng. **24**, 11–23 (2004)
13. Falborski, T., Jankowski, R.: Polymeric bearings—a new base isolation system to reduce structural damage during earthquakes. Key Eng. Mater. **569–570**, 143–150 (2013)
14. Falborski, T., Jankowski, R.: Experimental study on effectiveness of a prototype seismic isolation system made of polymeric bearings. Appl. Sci. **7**(8), https://doi.org/10.3390/app7080808 (2017)
15. Chopra, A.K.: Dynamics of Structures: Theory and Applications to Earthquake Engineering. Prentice Hall, New Jersey (1995)
16. Clough, R., Penzien, J.: Dynamics of Structures. McGraw-Hill, New York (1975)
17. Newmark, N.M.: A method of computing for structural dynamics. J. Eng. Mech. **85**, Paper No. 2094 (1959)

Accumulation of the Energy in Mechanical Resonance

Wiesław Fiebig

Abstract The resonance phenomena occurs when the frequency of the excitation force in an oscillating system is equal to the natural frequency of the system. It will be shown, that in resonance, the inertial forces are compensated with the spring forces and the energy delivered in one cycle of vibrations is equal to the energy dissipated in an oscillator. The mechanical energy will be stored in an oscillator. In this paper the differences between energy accumulation in an oscillator and in the flywheel will be discussed. Finally the possibilities of use of the energy from resonance in machines will be shown.

Keywords Mechanical resonance · Energy accumulation · Impact and piston machines

1 Introduction

Resonance in mechanical systems is in most cases unwanted. Increased vibrations are connected with accelerations and thus with dynamic loads acting on the components of the systems. Overload and fatigue may strongly influence the integrity of a construction or structure e.g. failure of Tacoma Bridge, footbridges, shaft critical speeds, etc. As result of resonance the vibration amplitude is increasing [1, 2].

There are not many studies of use of mechanical resonance in a positive sense in drive systems of machinery and equipment, although it is known that this phenomena is used in many other applications such as electromagnetic resonance, radio waves, laser technology, etc. There is extensive literature on vibration energy harvesting in micro scale [3–9], which states that efficiency in obtaining energy from vibration is highest when energy reception occurs under mechanical resonance conditions. Harvesting of vibration energy is used to power small onboard devices, sensors and

W. Fiebig (✉)

Faculty of Mechanical Engineering, Wroclaw University of Science and Technology, ul. Łukasiewicza 7/9, 51-370 Wrocław, Poland

e-mail: wieslaw.fiebig@pwr.edu.pl
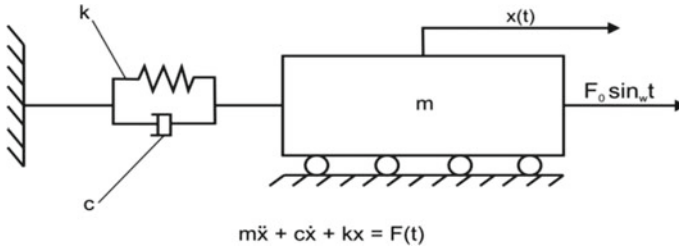
Fig. 1 Simple harmonic oscillator

electronics. The intentional use of mechanical resonance can be found in micro-scale systems—MEMS [8]. It has been stated that the most efficient energy harvesting occurs at the resonance conditions of the harvester [7, 9].

Large-scale energy harvesting has been described in [9]. Vibration energy may be harvestable in vehicle suspension systems, from the vibration of buildings and railway tracks, from human motion and from ocean waves etc. [9–11]. The paper [12] presents the case of a robotic arm where, due to the use of resonance, energy savings up to 56% were achieved.

The positive effects resulting from mechanical resonance are also used in the development of the optimal parameters of micro-propulsion systems to drive flying objects using wings [13]. Among other applications resonance is used in vibratory conveyors and in resonance drilling machines [14–16]. There is a very significant increase in the energy efficiency of such machines using resonance phenomena The main purpose of this paper is to explain the energy accumulation in mechanical resonance. That will be done with the assumption of linear viscous damping in the system. The effect of non-linear damping in different mechanical systems is analyzed at work [17]. Finally, the accumulation of energy at resonance and its use in impact working machines and in machines with crankshaft systems will be presented.

2 Energy in an Oscillator

In Fig. 1 the simple harmonic oscillator has been shown.

The general solution of equation of motion for a harmonic oscillator shown in Fig. 1 can be written as [3]:

$$x(t) = x_m * e^{-\beta t} * \cos\left(t * \sqrt{\omega^2 - \beta^2} + \Phi\right) + X_m * \cos(\omega_w * t + \varphi) \qquad (1)$$

$$\phi = arctg\left[\left(\frac{-\beta}{\sqrt{\omega^2 - \beta^2}}\right) * \left(1 + \frac{2 * \omega_w^2}{\omega^2 - \omega_w^2}\right)\right] \qquad (2)$$

$$\varphi = -arctg\left(\frac{2 * \beta * \omega_w}{\omega^2 - \omega_w^2}\right) \qquad (3)$$

Fig. 2 Displacement of the mass and energy of the oscillator at the frequency $\omega_w = 6\ \text{s}^{-1}$ (below resonance)
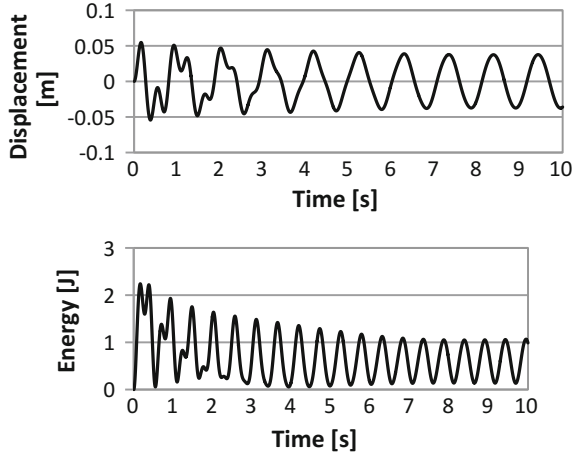
$$x_m = -X_m * \left[\frac{\cos(\varphi)}{\cos(\phi)} \right] \tag{4}$$

$$X_m = \frac{F_0}{\sqrt{m^2 * (\omega^2 - \omega_w^2)^2 + \left(c^2 * \omega_w^2\right)}} \tag{5}$$

where: $\omega = \sqrt{\omega_0^2 - \beta^2}$, $\beta = \frac{c}{2 * m}$, $\omega_0 = \sqrt{\frac{k}{m}}$, ω_w- excitation frequency.

The total energy of the mass in the oscillator will be defined as:

$$E_{osc} = \frac{1}{2} k X_m^2 \tag{6}$$

The calculations for excitation frequencies before resonance, in resonance and after the resonance have been performed to clear the differences in amplitude and total energy in an oscillator.

Following data have been used for calculations:

m = 5 kg—oscillating mass
k = 1500 N/m—spring stiffness
c = 5 Ns/m—damping factor
F_0 = 50 N—amplitude of the excitation force
Initial conditions: x(t = 0) = 0, dx/dt(t = 0) = 0.

For frequencies of excitation lower than resonance frequency (Fig. 2), the vibration amplitude is stabilized after define time and is relatively low. The peak value of the vibration energy of the oscillator achieves in steady state around 1 J.

The amplitude of vibrations is increased, as the frequency of excitation is closer to the natural frequency of the oscillator. Under resonance conditions (Fig. 3), the amplitude of vibrations increases up to the maximum by 0.6 m.

Fig. 3 Displacement of the
mass and energy of the
oscillator at the resonance
$\omega_w = 17.31\ \mathrm{s}^{-1}$
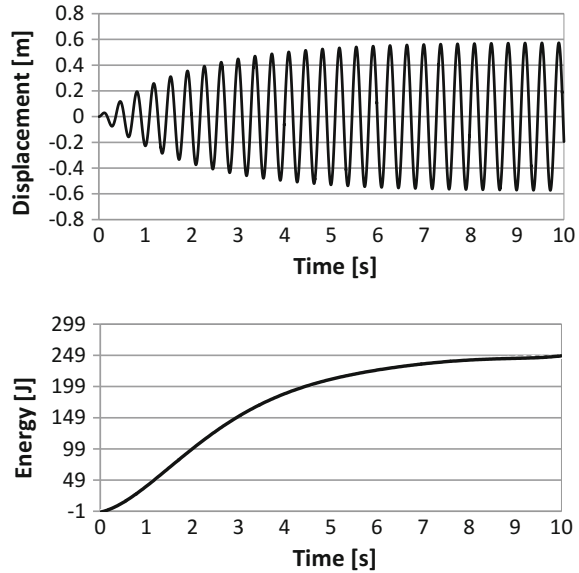
The energy is increasing with the increase of amplitude of vibrations and achieves the level of around 250 J. Under resonance conditions, the excitation force precedes the displacement of the mass at 90° so that the maximum possible vibration energy can be obtained.

At frequencies above resonance the amplitude of vibrations (Fig. 4) is again lower and the peak value of the energy in oscillator is decreasing up to 1.5 J.

3   Force Balance in Resonance

Figure 5 shows the time course of inertial force and spring force and Fig. 6 shows the excitation force and damping force in the oscillator.

At steady state of resonance, due to the 180° phase shift, the inertia force is compensated by the spring force, while the damping force is balanced by the external force. In the steady state conditions of resonance the excitation force is used to overcome the damping only. If theoretically no damping will be considered, the amplitude of vibration increase to infinity. Figure 8 shows that the energy stored in the oscillator is many times higher than the peak values of the instantaneous energy supplied to the oscillator resulting from the harmonic excitation.

It is important to underline that the amount of energy accumulated is closely related to the damping. The smaller the damping, the more energy will be accumulated in the oscillator at resonance.

Fig. 4 Displacement of the mass and energy of the oscillator at the frequency $\omega_w = 25 \ s^{-1}$ (above resonance)
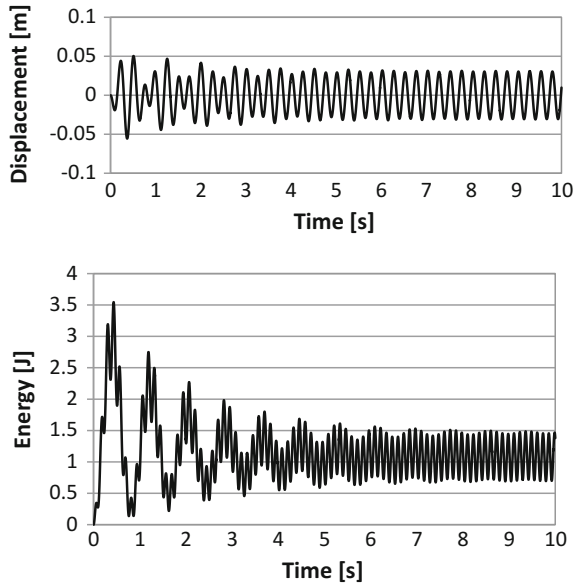
Fig. 5 Time courses of the inertial force and spring force at resonance
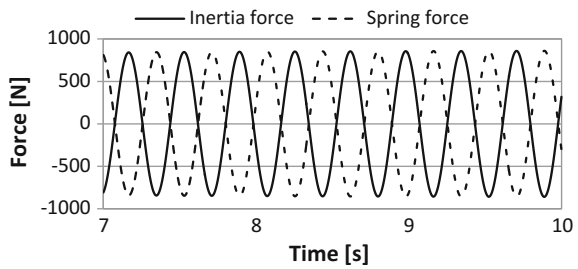
Fig. 6 Time courses of excitation force and damping force at resonance
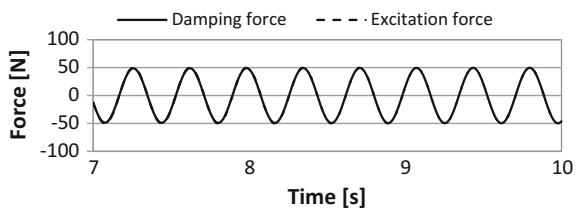
4 Energy Accumulation in an Oscillator and in a Fly-Wheel

The maximum of energy accumulated in an oscillator at resonance can be established from (Fig. 7):

$$E_{osc} = \tfrac{1}{2}kX_{max}^2 = \tfrac{1}{2}m\omega^2 X_{max}^2, \text{ where } X_{max} = \tfrac{F_0}{2m\beta\omega} \tag{7}$$
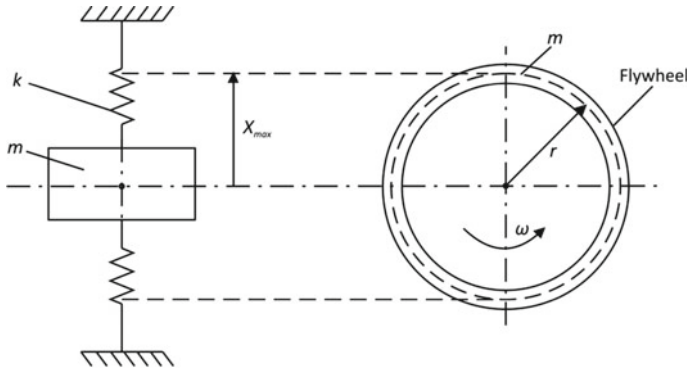
Fig. 7 Oscillator and flywheel (ring)

From Eq. (7) is to see, that the amplitude and the frequency has the biggest influence on the energy of an oscillator.

Kinetic energy accumulated in the flywheel (Fig. 7) can be calculated from:

$$E_{kf} = \frac{1}{2}I\omega^2 = \frac{1}{2}m\omega^2 r^2 \tag{8}$$

It is to see from Eqs. (7) and (8) that total energy of the oscillator is exactly the same as the kinetic energy of the flywheel $E_{osc} = E_{kf}$ if masses and frequencies are the same and radius of the flywheel is equal to the amplitude of the oscillator vibration at resonance $r = X_{max}$.

Comparison of the energy storage process in an oscillator at resonance and in the flywheel is shown in Fig. 8. In this calculation example the masses of the oscillator and flywheel are the same, $r = X_{max} = 0.6$ and $\omega_f = \omega_{osc.}$ The oscillator will be driven from the begin with the resonant frequency. At time t_0 the energy of the flywheel will reach the maximum energy of the oscillator.

The kinetic energy of the oscillator and of the flywheel will be the same at the time t_0. If the flywheel should be accelerated to achieve the kinetic energy of 250 J in time t_0, it should be driven with the torque M:

$$M = I\varepsilon = \frac{I\omega}{t_0} = \frac{mr^2\omega}{t_0} \tag{9}$$

The torque M acting on the flywheel is resulting from the inertia of the flywheel and the torque due to the motion resistance have been neglected. In case of the oscillator in resonance conditions, the inertia force is compensated by the spring force hence the increase of energy in the initial phase is faster than in the flywheel. The instantaneous energy delivered to the oscillator to accumulate the energy of 250 J is lower than the energy applied to drive the flywheel.
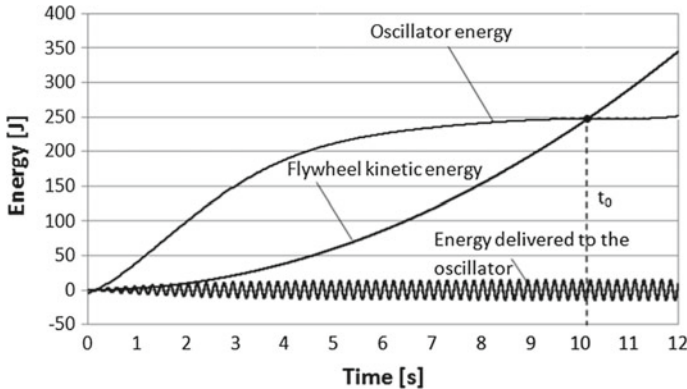
Fig. 8 Energy accumulated in an oscillator at resonance, flywheel energy and instant neous energy delivered to the oscillator

5 Application Examples of Using Mechanical Resonance

5.1 Impact Working Machines

In impact machines there is a sequential reception of energy, which is necessary to perform the process, for example, punching holes in metal sheet or pressing operation. The main element of the resonant press (Fig. 9) can be the resonant block, which is moving on a linear guides and is attached to the housing by means of springs. Driving to the resonance can occur inertial by rotating mass or with an hydraulic, pneumatic or electric actuator. The reception of energy from resonance block follows after the conjunction with the clutch actuated with the control system. After performing the punching operation the vibration amplitude of resonance block will increase up to the maximum value. This process may be repeated periodically. The drive needed to accumulate the energy in the resonance block is used only to overcome the friction forces. The time needed to accumulate the energy in the resonance block to the maximal value is dependent mainly from the friction/damping and the amplitude of the excitation force. The vibration amplitude of the resonance block should not decrease more than 10%, similar as the speed fluctuation ratio of flywheels in eccentric presses. That have also a big influence on the cycle time during the punching process.

In eccentric presses, the energy needed to perform the punching process is stored in the flywheel. The energy losses in such machines are higher due to the change of the rotary motion of the flywheel to the reciprocating motion of the slider. The degree of the design complexity of the eccentric press is also much higher than in a press with resonance block.

The mechanical resonance can be also used in many other machines like: impact drills, forging hammers, stamping machines, etc.
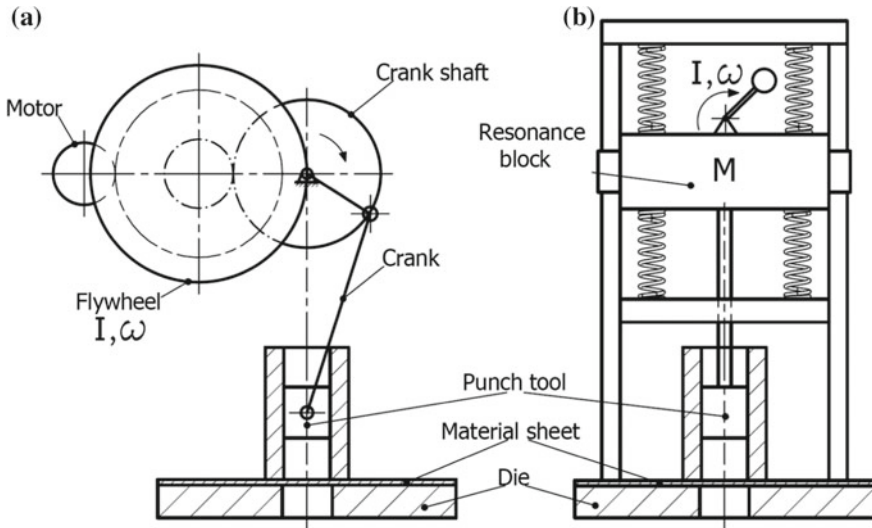
Fig. 9 Schematic view of the punching press: **a** with the flywheel, **b** with resonance block

Fig. 10 The piston machine
with spring damper element
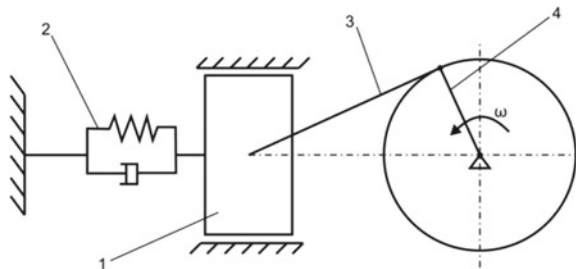
5.2 Piston Machines

In piston machines such as combustion engines, compressors, etc., usually crankshaft systems will be used. Figure 10 shows the crank-piston system in which the spring (2) has been introduced.

The spring takes and gives back the energy in the same way as in the oscillator. At the resonance conditions, the force amplitude in the connecting rod as well as the torque pulsation in the crankshaft system will be minimal, depending from the damping in the system.

In such arrangement the resonance will be achieved, when the frequency resulting from the crank speed is equal to the natural frequency resulting from the reduced piston mass and spring stiffness. The system with spring behaves like an oscillator, so during resonance, there is a compensation of the inertial force due to the piston mass by the force in spring that contributes to reducing the amplitude of the torque pulsation on the crankshaft. That solution can be used in many piston machines
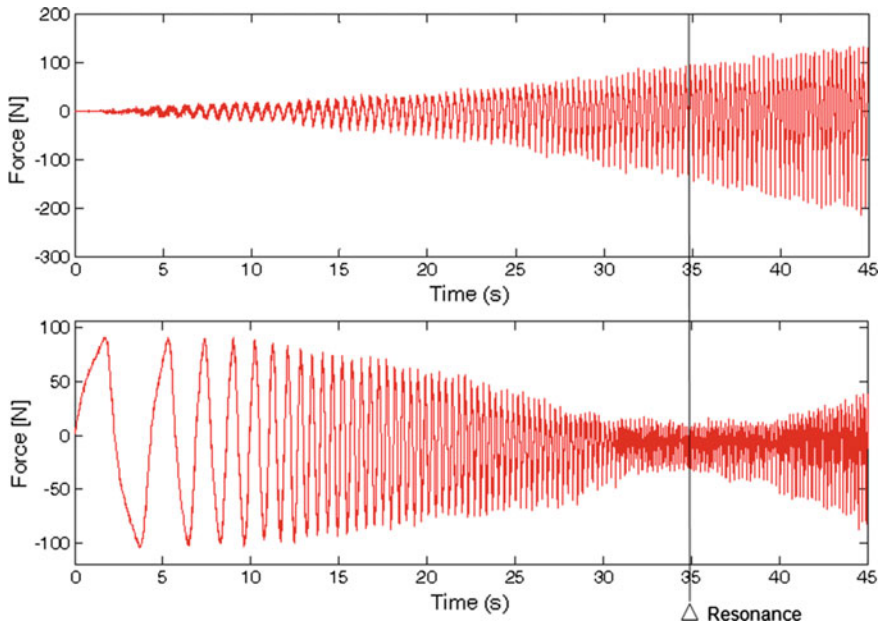
Fig. 11 Forces in the connecting rod in a crankshaft system with and without spring [16]

working with the constant rotational speed. It should be noted that the inertial forces in conventional crank-piston systems reach high values similar to those resulting from the working load, especially at higher speeds. Therefore the compensation of inertia forces at resonance should have an impact on the efficiency of these machines. The effect of reducing the amplitude of the torque pulsation in resonance was confirmed experimentally (Fig. 11). Use of mechanical resonance in machines with crankshaft systems can thus eliminate flywheels in some applications in order to reduce the torque pulsation in the crankshaft drives.

6   Conclusions

In this paper, an attempt was made to describe the process of mechanical energy accumulation under resonance conditions using the example of a harmonic oscillator. It has been found that energy accumulation is related to compensation of inertia forces with forces in the spring element of the oscillator. For low damping, the energy accumulated in the oscillator is many times greater than the energy needed to overcome the motion resistance. The process of energy accumulation in an oscillator has been compared with energy accumulation in a flywheel. This comparison shows that the accumulation process in oscillator while resonance is more efficient and faster than the energy accumulation in the flywheel assuming the same parameters for

both systems (as mass, rotational speed/vibration frequency, and radius/amplitude of vibration). The possibilities of use the mechanical resonance phenomenon in impact working machines and machines with crankshaft system have been presented. Further research will be aimed at investigations of energy consumption in machines using the mechanical resonance concept compared to conventional solutions.

References

1. Harris, C.M., Piersol, A.G.: Shock and Vibration Handbook. McGraw-Hill, New York (2002)
2. Ergaenzungen zu Physik 1, Script, University of Zurich, Switzerland (2016)
3. Stephen, N.G.: On energy harvesting from ambient vibration. J. Sound Vib. **239**, 409–425 (2006)
4. Glynne-Jones, P., Tudor, M.J., Beeby, S.P., White, N.M.: An electromagnetic, vibration-powered generator for intelligent sensor systems. Sens. Actuators, A **110**, 344–349 (2004)
5. Colins, L.: Harvesting for the world: energy harvesting techniques. IEEE Power Eng. **20**, 34–37 (2006)
6. Aldraihem, O., Baz, A.: Energy harvester with a dynamic magnifier. J. Intell. Mater. Syst. Struct. **22**(6), 521–530 (2011)
7. Kammer, A.S., Olgac, N.: Delayed-feedback vibration absorbers to enhance energy harvesting. J. Sound Vib. **363**(02), 54–67 (2016)
8. Horodinca, M., Saghedin, N.E.: Experimental investigations of power absorbed at mechanical resonance, experimental techniques SEM, 1–11 (2011)
9. Lei, Z., Xiudong, T.: Large-scale vibration energy harvesting. J. Intell. Mater. Syst. Struct. **24**(11), 1405–1430 (2013)
10. Zuo, L., Scully, B., Shestani, J., Zhou, Y.: Design and characterization of an electromagnetic energy harvester for vehicle suspensions. Smart Mater. Struct. 19 (2010)
11. Goldner, R.B., Zerigian, P.: A Preliminary study of energy recovery in vehicles by using regenerative magnetic shock absorbers. SAE technical paper series 2001-01-2071 (2001)
12. Plooij, M.C., Wisse, M.A.: Novel spring mechanism to reduce energy consumption of robotic arms, intelligent robots and systems (IROS). In: IEEE/RSJ International Conference, pp. 2901–2908 (2012)
13. Baek, S., Ma, K., Fearing R.: Efficient drive of flapping-wing robots. In: IEEE/RSJ International Conference on Intelligent Robots and Systems, 11-15 Oct. 2009 St. Louis, USA
14. Despotovic, Z, Ribic, A.: A comparison of energy efficiency of SCR phase control and switch mode regulated vibratory conveying drives. In: IX Symposium Industrial Electronics, INDEL, 2012, Banja Luka, 01-03 Nov. 2012
15. Fiebig, W., Wrobel, J.: Simulation of energy flow at mechanical resonance. In: 22nd ICSV Conference, 12–16 July 2015, Florence, Italy
16. Fiebig, W., Wrobel, J: Use of mechanical resonance in machines drive systems. In: 24th ICSV Conference, 12–16 July 2017, London, England
17. Awrejcewicz, J., Olejnik, P.: Analysis of dynamic systems with various friction laws. Appl. Mech. Rev. **58**(6), 389–411 (2005)

Application of Time-Frequency Methods for Assessment of Gas Metal Arc Welding Condition

Jacek Górka and Wojciech Jamrozik

Abstract Gas Metal Arc Welding (GMAW) is a popular method of material joining, widely used for a variety of critical industrial structures. Assuring high quality of joints is than a vital task. Welding is a highly dynamic and non-linear process, thus an application of time-domain or frequency-domain methods is often not suitable for evaluation of welded joints quality. To fully describe the correspondence between the geometry of welding arc, parameters that express the quality of joint, and the welding arc current, being the most important steerable parameter of a GMAW, time-frequency methods (TFM) of signal analysis should be applied. In the paper application of ensemble of STFT and EMD (Empirical Mode Decomposition)-based estimators to evaluate the stability of a GMAW process, that results in the quality of joint. Proposed method of feature extraction was applied on the real data taken during several GMAW realizations with different conditions (changes in welding current, arc voltage, shield gas flow, wire feed speed, etc.). In the active experiment process parameters were acquired. Performed investigations revealed that in comparison to traditional as well as separately used TFM, ensemble of TF estimators gave better performance in a GMAW condition assessment.

Keywords Welding · Time-frequency transform · Condition assessment

1 Introduction

Gas Metal Arc Welding (GMAW) is a technique commonly used for joining metal materials. It is a dynamic and non-linear process. The quality of seam and created joint is closely related to features of welding arc as well as droplet transfer mode. To obtain a desired mechanical and metallurgical properties of joint, several parameters,

J. Górka · W. Jamrozik (✉)
Silesian University of Technology, ul. Konarskiego 18a, 44-100 Gliwice, Poland
e-mail: wojciech.jamrozik@polsl.pl

J. Górka
e-mail: jacek.gorka@polsl.pl

especially electrical ones, are monitored and controlled. Monitoring of joint quality is a vital issue, especially in those branches of industry, where defective welds lead to losses in production and necessitate expensive repair [1]. Electrical signals describing the welding arc behaviour are typically non-linear and non-stationary. Because of those signal properties common signal processing and analysis methods, that can be executed in only time domain or frequency domain, are not suitable for assessment and evaluation of welding process stability and joint quality. Point estimators and classifier ensembles were used to identify inconsistencies appeared in GMAW [2]. Also autocorrelation peak coefficient of various welding parameters was used to describe process stability [3]. Modern and complex time-frequency analysis methods have been applied to assess condition of welding process and quality of joints. Most popular methods are Short Time Fourier transform (STFT) and Wigner-Ville distribution (WVD). Both of them were used to establish a correspondence between TF spectrum and process stability [4, 5]. To overcome main disadvantage of STFT, namely constant resolution for all frequencies, wavelets were introduced. This type of transformation was applied to determine seam geometrical parameters, penetration depth and process stability [6]. Recently Hilbert-Huang transform has been applied to arc stability evaluation in short-circuiting GMAW. There was found, that the welding was more stable when the time frequency entropy calculated for Hilbert-Huang transform of welding current signals, was larger [7]. Although many signal processing methods were successfully applied, there is no approach, that utilize extracted features fully to assess welding process and welded joints.

1.1 Time-Frequency Representation of Signals

Short Time Fourier Transform is an iterative procedure, consisted in applying Fourier Transform for a part of signal catted by window of certain length. Window is moved by time index until end of processed signal is reached. Formally STFT is given by following equation:

$$F_x(t, v; h) \int_{-\infty}^{+\infty} x(u)h^*(u - t)e^{-j2\pi vu}\mathrm{d}u \tag{1}$$

where $h(t)$ is a short time analysis window localized around $t = 0$ and $v = 0$. Main drawback of STFT is limited precision, given by size of window. Having high resolution in time domain, resolution in frequency domain will be relatively low. Moreover STFT gives same resolution for all frequencies, while sometimes it is valuable to have more flexible approach [8].

Wigner-Ville distribution (WVD) is a spectrum corresponding to each time based on this time as the centre, which conducts the Fourier transform to the results from the signal multiplied by the right and left of all parts [9]. The advantage of the WVD is the good resolution in both domain, namely time and frequency. The oscillation characteristics of the cross-terms can be reduced by the smoothing of WVD, that is, a

Fig. 1 Test stand with the computer station and the welding device

smooth window function is added in time domain, and then the Pseudo Wigner-Ville distribution (PW) is obtained for a discrete-time signal x:

$$PW_x(t, \nu) = \int_{-\infty}^{+\infty} h(\tau)x\left(t + \frac{\tau}{2}\right)x^*\left(t - \frac{\tau}{2}\right)e^{-j2\pi\nu\tau}\mathrm{d}\tau \qquad (2)$$

Empirical Mode Decomposition, EMD, decomposes the signal of interest into oscillatory functions intrinsic to the original signal, defined as Intrinsic Mode Functions (IMFs) [10].

The result of this procedure is a series of IMFs, plus a final residual, r(t). In its core form it was not done much to modify IMF extraction procedure. Modifications come in how some of the steps are carried out, including the maxima/minima detection, envelope formation (interpolation), the way a IMF is identified (i.e. stopping criteria) and how one stops the sifting process. Although EMD is a promising method is also several drawbacks. Most important of them are that the IMFs are not strictly orthogonal each other, mode mixing sometimes occurs between IMFs. The most important issue of EMD is that IMFs cannot be directly interpreted, in other words they don't have straight physical interpretation [11].

It can be noticed, that each of TFR methods has some advantages and disadvantages as well. According to that, it cannot be stated, which of those methods is most universal and generally best one for widest field of applications.

2 Case Study

Current and voltage signals were taken during welding of plates made of steel S235JR (EN 10027-1) with dimensions $300 \times 150 \times 5$ mm on the mechanised welding stand for rectilinear GAMW welding equipped in welding machine Castolin TotalArc 5000

Fig. 2 Exemplary joint made with **a** corroded wire (S4), **b** contaminated with oil (S6)

Table 1 Nominal GMAW parameters

Welding current [A]	Arc voltage [V]	Welding speed [cm/min]	Wire feeding rate [m/min]	Shield gas flow [l/min]	Electrode outlet [mm]
240	25	32	7.4	15	15

(see Fig. 1). The edges of the joined plates were bevelled at an angle of 60° and the offset between them was b = 1.0 mm. For joining a solid electrode wire with a diameter of 0.2 mm (Castolin CastoMag 45255) and a shield gas M21 (82%Ar+18%CO_2) were used. Nominal welding parameters are presented in Table 1. It was checked, that those parameters lead to correct joint made in a stable process.

Series of experiments simulating different faults of welding process were carried out. It permitted to record the collection of sequences of infrared and vision images for 12 different states of welding process classified in the following way: S1 - Correct welding process. S2 - Welding with decay of the shielding gas flow. S3 - Welding of the plates with distinct outbreaks of atmospheric corrosion on the welded surfaces. S4 - Welding with use of corroded wire. S5 - Welding of plates with irregularities of the plate edges from side of the weld root. S6 - Welding of plates with oil contamination. S7 - Welding with deviation of current. S8 - Welding of plates with different offset intervals. S9 - Welding with deviation of voltage. S10 - Welding of the plates with improper welding groove geometry. S11 - Welding with deviation of speed. S12 - Welding with use of worn rollers of wire feeder (see Fig. 2).

Welding current and arc voltage were measured during welding with frequency of 25 kHz. Then signals were down sampled and down pass filtered. Exemplary current signals were presented in Fig. 3.

2.1 TFR of Welding Signals

To generate features, that can be used for assessment of welding process stability and secondly the quality of welded joint, several TFR of acquired electrical signals

(a)

(b)

(c)

(d)
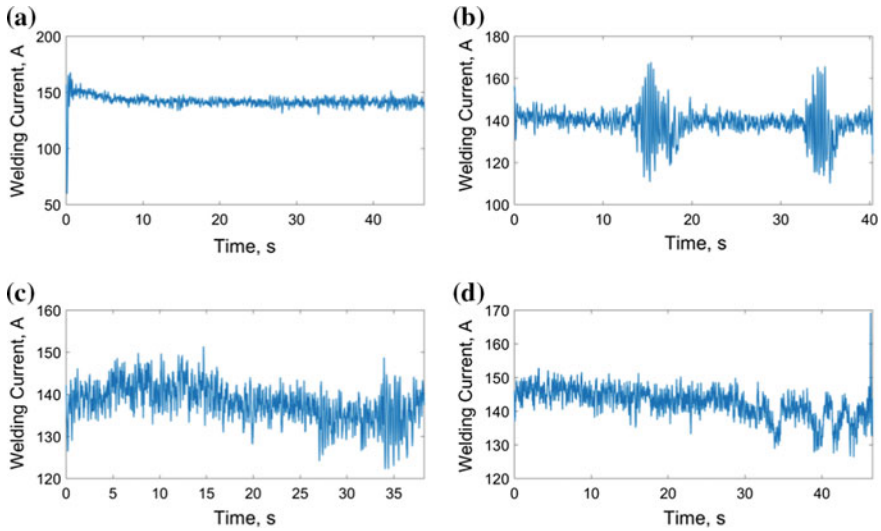
Fig. 3 Exemplary time signals for conditions: **a** S1- correct process, **b** S2 lack of shield gas, **c** S9 change of voltage, **d** S11 wrong groove geometry

(a)

(b)
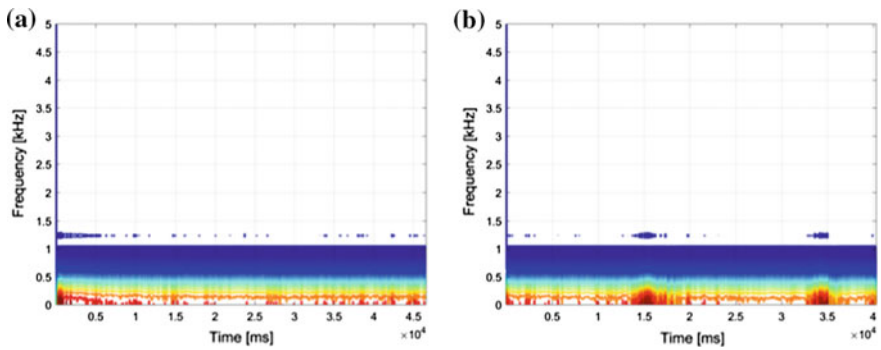
Fig. 4 STFT representation of welding current: **a** S1 condition correct process, **b** S2 condition lack of shielding gas

were calculated. First STFT of signal was calculated. The number of FFT points was 512 and the Hamming window of length 21 points was used. Exemplary results can be seen in Fig. 4. Comparing results it is clearly visible, that for lack of shield gas, that frequency components of higher amplitude appeared in time, when the gas flow was disturbed.

Applying to current signal PW distribution, result are similar to those obtained by STFT. Nevertheless, having better resolution, all frequency components are better distinguishable (Fig. 5).

To obtain more accurate results EMD was applied. It can give interesting information based on the local characteristic time scale of the signal. It can be seen, that
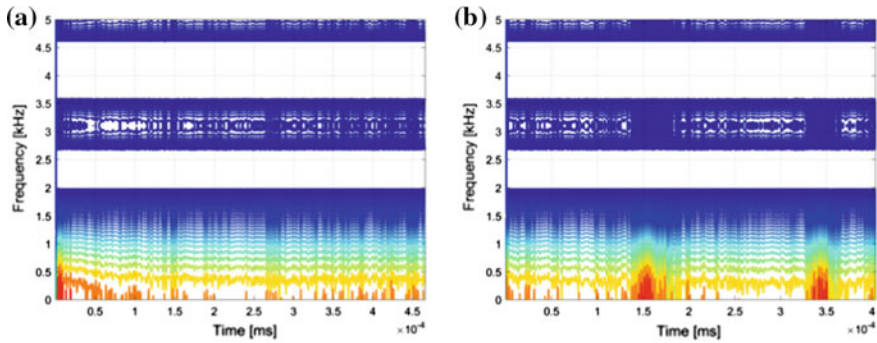
Fig. 5 Pseudo Wigner-Ville representation of welding current: **a** S1 condition correct process, **b** S2 condition lack of shielding gas

Fig. 6 First 10 IMFs and the rest of the welding current: **a** S1 condition - correct process, **b** S2 condition - lack of the shielding gas
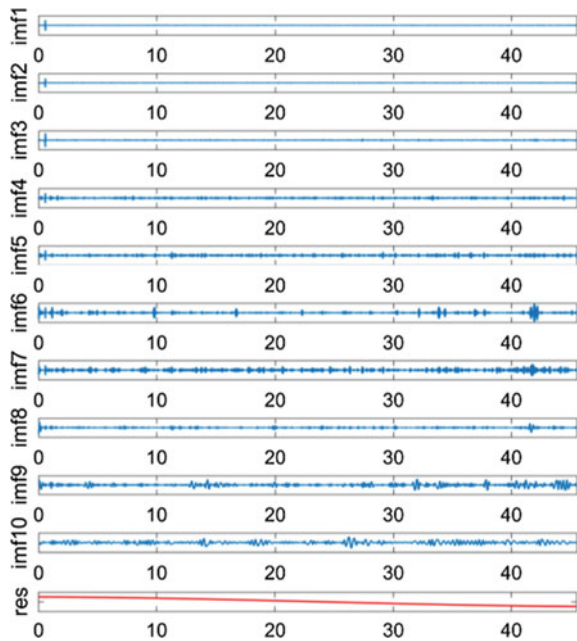
for stable, correct process IMF9 and IMF 10 of welding current signals, are low amplitude noise like signals and there are no visible disturbances, that can be result of the stability of the process (see Fig. 6). When the process disturbance appears, as in the case of decaying od shield gas flow, there are clear variation visible in IMF9 and IMF10 (see Fig. 7). Locations of those variations in time allows to indicate the position of welding instabilities results on the weld surface.

To quantify IMFs first the STFT of each mode was calculated. Spectrogram of the IMF10 of the current signal taken for correct process presents uniform distribution of frequency bands. Increased amplitudes in some time moments cannot be treated
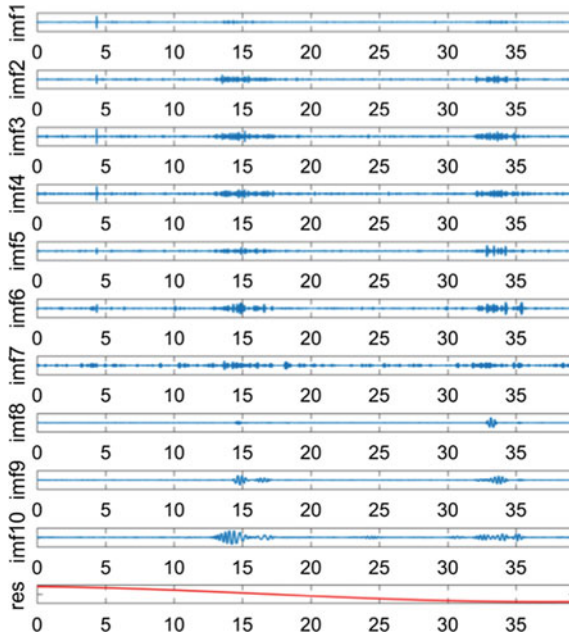
Fig. 7 First 10 IMFs and the rest of the welding current: **a** S1 condition correct process, **b** S2 condition - lack of the shielding gas

as symptoms of potential instabilities leading to joint inconsistencies. Spectrogram of IMF10 calculated for condition S2 point on presence of two time intervals, where process was disturbed (Fig. 8). Positioning of those regions is consistent with the time moment when flow of gas was present. Additionally there is no other signal processing technique needed, because application of thresholding, that was applied to cut out components with low amplitude was sufficient.

2.2 Detection of Welding Instabilities

In order to determine the condition of welding process, classification procedure was developed. For generated TFRs of GMAW electric signals, point features were used, to assess each process. RMS and entropy were used to assess signal in band of about 500Hz for STFT calculated for acquired signals and 200 Hz for IMFs. To validate usefulness of particular TFR method STSF spectrograms were used, as well as spectrograms generated for 9th, 10th and 11th IMFs. Classification was performed by simple K-Nearest Neighbours classifier, where number of neighbours was three, and Euclidean distance was used. Classifiers were validated k-using fold cross validation, for k = 10. The classification was made for detection case, thus there was no
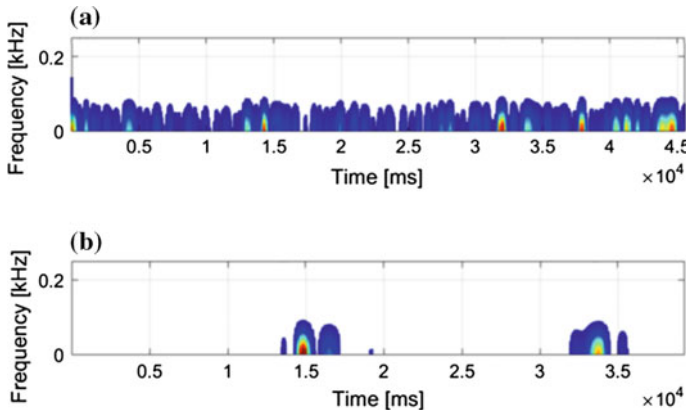
Fig. 8 STFT of the IMF10 for condition S1 (**a**) and S2 (**b**)

Table 2 Nominal GMAW parameters

Classifiers	Signal STFT RMS	Signal STFT Entropy	IMF9 STFT RMS	IMF10 STFT RMS	IMF11 STFT RMS	IMF9 STFT Entropy	IMF10 STFT Entropy	IMF11 STFT Entropy
1	0.0125	0.2	0.0625	0.025	0	0.05	0.2	0.075
5	0.0125	0.0125	0.0375	0	0	0.025	0	0

Table 3 Nominal GMAW parameters

Classifiers	IMF9-IMF11 STFT RMS	IMF9-IMF11 STFT Entropy	IMF9-IMF11 STFT RMS+Entropy
1	0.0125	0.3125	0.1125
5	0.0125	0.0625	0

differentiation between appeared inconsistencies. To increase classification accuracy bagging procedure was used, where there were maximal five classifier in ensemble Training samples for faulty condition were consisted of samples representing states form S2 to S12. Obtained classification errors are gathered in Tables 2 and 3. When single features were taken for classification, best one was the RMS calculated for the spectrogram of IMF11. Simple ensemble building technique, like bagging, increased the classification performance significantly. In the ensemble of classifiers, features calculated from IMF spectrograms were generally better than those calculated from current or voltage signals. Nevertheless detection results are satisfying. To reduce uncertainty of results, that can be connected connected with the selection of feature, classification in multidimensional feature space was performed. It was revealed that the use of all IMF features lead always to best classification accuracy. Nevertheless, there were no studies performed how different feature mixtures will affect classification results.

3 Conclusions

In the paper application of point features calculated for various Time-Frequency Representations of electric signals recorded during welding to detection of possible welding inconsistencies. It was found that spectrograms calculated for IMFs being result of empirical mode decomposition, can be a good basis for feature extraction. Those features have potential to be valuable diagnostic signals. Quantification of detection ability on the basis of extracted features was made using pattern recognition method. Classification has been performed using single classifiers, as well as classifier ensembles. It was found that features calculated for IMFs are best symptoms, having high ability to distinguish correct and incorrect joints. Presented results are preliminary. Further studies will cover application of Hilbert-Hunag Transform and more sophisticated features to quantify realizations of GMAW. Additionally method, that will allow detection of inconsistencies or process instabilities not only for whole process realization but also with indication of time point where disturbance occur.

References

1. Wu, C.S., Polte, T., Rehfeldt, D.: A fuzzy logic system for process monitoring and quality evaluation in GMAW. Weld. J. Supplement **80**(2), 33–38 (2001)
2. Jamrozik, W.: Contextual reliability discounting in welding process diagnostic based on DSmT. Expert Syst. **32**, 192–202 (2015)
3. Gao, L., Xue, J., Hui, C., Xue, Z., Wang, R.: Quantitative evaluation on metal transfer process stability of arc welding based on autocorrelation analysis. Trans. China Weld. Inst. **33**, 28–29 (2012)
4. Si-Wen, X., Wang, C., Zhi-Peng, Z., Kuan-Fang, H.: Arc Energy Characteristics Analysis of AC Square Wave Submerged Arc Welding using WVD. J. Appl. Mech. Eng. **5**, 204 (2016)
5. Luo, Y.: Application of joint time-frequency analysis to electrical signals of C02 arc welding. Trans China Weld. Institute **28**(2), 75–78 (2007)
6. Xue, J.X., Zhang, X.N., Huang, S.S.: De-noising in electric signals of arc welding process via wavelet soft threshold. Trans. China Weld. Inst. **21**(2), 18–21 (2000)
7. Huang, Y., Wang, K., Zhou, Q., et al.: Feature extraction for gas metal arc welding based on EMD and time frequency entropy. Int. J. Adv. Manuf. Technol. **92**, 14–39 (2017)
8. Allen, J., Rabiner, L.: A unified approach to short-time fourier analysis and synthesis. Proc. of the IEEE **65**, 1558–1564 (1977)
9. Claasen, T., Mecklenbrauker, W.: The wigner distribution? A tool for time-frequency signal analysis Part II: discrete time signals. Philips Jl Res. **35**, 276–300 (1980)
10. Huang, N.E., et al.: The empirical mode decomposition and the Hilbert spectrum for nonlinear and non-stationary time series analysis. Proc. Royal Soc. **454**, 903–995 (1998)
11. Rilling, G., Flandrin, P.: One or two frequencies? The empirical mode decomposition answers. IEEE Trans. Signal Process. **56**, 85–95 (2008)

A 3-Link Model of a Human for Simulating a Fall in Forward Direction

Dariusz Grzelczyk, Paweł Biesiacki, Jerzy Mrozowski and Jan Awrejcewicz

Abstract In this study we consider a 3-link biomechanical model of a human for simulating a forward fall. Individual segments of the human body are modelled as rigid bodies connected by the rotary elements which correspond to the human joints. The model implemented in Mathematica is constructed based on a planar mechanical system with a non-linear impact law modelling the hand-ground contact. Due to kinematic excitation in the joints corresponding to the hip and the shoulder, the presented fall model is reduced to a single-degree-of-freedom system. Parameters of the model are obtained based on the three-dimensional scanned human body model created in Inventor, while its kinematics (time histories of the angles in hip and shoulder joints) are obtained from the experimental observation with the optoelectronic motion analysis system. Validation of the model is conducted by means of comparing the simulation of impact force with experimental data obtained from the force plate. Finally, the obtained ground reaction forces can be useful in further studies, as a load conditions, for finite element analysis of the numerical model of the human upper extremity.

Keywords Forward fall · Ground reaction force · Fracture · Distal radius

D. Grzelczyk (✉) · P. Biesiacki · J. Mrozowski · J. Awrejcewicz
Department of Automation, Biomechanics and Mechatronics, Lodz University of Technology,
1/15 Stefanowski Street, 90-924 Lodz, Poland
e-mail: dariusz.grzelczyk@p.lodz.pl

P. Biesiacki
e-mail: pawelbiesiacki@o2.pl

J. Mrozowski
e-mail: jerzy.mrozowski@p.lodz.pl

J. Awrejcewicz
e-mail: jan.awrejcewicz@p.lodz.pl

135

1 Introduction

A fall onto outstretched arms is one of the main reasons of the upper limb bone injuries. The resulting bone fractures are a serious medical and social problem due to long-term sick leave, absence from work, and sometimes a complicated rehabilitation process, especially among the elderly [1, 2]. The aforementioned upper extremity injuries may be the result of forward falls, backward falls or side falls. However, most cases of upper extremity injuries occur as a result of a forward fall with direct impact on the fully extended upper extremities [3, 4]. Due to the compromised bone quality/density and the increased risk of falling in the older part of population, distal radius fractures are especially common in elderly women with osteoporosis.

The so-called Colles' fracture as an injury of distal radius is the most common type of fracture of the upper extremity resulting from a forward fall [5]. Colles' fracture is a direct result of exceeding the maximum value of force allowable for the radius. Estimation of this value as a distal radius fracture threshold has been the research goal of many scientists. For instance, distal radius fractures at a mean force equal to 1640 N were observed by Spadaro and his co-workers [6]. In other paper, Kim and Ashton-Miller used the value equal to 2400 N as a distal radius fracture threshold in their investigations [7]. In turn, in one of the recent papers Burkhart and his co-investigators tested the real bones from cadavers and obtained value of the distal radius fracture threshold approximately equal to 2150 N [8].

The literature review indicates that recent decades have brought different models related to the impact of the upper extremities to the ground as a result of a fall in a forward direction. A model proposed by Chiu and Robinovitch [9] applies to the human forward fall from a low height on the outstretched and fully extended hand, and it is constructed as a two degrees-of-freedom (DoFs) lumped-parameter mechanical system with spring-damper elements imitating properties of human muscles. DeGoede and Ashton-Miller [10] applied Adams software in order to develop a half-body, symmetric human forward fall model consisting of five segments (lower limb, half torso with neck and head, upper arm, forearm, and hand). Using this model, the authors studied the probability of injury in older women. In other paper, Kim and Ashton-Miller [7] showed another planar model of a forward fall as a two DoFs system constructed based on a mechanical double pendulum (rotating freely around the pivot corresponding to the ankles of lower human extremities). Finally, the mechanical system was reduced to a linear system with 2-DoFs and spring-damper elements responsible for attenuation action of the human muscles.

To conclude, the considered falling process is usually modeled on the basis on planar and linear mechanical systems consisting of two rigid bodies with masses moved by transverse motion and connected by linear spring-damper elements. Simple models have been presented in the form of the second-order ordinary differential equations of motion [9], or the appropriate equations have been developed in the state space [7]. On the other hand, more complex mechanical models have been implemented only using commercial software, for instance see paper [10]. In this work, we proposed a novel mathematical model of the human forward fall on the

outstretched arms. Mechanical, kinematical, and dynamical parameters of this model have been identified using experimental investigations of a real falling process of a faller. Moreover, we have investigated influence of different human speed just before a trip over an obstacle and starting the falling process, which affects the ground reaction force (GRF) acting on the upper extremity.

2 Biomechanical Model of a Human

The human forward fall on outstretched arms is presented schematically in Fig. 1 as a planar 3-DoFs mechanical model. The xy plane corresponds to the sagittal plane of the human body.

The bodies 1 (lower extremities), 2 (torso with neck and head) and 3 (upper extremities) have masses m_1, m_2, m_3 and moments of inertia about centres of the masses I_1, I_2, I_3, respectively. The angle $\theta_1(t)$ is the angle between the x axis and the longitudinal axis of the body 1, $\theta_2(t)$ is the angle measured from the axis of the body 1 to the axis of the body 2, while $\theta_3(t)$ denotes the angle between the axes of the bodies 2 and 3. Parameters a_1, a_2, a_3 denote distances between the centres of masses and rotation axes for bodies 1, 2 and 3, respectively, l_1 is the distance between the ankle joint and the hip joint, l_2 is the distance between the hip joint and the shoulder joint, whereas l_3 denotes the length of the upper limbs. The equations of motion of the considered system have been obtained by the Newton-Euler method.
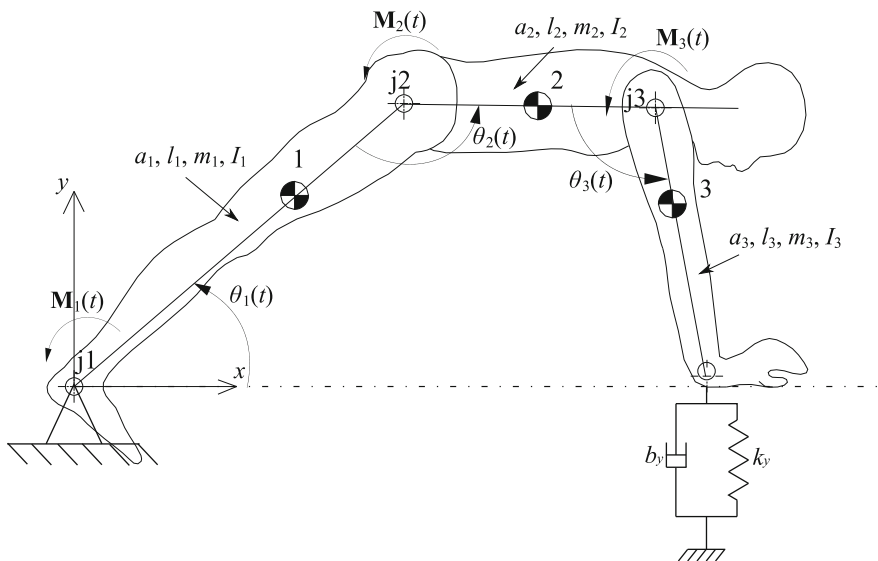
Fig. 1 The proposed forward fall biomechanical planar model with 3-DoFs embedded in the Cartesian coordinate system

In our model, we take the vectors $\boldsymbol{\theta}_1(t) = [0, 0, \theta_1(t)]^T$, $\boldsymbol{\theta}_2(t) = [0, 0, \theta_2(t)]^T$, $\boldsymbol{\theta}_3(t) = [0, 0, \theta_3(t)]^T$ of the angles in the joints j1, j2, j3, and the following vectors:

$$\mathbf{r}_1(t) = [x_1(t), y_1(t), 0]^T = [a_1 \cos\theta_1(t), a_1 \sin\theta_1(t), 0]^T, \tag{1}$$

$$\mathbf{r}_2(t) = [x_2(t), y_2(t), 0]^T = [l_1 \cos\theta_1(t) + a_2 \cos\alpha(t), l_1 \sin\theta_1(t) - a_2 \sin\alpha(t), 0]^T, \tag{2}$$

$$\begin{aligned}
\mathbf{r}_3(t) &= [x_3(t), y_3(t), 0]^T \\
&= [l_1 \cos\theta_1(t) + l_2 \cos\alpha(t) + a_3 \cos\beta(t), l_1 \sin\theta_1(t) \\
&\quad -l_2 \sin\alpha(t) - a_3 \sin\beta(t), 0]^T,
\end{aligned} \tag{3}$$

$$\mathbf{l}_1(t) = [l_1 \cos\theta_1(t), l_1 \sin\theta_1(t), 0]^T, \tag{4}$$

$$\mathbf{l}_2(t) = [l_1 \cos\theta_1(t) + l_2 \cos\alpha(t), l_1 \sin\theta_1(t) - l_2 \sin\alpha(t), 0]^T, \tag{5}$$

$$\mathbf{l}_3(t) = [l_1 \cos\theta_1(t) + l_2 \cos\alpha(t) + l_3 \cos\beta(t), l_1 \sin\theta_1(t) - l_2 \sin\alpha(t) - l_3 \sin\beta(t), 0]^T, \tag{6}$$

where $\alpha(t) = \pi - \theta_1(t) - \theta_2(t)$ and $\beta(t) = \pi + \alpha(t) - \theta_3(t)$. The forces $\mathbf{Q}_1 = [0, -m_1 g, 0]^T$, $\mathbf{Q}_2 = [0, -m_2 g, 0]^T$, and $\mathbf{Q}_3 = [0, -m_3 g, 0]^T$ are the gravity forces acting on centres of gravity of bodies 1, 2 and 3, where $g = 9.81$ m/s^2. The force $\mathbf{R}(t) = [R_x(t), R_y(t), 0]^T$ is the reaction force in the joint j1. The unknown joint forces (resulting from presentation of the system as a free body diagram) are denoted as $\mathbf{P}_1(t) = [P_{1x}(t), P_{1y}(t), 0]^T$ and $\mathbf{P}_2(t) = [P_{2x}(t), P_{2y}(t), 0]^T$, respectively. The force $\mathbf{F}(t) = [F_x(t), F_y(t), 0]^T$ is the ground reaction force acting on the body 3 at the moment of its impact to the ground. Let us assume further that torques $\mathbf{M}_1(t) = [0, 0, 0]^T$, $\mathbf{M}_2(t) = [0, 0, M_2(t)]^T$, and $\mathbf{M}_3(t) = [0, 0, M_3(t)]^T$ in joints j1, j2 and j3, correspond to the torques generated by human muscles in the ankle, hip and shoulder joints, respectively. Then, the analysed system can be described by the equations of motion in the following vector form:

$$m_1 \ddot{\mathbf{r}}_1(t) = \mathbf{R}(t) + \mathbf{Q}_1 + \mathbf{P}_1(t), \tag{7}$$

$$I_1 \ddot{\boldsymbol{\theta}}_1(t) = \mathbf{M}_1(t) - \mathbf{M}_2(t) + \boldsymbol{\tau}_\mathbf{R}(t) + \boldsymbol{\tau}_{\mathbf{P}12}(t), \tag{8}$$

$$m_2 \ddot{\mathbf{r}}_2(t) = -\mathbf{P}_1(t) + \mathbf{Q}_2 + \mathbf{P}_2(t), \tag{9}$$

$$I_2 \ddot{\boldsymbol{\theta}}_2(t) = \mathbf{M}_2(t) - \mathbf{M}_3(t) + \boldsymbol{\tau}_{\mathbf{P}21}(t) + \boldsymbol{\tau}_{\mathbf{P}23}(t), \tag{10}$$

$$m_3 \ddot{\mathbf{r}}_3(t) = -\mathbf{P}_2(t) + \mathbf{Q}_3 + \mathbf{F}(t), \tag{11}$$

$$I_3 \ddot{\boldsymbol{\theta}}_3(t) = \mathbf{M}_3(t) + \boldsymbol{\tau}_{\mathbf{P}32}(t) + \boldsymbol{\tau}_\mathbf{F}(t), \tag{12}$$

where

$$\boldsymbol{\tau}_\mathbf{R}(t) = [0, 0, \tau_R(t)]^T = -\mathbf{r}_1(t) \times \mathbf{R}(t), \tag{13}$$

$$\boldsymbol{\tau}_{\mathbf{P}12}(t) = [0, 0, \tau_{P12}(t)]^T = [\mathbf{l}_1(t) - \mathbf{r}_1(t)] \times \mathbf{P}_1(t), \tag{14}$$

$$\boldsymbol{\tau}_{\mathbf{P}21}(t) = [0, 0, \tau_{P21}(t)]^T = [\mathbf{l}_1(t) - \mathbf{r}_2(t)] \times [-\mathbf{P}_1(t)], \tag{15}$$

$$\boldsymbol{\tau}_{P23}(t) = [0, 0, \tau_{P23}(t)]^T = [\mathbf{l}_2(t) - \mathbf{r}_2(t)] \times \mathbf{P}_2(t), \tag{16}$$

$$\boldsymbol{\tau}_{P32}(t) = [0, 0, \tau_{P32}(t)]^T = [\mathbf{l}_2(t) - \mathbf{r}_3(t)] \times [-\mathbf{P}_2(t)], \tag{17}$$

$$\boldsymbol{\tau}_{\mathbf{F}}(t) = [0, 0, \tau_F(t)]^T = [\mathbf{l}_3(t) - \mathbf{r}_3(t)] \times \mathbf{F}(t), \tag{18}$$

are the torques generated by the forces $\mathbf{R}(t)$, $\mathbf{P}_1(t)$, $\mathbf{P}_2(t)$ and $\mathbf{F}(t)$, respectively, and

$$P_{2x}(t) = F_x(t) - m_3\ddot{x}_3(t), \tag{19}$$

$$P_{2y}(t) = F_y(t) - m_3\ddot{y}_3(t) - m_3g, \tag{20}$$

$$P_{1x}(t) = P_{2x}(t) - m_2\ddot{x}_2(t), \tag{21}$$

$$P_{1y}(t) = P_{2y}(t) - m_2\ddot{y}_2(t) - m_2g, \tag{22}$$

$$R_x(t) = m_1\ddot{x}_1(t) - P_{1x}(t), \tag{23}$$

$$R_y(t) = m_1\ddot{y}_1(t) + m_1g - P_{1y}(t). \tag{24}$$

In order to arrest and/or absorb the fall, the faller instinctively bends their body in the hip joints and pulls their upper extremities to the front. In the proposed fall model, these processes are described by functions $\theta_2(t)$ and $\theta_3(t)$, respectively. Taking into account the kinematic excitation as time histories of the angles $\theta_2(t)$ and $\theta_3(t)$, the considered system can be reduced to the 1-DoF model described by the following equation

$$I_1\ddot{\theta}_1(t) + I_2\ddot{\theta}_2(t) + I_3\ddot{\theta}_3(t) = \tau_R(t) + \tau_{P12}(t) + \tau_{P21}(t) + \tau_{P23}(t) + \tau_{P32}(t) + \tau_F(t) \tag{25}$$

with the function $\theta_1(t)$ as a solution of this equation of motion.

Ground reaction force

In order to predict the vertical component of the ground reaction force, we used a non-linear model of impact at the wrist-ground interface in the form [10–12]

$$F_y(t) = k_y|y(t)|^3(1 - b_y\dot{y}(t)) \cdot J(-y(t)), \tag{26}$$

where k_y and b_y denote ground stiffness and damping coefficient in the vertical direction, respectively, $y(t) = l_1\sin\theta_1(t) - l_2\sin\alpha(t) - l_3\sin\beta(t)$, and the function $J(-y(t))$ has the form

$$J(-y(t)) = \begin{cases} 1 \text{ for } y(t) < 0, \\ 0 \text{ for } y(t) \geq 0. \end{cases} \tag{27}$$

Initial conditions

At the beginning of the trip, a human is usually in a standing position. Therefore, we take initial angular position $\theta_1(0) = 90°$. Initial angular velocity $\dot{\theta}_1(0)$ is estimated based on the walking speed v_0 of human gait, (which is referring to the whole body
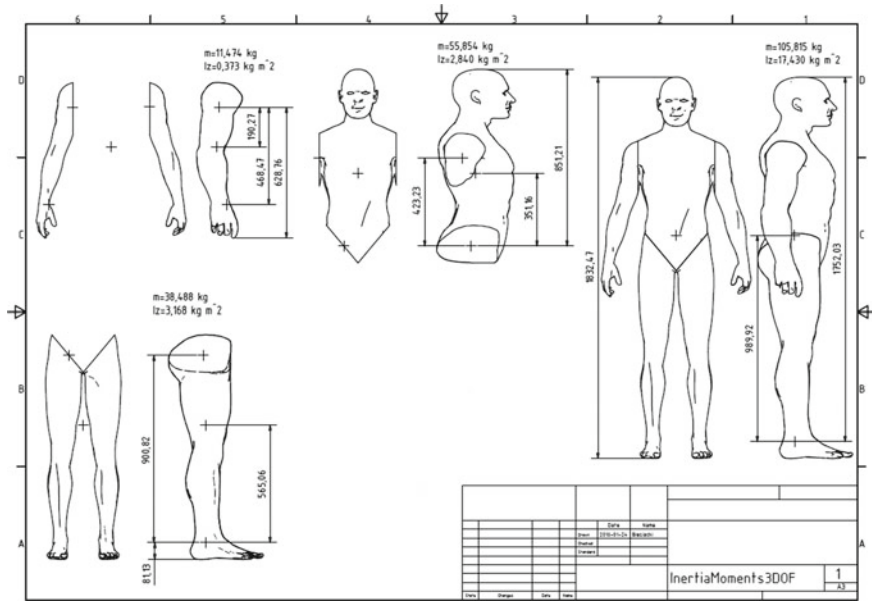
Fig. 2 3D scanned human body model analysed in Inventor

speed during walking) just before the moment of the trip, by using the principle of conservation of momentum according to the formula [12]

$$\dot{\theta}_1(0) = -\frac{(m_1 + m_2 + m_3)v_0 r}{I}, \tag{28}$$

where I is the moment of inertia of the human body about the axis of rotation placed in the ankle joint, and r is the distance between the human gravity centre and the ankle joint, in such position, when the upper extremities are adjusted along the body (it is a typical position of a human body during walking). As a result of the adopted assumptions, the proposed forward fall model allows for studying kinematic and dynamic parameters during the falling process for different walking speeds of the faller just before the moment of the trip over an obstacle.

Identification of the fall model parameters

To determine the appropriate lengths, masses, and moments of inertia of the faller's body, we used the full 3D scanned human body model (see Fig. 2). Even though human body does not consist of a homogenous structure, the abovementioned values were calculated assuming the average density $\rho = 1050$ kg/m^3. Parameters used in numerical simulations are presented in Table 1.

Table 1 Body segment lengths, masses, and moments of inertia

Quantity		Value	Unit
Parameters	$a_1; a_2; a_3$	0.565; 0.351; 0.190	m
	$l_1; l_2; l_3; r$	0.901; 0.423; 0.468; 0.990	m
	$m_1; m_2; m_3$	38.488; 55.854; 11.474	kg
	$I_1; I_2; I_3; I$	3.168; 2.840; 0.373; 121.14	kg·m^2

3 Experimental Investigations

In our experimental investigations, kinematics of the faller from the moment of tripping over an obstacle to hitting their hands to the force plate were observed using the Optitrack system. This motion capture system has been successfully used before, for instance, to track the falling process [12] or gait [13] of a human. The location of 37 individual markers placed on the body of the faller (one of the authors of this work) is presented in Fig. 3. Figure 4 shows the pictures of the faller's body configurations obtained at different times during the observation of the forward falling process. Time histories of angles $\theta_2(t)$ and $\theta_3(t)$, obtained from experiment and their analytical approximations by functions
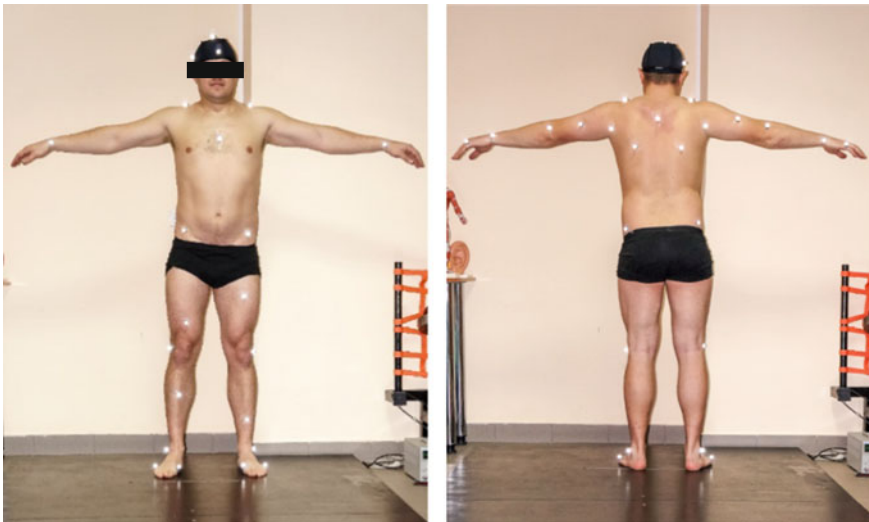
Fig. 3 Thirty seven passive reflective markers distributed on the faller's body for observation of a forward falling process by using the Optitrack system

Fig. 4 Faller's body configurations at different stages of the falling process obtained by the Opti-track system
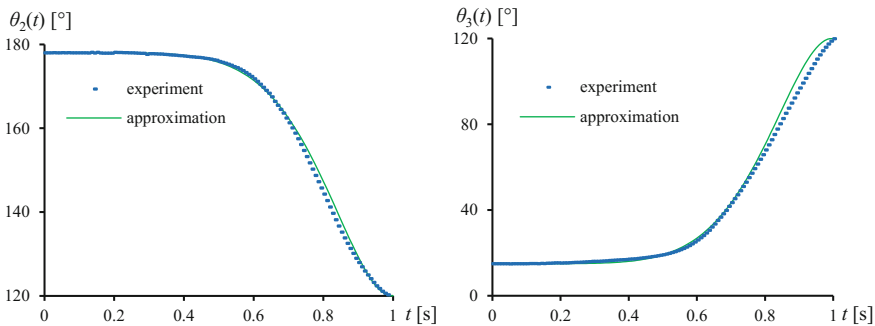
Fig. 5 Time histories of angles $\theta_2(t)$ and $\theta_3(t)$ obtained from the experiment and their approximations by analytical smooth functions

$$\theta_2(t) = \begin{cases} 178° - 58° \sin^2(\lambda t^3) & \text{for } t \leq T, \\ 120° & \text{for } t > T, \end{cases} \tag{29}$$

$$\theta_3(t) = \begin{cases} 15° + 105° \sin^2(\lambda t^3) & \text{for } t \leq T, \\ 120° & \text{for } t > T, \end{cases} \tag{30}$$

for $\lambda = 1.59$ 1/s^3 and duration of the fall $T = 1.00$ s (the time between tripping and hitting the ground), are presented in Fig. 5.

Figure 6 shows the real time histories of the average impact force acting on the single hand of the faller, registered during the experiment using the force plate. During the experimental test the forearms of the faller were arranged in pronation positions. The impact force increases from zero to the maximum value of about 1510 N during the time about 0.05 s. Next, the force changes periodically and decreases to about 400 N during the time interval 0.8–1.0 s.

The forward fall model proposed in this paper is constructed based on the three rigid bodies connected by two rotary joints, which correspond to the human hip and shoulder joints, as well as immobile joint, which corresponds to the ankle joint. To carry out numerical simulations, we adopted parameters $k_y = 3500$ kN/m^3 and $b_y =$

Fig. 6 Time history of ground reaction force, obtained experimentally by using the force plate
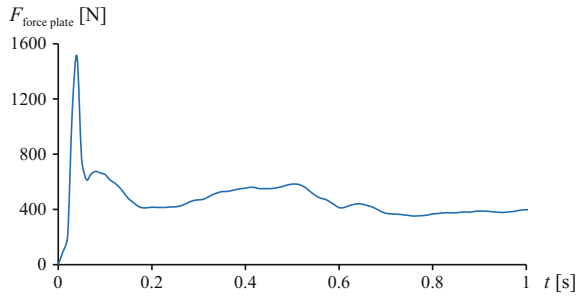
6.0 s/m based on the paper [10]. The human body is a complicated biomechanical system, which contains many different muscles that absorb the impact force during a fall. Therefore, in case of a real fall to the ground, a part of the impact energy is absorbed by the abovementioned muscles, which are not considered in the presented fall model. By comparing the real ground reaction force obtained from the force plate and the impact force generated by the proposed fall model, we estimated what a part of the impact energy (impact force) is transferred to the upper extremities, and what a part is dissipated in other parts of the human body. As a result, it is possible to estimate the real value of the impact force acting on the faller during the impact to the ground for different values of the walking speed v_0 by extrapolating the proposed fall model.

4 Numerical Results

The proposed forward fall model has been implemented and visualised in Mathematica software. Figure 7 shows animation snapshots of the faller's body, plotted at different stages of the fall from a standing position. The presented frames correspond to the fall tested experimentally and observed using the Optitrack system.
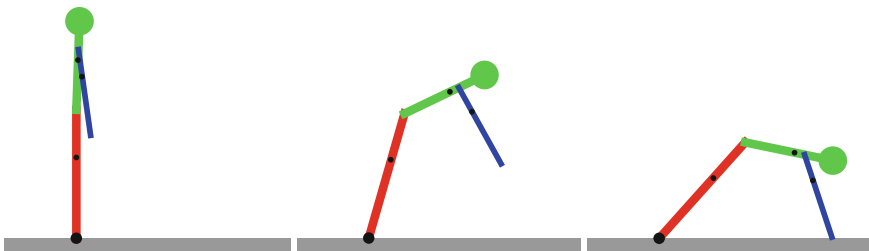
Fig. 7 Animation snapshots of the faller's body, plotted at different times of the fall from a standing position (obtained in Mathematica software)

Table 2 Values of parameters T and λ corresponding to different values of walking speed v_0

v_0 [m/s]	0.22	0.5	1.0	1.5	2.0	2.5	3.0
T [s]	1.00	0.85	0.65	0.50	0.40	0.35	0.30
λ [1/s^3]	1.59	2.59	5.79	12.72	24.84	37.08	58.89

Fig. 8 Distal radius fracture thresholds [6–8] and the maximum values of the ground reaction force as a function of velocity v_0
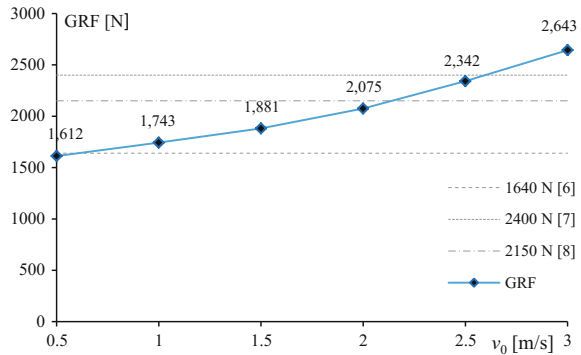
More detailed experimental observations with falls demonstrate that with an increase in the walking speed v_0, the faller instinctively bends the body around the hip joint and pulls their arms in the forward direction. As a result, duration of the fall T is shorter, whereas the value of the parameter λ is greater. Therefore, in our further numerical analysis we used the time histories of the angles $\theta_2(t)$ and $\theta_3(t)$ governed by Eqs. (29) and (30) with different parameters T and λ, depending on the speed v_0 of the human walking just before the trip. The mentioned parameters are presented in Table 2.

Figure 8 presents the maximum values of GRF as a function of the velocity v_0 and values of GRFs, which correspond to the distal radius fracture thresholds adopted by different authors [6–8]. As can be seen, the maximum value of GRF increases with the increasing speed v_0. For the lowest presented value of v_0 (equal to 0.5 m/s), the estimated maximum value of GRF is 1612 N. For the largest value of v_0 (equal to 3.0 m/s), the maximum value of GRF is 2643 N. For small values of v_0, the maximum value of GRF is less than the presented distal radius fracture thresholds. For large value of v_0, the maximum of GRF exceeds all the presented distal radius fracture thresholds. Concluding, it can be stated that for a large walking speed of human gait before the falling process, the value of the distal radius fracture threshold is usually exceeded, eventually leading to injuries and/or fractures of the upper extremities. Both the presented results as well as further extrapolations of the proposed fall model can be used as a load conditions in the finite element analysis of the numerical model of the human upper extremity.

5 Conclusions

The paper presents a 3-link mechanical model implemented in Mathematica, governing the forward fall on outstretched arms. The presented model is an extension of the fall models considered in papers [12, 14]. It enables to estimate the vertical ground reaction forces acting on the hands during the human falling process. Segments of the human body were modelled as three rigid bodies connected by rotary joints which correspond to the hip and shoulder human joints, as well as immobile joint, which corresponds to the ankle joint. In order to estimate parameters of the faller body we used three-dimensional scanned human body model, created and segmented in Inventor. Kinematics of the falling process was observed by the Optitrack system, while the real ground reaction force during impact to the ground was registered by the force plate. The proposed fall model allows one to estimate the value of the vertical ground reaction force acting on the hands of the faller during the impact to the ground for different speed just before a trip over an obstacle.

Concluding, it should be noted that the developed model has also some limitations. First, based on the scan of the human body, we are not able to determine accurately the distribution of human body mass density. Therefore, in our simulations we have adopted the average value resulting from the total weight and total body volume. Second, the movement of the shoulder with respect to the torso and stiffness/damping properties of the shoulder, hip and/or elbow joints were not implemented in the presented model. Eventually, only the vertical component of the ground reaction force was considered, whereas the horizontal component was omitted. In future studies, for instance, a two dimensional approach for modeling of human skeletal muscles, can also be considered [15, 16]. Nevertheless, the proposed forward fall model enables to obtain the results in the form of the time histories of the ground reaction force, which can be used as load conditions, for further finite element analysis of the human upper extremity.

References

1. Heijnen, M.J.H., Rietdyk, S.: Falls in young adults: perceived causes and environmental factors assessed with a daily online survey. Hum. Mov. Sci. **46**, 86–95 (2016)
2. Robinovitch, S.N., Feldman, F., Yang, Y., Schonnop, R., Leung, P.M., Sarraf, T., et al.: Video capture of the circumstances of falls in elderly people residing in long-term care: an observational study. The Lancet **381**, 47–54 (2013)
3. Nevitt, M.C., Cummings, S.R.: Study of osteoporotic fractures research group, type of fall and risk of hip and wrist fractures: the study of osteoporotic fractures. J. Am. Geriatrics Soc. **41**, 1226–1234 (1993)

4. Palvanen, M., Kannus, P., Parkkari, J., Pitkajarvi, T., Pasanen, M., Vuori, I., Jarvinen, M.: The injury mechanisms of osteoporotic upper extremity fractures among older adults: a controlled study of 287 consecutive patients and their 108 controls. Osteoporos. Int. **11**, 822–831 (2000)
5. Johnell, O., Kannis, J.A.: An estimate of the worldwide prevalence and disability associated with osteoporotic fractures. Osteoporos. Int. **17**, 1726–1733 (2006)
6. Spadaro, J.A., Werner, F.W., Brenner, R.A., Fortino, M.D., Fay, L.A., Edwards, W.T.: Cortical and trabecular bone contribute strength to the osteopenic distal radius. J. Orthop. Res. **12**, 211–218 (1994)
7. Kim, K.-J., Ashton-Miller, J.A.: Segmental dynamics of forward fall arrests: a system identification approach. Clin. Biomech. **24**, 348–354 (2009)
8. Burkhart, T.A., Andrews, D.M., Dunning, C.E.: Multivariate injury risk criteria and injury probability scores for fractures to the distal radius. J. Biomech. **46**, 973–978 (2013)
9. Chiu, J., Robinovitch, S.N.: Prediction of upper extremity impact forces during falls on the outstretched hand. J. Biomech. **31**, 1169–1176 (1998)
10. DeGoede, K.M., Ashton-Miller, J.A.: Biomechanical simulations of forward fall arrests: effects of upper extremity arrest strategy, gender and aging-related declines in muscle strength. J. Biomech. **36**, 413–420 (2003)
11. Gerritsen, K.G.M., van den Bogert, A.J., Nigg, B.M.: Direct dynamics simulation of the impact phase in heel-toe running. J. Biomech. **28**, 661–668 (1995)
12. Grzelczyk, D., Biesiacki, P., Mrozowski, J., Awrejcewicz, J.: Dynamic simulation of a novel "broomstick" human forward fall model and finite element analysis of the radius under the impact force during fall. J. Theor. Appl. Mech. **56**, 239–253 (2018)
13. Grzelczyk, D., Szymanowska, O., Awrejcewicz, J.: Gait pattern generator for control of a lower limb exoskeleton, Vibrations in Physical Systems, 29, 2018, 2018007, 10 pages
14. Biesiacki, P., Mrozowski, J., Grzelczyk, D., Awrejcewicz, J.: Modelling of forward fall on outstretched hands as a system with ground contact. Nonlinear dynamics of a vibration harvest–absorber system. Experimental Study, pp. 61–72 (2016)
15. Wojnicz, W., Zagrodny, B., Ludwicki, M., Awrejcewicz, J., Wittbrodt, E.: Mathematical model of pennate muscle. In: Awrejcewicz, J., Kaźmierczak, M., Mrozowski, J., Olejnik, P. (eds.) Dynamical Systems—Mechatronics and Life Sciences. TU of Lodz, Lodz, pp. 595–608 (2015)
16. Wojnicz, W., Zagrodny, B., Ludwicki, M., Awrejcewicz, J., Wittbrodt, E.: A two dimensional approach for modelling of pennate muscle behaviour. Biocybernetics Biomed. Eng. **27**, 302–315 (2017)

Reflectance and Transmittance of Cholesteric Liquid Crystal Sandwiched Between Polarizers

Dariusz Grzelczyk and Jan Awrejcewicz

Abstract In this paper we calculated reflection and transmission coefficients of the electromagnetic radiation (light) incident on the cholesteric liquid crystal sandwiched between two isotropic optical media and a pair of polarizers. To model optical phenomena (i.e. propagation and interference of the light waves) in liquid crystal, we applied the 4×4 matrix method. As a result of the performed computer simulation, we obtained some interesting reflection/transmission spectra and polar plots for different parameters of the considered system and arbitrary incident monochromatic light. The illustrated and discussed results can be useful for understanding different optical systems, especially liquid crystal displays. Moreover, the applied mathematical approach can be potentially used for modelling of more advances contemporary optical systems, i.e. photonic crystals.

Keywords Cholesteric liquid crystal · Polarizer · Reflectance · Transmittance

1 Introduction

Liquid crystals (LCs) are an interesting fourth state of matter lying between the crystalline solid and amorphous liquid states. Therefore, in some temperature ranges, they exhibit both the properties of liquids and the properties of crystalline solid state. Most of them are organic compounds with elongated molecules that influence their interesting physical properties. The classification of LCs distinguishes three types of liquid crystalline phases, namely: nematic, smectic and cholesteric liquid crystals (CLCs). The above listed groups differ in physical properties, especially in optical ones. However, due to the strongly periodic helical structure, cholesteric liquid crys-

D. Grzelczyk (✉) · J. Awrejcewicz
Department of Automation, Biomechanics and Mechatronics, Lodz University of Technology, 1/15 Stefanowski Street, 90-924 Lodz, Poland
e-mail: dariusz.grzelczyk@p.lodz.pl

J. Awrejcewicz
e-mail: jan.awrejcewicz@p.lodz.pl

tals exhibit unique optical properties. The first of these is the optical birefringence, i.e. two different refractive indices. In the birefringent medium, the propagating wave of the monochromatic radiation decomposes into two waves, which propagate with different velocities. In addition, CLCs are characterized by twisting of the plane of polarization and circular dichroism. However, the most popular engineering applications employ the selective reflection of incident radiation of the light. The colour of the reflected light depends on temperature, mechanical stress, external electric, magnetic fields, etc. Due to the abovementioned properties of LCs, they have been used in practical applications, especially in liquid crystal displays. Moreover, CLCs seems to be the promising candidates for numerous different photonic applications. Therefore, nowadays, a lot of attention is paid to the photonic crystals (PCs), whose optical properties are similar to the properties of liquid crystals due to their periodic dielectric structures. These substances contain a periodic distribution of both refractive indices in one, two, or three dimensions, and can be used to prohibit, confine, and control light propagation in a specific wavelength bandwidth. An interesting review of the fabrication of photonic band gap materials based on cholesteric liquid crystals is presented in the review paper [1]. In the present study, we tested the implemented computer algorithm of the 4×4 matrix method using CLC sandwiched within two isotropic media and optical polarizers. However, the used algorithm can be adopted to model optical phenomena in photonic crystals with a known distribution of the dielectric structure.

2 Methods—A Brief Literature Review

It should be noted that optical phenomena and the transmission of light through birefringent optical media (networks) have been treated by different methods. In the conventional Jones calculus, each optical element (wave plate, liquid crystal layer) is represented by a 2×2 matrix, and refraction and reflection of light at the plate surfaces (dielectric discontinuities) are neglected. This method is limited to normally incident light and does not explain the leakage of off-axis light through a pair of crossed ideal polarizers [2]. For treating the transmission of off-axis light in a general birefringent optical media, the extended Jones matrix method can be used, which takes into account the single reflection at the interfaces. This method is adequate for numerous practical applications, and has been widely used in the analysis of many optical systems [2–7]. In 2000, Li [8] applied the Jones matrix method to ellipsometry, i.e. for investigating the dielectric properties of a thin film. In turn, in 2010, Chen et al. [9] used a new 2×2 matrix method and discussed the polarization state of transmitted waves through the cholesteric liquid crystal.

On the contrary to the aforementioned methods dedicated to the birefringent networks, the exact solutions can be obtained by using the 4×4 matrix method, which takes into account both the effect of refraction and multiple reflections between plate interfaces [2]. This approach has been applied by many researches. For instance, Schwelb [10] analyzed lossy gyro electromagnetic layers in polar and longitudinal
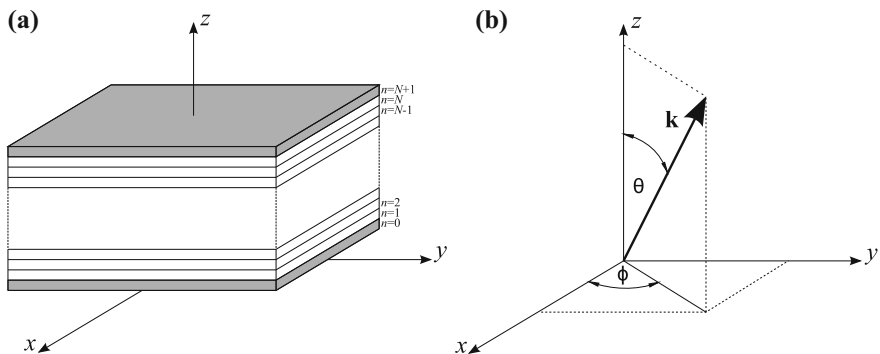
Fig. 1 Model of the investigated cholesteric liquid crystal sandwiched within two isotropic optical media (**a**) and the orientation of the wave vector **k** of the arbitrarily incident light (**b**)

orientation. Chen et al. [11] applied the 4×4 matrix method to liquid crystal displays. Using this method, Ivanov and Sementsov [12] described the propagation of electromagnetic waves in stratified bianisotropic chiral structures. Most recently, the 4×4 matrix method was used by Ortega et al. [13] to study different kinds of cells of cholesteric liquid crystal lasers. Due to abovementioned anisotropic properties of CLCs and PCs, we used the exact 4×4 matrix method also in this paper, which is shortly presented in Sect. 3.

3 Model of the Considered Optical System

Figure 1a presents the model of the cholesteric liquid crystal placed in the Cartesian coordinate system *xyz* and sandwiched between two (i.e. lower and upper) isotropic media. The considered CLC with thickness *d* is divided into *N* equal layers parallel to the *xy* plane. The incident light propagates in the lower medium ($n = 0$), and then partially propagates in the liquid crystal ($n = 1, 2, …, N$) and the upper isotropic medium ($n = N + 1$). The *c*-axis (optical axis) of the CLC lies in the *xy* plane and changes periodically along the *z*-direction. Periodical helical structure of the analyzed CLC is characterized by the pitch *p*. Both lower and upper isotropic media are quantified by a refractive index n_s. The liquid crystal has two refractive indices, n_o and n_e, for the ordinary and extraordinary waves, respectively. Figure 1b presents orientation (described by angles θ and ϕ) of the wave vector **k** of the incident non-polarized beam of monochromatic light with wavelength λ, in lower isotropic medium.

The 4×4 matrix method used in the paper was developed on the basis of mathematical formalism presented in monograph [14]. Therefore, only the main stages of this method, which are needed in the further part of the paper dedicated to the modeling of CLCs sandwiched within optical polarizers, are presented below. In this method, the optical *c*-axes and the dielectric tensors $\hat{\boldsymbol{\varepsilon}}(n)$ of the individual liquid

(a)   **(b)**
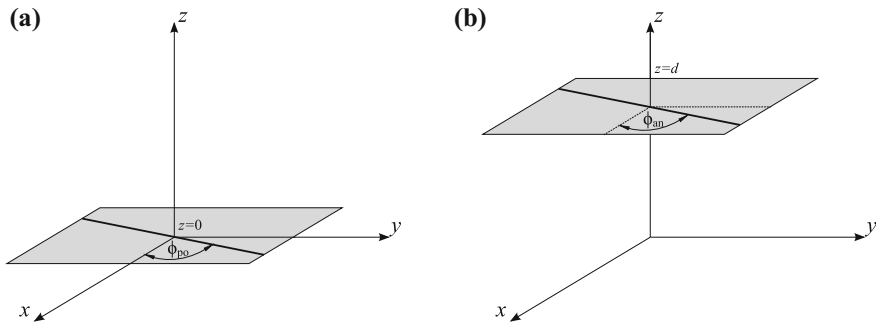
Fig. 2 Orientation of the polarization axes of the polarizer (**a**) and the analyzer (**b**)

crystal layers ($n = 1,2, \ldots, N$) and bounded plates ($n = 0$ and $n = N+1$) are determined first. In the second step, the wave vectors $\mathbf{k}_\sigma(n)$ of all four elementary waves ($\sigma = 1, 2, 3, 4$) in all layers are calculated. The third stage is devoted to computing of the optical polarization vectors $\mathbf{p}_\sigma(n)$ of individual elementary waves representing the directions of the electric field and the corresponding vectors $\mathbf{q}_\sigma(n)$ representing the directions of the magnetic field. In the fourth stage of this method, transition matrices between individual layers are calculated based on the assumption of continuity of the tangential components of the vectors $\mathbf{p}_\sigma(n)$ and $\mathbf{q}_\sigma(n)$ at the dielectric interfaces. The product of the abovementioned individual matrices is the 4×4 transition matrix, which describes the relationships between amplitudes of the electric field of the incident waves A_s, A_p, reflected waves B_s, B_p, and transmitted waves C_s, C_p, both for s and p waves, respectively. Finally, in the last stage of this method, the coefficients of reflection R and transmission T of the incident light are computed.

Let us consider now two ideal optical polarizers bounding the optical system presented in Fig. 1a. In general, a polarizer is an optical filter that transmits light waves of a specific polarization and blocks light waves of other polarizations. It can also be used to analyze the polarized light, and then it is called an analyzer. The dependence of the intensity of the transmitted light on the angle φ between polarization axes of the polarizer and analyzer is given by the Malus's law

$$I = I_0 \cos^2 \varphi, \tag{1}$$

where I_0 is the initial intensity of beam of light polarized by polarizer, whereas I is the intensity of the light that passes through the analyzer. In general, the optical polarizer can be characterized by the axis of polarization. In our system, these axes (both for polarizer and analyzer) lie in the xy plane and can be oriented arbitrarily (angles ϕ_{po} and ϕ_{an}) with respect to the x-axis, as it is shown in Fig. 2.

The polarization axes can be characterized by the following unit vectors

$$\mathbf{po} = [\cos \phi_{po}, \sin \phi_{po}, 0]^T, \tag{2}$$

$$\mathbf{an} = [\cos \phi_{an}, \sin \phi_{an}, 0]^{T}. \tag{3}$$

The vector of the optical polarization of the light transmitted through the polarizer is normal to the wave vector $\mathbf{k}_1(0)$, which denotes the wave vector of the incident s wave in the lower isotropic medium. Therefore, the unit vector $\mathbf{A}$ of the optical polarization of the polarized incident light can be determined as follows

$$\mathbf{A} = \frac{\mathbf{k}_1(0) \times [\mathbf{po} \times \mathbf{k}_1(0)]}{|\mathbf{k}_1(0) \times [\mathbf{po} \times \mathbf{k}_1(0)]|}. \tag{4}$$

The vector $\mathbf{A}$ can be decomposed into the components $\mathbf{A}_s$ and $\mathbf{A}_p$, with the amplitudes A_s and A_p, respectively. These amplitudes can be determined as follow

$$A_s = \mathbf{A} \cdot \mathbf{p}_1(0), \tag{5}$$
$$A_p = \mathbf{A} \cdot \mathbf{p}_3(0), \tag{6}$$

where $\mathbf{p}_1(0)$ and $\mathbf{p}_3(0)$ are the optical polarization vectors of incident s and p waves, respectively, in lower isotropic optical medium.

Knowledge of the amplitudes A_s and A_p allows one to determine the values B_s, B_p of the reflected s and p waves, and the values C_s and C_p of the transmitted s and p waves, respectively, using the 4×4 matrix method. As a result, the optical polarization vector $\mathbf{B}$ for the reflected wave and the vector $\mathbf{C}$ for the transmitted wave can be obtained as follow

$$\mathbf{B} = B_s \mathbf{p}_2(0) + B_p \mathbf{p}_4(0), \tag{7}$$
$$\mathbf{C} = C_s \mathbf{p}_1(N + 1) + C_p \mathbf{p}_3(N + 1), \tag{8}$$

where $\mathbf{p}_2(0)$ and $\mathbf{p}_4(0)$ denote optical polarization vectors of the reflected s and p waves, respectively. On the other hand, $\mathbf{p}_1(N + 1)$ and $\mathbf{p}_3(N + 1)$ stand for the optical polarization vectors of the transmitted to the upper isotropic medium s and p waves, respectively.

Let the vectors $\mathbf{PO}$ and $\mathbf{AN}$ be the unit vectors lying in the planes of the polarizer and the analyzer, which are normal to the wave vector $\mathbf{k}_2(0)$ of the reflected wave in the lower isotropic medium and the wave vector $\mathbf{k}_1(N + 1)$ of the transmitted wave to the upper isotropic medium, respectively. The unit vectors that have these properties have the following forms

$$\mathbf{PO} = \frac{\mathbf{k}_2(0) \times [\mathbf{pol} \times \mathbf{k}_2(0)]}{|\mathbf{k}_2(0) \times [\mathbf{pol} \times \mathbf{k}_2(0)]|}, \tag{9}$$

$$\mathbf{AN} = \frac{\mathbf{k}_1(N + 1) \times [\mathbf{pol} \times \mathbf{k}_1(N + 1)]}{|\mathbf{k}_1(N + 1) \times [\mathbf{pol} \times \mathbf{k}_1(N + 1)]|}. \tag{10}$$

The scalar product of the unit vectors is equal to the cosine of the angle between their directions. Therefore, both the reflection coefficient R and the transmission coefficient T can be determined from the formulas

$$R = \frac{B_s^2 + B_p^2}{A_s^2 + A_p^2} \left(\frac{\mathbf{B}}{|\mathbf{B}|} \cdot \mathbf{PO} \right)^2, \tag{11}$$

$$T = \frac{C_s^2 + C_p^2}{A_s^2 + A_p^2} \left(\frac{\mathbf{C}}{|\mathbf{C}|} \cdot \mathbf{AN} \right)^2. \tag{12}$$

4 Simulation Results

In what follows, we illustrated and discussed some calculations of the reflection and transmission coefficients R and T for different parameters of the considered optical system. In addition, we calculated values of these coefficients for different angles characterizing the orientation of the incident light in the form of colour polar plots.

To test the operation of the developed algorithm, at first, we considered the case when the non-polarized light propagated through the homogenous and lossless isotropic optical medium, i.e. we assumed that $n_s = n_o = n_e$. For this case, for arbitrary values of the parameters d, λ, θ, ϕ, $n_s = n_o = n_e$ and N, we obtained always $R = 0$ and $T = 1$. In such system, there are no dielectric discontinuities at the interfaces of the imaginary layers. Therefore there is a lack of reflection of the incident light, i.e. the incident light is completely transmitted through the analyzed optical medium.

In the next step of the performed tests, we took into account again a homogeneous isotropic medium sandwiched between two optical polarizers. Figure 3 shows the dependence of the transmission coefficient T of the normally incident light as a function of the angle φ (the angle between the axes of the polarizer and the analyzer). This dependence coincides with the theoretical dependence by means of Malus's law defined by the formula (1). It should be noted that the presented relationships also coincide for other values of the analyzed lossless, homogenous, and isotropic optical medium as well as different values of the wavelength of the incident light.

Figure 4 shows the polar plots of the transmission coefficient T as a function of the angles θ and ϕ of the incident non-polarized light for different orientations of the polarizer and the analyzer. It should be noted that in all polar plots presented in this paper, radial position corresponds to the angle θ (from 0 in the middle, to the 90° at the edges of the of the plotted polar distributions), whereas circumferential position corresponds to the angle ϕ (from 0 to 360°, as it is shown in plotted distributions). The presented results show that the values of the transmission coefficients depend both on the orientation of the wave vector of the incident light and relative orientations of the polarizer and analyzer.

In the next step of the analysis, we presented some characteristics of the transmission coefficient T for different parameters of the CLC sandwiched between two
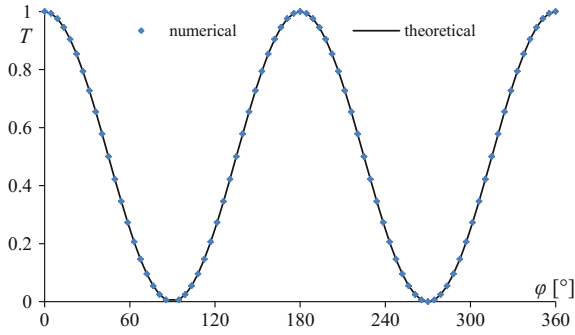
Fig. 3 Transmission coefficient T as a function of the angle φ between polarization axes of the polarizer and the analyzer, obtained numerically and theoretically (based on Malus's law)

$\phi_{po} = 0°, \phi_{an} = 45°$ $\qquad$ $\phi_{po} = 0°, \phi_{an} = 90°$ $\qquad$ $\phi_{po} = 0°, \phi_{an} = 135°$

$\phi_{po} = 45°, \phi_{an} = 90°$ $\qquad$ $\phi_{po} = 45°, \phi_{an} = 135°$ $\qquad$ $\phi_{po} = 45°, \phi_{an} = 180°$
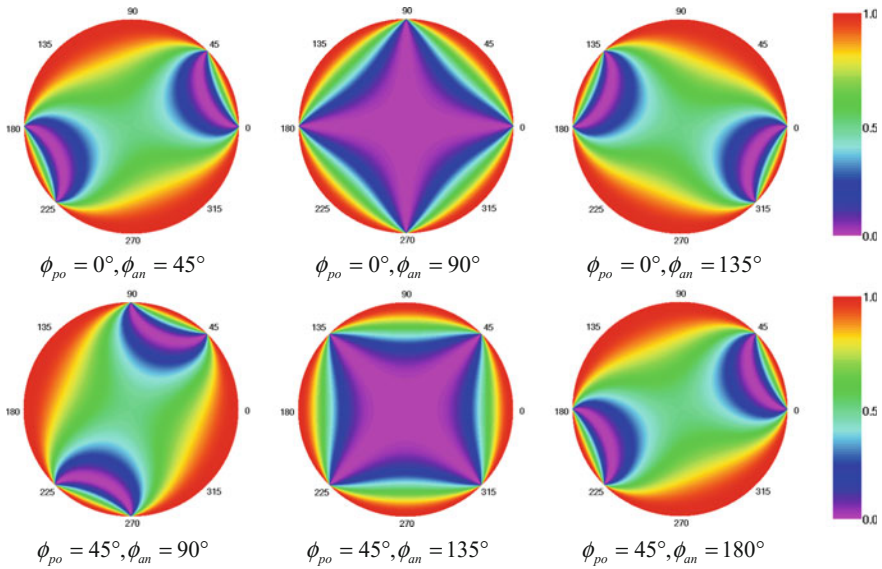
Fig. 4 Polar plots of the transmission coefficient T for different orientations of the polarizers

Table 1 Parameters of the investigated CLC and the bounding isotropic media

Quantity	d	p	n_s	n_o	n_e
Unit	μm	nm	–	–	–
Value	12	350	1.3	1.4	1.5

isotropic media. First, we investigated the system without polarizers. The parameters of the tested system are presented in Table 1. All calculations were carried out for $N = 1000$. Figure 5 shows the reflection R and transmission T spectra for normally incident non-polarized light.

Fig. 5 Reflection and transmission spectra of the normally incident non-polarized light. The colour scale below the plot corresponds to the colours of the light with wavelength presented on the x-axis. The sum of coefficients $R+T$ equals 1 (for each value of the wavelength λ)
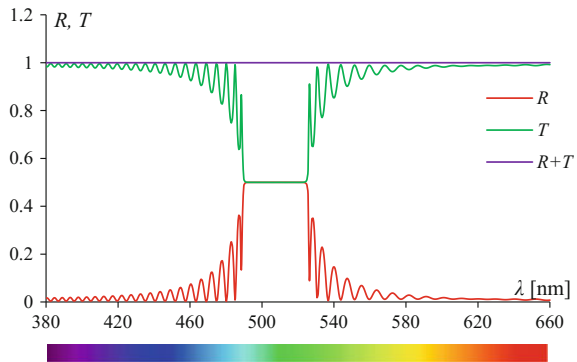
As can be seen, the presented curve is characterized by the reflection bandwidth, i.e. the range of the wavelength of the incident light where $R = 0.5$. The natural non-polarized incident light contains the same amount of both right- and left-circularly polarized light. Within the bandwidth, right-circularly polarized light is reflected by a right-handed helix, while left-circularly polarized light is transmitted by the cholesteric liquid crystal, and therefore values of both R and T coefficients are equal 0.5. Concluding, in our algorithm we confirmed the occurrence of the selective reflection of the incident radiation within the bandwidth and transmission of both polarization states outside the this bandwidth. Figure 6 presents reflection spectra for different parameters of the CLC.

The obtained calculations showed that the bandwidth and its position in the wavelength spectrum strongly depend on the refractive indices n_o and n_e (see Fig. 6a and b). The bandwidth depends also strongly on the pitch p of the helical structure of the CLC (see Fig. 6c), whereas the shape of the bandwidth is strongly dependent on the thickness d of the investigated CLC (see Fig. 6d). The obtained results of computer simulations allowed us to analyze the basic properties of the optical polarizers as well as the optical properties of cholesteric liquid crystals.

For later comparative purposes, in Fig. 7a we presented the polar plot of the coefficient T of the non-polarized light transmitted by the CLC, without polarizers. The calculations were performed for the parameters given in Table 1 and wavelength $\lambda = 507.5$ nm (the middle of the selective reflection bandwidth presented in Fig. 5). As can be seen, the obtained plot does not depend on the angle ϕ. However, we observed an interesting dependence on the angle θ presented in Fig. 7b, i.e. along the radius of the polar plot presented in Fig. 7a. For small values of angle θ, we obtained $T = 0.5$ (selective reflection of the incident non-polarized light). For larger values of angle θ, the transmission coefficient T increases, because both right- and left-circularly polarized light can be transmitted. In turn, for large values of the angle θ (i.e. $\theta \approx 90°$), the ray of the incident light slides on the surface and does not propagate within the investigated CLC.

(a)

(b)

(c)

(d)
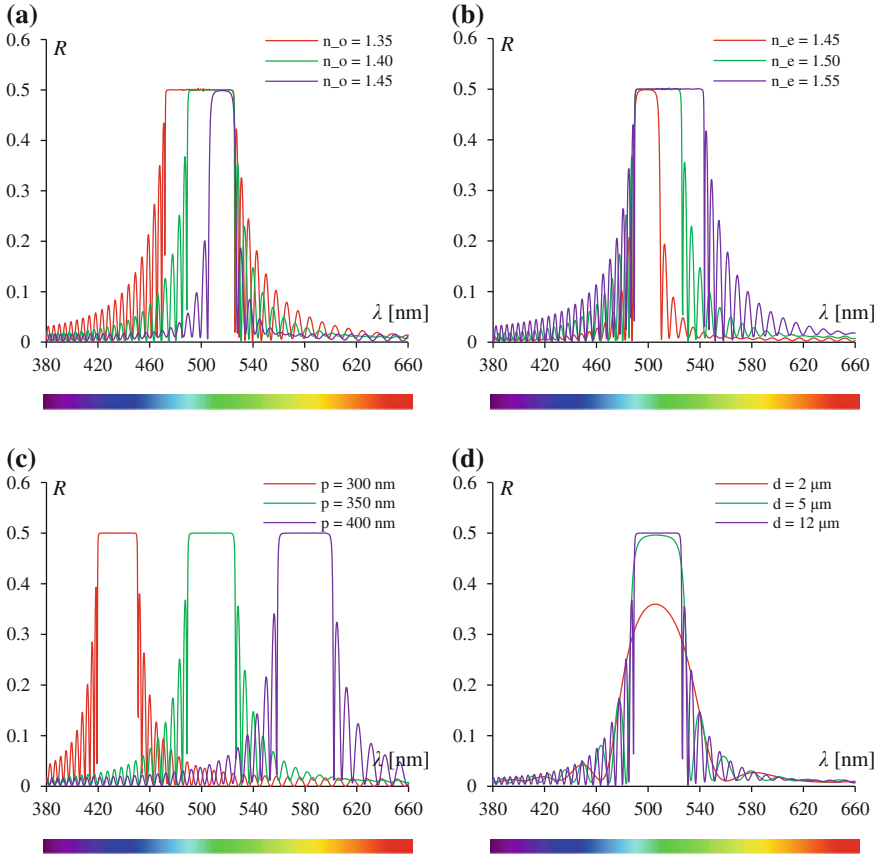
Fig. 6 Reflection spectra of the normally incident non-polarized light for different values of the parameters n_o, n_e, p and d. The colour scale below the picture corresponds to the colours of the light with wavelength presented on the x-axis

Figure 8 presents polar plots of the transmission coefficient T of the CLC sandwiched between differently oriented polarizers. All the presented distributions depend strongly on the angle ϕ and θ described orientation of the wave vector of the incident light. For instance, both for $\phi \approx \phi_{po}$ or $\phi \approx \phi_{an}$ we obtained $T \approx 0$. We also obtained a small value of the coefficient T for $\theta \approx 90°$ (as in Fig. 7). However, for other values of angle ϕ, the value of the coefficient T is characterized by large and frequent changes. The presented distribution is symmetrical only for small values of the angle θ.

(a)

(b)
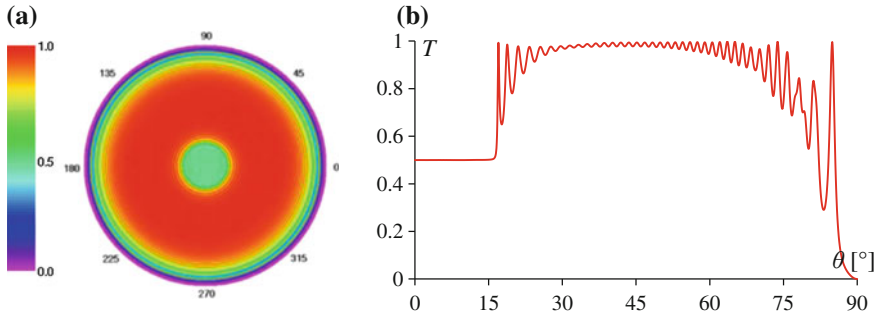
Fig. 7 Polar plot (**a**) and the plot profile along the radius (**b**) of the non-polarized light transmitted through the CLC

$\phi_{po} = -45°, \phi_{an} = 45°$

$\phi_{po} = 0°, \phi_{an} = 90°$

$\phi_{po} = 45°, \phi_{an} = 135°$

$\phi_{po} = 90°, \phi_{an} = 180°$
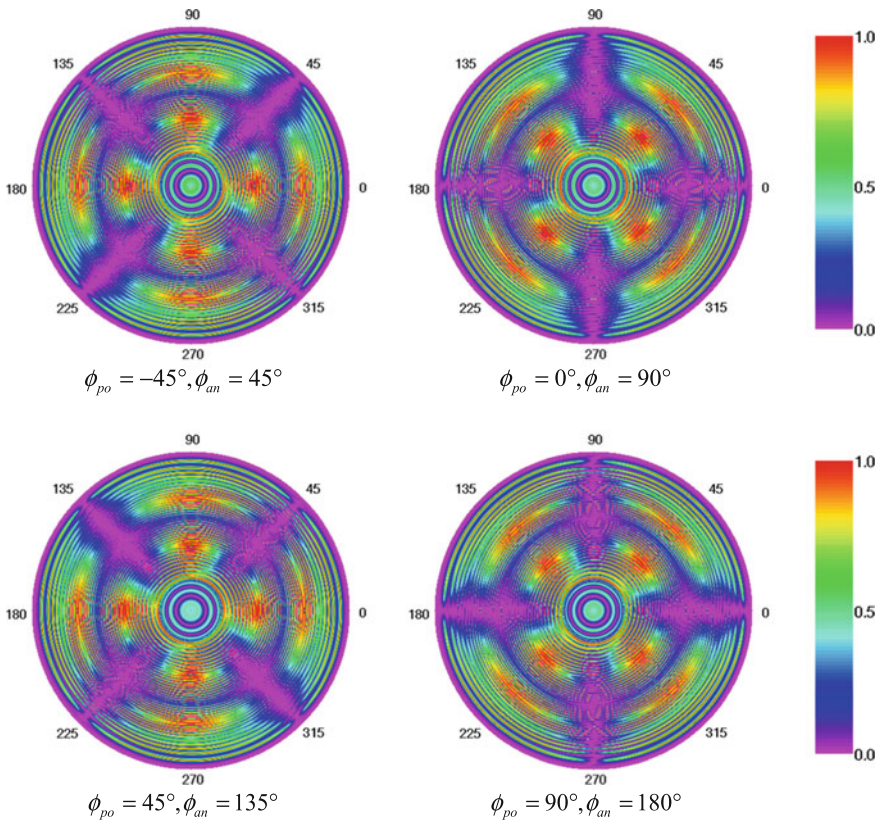
Fig. 8 Polar plots of the transmission coefficient T of the investigated CLC sandwiched within differently oriented polarizer and analyzer

5   Conclusions

In the paper, an attempt to model optical phenomena in cholesteric liquid crystals sandwiched between two isotropic media and optical polarizers has been presented. The influence of the orientation of the applied polarizers on the intensity of the transmitted light in relation to the investigated cholesteric liquid crystal has been mathematically considered. Optical phenomena in the CLC have been modeled using the 4×4 matrix method, which takes into account the effect of refraction and multiple reflections between plate interferences, both ordinary and extraordinary waves.

The developed computer algorithm has been tested using lossless homogenous isotropic medium first, and the same medium sandwiched within two optical polarizers. Next, we have calculated reflection and transmission coefficient of the monochromatic light incident on the investigated CLC sandwiched within isotropic media, both without and with optical polarizers. Some interesting reflection and transmission spectra as well as polar plots of the reflection or transmission coefficient have been obtained, illustrated, and discussed. The implemented computer algorithm of the 4×4 matrix method has allowed us to understand optical properties of the considered optical system for different parameters. The gained experiences can be potentially used to model optical phenomena in photonic crystals, which have attracted a large amount of attention in recent years. They offer unique optical properties, including ability to control the propagation of light, and can be used in the future as a basic elements of all-optical integrated circuits [1].

References

1. Balamurugan, R., Liu, J.-H.: A review of the fabrication of photonic band gap materials based on cholesteric liquid crystals. React. Funct. Polym. **105**, 9–34 (2016)
2. Gu, C., Yeh, P.: Extended Jones matrix method and its application in the analysis of compensators for liquid crystal displays. Displays **20**, 237–257 (1999)
3. MacGregor, A.R.: Method for computing homogeneous liquid-crystal conoscopic figures. J. Opt. Soc. Am. A **7**, 337–347 (1990)
4. Lien, A.: The general and simplified Jones matrix representations for the high pretilt twisted nematic cell. J. Appl. Phys. **67**, 2853–2856 (1990)
5. Lien, A.: Extended Jones matrix representation for the twisted nematic liquid-crystal display at oblique incidence. Appl. Phys. Lett. **57**, 2767–2769 (1990)
6. Ong, H.L.: Electro-optics of electrically controlled birefringence liquid-crystal displays by 2×2 propagation matrix and analytic expression at oblique angle. Appl. Phys. Lett. **59**, 155–157 (1991)
7. Ong, H.L.: Electro-optics of a twisted nematic liquid-crystal display by 2×2 propagation matrix at oblique angle. Jpn. J. Appl. Phys. Part 2—Lett. **30**, L1028–L1031 (1991)
8. Li, S.F.: Jones-matrix analysis with Pauli matrices: application to ellipsometry. J. Opti. Soc. Am. A **17**, 920–926 (2000)

9. Chen, T., Feng, S.M., Xie, J.N.: The new matrix and the polarization state of the transmitted light through the cholesteric liquid crystal. Optik **121**, 253–258 (2010)
10. Schwelb, O.: Stratified lossy anisotropic media: general characteristics. J. Opti. Soc. Am. A **3**, 188–193 (1986)
11. Chen, C.-J., Lien, A., Nathan, M.I.: 4×4 matrix method for biaxial media and its application to liquid crystal displays. Jpn. J. Appl. Phys. **35**, L1204–L1207 (1996)
12. Ivanov, O.V., Sementsov, D.I.: Light propagation in stratified chiral media. The 4×4 matrix method. Crystallogr. Rep. **45**, 487–492 (2000)
13. Ortega, J., Folcia, C.L., Etxebarria, J.: Upgrading the performance of cholesteric liquid crystal lasers: improvement margins and limitations. Materials, **11**, 24 p (2018)
14. Yeh, P., Gu, C.: Optics of liquid crystal displays. John Wiley and Sons, New York (1999)

Analysis of Nonlinear Dynamic Behavior of a Rotating Electrical Machine Rotor-Bearing System Using Optimal Auxiliary Functions Method

Nicolae Herisanu and Vasile Marinca

Abstract Rotating electrical machines are widely used in engineering and industry applications due to their reliability. The machines under study are subjected to a parametric excitation caused by an inertial thrust and a forcing excitation caused by an unbalanced force of the rotor while the entire system is being supported by nonlinear bearings with nonlinear stiffness characteristics and damping properties. The nonlinear suspension makes the analytical study very difficult, leading to strong nonlinear differential equations, which are hard to be solved through classical methods. Supplementary problems could arise in case of some horizontal rotating machines, when the gravity effect is not negligible for certain stiffness conditions. Also, the misalignment could occur in the electrical machine after some amount of running. In our paper, a new analytical approach, namely the Optimal Auxiliary Functions Method (OAFM) is employed to solve the problem of an electrical machine supported by nonlinear bearings characterized by nonlinear stiffness of Duffing type and the entire system is subjected to a parametric excitation due to the axial thrust and a forcing excitation caused by an unbalanced force of the rotor. This study contains an effective and easy to use procedure which is independent of the presence of small or large parameters in the nonlinear equations. The approximate analytical solution is in very good agreement with the numerical simulation results, which prove the reliability of this procedure.

Keywords Dynamic behavior · Rotating machine · Approximate analytical solution

N. Herisanu · V. Marinca
University Politehnica Timisoara, Timisoara, Romania

N. Herisanu (✉) · V. Marinca
Centre for Fundamental Technical Research, Romanian Academy, Timisoara, Romania
e-mail: nicolae.herisanu@upt.ro

159

1 Introduction

Rotating electrical machines are widely used in engineering and industry applications due to their reliability. Having in view that there is a need to continuously increase the performance of this kind of machines, they are intensively studied from both mechanical and electrical point of view, since these complex engineering systems combine electrical and mechanical concepts.

Reliable analytical and numerical tools should be developed and implemented in order to predict and analyze possible problems related to dynamic behavior of these systems, which could be described by nonlinear and strongly nonlinear differential equations. The most often encountered problems could be generated by unbalanced forces of the rotor, electrical unbalances, coupling or driven equipment, shaft misalignment and nonlinearity of the bearing stiffness, bad bearings and mechanical looseness, resonance, critical speeds, etc. Specific for this type of systems is the interaction of mechanical and electrical phenomena, which should be understood and taken under control in order to avoid problems occurrence and making the machine to run smoothly and reliably to higher speeds and loads.

Many scientists are concerned in investigating the nonlinear behavior of rotating electrical machines using various techniques. Raja et al. [1] exploited bio-inspired computational intelligence to analyze the nonlinear vibrational dynamics of rotating electrical machine model by applying artificial neural networks, genetic algorithms and active-set methods. In [2] it is introduced an optimal variational method to investigate the nonlinear behavior of a rotating electrical machine modeled as an oscillator with cubic elastic restoring force and time variable coefficients. An analytical approach for expeditiously understanding and solving specific problems encountered by rotating electrical machines is presented in [3]. Martinez et al. [4] developed a Finite Element Model in order to study the vibrations in induction motors under steady-state introducing a model which utilizes a weak coupling strategy between both magnetic and elastodynamic fields on the structure. Xu et al. [5] investigated the vibration characteristics of an inclined rotor with both static and displacement eccentricity and the static angle eccentricity in the three-dimensional space. Kirschneck et al. [6] introduced an approach for a multiphysical modal analysis that makes it possible to predict the dynamics of the strongly coupled magnetomechanical system proposing a method applied to a single-bearing design direct-drive wind turbine generator rotor to calculate the changes of the structural dynamics caused by the electromagnetomechanical coupling.

The machines understudy in this paper are subjected to a parametric excitation caused by an initial trust and a forcing excitation caused by an unbalanced force of the rotor while the entire system is being supported by nonlinear bearings with nonlinear stiffness characteristics and damping properties. The nonlinear suspension makes the analytical study very difficult, leading to strong nonlinear differential equations, which are hard to be solved through classical methods. Supplementary problems could arise in case of some horizontal rotating machines, when the gravity effect is not negligible for certain stiffness conditions. For the gravity deflection the

shaft center leaves the bearing centerline, which leads to vibration occurrence. Also, the misalignment could occur in the electrical machine after some amount of running.

In general, such nonlinear vibration problems are usually solved using perturbation methods which are the most used analytical techniques. Some of the most used methods are weighted linearization method [7], δ-method [8], Adomian decomposition method [9], Lindstedt-Poincare method [10], the Krylov-Bogoliubov-Mitropolski method [11] and other perturbation methods [12]. Unfortunately it is well-known that perturbation methods have their limitations since they are based on the existence of a small parameter and especially in strongly nonlinear system these classical methods fail. Therefore scientist are continuously concerned in the developing new analytical techniques which aim at surmounting these limitations. Recently new powerful analytical tools were developed, such as the parameter expanding method [13], the variational iteration method [14], the optimal homotopy perturbation method [15], the optimal homotopy asymptotic method [16, 17], and so on. Moreover, for an exhaustive investigation of general problems of dynamical systems, analytical and numerical developments are often combined with experimental investigations [18–21].

In this paper a new analytical procedure, namely the optimal auxiliary functions method is employed in order to study the problem of nonlinear vibrations of an electrical machine. The investigated electrical machine is considered to be supported by nonlinear bearings characterized by nonlinear stiffness of Duffing and Van der Pol type. The entire dynamical system is subjected to parametric excitation caused by an axial trust and forcing excitation caused by an unbalanced force of the rotor, which is obviously harmonicallyshaped. In this conditions the dynamical behavior of the investigated electrical machine will be governed by the following second-order strongly nonlinear differential equation with variable coefficients

$$m\ddot{x} + k_1(1 - q\sin\omega_2 t)x + k_2 x^3 = f\sin\omega_1 t \quad x(0) = A, \ \dot{x}(0) = 0. \tag{1}$$

This equation may be written in the more convenient way

$$\ddot{x} + \omega^2 x - a\sin\omega_2 tx + bx^3 - c\sin\omega_1 t = 0 \quad x(0) = A, \ \dot{x}(0) = 0, \tag{2}$$

where $\omega^2 = \frac{k_1}{m}, a = \frac{k_1 q}{m}, b = \frac{k_2}{m}, c = \frac{f}{m}$ and the dot denotes derivative with respect to time and A is the amplitude of the oscillations. It should be emphasized that it is unnecessary to suppose the existence of any small or large parameters in Eq. (2).

The main objective of this work is to use the Optimal Auxiliary Functions Method (OAFM) to obtain approximate analytical solutions of strongly nonlinear vibration of the electrical rotating machine [22].

2 Application of OAFM to the Investigation of Nonlinear Vibration of the Considered Electrical Machine

The validity of our procedure is illustrated on the electrical machine whose dynamic behavior is governed by Eq. (2). The Eq. (2) describes a system of oscillating with an unknown period T. We switch to a scalar time $\tau = \frac{2\pi t}{T} = \Omega t$. Under the transformations

$$\tau = \Omega t, \quad x(t) = Ay(\tau), \tag{3}$$

the original Eq. (2) becomes

$$\Omega^2 y'' + \omega^2 y - ay\sin\frac{\omega_2}{\Omega}\tau + bA^2 y^3$$
$$- \frac{c}{A}\sin\frac{\omega_1}{\Omega}\tau = 0, \quad y(0) = 1, \ y'(0) = 0, \tag{4}$$

where the prime denotes derivative with respect to τ.

By means of OAFM we define the linear and nonlinear operators, respectively

$$L[y(\tau)] = \Omega^2(y'' + y), \tag{5}$$

$$N[y(\tau)] = (\omega^2 - \Omega^2)y - ay\sin\frac{\omega_2}{\Omega}\tau + bA^2 y^3 - \frac{c}{A}\sin\frac{\omega_1}{\Omega}\tau. \tag{6}$$

For Eq. (4) we demand an approximate analytical solution $\widetilde{y}(\tau)$ in two components

$$\widetilde{y}(\tau) = y_0(\tau) + y_1(\tau, C_i), \ i = 1, 2, \ldots, n, \tag{7}$$

where C_i are unknown parameters at this moment.

The initial approximation $y_0(\tau)$ is determined from the linear equation

$$L[y_0(\tau)] = 0, \quad y_0(0) = 1, \ y_0'(0) = 0 \tag{8}$$

The solution of Eq. (8) is

$$y_0(\tau) = \cos\tau. \tag{9}$$

The nonlinear operator for (6) the initial approximation (9) becomes

$$N[y_0(\tau)] = \left(\omega^2 - \Omega^2 + \frac{3}{4}bA^2\right)\cos\tau + \frac{1}{4}bA^2\cos3\tau$$
$$- \frac{1}{2}a\left[\sin\left(\frac{\omega_2}{\Omega} + 1\right)\tau + \sin\left(\frac{\omega_2}{\Omega} - 1\right)\tau\right] - \frac{c}{A}\sin\frac{\omega_2}{\Omega}\tau \tag{10}$$

The first approximation $y_1(\tau, C_i)$ can be determined from the equation

$$L[y_1(\tau, C_i)] + A(y_0(\tau), C_j) P[N(y_0(\tau))]$$
$$+ B(y_0(\tau), C_k) = 0, \; y_1(0) = 0, \; y_1'(0) = 0, \tag{11}$$

where, taking into consideration the expression (10), we have the freedom to choose the functions

$$A(y_0(\tau), C_j) = -(C_1 + 2C_2\cos 2\tau)$$

$$P[N(y_0(\tau))] = \left(\omega^2 - \Omega^2 + \frac{3}{4}bA^2\right)\cos\tau + \frac{1}{4}bA^2\cos 3\tau$$

$$B(y_0(\tau), C_k) = -\left[C_3\cos 5\tau + C_4\sin\left(\frac{\omega_2}{\Omega} + 1\right)\tau + C_5\sin\left(\frac{\omega_2}{\Omega} - 1\right)\tau + C_6\sin\frac{\omega_1}{\Omega}\tau\right]. \tag{12}$$

However, the choices (12) are not unique. We can choose another alternative

$$A(y_0(\tau), C_j) = -(C_1 + 2C_2\cos 2\tau + 2C_3\cos 4\tau)$$

$$P[N(y_0(\tau))] = \left(\omega^2 - \Omega^2 + \frac{3}{4}bA^2\right)\cos\tau$$

$$B(y_0(\tau), C_k) = -\left[C_4\sin\left(\frac{\omega_2}{\Omega} + 1\right)\tau + C_5\sin\left(\frac{\omega_2}{\Omega} - 1\right)\tau\right], \tag{13}$$

or

$$A(y_0(\tau), C_j) = -C_1$$

$$P[N(y_0(\tau))] = \left(\omega^2 - \Omega^2 + \frac{3}{4}bA^2 - \frac{1}{4}bA^2\cos 3\tau - \frac{1}{2}a\sin\left(\frac{\omega_2}{\Omega} + 1\right)\tau\right)\cos\tau$$

$$B(y_0(\tau), C_k) = -[C_2\sin\left(\frac{\omega_2}{\Omega} + 1\right)\tau + C_3\sin\left(\frac{2\omega_2}{\Omega} + 1\right)\tau$$

$$+ C_4\sin\left(\frac{\omega_2}{\Omega} - 1\right)\tau + C_5\sin\left(\frac{2\omega_2}{\Omega} - 1\right)\tau + C_6\sin\frac{\omega_1}{\Omega}\tau, \tag{14}$$

and so on.

Having in view Eqs. (12) and (5), Eq. (11) becomes

$$\Omega^2(y_1'' + y_1) = \left[(C_1 + C_2)\left(\omega^2 - \Omega^2 + \frac{3}{4}bA^2\right) + \frac{1}{4}bA^2C_2\right]\cos\tau$$

$$+ \left[C_2\left(\omega^2 - \Omega^2 + \frac{3}{4}bA^2\right) + \frac{1}{4}bA^2C_1\right]\cos 3\tau + \left(C_3 + \frac{1}{4}bA^2C_2\right)\cos 3\tau$$

$$+ C_4\sin\left(\frac{\omega_2}{\Omega} + 1\right)\tau + C_5\sin\left(\frac{\omega_2}{\Omega} - 1\right)\tau + C_6\sin\frac{\omega_1}{\Omega}\tau,$$

$$y_1(0) = y_1'(0) = 0. \tag{15}$$

Avoiding the presence of secular terms in Eq. (15) we have

$$(C_1 + C_2)\left(\omega^2 - \Omega^2 + \frac{3}{4}bA^2\right) + \frac{1}{4}bA^2 = 0. \tag{16}$$

From Eq. (16) we obtain the frequency of the system in the form

$$\Omega^2 = \omega^2 + \frac{3}{4}bA^2 + \frac{1}{4}bA^2\frac{C_2}{C_1 + C_2}. \tag{17}$$

The solution of Eq. (15) is

$$
\begin{aligned}
y_1(\tau) = {}& \frac{1}{8\Omega^2}\left[C_2\left(\omega^2 - \Omega^2 + \frac{3}{4}bA^2\right) + \frac{1}{4}bA^2C_1\right](\cos\tau - \cos3\tau) \\
& + \frac{1}{24\Omega^2}\left(C_3 + \frac{1}{4}bA^2C_2\right)(\cos\tau - \cos5\tau) \\
& + \frac{\Omega^2C_4}{\omega_2^2 + 2\omega_2\Omega}\left[\left(\frac{\omega_2}{\Omega} + 1\right)\sin\tau - \sin\left(\frac{\omega_2}{\Omega} + 1\right)\tau\right] \\
& + \frac{\Omega^2C_5}{\omega_2^2 - 2\omega_2\Omega}\left[\left(\frac{\omega_2}{\Omega} - 1\right)\sin\tau - \sin\left(\frac{\omega_2}{\Omega} - 1\right)\tau\right] \\
& + \frac{\Omega^2C_6}{\Omega^2 - \omega_1^2}\left(\sin\frac{\omega_1}{\Omega}\tau - \frac{\omega_1}{\Omega}\sin\tau\right). \tag{18}
\end{aligned}
$$

Substituting Eqs. (9), (18) and (3) into Eq. (9) we obtain the solution of Eq. (1) in the first order of approximation of the form:

$$
\begin{aligned}
x(t) = {}& A\cos\Omega t + \frac{A}{8\Omega^2}\left[C_2\left(\omega^2 - \Omega^2 + \frac{3}{4}bA^2\right) + \frac{1}{4}bA^2C_1\right](\cos\Omega t - \cos3\Omega t) \\
& + \frac{A}{24\Omega^2}\left(C_3 + \frac{1}{4}bA^2C_2\right)(\cos\Omega t - \cos5\Omega t) \\
& + \frac{\Omega^2 AC_4}{\omega_2^2 + 2\omega_2\Omega}\left[\left(\frac{\omega_2}{\Omega} + 1\right)\sin\Omega t - \sin(\omega_2 + \Omega)t\right] \\
& + \frac{\Omega^2 AC_5}{\omega_2^2 - 2\omega_2\Omega}\left[\left(\frac{\omega_2}{\Omega} - 1\right)\sin\Omega t - \sin(\omega_2 - \Omega)t\right] \\
& + \frac{\Omega^2 AC_6}{\Omega^2 - \omega_1^2}\left(\sin\omega_1 t - \frac{\omega_1}{\Omega}\sin\Omega t\right). \tag{19}
\end{aligned}
$$

3   Numerical Examples

In order to validate the obtained approximate results, two numerical applications are considered, for two particular cases, as follows:

Fig. 1 Comparison between the approximate solution (21) and corresponding numerical results in case 1
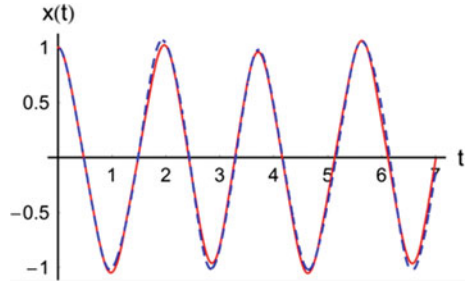
3.1 Case 1

For $A = 1$, $a = 2.95122$, $b = 12.1951$, $c = 0.195122$, $\omega_1 = 1.21$, $\omega_2 = 1.51$, $\omega = 1.63796$, following the described procedure, the optimal values of the convergence-control parameters obtained by minimizing the residual generated by the approximate solution (19) are:

$$C_1 = -0.12949743551566287, \quad C_2 = -8.6126665038499,$$
$$C_3 = 25.324695766371054, \quad C_4 = 0.09686844412991548,$$
$$C_5 = 0.07534250937939393, \quad C_6 = 0.01. \tag{20}$$

In this case, the approximate analytical solution of the first-order of approximation (19) becomes

$$
\begin{aligned}
x(t) = {} & \cos[3.38829t] - 0.0370021(\cos[3.38829t] - \cos[10.1649t]) \\
& - 0.00338774(\cos[3.38829t] - \cos[16.9415t]) \\
& - 0.108767(\sin[1.87829t] - 0.554348\sin[3.38829t]) \\
& + 0.0114617(\sin[1.21t] - 0.357112\sin[3.38829t]) \\
& + 0.0888774(1.44565\sin[3.38829t] - \sin[4.89829t]). \tag{21}
\end{aligned}
$$

Figure 1 shows the comparison between our approximate solution (21) and numerical integration results obtained by means of a fourth-order Runge-Kutta method.

3.2 Case 2

For $A = 2$, $a = 2.70976$, $b = 9.7561$, $c = 0.170732$, $\omega_1 = 1.21$, $\omega_2 = 1.51$, $\omega = 1.63796$, the optimal values of the convergence-control parameters are:

Fig. 2 Comparison between the approximate solution (23) and corresponding numerical results in case 2
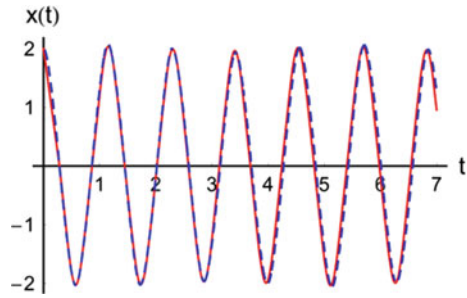
$$C_1 = 0.2819607928355029, \ C_2 = -6.540488872738153,$$
$$C_3 = 57.43354947958066, \ C_4 = 0.013110981874304229,$$
$$C_5 = 0.023582738555140967, \ C_6 = 0.011. \tag{22}$$

In this case, the approximate analytical solution (19) becomes:

$$\begin{aligned} x(t) = {} & 2\cos[5.51293t] - 0.0626977(\cos[5.51293t] - \cos[16.5388t]) \\ & - 0.0166043(\cos[5.51293t] - \cos[27.5646t]) \\ & - 0.0980561(\sin[4.00293t] - 0.726098\sin[5.51293t]) \\ & + 0.0210122(\sin[1.21t] - 0.219484\sin[5.51293t]) \\ & + 0.0424509(1.2739\sin[5.51293t] - \sin[7.02293t]). \end{aligned} \tag{23}$$

Figure 2 shows the comparison between our approximate solution (23) and numerical integration results obtained in the second case.

It can be seen that the solutions obtained using our technique are nearly identical with that obtained through numerical method, which validates the solution approach.

4 Conclusions

In this investigation, an approximate analytical solution for an electrical machine has been given. The proposed system is parametrically excited by an axial thrust and at the same time are forcing excitation caused by an unbalanced force of the rotor is acting on the system. The governing equation takes into consideration the sources of nonlinearity and the corresponding equation is solved using the Optimal Auxiliary Functions Method to graphically obtain the time history of nonlinear response. Our procedure is valid even if the nonlinear equation does not contain any small or large parameter. The convergence of the OAFM is demonstrated by the auxiliary functions A and B. These procedures provide us with a simple way to optimally control and adjust the convergence of the approximate analytical solutions and can give good approximations in a few terms. The obtained approximate analytical solution is in

very good agreement with the numerical simulation results, which proves the validity of the method.

The present paper shows one step in the attempts to develop a new nonlinear analytical technique which is valid in the absence of a small or large parameter.

References

1. Raja, M.A.Z., Niazi, S.A., Butt, S.A.: An intelligent computing technique to analyze the vibrational dynamics of rotating electrical machine. Neurocomputing **219**, 280–299 (2017). https://doi.org/10.1016/j.neucom.2016.09.032
2. Herisanu, N., Marinca, V.: An optimal approach to study the nonlinear behavior of a rotating electrical machine. J. Appl. Math. ID-465023 (2012). https://doi.org/10.1155/2012/465023
3. Finley, W.R., Hodowanec, M.M., Holter, W.G.: An analytical approach to solving motor vibration problems. IEEE Trans. Ind. Appl. **36**, 1467–1480 (2000). https://doi.org/10.1109/PCICON.1999.806440
4. Martinez, J., Belahcen, A., Detoni, J.G.: A 2D magnetic and 3D mechanical coupled finite element model for the study of the dynamic vibrations in the stator of induction motors. Mech. Syst. Signal Process. **66**, 640–656 (2016). https://doi.org/10.1016/j.ymssp.2015.06.014
5. Xu, X.P., Han, Q.K., Chu, F.L.: A four degrees-of-freedom model for a misalignment electrical rotor. J. Sound Vibr. **358**, 356–374 (2015). https://doi.org/10.1016/j.jsv.2015.08.006
6. Kirschneck, M., Rixen, D.J., Polinder, H., van Ostayen, R.A.J.: Electromagnetomechanical coupled vibration analysis of a direct-drive off-shore wind turbine generator. J. Comput. Nonlinear Dynam. **10**, 041011 (2015). https://doi.org/10.1115/1.4027837
7. Agrwal, V.P., Denman, H.: Weighted linearization technique for period approximation of large amplitude nonlinear oscillations. J. Sound Vibr. **57**, 463–470 (1985). https://doi.org/10.1016/0022-460X(85)90534-6
8. Awrejcewicz, J., Andrianov, I.V., Manewitch, L.I.: Asymptotic Approaches in Nonlinear Dynamics. New Trends and Applications. Springer, Heidelberg (1998)
9. Adomian, G.: A review of the decomposition methods in applied mathematics. J. Math. Anal. Appl. **135**, 501–544 (1998). https://doi.org/10.1016/0022-247X(88)90170-9
10. Cheung, Y.K., Chen, S.H., Lau, S.L.: A modified Lindstedt-Poincare method for certain strongly nonlinear oscillators. Int. J. Nonlinear Mech. **26**, 367–378 (1991). https://doi.org/10.1016/0020-7462(91)90066-3
11. Cveticanin, L.: Free vibration of a Jeffcott with pure cubic non-linear elastic property of the shaft. Mechanisms and Machine Theory **40**, 1330–1334 (2005). https://doi.org/10.1016/j.mechmachtheory.2005.03.002.
12. Nayfeh, A.H.: Introduction to perturbation techniques. Wiley, New York (1981)
13. Ramos, J.I.: Series approach to the Lane-Emden equation and comparison with the homotopy perturbation method. Chaos Solitons Fractals **30**, 400–408 (2008). https://doi.org/10.1016/j.chaos.2006.11.018
14. He, J.H.: Variational iteration method for autonomous ordinary differential systems. Appl. Math. Comput. **114**, 115–122 (2000). https://doi.org/10.1016/S0096-3003(99)00104-6
15. Marinca, V., Herisanu, N.: Nonlinear dynamic analysis of an electrical machine rotor-bearing system by optimal homotopy perturbation method. Comp. Math. Appl. **61**, 2019–2024 (2011). https://doi.org/10.1016/j.camwa.2010.08.056
16. Marinca, V., Herisanu, N.: The optimal homotopy asymptotic method. Eng. Appl. Springer Cham. (2015). https://doi.org/10.1007/978-3-319-15374-2
17. Marinca, V, Herisanu, N.: On the flow of a Wlaters-type B' viscoelastic fluid in a vertical channel with porous wall. Int. J. Heat. Mass. Transf. **79**, 146–165 (2014). https://doi.org/10.1016/j.ijheatmasstransfer.2014.07.094

18. Awrejcewicz, J., Wasilewski, G., Kudra, G., Reshmin, S.A.: An experiment with swinging up a double pendulum using feedback control. J. Comput Syst Sci Int **51**, 176–182 (2012). https://doi.org/10.1134/S1064230712020037

19. Awrejcewicz, J., Kudra, G., Wasilewski, G.: Chaotic zones in triple pendulum dynamics observed experimentally and numerically. Appl. Mech. Mater. **9**, 1–17. (2008). https://doi.org/10.4028/www.scientific.net/AMM.9.1

20. Awrejcewicz, J., Kudra, G., Wasilewski, G.: Experimental and numerical investigation of chaotic regions in triple physical pendulum. Nonlinear Dyn. **50**, 755–766 (2007). https://doi.org/10.1007/s11071-007-9235-0

21. Awrejcewicz, J., Kudra, G.: Mathematical modelling and simulation of the bifurcational wobblestone dynamics. Discontinuity Nonlinearity Complexity **3**, 123–132 (2014). https://doi.org/10.5890/DNC.2014.06.002

22. Herisanu, N., Marinca, V.: Approximate analytical solutions to jerk equations. Springer Proc. Math. Statist. **182**, 169–176 (2016). https://doi.org/10.1007/978-3-319-42408-8_14

Development of a Computational Based Reference Dynamics Model of a Flexible Link Manipulator

Elżbieta Jarzębowska, Krzysztof Augustynek and Andrzej Urbaś

Abstract Development of a new derivation method of a reference dynamics model of a flexible link manipulator is presented in the paper. The model including flexibility can map dynamics and performance of lightweight and fast manipulators correctly and may serve their motion analysis and control design in the presence of kinematic or programmed constraints, which are assumed to be position or first order non-holonomic. The reference dynamics model is derived using the formalism of joint coordinates and homogeneous transformation matrices. This approach allows generating dynamics equations of a manipulator without formulating additional material constraint equations. The constraints present in the reference dynamics model are the programmed ones only. The flexibility of a link is modelled using the rigid finite element method. The main advantage of this method is its ability of application of the rigid-body approach to modeling dynamics of multi-body systems with flexible links. The novelty of the presented method relies on the combination of dynamics modeling of flexible system models with the programmed constraints satisfaction problem for them. The computational algorithm underlying the derivation method presented in the paper is based on Generalized Programmed Motion Equations (GPME) approach. The reference dynamics model derivation is demonstrated for a flexible link manipulator model.

Keywords Reference dynamics model · Manipulator · Links flexibility · The Rigid Finite Element method · Joint coordinates

E. Jarzębowska
Department of Power and Aeronautical Engineering, Warsaw University of Technology, Nowowiejska 24, 00-665 Warsaw, Poland
e-mail: elajarz@meil.pw.edu.pl

K. Augustynek (✉)
Department of Computer Science and Automatics, University of Bielsko-Biala, Willowa 2, 43-309 Bielsko-Biala, Poland
e-mail: kaugustynek@ath.bielsko.pl

A. Urbaś
Department of Mechanical Engineering Fundamentals, University of Bielsko-Biala, Willowa 2, 43-309 Bielsko-Biala, Poland
e-mail: aurbas@ath.bielsko.pl

Nomenclature

rfe(l, r)	rigid finite element r of a link l
sde(l, s)	spring-damping element s of a link l
$n_{sde}^{(l)}$	number of spring-damping elements of a link l
$n_{rfe}^{(l)}$	number of rigid finite elements of a link l, $n_{rfe}^{(l)} = n_{sde}^{(l)} + 1$
g	acceleration of gravity
i_{i_c}, i_{d_c}	index of independent and dependent coordinates
$l^{(l)}$	length of a link l
$m^{(l)}, m^{(l,r)}$	mass of a link l (rfe(l, r))
$n_{dof}^{(l)}, n_{dof}^{(l,r)}$	number of generalized coordinates describing motion of a link l (rfe(l, r)) with respect to the reference frame
n_{dof}	number of generalized coordinates describing motion of the manipulator
n_l	number of links
$c_\alpha^{(l,s)}\big|_{\alpha \in \{\psi, \theta, \varphi\}}$	rotational stiffness coefficient of sde(l, s)
$t_{dr}^{(l)}$	drive torque acting on a link l
$r_{E,a}$	radius of a reference circle
$y_{E,a}^{(0)}$	assumed time course of y coordinate of a point E
E_k	kinetic energy of a system
E_p	potential energy of a system
$E_{p,f}$	potential energy resulting from spring deformations of flexible links
$E_{p,g}$	potential energy of gravity forces
$\mathbf{r}_E^{(l)}$	position vector of a point E defined in a local coordinate frame of a link l
$\mathbf{H}^{(l)}, \mathbf{H}^{(l,r)}$	pseudo-inertia matrix of a link l (rfe(l, r))
$\mathbf{T}^{(l)}, \mathbf{T}^{(l,r)}$	homogeneous transformation matrix from a local coordinate frame of a link l or rfe(l, r) to the inertial reference frame $\mathbf{T}_i^{(l)} = \frac{\partial \mathbf{T}^{(l)}}{\partial q_i^{(l)}}$, $\mathbf{T}_{i,j}^{(l)} = \frac{\partial \mathbf{T}_i^{(l)}}{\partial q_j^{(l)}} = \frac{\partial^2 \mathbf{T}^{(l)}}{\partial q_i^{(l)} \partial q_j^{(l)}}$

1 Introduction

Dynamics modeling methods, both analytical and computational, for rigid models of multibody systems are well developed and many of their specializations for specific classes of systems are available. Due to the presence of friction, compliance, flexibility and other real system properties that need to be accounted for in modeling to obtain reliable dynamics models, many specializations of the modeling methods were developed within the classical mechanics approach. Also, constraints that are present in mechanical systems, both material and task-based, are merged into system dynamics using the classical mechanics approach. However, demands for high

fidelity and accurate dynamical models from one hand and fast and simple derivations from the other hand, make room for new development methods for dynamics models of rigid-flexible and constrained multibody systems.

The paper presents a development of a new derivation method of a reference dynamics model of a rigid-flexible system model. The model including flexibility may describe dynamics and performance of lightweight and fast systems, e.g. ground or space manipulators, correctly and may serve their motion analysis and control design in the presence of constraints put upon them. The reference dynamics is the system model dynamics including all constraints upon it, i.e. kinematic or programmed constraints, which are assumed to be position or first order nonholonomic. The new derivation method of reference dynamics model of a rigid-flexible system models combines latest research results in dynamics of flexible multibody systems, a finite element method for modelling flexibility of spatial linkage links [1, 7, 8] as well as the dynamics modeling method for constrained systems, which does not use the Lagrange approach, i.e. both material and programmed constraints can be merged into a system dynamics [3–5]. The modeling method is referred to as the generalized programmed motion equations (GPME) method and it was originally developed for rigid system models [5]. The GPME method was automated for computational generation of constrained rigid body models in Jarzębowska et al. [6].

The reference dynamics model presented in the paper is derived for a rigid-flexible system model using the formalism of joint coordinates and homogeneous transformation matrices. This approach allows generating dynamics equations of a system, which is a manipulator model, without formulating additional material constraint equations. The constraints present in the reference dynamics model are the programmed ones only. The flexibility of a link is modeled using the rigid finite element method. The main advantage of this method is its ability of application of the rigid-body approach to modeling dynamics of multi-body systems with flexible links. The novelty of the presented method relies on the combination of dynamics modeling of flexible system models with the programmed constraints satisfaction problem for them. The computational algorithm underlying the derivation method presented in the paper is based on Generalized Programmed Motion Equations (GPME) approach. The reference dynamics model derivation is demonstrated for a flexible link manipulator model.

The paper is organized as follows. Section 1 delivers a short introduction of the ideas, motivation and the origin of the presented modeling approach. Section 2 details a mathematical model of a three link manipulator with a flexible link. Simulation studies illustrating the application of the derivation of the reference dynamics for the manipulator are presented in Sect. 3. The paper ends with conclusions and a reference list.
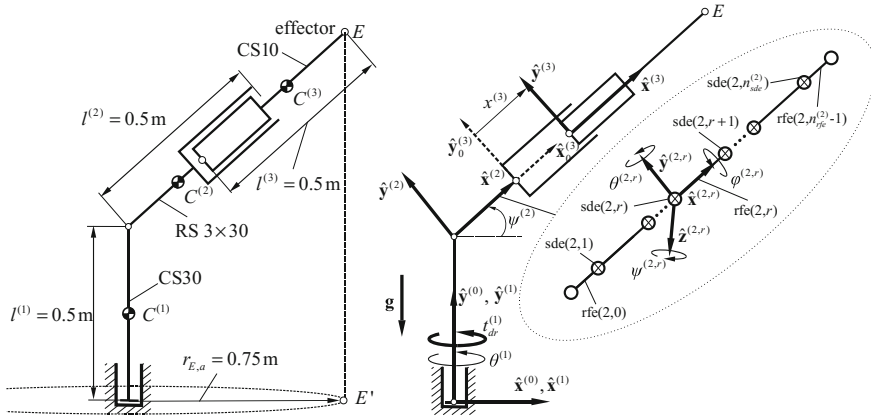
Fig. 1 Model of spatial manipulator with a flexible link

2 Mathematical Model of a Three Link Manipulator Model with a Flexible Link

Three link spatial manipulator model composed of a rotary column 1, a rotary arm 2 and a slider 3 (Fig. 1) is analysed in the paper. It is assumed that the link 2 can be flexible and other links are treated as non-deformable. All joints are modelled as ideal, i.e. friction and clearance are neglected, and the rotary column 1 is driven by a driving torque $t_{dr}^{(1)}$. Motion of each link is described by homogeneous transformations and joint coordinates. The flexible link 2 is discretized by means of the modified Rigid Finite Element Method proposed in [1, 7, 8]. In this method flexible links are replaced by a set of rigid finite elements (rfe) connected by massless and dimensionless spring-damping elements (sde).

The vector of generalized coordinates of the manipulator is composed of the following sub-vectors:

$$\mathbf{q} = (q_i)_{i=1,\dots,n_{dof}} = \begin{bmatrix} \tilde{\mathbf{q}}^{(1)^T} & \tilde{\mathbf{q}}^{(2)^T} & \tilde{\mathbf{q}}^{(3)^T} \end{bmatrix}^T$$
$$= \begin{bmatrix} \theta^{(1)} & \psi^{(2)} & \tilde{\mathbf{q}}_f^{(2)^T} & x^{(3)} \end{bmatrix}^T, \tag{1}$$

where

$\tilde{\mathbf{q}}_f^{(2)}$ vector containing generalized coordinates of rfes,

$$\tilde{\mathbf{q}}_f^{(2)} = \begin{cases} \varnothing, & \text{if the link is rigid } (n_{rfe}^{(2)} = 1), \\ \begin{bmatrix} \tilde{\mathbf{q}}^{(2,1)^T} & \dots & \tilde{\mathbf{q}}^{(2,r)^T} & \dots & \tilde{\mathbf{q}}^{(2,n_{rfe}^{(2)}-1)^T} \end{bmatrix}^T, & \text{if the link is flexible } (n_{rfe}^{(2)} > 1), \end{cases}$$

$\tilde{\mathbf{q}}^{(2,r)} = \left[\psi^{(2,r)} \ \theta^{(2,r)} \ \varphi^{(2,r)} \right]^T$ vector of generalized coordinates of rfe(2, r).

The motion of the manipulator is subjected to programmed constraints, which specify a desired motion of the manipulator end effector E, in z direction. It is assumed that a circle of radius $r_{E,a}$ is the desired trajectory of the end-effector E in the plane $\hat{\mathbf{x}}^{(0)}\hat{\mathbf{z}}^{(0)}$.

The programmed position constraints can be written in the form of algebraic equations as

$$\Phi_1 \equiv \left(x_E^{(0)} \right)^2 + \left(z_E^{(0)} \right)^2 - r_{E,a}^2 = 0, \tag{2}$$

$$\Phi_2 \equiv y_E^{(0)} - y_{E,a}^{(0)}(t) = 0, \tag{3}$$

where $\mathbf{r}_E^{(0)} = \left[x_E^{(0)} \ y_E^{(0)} \ z_E^{(0)} \right]^T = \Theta \mathbf{T}^{(3)} \mathbf{r}_E^{(3)}$, $\Theta = \begin{bmatrix} \Theta_1 \\ \Theta_2 \\ \Theta_3 \end{bmatrix} = \begin{bmatrix} 1 & 0 & 0 & 0 \\ 0 & 1 & 0 & 0 \\ 0 & 0 & 1 & 0 \end{bmatrix}$.

The derivation method of a reference dynamics model for a constrained system based upon the GPME requires double differentiation of the position constraints (2) and (3). After their differentiation with respect to time, velocity level programmed constraints are obtained as

$$\dot{\Phi}_1 \equiv \mathbf{D}_r(\mathbf{q}) \, \dot{\mathbf{q}} = 0, \tag{4}$$

$$\dot{\Phi}_2 \equiv \mathbf{D}_2(\mathbf{q}) \, \dot{\mathbf{q}} - \dot{y}_{E,a}^{(0)}(t) = 0, \tag{5}$$

where $\mathbf{D}_r = \dot{x}_E^{(0)}\mathbf{D}_1 + \dot{z}_E^{(0)}\mathbf{D}_3$, $\mathbf{D} = \begin{bmatrix} \mathbf{D}_1 \\ \mathbf{D}_2 \\ \mathbf{D}_3 \end{bmatrix} = \left[\mathbf{T}_1^{(3)}\mathbf{r}_E^{(3)} \ \dots \ \mathbf{T}_{n_{dof}}^{(3)} \, \mathbf{r}_E^{(3)} \right]$.

Differentiating (4) and (5) again with respect to time leads to the programmed constraint equations at the acceleration level:

$$\ddot{\Phi}_1 \equiv \mathbf{D}_r(\mathbf{q}) \, \ddot{\mathbf{q}} - \xi_1(\mathbf{q}, \dot{\mathbf{q}}) = 0, \tag{6}$$

$$\ddot{\Phi}_2 \equiv \mathbf{D}_2(\mathbf{q}) \, \ddot{\mathbf{q}} - \xi_2(\mathbf{q}, \ \dot{\mathbf{q}}) - \ddot{y}_{E,a}^{(0)}(t) = 0, \tag{7}$$

where $\xi_1 = -\left(\dot{x}_E^{(0)} \, \mathbf{D}_1 + x_E^{(0)} \, \dot{\mathbf{D}}_1 + \dot{z}_E^{(0)} \, \mathbf{D}_3 + z_E^{(0)} \, \dot{\mathbf{D}}_3 \right) \dot{\mathbf{q}}$, $\xi_2 = -\dot{\mathbf{D}}_2 \, \dot{\mathbf{q}}$.

In the considered manipulator model the number of control inputs $n_c = 2$ is less than the number degrees of freedom of the manipulator, $n_c < n_{dof}$, and it means that the considered model is underactuated.

Let us define sets containing dependent and independent coordinates of indices i_{i_c} and i_{d_c}, respectively, in the generalized coordinate vector $\mathbf{q}$. The resultant vector $\mathbf{q}$ can be thus partitioned into the set of independent coordinates $\mathbf{q}_{i_c}$ and the set of dependent coordinates $\mathbf{q}_{d_c}$. Indices of dependent and independent coordinates can be selected as follow:

$$i_{i_c} \in \left\{ 1, 3, 4, \ldots, n_{dof} - 1 \right\}, \tag{8}$$

$$i_{d_c} \in \left\{ 2, n_{dof} \right\}. \tag{9}$$

The corresponding generalized coordinate vector contains elements:

$$\mathbf{q}_{i_c} = \left[\theta^{(1)} \; \psi^{(2,1)} \; \theta^{(2,1)} \; \varphi^{(2,1)} \; \ldots \; \psi^{(2,n_{rfe}^{(2)}-1)} \; \theta^{(2,n_{rfe}^{(2)}-1)} \; \varphi^{(2,n_{rfe}^{(2)}-1)} \right]^{T}, \tag{10}$$

$$\mathbf{q}_{d_c} = \left[\psi^{(2)} \; x^{(3)} \right]^{T}. \tag{11}$$

Dynamical equations of motion of the spatial manipulator with the first programmed constraints are derived using the algorithm based upon the GPME [3–6] and can be presented as follows:

$$\frac{\partial R_1}{\partial \dot{\mathbf{q}}_{i_c}} + \sum_{j \in i_{d_c}} \frac{\partial R_1}{\partial \dot{q}_j} \frac{\partial \dot{q}_j}{\partial \dot{\mathbf{q}}_{i_c}} = \mathbf{0}, \tag{12}$$

where

$$R_1 = \dot{E}_k - 2 \sum_{i=1}^{n_{dof}} \left[\frac{\partial E_k}{\partial \mathbf{q}} \right]^{T} \dot{\mathbf{q}} + \sum_{i=1}^{n_{dof}} \left[\frac{\partial E_p}{\partial \mathbf{q}} \right]^{T} \dot{\mathbf{q}} - \sum_{i=1}^{n_{dof}} \mathbf{Q}^{T} \dot{\mathbf{q}},$$

$$E_k = \sum_{l=1}^{n_l} E_k^{(l)}, \; E_k^{(l)} = \begin{cases} \frac{1}{2} \mathrm{tr} \left\{ \dot{\mathbf{T}}^{(l)} \mathbf{H}^{(l)} \left(\dot{\mathbf{T}}^{(l)} \right)^{T} \right\}, & n_{rfe}^{(l)} = 1 \\ \sum_{r=0}^{n_{sde}^{(l)}} \frac{1}{2} \mathrm{tr} \left\{ \dot{\mathbf{T}}^{(l,r)} \mathbf{H}^{(l,r)} \left(\dot{\mathbf{T}}^{(l,r)} \right)^{T} \right\} & n_{rfe}^{(l)} > 1 \end{cases},$$

$$E_p = E_{p,g} + E_{p,f},$$

$$E_{p,g} = \sum_{l=1}^{n_l} E_{p,g}^{(l)}, \; E_{p,g}^{(l)} = \begin{cases} m^{(l)} g \, \mathbf{\Theta}_2 \mathbf{T}^{(l)} \mathbf{r}_{C^{(l)}}^{(l)}, & n_{rfe}^{(l)} = 1 \\ \sum_{r=0}^{n_{sde}^{(l)}} m^{(l,r)} g \, \mathbf{\Theta}_2 \mathbf{T}^{(l,r)} \mathbf{r}_{C^{(l,r)}}^{(l,r)}, & n_{rfe}^{(l)} > 1 \end{cases},$$

$$E_{p,f} = \sum_{l=1}^{n_l} \sum_{s=1}^{n_{sde}^{(2)}} E_{p,f}^{(l,s)}, \; E_{p,f}^{(l,s)} = \frac{1}{2} \tilde{\mathbf{q}}^{(l,s)^{T}} \mathbf{C}^{(l,s)} \tilde{\mathbf{q}}^{(l,s)},$$

$$\mathbf{C}^{(l,s)} = \mathrm{diag} \left\{ c_{\psi}^{(l,s)}, \; c_{\theta}^{(l,s)}, \; c_{\varphi}^{(l,s)} \right\},$$

$$\mathbf{Q} = \left[t_{dr}^{(1)} \; \mathbf{0} \right]^{T}.$$

After performing computations as indicated in (18), the generalized program motion equations (GPME) can be presented in the following form:

$$
\begin{bmatrix}
\mathbf{M}_{i_c} + \Delta\mathbf{M}_{i_c} & & \\
& \mathbf{D}_r & \\
& & \mathbf{D}_y
\end{bmatrix}
\ddot{\mathbf{q}} =
\begin{bmatrix}
\mathbf{f}_{i_c} + \Delta\mathbf{f}_{i_c} \\
\xi_1 \\
\ddot{y}_{E,a}^{(0)} + \xi_2
\end{bmatrix},
\tag{13}
$$

where

$$
\mathbf{M}_{i_c} = \left(m_{i,j}\right)_{\substack{i \in i_c, \\ j=1,\ldots,n_{dof}}}, \mathbf{M} = \left(m_{i,j}\right)_{i,j=1,\ldots,n_{dof}} = \sum_{l=1}^{n_l} \mathbf{M}_{(l)},
$$

$$
\mathbf{M}^{(l)} =
\begin{cases}
\left(m_{ij}^{(l)}\right)_{i,j=1,\ldots,n_{dof}^{(l)}}, & n_{rfe}^{(l)} = 1 \\[4mm]
\sum_{r=0}^{n_{rfe}^{(l)}-1} \mathbf{M}^{(l,r)}, & n_{rfe}^{(l)} > 1
\end{cases}
, \mathbf{M}^{(l,r)} = \left(m_{ij}^{(l,r)}\right)_{i,j=1,\ldots,n_{dof}^{(l,r)}},
$$

$$
m_{ij}^{(b)}\Big|_{b\in\{l,(l,r)\}} = \mathrm{tr}\left\{\mathbf{T}_i^{(b)}\mathbf{H}^{(b)}\left(\mathbf{T}_j^{(b)}\right)^T\right\},
$$

$$
\Delta\mathbf{M}_{i_c} = \left(\Delta m_{i,j}\right)_{\substack{i \in i_c \\ j=1,\ldots,n_{dof}}}, \Delta m_{i,j} = \sum_{k \in i_{dc}} m_{k,j}\frac{\partial \dot{q}_k}{\partial \dot{q}_i},
$$

$$
\mathbf{f}_{i_c} = (f_i)_{i \in i_c}, \mathbf{f} = \left(f_{i,j}\right)_{i,j=1,\ldots,n_{dof}} = \mathbf{Q} + \sum_{l=1}^{n_l}\left(\mathbf{h}^{(l)} - \mathbf{g}^{(l)}\right) - \mathbf{C}\,\mathbf{q},
$$

$$
\mathbf{h} = \left(h_i\right)_{i=1,\ldots,n_{dof}} = \sum_{l=1}^{n_l}\mathbf{h}^{(l)}, \mathbf{h}^{(l)} =
\begin{cases}
\left(h_i^{(l)}\right)_{i=1,\ldots,n_{dof}^{(l)}}, & n_{rfe}^{(l)} = 1 \\[4mm]
\sum_{r=0}^{n_{rfe}^{(l)}-1}\mathbf{h}^{(l,r)}, & n_{rfe}^{(l)} > 0
\end{cases}
,
$$

$$
\mathbf{h}^{(l,r)} = \left(h_i^{(l,r)}\right)_{i=1,\ldots,n_{dof}^{(l,r)}},
$$

$$
h_i^{(b)}\Big|_{b\in\{l,(l,r)\}} = \sum_{m=1}^{n_{dof}^{(b)}}\sum_{n=1}^{n_{dof}^{(b)}}\mathrm{tr}\left\{\mathbf{T}_i^{(b)}\mathbf{H}^{(b)}\left(\mathbf{T}_{m,n}^{(b)}\right)^T\right\}\dot{q}_m^{(b)}\dot{q}_n^{(b)}
$$
$$
+ 2\sum_{m=1}^{n_{dof}^{(b)}}\sum_{n=1}^{n_{dof}^{(b)}}\mathrm{tr}\left\{\mathbf{T}_m^{(b)}\mathbf{H}^{(b)}\left(\mathbf{T}_{i,n}^{(b)}\right)^T\right\}\dot{q}_m^{(b)}\dot{q}_n^{(b)},
$$

$$\mathbf{g} = (g_i)_{i=1,\dots,n_{dof}} = \sum_{l=1}^{n_l} \mathbf{g}^{(l)}, \mathbf{g}^{(l)} = \begin{cases} \left(g_i^{(l)}\right)_{i=1,\dots,n_{dof}^{(l)}}, & n_{rfe}^{(l)} = 1 \\ \sum_{r=0}^{n_{rfe}^{(l)}-1} \mathbf{g}^{(l,r)}, & n_{rfe}^{(l)} > 1 \end{cases},$$

$$\mathbf{g}^{(l,r)} = \left(g_i^{(l,r)}\right)_{i=1,\dots,n_{dof}^{(l,r)}},$$

$$g_i^{(b)}\Big|_{b\in\{l,(l,r)\}} = m^{(b)} g\Theta_2 \mathbf{T}_i^{(b)} \mathbf{r}_{C^{(b)}}^{(b)},$$

$$\mathbf{C} = \mathrm{diag}\{\mathbf{C}^{(1)}, \dots, \mathbf{C}^{(n_l)}\},$$

$$\mathbf{C}^{(l)} = \left(c_{i,j}^{(l)}\right)_{i,j=1,\dots,n_{dof}^{(l)}} = \begin{cases} \mathbf{0}, & n_{sde}^{(l)} = 0 \\ \mathrm{diag}\{\mathbf{0}, \mathbf{C}^{(l,1)}, \dots, \mathbf{C}^{(n_{sde}^{(l)},1)}\}, & n_{sde}^{(l)} > 0 \end{cases},$$

$$\Delta\mathbf{f}_{i_c} = (\Delta f_i)_{i\in i_{i_c}}, \Delta f_i = \sum_{k\in i_{d_c}} f_k \frac{\partial \dot{q}_k}{\partial \dot{q}_i}.$$

Partial derivatives of dependent coordinates with respect to independent coordinates $\frac{\partial \dot{q}_k}{\partial \dot{q}_i}\Big|_{k\in\{2,\,n_{dof}\}}$ can be obtained from the solution of the following system of linear equations:

$$\frac{\partial \dot{q}_2}{\partial \dot{q}_i} + \frac{D_{r,n_{dof}}}{D_{r,2}} \frac{\partial \dot{q}_{n_{dof}}}{\partial \dot{q}_i} = -\frac{D_{r,i}}{D_{r,2}}, \tag{14}$$

$$\frac{\partial \dot{q}_{n_{dof}}}{\partial \dot{q}_i} + \frac{D_{2,2}}{D_{2,n_{dof}}} \frac{\partial \dot{q}_2}{\partial \dot{q}_i} = -\frac{D_{2,i}}{D_{2,n_{dof}}}. \tag{15}$$

Constraints violation at the position and velocity levels is eliminated using the Baumgarte stabilization method [2]. The final form of the GPME is as follows:

$$\begin{bmatrix} \mathbf{M}_{i_c} + \Delta\mathrm{M}_{i_c} \\ \mathbf{D}_r \\ \mathbf{D}_2 \end{bmatrix} \ddot{\mathbf{q}} = \begin{bmatrix} \mathbf{f}_{i_c} + \Delta\mathbf{f}_{i_c} \\ \xi_1 - 2\alpha_1\dot{\Phi}_1 - \beta_1^2\Phi_1 \\ \ddot{y}_{E,a}^{(0)} + \xi_2 - 2\alpha_2\dot{\Phi}_2 - \beta_2^2\Phi_2 \end{bmatrix}. \tag{16}$$

In numerical simulations it has been assumed that $\alpha_i|_{i=1,\,2} = 100$, $\beta_i|_{i=1,\,2} = 50$.

3   Numerical Study Results for the Flexible Link Manipulator Model

Numerical simulation results obtained for analysing the reference motion of the spatial manipulator subjected to the programmed constraints (2) and (3) are presented in this section. It is assumed that the driving torque is applied to the vertical column (1) and its time course is described by the following formula:

$$t_{dr}^{(1)}(t) = \begin{cases} 10\, t_{dr,0}^{(1)} \left(\dfrac{t}{t_0}\right)^3 - 15\, t_{dr,0}^{(1)} \left(\dfrac{t}{t_0}\right)^4 + 6\, t_{dr,0}^{(1)} \left(\dfrac{t}{t_0}\right)^5, & t < t_0 \\[2mm] t_{dr,0}^{(1)}, & t \geq t_0 \end{cases}, \qquad (17)$$

where $t_{dr,0}^{(1)}$ is an assumed value of the driving torque at time $t \geq t_0$. In simulations it is assumed $t_0 = 5\,\mathrm{s}$ and $t_{dr,0}^{(1)} = 1\ \mathrm{Nm}$.

The flexible link is divided into 5 rfes. Such division is a good compromise between numerical effectiveness and sufficient results quality. The GPME has been integrated using Runge-Kutta 4th order method. The presented numerical simulations are performed with a constant integration step $\Delta h = 10^{-5}\,\mathrm{s}$. The initial configuration of the system results from the solution of the statics task for increasing values of the
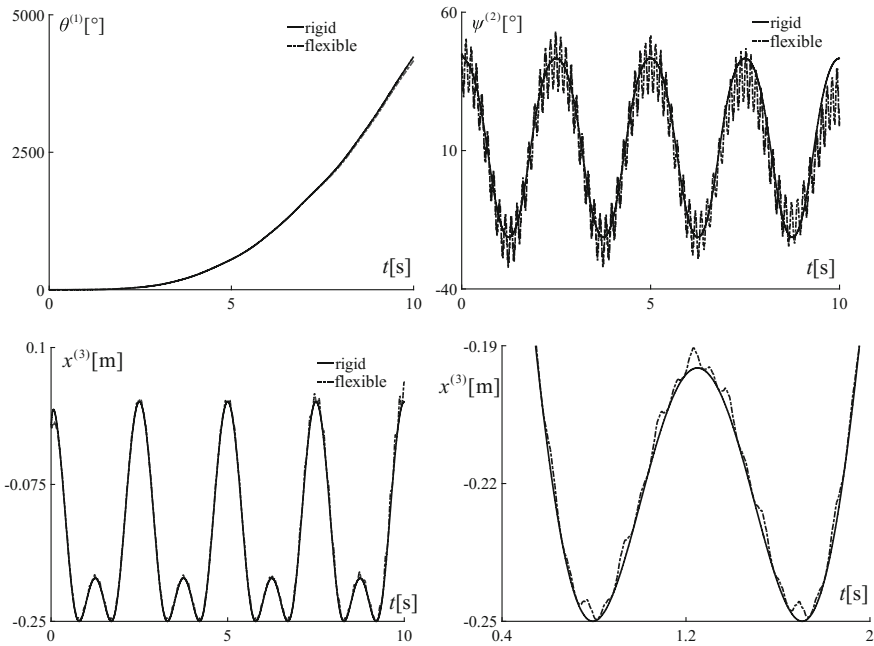
Fig. 2 Time courses of the joint coordinates

gravity $g = 0, 1, 2, \ldots, 9.81$. The initial values of the configuration variables used in the statics problem for $g = 0$ are as follows: $\theta^{(1)} = 0°$, $\psi^{(2)} = 45°$, $x^{(3)} = 0\,\mathrm{m}$. Newton-Raphson method is applied to solve the statics task. When the rotary arm 2 is treated as flexible, the initial position of the slider (Fig. 2) and end-effector E (Fig. 4) change due to deformation of the flexible link. Vertical motion of the end-effector E is defined by:

$$y_{E,a}^{(0)}(t) = y_0 + A \, \cos\left(\frac{2\pi}{T}t\right), \qquad (18)$$

where y_0 is the initial position of the end-effector, A is the amplitude and T is a time period of oscillations. It is assumed that $A = 0.5\,\mathrm{m}$ and $T = 2.5\,\mathrm{s}$.

Time courses of the configuration variables of the manipulator obtained from simulations are presented in Fig. 2.

It can be observed that for the arm 2, which is flexible, additional oscillations appear in time courses of displacements of the rotary arm 2 and the slider 3. It can be concluded that influence of the flexibility on the programmed motion of the manipulator is compensated by the appropriate combination of the rotation angle of the arm 2 and the displacement of the slider 3.

Figure 3 shows time courses of the global Cartesian coordinates of the end-effector E.

A good agreement of the time course of y-component of the end-effector E displacement with the ones assumed by the programmed constraints can be observed.

A trajectory of the end effector E in the planes $\hat{\mathbf{x}}^{(0)}\,\hat{\mathbf{z}}^{(0)}$ and $\hat{\mathbf{x}}^{(0)}\,\hat{\mathbf{y}}^{(0)}$ is presented in Fig. 4.

A starting point of the end-effector E is different for each considered model of the manipulator. The gravity forces cause bending of the flexible arm 2 and as a result the end-effector moves in the plane $\hat{\mathbf{x}}^{(0)}\,\hat{\mathbf{y}}^{(0)}$ from the position E_r' to the position E_f'. It can also be observed that the required circular trajectory of the end-effector in the plane $\hat{\mathbf{x}}^{(0)}\,\hat{\mathbf{z}}^{(0)}$ is achieved.

4   Conclusions

A dynamics model of the spatial manipulator with a flexible link whose end-effector motion is limited by first order programmed constraints is presented in the paper. Flexible links are modeled by means of modified approach of the Rigid Finite Element Method. An algorithm of generation of the generalized program motion equations formulated in the paper can be applied to any open-loop kinematic chain whose links can be flexible. Thanks to homogeneous transformations and joint coordinates dynamics of the system is described by a minimal set of coordinates without the need for determination of constraints reaction forces. It can be seen that constraint reaction forces are also eliminated at the derivation level. As a result, dynamics of the system is described by a set of ordinary differential equations. Numerical simulation
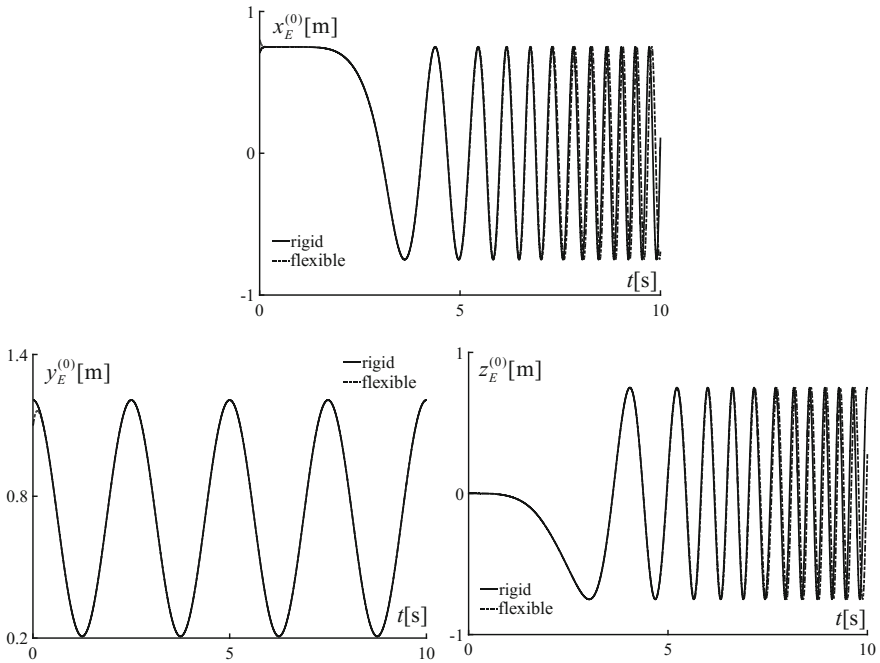
Fig. 3 A time course of the end-effector E coordinates
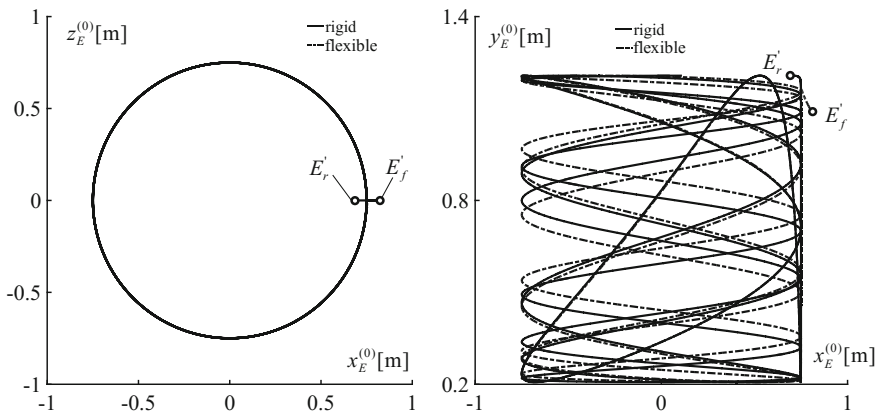
Fig. 4 Trajectory of the end-effector, where $E_i'\big|_{i \in \{r, f\}}$ is a starting point of the end-effector for a rigid (r) and flexible (f) model of the arm 2

results show that flexibility of links has significant influence on driving function courses realizing the desired programmed motion. In further works it is planned to

extend the presented algorithm to model dynamics and control of spatial linkages with flexible links.

References

1. Augustynek, K., Urbaś, A.: Two approaches of the rigid finite element method to modelling the flexibility of spatial linkage links. In: Proceedings of the ECCOMAS Thematic Conference on Multibody Dynamics, Prague, pp. 19–22 (June 2017)
2. Baumgarte, J.: Stabilization of constraints and integrals of motion in dynamic systems. Comput. Methods Appl. Mech. Eng. **1**, 1–16 (1972)
3. Jarzębowska, E.: On derivation of motion equations for systems with non-holonomic high-order program constraints. Multibody Sys. Dyn. **7**, 307–329 (2002)
4. Jarzębowska, E.: Advanced programmed motion tracking control of nonholonomic mechanical systems. IEEE Trans. Robot. **24**(6), 1315–1328 (2008)
5. Jarzębowska, E.: Model-based tracking control of nonlinear systems. Taylor & francis group, series: modern mechanics and mathematics, Boca Raton (2012)
6. Jarzębowska, E., Augustynek, K., Urbaś, A.: Computational reference model of dynamics of multibody system with first order constraints. In: Proceedings of the ASME 2017 International Design Engineering Technical Conferences & Computers and Information in Engineering Conference IDETC2017, Cleveland, pp. 6–9 (August 2017)
7. Urbaś, A.: Computational implementation of the rigid finite element method in the statics and dynamics analysis of forest cranes. Appl. Math. Modell. **46**, 750–762 (2017). https://doi.org/10.1016/j.apm.2016.08.006
8. Wittbrodt, E., Adamiec-Wójcik, I., Wojciech, S.: Dynamics of flexible multibody systems. Rigid finite element method, Springer, Berlin (2006)

Optimization of Geometry of Cavitational Tunnel Using CFD Method

Robert Jasionowski and **Waldemar Kostrzewa**

Abstract The liquid flow through a various kind of installation or devices is still not fully clarified issue. The liquid flow is assisted by a stream swirling, local pressure drops or changes of flow rates or temperature. CFD methods have been already implemented for few years to analyze phenomena related to the liquid flow. In this work Autodesk CFD Design Study Environment 2018 was used to simulate a new geometry of cavitational tunnel—a laboratory stand for examinations of cavitational resistance of structural materials. Three different geometries of the tunnel were analyzed in this work: with a cavitation initiator made of barricade and counter-barricade systems, with a cavitation initiator having a cylindrical pocket in counter-barricade and with a cavitation initiator having a double wedge shape. The introduced change of geometry allows multiplying the area of local pressure drop (i.e. the area of cavitation phenomenon). Obtained results of will serve in future (after building the new laboratory stand) to verify CFD simulations in a real testing conditions. The new tunnel geometry developed in CFD simulations should shorten evaluation time, what in turn, will give direct economic benefits (i.e. lower exploitation rate of the laboratory stand as well as lower costs of electrical energy).

Keywords Cavitation · Cavitational tunnel · CFD

1 Introduction

Computational Fluid Dynamics (CFD) is a software based on numerical methods describing a fluid movement. The methods implemented in CFD are mostly based

R. Jasionowski (✉) · W. Kostrzewa
Institute of Basic Technical Sciences, Maritime University of Szczecin, 2-4 Willowa Str, 71-650 Szczecin, Poland
e-mail: r.jasionowski@am.szczecin.pl

W. Kostrzewa
e-mail: w.kostrzewa@am.szczecin.pl

on Navier-Stokes equation describing the motion of an viscous fluid [1–6]. Beside the Navier-Stokes equation following mathematical tools are also involved:

– Euler equation describing the motion of an inviscid fluid [1–6];
– Laplace's equation describing the irrotational flow [1, 3, 4, 6];
– Orr-Sommerfeld equation describing the hydrodynamic stability [3];
– The Reynolds numbers [1–5].

A solving of aforementioned equations (under properly pre-assumed boundary conditions) allows analyzing incompressible, inviscid and turbulent liquid flows, as well as simulating their interaction with other surrounding liquids or gases.

In order to provide a full description of liquid flow, the CFD software utilizes four different methods: finite difference method, finite element method, finite volume method and spectral method.

An involvement of these methods gives a new interdisciplinary nature to the CFD as the engineering tool. It offers a full range of analytical possibilities e.g. performing large-scale complex related to liquid flows, conducting of new experiments in conjunction with the CFD results or a detailed visualization of a flow.

A reliability of the CFD method mainly depends on: the accuracy of applied geometrical model; generate the grid and a correctness of the boundary conditions. During building the geometrical model it is acceptable to skip some small, not important details (e.g. roundness, holes) that do not significantly affect the final results of numerical simulations. The obtained model is like a grid of the mesh. The mesh model directly determines the accuracy of obtained results, but on the other hand, increasing the number of nodes might elongate the processing time. In order to avoid time-consuming analyses, it is acceptable to add some extra nodes only in most crucial parts of the model (e.g. those giving highly scattered results). The correctness of CFD analyses is also strongly determined by pre-assumed boundary conditions, that may even lead to erroneous or contradicted results. The following types of boundary conditions are distinguished in the CFD:

– Inlet—a determination of boundary conditions for inlets;
– Outflow—a determination of boundary conditions for outlets;
– Wall—a determination of boundary conditions for rigid walls;
– Symmetry—a determination of boundary conditions in sites having a mirror-like symmetry;
– Periodic—a determination of boundary conditions in sites having a rotational or translational symmetry.

The aviation is the pioneering industry branch that has started to use the CFD methods. In the early 70s, the CFD was implemented in industrial plants of Boeing Company [7], Lockheed Corporation [8], Douglas Aircraft [9], McDonnel Aircraft [10] and NASA [11] to analyze aircraft bodies. Nowadays, the CFD is also applied upon a fabrication of submarines, cars, helicopters, wind and water turbines, and also in biomedicine, electronics, mining and metallurgy. Such high popularity of the CFD is mostly related to a given opportunity of visualizing un-recognized flow phenomena, and to a lowering of costs associated with very expensive experiments.

In this work, the CFD method was utilized to simulate and analyze changes of geometry of cavitational tunnel. The tunnel is intended to experimentally evaluate a cavitational erosion resistance of structural materials. Three different geometries of the tunnel were analyzed in this work:

– variant #1—with a cavitation initiator made of barricade and counter-barricade systems; similar to that used in laboratory stands of University of Hannover and Hiroshima University and Institute of Fluid-Flow Machinery of the Polish Academy of Sciences. This tunnel geometry is also exploited in Institute of Basic Technical Sciences in Szczecin.
– variant #2—with a cavitation initiator having a cylindrical pocket (with diameter of 20 mm and depth of 25 mm) in counter-barricade that reduces the pressure. This design was originally developed by J. Griggs in a power cavitation reactor [12];
– variant #3—with a cavitation initiator having a double wedge shape that allows obtaining an under pressure below the examined sample, and thus increasing the liquid flow.

The basic purpose of the CFD analyzes was to determine an optimal shape of counter-barricade (a spare part of the tunnel) in terms of receiving the largest low-pressure area that induces the cavitation phenomenon. A selection of the optimal tunnel geometry will result in a reduction of time needed to examine new materials; as well as will allow properly arrange the measurement device controlling a correctness of CFD calculations.

2 Numerical Model

2.1 Physical Model

In the present work, a cavitational tunnel (Fig. 1) being a part of cavitational resistance measurement device, has been subjected to the analysis.

A PML2 80/200 type pump driven by 15 kW engine and LG iG5A inverter pushes water through the tunnel. In previous experiments a rotor inside the PML2 80/200 type pump rotated with 2900 rpm giving a flow rate of 9.95 m/s (measured in the tunnel inlet). The application of LG iG5A inverter allows setting a freely chosen rotational speed of the rotor, thus controlling the flow rate. The cavitation induction system in the tunnel is made of barricade (upper) and counter-barricade (lower) systems.

Fig. 1 Cavitational tunnel
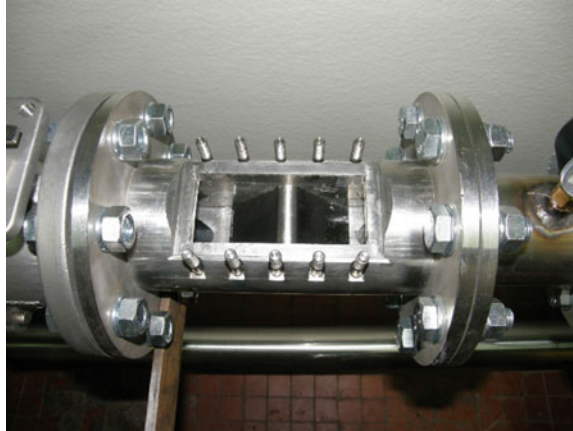
2.2 The Geometric Model of Cavitational Tunnel and Boundary Conditions

The geometric model of cavitational tunnel was designed in AutoDesk Inventor Professional 2018 software by using a dimensional accuracy of 0.1 mm. The geometric model of cavitational tunnel is made of six own-designed components (a body, a cover, barricades systems, two flanges and 53 components from preexisted libraries (Fig. 2).

Analyzed three different variants of counter-barricade geometry are shown in Fig. 3.

The tunnel was made of 0H18N9 stainless steel, so the same material was also used upon the simulation of flow. Volume mesh model (Fig. 4) and numerical analysis of liquid flow in cavitational tunnel was designed in AutoDesk CFD 2017 software. In

Fig. 2 The geometric model—components (1—body, 2—cover, 3—upper barricade, 4—lower barricade, 5—sample, 6—flange)
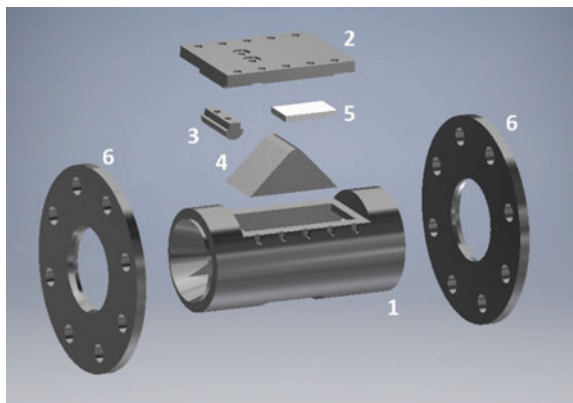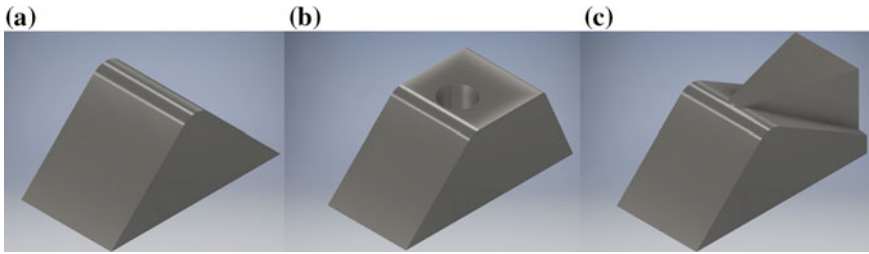
Fig. 3 The geometry of the lower barricade: **a** counter-barricade, **b** counter-barricade with cylindrical pocket, **c** the double wedge shaped counter-barricade
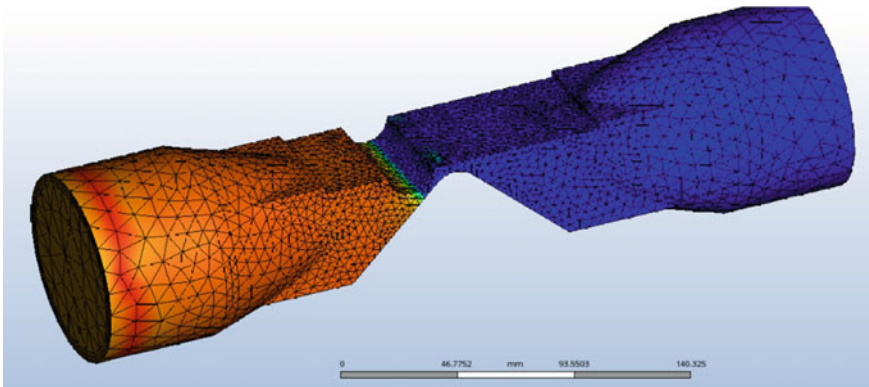
Fig. 4 Volume mesh model for variant #1

order to increase the precision of measurements was performed tenfold concentration of mesh nodes between upper and lower barricades and under test sample (size adjustment parameter was 0.1). Additionally components that do not have a direct contact with the flowing liquid as well as the roundness and chamfers of edges below 0.1 mm were excluded from the analysis.

The volume mesh models containing 888,049, 1,087,767 and 1,041,989 nodes were obtained for variants #1, #2 and #3, respectively.

The following chemical and physical parameters of flowing water were used upon the analysis: density of 0.9982 g/cm^3, viscosity of 0.001003 Pa s, temperature of 25 °C, thermal conductivity of 0.0006 W/mm K, bulk modulus of 2.18565 GPa.

The numerical analysis was carried out by using a liquid temperature of 25 °C and velocity in the tunnel inlet 9.95 m/s.

3 Analysis of Simulation and Test Results

The conducted analyzes include examinations of velocity and pressure distributions; and a formation of swirls inside the beam flowing through a tunnel with three different geometries.

3.1 Analysis of Velocity

The analysis of velocity distribution for considered three different geometries of the counter-barricade was performed in two planes: a vertical one located in the tunnel axis (Fig. 5) and in a horizontal plane shifted from the sample surface at a distance of 1 mm (Fig. 6).
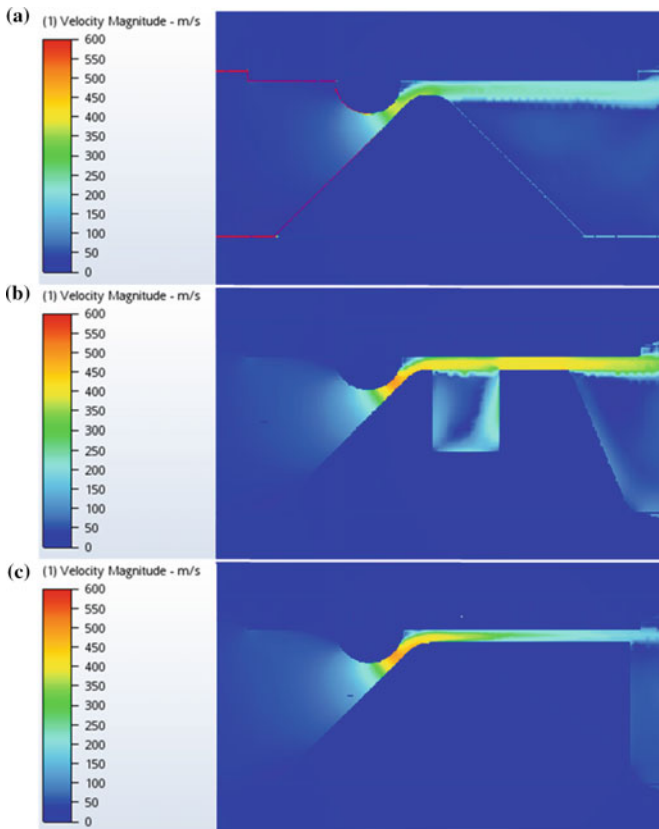
Fig. 5 The results of the velocity in the vertical plane: **a** variant #1, **b** variant #2, **c** variant #3
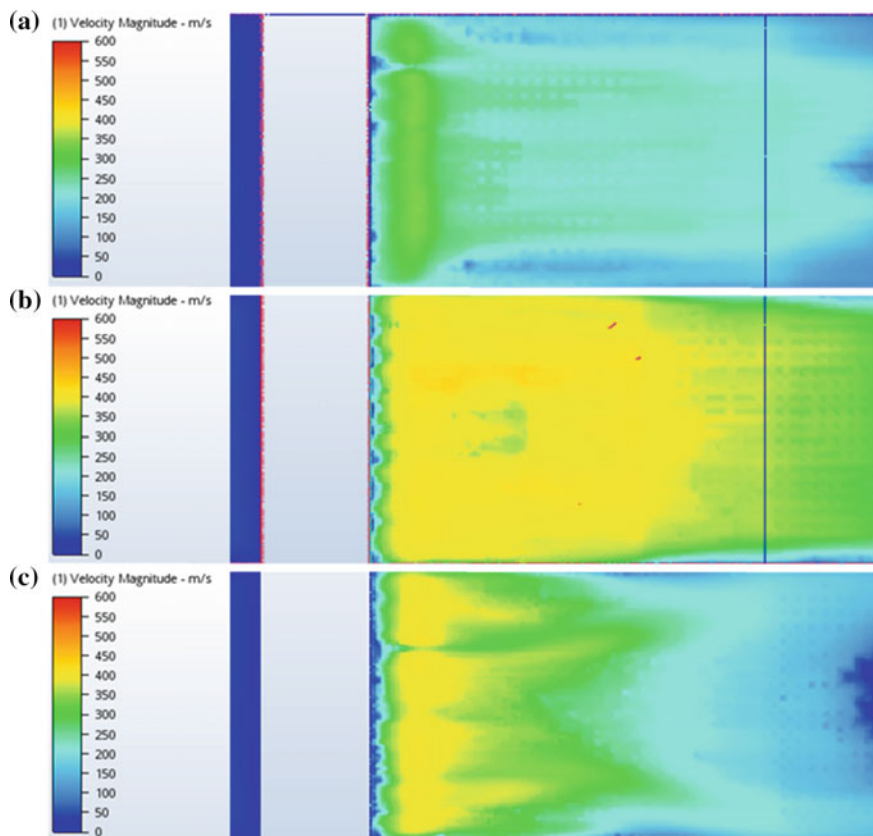
Fig. 6 The results of the velocity in the horizontal plane: **a** variant #1, **b** variant #2, **c** variant #3

The analysis carried out in the vertical plane allows establishing a maximum flow velocity between barricade and counter-barricade. The highest value (520 m/s) was obtained for the variant #2, while that for the variant #3 (with the double wedge shaped counter-barricade) was only slightly lower (500 m/s). Finally, the lowest value was received for the first analyzed case of tunnel geometry (350 m/s).

Interesting results were obtained upon the analysis of liquid flow in the horizontal plane (Fig. 6). As in the case of the other considered plane, the highest velocity was also noted for the second variant.

The average flow velocity at a distance of 1 mm from the sample surface was over 410 m/s, while the lowest (350 m/s) was recorded near the pocket area and at the end of the sample.

The results obtained for double wedge-shaped counter barricade, were qualitatively and quantitatively different. For this case, the highest velocities were around 420 m/s, while the lowest (200 m/s) were found at the end of the sample. The average velocity in analyzed plane of the variant #2 was equal to 330 m/s. The lowest

velocities were received for the already existed geometry of the tunnel. The average flow velocity below the sample was around 210 m/s.

3.2 Analysis of Pressure

The flow pressure distributions for each of examined geometries were performed in the same manner as in the case of velocity distributions. The pressure distributions in vertical and horizontal planes are shown in Figs. 7 and 8, respectively.
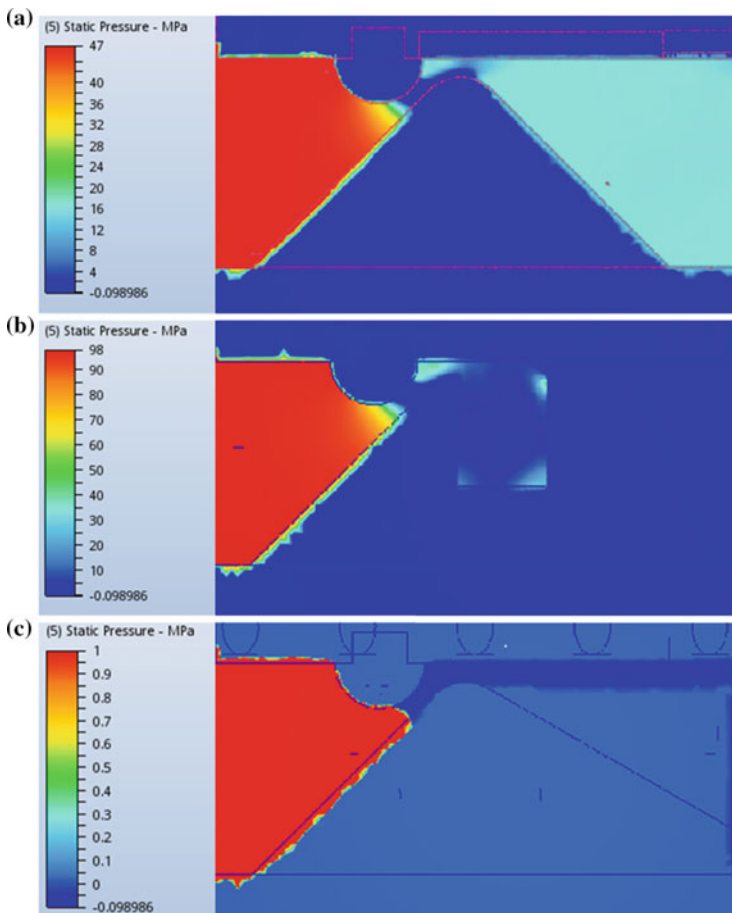
Fig. 7 The results of the pressure in the vertical plane: **a** variant #1, **b** variant #2, **c** variant #3
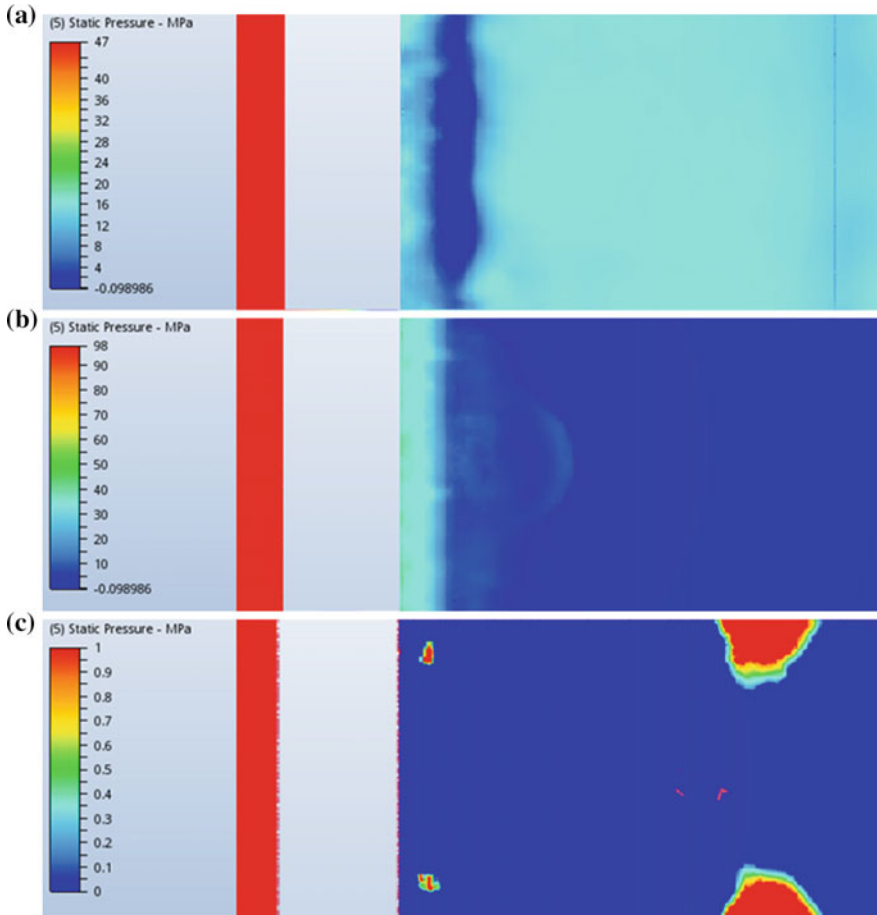
Fig. 8 The results of the pressure in the horizontal plane: **a** variant #1, **b** variant #2, **c** variant #3

The main intention of our numerical analyses was to determine areas of lowered pressure by using a different range. In the first analyzed variant the area of lowered pressure was located between the upper and lower barricades and also over the top of counter-barricade. For the variant with cylindrical pocket the area of lowered pressure was located in three sites:

– in a small region between lower and upper barricades;
– inside the pocket. In order to precisely determine the pressure value inside the pocket 25 additional points were introduced. The points were arranged in 5 planes separated by 5 mm distance (5 points were located in each plane—one in pocket axis and four at the periphery). The first plane was moved 2.5 mm away from the pocket's bottom. The arrangement of points and results of analyses are presented in Fig. 9 and in Table 1.
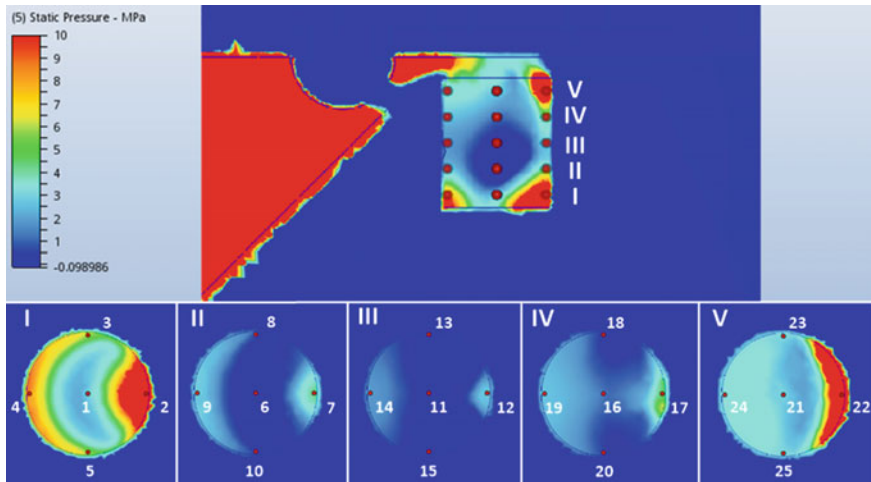
Fig. 9 The arrangement of points inside the pocket

Table 1 The values of pressure inside the pocked

Plane I	Point number	1	2	3	4	5
	Value of pressure / MPa	2.4091	17.0716	5.7181	8.8096	5.6036
Plane II	Point number	6	7	8	9	10
	Value of pressure / MPa	−0.0989	4.1914	0.1158	0.4371	2.3695
Plane III	Point number	11	12	13	14	15
	Value of pressure / MPa	−0.0970	2.2543	−0.0989	1.3742	−0.0989
Plane IV	Point number	16	17	18	19	20
	Value of pressure / MPa	0.9580	4.4622	0.1406	2.1506	0.3603
Plane V	Point number	21	22	23	24	25
	Value of pressure / MPa	2.4613	25.2419	2.6597	3.3549	2.6429

Results obtained for the counter-barricade having double-wedge shape revealed existence of the largest region of lowered pressure that starts between upper and lower barricades and ends beyond the counter-barricade.

3.3 Analysis of Stream of Liquid

Beside of analyzing velocity and pressure distributions, additionally conducted examinations were associated to the course of liquid beams. The results presented in graphical form are shown in Fig. 10. The graphs show a liquid beam that take into account its velocity of liquid.
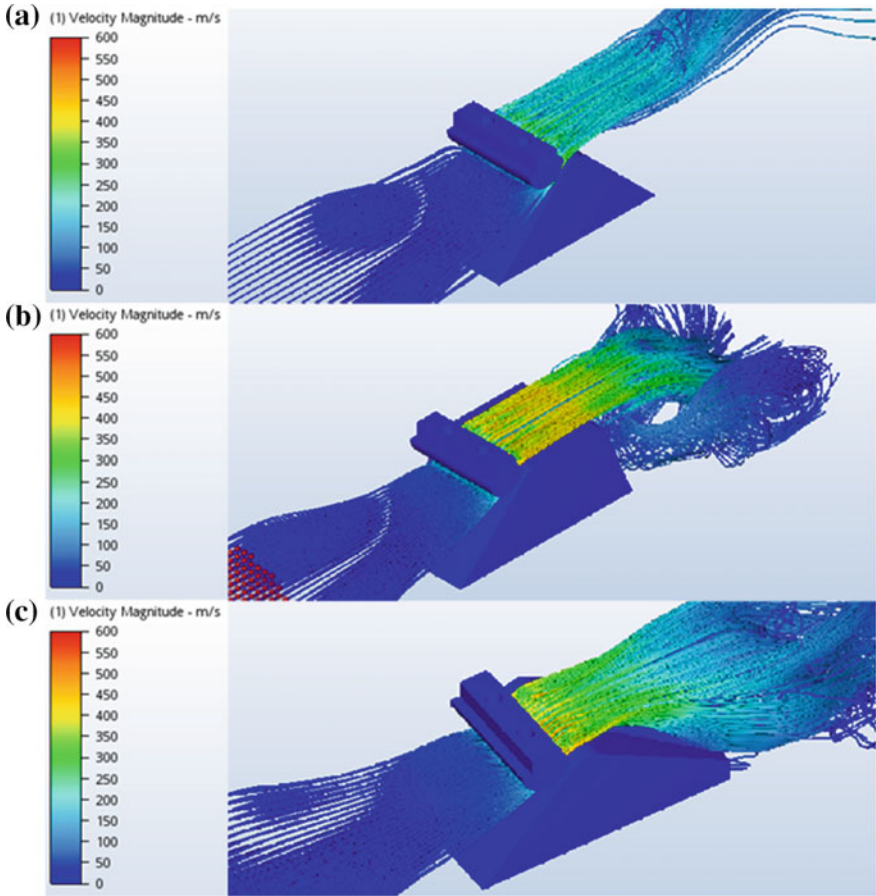
Fig. 10 The results of the stream of liquid: **a** variant #1, **b** variant #2, **c** variant #3

For the variant #1 the liquid beams were located in the upper part of the tunnel (i.e. below the surface of analyzed sample). In other examined cases the whirpools leading to a formation of local drops of pressure and velocity, were observed. However, since these whirpools do not affect the cavitational resistance of sample placed on the counter-barricade, they were not taken into the consideration.

4 Conclusions

Experiments on the resistance of structural materials tested in cavitational tunnels are assisted by a presence of hydrodynamic cavitation phenomenon. The cavitational tunnels are laboratory stands characterized by a similarity of the cavitation course

and its low intensity, what significantly increases the overall evaluation time. A new geometry of cavitational tunnels (in terms of increasing the area of lowered pressure) is needed to shorten time of experimental procedures. This purpose might accomplished through a modification of the tunnel geometry leading to a simultaneous drop of pressure and increase of velocity.

The proposed changes of counter-barricade geometry and conducted CFD simulations revealed an increase of lowered pressure area, as compared to actually applied geometry.

The results of CFD analyses carried out for three different geometries of the tunnel confirm advantages of using this type of software during designing of new devices or improvement of already existed ones.

The conducted analyses allows determining velocity and pressure distributions (i.e. maximum and average values of flow velocities below the sample, were established). Nevertheless, the obtained results did not clearly point the best considered modification of the tunnel geometry. Thus, all of them will be experimentally verified in our further research. Furthermore, in the case of the variant #3, it is planned to perform analyses on samples placed inside the pocket.

References

1. Blazek, J.: Computational Fluid Dynamics: Principles and Applications. Elsevier, Oxford (2001)
2. Chung, J.: Computational Fluid Dynamics. Cambridge University Press, Cambridge (2002)
3. Cebeci, T., Shao, J.R., Kafyeke, F., Laurendeau, E.: Computational Fluid Dynamics for Engineers. Springer, Berlin (2005)
4. Sayma, A.: Computational Fluid Dynamics, Ventus (2009)
5. Lomax, H., Pulliam, T.H., Zingg, D.W.: Fundamentals of Computational Fluid Dynamics. Springer, Berlin (2001)
6. Anderson Jr., J.D.: Computational Fluid Dynamics. The Basics with Applications. McGraw-Hill, New York (1995)
7. Carmichael, R., Erickson, L.L.: PAN AIR—a higher order panel method for predicting subsonic or supersonic linear potential flows about arbitrary configurations. In: 14th Fluid and Plasma Dynamics Conference, Palo Alto, CA, USA (1981)
8. Youngren, H.H., Bouchard, E.E., Coopersmith, R.M., Miranda, L.R.: Comparison of panel method formulations and its influence on the development of QUADPAN, an advanced low order method. In: Applied Aerodynamics Conference Danvers, MA, USA (1983)
9. Hess, J.L., Friedman, D.M.: Analysis of complex inlet configurations using a higher-order panel method. In: Applied Aerodynamics Conference Danvers, MA, USA (1983)
10. Bristow, D.R.: Development of panel methods for subsonic analysis and design, NASA (1980)
11. Ashby, D.L., Dudley, M.R. Iguchi, S.K. Browne, L., Katz, J.: Potential Flow Theory and Operation Guide for the Panel Code PMARC, NASA (1991)
12. Griggs, J.L.: Apparatus for heating fluids, US 5385298 A, US 08/015.809 (1995)

Application of Numerical Simulations on 10GN2MFA Steel Multilayer Welding

Tomasz Kik, Jaromír Moravec and Iva Nováková

Abstract 10GN2MFA steel is used to produce wire and manufacturing of steam generators, pressure compensators, collectors and other equipment for nuclear power plants. In this area, there is no place to do any mistakes during manufacturing or carrying out extensive tests and producing a lot of prototypes. It is the main reason why we used modern software for numerical simulation of welding and heat treatment processes also on the very early stage of development. The aim of this paper is to describe how can welding processes be optimized by means of the numerical simulations mainly with respect to the structural changes, stresses and hardness distribution in the Heat Affected Zone (HAZ). On the real multilayer weld how to arrange whole experiment in order to obtain not only relevant input data but also verification data will be described. Additional aim of this paper is to propose mathematical description of the computational model that is usable for simulation computations of welding and heat treatment of real structure components.

Keywords Numerical simulation · 10GN2MFA steel · Welding · FEM SYSWELD · Hardness prediction

1 Introduction

Energy sector is generally responsible for substantial and comprehensive public development. Even that we have a lot of alternative energy sources, still the most

T. Kik (✉)
Department of Welding, Faculty of Mechanical Engineering, Silesian University of Technology, Konarskiego 18A, 44-100 Gliwice, Poland
e-mail: tomasz.kik@polsl.pl

J. Moravec · I. Nováková
Technical University of Liberec, Liberec, Czech Republic, Studentska 2, 461 17 Liberec, Czech Republic
e-mail: jaromir.moravec@tul.cz

I. Nováková
e-mail: iva.novakova@tul.cz

critical for energy sector are two method: producing energy in coal steam power plants (powered by coal and others fossil fuels) and nuclear power plants (where the energy is produced from nuclear fusion).

As for April 2017 in 30 countries worldwide are operating 449 nuclear reactors for electricity generation. Another 60 new nuclear plants are under construction in 15 countries. Nuclear power plants provided 11% of the world's electricity production in 2014. In 2016, 13 countries relied on nuclear energy to supply at least one-quarter of their total electricity [1, 2].

In nuclear energy reactors, the heat from nuclear fusion is used to produce a steam. Steam next is transported to turbines and used to produce electricity. From a single uranium fuel pellet (size is like a pencil eraser) it is possible to produce same energy amount as from 17,000 cubic feet of natural gas, 1780 lb of coal or 149 gallons of oil [1]. It is important that proper used nuclear reactors do not emit any pollutions. There is no carbon dioxide, nitrogen oxides and sulfur dioxides as well. It can be also called second generation of clean energy because of no environment degradation comparing to wind turbines or dams. For example, the amount of electricity produced by a multi-reactor nuclear power plant would require about 45 square miles of photovoltaic panels or about six times more square miles of wind turbines. Additional advantage is that renewable energy sources is limited by their fuel—wind, sun or water. Nuclear energy produces electricity continuously, without breaks. Also it is important that there is enough uranium in the world to fuel reactors for 100 years or more [1–4].

Of course some of people can be afraid about the radiation, but it is worth to say, that normally operated nuclear power plant do not emits radiation. Of course they are also real-time monitored and the risk on some hazardous accident is very limited [1, 2, 4]. To assure the proper safety level, important is also to ensure the highest quality level of nuclear island equipment elements. 10GN2MFA steel is a widely used as also 16MND5 and A508 tempered bainitic pressure vessel steel used mainly in production of WWER-1000 reactor equipment as steam generator cases, collectors and pipes. Due to the big dimensions of elements, different conditions of plastic deformation involve in the manufacturing process can have big influence on mechanical properties [5, 6].

Due to the specific use and technologies for joining of these material, important is also to investigate properties of used materials as well as it possible. To achieve best results and also claim specific working conditions, applications of these materials and development of the technological processes for their processing is still more and more aided by numerical simulation computations. These computations help to understand the processing which takes place in the individual phases of a simulated process and with respect to that it is possible to process optimize. Eventually risks associated with unacceptable defects can be significantly eliminated. The information obtained from the simulations can be used to support or develop a methodology how to obtain not only input data, but also data which verify the validity and suitability of the computational procedures that are used [7, 8].

Fig. 1 Scheme of specimen
preparation for welding tests
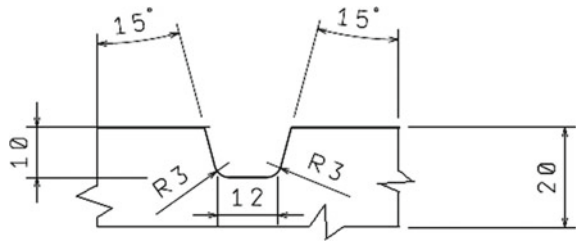
2   Realization of the Welding Experiment on 10GN2MFA Steel Specimens

Main aim of real tests was not achieve the best quality of welds but collect as more as it possible of input data's for numerical simulations. These data will help us to define boundary conditions and verification of calculation results, mainly hardness after welding and after post weld heat treatment.

For real tests, $180 \times 80 \times 20$ mm specimen was prepared with milled grove for welding as on Fig. 1. Chemical composition of 10GN2MFA measured on TASMAN Q4 spectrometer was shown at Table 1. Complete specimen was welded by 8 beads in 4 layer by manual arc welding, where two beads were placed side-by-side in each layer using Boehler FOX EV 85 electrode, Table 2. All process was completely monitored by the Weld Monitor system and all information's about the relevant processes parameters were available. Test specimen monitored by six thermocouples and partially coated with Sibral isolation (Fig. 2) was placed into the furnace and heated on temperature 200 °C with heating rate about 1.5 °C/min. After reaching preheating temperature on whole specimen, Sibral isolation was also placed on the top and welded. During all welding procedure the interpass temperature at 350 °C was respected. After welding, specimen with welds was heat treated by heating up to the 650 °C and cooled with furnace to the 300 °C and then in the free air to the ambient temperature.

3   Numerical Simulation of Welding Process in SYSWELD Software

SYSWELD software package is the most used commercial simulation software for welding and heat treatment processes. The whole computation process consists of two separate analyses—the thermo-metallurgical and the mechanical one. First of them makes it possible to compute non-stationary temperature fields, phase transformations, hardness or size of the austenitic grain. The second part of analysis—mechanical analysis uses the results of the temperature-metallurgical analysis as input

Table 1 Chemical composition tested on TASMAN Q4 spectrometer, % and basic mechanical properties of 10GN2MFA steel

C	Mn	Si	P	S	N	Cu	Ni	Cr	Mo
0.117	0.954	0.223	<0.005	<0.15	<0.02	0.048	1.970	0.041	0.583
V	Al	B	Ti		Nb	As	Sn		Fe
0.052	0.014	0.001	0.0012		0.001	0.012	<0.005		95.71
Yield point, MPa			Tensile strength, MPa			Elongation, %			
345–590			540–700			18			

Table 2 Chemical composition of the Boehler FOX EV 85 filler material, %

C	Mn	Si	P	S	N	Cu	Ni	Cr	Mo
0.05	1.7	0.4	–	–	–	–	2.1	0.4	0.5

Fig. 2 View of 10GN2MFA steel specimen with thermocouples and Sibral isolation before heating (on the left side) and during welding (on the right side)

Fig. 3 Double ellipsoid heat source model [10]
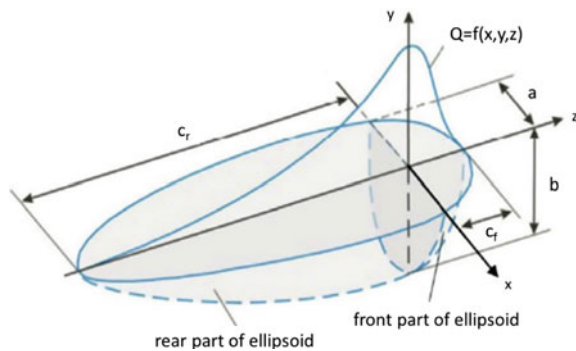
data and the most common results here are mainly stress and strain fields but also distortions [7–9].

Nowadays there are known a many numerical heat source models used in the welding FEM simulations. One of the most popular for typical arc welding methods is a double-ellipsoidal heat source model also called Goldak's model. This heat source model (defined as heat flux density into material) is described by Eqs. (1) and (2). The efficiency of the heat transfer into parent material is given by the applied welding method [4]. Geometry of double-ellipsoidal model can be modified by changing coefficients 'a', 'b' and 'c' in the Eqs. (1) and (2) [9–11] (Fig. 3).

Transferred heat is described by equations below [9]:

for the front part of heat source model is

$$Q_f(x, y, z) = \frac{6\sqrt{3} f_f Q}{abC_f \pi \sqrt{\pi}} exp\left(\frac{-3x^2}{a^2}\right) exp\left(\frac{-3y^2}{b^2}\right) exp\left(\frac{-3z^2}{c^2}\right) \qquad (1)$$

and for the rear part of heat source model is
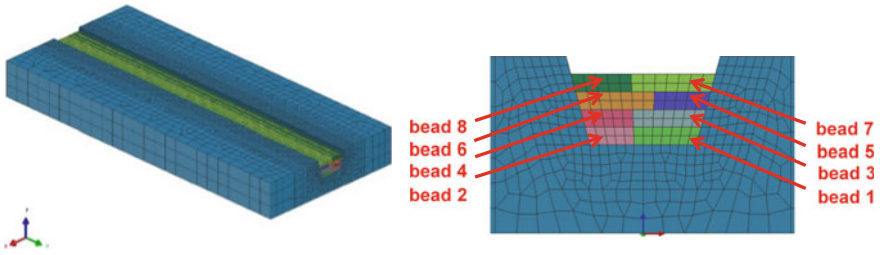
Fig. 4 View of 3D discrete model of weld created on the basis of real experiment and cross section with each bead description and model mesh

$$Q_r(x, y, z) = \frac{6\sqrt{3}\,f_r\,Q}{abC_r\pi\sqrt{\pi}}exp\left(\frac{-3x^2}{a^2}\right)exp\left(\frac{-3y^2}{b^2}\right)exp\left(\frac{-3z^2}{c^2}\right) \qquad (2)$$

where:

Q_f, Q_r heat introduced into the front and the rear part of the model,
Q total power source,
a width of the molten pool,
b depth of the molten pool,
c_f, c_r length of the front and the rear part of the molten pool,
f_f, f_r constants which influence energy flow intensity into the material.

Total energy introduced by the heat source model to the welded material is [9]:

$$P = \int_{structure} Q_R \qquad (3)$$

Hardness and stresses calculations in SYSWELD requires to calculate the temperature distribution on the welded specimen. That is why the proposal of the experiment to optimize the computational model in program SYSWELD arises both from such requirement to define Goldak´s heat source model and from the necessity to know the change of the hardness in multilayer welding. Therefore the aim of the experiment was not only to define the geometry of every weld (including necessary welding parameters used in process) but also to determine hardness changes in the parent material, HAZ and in the weld at application of at application of multiple multiple temperature cycle. Very important is also an unambiguous definition of boundary conditions for the experiment which are given both by used clamping method and the technological parameters (preheating, interpass temperature) but also by the way of thermal conductivity into surrounding. For the possibilities of beads geometry and HAZ areas examinations, in real experiments beads were moved each other.

Thanks to this it was possible just by means of one experiment to gain all necessary data both for a definition of Goldak´s heat source model and also for subsequent verification and eventual optimization of computational model. Numerical model was built from 50,704 3D elements and 44,999 nodes, Fig. 4.
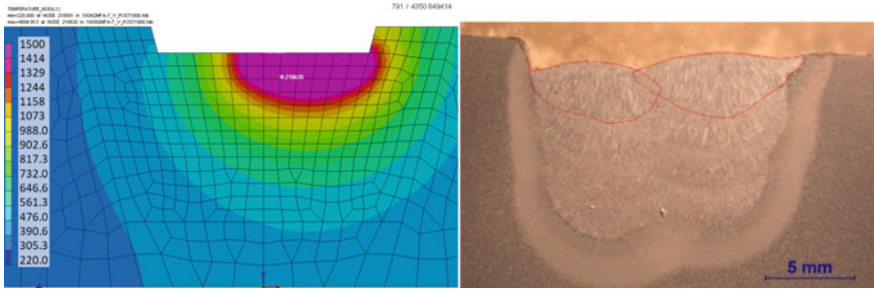
Fig. 5 An example of temperature distribution during heat source calibration for 8th bead (on the left) and macro view of real welded beads used for calibration comparison
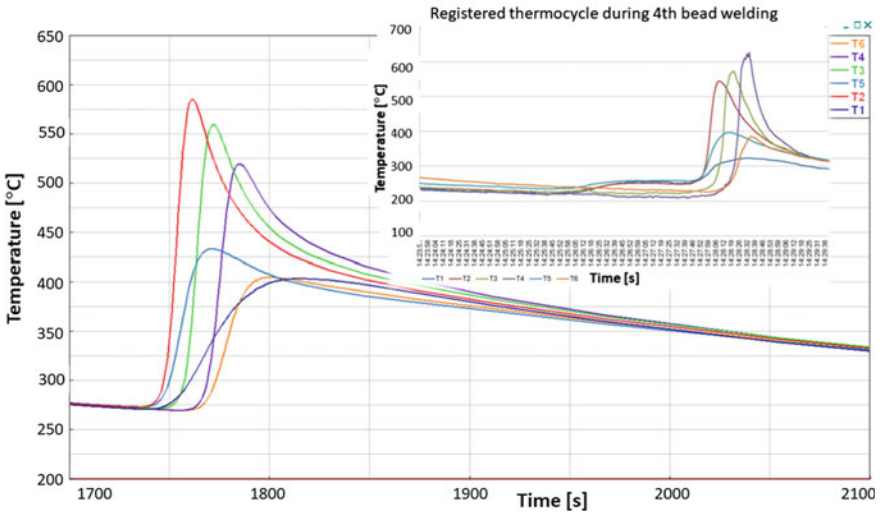
Fig. 6 Comparison of registered and calculated thermal cycles for all six thermocouples during welding 4th bead

For each welded bead, individual 3D model was calculated. Heat source model was calibrated to achieve the best correspond with real welding tests (comparison of molten areas on macro views and registered thermal cycles) as on Figs. 5 and 6. Based on the our experience, main attention was placed on the size and dimensions of the molten area as more efficient in heat source calibration procedure. Differences between the measured and calculated thermal cycles were because of the numerical model do not take into consideration that some of the beads were not welded to the end of specimen due to the macro investigation and hardness measurements (as it was explained earlier). As it was mentioned earlier, in the real experiment, first layer was welded to the end, second to 4/5 of the specimen length, third to the 3/5 etc. It means that in numerical model, total heat input was finally higher.
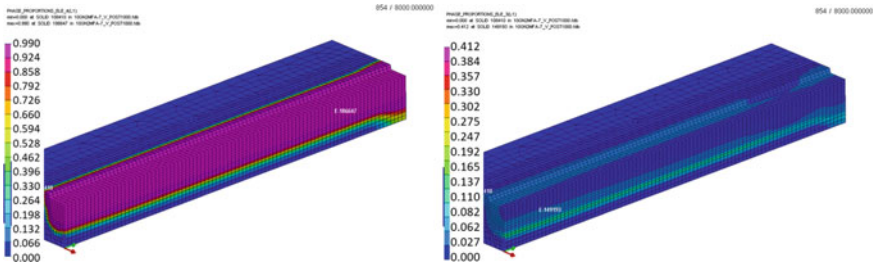
Fig. 7 Calculated bainite and martensite distribution after welding (longitudinal cross section in weld axis)
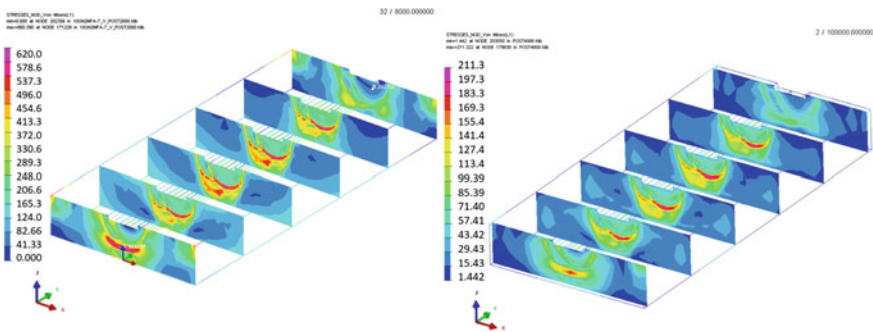
Fig. 8 Cross sections of calculated equivalent stresses (vonMises) distribution after welding (on the left side) and after post weld heat treatment (on the right side)

Metallurgical phases calculation indicates that in the area of weld is almost 100% bainitic structure. In the heat affected zone are present also small areas of martensite, up to the 15%, Fig. 7. Calculated values corresponds with the material properties and provided welding technology, especially used preheating and interpass temperatures.

Numerical analyses of stresses distribution confirms the thermo-metallurgical results. Values of calculated equivalent stresses (vonMises) and cumulative plastic strains are corresponds with used material. Maximal values of equivalent stresses are about 700 MPa which corresponds well with bainitic structure. After post weld heat treatment, values of stresses were decreased on level about 200 MPa. Also cumulative plastic strains values about 8% are acceptable for used base material, Figs. 8 and 9.

As it was written above, also results of hardness are important in this kind of analyses. Hardness on real specimen was measured in horizontal lines on the cross section of specimen on every welded layer. On Fig. 10 was shown as an example, distribution of hardness measured and calculated. Additionally there was presented standard and modified hardness calculation model. In case on 10GN2MFA steel differences are small because due to the chemical composition of welds it is possible to use standard SYSWELD hardness calculation model. In the area of base material these differences are higher. It can be explained with thesis that most of the hardness
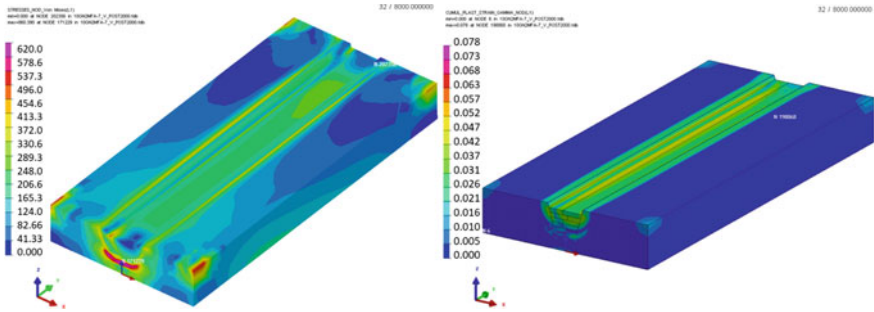
Fig. 9 Calculated equivalent stresses (vonMises) distribution after welding (on the left side) and cumulative plastic strength distribution (on the right side)
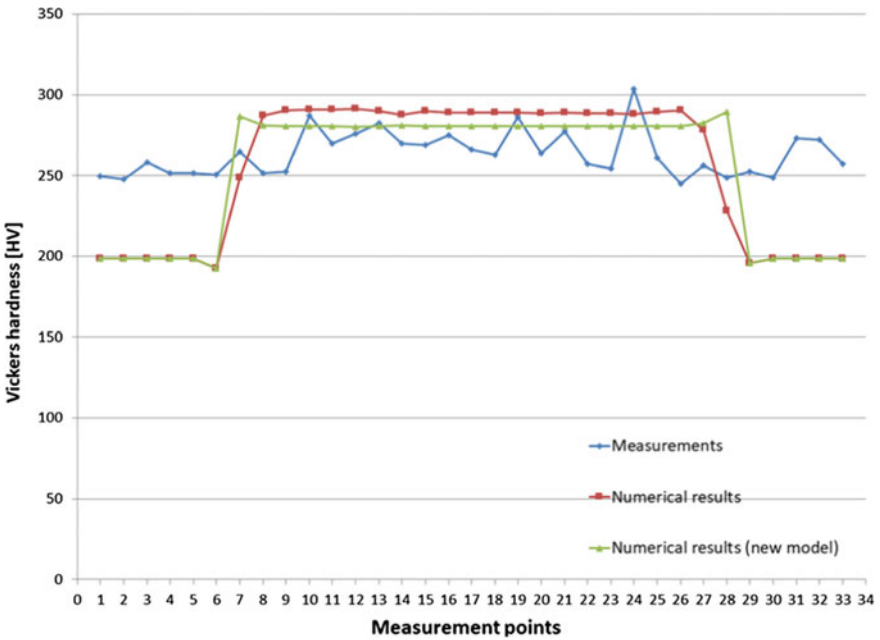
Fig. 10 Comparison of measured and calculated hardness distribution on 4th welded bead

prediction model are calibrated usually for "primary hardened" structures but in this case, base material of 10GN2MFA steel is usually hardened and tempered. And then, in case of primary structure definition for example martensite, values for primary hardened martensite are automatically calculated. In the results high values are calculated. Summarizing, it is recommended to define in every numerical analysis so-called initial hardness value independent on present primary structure [12].

4   Conclusions

Welding experiments are the most frequent method of numerical simulations input or verification data's collection. Aim of this work was to show how to correctly prepare and provide these experiments which are useful during acquiring input data's for numerical simulation of welding with preheating. It is good to provide the experiments for multilayer welds, because of every next bead multiplying eventually inaccuracy of simulation previous layer. Second thing is, that usually after 3 beads it is visible if used numerical model is correct or not. At multilayer welds is questionable mainly hardness calculation after application individual weld runs. New methodology of calculating hardness in SYSWELD results in situation that calculated values are closer to the measured in real tests. Of course it is still needed to improve hardness calculation models, because in the present, commercial simulation software unfortunately there is no exist hardness prediction models for high-alloy martensitic and bainitic steels. It is also very difficult to generally determine the influence of individual alloy elements on substitution reinforcement of solid solution and also precipitations with different thermodynamical stability. Because of it now is developed new equation which will be suitable for hardness calculations on tempering for martensitic and bainitic Cr-steels.

References

1. Nuclear Energy Institute website. https://www.nei.org
2. World Nuclear Association (WNA) US Nuclear Power Policy. http://www.world-nuclear.org/info/inf41_US_nuclear_power_policy.html
3. Nuclear Regulatory Commission (NRC) Power uprates for nuclear plants http://www.nrc.gov/reading-rm/doc-collections/fact-sheets/power-uprates.html
4. https://ocw.mit.edu/courses/nuclear-engineering/22–06-engineering-of-nuclear-systems-fall-2010/lectures-and-readings/MIT22_06F10_lec01.pdf
5. Jonšta, P., Vlčková, I., Krišták, L., Špička, I., Jonšta, Z.: Contribution to the thermal properties of selected steels. Metalurgija **54**(1), 187–190 (2015)
6. Coret, M., Calloch, S., Combescure, A.: Experimental study of the phase transformation plasticity of 16MND5 low carbon steel under multiaxial loading. Int. J. Plast **18**, 1707–1727 (2002)
7. Kik, T., Slovacek, M., Moravec, J., Vanek, M.: Numerical Simulations of heat treatment processes. Appl. Mech. Mater. **809–810**, 799–804 (2015)
8. Moravec, M., Kik, T., Novakova, I.: Application of numerical simulations on X10CRWMOVNB9-2 steel multilayer welding. MM Sci. J. **11**, 1190–1193 (2016). https://doi.org/10.17973/MMSJ.2016_11_201628
9. Welding simulation user guide 2016, Sysweld manual ESI Group
10. Joshi, S., Hildebrand, S., Aloraier, A., Rabczuk, T.: Characterization of material properties and heat source parameters in welding simulation of two overlapping beads on a substrate plate. Comput. Mater. Sci. **69**, 559–565 (2013)

11. Bergheau, J.M., Leblond, J.B.: Coupling between heat flow, metallurgy and stress-strain computations in steels—the approach developed in the computer code SYSWELD for welding or quenching. In: Proceedings of the vth Engineering Foundation Conference on Modeling of Casting, Welding and Advanced Solidification Processes Davos, Switzerland 1990
12. Kik, T., Slovacek, M.: Numerical simulation of 10GN2MFA welded plates post weld heat treatment, Technical report M_Z_13_021_r01. Plzen: Mecas ESI, 2013

Application of Time-Frequency Analysis of Acoustic Signal to Detecting Flat Places on the Rolling Surface of a Tram Wheel

Pawel Komorski, Tomasz Nowakowski, Grzegorz M. Szymanski and Franciszek Tomaszewski

Abstract The article presents the problematic aspects of detection of flat places on tram wheels using time-frequency analysis of acoustic signals. A number of pass-by tests were conducted during real life exploitation. The objects of research are light rail vehicles exploited in Poznan. Some of them were characterized by flat places on tram wheels. The research aimed to apply the wrought method for detection of flat places on tram wheels.

Keywords Wheel flats monitoring · Time-frequency analysis · Acoustic signal processing

1 Introduction

Public rail transportation is one of the most attractive modes of transportation in larger European agglomerations. Comfort is a very important factor on the basis of which passengers choose their mode of transportation. Vibroacoustic phenomena generated during a ride have a significant impact on the comfort of both the passengers and the nearby city dwellers. Number of inhabitants and passengers complain on annoyance vibroacoustic signals emitted by Poznan public rail transport during passage rise up [4]. Also public transportation operators and cities authorities are noticed the noise problem and the scale of this issue has to be reduced. The noise requirements for

P. Komorski (✉) · T. Nowakowski · G. M. Szymanski · F. Tomaszewski
Department of Rail Vehicles, Poznan University of Technology, 3 Piotrowo Street, 61-138
Poznan, Poland
e-mail: pawel.komorski@put.poznan.pl

T. Nowakowski
e-mail: tomasz.nowakowski@put.poznan.pl

G. M. Szymanski
e-mail: grzegorz.m.szymanski@put.poznan.pl

F. Tomaszewski
e-mail: franciszek.tomaszewski@put.poznan.pl

producers and also tram maintenance operators are increasing in terms of reduce the
main sound sources—rolling and traction noise [5, 8]. Particularly important is a
correct interaction between the rolling surface of a wheel and the rail. Imperfections
on rolling surfaces of wheels and rails—flat places in particular—contribute to the
increased level of noise and vibrations. One of the most annoying sounds during
rail journeys is the impact rolling noise which is caused by rail joints, switches and
crossings or irregularities on rail and wheel surfaces, called wheel/rail flats [7, 9, 10].
The example of the wheel flat, which was located on the both wheels on the last bogie
axis of examined tram, is shown in Fig. 1. When only wheel flats will be taken to con-
sideration, it is worth to diagnose and monitor them by the acoustic signal processing
in normal technical conditions. Another aspect confirming the necessity of detection
of flat places on tram wheels is minimizing tram exploitation costs. Moreover, early
detection of the problem increases the dependability of the transportation process.
Those are essential factors to rail vehicles and rail infrastructure managers.

The aim of the article is detection of tram wheel flats using the time-frequency
method on acoustic signals processing. Firstly, several exterior acoustic measure-
ments in pass-by test were carried out. Trams, which are still operated on Poznan
tram infrastructure, were taken as the research objects. Some of light rail vehicles
were equipped with wheels where the flat places are. Secondly, the acoustic signals
processing using proposed method based on the STFT (Short Time Fourier Trans-
form) analysis was performed. The results of research are presented and the proposed
method is applied on.

2   The JTFA Analysis Method

Joint Time-Frequency Analysis is an analysis method for non-stationary signals. This kind of method includes the STFT analysis and Wavelet Transform. Short Time Fourier Transform concerns short signal sequences FFT analysis in which it can be treated as quasi stationary. Extraction of the input signal of subsequent data segments for the FFT analysis is performed by means of the floating window method [2]. The comparison of spectra achieved in this manner gives, as a result, a time-spectra map of the analyzed process. Definitional STFT record can be presented by means of the dependence (1).

The STFT result can be treated as a series of spectra determined for local, short time segments of time history. The advantages of this method include, among others, short calculation time necessary to define time-frequency map, easy, intuitive interpretation of results and constant resolution within the whole frequency range.

$$STSF[x_w(t, \tau)] = X_w(f, \tau) = \int_{-\infty}^{\infty} w(t, \tau)x(t) \cdot e^{-i2\pi ft} \, dt \tag{1}$$

where: x(t)—time course representing analyzed input signal; w(t)—time window function (tapering function); τ—position of time window in time domain.

The form of analysis result depends on the assumed time window function and signal processing parameters: the number of samples in data segment and time step of the analysis. There are some limitations of this method which include, for example, lack of possibility to achieve, at the same time, high resolution in time and frequency domains. Resolution in time domain can be improved by applying overlapping which is partial covering of analyzed segments of the signal. The error of amplitude and frequency estimations for local maximum values of a map can be minimized by applying amplitude—frequency AFC correction [1, 3].

In Wavelet Transform, any functions [6] can be used as mother functions. Due to the simplification of the calculation process, in many cases Morlet's function is used as mother function. Its application allows using the FFT procedure which effectively accelerates the calculation process. The result form, to a great extent, depends on the assumed mother functions. The definition of Wavelet Transform is presented by the following dependence (2) [6]:

$$WT(a, b) = \frac{1}{\sqrt{a}} \int_{-\infty}^{\infty} x(t)\Psi^*\left(\frac{t - b}{a}\right) dt \tag{2}$$

where: Ψ (t-τ)—mother function (wavelet); a—scale, parameter connected with localization in frequency domain (dilation, scale); b—parameter indicating position in time domain (translation); Ψ^*—conjugate function of Ψ function (.).

This type of analysis can be compared to filtration with the constant relative width of the Δf/fs band. The position of filter on the time-frequency map is defined by scale

and translation parameters (a—dilation, b—translation). Together with the translation towards higher frequencies, analysis band width increases (analysis resolution is decreased in domain of frequency), whereas, resolution in domain of time is increased and the other way round. This feature can be very useful in case of simultaneous analysis and observation with a different time step of quick-changing high frequency (e.g. vibrations of car body or vibrations of the wheel) and slow-changing low-frequency processes. One of the disadvantages of this method is dependability of the result form on the assumed mother function, and not always intuitive interpretation of the graphical form of result.

To summarize the overview of vibration signals analysis methods, it has been concluded that in order to obtain diagnostics opinion about examined object, simple analysis methods e.g. assigning point measures, as well as highly advanced methods—from the signal processing point of view, e.g. time-spectrum analysis, can be used. In this work, to monitor the impact noise caused by wheel flat during tram passage, the analysis of acoustic signals was used.

3 Research Methodology

3.1 Measurements Assumptions

The experimental research stage involved exterior acoustic measurements during pass-by test. Measurements were carried out on a straight section of the track, located in the Poznan Franowo depot. The tram's speed was about 10–20 km/h. Furthermore, measurements have performed during late evening hours, when all trams were going back to depot. Thus, all types of light rail vehicles, which are operated on Poznan tram infrastructure, were a research objects. Among all research objects, one of the trams had wheels flat, which was very important aspect in case of next research analysis. Furthermore, there was made few more acoustic measurement series on the selected tram, with different tram's speed −20, 30 and 40 km/h. Impact noise emitted by this tram was taken to further signal processing.

3.2 Measurement Points

In Fig. 2 is shown the scheme of measuring position. Three microphones were used to acoustic measurements, located in proximity of 2 m from the track. All electroacoustic transducers were spread along the track at a distance of 2.04 m which is the length of each tram wheel circumference. It means one full wheel rotation period during passage will be made at this distance. Thus, authors have made sure that all acoustic signals caused by wheel flats will be recorded in proper way.
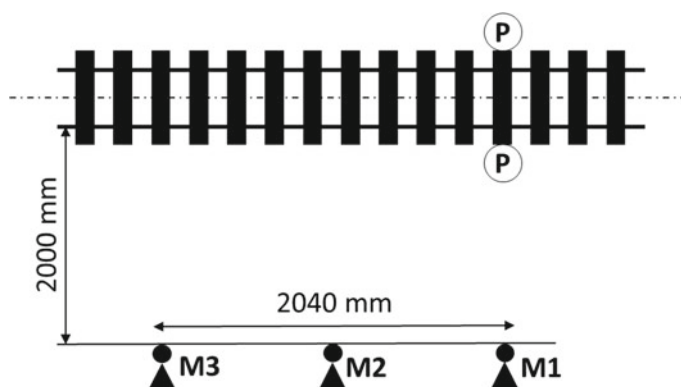
Fig. 2 The scheme of measuring position in the pass-by test; M—Microphones, P—photocells

In the measurement cross section, between the tracks, a transmitter-receiver type photocell was placed (Fig. 2). It allowed for introduction of time selection of the processed signals, in which the tram was found in the measuring cross section of the track—on the microphone1-photocell line. Also, the speed of tram's ride was calculated on the basis of the recorded signal.

3.3 Measurement Devices

Recording of acoustic signals was conducted with use of measurement devices from a Danish firm Brüel and Kjær Sound and Vibration A/S. The measuring equipment scheme is shown in Fig. 3.

To acoustic measurements were used following equipment:

- microphones type 4189-A-021,
- two Autonics Photocells type BX15M-TDT,
- the data acquisition system PULSE LAN-XI type 3050-A-060,
- mobile computer,
- router Wi-Fi.

Before the measurements, the calibration process of each measuring devices, was performed.

3.4 Parameters of Recording Acoustic Signals

Registering of acoustic signals for exterior measurements was conducted constantly in a full measurement spectrum of 25.6 kHz, with sampling frequency of 65,536
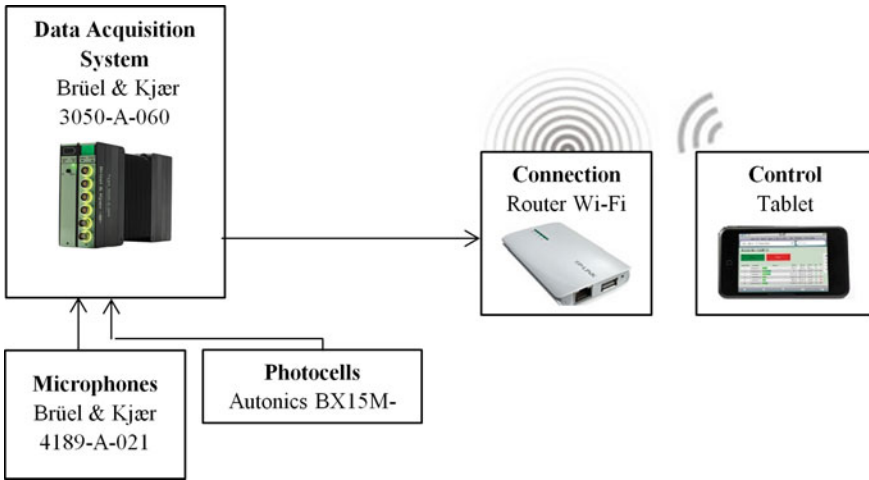
Fig. 3 The measuring equipment scheme used to research

samples per second. The signals were recorded synchronously in all measurement points and channels. Duration of signals was dependent on the speed and length of the tram passing through the measurement cross section, and was about 4–10 s.

4 Research Results

4.1 Research Analysis

After acoustic measurements, authors have picked four sound records for further analysis. The four STFT analyses are shown in Fig. 4. Sound records from the first microphone were taken to all analysis. The Mik1_Good chart presents the reference sound recorded during the Moderus Beta No. 916 ride. There was no wheel flat problem in this case. While next three charts (Mik1_20, Mik1_30 and Mik1_40) show the Moderus Beta No.920 rides with different tram's speed. The sound pressure was much higher than in the first example. Especially in the low and medium frequency range, the regular brighter stripes (higher sound pressure) can be observed. Wheel flats are the reason of the impact noise occurring.

Based on the STFT analysis, two main frequency bands were chosen: 100–300 and 1150–2125 Hz. The filtered FFT analyses of four acoustic signals are shown in Figs. 5 and 6. Sound pressure of Mik1_30 and Mik_40 are the highest on both figures. While the sound pressure of Mik1_20 is higher than Mik1_good only in the Fig. 5. It means that tram's speed has influence on the impact noise magnitude and
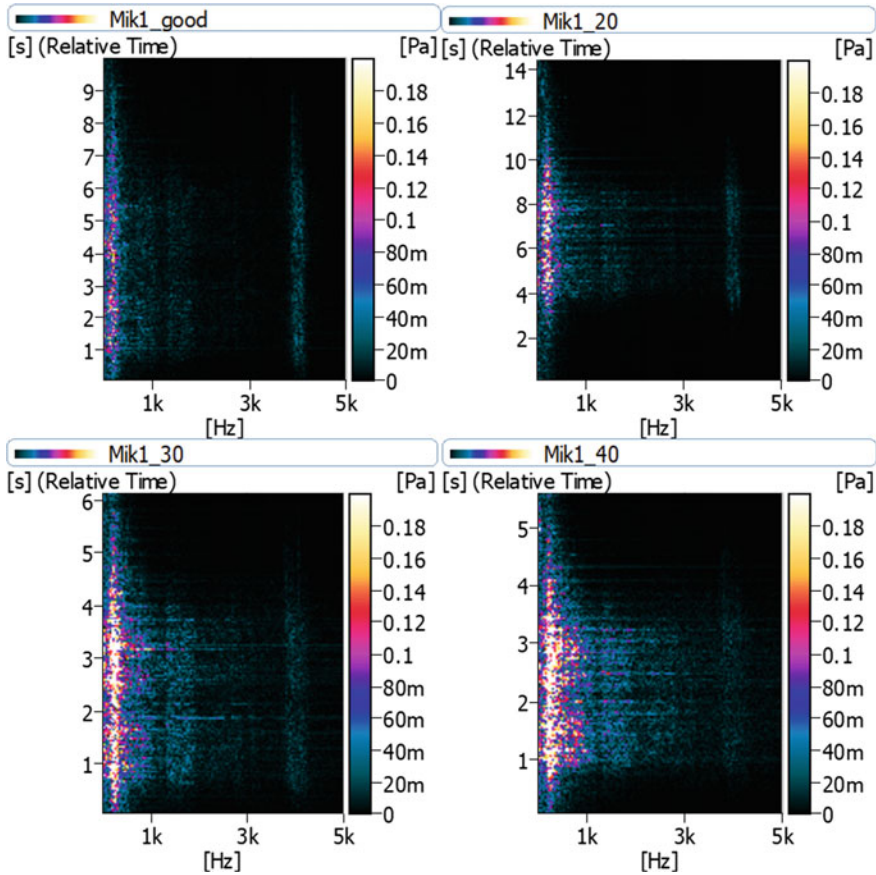
Fig. 4 The first step of acoustic data processing—the STFT analysis

frequency. Therefore, if tram's speed is about 20 km/h and lower it will be hard to find the wheel flat based on the second filtered FFT analysis.

All RMS values were calculated in accordance to the Eq. (3)—which is an energetic averaged root mean square value taken from filtered FFT analysis:

$$S_{rms} = \sqrt{\sum_{i=1}^{n} |x_i|^2}$$

(3)

where: x_i—is the sound pressure value in the ith frequency band.

The reference RMS value S_{ref} was calculated from Mik1_good sample and it is equal to 11 mPa (nearly 55 dB) in case to the first filtered FFT range (Tables 1 and 2). This is 1.5 times (3.5 dB) less than in the Mik1_20 case and about 3 times (about 9.5 dB) less than next two examined cases. It means the wheel flat problem has
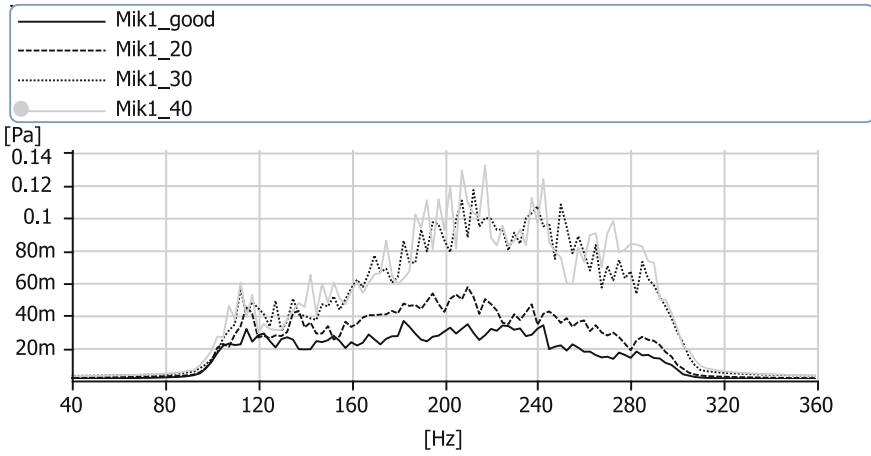
Fig. 5 Filtered FFT analysis in the first frequency range: 100–300 Hz
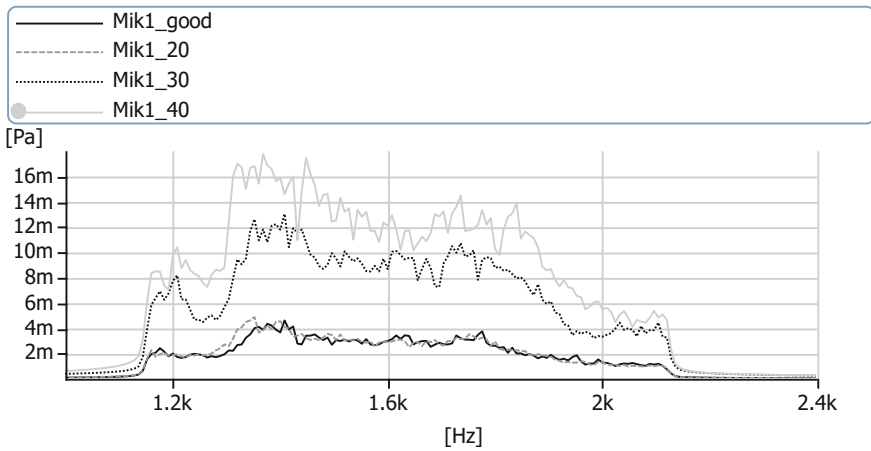
Fig. 6 Filtered FFT analysis in the second frequency range: 1150–2125 Hz

occurred and tram wheels should be serviced. In case to the second filtered frequency range, only the S2 and S3 RMS values are significant higher (by 3–4 times) than S_{ref} which means the impact noise problem. The differences expressed in decibels unit are even higher—nearly by 10 and 13 dB (Table 2).

Table 1 Root mean square values and differences related to the reference value S_{ref} in mPa

		RMS values			
		f: 100–300 Hz		f: 1150–2125 Hz	
		mPa	S_{ref}/S_i	mPa	S_{ref}/S_i
Mik1_good	S_{ref}	10.97	–	1.44	–
Mik1_20	S1	16.48	1.50	1.49	1.03
Mik1_30	S2	32.04	2.92	4.45	3.09
Mik1_40	S3	33.84	3.09	6.24	4.33

Table 2 Root mean square values and differences related to the reference value S_{ref} in dB

		RMS values			
		f: 100–300 Hz		f: 1150–2125 Hz	
		dB	$S_{ref} - S_i$	dB	$S_{ref} - S_i$
Mik1_good	S_{ref}	54.78	–	37.15	–
Mik1_20	S1	58.32	3.54	37.44	0.29
Mik1_30	S2	64.09	9.31	46.95	9.80
Mik1_40	S3	64.57	9.79	49.88	12.74

4.2 Algorithm of the Acoustic Signals Processing

Authors elaborated the algorithm for sound pressure processing in case to monitor and diagnose wheel flats (Fig. 7). Based on recorded acoustic signals and proposed time-spectrum analysis method, the decision can be made if tram wheels should be serviced. First step is to carry out acoustic measurements s(t) during tram ride. Authors used three measurement points however one microphone placed near track should also be good for further analysis. Also tram's speed is very important parameter and has to be calculated or measured. If tram's speed is less than 30 km/h, the tram's ride should be repeated with higher speed, to make sure of proposed method validity. The STFT analysis in the full range of signal spectrum is the next step of the algorithm. Characteristic frequency bands, where sound pressure amplitude increased in unnatural way (in comparison to reference acoustic signals where no wheel flat problem occurred), are pointed. The frequency filter to reject unwanted bands is applied in next algorithm step. Then, energetic root mean square value is calculated. Critical RMS value S_c should be averaged from the same types of vehicle. Also the standard deviation should be added. If examined RMS sound pressure value S is bigger than critical value S_c, it means there is a wheel flat problem and service or technical checking of tram wheels should be made.
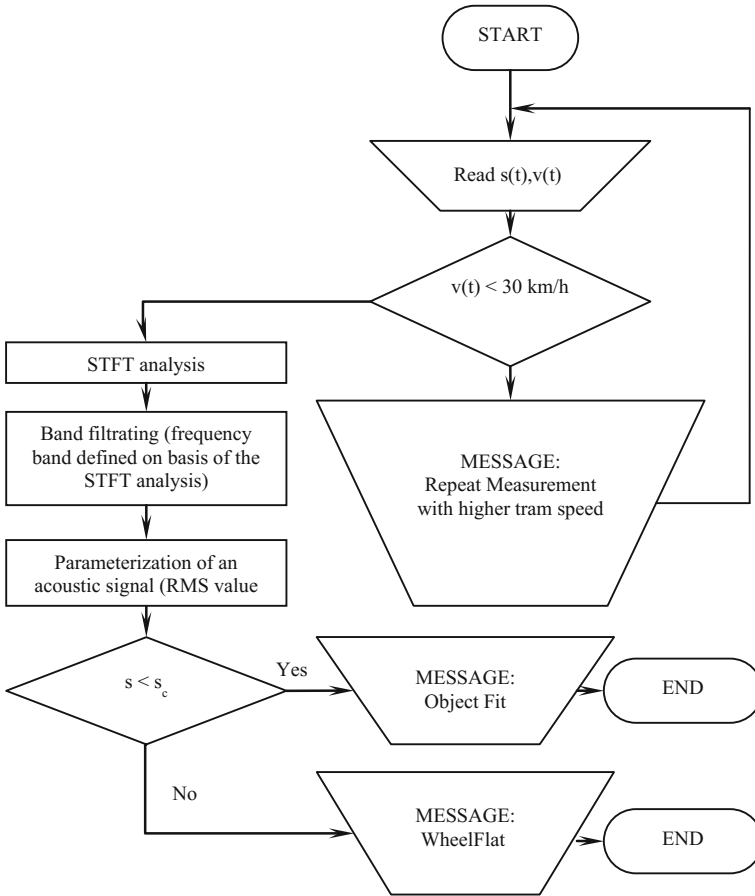
Fig. 7 Algorithm of the acoustic signal processing to diagnose wheel flats

5 Conclusions

Based on the research, authors proved that there is a possibility to monitor and diagnose wheel flats using acoustic signal processing—the algorithm of analysis was proposed. The time-spectrum method allows locating the wheel flat on the rail vehicle. Furthermore, the STFT analysis enables the frequency band detection, in which the system response to the impact excitation. Here, the impact excitation means dynamic wheel-track interaction when the wheel flat appears. The 100–300 and 1150–2125 Hz frequency bands are characteristic spectrum for examined tram. Research shows that analysis is not suitable when rail vehicle velocity is about 20 km/h because the difference between examined RMS sound pressure and critical sound pressure S_c should be at least 6 dB (in the research it was equal to 3.5 dB). Above the rail vehicle velocity of 25–30 km/h, proposed algorithm is well-founded.

There is a lot of different kind of methods and approaches for detection of rail wheel defects. A vibration technique (where vibration signal is processed) seems to be the most popular one. In this article authors proposed acoustic approach which is also easy in usage and cheap in production. Based on proposed method can be designed the monitoring system which can be applied on every tram depot. This could successfully contribute to decrease vibroacoustic emission around tram infrastructure and improve the passengers' comfort.

References

1. Barczewski, R.: AFC—the method of amplitude spectrum correction. In: Proceedings of The Congress of Technical Diagnostics, vol. 2, 17-20.09.1996, Gdansk, pp. 79–54 (1996)
2. Barczewski, R.: Application of the short time fourier transform (STFT) with amplitude and frequency correction (AFC) to non-linear system free vibration signal analysis. Report: CRI Universitat Hannover, Nov 1997 (1997)
3. Barczewski, R.: Analysis of non-linearity using STSF-AFC as a diagnostic method. In: Proceedings of The II International Congress of Technical Diagnostics. 19-22.09.2000, Warsaw, pp. 29–30 (2000)
4. Facebook Social Group "Spotted: MPK Poznan" (2017) P: Tymczasem w tatrze… Przecież to się jechać nie da https://www.facebook.com/332551400182715/videos/1127014797403034/. Accessed 27 Apr 2017
5. Komorski, P., Nowakowski, T., Szymański, G.M., Motyl, M.: The Comparison analysis of sound level emitted by various tram bogies under normal operating conditions. In: 24th International Congress on Sound and Vibration. 23-27.07.2017, London, pp. 1–8 (2017)
6. Newland, D.: Practical signal analysis: do wavelets make any difference? In: Proceedings of DTC'97 ASME Design Engineering Technical Conference. 14-17.09.1997, Sacramento, California (1997)
7. Nielsen, J.C.O., Igeland, A.: Vertical dynamic interaction between train and track influence of wheel and track imperfections. J. Sound Vib. **187**, 825–839 (1995). https://doi.org/10.1006/jsvi.1995.0566
8. Orrenius, U., Carlsson, U.: Attractive train interiors: minimizing annoying sound and vibration. KTH Railw Gr. (2013). https://doi.org/10.1007/978-3-662-44832-8_84
9. Wu, T.X., Thompson, D.J.: On the impact noise generation due to a wheel passing over rail joints. J. Sound Vib. **267**, 485–496 (2003). https://doi.org/10.1016/S0022-460X(03)00709-0
10. Yang, J., Thompson, D.J.: Time-domain prediction of impact noise from wheel flats based on measured profiles. J. Sound Vib. **333**, 3981–3995 (2014). https://doi.org/10.1016/j.jsv.2014.04.026

Development of a Prototype Dynamic Weighing System for Single Bucket Excavator

Andrzej Kosiara, Jakub Chołodowski and Aleksander Skurjat

Abstract Some earthmoving works performed by single bucket excavators require on-line weighing of material transported by excavator's bucket. Such measurements are critical e.g. for optimal loading of dump trucks. The first commercially available payload weighing systems for single bucket excavators were called static systems. To properly estimate bucket load, the machine equipped with them had to be kept in a standstill condition for a few seconds. Consequently, productivity of the machine was low. Recently dynamic weighing systems have been introduced. These systems enable to precisely weigh the material collected in the bucket while swinging excavator's house as well as moving its boom, arm or bucket. Thus, they do not influence productivity of the machine. Such systems are commercially available nowadays. Development of reliable dynamic weighing systems requires certain problems to be resolved. Firstly, the influence of acceleration acting on excavator's bodies and bucket payload has to be taken into account. Values of pressure inside cylinders supporting excavator's boom, which are usually used as input signals for payload mass computation, significantly differ in dynamic and static conditions. In order to provide satisfactory weighing performance, internal friction of hydraulic cylinders cannot be also omitted. A prototype dynamic weighing system for single bucket excavator developed in The Department of Off-Road Machine and Vehicle Engineering (Wrocław University of Science and Technology) will be presented in the article. While estimating bucket payload the system allows for acceleration acting on excavator bodies as well as hydraulic cylinders friction.

Keywords Single bucket excavator · Operator assistance system · Payload monitoring

A. Kosiara (✉) · J. Chołodowski · A. Skurjat
The Department of Off-Road Machine and Vehicle Engineering, Wrocław University of Science and Technology, ul. Łukasiewicza 7/9, 50-371 Wrocław, Poland
e-mail: andrzej.kosiara@pwr.edu.pl

J. Chołodowski
e-mail: jakub.cholodowski@pwr.edu.pl

A. Skurjat
e-mail: aleksander.skurjat@pwr.edu.pl

1 Introduction

Single bucket excavators are often utilized to load different types of loose materials onto dump trucks. The tucks might be loaded with material deposited on heaps as well as with winnings dug directly from the ground. In both cases current weighing of the material loaded onto dump truck's bed is a crucial issue. If mass of the material is monitored while loading, actual overall truck's payload can be set very close to the maximum permissible load of the truck with no risk of overload. Consequently, amount of material transported by the truck is maximized and regulations concerning maximum permissible axle loads are respected.

In practice, weight of dump truck payload might be monitored in two ways. Firstly, an excavator can be fitted with an onboard payload weighing system. Secondly, stationary weighing devices, so called weighbridges, might be applied. In the vast majority of cases weighbridges located on construction sites are situated remotely from the places where excavators operate. Thus, they are not as convenient as mentioned onboard weighing systems.

Onboard payload weighing systems weigh the material loaded with excavator's bucket onto truck's bed in every work cycle of the machine. Consequently, overall truck's payload is calculated as a sum of masses measured in consecutive work cycles. Nowadays, two main types of onboard weighing systems may be distinguished—static systems and dynamic systems.

"Static system" and "dynamic system" phrases are trade names widely used by vendors to promote their products as well as to define key capabilities of the systems. In case of static systems, in order to determine bucket payload with acceptable precision, the excavator has to be kept in a standstill condition for a short period of time during every work cycle. On the other hand, dynamic systems, introduced recently to the market, do not require any machine holdups to properly estimate weight of the payload. Hence, productivity of the machine is improved and operator's work becomes easier.

1.1 Dynamic Payload Weighing Systems for Single Bucket Excavators—Overview

Numerous dynamic onboard weighing systems for single bucket excavators are available nowadays. Some of them have been discussed in work [1]. X2350 by Trimble Loadrite Auckland Ltd. and Loadex 100 by RDS Technology Ltd. are great examples of such systems.

Dynamic weighing systems are typically composed of sensors which measure angular position of boom and arm of an excavator as well as oil pressure inside hydraulic cylinders supporting the boom (see Fig. 1). Inclination sensors are also attached to the excavator's house to compensate bucket load estimation error caused by ground surface inclination. Furthermore, the excavator might be optionally fitted

Fig. 1 Components of Load Rite X2350 system by Trimble [6]: 1—inclination sensor for determination of angular position of bucket, 2—inclination sensor for determination of angular position of boom, 3—control panel (HMI), 4—sensors for determination of ground inclination, 5—wireless data transmission device (wi-fi, GPRS, radio communication), 6—printer, 7—sensors for determination of oil pressure inside boom positioning hydraulic cylinder/cylinders

with sensor for determination of work tool angular position, which also improves accuracy of the system.

Most of manufacturers of dynamic weighing systems claim that accuracy of their products is at least ±3%. Nevertheless, such accuracy can be obtained only under some specific conditions:

- excavator performs smooth movements,
- bucket is located in so called weighing zone (see Fig. 2),
- calibration of the system is periodically repeated by the operator during machine operation.

In order to calibrate the system, excavator performs certain sequence of movements. There is no universal calibration motion sequence. Sequences for systems elaborated by various manufacturers are different. However, all calibration procedures involve some motions of excavator's bodies, including motions of empty bucket. In case of some particular systems, movements of excavator's bodies and the bucket filled with the material are also required.

During calibration the system collects data vital for determination how oil pressure inside cylinders supporting excavator's boom is affected by mass of excavator's bodies and cylinder/cylinders internal friction, i.e. friction between barrel, piston, rod and seals. As it was previously mentioned, while the machine is being operated, calibration has to be periodically repeated in order to maintain accuracy of the system at

Fig. 2 Weighing zone of Trimble Loadrite X2350 payload weighing system [6]
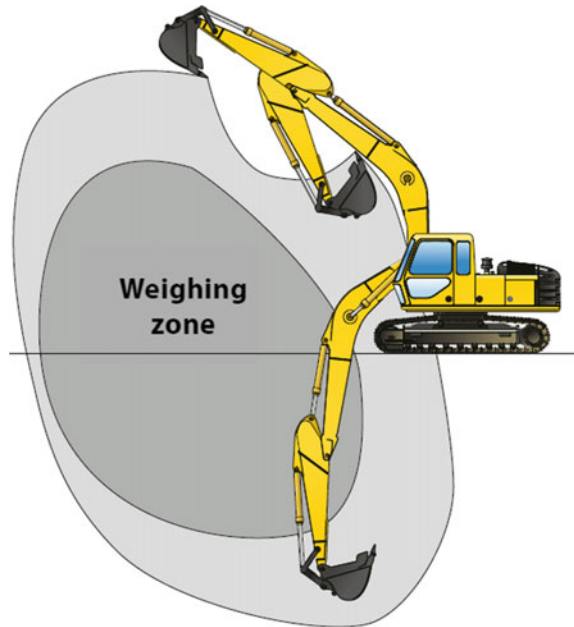
level claimed by the manufacturer. Such a need results from fluctuations in hydraulic cylinders internal friction. Actually, cylinder internal friction strictly depends on oil temperature which significantly changes while excavator is being operated.

Operation algorithms of commercially available weighing systems are know-how of their manufacturers. Hence, they are not published. On the other hand, exemplary weighing systems developed at technical universities around the world have been presented in following papers [2–5]. These systems are based on various computational algorithms, however, the systems involving neural networks are particularly interesting [3, 5].

2 Concept of Original Onboard Payload Weighing System for Single Bucket Excavators

Concept of weighing system developed by the authors have been elaborated in such a way that various modifications and improvements might be easily introduced. Basically, the concept was intended to be a test platform that would enable to verify wide spectrum of weighing system variants and solutions. After research and development phase, basing on gained experience, a new, comprehensive, innovative weighing system was intended to be built using the same hardware.
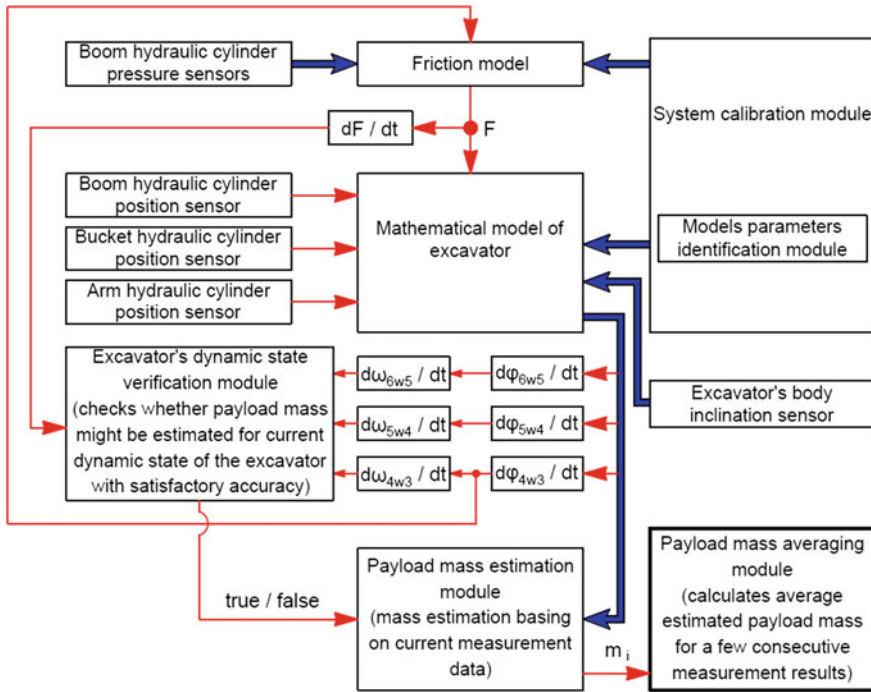
Fig. 3 Flow chart of onboard payload weighing system for single bucket excavators presented in the article

According to nomenclature introduced by Trimble Loadrite Auckland Ltd., the developed concept is a 2D-type weighing system. It means that bucket load can be determined by the system only if excavator's house does not perform swing motion.

Figure 3 depicts a flow chart of the system which has been designed and built by the authors. At the very beginning of operation, calibration procedure is performed. Firstly, constants defining kinematic structure of the excavator are uploaded. In the following calibration phase parameters of boom cylinder internal friction model are estimated. Eventually, mass as well as center of mass coordinates for each main body of the excavator are identified.

Mentioned parameters are mostly the parameters of mathematical model of the excavator. The model is based on equations of static equilibrium and enables to determine mass of the material collected inside the bucket. Apart from above parameters, in order to calculate the payload, value of force delivered by hydraulic cylinder supporting excavator's boom is required by the model. In case of the developed system, force delivered by excavator's boom cylinder is calculated on the basis of oil pressure measured inside both chambers of this cylinder, according to equations presented below:

$$F = \begin{cases} p_d \cdot A_d - p_g \cdot A_g - F_{T\text{-}P} & \text{if the boom is raised} \\ p_d \cdot A_d - p_g \cdot A_g + F_{T\text{-}O} & \text{if the boom is lowered} \end{cases} \tag{1}$$

Nomenclature applied in Eq. (1) is as follows:

- p_d—oil pressure measured in lower chamber of the cylinder (cap end side chamber),
- p_g—oil pressure measured in upper chamber of the cylinder (rod end side chamber),
- A_d—piston area at cap end side,
- A_g—piston area at rod end side,
- $F_{T\text{-}P}$—cylinder internal friction force during raising the boom,
- $F_{T\text{-}O}$—cylinder internal friction force during lowering the boom.

Internal friction of a hydraulic cylinder depends on numerous factors, e.g.: current rod velocity and acceleration, oil pressure inside both chambers of the cylinder, oil temperature etc. Hence, only sophisticated models provide comprehensive and precise description of cylinder internal friction. Static friction models, such as Tustin's model, are definitely not suitable in this case. So called dynamic friction models had to be applied to properly describe all triblogical phenomena occurring in hydraulic cylinders. One of the first models used to estimate internal friction of hydraulic cylinders was LuGre model. Unfortunately, it quickly turned out to be insufficient. Thus, numerous modifications of LuGre model have been elaborated so as to increase its accuracy in cylinder internal friction estimation. The problem of theoretical description of hydraulic cylinders internal friction has been discussed in more details in [7].

Nevertheless, in practice implementation of such sophisticated friction models brings serious problems, since numerous parameters have to be identified as well as complex identification procedures need to be carried out. Consequently, cylinder internal friction model applied in the developed weighing system was simplified. The following key assumption was made: if the cylinder's rod moves in certain direction at specified speed, cylinder internal friction force does not change. Research discussed below was carried out to verify whether such assumption would diminish the accuracy of bucket payload weight estimation.

Basing on mathematical model of the excavator two moments acting on excavator's boom are determined. The first moment (M_Q) is caused by manipulator's weight, whereas the second one (M_F) by the force delivered by boom cylinder. Both moments are calculated about a reference axis that coincides with the axis of rotation of the boom with respect to the excavator's house. Mathematical model of the excavator is also involved in determination of a horizontal distance (d_l) between center of mass of the bucket payload and axis of rotation of the boom with respect to the excavator's house. Both moments M_F and M_Q as well as distance d_l are put into the Eq. (2) to estimate mass of the material collected inside the bucket.

$$m_i = \frac{(M_Q - M_F) \cdot g}{d_l} \tag{2}$$

The mass of payload is calculated only if specified module of the weighing system positively verifies dynamic state of the excavator. Excavator's dynamic state is accepted by the module if conditions listed below are fulfilled:

- rod of the cylinder supporting the boom moves at velocity higher than predefined threshold speed,
- boom cylinder oil pressure change rate is smaller than predefined maximum pressure change rate,
- angular acceleration of the boom measured with respect to the excavator's house is smaller than predefined threshold angular acceleration,
- angular acceleration of the arm measured with respect to the boom is smaller than predefined threshold value,
- angular acceleration of the bucket measured with respect to the arm is smaller than predefined threshold value.

Despite constraints given above, at least tens of payload mass estimates can be successfully calculated during every work cycle of the excavator. The average value of several consecutive results, which is continuously calculated during system operation, is treated as an ultimate payload mass measurement result.

3 Estimation of Mass Parameters of Excavator's Manipulator Bodies

Estimation of mass parameters of excavator's bodies is crucial for successful calibration of the weighing system developed herein. What is more, other operator assistance systems might require these parameters as well [8].

The procedure for identification of mass parameters of the excavator, which has been developed and tested in the article, comprises of measurement phase and computational phase.

During the measurement phase length of each cylinder of the excavator's work gear as well as oil pressure inside the cylinder/cylinders supporting the boom are measured. The measurements are conducted for different manipulator configurations, while the boom is being lifted up and lowered at constant, relatively low, angular speed.

Afterwards, the measured values are uploaded to a computational module of the system and applied to create a criterion function, whose minimum is sought. Criterion function is a mathematical function which equals to zero if there is no difference between actually measured boom cylinder force and its respective value calculated on the basis of mathematical model of excavator's manipulator. The bigger the difference becomes, the higher the value of the criterion function is. As a result of optimization process, parameters of manipulator model are adjusted in such a way that the value of criterion function is set as close to zero as it is possible. The criterion function in generally represented by following equation:

$$\min\left\{\sum_{i=1}^{n}(F_i(F_{T\text{-}P}, F_{T\text{-}O})\right.$$

$$\left.-[F_{s:i}(x_{CG\text{-}III}, \ldots, x_{CG\text{-}n}, z_{CG\text{-}III}, \ldots, z_{CG\text{-}n}, m_{III}, \ldots, m_n)]_{L_{1:i}, L_{2:i}, L_{3:i}}\right)^2\right\} \qquad (3)$$

Nomenclature applied within Eq. (3) is as follows:

- i—index of manipulator configuration,
- F_i—estimate of force delivered by boom cylinder/cylinders calculated using oil pressure measured for i-th manipulator configuration; force F_i depends on one of optimization variables (friction force) F_{T_P} or F_{T_O},
- $[F_{s:i}(\ldots)]_{L1:i, L2:i, L3:i}$—mathematical function representing force delivered by hydraulic cylinder/cylinders supporting the boom; the function depends on mass parameters of the manipulator bodies as well as length of hydraulic cylinders determined in measurement phase,
- $L_{k:i}$—length of k-th hydraulic cylinder measured for i-th manipulator configuration,
- $x_{CG\text{-}III}, \ldots, x_{CG\text{-}n}, z_{CG\text{-}III}, \ldots, z_{CG\text{-}n}, m_{III}, \ldots, m_n$—sought mass parameters of movable bodies of manipulator—optimization variables,
- $x_{CG\text{-}j}, z_{CG\text{-}j}$—coordinates of center of mass of j-th manipulator's body represented in local coordinate system of j-th body,
- m_j—mass of j-th manipulator's body,
- n-3—number of movable bodies of the manipulator taken into account by manipulator's model.

In case of the prototype weighing system presented herein, computational module for determination of parameters of particular mathematical models implemented in the system was created in MATLAB environment. In order to find minimum value of criterion function given by Eq. (3) the module uses fmincon function which is a standard solver available in MATLAB environment for finding minimum of constrained nonlinear multivariable function.

Discussed method for estimation of mass parameters of excavator's manipulator model was verified indirectly. To do so, a test stand fitted with a mini-excavator's arm depicted in Fig. 4 was used. Firstly, oil pressure in both chambers of boom cylinder was measured for specified configurations of the manipulator and actual forces delivered by the cylinder were calculated. Secondly, manipulator's mathematical model as well as cylinder internal friction model were applied to calculate mentioned forces for respective manipulator configurations. Difference between actually measured and calculated forces became a measure of overall accuracy of the elaborated model as well as effectiveness of mass parameters and friction model parameters estimation. Comparison between forces estimated by means of mathematical models with forces calculated directly on the basis of oil pressure revealed that relative error of force estimation did not exceed 1%. Thus, accuracy of the models is satisfactory.

Fig. 4 Test stand fitted with
a mini-excavator's
manipulator for validation of
mathematical models'
parameters identification
procedure and testing of the
prototype weighing system
for single bucket excavators

4 Original Onboard Weighing System for Single Bucket Excavators—Implementation and Research

A prototype onboard payload weighing system for single bucket excavators based on the concept presented in paragraph 2 had been built, which enabled to check whether assumed simplifications of implemented computational algorithms were allowable. Efficiency of the algorithms could have been also verified.

Control unit as well as HMI control panel, typical for commercially available weighing systems, were replaced with a single National Instruments industrial PC, which reduced prototype implementation cost. The PC was fitted with NI PXIe-6341 multifunction I/O module which provided appropriate connection between the PC and all sensors of the system.

Two ATM.1ST pressure sensors by STS Sensor Technik Sirnach AG were applied to measure oil pressure inside chambers of hydraulic cylinder supporting excavator's boom. To avoid errors caused by oil temperature fluctuations, which usually occur during excavator's operation, pressure sensors with temperature compensation were applied. Current length of hydraulic cylinders was determined by means of Baluff BTL5 magnetostrictive linear position sensors which were embedded inside the cylinders. BTL5 sensors are capable of linear position measurement with 1 kHz frequency, 5 μm resolution and accuracy better than $\pm 0.02\%$ F.S.O. Software of the weighing system was implemented in LabView development environment.

The prototype weighing system was installed on a test stand equipped with a mini-excavator manipulator, depicted in Fig. 4. Before main series of experiments calibration procedure was carried out using software implemented in MATLAB environment (as discussed in paragraph 3).

Every conducted experiment came down to a comparison between mass of a weight put into bucket estimated by the system and actual mass of the weight, which was known a priori. During weight mass estimation bodies of excavator performed certain, defined in advance, sequences of motions. Multiple experiments in different test conditions were conducted. During every experiment mass of the weight put inside the bucket as well as acceleration of manipulator bodies were different. The experiments were also conducted in various areas of excavator's working zone. Exemplary results are depicted in Fig. 5. In the Fig. 5, full red line represents mass of bucket payload estimated by the system using only equations of static equilibrium for all dynamic states of the manipulator. On the other hand, full black line represents average payload mass estimated only for dynamic states identified by the system as the states in which payload mass could have been calculated with acceptable accuracy (see conditions listed in paragraph 2). Analysing the data obtained as a result of the whole series of experiments, it might be stated that relative error of payload mass estimation did not exceed 5%. Moreover, the research reveals that during typical work cycle of an exemplary excavator the system is able to identify 60…100 dynamic states in which mass of payload can be estimated with acceptable precision. Eventually, it was observed, that mass estimation error increases if the piston of the boom cylinder reaches one of its end positions.
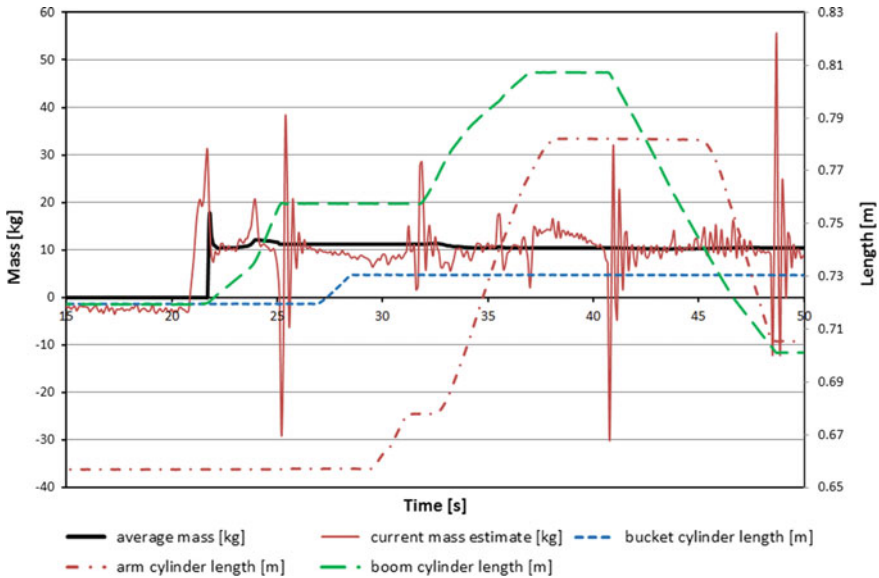
Fig. 5 Exemplary results obtained during research on the developed payload weighing system for single bucket excavators

5   Conclusions

Summing up, the results of the research presented herein indicate that the developed system is capable of reliable weighing of payload transported inside excavator's bucket. Accuracy of the system is relatively good. Maximum error of bucket payload mass estimation did not exceed 5%. What is more, the accuracy may be easily improved in the future. To do so, first of all, more sophisticated mathematical model of hydraulic cylinder internal friction should be involved in system's operation algorithm. Calculation of cylinder internal friction force on the basis of oil pressure measured inside both chambers of boom cylinder will definitely contribute to increase in accuracy of the system. Secondly, system's computational algorithm should take into account centrifugal forces acting on excavator's manipulator bodies and bucket payload. Performance of the system would also improve if some kind of weighing zone were introduced, i.e. if estimates of payload mass were not calculated for end positions of boom cylinder.

References

1. Leski, M.: Projekt systemu, dynamicznego, automatycznego ważenia materiału transportowanego w łyżce koparki jednonaczyniowej. Master thesis, Wrocław University of Science and Technology. Andrzej Kosiara, Supervisor (2017)
2. Bennett, N., Walawalkar, A., Schindler, Ch.: Payload estimation in excavators: model-based evaluation and comparison of current payload. In: 3rd Commercial Vehicle Technology Symposium, Kaiserslautern, Germany, 2014
3. Saviaa, M., Koivo, H.N.: Neural-network-based payload determination of a moving loader. Control Eng. Practice **12**, 555–561 (2004)
4. Yung, I., Freidovich, L., Vázquez, C.: Payload estimation in front-end loaders. In: 5th International Conference on Machine Control and Guidance, Vichy, France, October 5–6th, 2016
5. Hindman, J.J.: Dynamic payload estimation in four wheel drive loaders. Ph.D Dissertation, University of Saskatchewan, Canada, 2008
6. Materiały reklamowe firmy Trimble Loadrite Auckland Ltd. 2015
7. Tran, X.B., Hafizah, N., Yanada, H.: Modeling of dynamic friction behaviors of hydraulic cylinders. Mechatronics **22**, 65–75 (2012)
8. Kosiara, A.: Development and Validation of a system for monitoring of tip over stability of a single bucket excavator. In: 9th International and 14th European-African Regional Conference of the ISTVS, Budapest, 2017

Design of Illumination and Lighting Visualization by Simulation Methods

Ruzena Kralikova, Miroslav Badida, Lydia Sobotova and Anna Badidova

Abstract This article deals with designing internal artificial lighting as part of the working environment, which is subject to certain rules, derived from the nature of lighting. Good lighting exerts an impact on visual comfort, which contributes to overall psychological well-being, and indirectly also to the quality and productivity of performance, to reliability and to visual performance. Currently the development of computer graphics software products exist to enable a comprehensive design and calculation of the parameters of lighting systems, which would reflect light effects that arise in artificial and day lighting. For the purposes of this paper, as to the possibilities utilisation simulations of light—technical parameters are presented simulations of the lighting design of mechanical engineering workshop created in the software DIALux.

1 Introduction

Modelling and simulation technologies are tools to streamline the presentation and assess the risks for the implementation. Lighting can have other significance than just to light a dark room. It can improve the functions and the design of environment, improve occupational safety and create flexible spaces that are adapting themselves to the tasks according to the type of the carried out activity. A good lighting solution delivers the right level of light at different times of the day and enhances people's sense of wellbeing, improving concentration, motivation and performance [7]. The project of a lighting system is a complex and laborious task that requires not only technical knowledge, but also knowledge of architecture, production, and the physiology of vision.

R. Kralikova (✉) · M. Badida · L. Sobotova · A. Badidova
Faculty of Mechanical Engineering, Department of Process and Environmental Engineering, Technical University of Kosice, Letna 9, 042 00 Kosice, Slovakia
e-mail: ruzena.kralikova@tuke.sk

The role of the designer is not only to select the type of solution; this task is often complex and might be of a research character, leading to the development and manufacture of the lighting systems testing, analysis, and finding the optimum lighting conditions of the workplace and the area as a whole. The lighting of workplaces puts on light-technical solution the following requirements:

- Sufficient horizontal and vertical lighting value for a particular type of the work performed.
- Appropriate radiant flux distribution in the area.
- Suppressing the creation of glare and protecting against it.
- Satisfactory psychological impact of the colour of the light and colour of the administration premises.
- Appropriate colour change in the environment.
- Stable lighting undispersional refraction transparency.
- Reasonable uniformity.
- Suitable orientation of the impact of light on the desktop.

In compliance with all the quantitative and qualitative parameters of illumination, we must design a lighting system based on the principles of maximum performance. Lighting systems with streamlined operation, regulation and management of lighting may also significantly contribute to energy savings [8].

2   Light-Technical Models Creation

In the past there were three basic types of light-technical models:

1. Calculation—without taking into account the actual dimensions, with Tables
2. Accurate (for models in—the scale 1:1)
3. Using of mock-ups that generate a display similar to visual perception designed lighting system

Modern visualization programs can reproduce the luminance, colour and surface structure of the complex three-dimensional space rather realistic, since in the calculations include inter reflection of light between surfaces in space and in many optical effects arising in the day, an artificial joint or lighting. Simulation methods are based on classical optical, thermodynamic, respectively light-technical models of the radiation transfer.

3   Methods Used in Computer Simulation

The lighting research often requires human surveys for defining subjective qualities, creating new settings, new test scenarios which are usually a time and resource-

consuming task. There are two basic methods used in computer simulations luminous environment:

1. Ray tracing—Monte Carlo method is an image-space algorithm, if the camera is moved, we have to start over. Apply technology tracking light beams ray tracing, this name is used for follow-up of beams, also used the term ray casting sending light beam when a beam of light comes from the light source [6].
2. Radiosity is computed in object-space, view-independent (just don't move the light), can pre-compute complex lighting to allow interactive walkthroughs. The Radiosity method is based on the numerical solution of the shading equation by the finite element method.

From a physical point of view both methods are similar, the difference lies in algorithmization. The method of monitoring the beam has a very small spot stochastic manner (results of re-calculation may differ slightly).

3.1 Ray Tracing Technique

Monte Carlo simulation thus provides a very simple method for the computation of the global illumination in the three dimensional environment. Monte Carlo methods have been applied to stochastic ray tracing and to find solutions to the rendering equation. In principle, the ray tracing technique solves the following integral Eq. (1) for the energy balance of each nearly the same surfaces in space.

$$L_r(\theta_r, \varphi_r) = L_e(\theta_r, \varphi_r) + \iint L_i(\theta_i, \varphi_i).\rho_{bd}(\theta_i, \varphi_i, \theta_r, \varphi_r).|\cos\theta_i|.\sin\theta_i.d\theta_i.d\varphi_i$$

(1)

where

θ	polar angle measured from the surface at normal levels
φ	azimuthal angle of the surface at normal levels
$L_e(\theta_r, \varphi_r)$	its own radiance [W sr^{-1} m^{-2}]
$L_r(\theta_r, \varphi_r)$	the total radiance [W sr^{-1} m^{-2}]
$L_i(\theta_i, \varphi_i)$	incident radiance [W sr^{-1} m^{-2}]
$\rho_{bd}(\theta_i, \varphi_i, \theta_r, \varphi_r)$	bidirectional reflectance distribution function [sr^{-1}]

Although the ray tracing algorithm produces perfect results in modelling the mirror reflectivity and undispersional refraction transparency, the algorithm has a shortcoming; specifically, it does not take into account the physical laws of some of the important visual effects, for example colour bleeding by the influence of the reflection of light from another object. It is due to the fact that ray tracing only monitors the finite number of rays emanating from the observer's eye.

3.2 Radiosity Method

The Radiosity method of working with larger surfaces deterministically (repeated calculation results are always the same) [2]. The Radiosity method is attempts to remove this shortcoming [1]. The Radiosity method is based on the principles of the spread of light energy and the energy balance. Stages in a Radiosity solution are on the Fig. 1.

Consider the distribution of the environment as a finite number of n discrete surfaces (patches), each of which have its finite respective size and emit and reflect light evenly across its surface. The scene then consists of surfaces acting both as light sources and reflective surfaces creating a closed system. If we consider each of the surfaces as an opaque Lambertian diffuse emitter and reflector, then the following Eq. (2) applies for the surface due to energy conservation:

$$B_i = E_i + p_i \sum_{1 \le j \le n} B_j F_{ji} \frac{A_j}{A_i} \tag{2}$$

where:

B_i, B_j irradiance areas i and j measured in units of radiant power per unit area (W m^{-2})

E_i power of light radiated from the surface i and has the same dimension as radiation

p_i the reflection coefficient (reflectivity) of the surface i and is dimensionless

F_{ij} dimensionless configuration factor called *form factor*, which specifies the surface i and the energy incoming to the surface j and taking into account the shape, relative orientation of both of the surfaces, as well as the presence of any areas that could create an obstacle. The configuration factor takes its values from the interval <0, 1>, while for the fully covered surfaces it takes the value of 0.

Fig. 1 Stages in a Radiosity solution
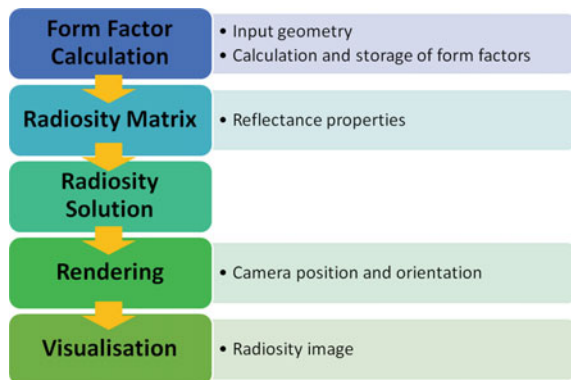
A_i, A_j surface levels i and j

Equation (2) shows that the energy leaving the unit part of the surface is the sum total of both light emitted and reflected. The reflected light is calculated as a product of the reflection coefficient and the sum total of the incident light [10].

On the contrary, the incident light is the sum total of the light leaving the whole surface changed in the part of the light which reaches the receiving unit content of the receiving surface. $B_j F_{j\text{-}i}$ is the amount of light leaving the unit content of the surface A_j area and incident on the entire surface of A_i. It is therefore necessary to multiply the equation by the ratio of A_j/A_i for the determination of light leaving the entire surface A_j and incident on the entire surface A_i. A simple relationship is valid between the configuration factors in the diffuse medium:

$$A_i F_{ij} = A_j F_{ji} \tag{3}$$

The most obvious way to solve a linear equation is to apply the Gauss elimination method [9]. By simplifying Eq. (2) using Eq. (3) we obtain the equation:

$$B_i = E_i + p_i \sum_{1 \leq j \leq n} B_j F_{ij} \tag{4}$$

By subsequent treatment we get the equation in the form:

$$B_i - p_i \sum_{1 \leq j \leq n} B_j F_{ij} = E_i \tag{5}$$

Interaction of light between the surfaces may be expressed in the matrix form [2]. The Eq. (4) can be written for all surfaces, yielding a linear equation where the unknown components are the surface radiosities (B_i):

$$\begin{bmatrix} 1 - p_1 F_{11} & -p_1 F_{12} & \dots & -p_1 F_{1n} \\ -p_2 F_{21} & 1 - p_2 F_{22} & \dots & -p_2 F_{2n} \\ . & . & \dots & . \\ -p_n F_{n1} & -p_n F_{n2} & \dots & 1 - p_n F_{nn} \end{bmatrix} \begin{bmatrix} B_1 \\ B_2 \\ . \\ B_n \end{bmatrix} = \begin{bmatrix} E_1 \\ E_2 \\ . \\ E_n \end{bmatrix} \tag{6}$$

or in matrix form, having introduced matrix $R_{ij} = p_i.F_{ij}$:

$$(1 - R) \cdot B = E \tag{7}$$

where 1 is the standard for the unit matrix.

Note that the contribution of a part of the surface to its own reflected energy (which may be hollow, concave) must be taken into account. Thus, in general, each term on the diagonal need not necessarily equal to 1. Equation (6) must be solved for each group of wavelengths of light in the model, since p_i and E_i depend on the

wavelength. The most critical issue in the radiosity method is efficient form factor calculation.

4   Simulation of Lighting in Dialux

Currently, the development of computer graphics software products exist to enable a comprehensive design and calculation of the parameters of lighting systems, which would reflect light effects that arise in artificial and day lighting. In consequence, there are on the market several light-technical programs with different purposes and uses. Light simulation is often incorporated in standard 3D modelling software. They incorporate calculations for luminance, contrast, glare, etc. To meet recommended standards like EN12464-1: Lighting of indoor workplaces.

A workflow for light planning basically consists of three parts (Fig. 2):

- Design of the lighting concept
- Simulation of the lighting situations
- Visualization of the room/space with lighting.

The above simulation program offers the following options of the selected lighting system and various options for the presentation of results as chart values, isofotic lines, light maps (colour scale), false colour rendering, summary tables of lighting or brightness, a three-dimensional model lighting, economic evaluation of brightness of the lighting project in terms of power consumption, visualization of sunshine, and so on.

Calculation of lighting systems and of lighting characteristics can be realized by using modern computer programs, which, in addition to the results of lighting technologies, offer both 2D and 3D visualization of the illuminated facilities and enable processing of a complete drawing documentation to a project of implementation of lighting technologies. With lighting design simulation software such as DIALux, Relux, DIAL, Autodesk 3D MAX design lighting etc., we can design exactly the right lighting from individual house lighting to large-scale industrial illumination. One is more widely used Dialux and Relux in Europe [4]. Both software were developed

Fig. 2 Light planning workflow [5]
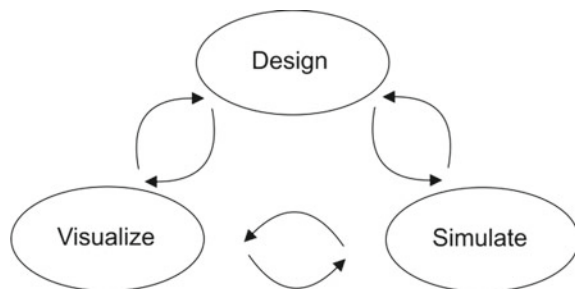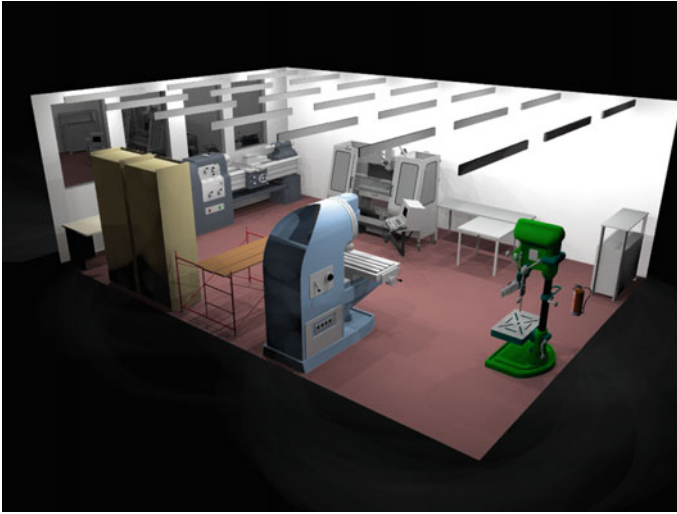
Fig. 3 3D model of mechanical engineering workshop

in Europe and have a strong connection with many lighting manufacturers which supply downloadable plunging for Dialux and Relux software, which facilitates the importing of photometric data and may speed up simulation process.

For the purposes of this paper, as to the possibilities utilisation simulations of light—technical parameters are presented the outputs created in the software DIALux [11]. DIALux is not limited to indoor scenes; you can work with your room surfaces, render general outdoor scenes, setup maintenance plans and more. This program even integrates calculations and radiosity rendering. In this application after calculation and creation of 3D model (Fig. 3), we can go to the false colour display to choose either illuminance.

By DIALux we can switch on the 3D Light distribution curve, Fig. 4. The light distribution curve, which exists for every lamp, illustrates the areal light intensity distribution as the so called polar diagram. These diagrams, which are unique for every lamp, are very important for design. The figures, i.e. Figs. 4, 5 and 6 show the graphical outputs, which is one of the computer programs serving for designing lighting applications.

False colour rendering refers to a group of colour rendering methods used to display images in colour which were recorded in the visible or non-visible parts of the electromagnetic spectrum [3], see Fig. 5.

With DIALux the user has the option to display the 3D rendering in a false colour rendering presentation. The presentation of illuminance and luminance with freely scalable value ranges and definable colour gradients are available. An isoclines' diagram can also be created in this program. This is a plan view, indicating light levels in the space, almost like a topographical map and view network of intensity illumination values, i.e. Fig. 6.
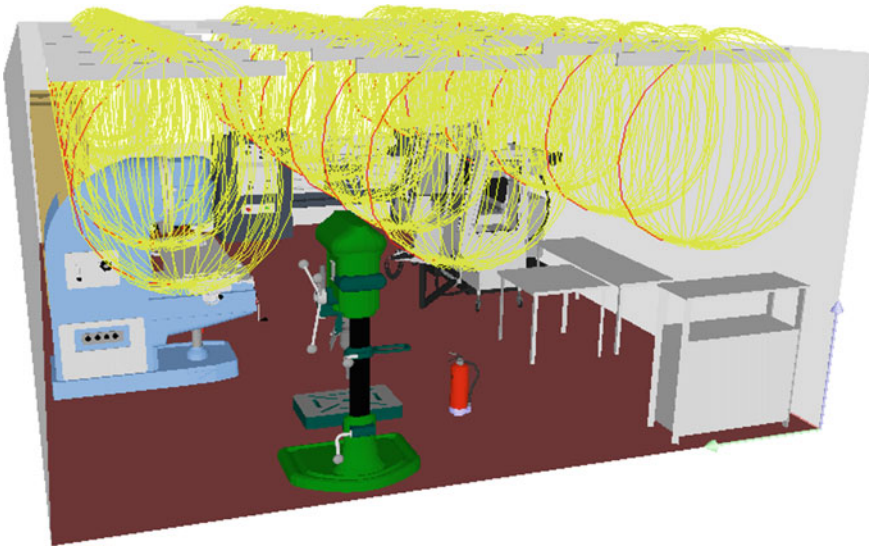
Fig. 4 Curves of illumination
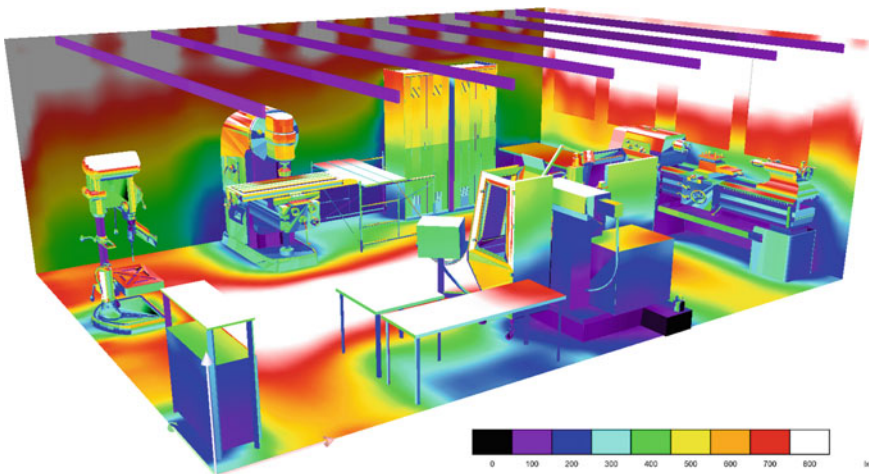
Fig. 5 Rendering with phantom colours

The presented results deal with simple example of lighting design, which were applicated for mechanical workshop. After the project realisation there was the solution objectified by measuring of light intensity with luxmeter Radiolux of Krochman firm. It was occurred the differences between software calculated values and corrected measured values (uncertainty of measurement U = 11%) of real state of indoor light intensity of workshop. Into the lighting system after installation were added next
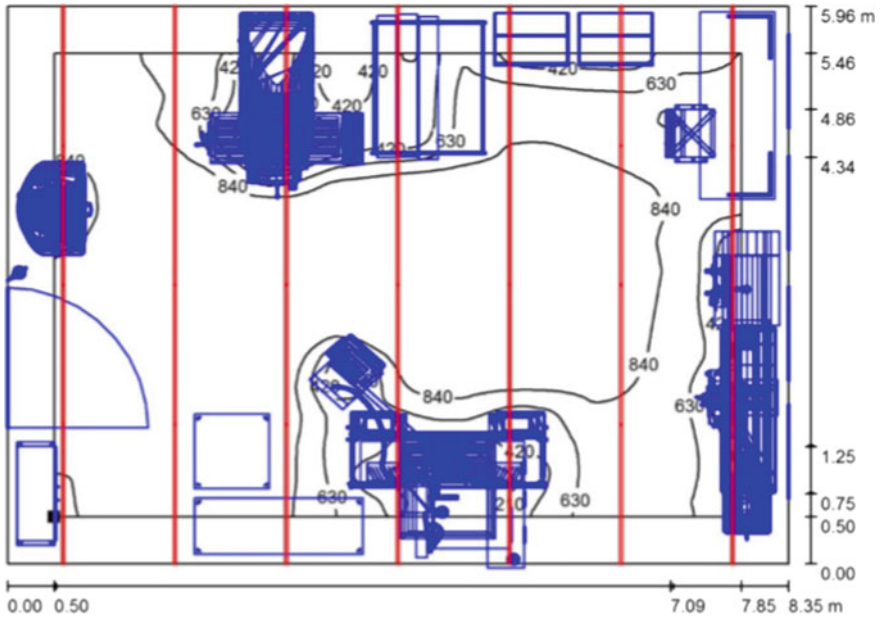
Fig. 6 Isolines with the values of illumination

the lighting sources, which meant account 20% of increasing this overall number of installed lighting sources.

We can encounter this problem in practice several times in lighting projects that may not have to do with the calculated error in the use programs. By using of lighting sources with the same parameters but from producers can be occurred the problems or the problems with the inadequate definition of certain inputs (the colour shades, the lightning effects on the scattering characteristics of light sources, etc.). In the future practice we need to thing about better dimension of lighting requirement calculation, to eliminate the causal differences by qualified estimate. This suggestion will not increase the cost on the lighting system so much, but will keep the hygienic condition for vision according the legislative and standards.

5   Conclusions

The primary role in creating the work environment is to ensure optimal conditions of vision and ensure a safe working environment. Visibility must therefore be seen as a precondition for the implementation of high quality, safe, and reliable work operations. Additionally, one should consider the roles of the involved persons as the designer might have a focus on qualitative light design and the light-technical engineer will possess the necessary knowledge of quantitative parameters and the

standards that have to be met at certain use cases. It is necessary to pay close attention to this issue.

Further improvements continue to appear from time to time, to reduce costs or extend the application areas of visualisation techniques. Thus environments with complex light sources or unevenly illuminated large surfaces or with participating media can be treated with greater flexibility, simplicity and speed. When dealing with light-technical projects, the visualization of lighting parameters is a useful tool by using programmes realistically displaying the lighting parameters. Despite numerous possibilities that the current software tools offer, in some cases there is a difference between the modelled and actual light-technical parameters. One of the reasons affecting the result of the computer output may be the inadequate definition of certain inputs (the colour shades and quality of the room's surfaces, the lightning effects on the scattering characteristics of light sources, etc.).

However, these differences do not affect the overall relevance of computer outputs and may be virtually eliminated by qualified estimation. In this contribution we could demonstrate the light simulation solutions, which can be integrated into a real time visual framework and these resulting inputs from Dialux shows on a lot of potential for future extensions. Another interesting extension would be to use image based lighting with high dynamic range images (HDRI), which is currently not possible in DIALux, but could be integrated into other visualisation software packages as Cryengine, Unity, Blender etc.

References

1. Baum, D.R., Winget, J.M.: Real time radiosity through parallel rocessing and hardware acceleration. Comput. Graph. **24**(2), 67–75 (1990)
2. Cohen, M.F., Greenberg D.P.: The hemi cube: a radiosity solution for complex environments. In: Symposium on Computational Geometry, pp. 31–40 (July 1985)
3. Dachsbacher, C., Krivanek, J., Hasan, M., Arbree, A., Walter, B., Novak, J.: Scalable realistic rendering with many-light methods. Comput. Graphics Forum **33**(1), 88–104 (2014). Wiley Online Library
4. Despotovic-Zrakic, M., Barac, D., Bogdanovi Z., Jovanic B., Radenkovic B.: Software environment for learning continuous system simulation. Acta. Polytech. Hungarica **8**(2), pp 187–202 (2014) ISSN: 1785-8860 (2014)
5. Ferschin, P., Di Angelo, M., Suter, G.: Exploring the potential of game engines for real-time light simulation. In: Third German-Austrian IBPSA Conference, BauSim 2010. Viena, pp. 449–504 (2010)
6. Fujiomoto, A., Tanaka, T., Iwata, K.: ARTS accelerated ray tracing system. IEEE Comput. Graphics Appl. **6**(4), 16–26 (1986)
7. Gligor, V.: Luminous environment and productivity at workplaces. Thesis, 2004. Helsinki University of Technology, Espoo (2004)
8. Micieta, B., Markovic, J., Binasova, V. (2016) Advances in sustainable energy efficient manufacturing system, MM Sci. J. pp. 918–926 (2016-June). ISSN 1803-1269

9. Press, W.H., Flannery, B.P., Teukolsky, S.A., Vetterling, W.T.: Numerical Recipes in C, 3rd edn. Cambridge University Press, Cambridge, USA (2007)
10. Tilinger, A., Madar, G.: Spectral Radiosity rendering application for lighting researches. Acta Polytech. Hungarica **5**(3), 141–145 (2008)
11. www.dialux.com

Optimal Design of Multibody Systems Using the Adjoint Method

Paweł Maciąg, Paweł Malczyk and Janusz Frączek

Abstract Optimal design of multibody systems (MBS) is of primary importance to engineers and researchers working in various fields, e.g.: in robotics or in machine design. The goal of this paper is a development and implementation of systematic methods for finding design sensitivities of multibody system dynamics with respect to design parameters in the process of optimization of such systems. The optimal design process may be formulated as finding a set of unknown parameters such that the objective function is minimized under the assumption that design variables may be subjected to a variety of differential and/or algebraic constraints. The solutions of such complex optimal problems are inevitably connected with evaluation of a gradient of the objective function. Herein, a multibody system is described by redundant set of absolute coordinates. The equations of motion for MBS are formulated as a system of differential-algebraic equations (DAEs) that has to be discretized and solved numerically forward in time. The design sensitivity analysis is addressed by using the adjoint method that requires determination and numerical solution of adjoint equations backwards in time. Optimal design of sample planar multibody systems are presented in the paper. The properties of the adjoint method are also investigated in terms of efficiency, accuracy, and problem size.

Keywords Multibody dynamics · Sensitivity analysis · Adjoint method
Optimization · Optimal control

P. Maciąg (✉) · P. Malczyk · J. Frączek
Division of Theory of Machines and Robots,
Faculty of Power and Aeronautical Engineering,
Institute of Aeronautics and Applied Mechanics,
Warsaw University of Technology, Nowowiejska Str. 24,
00-665 Warsaw, Poland
e-mail: pmaciag@meil.pw.edu.pl

P. Malczyk
e-mail: pmalczyk@meil.pw.edu.pl

J. Frączek
e-mail: jfraczek@meil.pw.edu.pl

1 Introduction

Optimization methods and tools are commonly exploited in early design stage of many various systems encompassing, e.g.: industrial or space robots, mechanisms, multi-purpose vehicles or bio-mechanical systems. Systematic design improvements of multibody systems for multiple design parameters and complex performance indices are rather difficult to obtain without a suitable optimization strategy. A reliable and efficient procedures for gradient calculation are indispensable steps in the development of general purpose multibody design tools.

There are multiple ways of calculating a gradient of a cost function, each method distinguished by particular advantages as well as encumbered with certain flaws. Both finite difference method and direct differentiation method are simple to implement, yet quite inefficient from a numerical point of view. This fact may be a prohibitive disadvantage for the optimization of large scale problems. More sophisticated algorithms such as automatic differentiation [7] or complex differentiation methods offer some improvement, however, this is not the case when the number of design variables is large and the systems under consideration are complex. A tremendous asset of the adjoint method investigated here is the fact that its computational efficiency does not depend on the number of design variables. This property fills the gap which arises from the concepts listed above. One drawback of this approach is its difficult implementation in general applications. This, however, motivates further investigation of the adjoint method in the pursuit of additional development.

The adjoint method originates from the optimal control theory, and although initially it had been employed mostly in fluid dynamics problems, this method has been recently widely expanded onto the field of multibody dynamics [2, 3, 5]. Combined with the optimization theory, the mathematical apparatus can be utilized not only in optimal design but also in parameter estimation of complex MBS [6, 8, 9]. This field is still open for new research directions and the goal of this paper is to recapitulate the general key points of the adjoint method as well as to implement systematic methods for calculating design sensitivity vector for a multibody system in a reliable and efficient manner.

The primary goal of this paper is to present the adjoint method for the process of optimal design of multibody systems. Newmark scheme is employed in the paper in order to efficiently solve the equations of motion forward in time and the adjoint equations backwards in time. Sample test cases are reported in the text to verify the formulation and show its properties.

2 Design Sensitivity Analysis

The following section is a theoretical introduction to the discussed subject. The first step of the adjoint based procedure is to solve dynamic equations of motion forward

in time. This issue is discussed in Sect. 2.1. Following this, in Sect. 2.2 the adjoint equations are derived as well as their solution backward in time is briefly described.

2.1 Forward Solution of Equations of Motion

For simplicity's sake, only planar mechanisms are taken into consideration, where position of ith body is described by a vector of three absolute coordinates: $\mathbf{q}_i = [x_i, y_i, \varphi_i]^T$. The quantities x_i and y_i are Cartesian coordinates of the body-fixed centroidal coordinate frame and φ_i is an angle of orientation of ith body with respect to the global frame [2]. The classical formulation of the equations of motion with multipliers reads as:

$$\mathbf{M}(\mathbf{q}, \mathbf{z}) \cdot \ddot{\mathbf{q}} + \boldsymbol{\Phi}_{\mathbf{q}}^T(\mathbf{q}) \cdot \lambda = \mathbf{Q}(t, \mathbf{q}, \dot{\mathbf{q}}, \mathbf{z}), \tag{1a}$$

$$\boldsymbol{\Phi}(\mathbf{q}) = \mathbf{0}, \tag{1b}$$

where $\mathbf{M} \in \mathcal{R}^{n \times n}$ is the mass matrix of MBS, $\boldsymbol{\Phi} \in \mathcal{R}^m$ is a set of kinematic constraints imposed on dependent coordinates vector $\mathbf{q}$, $\boldsymbol{\Phi}_{\mathbf{q}} \in \mathcal{R}^{m \times n}$ denotes the Jacobi matrix, $\lambda \in \mathcal{R}^m$ is a vector of Lagrange multipliers that provide the constraint loads at joints, $\mathbf{Q} \in \mathcal{R}^n$ describes generalized forces acting on the system, and $\mathbf{z} \in \mathcal{R}^c$ is a vector of design variables. Scalar values n, m and c denote the number of introduced coordinates, kinematic constraints and design variables, respectively.

Equation (1) is a mixed system of differential - algebraic equations (DAE) of differential - index 3, which herein is discretized by using fixed time-step Newmark scheme [10]:

$$\dot{\mathbf{q}}_{n+1} = \frac{\gamma}{\beta h}\mathbf{q}_{n+1} + \hat{\dot{\mathbf{q}}}_n \,, \text{ where } \quad \hat{\dot{\mathbf{q}}}_n = -\left[\frac{\gamma}{\beta h}\mathbf{q}_n + \left(\frac{\gamma}{\beta} - 1\right)\dot{\mathbf{q}}_n + h\left(\frac{\gamma}{2\beta} - 1\right)\ddot{\mathbf{q}}_n\right], \tag{2}$$

$$\ddot{\mathbf{q}}_{n+1} = \frac{1}{\beta h^2}\mathbf{q}_{n+1} + \hat{\ddot{\mathbf{q}}}_n \,, \text{ where } \quad \hat{\ddot{\mathbf{q}}}_n = -\left[\frac{1}{\beta h^2}\mathbf{q}_n + \frac{1}{\beta h}\dot{\mathbf{q}}_n + \left(\frac{1}{2\beta} - 1\right)\ddot{\mathbf{q}}_n\right], \tag{3}$$

where h is a time-step, while β, and γ are the integrator parameters. By setting the parameters to values $\beta = \frac{1}{4}$ and $\gamma = \frac{1}{2}$ a second order accuracy is obtained whilst the stability of the integrator is maintained within the whole left-hand portion of complex plane (A-stability) [10]. Such numerical scheme is also known as *trapezoidal rule* and it is often used in real-time multibody dynamics applications. Let us insert the Newmark integrator from Eqs. (2) and (3) into the equations of motion (1), to obtain a nonlinear system of algebraic equations with $\mathbf{q}_{n+1}$ and λ_{n+1} as sole unknowns. If we additionally multiply Eq. (1) by a factor of βh^2, we get the following formula:

$$\mathbf{M}_{n+1} \cdot \mathbf{q}_{n+1} + \beta h^2 \cdot \left(\left[\mathbf{\Phi}_{\mathbf{q}}^T \lambda \right]_{n+1} - \mathbf{Q}_{n+1} + \mathbf{M}_{n+1} \cdot \hat{\dot{\mathbf{q}}}_n \right) = \mathbf{0},$$

$$\beta h^2 \cdot \mathbf{\Phi}_{n+1} = \mathbf{0}, \tag{4}$$

Since the numerical integration method used here is implicit, an iterative scheme such as Newton - Raphson method has to be employed in order to solve it for positions $\mathbf{q}_{n+1}$ and Lagrange multipliers λ_{n+1} at the next time-instant:

$$\begin{bmatrix} \mathbf{M}^* & \beta h^2 \cdot \mathbf{\Phi}_{\mathbf{q}}^T \\ \beta h^2 \cdot \mathbf{\Phi}_{\mathbf{q}} & \mathbf{0} \end{bmatrix}^{(i)} \cdot \begin{bmatrix} \Delta \mathbf{q} \\ \Delta \lambda \end{bmatrix}^{(i+1)} = \begin{bmatrix} \mathbf{M} \mathbf{q}_{n+1} + \beta h^2 \cdot \left(\mathbf{\Phi}_{\mathbf{q}}^T \lambda - \mathbf{Q} + \mathbf{M} \hat{\dot{\mathbf{q}}}_n \right) \\ \beta h^2 \cdot \mathbf{\Phi} \end{bmatrix}^{(i)}, \tag{5}$$

where $\mathbf{M}^*$ denotes the matrix $\mathbf{M}^* = \mathbf{M} + \beta h^2 \cdot (\mathbf{\Phi}_{\mathbf{q}}^T \lambda)_{\mathbf{q}} - \gamma h \cdot \mathbf{Q}_{\mathbf{v}} - \beta h^2 \cdot \mathbf{Q}_{\mathbf{q}}$. The quantities $\Delta \mathbf{q}$ and $\Delta \lambda$ are the corrector values for each iteration and are used to update displacement and Lagrange multipliers in the following way:

$$\mathbf{q}_{n+1}^{(i+1)} = \mathbf{q}_n^{(i+1)} + \Delta \mathbf{q}_{n+i}^{(i+1)}, \qquad \lambda_{n+1}^{(i+1)} = \lambda_n^{(i+1)} + \Delta \lambda_{n+i}^{(i+1)}. \tag{6}$$

It is important to distinguish that index n refers to currently calculated time step, whereas index i describes ith iteration within Newton - Raphson procedure. Each iteration, new values obtained from Eq. (6) are inserted into (2) and (3); moreover, updated $\mathbf{q}_{n+1}^{(i+1)}$ and $\dot{\mathbf{q}}_{n+1}^{(i+1)}$ are used to recalculate coefficients $\mathbf{M}, \mathbf{\Phi}_{\mathbf{q}}, \mathbf{Q}_{\mathbf{q}}, \mathbf{Q}_{\mathbf{v}}$ and $\mathbf{\Phi}$ before invoking Eq. (5) again. This process is carried on until $\mathbf{q}_{n+1}$ and λ_{n+1} fulfills Eq. (1) at a proper time step within a desired tolerance.

The solution of Eq. (5) fulfills position level constraint equations (1b) at a current time step up to the accuracy defined by the user. Since the Newton-Raphson procedure takes into account only position level constraints and neglects its counterparts imposed on velocity and acceleration level, the values $\dot{\mathbf{q}}_{n+1}^*$ and $\ddot{\mathbf{q}}_{n+1}^*$ calculated from Eqs. (2) and (3) do not fulfill first and second time-derivatives of (1b). Thus, this emerges a need of finding clean values of $\dot{\mathbf{q}}_{n+1} = \mathbf{0}$ and $\ddot{\mathbf{q}}_{n+1} = \mathbf{0}$ that fulfill velocity level constraints $\dot{\mathbf{\Phi}} = \mathbf{0}$ and acceleration level constraints $\ddot{\mathbf{\Phi}} = \mathbf{0}$. One way is to project them onto appropriate constraint hyper-surfaces. This approach comes from the optimization theory and has various implementations. A simple and practical solution of the problem is a mass - orthogonal projection proposed by Cuadrado [1]. Its huge asset is the utilization of the tangent matrix from Eq. (5). The velocity and acceleration level mass-orthogonal projections can be expressed as:

$$\begin{bmatrix} \mathbf{M}^* & \beta h^2 \cdot \mathbf{\Phi}_{\mathbf{q}}^T \\ \beta h^2 \cdot \mathbf{\Phi}_{\mathbf{q}} & \mathbf{0} \end{bmatrix} \cdot \begin{bmatrix} \dot{\mathbf{q}} \\ \sigma \end{bmatrix} = \begin{bmatrix} \mathbf{M}^* \cdot \dot{\mathbf{q}}^* \\ -\beta h^2 \cdot \mathbf{\Phi}_t \end{bmatrix}, \tag{7}$$

$$\begin{bmatrix} \mathbf{M}^* & \beta h^2 \cdot \mathbf{\Phi}_{\mathbf{q}}^T \\ \beta h^2 \cdot \mathbf{\Phi}_{\mathbf{q}} & \mathbf{0} \end{bmatrix} \cdot \begin{bmatrix} \ddot{\mathbf{q}} \\ \kappa \end{bmatrix} = \begin{bmatrix} \mathbf{M}^* \cdot \ddot{\mathbf{q}}^* \\ -\beta h^2 \cdot \left(\dot{\mathbf{\Phi}}_{\mathbf{q}} \dot{\mathbf{q}} + \dot{\mathbf{\Phi}}_t \right) \end{bmatrix}, \tag{8}$$

where σ and κ are the Lagrange multipliers associated with the projection process. It should be pointed out that the formulation described here works well

for non-redundant systems. In the case of redundant constraints one may employ augmented Lagrangian methods, [1, 4] with special caution associated with the uniqueness of constraint loads at joints [11].

Before the simulation is run, it is essential to estimate initial values of λ and $\ddot{\mathbf{q}}$, since they are usually not available at the first time-instant. This can be achieved by transforming Eq. (1) into index 1 formulation, i.e. by differentiating (1b) twice. The corresponding set of equations can be expressed as:

$$\begin{bmatrix} \mathbf{M} & \mathbf{\Phi_q}^T \\ \mathbf{\Phi_q} & \mathbf{0} \end{bmatrix}_{t=0} \cdot \begin{bmatrix} \ddot{\mathbf{q}}_0 \\ \lambda_0 \end{bmatrix} = \begin{bmatrix} \mathbf{Q} \\ -\dot{\mathbf{\Phi}}_{\mathbf{q}}\dot{\mathbf{q}} - \dot{\mathbf{\Phi}}_t \end{bmatrix}_{t=0}. \tag{9}$$

It should be emphasized that efficient and reliable solution of the equations of motion for a MBS is an important factor for evaluation of design sensitivities for an optimized system.

2.2 Backward Solution of Adjoint Equations

The forward dynamics problem yields a set of kinematic parameters that allow for evaluation of a cost function. Forward integration of the equations of motion provides the quantities that are required to be stored on a computer. Subsequently, the relevant terms are used in the process of finding design sensitivity vector. Let us define the following cost function to be minimized:

$$J(t, \mathbf{z}, \mathbf{q}, \mathbf{v}) = \int_0^{T_f} g(\mathbf{q}, \mathbf{v}, \mathbf{z}) \, dt + S(\mathbf{q}, \mathbf{v})|_{T_f}, \tag{10}$$

where g is a function of state of a system and S is a terminal cost allowing for the additional settings at final time T_f. The problem investigated here is to find at least a local minimum of a performance index (10) under the assumption that there are mixed differential and algebraic constraints imposed on the design variables. The key idea of the adjoint method is to incorporate constraint equations into the cost function by adding additional Lagrange multipliers to be evaluated from time T_f to initial time.

In order to insert equations of motion into (10), it is convenient to decrease order of Eq. (1) by introducing additional variable $\mathbf{v}(t) = \dot{\mathbf{q}}(t)$. Next, one can move all components to the left-hand side of the equation, and multiply each equation by a vector function of arbitrary values $\mathbf{p}^T(t)$, $\mathbf{w}^T(t)$, $\mu^T(t)$, called Lagrange multipliers or adjoint variables. Ultimately, it is valid to integrate these expressions from time $t = 0$ up to $t = T_f$. These operations yield the following result:

$$\int_0^{T_f} \mathbf{p}^T \cdot (\dot{\mathbf{q}} - \mathbf{v}) \, dt = 0, \int_0^{T_f} \mathbf{w}^T \cdot \left(\mathbf{M}\dot{\mathbf{v}} + \mathbf{\Phi}_{\mathbf{q}}^T \cdot \lambda - \mathbf{Q}\right) \, dt = 0, \int_0^{T_f} \mu^T \cdot \mathbf{\Phi} \, dt = 0. \tag{11}$$

Since the RHS of Eq. (11) equals zero, inserting them into Eq. (10) does not bring any quantitative change to the cost function:

$$J = \int_0^{T_f} \left[g + \mathbf{p}^T \cdot (\dot{\mathbf{q}} - \mathbf{v}) + \mathbf{w}^T \cdot (\mathbf{M}\dot{\mathbf{v}} + \mathbf{\Phi}_\mathbf{q}^T \cdot \lambda - \mathbf{Q}) + \mu^T \cdot \mathbf{\Phi} \right] \mathrm{d}t + S|_{T_f}.$$
(12)

It is possible to calculate variation of J in Eq. (12) by expressing it as a collective variation of other variables:

$$\delta J = \int_0^{T_f} \left\{ g_\mathbf{q}\delta\mathbf{q} + g_\mathbf{v}\delta\mathbf{v} + g_\mathbf{z}\delta\mathbf{z} + \mathbf{p}^T (\delta\dot{\mathbf{q}} - \delta\mathbf{v}) + \mathbf{w}^T \left[\mathbf{M}\delta\dot{\mathbf{v}} + (\mathbf{M}\dot{\mathbf{v}})_\mathbf{q}\delta\mathbf{q} + (\mathbf{M}\dot{\mathbf{v}})_\mathbf{z}\delta\mathbf{z} \right. \right.$$
$$\left. \left. - \mathbf{Q}_\mathbf{q}\delta\mathbf{q} - \mathbf{Q}_\mathbf{v}\delta\mathbf{v} - \mathbf{Q}_\mathbf{z}\delta\mathbf{z} + (\mathbf{\Phi}_\mathbf{q}^T \lambda)_\mathbf{q}\delta\mathbf{q} + \mathbf{\Phi}_\mathbf{q}^T \delta\lambda \right] + \mu^T \mathbf{\Phi}_\mathbf{q}\delta\mathbf{q} \right\} \mathrm{d}t + S_\mathbf{q}\delta\mathbf{q}|_{T_f} + S_\mathbf{v}\delta\mathbf{v}|_{T_f}.$$
(13)

The quantities $\delta\dot{\mathbf{q}}$ and $\delta\dot{\mathbf{v}}$ can be integrated by parts, yielding expressions containing only variations of $\delta\mathbf{q}$ and $\delta\mathbf{v}$:

$$\int_0^{T_f} \mathbf{p}^T \delta\dot{\mathbf{q}} \ \mathrm{d}t = -\int_0^{T_f} \dot{\mathbf{p}}^T \delta\mathbf{q} \ \mathrm{d}t + \mathbf{p}^T \delta\mathbf{q}|_{T_f} - \mathbf{p}^T \delta\mathbf{q}|_{t=0}$$
(14a)

$$\int_0^{T_f} \mathbf{w}^T \mathbf{M}\delta\dot{\mathbf{v}} \ \mathrm{d}t = -\int_0^{T_f} \dot{\mathbf{w}}^T \mathbf{M}\delta\mathbf{v} \ \mathrm{d}t + \mathbf{w}^T \mathbf{M}\delta\mathbf{v}|_{T_f} - \mathbf{w}^T \mathbf{M}\delta\mathbf{v}|_{t=0}.$$
(14b)

It is a common requirement to treat some state parameters of MBS as design variables. One can take this into account by expressing variation of initial state in terms of variation of design variables:

$$\delta\mathbf{q}|_{t=0} = \nabla_\mathbf{z}\mathbf{q}\delta\mathbf{z}|_{t=0} \qquad \delta\mathbf{v}|_{t=0} = \nabla_\mathbf{z}\mathbf{v}\delta\mathbf{z}|_{t=0}.$$
(15)

Substituting all the above terms into Eq. (10) and rearranging them in terms of adjoint variables yields:

$$\delta J = \int_0^{T_f} \left\{ \left[g_\mathbf{q} - \dot{\mathbf{p}}^T + \mathbf{w}^T \left((\mathbf{M}\dot{\mathbf{v}})_\mathbf{q} + (\mathbf{\Phi}_\mathbf{q}^T\lambda)_\mathbf{q} - \mathbf{Q}_\mathbf{q} \right) + \mu^T \mathbf{\Phi}_\mathbf{q} \right]\delta\mathbf{q} + \left[\mathbf{w}^T \mathbf{\Phi}_\mathbf{q}^T \right]\delta\lambda \right.$$
$$+ \left[g_\mathbf{v} - \mathbf{p}^T - \mathbf{w}^T \mathbf{Q}_\mathbf{v} - \dot{\mathbf{w}}^T \mathbf{M} \right]\delta\mathbf{v} + \left[g_\mathbf{z} - \mathbf{w}^T \mathbf{Q}_\mathbf{z} + \mathbf{w}^T (\mathbf{M}\dot{\mathbf{v}})_\mathbf{z} \right]\delta\mathbf{z} \right\} \mathrm{d}t$$
$$+ \left[S_\mathbf{q} + \mathbf{p}^T \right]\delta\mathbf{q}|_{T_f} + \left[S_\mathbf{v} + \mathbf{w}^T \mathbf{M} \right]\delta\mathbf{v}|_{T_f} - \mathbf{p}^T \nabla_\mathbf{z}\mathbf{q}\delta\mathbf{z}|_{t=0} - \mathbf{w}^T \mathbf{M}\nabla_\mathbf{z}\mathbf{v}\delta\mathbf{z}|_{t=0}.$$
(16)

The goal is to find such values of arbitrary functions $\mathbf{p}(t)$, $\mathbf{w}(t)$, $\mu(t)$ that will allow to express δJ solely in terms of design variables. Since the variations $\delta\mathbf{q}$, $\delta\mathbf{v}$, $\delta\lambda$ are arbitrary and the necessary condition $\delta J = 0$ for the minimization of performance index holds, we equate the terms in brackets to zero, to generate a set of DAEs called adjoint equations:

$$\dot{\mathbf{p}} = g_{\mathbf{q}}^T + \left[(\mathbf{M}\dot{\mathbf{v}})_{\mathbf{q}}^T + (\mathbf{\Phi}_{\mathbf{q}}^T \lambda)_{\mathbf{q}}^T - \mathbf{Q}_{\mathbf{q}}^T \right]\mathbf{w} + \mathbf{\Phi}_{\mathbf{q}}^T \mu \tag{17a}$$

$$\mathbf{M}\dot{\mathbf{w}} = g_{\mathbf{v}}^T - \mathbf{p} - \mathbf{Q}_{\mathbf{v}}^T \mathbf{w} \tag{17b}$$

$$\mathbf{\Phi}_{\mathbf{q}}\mathbf{w} = \mathbf{0} \tag{17c}$$

$$S_{\mathbf{q}}^T|_{T_f} + \mathbf{p}(T_f) = \mathbf{0} \tag{17d}$$

$$S_{\mathbf{v}}^T|_{T_f} + \mathbf{M}\mathbf{w}(T_f) = \mathbf{0}, \tag{17e}$$

Solving the DAE system (17) from final time up to initial time yields uniquely defined set of adjoint variables for which the expression (16) simplifies to:

$$\delta J = \int_0^{T_f} \left[g_{\mathbf{z}} - \mathbf{w}^T \left(\mathbf{Q}_{\mathbf{z}} + (\mathbf{M}\dot{\mathbf{v}})_{\mathbf{z}} \right) \right] \delta \mathbf{z} \; dt - \mathbf{w}^T \mathbf{M} \nabla \mathbf{v} \, \delta \mathbf{z}|_{t=0} - \mathbf{p}^T \nabla \mathbf{q} \, \delta \mathbf{z}|_{t=0}. \tag{18}$$

Thus the gradient of the objective function J can therefore be expressed as:

$$\nabla J = \int_0^{T_f} g_{\mathbf{z}}^T + \left((\mathbf{M}\dot{\mathbf{v}})_{\mathbf{z}}^T - \mathbf{Q}_{\mathbf{z}}^T \right)\mathbf{w} \; dt - \left(\mathbf{M} \nabla \mathbf{v} \right)^T \mathbf{w}|_{t=0} - \left(\nabla \mathbf{q} \right)^T \mathbf{p}|_{t=0}. \tag{19}$$

Since Eqs. (17d) and (17e) can be treated as boundary conditions, the solution of the adjoint equations is carried out backwards in time with dynamic parameters $\mathbf{q}$, $\dot{\mathbf{q}}$, $\ddot{\mathbf{q}}$, λ as coefficients.

As in the case of forward dynamics problem, Eq. (17) can be discretized by means of trapezoidal rule and the resulting equations may again be resolved with the use of the Newton-Raphson procedure. Since this system of equations is linear, only one iteration per time step will be required. Again, there is a need of finding initial value $\mu(T_f)$, since it is not provided by boundary conditions. Information on both initial iteration and additional consistency of boundary conditions for adjoint equations can be found in Ref. [5].

The gradient calculated in Eq. (19) shows a direction along which the objective function is guaranteed to decrease (unless the considered point is already a local minimum). This information can be utilized by an appropriate optimization procedure, e.g. the steepest descent method, to get the optimal solution.

3 Numerical Examples

Two sample test cases are further discussed. The example presented in Sect. 3.1 contains an analytical solution of the problem and includes a comparison between the adjoint method and the finite differences method. Section 3.2 investigates the problem of vibration suppression of a 2 DOF mass, spring and damper system.
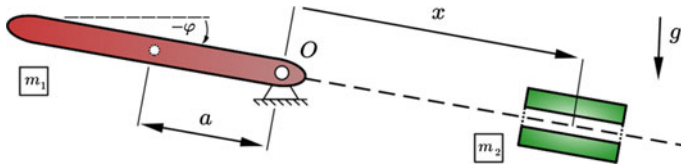
Fig. 1 Physical pendulum with attached mass

3.1 Optimization of a Mass Attached to a Pendulum

The first test example is a simple system of physical pendulum with additional point-mass. The system is described in minimal coordinate formulation. Intentionally, the example is chosen to be simple to get an analytic optimal solution in a closed form. Let us consider the pendulum depicted in Fig. 1. The pendulum is attached to the ground by pin joint at point **O**, whereas additional mass moves along the pendulum's axis on a weightless rod.

Masses of the bodies are $m_1 = 1$ kg and m_2, respectively. The center of gravity of the pendulum is at distance of $a = 0.5$ m from the point **O**. Initially, the pendulum is aligned horizontally ($\varphi_0 = 0$), the position of the box is x_0 and velocities are equal to zero. The objective is to find an initial position of the second body $z_1 = x_0$ and its mass $z_2 = m_2$ that will keep the system in equilibrium. The cost function for the optimization problem as well as the equations of motion have the following form:

$$
J = \int_0^{T_f} \varphi^2 \, dt , \qquad
\begin{bmatrix} \dot{\mathbf{q}} \\ \dot{\mathbf{v}} \end{bmatrix} =
\begin{bmatrix} \dot{x} \\ \dot{\varphi} \\ \dot{v} \\ \dot{\omega} \end{bmatrix} =
\begin{bmatrix}
v \\
\omega \\
x\omega^2 - g \sin \varphi \\
-\dfrac{(m_2 x - m_1 a)g \cos \varphi - 2m_2 x v \omega}{I_O + m_2 x^2}
\end{bmatrix} . \qquad (20)
$$

where g denotes gravitational constant and I_O is a moment of inertia of the pendulum with respect to the axis passing through point **O** and perpendicular to the plane of motion. Vectors **q** and **v** are the state variables and become known parameters while solving the adjoint equations. The minimal-coordinate formulation used here simplifies slightly the adjoint equations, since there are no constraints imposed on the system, which renders as $\mathbf{\Phi} \equiv \mathbf{0}$ and $\mu \equiv \mathbf{0}$. As mentioned above, the solution curve of the optimization problem can be easily calculated. It reads as: $m_2 = \dfrac{m_1 \cdot a}{x_0} = \dfrac{1}{2x_0}$.

Multiple simulations at time step $dt = 0.01$ s adopted for both forward and backward simulations, and with different initial guesses of the design have been performed. The following results were obtained using Interior Point optimization algorithm. Figure 2 shows the outcome of the simulations for different initial guesses and various methods used for the gradient calculation. Let us observe that both finite difference and adjoint methods converge to the optimal solution marked by a solid line. Both methods, however, produce significantly different solutions, e.g. starting from point $\mathbf{z}_0 = [2, 1]^T$ we obtain $\hat{\mathbf{z}} = [0.765, 0.654]^T$ for finite differences method,

(a) Starting point and the associated solutions.

(b) History of intermediate points.
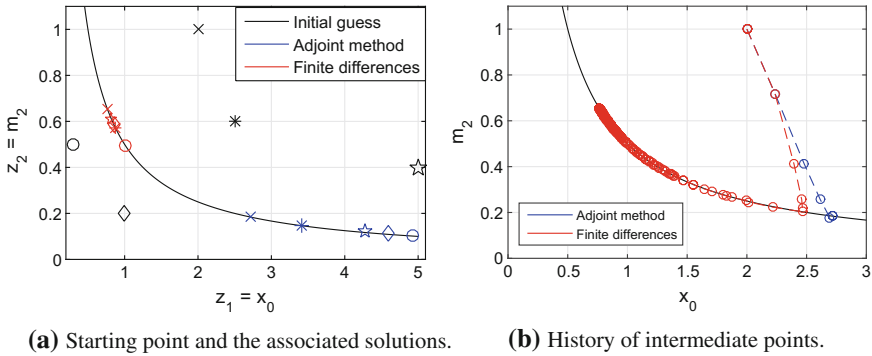
Fig. 2 Solutions for different starting points with the distinction of adjoint and finite differences method of gradient calculation

(a) Cost measure.

(b) First order optimality measure.
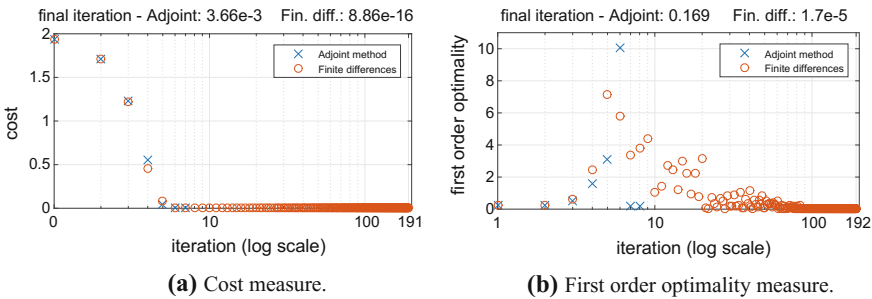
Fig. 3 History of cost and optimality measure for both methods of gradient calculation

whereas the adjoint method yields $\hat{\mathbf{z}} = [2.717, 0.187]^T$. The observed discrepancy comes from the small perturbations between numerical values of each gradient. It can be captured with the aid of Fig. 2b, which shows the trajectory taken by the optimization algorithm for both methods. Let us note that in the case of finite differences method, the algorithm slowly converges to the optimal solution and performs many iterations to reach that point. The comparison of the cost and fulfillment of the first order optimality conditions is shown in Fig. 3. The optimal solution is found significantly faster in case of the adjoint method, however, finite differences method ultimately reaches higher convergence.

3.2 Vertical Double Mass Damping System

Consider two rigid bodies having the masses m_1, m_2, which are aligned vertically, and constrained in such way that only vertical motion is possible (see Fig. 4). Since in this example each body is described in accordance with Sect. 2.1 (redundant coordinate

Fig. 4 Vertical double mass oscillator
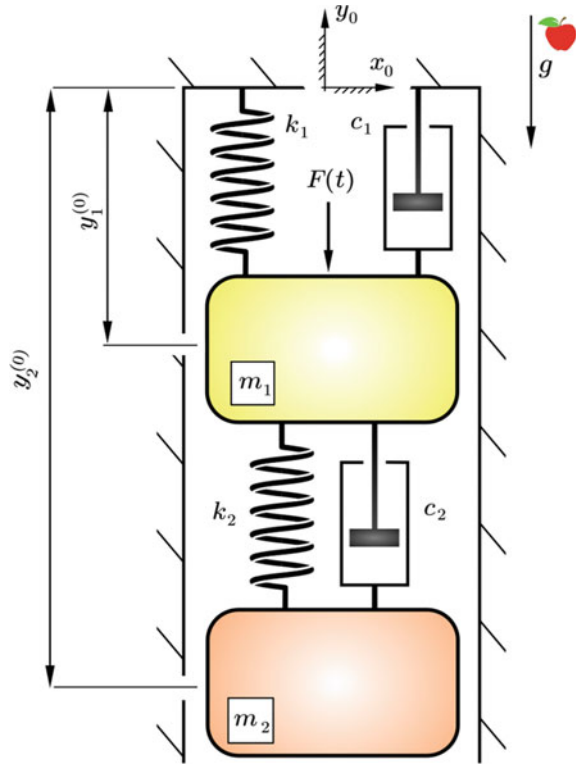
formulation), constraint equations $\mathbf{\Phi}_{4 \times 1} = \mathbf{0}$ has to be imposed on the system and furthermore taken into consideration while solving adjoint equations. Both parts are affected by gravity forces and two linear spring - damper systems located as in Fig. 4. Moreover, the upper part is subjected to sinusoidal excitation $F(t)$. The design variables are defined as coefficients of springs and dampers, i.e. $\mathbf{z} = [k_1, c_1, k_2, c_2]^T$. Numerical parameters used in the simulation are gathered in the Table 1. The goal of the optimization process is to reduce oscillations of upper mass (described by y_1 coordinate) from its initial state $y_1^{(0)}$. The performance index can be expressed as:

$$J = \int_0^{T_f} \left(y_1 - y_1^{(0)}\right)^2 \; \mathrm{d}t. \tag{21}$$

There are lower and upper bound constraints imposed on the design variables: $\mathbf{z}^{min}$ and $\mathbf{z}^{max}$, respectively. Different optimization algorithms were compared: Sequential Quadratic Programming (SQP) and Trust Region Reflective (TRR). Solutions obtained with each procedure are set together in Table 1. One can notice that majority of the optimal parameters converged to the boundary constraints. Sample numerical results obtained with the aid of the adjoint method are depicted in Fig. 5a, b. Figure

Table 1 Numerical parameters

Symbol	Value
$\mathbf{z}_0$	$[5500, 25, 3520, 15]^T$ $[\frac{N}{m}, \frac{Ns}{m}, \ldots]$
$\mathbf{z}^{min}$	$[3000, 5, 3000, 5]^T$
$\mathbf{z}^{max}$	$[6000, 30, 6000, 30]^T$
$y_1^{(0)}$	$-5.5\,\mathrm{m}$
$y_2^{(0)}$	$-10.5\,\mathrm{m}$
m_1, m_2	$20\,\mathrm{kg}$
$F(t)$	$1000 \cdot \sin(4\pi t)\ N$
T_f	$1\,\mathrm{s}$
$\hat{\mathbf{z}}_{SQP}$	$[5748, 30, 3000, 12.4]^T$
$\hat{\mathbf{z}}_{TRR}$	$[6000, 30, 3000, 11.8]^T$
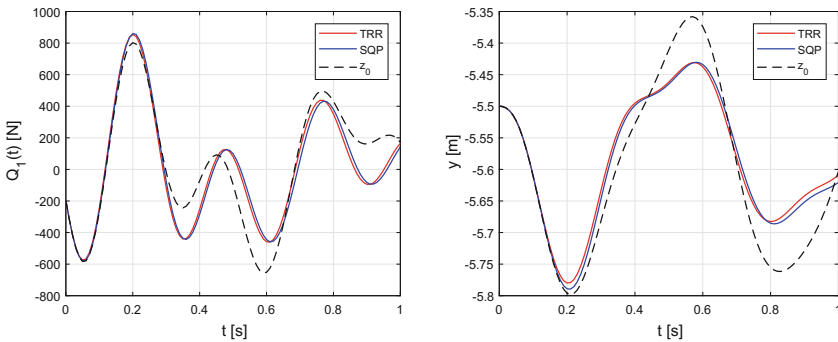
(a) Cumulative force acting on the first body: $Q_1 = m_1 g + F(t) + F_{damp} + F_{spring}$.

(b) Displacement of the first body for different design values.

Fig. 5 Numerical results for the double mass oscillator

5a reports resultant force acting on the first body for optimized and non-optimized systems. A similar comparison is carried out in Fig. 5b, where the first mass displacement is shown.

Some of the performance measures for each of optimization algorithm used for calculations are shown in Fig. 6a. One can see that although both solutions represent a similar value of the cost function, TRR algorithm converged in significantly fewer iterations than SQP algorithm. Figure 6b compares numerical agreement between gradients in case of finite difference and adjoint methods at the starting point $\mathbf{z}_0$. The comparison is performed for constant relative step of central finite difference method $h_i = k \cdot z_i$, where $k = 10^{-8}$. The varying quantity is the step size dt of both forward and backward integration process.

One can notice that there is an optimal step size at which both methods produce similar results. Incrementing time step over the value of 10^{-2} results in incorrect solutions of adjoint equations. On the other hand, decreasing the time-step to the

(a) History of cost and optimality measure for SQP and TRR algorithms.

(b) Consistency of solutions for different time steps of the adjoint method.
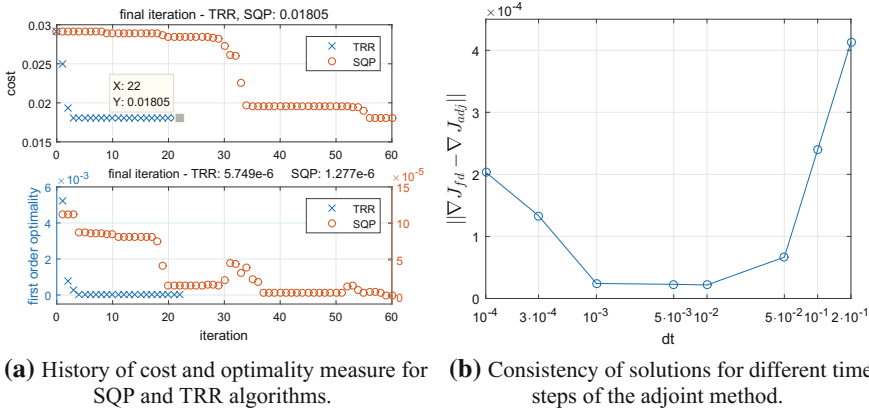
Fig. 6 Performance measures of the optimization process

values below 10^{-3} leads to the ill-conditioning of the tangent matrix in the Newton-Raphson procedure. This way a very small change in design has a great effect on the cost function, which leads to inappropriate solutions obtained with the finite differences method.

4 Summary and Conclusions

A brief insight into the multibody systems' optimization has been presented in this paper. An efficient solution strategy based on the Newmark scheme for forward dynamics problem formulated in descriptor form with mass - orthogonal projections at the velocity and acceleration level is also demonstrated. Furthermore, a general concept of the adjoint method is introduced and subsequently utilized throughout the solution of optimization problems associated with two representative sample test cases. Finally, the numerical outcome is compared with results obtained by finite difference method. The proposed computational algorithm delivers a gradient vector in an efficient and reliable manner with good convergence properties guaranteed by the Newmark scheme. The extension of the method for more elaborated examples including spatial systems are under current development for the authors.

References

1. Cuadrado, J., Cardenal, J., Morer, P., Bayo, E.: Intelligent simulation of multibody dynamics: space-state and descriptor methods in sequential and parallel computing environments. Multibody Syst. Dyn. **4**(1), 55–73 (2000)
2. Haug, J.: Computer Aided Kinematics and Dynamics of Mechanical Systems. Allyn and Bacon, Boston (1989)
3. Haug, J., Wehage, R., Mani, N.: Design sensitivity analysis of large-scale constrained dynamic mechanical systems. J. Mech. Transmissions Autom. Des. **106**(2), 156–162 (1984)
4. Malczyk, P., Frączek, J.: A divide and conquer algorithm for constrained multibody system dynamics based on augmented Lagrangian method with projections-based error correction. Nonlinear Dyn. **70**(1), 871–889 (2012)
5. Nachbagauer, K., Oberpeilsteiner, S., Sherif, K., Steiner, W.: The use of the adjoint method for solving typical optimization problems in multibody dynamics. J. Comput. Nonlinear Dyn. **10**(6), 061011 (2015)
6. Nachbagauer, K., Oberpeilsteiner, S., Steiner, W.: Enhancement of the adjoint method by error control of accelerations for parameter identification in multibody dynamics. Univ. J. Control Autom. **3**(3), 47–52 (2015)
7. Nocedal, J., Wright, S.: Numerical Optimization. Springer, Berlin (1999)
8. Oberpeilsteiner, S., Lauss, T., Nachbagauer, K., Steiner, W.: Optimal input design for multibody systems by using an extended adjoint approach. Multibody Syst. Dyn. **40**(1), 43–54 (2017)
9. Serban, R., Freeman, J.: Identification and identifiability of unknown parameters in multibody dynamic systems. Multibody Syst. Dyn. **5**(4), 335–350 (2001)
10. Suli, E., Mayers, D.F.: An Introduction to Numerical Analysis. Cambridge University Press, New York (2003)
11. Wojtyra, M., Frączek, J.: Comparison of selected methods of handling redundant constraints in multibody systems simulations. ASME. J. Comput. Nonlinear Dyn. **8**(2), 1–9 (2012)

Non-linear Modelling of Human Body Dynamic

Tomasz Mirosław and Adam Zawadzki

Abstract In the paper authors present a concept and a modelling method of the static and dynamic loads of human body's parts: bones and muscles during movement. Currently the problem of human body modelling is very important for many domains of our "better life" programs e.g.: an automotive—to find the best solution for human protection during accidents, sport—to find the most efficient and least tiring movements, to the health protection or extend the active life of the elderly. The human body is not a rigid multi-body system, but elastic, flexible and varying according to time. It consists of semi-stiff bones, elastic muscles and tendons. Other parts like stomach or liver are hanging on elastic wires and move relatively to each other during the whole acceleration process etc. All those elements can be broken or fatigued under some load. So the model of human body is not linear and shouldn't be modelled by linear equation sets. Authors present the concept of human body modelling based on three types element chain. One type are "bones" that are coupled in joints and conduct loads to the support surface; the elastic tendons that keep the joints and propel bones rotation in joints, and muscles that generate forces for stabilization system or for propelling the bones. In paper the simplified model of human body built in MATLAB/Simulink software is presented. Some results of simulation e.g. load of a knee during squat or landing after jump are compared with real test results.

Keywords Multibody systems · Human body dynamics · Computer modeling

T. Mirosław · A. Zawadzki (✉)
Faculty of Automotive and Construction Machinery, Institute of Construction Machinery
Engineering, Warsaw University of Technology, 84 Narbutta str., 02-524 Warsaw, Poland
e-mail: azawadzki@simr.pw.edu.pl

T. Mirosław
e-mail: tmiroslaw@simr.pw.edu.pl

1 Introduction

A problem of human body modelling is getting more and more popular, because we pay more attention to health, body comfort and work effort. In our longer life we expect some problems with our skeleton like pain in neck, backbone or knees. It is a result of an injury that we had in youth. These injuries some times are the effect of accidents or the result of wrong movement during normal activities or sport. We try to avoid injuries by creating the passive and active safety systems in vehicles, creating more ergonomic furniture, better clothes—especially footwear.

To find the real risk of serious injury we develop tests and measurements—for validation of equipment. On the other hand we develop modelling methods. One of the methods used for evaluation of the effect of vehicle crash are phantoms (physical model) build with special materials that have similar structure to skin, muscle, fat and bones. This physical model is put on the driver's and passenger's seats and the crash test is carried out. After that the artificial body parts are examined. Those phantoms are very expensive and very often one-use-only, so these tests are very costly. When we could build a computer model of the vehicle's construction and provide some dynamics simulation we would like to have a similar model for a human body.

Other domain where modelling of the body behaviour is very important is the safety of work or sport. During jogging on rigid surface our heels and knees are exposed on shocks which can be absorbed by sport shoes.

We can reduce those forces by improving the knowledge about our body and by developing good habits and right pattern of our muscle work.

Our body is still an attractive subject for research not only for medics. The technology that compensates disabilities appears to be more and more realistic (Fig. 1).

Our body is composed of bones joined with joints or cartilage, muscles and tendons. All of them are flexible and have possibilities of energy absorption and dissipation on the other hand can be damaged or destroyed during the lifecycle. Currently we can treat our joints, muscles and tendons, with some medicines or in the worst case we can replace them with artificial implants or prosthesis. The analyses of forces acting in a human biological joint or in an artificial implants composed into natural system can help us to better design or use these implants.

2 Model of a Human Body

For many years scientists have built human body models using the theory of multi-body modelling [1–4]. As the first approach and simplified model of movement system we can assume that our skeleton is made of rigid elements with joints which enable the relative movement between them. The movement is effected by muscles which generate the propelling torques.

Depending on the main purpose of modelling we can find more or less precise reflection of human bones in model [5–7]. In Fig. 2 the simplified model of movement

Fig. 1 An active prosthesis of human leg. Photo (Tomasz Mirosław, Milipol 2015 Paris)

system dedicated for basic movement (like standing, walking, running) analyses is presented. This model consist of: head, neck, shoulders, arms, forearms, joined part of backbone, pelvic bone, femurs and calves, and 2 toes for foot (big toe and rest). This model is called 17 segment models. Each part of this model has their mass, inertia, dimensions (presented in Fig. 3).

This model is good enough for kinematic analyses during typical movement like walking. An example of moment analyses with mass centre trajectory is presented in Fig. 4.

This model can be described with forces in joints that can be calculated based on geometry processing methods GP [8]. When we assume that propelling torques are generated in joints we can implement this model to computer software in an easy to process form i.e. the Kroneker product is used to build the synthetic matrix equation.

Those approach is quite effective as it is proved by D. Grzelczyk and others (2018) [9] where Authors used the methodology of rigid body system modelling to solve very important problem of the human bone brake risk estimation during a "broomstick" human forward fall", which especially consider elder people.
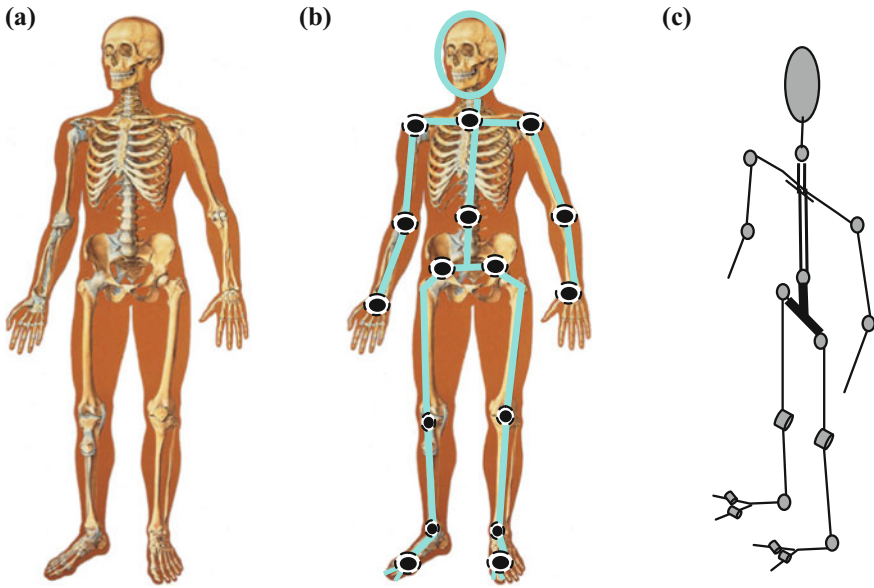
Fig. 2 The model of human body motion system. The simplified model of human skeleton [18]
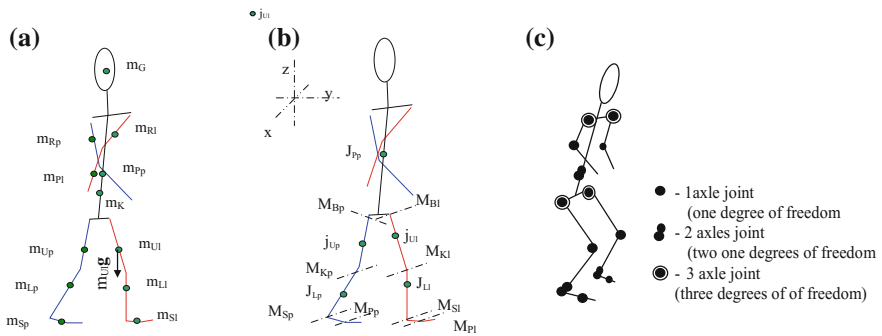
Fig. 3 Mass and forces, inertia moment and torques, joints types of human body system model

But in our body the moment comes from muscle forces or from gravity. Joints do not generate any torques. The muscles with tendons can generate forces and accumulate the potential energy and the muscle can dissipate it. But in more precise analyses we can find in our body bone and tendon bow-like structure for shock absorption and short term energy accumulation. Some bones are prepared to work as safety system—like a fuse, which can be broken when the load is too high.

In a typical model we assume that bones of the skeleton are propelled by muscles controlled by brain.

The model of a muscle and whole simplified movement system of skeleton with muscles is presented in Fig. 5 (based on [10, 11]).
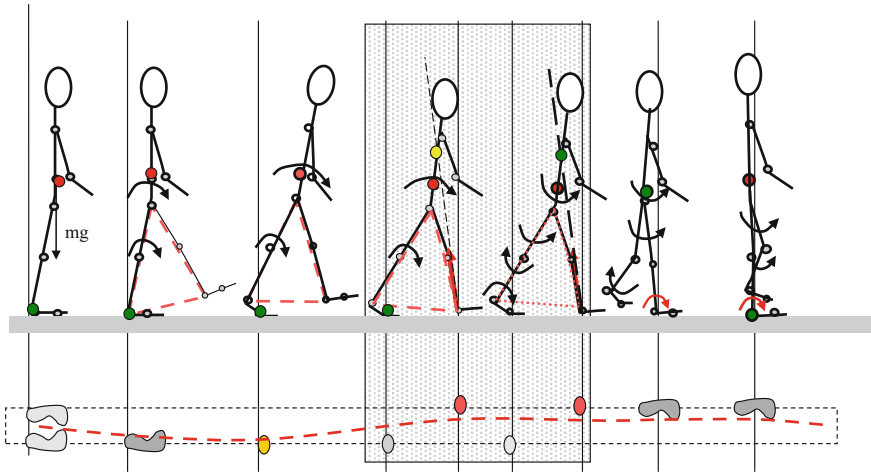
Fig. 4 The walking model with 17 segment human body model
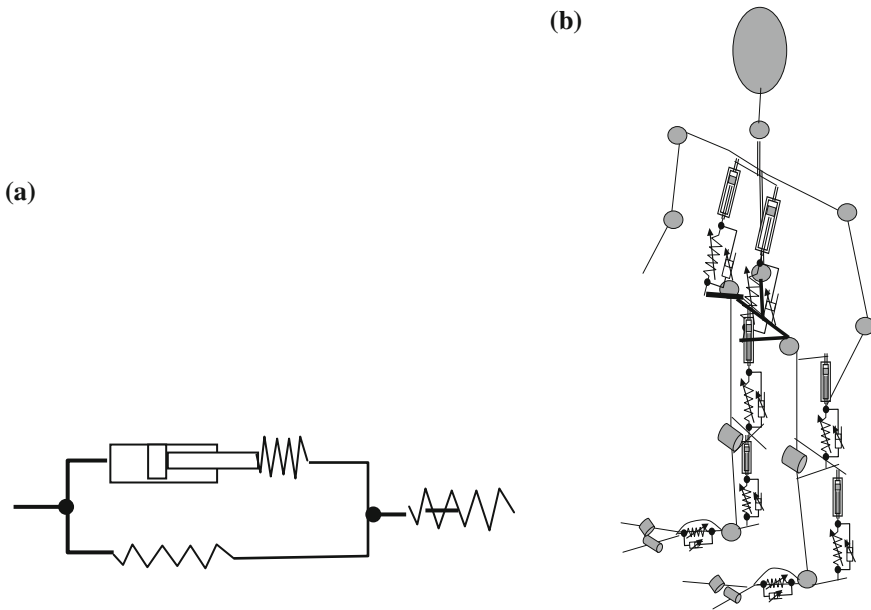
Fig. 5 a Model of human muscle that consists of three passive elements: a series elastic element corresponding to tendon and connective tissue, parallel elastic element and damper. **b** The model skeleton with muscles

When we introduce muscles flexible elements the other method of analyses is recommended. The modelling with flexible elements like ACNF should be more efficient in reference to human body [8].
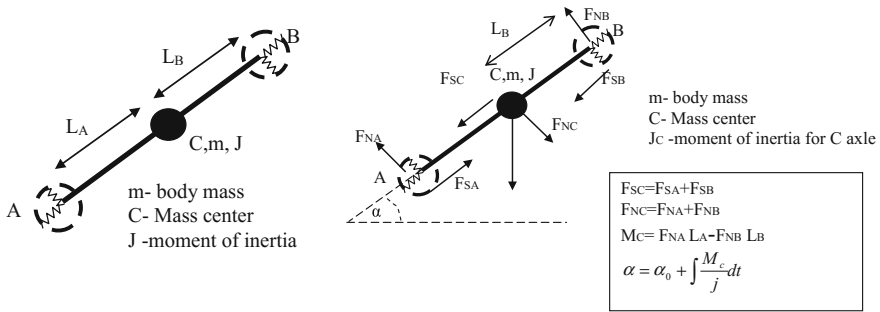
Fig. 6 A model of human bone with rigid body and flexible (resilient/spring ball) ends

The joints that connect bones are different. Almost all joints between different bones have different structure optimized to specific movement and load [12–16]. Usually for moment analyses we can differ them according to their degrees of freedom, but for other analyses for instance of load resistance we have to take into account much more construction details, that will be presented in further part of this paper.

The motion system is not a rigid system. The flexible part can be modelled by adding the parallel system of flexible elements which represent the muscles with tendons. It is the next simplification. Of course such a model reflects the energy accumulation function of muscles.

Although the bones are still rigid. But as it was mentioned above, one of the interesting problems is to estimate the forces in joints during dynamic process [9]. This forces can cause the rapid damage of joint when it overcomes the critical limit value or can cumulate the small damages when the load is too big.

For few years authors used the model developed for exoskeleton cooperation with human body. The method and model of human lower limbs was described in authors other paper [17].

In that paper the bones are modelled as the flexible body with geometrical size, mass, inertia and elastic ends (Fig. 6). Those are combined into multi-body system of bones joined with invisible tendons into the limb (Fig. 7). Forces affecting bones come from displacement of flexible ends.

Those methods were prepared to be implemented with MATLAB/Simulink software.

The example of 2D (two dimension) bone model is presented in Fig. 8. It consists of two terminals A and B (modelled in the same way) and mass centre. The body block have inputs for forces represented by components in horizontal and vertical reference systems) for two terminals A and B: FBXR (terminal B component X reaction force), FBYR (terminal B component Y reaction force) and external forces: FBXE and FBYE, analogous FAXR, FAYR, FAXE, FAYE for terminal A. The input Mext—represents the external torque for body rotation—which can represent the torque produced by muscles. Additionally the start position of mass centre X0 and Y0 with start angle ALFA and distances of terminals from the mass centre DLA and
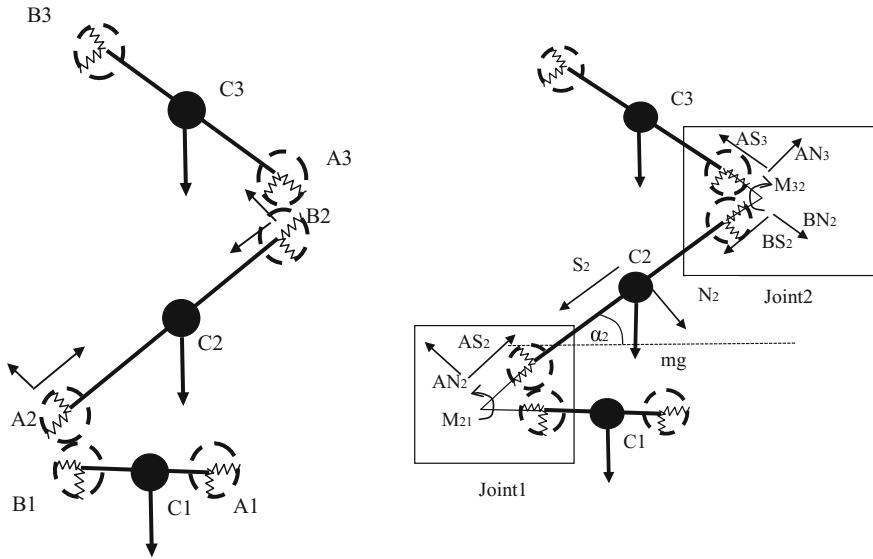
Fig. 7 Model of leg-as the bones joined with contact of flexible ends

DLB are given. The outputs are: coordinated of real position terminal BX, CY, AX, AY and mass centre CX and CY and real angle. Additionally two outputs of MA and MB, representing torques generated in terminals, are present for tests.

The structure of terminal model is presented in Fig. 9. This model consists of terminal position calculator marked as DBXY. The effect of calculation is given to outputs EY and EX. Forces from inputs Fx, FXr and Fy, FYr are summed and given together with real angle to XY2SN transformation block, where XY components are converted to SN component. The orthogonal force component is used for torque calculation. These forces and torques are sent to mass centre model.

Model of mass centre is presented in Fig. 8. In this block the weight force appear and is transformed into SN components basing on actual rotation angle. These forces are summed with forces coming from terminal and, after dividing by mass value, appear the acceleration in axles N and S. This acceleration is converted to XY coordinate and integrated for real speed and XY position. The real speed is reversely converted to SN coordinates for damping force calculations. The CX and Y position is estimated in reference to Y0, X0—the start position.

In this block the torque is calculated as the sum of torques coming from both terminals and from the outside. This torque accelerates the rotation proportionally to inversion of body inertia moment. After its double integration we get real angle of body bending. So the model is geometrically oriented multimode system model, but the movement of element depend on interaction with joined bodies (Figs. 10 and 11).

The structure of joint is presented in Fig. 12. It consist of two blocks: Torque and reaction force generator. Their structure is shown in Figs. 13 and 14. The forces and
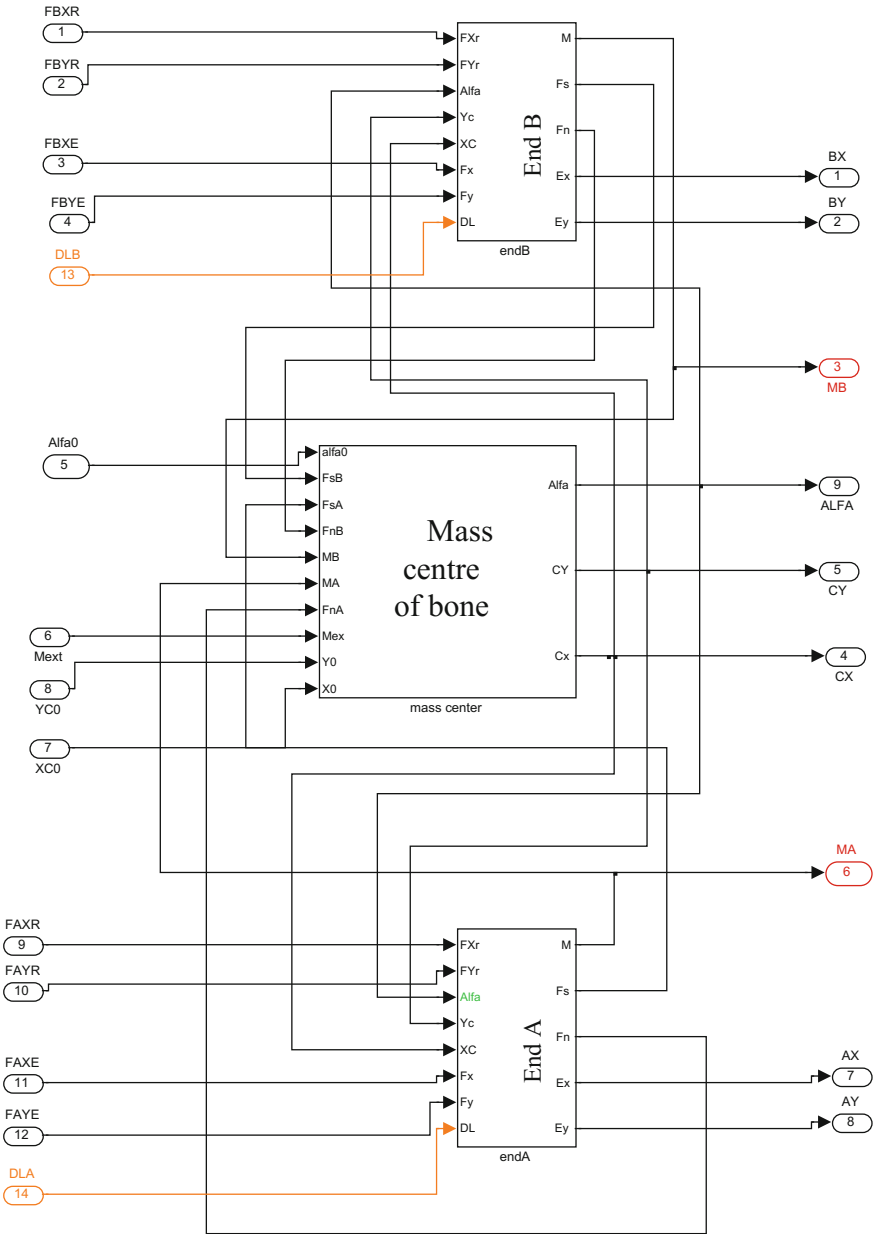
Fig. 8 The bone SIMULINK/MATLAB model. In reference to Fig. 6

torques are calculated in reference to displacement or bending flexible elements. So the forces are generated where displacement appears, not as the free vector. In the
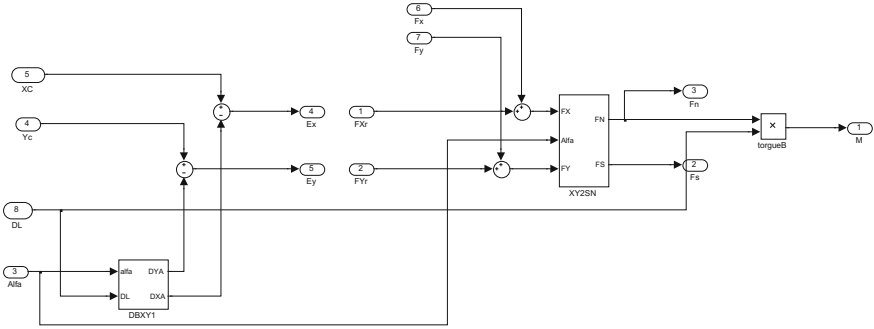
Fig. 9 The bone terminal model
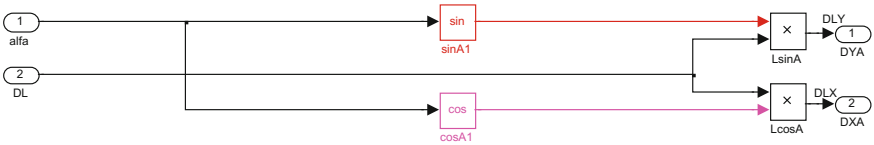
Fig. 10 The terminal position calculator
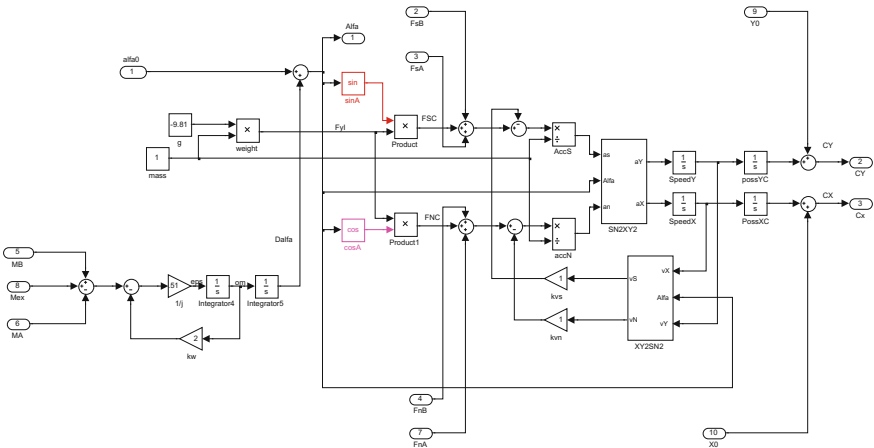
Fig. 11 The mass centre block internal structure

torque generator the input gamma is the value of the angle between bodies when torque of torsion is equal to zero. Each force and torque are multiplied by "−1" to give the action and reaction forces which are sent to both cooperating bodies. As we can see these structure are very simple and adjustable by setting various gains coefficients (Fig. 15).
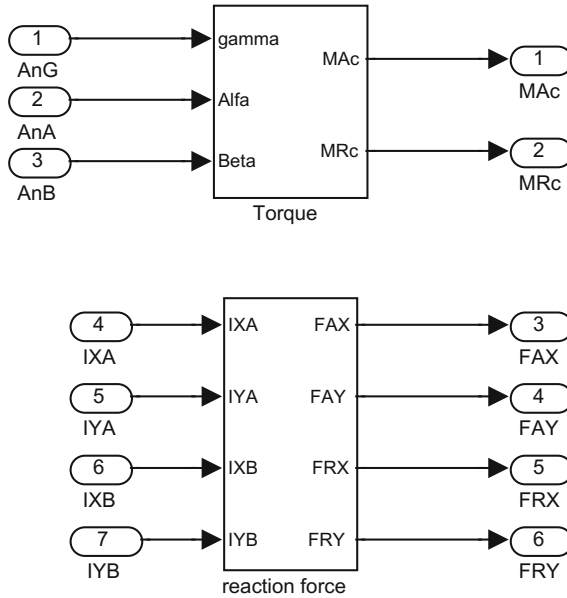
Fig. 12 Structure of joint model

3 Model Verification

The experiment with falling body (jump) down on the ground was chosen as the example of the model verification. It seems to be important because of potential to kinetic energy conversion and the dynamic changes of the system structure from free to open one. A damping and elasticity coefficient was set to constant value. In Fig. 16 the result for different values of coefficients is presented.

The diagram of movement of the free end and mass centre of highest body is shown in Fig. 16. We can see that after landing this body is bending and rising. In Fig. 17 (right side) we can see the trajectory of mass centres of lower and middle part of the system. They are moved almost in a straight line.

But for more reliable analyses we should take account the structure of joint. The most often damaged joint is the knee. Probably each of us experienced pain in it or for sure know someone who have or had knee injury. Fortunately the joint is much more complicated in its structure than hinge joint. Proposed spring ball-terminated ball model is more adequate for knee joint simulation than typical one axle hinge joint. The rolling heads of joined bones change the contact point and tangential forces acting with knee bent angle. The normal force creating the rotation torque goes though ligaments of the knee and muscles. The torque depends not only on muscles forces but on the angle of rotation and moving rotation point as it is shown in Fig. 17.
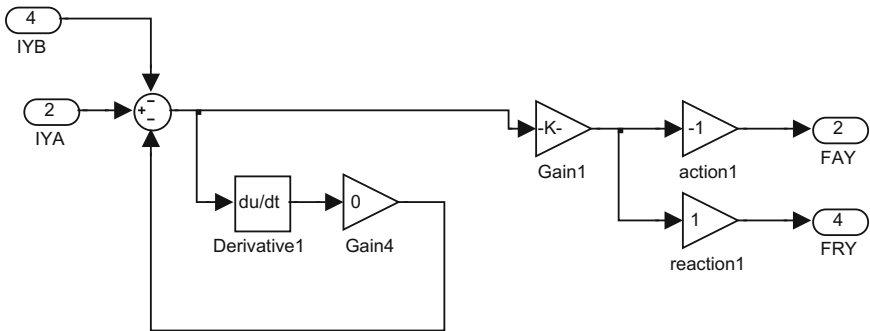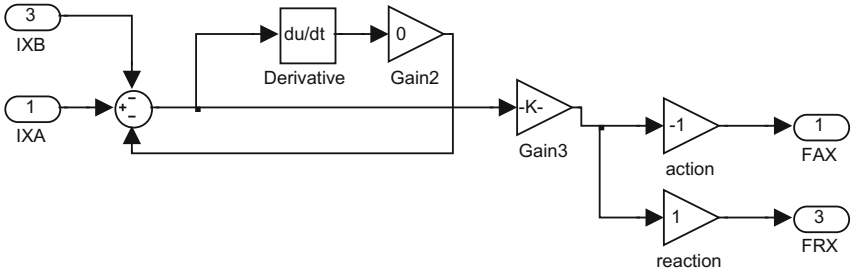
Fig. 13 Structure of reaction force generator
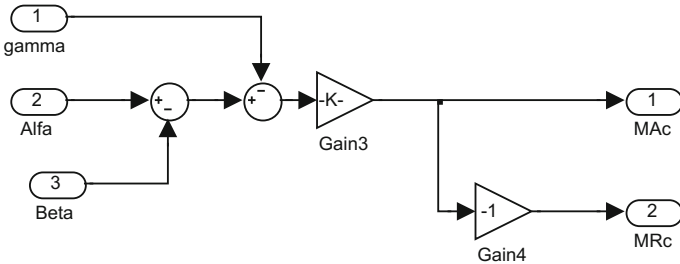
Fig. 14 Generator of reaction torque

4 Conclusions

This model of limb, seems to be easily understandable and worked properly, so it has been the base for further development of modelling focused on forces acting in the heads of bones, muscles and tandems. These simulation results seems to be interesting and model can show the forces which appear in joints.
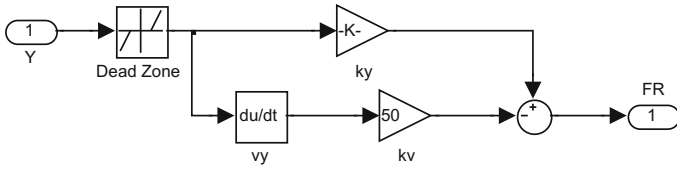
Fig. 15 Block of ground reaction
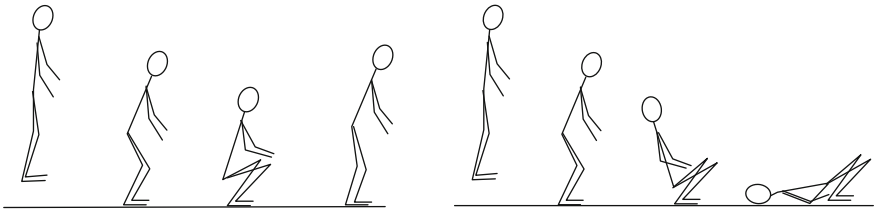
Fig. 16 Examples of simulation results
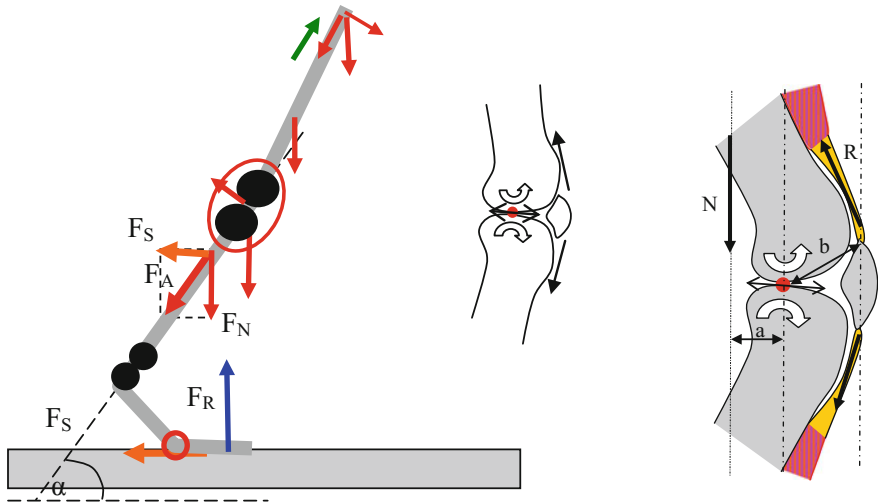
Fig. 17 Forces acting on a knee joint

References

1. Pons, J.L.: Wearable Robots: Biomechatronic Exoskeletons, CSIC, Madrid, Spain. Wiley (2008)

2. Dollar, A., Her, H.: Lower extremity exoskeletons and active orthoses: challenges and state-of-the-art. IEEE Trans. Robot. **24**(1), 144–158 (2008)
3. Zoss, A., Kazerooni, H., Chu, A.: Biomechanical design of the Berkeley Lower Extremity Exoskeleton (BLEEX). IEEE/ASME Trans. Mechatron. **11**(2), 128–138 (2006)
4. Bortole, M., Venkatakrishman, A., Hill, A.V.: First and Last Experiments on Muscle Mechanics. Cambridge University Press, Cambridge (1970)
5. Ghan, J., Kazerooni, H.: System identification for the Berkeley Lower Extremity Exoskeleton (BLEEX). In: Proceedings of the International Conference on Robotics and Automation, Orlando, Florida (2006)
6. Low, K., Yin, Y.: An integrated lower exoskeleton system towards design of a portable active orthotic device. Int. J. Robot. Autom. **22**(1), 32 (2007)
7. Pillai, M., Kazerooni, H., Hurwich, A.: Design of a semi-active knee-ankle prosthesis. In: IEEE International Conference on Robotics and Automation. Shanghai, China (2011)
8. Mikkola, A., Shabana, A., Sanchez-Rebollo, A., Jimenez-Octavio, C.: Comparison between ANCF and B-spline surfaces. Multibody Syst. Dyn. **30**(2), 119–138 (2013)
9. Grzelczyk, D., Biesiacki, P., Mrozowski, J., Awrejcewicz, J.: Dynamic simulation of a novel "broomstick" human forward fall model and finite element analysis of the radius under the impact force during fall. J. Theor. Appl. Mech. **56**(1), 239–253 (2018) (Warsaw)
10. Valiente, A.: Design of a quasi-passive parallel leg exoskeleton to augment load carrying for walking. Master's thesis, Department of Mechanical Engineering, Massachusetts Institute Technology, Cambridge (2005)
11. Sawicki, G.S., Khan, N.S.: A simple model to estimate plantar flexor muscle-tendon mechanics and energetics during walking with elastic ankle exoskeletons. TBME 2015
12. Kumar, V.: Modeling, analysis and simulation of multibody systems with contact and friction, Peng Song (2002)
13. Otter, M., Elmqvist, H., Cellier, F.E.: Modeling of multibody system with the object-oriented modeling language dymola. Nonlinear Dyn. **9**(1), 91–112 (1996)
14. Liu, Y., Schmiedeler, J., Wensing, P., Orin, D.: A 3D Dual-SLIP model of human walking over a range of speeds. http://biomechanics.osu.edu/dynamic-walking/AbstractsFolder/Liu_2015_DW.pdf
15. Bertholdt, M., Kapper, J., Schmodt, S., Schnorr, C.: A study of parts based object class direction using complete graphs. Int. J. Comput. Vis. (2010)
16. Zahariev, E.: Computer system for kinematic and dynamic analysis synthesis of rigid and flexible multibody systems. PAMM **8**(1), 10163–10164 (2008)
17. Miroslaw, T.: The method of modeling of human skeletons multi-body system. In: Awrejcewicz, J. (eds.) Dynamical Systems: Modelling. DSTA 2015. Springer Proceedings in Mathematics & Statistics, vol. 181. Springer, Cham (2016)
18. https://www.anatomystuff.co.uk/media/catalog/product/cache/1/image/1000x/9df78eab3352 5d08d6e5fb8d27136e95/i/m/img_1000012-the-human-skeleton-back-view-oversized-chart-_ with-rods.jpg

Dynamics of a Portable Module Handling System

Robert Mitoraj and Marek Szczotka

Abstract The paper describes a model of a light module handling system (LMHS) developed for IMR (Inspection, Maintenance and Repair) services typically performed for the seabed-located oil and gas production facilities. In order to describe dynamic performance and loads during the operation, the system is characterized by means of a multi-body model consisting both rigid and flexible links. Using the joint coordinates and homogeneous transformations the dynamics can be described by a set of differential equations of the second order and some constraint equations. The system forms several tree-like structures of bodies. The interaction between them takes place on guiding elements and lifting ropes. An important features of the handling system are flexible guide beams and prongs. The flexibility provided by those elements helps to limit some impact loads during the module docking phase. This functionality is modelled by the rigid finite elements. Lifted objects (subsea modules) are described by a set of special elements defining the hydrodynamic interaction. The work will also show some simulation results reflecting a typical operation.

Keywords Module handling systems · Dynamics · Subsea installations

1 Introduction

Subsea modules are complex units installed on the seabed and operated remotely. These units process the natural resources and differ in size and functions. Typically, they serve as separation valves, pumps or compressors, coolers, dischargers or other

R. Mitoraj · M. Szczotka (✉)
AXTech AS, Fannestrandsvegen 85 PO Box 2008, 6402 Molde, Norway
e-mail: mszczotka@axtech.no

R. Mitoraj
e-mail: rmi@axtech.no

M. Szczotka
Department of Transport Willowa 2, University of Bielsko-Biała,
43-309 Bielsko-Biała, Poland

units. Beside the installation, it is required to perform maintenance on these objects. Despite rough sea conditions, damaged modules must be safely replaced with new ones. To address these challenges, a "small" special module handling system has been developed. Several new functions makes this tool unique. As the majority of subsea modules weight up to 25 tons, the LMHS can be easily applied in existing and future installations. One of the most important futures of the LMHS is its ability to be installed on an "average" supply vessel. No special vessel is required, in contrast to a typical crane-based constructions with detailed specified hull requirements. Moreover, the LMHS can be relocated within 48 h to an another ship (it can be packed in two containers for road transportation).

There are many examples of computational models of offshore systems. Often coupled, complex hydrodynamic motion analyses are conducted for ship cranes and payloads, for example in [1, 3, 4]. Numerical and experimental tests are performed for vessels and equipment where design loads (the wire rope tension) are calculated during installination, such as a 150 ton subsea manifold investigated in [5]. The calculations require hydrodynamic coefficients to be determined by CFD, which is a common practice when ships [9] and lifted objects [7] are analysed. Crane booms are can be very large and its flexibility shall be also considered [6], which makes an additional challenge for designers.

A mathematical model developed is presented in this work. It allows us to calculate dynamic loads acting on the LMHS structure and modules. Assumed vessel and weather criteria can be tested with respect to design criteria. The main goal was to provide a simple, convenient method that allows an engineer to perform qualitative assessment without access to a large and expensive computation systems.

2 LMHS Basic Assumptions and Layout

The design concept considers a safe launch and recovery of subsea modules performed on typical supply vessels having an average performance on moderate sea states. An installation over the vessel side as well as over a moonpool are taken into account. The main components are shown in Fig. 1.

The CGS (cursor guide system) is specially designed to guide the module safely and consist of (Fig. 1b) the following main parts: guide rails (integral part of the slewing column), guide frame, slide frame, two prong beams with prongs. An easy adjustments of prongs towards required module geometry (funnels) is crucial.

3 Mathematical Model

Dynamic analysis must be conducted in order to predict loads and check for the limitations of the LMHS. A mathematical model is developed for that purpose. The LMHS is modelled as a multibody system with both rigid and flexible bodies
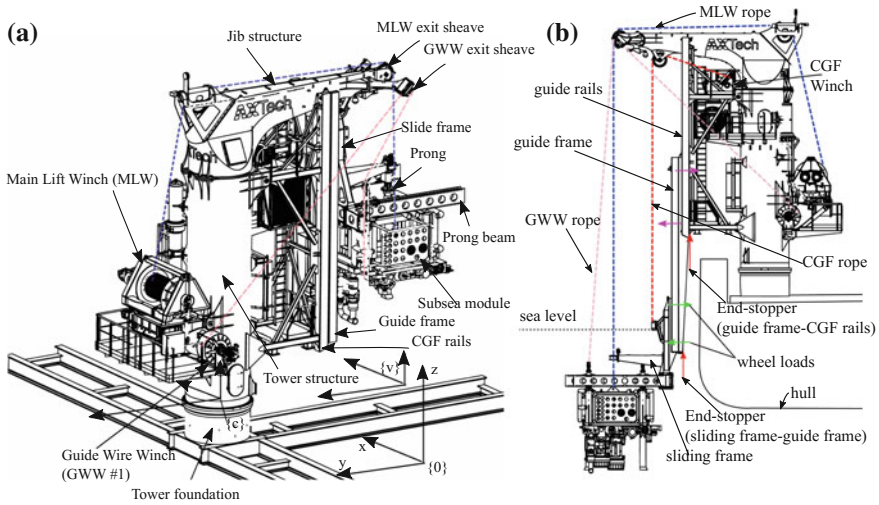
Fig. 1 LMHS - main components, **a** system with module over deck (CGF frames retracted), **b** over-boarded position with module launched (CGF frames extracted)

consisting of multiple, tree-like structures. The flexibility of selected bodies is considered using the rigid finite element method [12].

3.1 Transformation of Coordinates

The inertial coordinate system is designated as $\{0\}$, while the coordinate system $\{p\}$ will be attached to a body (p) (which may be dependent on proceeding bodies in kinematic chain, [2]). The homogeneous transformation matrix to transform coordinates from the coordinate system $\{p\}$ to the inertial system $\{0\}$ denotes $_p^0\mathbf{T}$. This matrix depends on all the generalized coordinates of the body (p) in chain, i.e.

$$
_p^0\mathbf{T} = \mathbf{T}^{(p)}\left(\mathbf{q}^{(p)}\right) = \mathbf{T}^{(p-1)}\left(\mathbf{q}^{(p-1)}\right) \cdot \mathbf{T}^{(p)}\left(\tilde{\mathbf{q}}^{(p)}\right) = \mathbf{T}^{(p-1)}\left(\mathbf{q}^{(p-1)}\right) \cdot \prod_{i=1}^{n_p} \mathbf{U}\left(q_i^{(p)}\right)
$$

(1)

where $\mathbf{q}^{(p)} = \left[q_1^{(p)} \ \ldots \ q_{n_p}^{(p)} \right]^T = \left[\left(\mathbf{q}^{(p-1)}\right)^T \ \left(\tilde{\mathbf{q}}^{(p)}\right)^T \right]^T$, $\mathbf{q}^{(p-1)}$ is the vector of generalized coordinates of proceeding body $(p-1)$ in chain, $\tilde{\mathbf{q}}^{(p)} = \left[\tilde{q}_1^{(p)} \ \ldots \ \tilde{q}_{\tilde{n}_p}^{(p)} \right]^T$ is the vector of generalized coordinates describing the relative motion of the body (p) with respect to $(p-1)$, n_p is the number of generalized coordinates of the body p in kinematic chain, $\mathbf{U}_i^{(p)}\left(\tilde{q}_i^{(p)}\right)$ is transformation matrix which depends only on one generalized coordinate $\tilde{q}_i^{(p)}$, $i = 1, \ldots, \tilde{n}_p$, $\tilde{n}_p \le 6$.

For some bodies the vector $\mathbf{q}^{(p-1)} = \emptyset$ (no proceeding body - applies to the vessel, guide frame, slide frame and module bodies).

3.2 Generalized Coordinates of the System

In this work we consider that the vessel's motion can be defined by known functions. For practical reasons we simplify the vessel's response to a simple harmonic input (see Fig. 3). Therefore the first body's motion is constrained by the six motion parameters ($x^{(v)}$-surge, $y^{(v)}$-sway, $z^{(v)}$-heave, $\psi^{(v)}$-yaw, $\theta^{(v)}$-pitch and $\varphi^{(v)}$-roll):

$$\mathbf{q}^{(v)}(t) = \left[x^{(v)}(t) \; y^{(v)}(t) \; z^{(v)}(t) \; \psi^{(v)}(t) \; \theta^{(v)}(t) \; \varphi^{(v)}(t) \right]^{T} \tag{2}$$

where $x^{(v)}(t), \ldots, \varphi^{(v)}(t)$ are known (assumed) functions of time t and other parameters depending on vessel design and operational conditions.

The homogeneous transformation matrix of the vessel, $\mathbf{T}^{(v)}\left(\mathbf{q}^{(v)}\right) = \mathbf{T}^{(v)}\left(\mathbf{q}^{(v)}(t)\right)$, is also known and can be found for example in [12] where also the detailed approach is presented.

The LMHS column (regarded in this work as a rigid body) may rotate around the vertical axis of a local coordinate system $\{c\}$ (Fig. 1), therefore its vector of generalized coordinates is:

$$\tilde{\mathbf{q}}^{(c)} = \left[\tilde{\psi}_c \right] \tag{3a}$$

$$\mathbf{q}^{(c)} = \left[\mathbf{q}^{(v) \, T} \; \tilde{\mathbf{q}}^{(c) \, T} \right] \tag{3b}$$

while the jib is regarded as a flexible part divided into $n_f^{(j)}$ rigid finite elements (rfe) (element $i = 0$ is part of the column):

$$\tilde{\mathbf{q}}^{(j)} = \left[\tilde{\mathbf{q}}_1^{(j) \, T} \; \cdots \; \tilde{\mathbf{q}}_{n_f^{(j)}}^{(j) \, T} \right]^{T} \tag{4a}$$

$$\mathbf{q}^{(j)} = \left[\mathbf{q}^{(v) \, T} \; \tilde{\mathbf{q}}^{(c)} \; \tilde{\mathbf{q}}^{(j) \, T} \right]^{T} \tag{4b}$$

where $\tilde{\mathbf{q}}_i^{(j)} = \left[\tilde{\psi}_i^{(j)} \; \tilde{\theta}_i^{(j)} \; \tilde{\varphi}_i^{(j)} \right]^{T}$, $\tilde{\psi}_i^{(j)}, \ldots, \tilde{\varphi}_i^{(j)}$ are the rotation angles due to deformation of the i-th rfe with respect to its proceeding body (or rfe), $i = 1, \ldots, n_f^{(j)}$. Four winch drums are included in the similar way as the slewing column. The generalized coordinates defining drum rotation can be formulated as (these bodies are added to the slewing column body):

$$\mathbf{q}^{(w)} = \left[\mathbf{q}^{(c) \, T} \; \varphi^{(w)} \right]^{T} \Big|_{w \in \{M, C, G_1, G_2\}} \tag{5}$$

where M depicts for main lifting winch (MLW), C stands for cursor guide winch (CGFW) and G_1, G_2 for the two guide wire winches (GWW #1 and GWW #2).

Guide frame (g) and sliding frame (s) bodies are assumed to be rigid as well and the vectors of generalized coordinates (both $\mathbf{q}^{(g)}$ and $\mathbf{q}^{(s)}$) take the form:

$$\mathbf{q}^{(f)} = \left[x^{(f)} \ y^{(f)} \ z^{(f)} \ \psi^{(f)} \ \theta^{(f)} \ \varphi^{(f)} \right]^T, \ f \in \{g, s\} \tag{6}$$

and the generalized coordinates for these parts are independent, hence $\mathbf{q}^{(f)} = \tilde{\mathbf{q}}^{(f)}$ and $\mathbf{q}^{(f-1)} = \emptyset$, $f \in \{g, s\}$.

Flexible prong beams (b_k), $k = 1, 2$ are attached to the sliding frame using hinge connections. The vectors of generalized coordinates are:

$$\mathbf{q}^{(b_k)} = \left[\mathbf{q}^{(s) \ T} \ \tilde{\mathbf{q}}^{(b_k) \ T} \right]^T \tag{7}$$

where $\tilde{\mathbf{q}}^{(b_k)} = \left[\tilde{\mathbf{q}}^{(b_k,0) \ T} \ \ldots \ \tilde{\mathbf{q}}^{\left(b_k, n_f^{(b_k)} \right) \ T} \right]^T$,

$$\tilde{\mathbf{q}}^{(b_k,i)} = \begin{cases} \left[\psi^{(b_k,i)} \ \theta^{(b_k,i)} \ \varphi^{(b_k,i)} \right]^T & \text{for } i = 1, \ldots, n_f^{(b_k)} \\ \left[\psi^{(b_k,i)} \right] & \text{if } i = 0 \end{cases}$$

The module is considered as a single rigid body with six degrees of freedom:

$$\mathbf{q}^{(m)} = \left[x^{(m)} \ y^{(m)} \ z^{(m)} \ \psi^{(m)} \ \theta^{(m)} \ \varphi^{(m)} \right]^T \tag{8}$$

which again yields to $\mathbf{q}^{(m-1)} = \emptyset$ and its equations of motion are coupled with the LMHS system by wire forces and contact forces between funnels and prongs.

3.3 Guiding Elements

Figure 2 shows guiding elements transmitting loads in the cursor guide system. Figure 2a presents CGF rails, which are an integral part of the slewing structure. CGF rails "constrain" the guide frame body motion (together with the mechanical end-stoppers to limit its vertical motion) using eight wheels: four of them transfer the loads in "Y" direction, and the other four along the "X" direction. The guide frame also posses its own guiding rails - for guiding the sliding frame. The sliding frame (Fig. 2b), is equipped with eight wheels, too. A similar wheel arrangement is used for the slide frame - guide frame interface.

In addition to the wheels, there are also mechanical end-stoppers (indicated Fig. 1b), limiting the movement of guide and sliding frames. When the module is lowered into the sea, the guide frame rests on stoppers, and the sliding frame continues to slide downward, until it reaches the end position (by end stoppers) with fully submerged module. In the other case, whenever the module is handled over the sea/deck, the guide frame is resting on the end-stoppers transferring its weight into the slide frame.
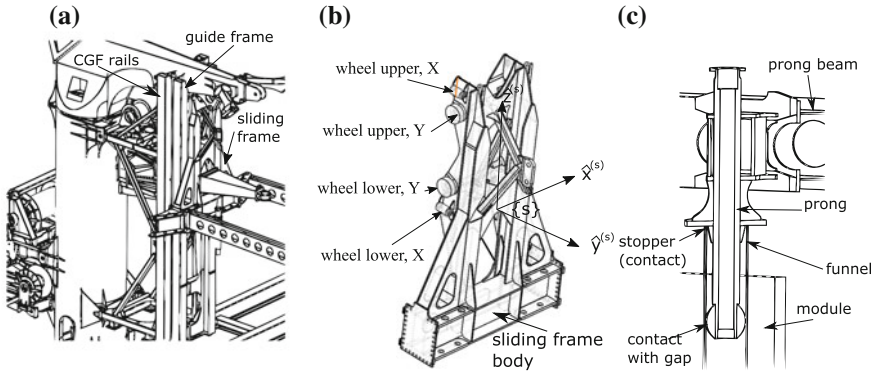
Fig. 2 Guiding elements: **a** CGF rails, **b** sliding frame wheels, **c** prong-module interface

Wheels and stoppers are simulated by introducing a special spring-damping elements, with a non-linear characteristics and arbitrary selected clearances. A proper modelling of the stiffness curve allows us to overcome some numerical difficulties due to changing conditions (sudden contacts) as well as the clearance can be introduced (design constants). Suitable models for such elements are developed, some similar approaches can be found in [10] or [11]. The interaction between the module and prongs is handled similarly. Figure 2c shows contact pairs that guide the module: the upper plate of the prong is working as a stopper, and a soft material forms a spherical shape, that guides the prongs inside the funnels. The upper plate (stopper) plays also other important function - provides required down-force to the module.

3.4 Drive Elements

Slewing column, the jib angle and winches (drum rotations) motions are controlled, which can be realised in the form of kinematic constraints:

$$\varphi^{(i)} = \varphi^{(i)}(t) \tag{9}$$

where $\varphi^{(i)} \in \left\{ \tilde{\psi}^{(c)}, \tilde{\varphi}_1^{(j)}, \tilde{\varphi}^{(M)}, \tilde{\varphi}^{(C)} \right\}$ is the appropriate degree of freedom specified in (3a), (4a) or (5).

In order to obtain a desired motion of driven components, additional unknown reactions must be formulated. These driving moments (unknown reactions), ensuring the courses of selected in (9) degrees of freedom, are the components the vector:

$$\mathbf{R}_d = \begin{bmatrix} M_c & M_{j_1} & M_M & M_C \end{bmatrix}^T \tag{10}$$

which must be included in the equations of motion.

3.5 Equations of Motion

The equations of motion for the whole system dynamics can be written in the form:

$$\mathbf{A}\ddot{\mathbf{q}} - \mathbf{D}\mathbf{R} = \mathbf{F} \tag{11a}$$

$$\mathbf{D}^T\ddot{\mathbf{q}} = \mathbf{W} \tag{11b}$$

where $\mathbf{A}$ is the inertia matrix (non-diagonal, with variable elements), $\mathbf{q} = \left[\mathbf{q}^{(H)\,T}\ \mathbf{q}^{(f)\,T}\ \mathbf{q}^{(s)\,T}\ \tilde{\mathbf{q}}^{(b_1)\,T}\ \tilde{\mathbf{q}}^{(b_2)\,T}\ \mathbf{q}^{(m)\,T}\right]^T$ is the vector of generalized coordinates, $\mathbf{q}^{(H)} = \left[\mathbf{q}^{(v)\,T}\ \tilde{\psi}^{(c)}\ \tilde{\mathbf{q}}^{(j)\,T}\ \tilde{\varphi}^{(M)}\ \tilde{\varphi}^{(C)}\ \tilde{\varphi}^{(G_1)}\ \tilde{\varphi}^{(G_2)}\right]$, $\mathbf{R} = \left[\mathbf{R}^{(v)\,T}\ \mathbf{R}_d^T\right]^T$ is the vector of unknown reactions, $\mathbf{R}^{(v)}$ is the vector of reactions ensuring realisation of the vessel motion, $\mathbf{D}$ is the constraint coefficient matrix, $\mathbf{F} = \mathbf{F}(t, \mathbf{q}, \dot{\mathbf{q}})$, $\mathbf{G} = \mathbf{G}(t, \mathbf{q}, \dot{\mathbf{q}})$

When $n_f^{(j)} = n_f^{(b_1)} = n_f^{(b_2)} = 0$, Eq. (11) represent a system of minimum $M_{\mathbf{q}} = 30$ differential equations and $N_{\mathbf{R}} = 10$ constraint equations. The equations are solved by numerical integration using the Runge-Kutta method of the fourth order with fixed time step. The initial conditions were found assuming $\ddot{\mathbf{q}} = \dot{\mathbf{q}} = \mathbf{0}$ in (11) and solving for $\mathbf{q}$ and $\mathbf{R}$ with the Newton's method [8].

4 Example Simulations

Principal parameters of the vessel, sea conditions and LMHS location considered in example simulations are listed in Table 1.

The motion of the vessel is approximated based on available hydrodynamic calculations and shown in Fig. 3.

Two cases are investigated, where the slewing function is assumed as in Fig. 4a:

- LC-A: operation without the module (governing load case for the CGF winch)
- LC-B: operation with 20 t module (governing loads for the crane structure and MLW drive)

Time histories of calculated slew drive reactions are presented in Fig. 4a. The drive torque equivalent for operation of empty LMHS, despite lower values obtained, is

Table 1 Main parameters of vessel and LMHS

Parameter	Value (m)	Parameter	Value
Vessel's length	120	Sig. wave height	3 m
Vessel's breadth	22	Wave headings	0°, 45°, 90°
Vessel's draught	7.5	LMHS base loc:	$\tilde{\mathbf{r}}_c^{(v)} = \begin{bmatrix} 0 & 10.0 & 1.8 \end{bmatrix}^T$
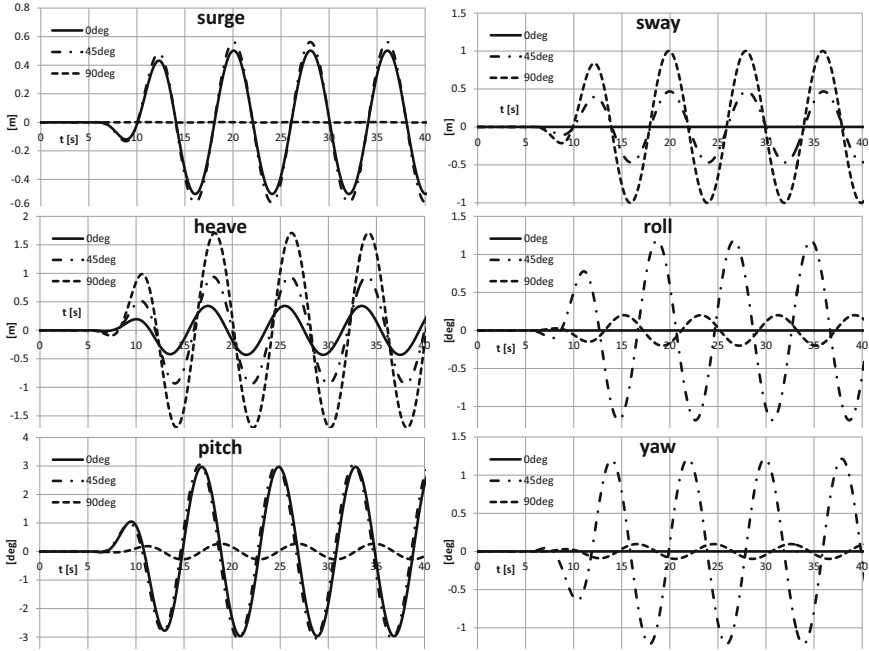
Fig. 3 Vessel motion assumed, headings 0°, 45° and 90°
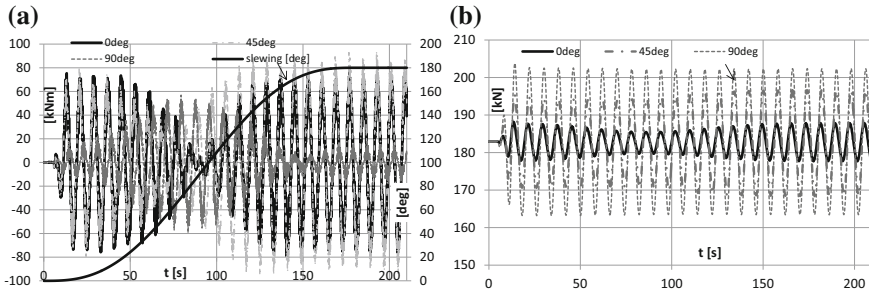
Fig. 4 Results for LC-A **a** slew rotation and moment M_c, **b** CGF winch tension force

important for dimensioning of the gear box life time (spectrum definition). It's also important that representative loads acting on CGF rope are determined (Fig. 4b). This allows for dimensioning of the CGF winch drive including fatigue loads for the drive gears as well as for the rope.

Similar results are presented when the module is present, Fig. 5 (same slewing function as in LC-A case). Slew drive moments for three headings are presented in Fig. 5a, where the moment peaks have increased up to 250 kNm which is caused by the module's inertia forces. The MLW rope tension force is shown in Fig. 5b: it equals the module and all CGF frame masses (i.e. all objects handled by MLW, excluding
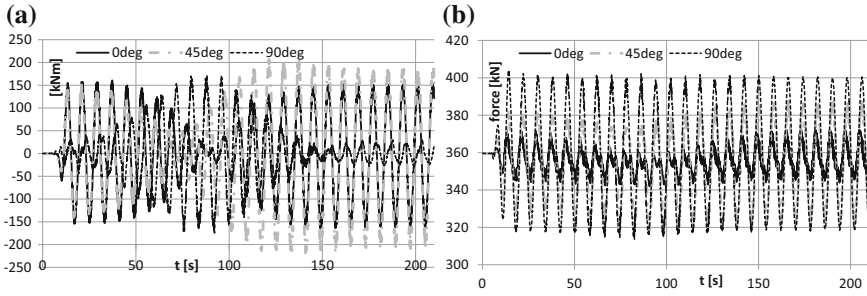
Fig. 5 Results for LC-B **a** slew drive moment M_c, **b** MLW rope force
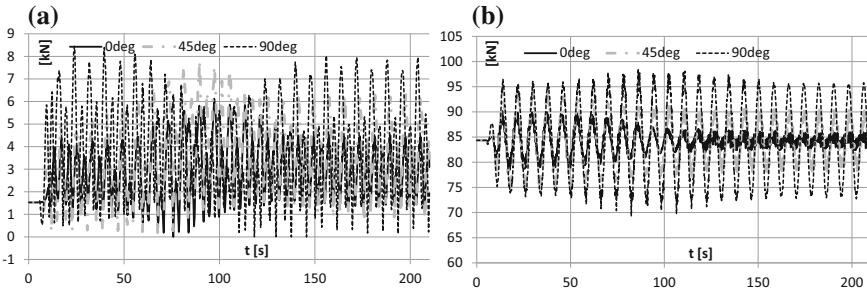
Fig. 6 Results for LC-B **a** radial contact force on funnel-prong sphere, **b** contact force on funnel-vertical prong stopper

20 kN constant tension generated by the CFG winch). Such a winch working mode is typical for the launch and recovery and provides the required down-force level.

Module interaction loads with prong sphere (contact forces) are shown in Fig. 6a. Forces presented in Fig. 6b present the contact loads between module funnel and prong vertical stopper. Forces acting on the second prong are similar, some difference is dictated by the prong beam-funnel geometry. The down-force level (the sum of contact forces on both prong stoppers) is an important parameter to consider. If the down-force is not sufficient, the module can slide out from prongs and a dangerous situation may occur (like a damage of the module due to impact with the CGF rails or hull). Therefore, the MLW capacity must be high enough to cover the loads generated by module itself and all cursor guiding elements resting on it.

5   Conclusions

The numerical model developed and elaborated computer programme enable us to predict the loads in various conditions and configurations. The assumptions made in the project design phase (i.e. design loads) should be confirmed whenever a new

installation is planned. Due to various possible vessels, different modules and deck arrangements, detailed engineering must performed for the verification if the governing loads are not exceeded. Winch drives and ropes capacities and life times are also important factors to monitor. For this purpose, as well as due to requirements of an external approval, the developed computer programme could be an useful tool.

The system was developed assuming SWL 25 t and the significant wave height up to 4.5 m. However, due to complexity of module handling operations and variety of possible input parameters (including large variety of module types), it is difficult to asses the limits without running several analyses for each significant input modification. Assisting engineers and vessel managers during such operations was the main motivation behind developing the model presented.

References

1. Cha, J.-H., Roh, M.-I., Lee, K.-Y.: Dynamic response simulation of a heavy cargo suspended by a floating crane based on multibody system dynamics. Ocean Eng. **37**, 1273–1291 (2010)
2. Craig, J.J.: Introduction to robotics. Prentice-Hall (2005)
3. Ellermann, K., Kreuzer, E.: Nonlinear hydrodynamic responses of submerged moving payload in vicinity of a crane barge in waves nonlinear dynamics in the motion of floating cranes. Multibody Sys. Dynamics. **9**, 377–387 (2003)
4. Hannan, M.A., Bai, W.: Nonlinear hydrodynamic responses of submerged moving payload in vicinity of a crane barge in waves. Mar. Struct. **41**, 154–179 (2015)
5. Nam, B.W., Kim, N.W., Hong, S.Y.: Experimental and numerical study on coupled motion responses of a floating crane vessel and a lifted subsea manifold in deep water. Int. J. Naval Architec. Ocean Eng. **9**, 552–567 (2017)
6. Park, K.P., Cha, J.H., Lee, K.Y.: Dynamic factor analysis considering elastic boom effects in heavy lifting operations. Ocean Eng. **38**, 1100–1113 (2011)
7. Park, Y.S., Kim, W.J., Nam, B.W.: CFD simulation of hydrodynamic forces acting on subsea manifold templates at wave zone. In: Proceedings of the International Offshore and Polar Engineering Conference. Anchorage, Alaska, USA pp. 654–661 (2013)
8. Ralston, A., Rabinowitz, P.: A First Course in Numerical Analysis. McGraw-Hill (1978)
9. RoyChoudhury, S., Dash, A.K., Nagarajan, V., Sha, O.P.: CFD simulations of steady drift and yaw motions in deep and shallow water. Ocean Eng. **142**, 161–184 (2017)
10. Szczotka, M., Maczynski, A., Wojciech, S.: Mathematical model of a pipelay spread. Arch. Mechanical Eng. LIV **1**, 26–46 (2007)
11. Urbas, A., Szczotka, M., Maczynski, A.: Analysis of movement of the BOP crane under sea weaving conditions. JTAM **48**(3), 677–701 (2010)
12. Wittbrodt, E., Szczotka, M., Maczynski, A., Wojciech, S.: Rigid Finite Element Method in Analysis of Dynamics of Offshore Structure. Springer, Berlin-Heidelberg (2013)

Dynamic Analysis of a Beam with Additional Auxiliary Mass Spatial Via Spectral Element Method

E. U. L. Palechor, M. R. Machado, M. V. G. de Morais and L. M. Bezerra

Abstract This paper aims to propose a new spectral element with additional mass. Methodologies for structural health monitoring are used to include additional auxiliary mass in the structure to change of natural frequencies. Therefore, the additional auxiliary mass can enhance the effects of discontinuities in the structural dynamics response, which could improve the identification and location of the discontinuities. The proposed approach deals with the wave propagation in structures regarding the spectral analysis method. The change in the natural frequencies due the mass is examined by comparing the differences between the dynamic responses of the beam with and without additional auxiliary mass. Similar analyses also performed with the Galerkin assumed modes technique to validate the new spectral element. The proposed technique is validated with numerical simulation and then compared to experimental data.

Keywords Spectral element method · Auxiliary mass spatial probing · Galerkin assumed modes technique.

E. U. L. Palechor · L. M. Bezerra
Civil Engineering Department, Faculty of Technology, University of Brasília,
Campus Universitário Darcy Ribeiro, Asa Norte, Brasília, DF 70910-900, Brazil
e-mail: erwinlopezpalechor@hotmail.com

L. M. Bezerra
e-mail: lmbz@unb.br

M. R. Machado (✉) · M. V. G. de Morais
Mechanical Engineering Department, Faculty of Technology, University of Brasília,
Campus Universitário Darcy Ribeiro, Asa Norte, Brasília, DF 70910-900, Brazil
e-mail: marcelam@unb.br

M. V. G. de Morais
e-mail: mvmorais@unb.br

1   Introduction

The spectral element method (SEM) consists in the exact displacement of the wave equation of the analytical solution in the frequency domain. It is equivalent to an infinite number of finite elements. SEM is a meshing method similar to FEM, where the approximated element shape functions are substituted by exact dynamic shape functions obtained from the exact solution of governing differential equations. As the SEM assumes the exact frequency-domain solution, it implies high accuracy. Other advantages of this method are the reduction of the problem size and DOFs, low computational costs, effectiveness in dealing with frequency-domain problems, adequate to deal with the non-reflecting boundary conditions of the infinite or semi-infinite-domain problems [11]. This characteristic and the spectral domain make SEM more suitable to solve the structural discontinues detection. The advantage of SEM is the reduced number of elements required to model the system as compared to other computational methods. Due to the SEM be formulated with the exact wave propagation solution, it became a suitable technique to model structural damage detection. In general, changes in either global or local structural properties can be associated with an imperfection or damage. In the last decades, damage detection researchers are focused on methods that use elastic wave propagation at medium and high-frequency bands [7, 8, 12, 14, 18, 20]. Some techniques in health structural monitoring use to add a traversing auxiliary mass change in the structure to enhance the effects of the discontinuities on the dynamic response and facilitate the identification and location, i.e., of damage. Zhong [21] presented damage detect technique that uses auxiliary mass spatial probing.

The modal analysis aims to reduce a complex system of partial differential equations that describe the dynamical behaviour of a continuous structure. This approach is less complicated and is described by a system of ordinary differential equations that considers the motion of an equivalent one-dimensional structure, such approach and numerical model especially in a non-linear analyses lead to errors in solution and must be treated with particular attention. Although the reduction of PDEs, especially non-linear systems analysis to ODEs and possibly algebraic equations to consideration of only a few degrees of freedom can lead to erroneous results. This approach in beam-like structure can be found in the references [2–4, 9]. A theoretical treatment of modal analysis is given in Meirovitch [13]. In literature, we found several examples of model reduction, for example, vortex induced vibration [5] or stochastic problems [17], or wind turbine analysis [16]. The order reduction can be made in the analysis. One of these techniques is to reduce the continuous system to a few degrees of freedom MDOF through modal analysis [1, 19]. Reducing continuous mechanical systems into discrete ones is advantageous. According to Galerkin's method [15].

The aim of this paper is to propose a new spectral element with additional mass. The proposed approach deals with the wave propagation in structures regarding the spectral analysis method. Methodologies for structural health monitoring are used to include additional auxiliary mass in the structure in order to change of natural frequencies. The change in the natural frequencies due the mass is examined by

comparing the differences between the dynamic responses of the beam with and without additional auxiliary mass. Similar analyse was also performed with the Galerkin assumed modes technique in order to validate the new spectral element with additional mass. The proposed model is validated with a numerical simulation and then compared to experimental data.

2 Beam Spectral Element with Additional Mass

A spectral damaged Euler-Bernoulli beam element with an auxiliary mass is addressed. Figure 1 shows a two-nodes auxiliary mass beam element with uniform rectangular cross-section, length L and auxiliary mass position L_1. The auxiliary mass is modelled with a tip mass ($\vartheta \delta(x - L)$) added in the beam mass. The undamped equilibrium equation with the auxiliary mass in frequency domain can be written as:

$$EI\frac{d^4v(x)}{dx^4} + \omega^2[\rho A + \vartheta\delta(x - L)]v(x) = p(x), \tag{1}$$

where I is the inertia moment, v is the transverse displacement, and p is the distributed external transversal force. A structural internal damping is introduced into the beam formulation as $EI = EI + c_{EI_0}$ with $c_{EI_0} = i\eta$ where η is the hysteretic structural damping factor. The auxiliary mass is described by a impulse force described by a Dirac delta function ($\delta(x - L/2)$) multiplied by a mass value ϑ. The homogeneous displacement solution for Eq. (1) must be described in two parts, one for the left-hand side of the mass, it has

$$v_L(x) = a_1 e^{-i(k_b x)} + a_2 e^{-(k_b x)} + a_3 e^{-ik_b(L_1-x)} + a_4 e^{-k_b(L_1-x)} \quad (0 \le x \le L_1)$$
$$= \mathbf{s}_L(x, \omega)\mathbf{a}_L \tag{2}$$

where $k_b = \sqrt{\omega}(\rho A/EI)^{1/4}$ is the beam wavenumber, $\mathbf{s}_L(x, \omega) = \big[e^{-i(k_b x)} \ e^{-(k_b x)}$ $e^{-ik_b(L_1-x)} \ e^{-k_b(L_1-x)}\big]$, and $\mathbf{a}_L = \{a_1 \ a_2 \ a_3 \ a_4\}^T$. Other, for the right-hand side of the mass

$$v_R(x) = a_5 e^{-ik_b(L_1+x)} + a_6 e^{-k_b(L_1+x)} + a_7 e^{-ik_b(L-(L_1+x))}$$
$$+ a_8 e^{-k_b(L-(L_1+x))} \quad (0 \le x \le L - L_1)$$
$$= \mathbf{s}_R(x, \omega)\mathbf{a}_R \tag{3}$$

where $\mathbf{s}_R(x, \omega) = \big[e^{-ik_b(L_1+x)} \ e^{-k_b(L_1+x)} \ e^{-ik_b(L-(L_1+x))} \ e^{-k_b(L-(L_1+x))}\big]$, and $\mathbf{a}_R = \{a_5 \ a_6 \ a_7 \ a_8\}^T$. Writing Eqs. (2) and (3) in a matrix form,

$$\begin{Bmatrix} v_L(x) \\ v_R(x) \end{Bmatrix} = \mathbf{d} = \begin{bmatrix} \mathbf{s}_L(x, \omega) & \mathbf{0} \\ \mathbf{0} & \mathbf{s}_R(x, \omega) \end{bmatrix} \begin{Bmatrix} \mathbf{a}_L \\ \mathbf{a}_R \end{Bmatrix} = \mathbf{s}(x, \omega)\mathbf{a} \tag{4}$$
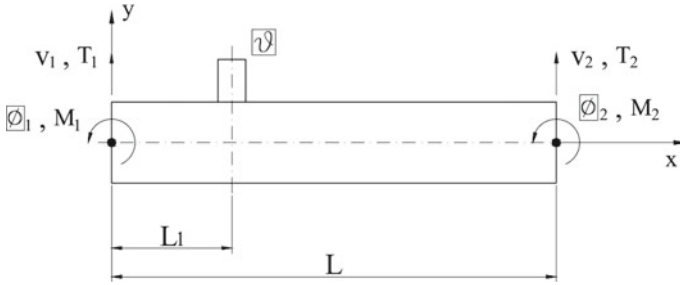
Fig. 1 Two-node damaged beam spectral element

where $\mathbf{d}$ is the nodal displacement vector, $\mathbf{a}$ is the coefficient vector, and $\mathbf{s}$ is a matrix dependent of the element boundary and compatibility conditions. The element boundary conditions are considered as following form:

- at node 1

$$v_L(0) = v_1 \quad \text{and} \quad \frac{\partial v_L(0)}{\partial x} = \phi_1 \tag{5}$$

- at the mass location ($x = L_1$ for $v_L(x)$ and $x = 0$ for $v_R(x)$)

$$v_L(L_1) = v_R(0),$$
$$\frac{\partial v_L(L_1)}{\partial x} = \frac{\partial v_R(0)}{\partial x},$$
$$\frac{\partial^2 v_L(L_1)}{\partial x^2} = \frac{\partial^2 v_R(0)}{\partial x^2},$$
$$\frac{\partial^3 v_L(L_1)}{\partial x^3} - \frac{\partial^3 v_R(0)}{\partial x^3} = -\vartheta \frac{\partial^2 v_L(L_1)}{\partial t^2} \tag{6}$$

- at node 2

$$v_R(L - L_1) = v_2 \quad \text{and} \quad \frac{\partial v_R(L - L_1)}{\partial x} = \phi_2 \tag{7}$$

Applying boundary and compatibility conditions in Eq. (4) it has,

$$\underbrace{\begin{bmatrix} 1 & 1 & \mathsf{m} & \mathsf{n} & 0 & 0 & 0 & 0 \\ -ik & -k & ik\mathsf{m} & k\mathsf{n} & 0 & 0 & 0 & 0 \\ -\mathsf{m} & -\mathsf{n} & 1 & 1 & \mathsf{m} & \mathsf{n} & \mathsf{o} & \mathsf{p} \\ \mathsf{m}ik & \mathsf{n}k & -ik & -k & -ik\mathsf{m} & -k\mathsf{n} & ik\mathsf{o} & k\mathsf{p} \\ -k^2\mathsf{m} & k^2\mathsf{n} & -k^2 & k^2 & k^2\mathsf{m} & -k^2\mathsf{n} & k^2\mathsf{o} & -k^2\mathsf{p} \\ ik^3\mathsf{m}+\vartheta ik^2\mathsf{m} & -k^3\mathsf{n}+\vartheta k^2 & -ik^3+\vartheta ik^2 & k^3+\vartheta k^2 & -k^3\mathsf{m} & k^3\mathsf{nn} & ik^3\mathsf{o} & -k^3\mathsf{p} \\ 0 & 0 & 0 & 0 & \mathsf{r} & \mathsf{t} & 1 & 1 \\ 0 & 0 & 0 & 0 & -ik\mathsf{r} & -k\mathsf{t} & ik & k \end{bmatrix}}_{\mathbf{G}_b} \begin{Bmatrix} a_1 \\ a_2 \\ a_3 \\ a_4 \\ a_5 \\ a_6 \\ a_7 \\ a_8 \end{Bmatrix} = \begin{Bmatrix} v_1 \\ \phi_1 \\ 0 \\ 0 \\ 0 \\ 0 \\ v_2 \\ \phi_2 \end{Bmatrix}$$

$$\tag{8}$$

where $\mathsf{m} = e^{ikL_1}$, $\mathsf{n} = e^{-kL_1}$, $\mathsf{o} = e^{-ik(L-L_1)}$, $\mathsf{p} = e^{k(L-L_1)}$, $\mathsf{r} = e^{-ikL}$, $\mathsf{t} = e^{-kL}$. From the Eq. (8) it can relate the coefficient vector with the nodal displacement vector by:

$$\mathbf{a} = \mathbf{G}_{br}^{-1}\mathbf{d} \tag{9}$$

where $\mathbf{G}_{br}^{-1}$ is the inverse of $\mathbf{G}_b$ reduced to the order $[8 \times 4]$ due to the zeros into the displacement vector $\mathbf{d}$. Substituting Eq. (9) into (4) it has,

$$\left\{ \begin{array}{c} v_L(x) \\ v_R(x) \end{array} \right\} = \begin{bmatrix} \mathbf{s}_L(x, \omega) & \mathbf{0} \\ \mathbf{0} & \mathbf{s}_R(x, \omega) \end{bmatrix} \mathbf{G}_{br}^{-1}\mathbf{d} = \mathbf{g}(x, \omega)\mathbf{d} \tag{10}$$

Note that $\Gamma(\omega) = \mathbf{G}_{br}^{-1}$. For instance the deterministic flexibility rigidity and mass per unit of length parameters, $EI(x)$ and $\rho A(x)$, are assumed as deterministic constants. The stiffness operator is given by $\partial^2(\bullet)/\partial x^2 = (\bullet)''$. Due spacial reference in the model the equations must be integrated according to the corresponding limits, then

$$\mathbf{K}(\omega) = EI\Gamma_d^T(\omega) \begin{bmatrix} \mathbf{Sk}_{0L} & \mathbf{0} \\ \mathbf{0} & \mathbf{Sk}_{0R} \end{bmatrix} \Gamma(\omega), \tag{11}$$

and

$$\mathbf{M}(\omega) = \rho A\ \Gamma_d^T(\omega) \begin{bmatrix} \mathbf{Sm}_{0L} & \mathbf{0} \\ \mathbf{0} & \mathbf{Sm}_{0R} \end{bmatrix} \Gamma(\omega), \tag{12}$$

where

$$\mathbf{Sk}_{0L} = \int_0^{L_1} \mathbf{s}''^T_L(x, \omega)\mathbf{s}''_L(x, \omega)dx, \qquad \mathbf{Sk}_{0R} = \int_0^{(L-L_1)} \mathbf{s}''^T_R(x, \omega)\mathbf{s}''_R(x, \omega)dx \tag{13}$$

$$\mathbf{Sm}_{0L} = \int_0^{L_1} \mathbf{s}^T_L(x, \omega)\mathbf{s}_L(x, \omega)dx, \qquad \mathbf{Sm}_{0R} = \int_0^{(L-L_1)} \mathbf{s}^T_R(x, \omega)\mathbf{s}_R(x, \omega)dx \tag{14}$$

Substituting Eqs. (13) in (11), and Eqs. (14) in (12) the deterministic stiffness and mass matrices as closed-form expressions can be obtained. Then, the spectral beam with auxiliary dynamic stiffness matrix can be obtained as $\mathbf{D}(\omega) = \mathbf{K}(\omega)\omega^2\mathbf{M}(\omega)$.

3 Experimental Procedure

Experimental results are performed for a I-beam 102×11.4 (exact dimensions 101.6×67.6 mm^2) of steel MR-250 with length of 6 m. Figure 2 show in detail the nominal geometric properties of I-beam. The Young's modulus is $E = 200.0474 \pm 2.0675$ (nominal 200) GPa, cross-sectional area $A = 14.3156$ cm^2, density $\rho = 7848.156$ kg/m^3 and moment of inertia $I_x = 245.13$ cm^4 were obtained

Dimension	Nominal
h (mm)	101.6
h_o (mm)	86.8
h_o (mm)	7.4
t_f (mm)	4.84
t_o (mm)	15.9
b (mm)	67.6
S (cm^2)	14.5
I_x (cm^4)	252
W_x (cm^3)	49.7
i_x (mm)	41.7
I_y (cm^4)	31.7
W_y (cm^3)	9.37
i_y (mm)	14.8
L (mm)	6000.0
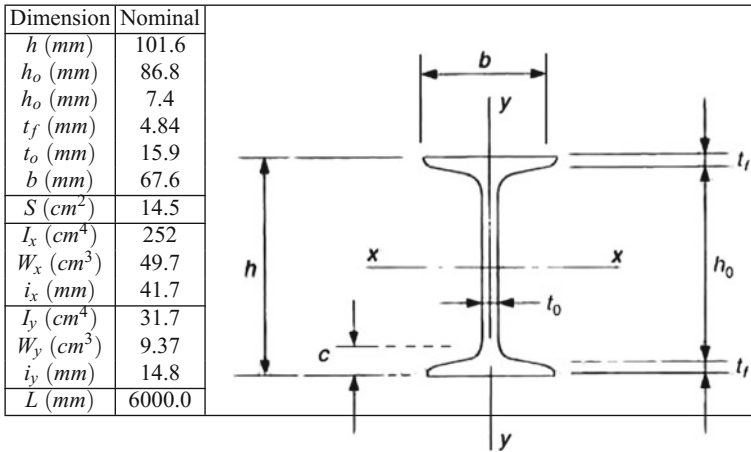
Fig. 2 Geometrical properties of I-shape 102×11.4
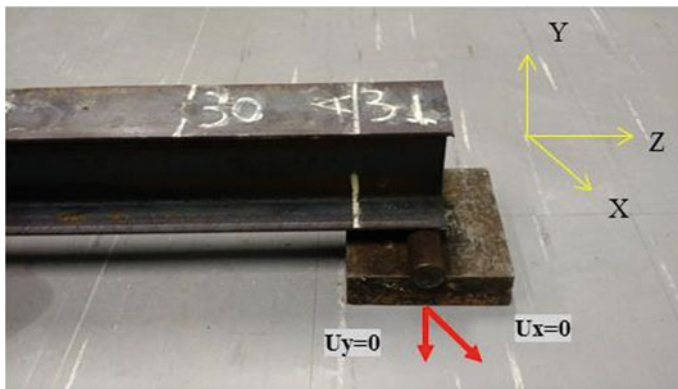
Fig. 3 Simply supported condition at both ends

experimentally. The dynamic tests were developed in laboratory of Mechanical Engineering Department of University of Braslia.

Geometric properties (area A and inertia I_x) was determined by articulated arm coordinate measuring machine (model Arm100 - uncertainty of 0.070 mm) of Metrology Laboratory (UnB-FT/EnM/LabMetro). With Archimedes principle, we obtain an density estimation of material. The experimental verification of Young modulus was performed by FRF estimation of a free-free and simply supported Euler-Bernoulli beam. With a modal impact testing, Young modulus was estimated by report to the best fit to natural frequencies identified. The tested beam has simply supported condition guarantee by steel rollers lean on steel plates, as show by Fig. 3.

(a) Schematic representation   (b) Assembly view
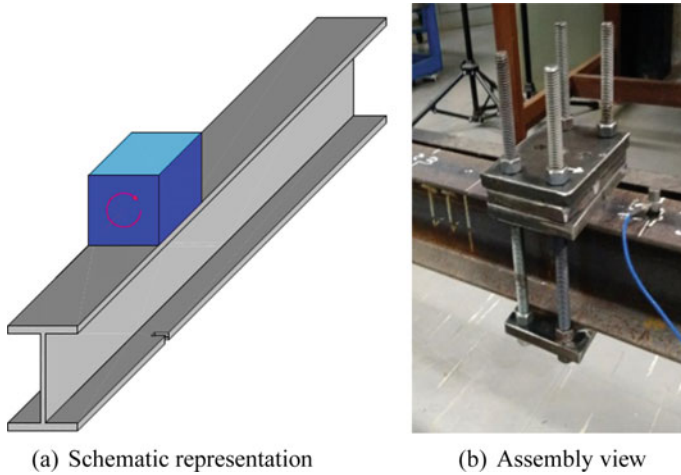
Fig. 4 Additional mass

The additional mass was composed by steel plates fixed with four threaded rod and nuts as shown in Fig. 4. Each steel plate weighted $5714 \pm 2g$. The added mass system was fast to avoid any accidental motion.

Instrumentation and Experimental Procedure

Figure 5 describe experimental setup in Laboratory of Vibration in University of Braslia to estimate FRF between modal hammer and accelerometer. The list of equipments are NI cDAQ-91 and NI-9124, accelerometers PCB352C34/PCB352C33, modal hammer PCB086C0, and a PC desktop with LabView to data acquisition. For experimental tests, one accelerometers located in $L/4$ from the right support and an impact in force in the $L/4$ from the right support.

The additional mass was placed along the beam every 20 cm. Once the masses were positioned, the modal hammer tests were performed to obtain the FRFs. The first and second frequencies for each position of the additional mass were identified by spectral centre correction method [21] (Table 1).

4   Numerical Results

In the first numerical example, a simply supported beam boundary conditions with the same material properties and geometry presented in Sect. 3. The impact and measured points are also assumed likewise in the experimental test setup. It is compared the firsts natural frequencies of the beam with and without auxiliary mass spatial probing. In Fig. 6 shows that when no mass is added to the structure the first natural frequency is constant, while that the beam with additional mass the first natural frequency

Fig. 5 General view of
experimental setup
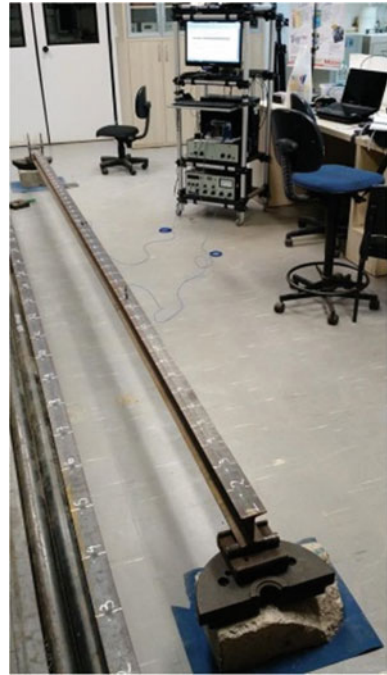
Table 1 First and second frequency (Hz) as function of position of additional mass (cm)

x(cm)	0.0	0.2	0.4	0.6	0.8	1.0	1.2	1.4	1.6	1.8
f_1	9.329	9.336	9.320	9.270	9.219	9.168	9.106	9.034	8.956	8.893
f_2	36.804	36.719	36.501	36.211	35.890	35.593	35.392	35.281	35.300	35.432
x(cm)	2.0	2.2	2.4	2.6	2.8	3.0	3.2	3.4	3.6	3.8
f_1	8.836	8.793	8.746	8.709	8.694	8.683	8.686	8.711	8.747	8.792
f_2	35.656	35.940	36.249	36.517	36.709	36.794	36.728	36.539	36.278	35.975
x(cm)	4.0	4.2	4.4	4.6	4.8	5.0	5.2	5.4	5.6	5.8
f_1	8.838	8.900	8.964	9.031	9.100	9.167	9.224	9.263	9.298	9.327
f_2	35.685	35.448	35.310	35.278	35.373	35.578	35.871	36.192	36.489	36.694

change when the auxiliary mass change position. The additional auxiliary mass
approximately 10% of the beam mass ($\vartheta = 0.54$ kg).

For the second example compare the firsts frequencies obtained with the SEM
model, Galerkin [1] and experimental measured. Figure 7 presents experimental
results and SEM simulation of accelerometer 2 ($x = L/4$) FRF with additional mass
at middle span. This figure compare experimental results and SEM simulation with
a reasonable agreement. The error are more notable to second frequency.
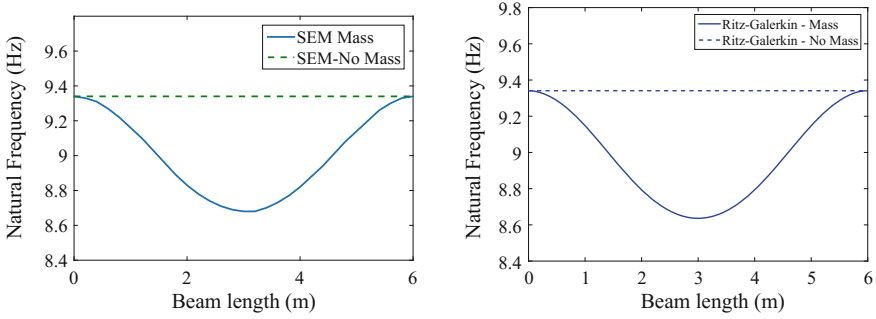
Fig. 6 First frequency as function of position of additional mass obtained using the SEM and Ritz-Galerkin with and without auxiliary added mass
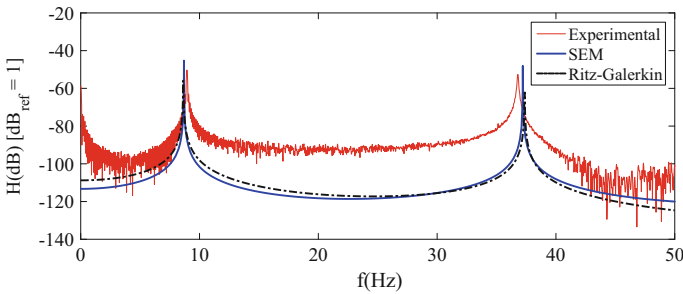
Fig. 7 FRF of accelerometer 2 ($x = L/4$) with additional mass at middle span: comparison of SEM, Ritz-Galerkin and experimental results

(b) First Frequency   (b) Second Frequency
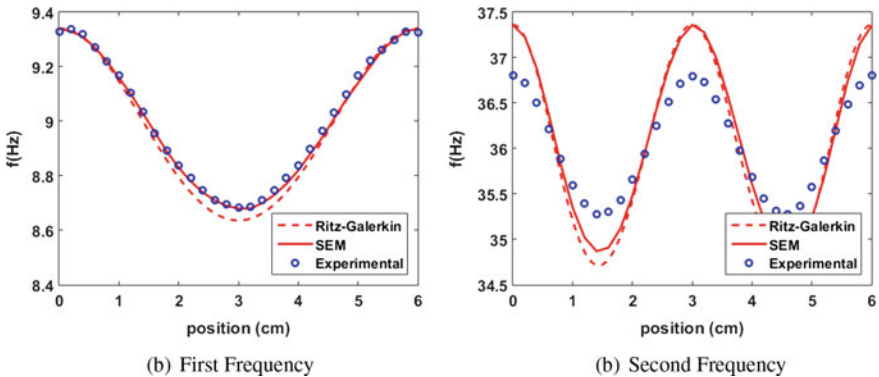
Fig. 8 Natural frequencies of beam $f_i (i = 1, 2)$[Hz] as function of additional mass x[cm]

Figure 8 show the first two natural frequency of essayed beam as function of addition mass position x[cm]. The error between SEM simulation and experimental are inferior of 1.2%.

5 Conclusions

This paper present a new spectral element with additional mass. The natural frequencies change due to position of the mass along x-axis. Similar analyse was also performed with the Galerkin assumed modes technique in order to validate the new spectral element with additional mass. Galerkin technique presents similar results to spectral element method even needing some assumed modes to converge ($N \geq 6$).

The proposed model is validated with a numerical simulation and then compared to experimental data. The spectral element results shows a good agreement with experimental first natural frequencies. Comparing the second natural frequencies experimentally identified, the spectral element observe a difference inferior to 1.2%.

Appendix

According to Galerkin's method [15], the solution of Eq. (1) can be expanded as function of:

$$w(x,t) \cong w_h(x,t) = \sum_{j=1}^{N} \psi_j(x) \, q_j(t) \qquad (15)$$

where $\psi_j(x)$ are test functions in domain $\mathbb{D} = [0, L]$ that satisfying boundary conditions of problem, $q_j(t)$ are generalized coordinates of discretized system. By substituting (15) into (1) to obtain residual function $\mathscr{R}$. As base functions are not exact solutions of problem (1), the residual function $\mathscr{R}$ results a non-null function. But, according to Garlerkin's method, a kind of weighted residual method [6, 10], we search minimize the residual function $\mathscr{R}$ in domain $\mathscr{D} \in [0, L]$,

$$\int_{\mathscr{D}} \mathscr{R} \left[w_h(x,t) \right] \cdot \psi_i(x) dx = 0, \qquad i = 1, 2, \ldots, N \qquad (16)$$

This problem can be solved by a numerical time integrator, e.g., Newmark method, Hilbert-Hughes-Taylor method, or a simple Runge-Kutta.

References

1. Avila, S.M., Shzu, M.A.M., Pereira, W.M., Santos, L.S., Morais, M.V.G., Prado, Z.J.G.: Numerical modeling of the dynamic behavior of a wind turbine tower. J. Vibr. Eng. Technol. **4**(3), 249–257 (2016)

2. Awrejcewicz, J., Krysko, A.V., Kutepov, I.E., Zagniboroda, N.A., Dobriyan, V., Krysko, V.A.: Chaotic dynamics of flexible Euler-Bernoulli beams. Chaos: an Interdisciplinary. J. Nonlinear Sci. **23**(4), 36–43 (2013)

3. Awrejcewicz, J., Krysko, A.V., Mrozowski, J., Saltykova, O.A., Zhigalov, M.V.: Analysis of regular and chaotic dynamics of the Euler-Bernoulli beams using finite difference and finite element methods. Acta. Mech. Sin. **27**(1), 36–43 (2011)

4. Awrejcewicz, J., Saltykova, O.A., Zhigalov, M.V.: Analysis of non-linear vibrations of single-layered Euler-Bernoulli beams using wavelets. Int. J. Aerosp. Lightweight Struct. **1**(2), 203–219 (2011)

5. Blevins, R.: Flow-Induced Vibration. Krieger Publishing Company, New York (2001)

6. Finlayson, B.A., Scriven, L.E.: The Method of Weighted Residuals - A Review (1966)

7. Krawczuk, M.: Application of spectral beam finite element with a crack and iterative search technique for damage detection. Finite Elem. Anal. Des. **80**, 1809–1816 (2002)

8. Krawczuk, M., Grabowska, J., Palacz, M.: Longitudinal wave propagation. Part I- comparison of rod theories. J. Sound Vib. **295**, 461–478 (2006)

9. Krysko, V.A., Awrejcewicz, J.: On the vibration of the Euler-Bernoulli beam with clamped ends deflection constraints. Int. J. Bifurcat. Chaos **15**(6), 1867–1878 (2005)

10. Kwon, Y.W., Bang, H.: The Finite Element Method Using Matlab. CRC Press, Boca Raton, FL (2000)

11. Lee, U.: Spectral Element Method in Structural Dynamics. Inha University Press, Incheon (2004)

12. Machado, M.R., Santos, J.M.C.D.: Reliability analysis of damaged beam spectral element with parameter uncertainties. Shock Vib. **2015** (2015) 12 p

13. Meirovitch, L.: Analytical Methods in Vibrations. Macmillan, New York (1967)

14. Ostachowicz, W.M.: Damage detection of structures using spectral finite element method. Comput. Struct. **86**, 454–462 (2008)

15. Paidoussis, M.P.: Fluid Structure Interactions. Slender Structures and Axial Flow, vol. 1. Elsevier Academic Press, Amsterdam (1998)

16. Peeters, J.L., Vandepitte, D., Sas, P.: Analysis of internal drive train dynamics in a wind turbine pp. 141–161

17. Ritto, T.G., Sampaio, R., Cataldo, E.: Timoshenko beam with uncertainty on the boundary conditions. J. Braz. Soc. Mech. Sci. Eng. **30**(4), 295–303 (2008)

18. Santos, E., Arruda, J., Santos, J.D.: Modeling of coupled structural systems by an energy spectral element method. J. Sound Vib. **36**, 1–24 (2008)

19. Soong, T.T., Dargush, G.F.: Passive Energy Dissipation Systems in Structural Engineering. Wiley, New York (1997)

20. Su, Z., Ye, L.: Identification of Damage Using Lamb Waves. Springer, Berlin (2009)

21. Zhong, S., Oyadiji, S.O., Ding, K.: Response-only method for damage detection of beam-like structures using high accuracy frequencies with auxiliary mass spatial probing. J. Sound Vib. **311**, 1075–1099 (2008)

Influence of Air Temperature on Dynamic Properties of Pipes Supplied with Pulsating Flow

Tomasz Pałczyński[ID]

Abstract Air temperature has a significant influence on the dynamic properties of pipes supplied with pulsating flows. In many applications (power plants, pipelines, intake and exhaust systems for internal combustion engines), air temperature has an effect on resonance. Depending on the air temperature and its influence on transient flow parameters (pressure, temperature, density, speed of sound), there may be significant changes in the dynamic properties of the test pipe, such as resonant frequencies and the damping coefficient. In this study, experiments were conducted in an air temperature range of between 288 and 343 K, with a very a short air temperature step of around 5 K. Each measurement series was performed in triplicate. The results were processed in the Matlab environment using Fast Fourier Transforms. The empirical coefficients were visualized as 3D maps, including the influence of air temperature on pulsation dynamics in pipes. Finally, the experimental results were compared with the author's 1D model (based on the method of characteristics). The results are significant both for the theoretical understanding of flows in pipelines with pulsating flows and for practical applications in industry..

Keywords Air temperature · Pulsating flow · Dynamic properties

1 Introduction

Air temperature has a significant influence on the dynamic properties of pipes supplied with pulsating flows. In many applications (power plants, pipelines, intake and exhaust systems for internal combustion engines), air temperature has an effect on resonance. Depending on the air temperature and its influence on transient flow parameters (pressure, temperature, density, speed of sound), there may be significant changes in the pipe dynamic properties of the test pipe, such as resonant

T. Pałczyński (✉)
Flow Metrology Division, Institute of Turbomachinery, Lodz University of Technology,
219/223 Wólczańska Street, 90-924 Łódź, Poland
e-mail: tomasz.palczynski@p.lodz.pl

frequencies and the damping coefficient. Pulsating flow implies pulsating pressure, which causes vibrations and noise. It is thus one of the most important problems currently facing industry [1–3]. Numerous studies in the literature include mathematical modeling of the dynamics of pipeline systems interacting with a medium [4–9]. In this study, experiments were conducted into the amplitude and phase characteristics, resonant frequencies, damping coefficient and quality of approximation for pipes sup-plied with pulsating flows, fitted with relative nozzle diameters of between 3 and 9%. The experiments were supported by the author's hybrid measurement method detailed in [10]. The National Instrument NI USB-6259 measurement card is designed to operate in the LabView environment, and is not supported by Matlab. Therefore, the experimental part of this project was based on LabView software. The second part, focusing on analog data processing, FFT (Fast Fourier Transform) analysis and Fourier series approximation, was conducted in Matlab. This clear division of process requirements demanded hybridization of the measurement process. Automated testing and recording was performed with LabView 2013 software. Calibration was performed using reference transmitters. Pressure transducers (Endevco 8510C-15 and 8510C-50) were calibrated using the glass tube water level gauge and a Vaisala PTB 330 reference barometer. Steady-state characteristics and performance were estimated using this procedure. Constant current thermometers (CCTs) were calibrated using a Type E reference thermoelectric element. Constant temperature anemometers (CTAs)—mass flow rate transducers—were calibrated using an Annubar-type flow meter. The experimental results were compared with the author's 1D model, based on the method of characteristics (MOC).

2 Principles of Method of Characteristics

Benson's [11] non-dimensional notation was used for first step approximation, where heat transfer and friction in pipes are often omitted (Fig. 1). The flow can be defined as homentropic, and there is no area section change. The two non-dimensional Riemann invariants (α and β) can be defined along the characteristics lines C^+ and C^- [12]:

Fig. 1 Method of characteristics in the space-time domain [12]
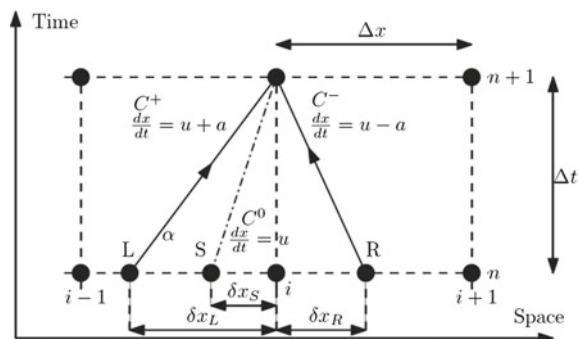
$$\alpha = A_i^{n+1} - \frac{\kappa - 1}{2} * U_i^{n+1} = A_R^n - \frac{\kappa - 1}{2} U_R^n, \tag{1}$$

$$\beta = A_i^{n+1} - \frac{\kappa - 1}{2} * U_i^{n+1} = A_L^n + \frac{\kappa - 1}{2} U_L^n, \tag{2}$$

where:

L, R, S   nodes at time space domain due to C^+, C^-, C^0 characteristics;
i   space point;
n   natural value in the time domain;
A   non-dimensional speed of sound $A = \frac{a}{a_{ref}}$;
U   non-dimensional velocity $U = \frac{u}{a_{ref}}$;
a_{ref} reference speed of sound

Using MOC, it appears that when all parameters at time step n are known, the Riemann characteristics (Eqs. 1 and 2) can be calculated. Using this information, the next step can be calculated.

For homentropic flow, contraction of the gas between S and the mesh node (i, $n+1$) can be defined:

$$\frac{p_S^n}{\left(\rho_S^n\right)^\kappa} = \frac{p_i^{n+1}}{\left(\rho_i^{n+1}\right)^\kappa}, \tag{3}$$

Having found δx_L, δx_R, δx_S (the distance between i node and L, S, R points) the thermodynamic states can be determined at nodes L, R and S using linear interpolation. There should be calculated: ρ_i^{n+1}, u_i^{n+1}, and p_i^{n+1}.

On the other hand, the transient speed of sound is determined as follows:

$$a = \sqrt{\kappa \cdot R \cdot T}, \tag{4}$$

where:

R individual gas constant 286,9 [J/(kg K)];
κ isentropic expansion factor;
T transient temperature (K);
a speed of sound (m/s)

Finally, the pipe length was estimated using the following equation:

$$f_n = \frac{a}{4 * L}, \tag{5}$$

where:

L pipe length (m)

Assuming the relationship presented above between the speed of sound, natural frequency and particle velocity, the following can be stated:

(a) speed of sound strongly depends on the temperature of medium (Eq. 4);
(b) the velocity of medium u is the additional speed propagating small amplitude disorders in air. This influences the course of the characteristic C^+, C^-, C^0 lines, changing the dynamic properties of the analyzed pipes supplied with pulsating flows.
(c) changes in the speed of sound change the natural frequency of the test pipe (Eq. 5).

3 Test Rig—Main Assumptions

The following assumptions were made:

– Real measurements taken of transitional states during pulsation frequency changes (from 20 to 180 Hz) in pipes. The main features of the test rig are presented in Fig. 2, including the pulse generator (PG) and three control sections (1, 2, 3).
– A simplified Simulink model, designed to estimate the local pulsation amplitude and amplitude-frequency characteristics [10].
– An analysis of the influence of frequency change in a range of amplitudes from 20 to 180 Hz on air pressure during pulsation changes at three control sections.
– Measurements showing resonant frequency changes with increasing and decreasing pulsation frequencies.
– Proposed parameters for estimating second-order inertial elements (the damping coefficient and resonant frequency), to describe the observed phenomena.
– Assessment of the impact of the sine swept constraint on amplitude-frequency characteristics.

The main parameters were as follows:
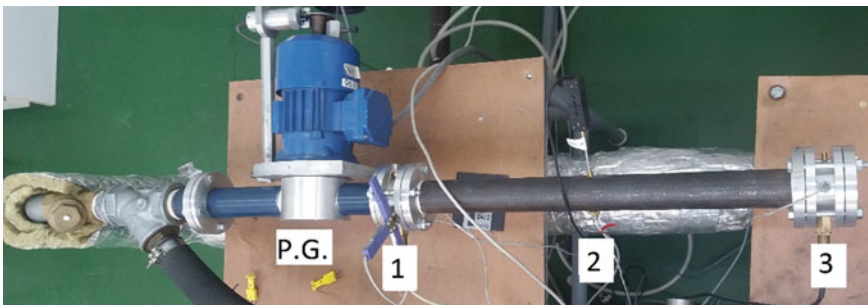
Fig. 2 Main elements of the test rig [1]. P.G.—pulse generator, 1, 2, 3—tested cross sections

- Range of desired values for the frequency of the pulse generator $f = (20 \div 180)$ (Hz).
- Pipe diameter $D_p = 42 \times 10^{-3}$ (m).
- Pipe length $L_p = 0.544$ (m), determined with resonance at 70 and 140 Hz.
- Nozzle diameters $D_n = 7.5 - 12.5 \times 10^{-3}$ (m). The nozzles were mounted at one end of the pipe, at cross section (3).
- Desired flow temperature from 313.15 to 343.15 (K).

   Transient and mean values for pressure, temperature and specific mass flow rate were measured at control sections (1) and (3), shown in Fig. 2. Transient pressure was also measured in section (2), located in the middle of the length of pipe. Analysis of the dynamic properties of the pipe was performed using the second-order oscillating element as the reference, parametrizing objectively the differences between particular cases. It was thereby possible to approximate the swept frequency probe with a coefficient of determination greater than 95% ($R^2 > 0.95$). Second-order oscillating elements were estimated using Eq. (6) and the Curve Fitting Tool, with custom equation settings and default 95% confidence bounds [13]:

$$M(f) = \left\{ \left[1 - \left(\frac{f}{f_n} \right)^2 \right]^2 + \left[\frac{2\zeta f}{f_n} \right]^2 \right\}^{-1/2}, \tag{6}$$

where:

$M(f)$ magnitude of oscillations (−)
f_n natural frequency (Hz)
ζ relative damping coefficient (−)

   Resonant frequency was calculated using the equation [13]:

$$f_r = f_n \sqrt{1 - \zeta^2}, \tag{7}$$

   Magnitude of oscillations were calculated as an relative amplitude of oscillations from the cross section 2 or 3 referenced to cross section 1.

4   Experimental and Simulation Results

Table 1 shows values for the damping coefficient and resonant frequencies in the studied cases. Each three rows represent the same temperature for three investigated mass flows (20, 24, 28 kg/s). The first group of columns represents experimental results according to p_3/p_1 (quotient of pressure pulsation of the third to the first cross-section) and the second group p_2/p_1 (quotient of pressure pulsation of the second to the first cross section). For each group, the natural frequency and relative damping coefficient were estimated (Eq. 1), together with R^2—the coefficient of
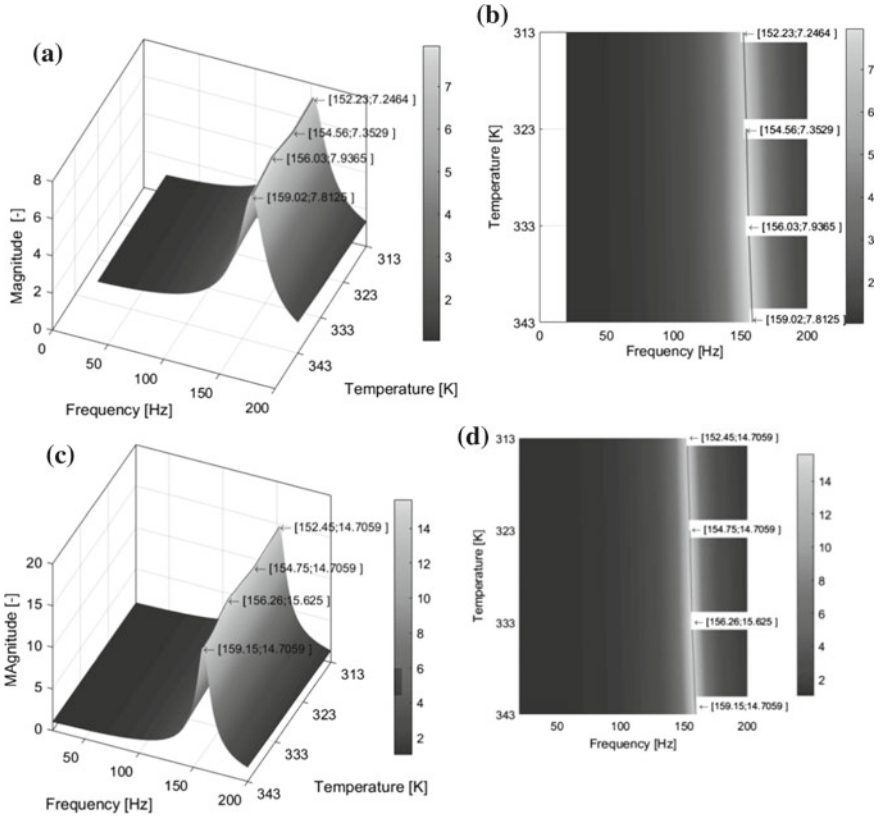
Fig. 3 **a** Magnitude p_2/p_1–3D plot in the frequency and temperature domains. **b** Magnitude p_2/p_1—contour plot in the frequency and temperature domains. **c** Magnitude p_3/p_1–3D plot in the frequency and temperature domains. **d** Magnitude p_3/p_1—contour plot in the frequency and temperature domains

determination and resonant frequency (Eq. 2). The whole spectrum of investigated temperatures was from 313.15 to 343.15 K with a 10 K step.

Figure 3 presents magnitude-frequency characteristics in the temperature domain. Figure 3a shows magnitude for p_2/p_1 as a 3D map in the frequency and temperature domains. Figure 3b provides a view from above, to show more clearly the influence of air temperature. As can be seen, air temperature increases from 313.15 to 343.15 K as resonant frequency increases from 152 to 159 Hz (4.5%). Similarly, Fig. 3a shows magnitude for p_3/p_1 as a 3D map in the frequency and temperature domains. A view from the top is presented in Fig. 3d to make more visible the influence of air temperature. As can be seen, air temperature increased from 313.15 to 343.15 K as resonant frequency increased from 152 to 159 Hz (4.5%).

In Fig. 4, there is significant noticeable increase from 7 to 14 magnitudes due to movement from the second to the third cross section.

Table 1 Experimental results

Temp. (K)	Mass flow (kg/s)	p_3/p_1				p_2/p_1			
		f_n (Hz)	Z (−)	f_r (Hz)	R^2 (−)	f_n (Hz)	ζ (−)	f_r (Hz)	R^2 (−)
313,15	20	152.44	0.043	152.16	0.850	151.78	0.083	151.72	0.984
313,15	24	152.45	0.034	152.16	0.860	152.23	0.069	151.51	0.973
313,15	28	152.64	0.029	152.51	0.870	151.51	0.053	151.08	0.986
323,15	20	154.81	0.043	154.52	0.870	154.53	0.084	153.44	0.990
323,15	24	155.81	0.032	155.52	0.850	156.42	0.061	153.50	0.863
323,15	28	154.76	0.028	154.64	0.878	154.37	0.055	153.91	0.997
333,15	20	157.17	0.041	156.91	0.882	156.83	0.079	155.83	0.994
333,15	24	156.26	0.032	156.10	0.876	156.03	0.063	155.41	0.996
333,15	28	156.92	0.025	156.82	0.894	156.85	0.050	156.45	0.988
343,15	20	158.72	0.040	158.46	0.895	158.85	0.079	157.86	0.987
343,15	24	158.66	0.030	158.52	0.898	158.25	0.057	157.73	0.973
343,15	28	157.95	0.025	157.18	0.829	158.59	0.055	157.73	0.972
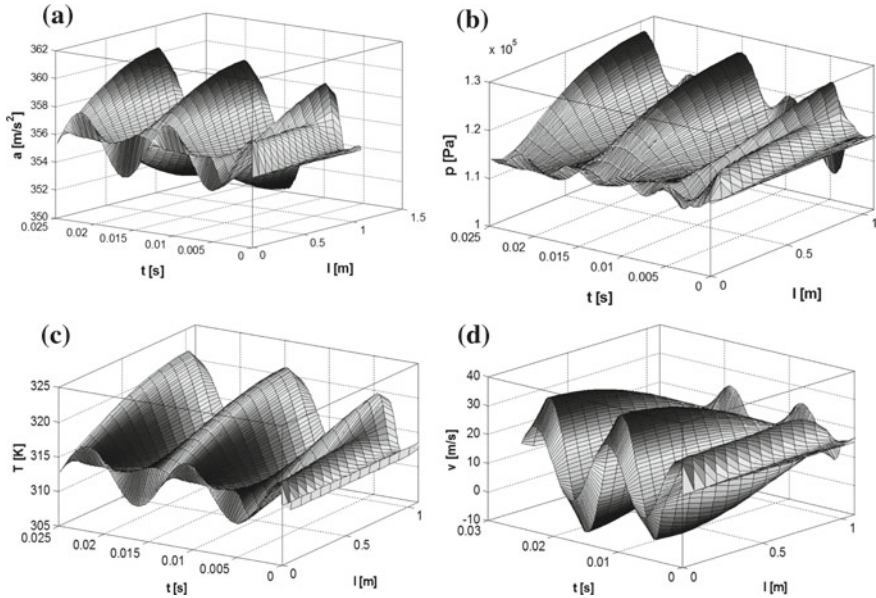
Fig. 4 Numerical simulation results for the resonant frequency $f_r = 145.16$ (Hz) and nozzle diameter 10×10^{-3} m and temperature 313,15 K: **a** local speed of sound in the time-space domain, **b** transient pressure in the time-space domain, **c** transient temperature in the time-space domain, **d** particle transient velocity in the time-space domain

The amplitudes of the oscillations at cross sections 1 and 2 were estimated and the magnitudes p_2/p_1 calculated. Magnitudes were assigned to the pulse generator frequencies. The coefficient of determination for the magnitude curve approximation is very good for p_2/p_1, with an average value $R^2 = 0.98$ and for p_3/p_1 the average value is $R^2 = 0.87$. This proves that the second-order oscillating element is sufficient for approximating the dynamic states of pulsating flows in pipes with partially-closed ends, including the influence of air temperature and the mass flow rate (especially for p_2/p_1 cases).

Calculations using the Simulink model (based on the method of characteristics) were performed in parallel with the experimental studies. Sample simulation results are presented in Fig. 4, which shows flow parameters in the time-space domain. The simulation of acoustic phenomena for the initial time steps is clearly visible. The propagating wave is divided into two parts, and is proportional to the cross-section area change coefficient. The reflected part of the propagating wave has closed-end type boundary conditions. The rest of the falling wave propagates outside the nozzle. Qualitative comparison of the results of the numerical studies reveals a good match with experimental measurements.

The assumed air temperature change was confirmed. The assumed reference speed of sound conditions for the partially-closed end were verified against the model of air temperature. Acoustic phenomena were confirmed for the analyzed flows. Nodes

and antinodes were found for the standing wave. At resonant frequency pulsations, the pressure nodes were located at the beginning of the pipe. Velocity antinodes can also be seen at the pipe end (cross section 3).

4.1   Experimental and Simulation Results—Discussion

Figures 5 and 6 provide a graphical interpretation of the results from Table 1. The influence of the mass flow rate and air temperature on the relative damping coefficient was estimated for p_3/p_1 (quotient of pressure pulsation of the third to the first cross-section) and p_2/p_1 (quotient of pressure pulsation of the second to the first cross section).

A significant decrease in the relative damping coefficient can be noticed, due to the increase in the mass flow rate. Case p_3/p_1 has much lower values for the relative damping coefficient, compared to p_2/p_1. This is caused by the flow phenomenon illustrated in Fig. 4b. The amplitudes of the pressure pulsation in the middle length of the tested pipe are lower. In the case of p_2/p_1, with a low mass flow rate there is a slight decrease in the relative damping coefficient, from 0.083 to 0.079 (−5%). A significant decrease in the relative damping coefficient was observed, from 0.069 to 0.057 (−21%), in the case of p_2/p_1 with medium mass flow rates [24 (kg/s)]. In the
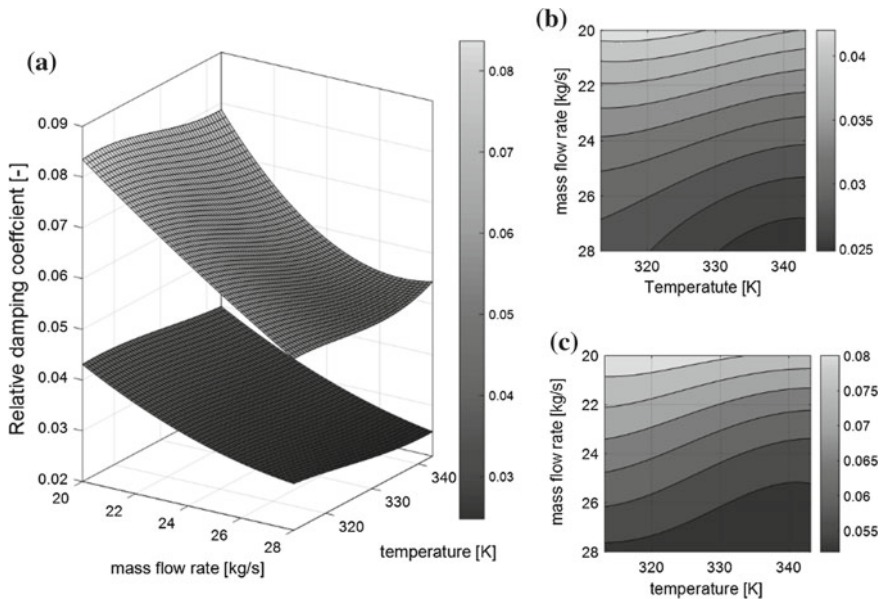
Fig. 5   a Damping coefficient relative to mass flow rate and air temperature (p_3/p_1 upper, p_2/p_1 bottom). **b** 2D plot—damping coefficient relative to mass flow rate and air temperature p_2/p_1. **c** 2D plot—damping coefficient relative to mass flow rate and air temperature p_3/p_1
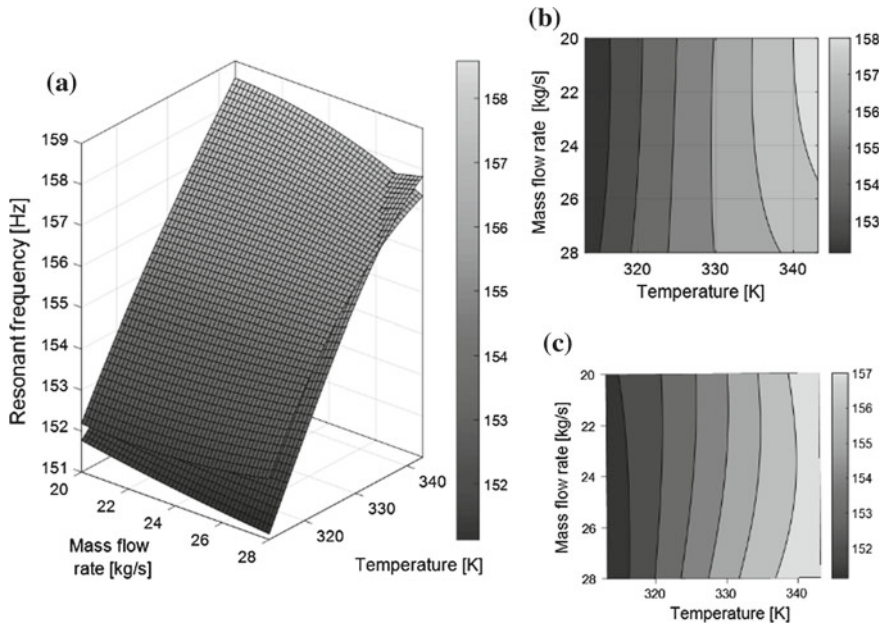
Fig. 6 a Resonant frequency relative to mass flow rate and air temperature (p_3/p_1 upper, p_2/p_1 bottom). **b** 2D plot—resonant frequency relative to mass flow rate and air temperature p_2/p_1. **c** 2D plot—resonant frequency relative to mass flow rate and air temperature p_3/p_1

case of p_3/p_1, the influence of air temperature on the relative damping coefficient was very slight. However, the mass flow rate was found to have a significant influence on the relative damping coefficient in both cases p_3/p_1 and p_2/p_1. In the case of p_3/p_1, there is a significant decrease in the relative damping coefficient, from 0.043 to 0.029 (-48%) at low temperatures, independent of air temperature. The decrease in the relative damping coefficient in case p_3/p_1 is greater at high air temperatures, from 0.040 to 0.025 (-60%). In the case of p_2/p_1, there is a significant decrease in the relative damping coefficient, from 0.083 to 0.053 (-57%).

The impact of air temperature and mass flow rate on resonant frequencies stands in contrast to the variability of the relative damping coefficient. Of course, this contrast is only apparent because these physical quantities were conjugated in the manner presented above. Changes in resonant frequencies with changes in air temperature were also significant, with an increase of around 9% (from 313.15 to 343.15 K), increasing to 3.2% (from 152.16 to 157.18 Hz) in the case of p_3/p_1 and increasing to 3.8% (from 151.72 to 157.73 Hz) in the case of p_2/p_1.

The significant influence of air temperature on the relative damping coefficient, and of mass flow rate on resonant frequencies, is of great importance for understanding the dynamic properties of pipes supplied with pulsating flows. All kinds of pipelines and compressed air lines suffer due to vibrations induced by resonance frequencies. The experimental results presented in Figs. 5 and 6 as three-dimensional
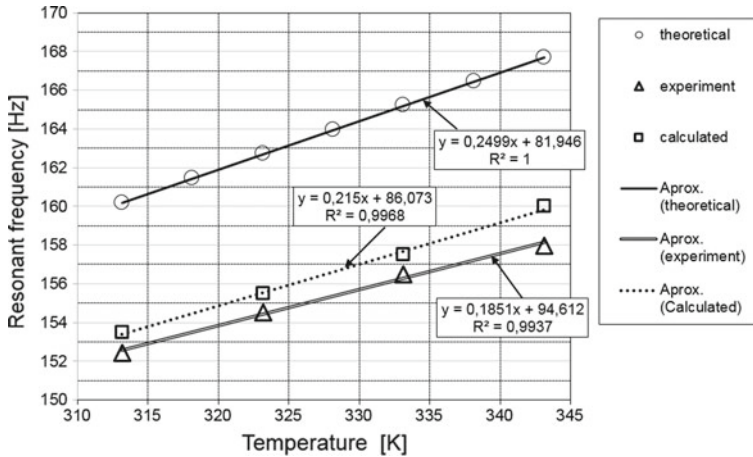
Fig. 7 Resonant frequency versus temperature (theoretical, experimental and calculated from simulation model based on MOC)

maps of the real relative damping coefficient and resonant frequencies could be used as corrective steering or process engineering maps. The research results presented here could also help to protect large industrial systems against defects caused by uncontrolled changes in the dynamic characteristics of pipelines.

A comparison of the theoretical (Eq. 5) and experimental results is presented in Fig. 7. The much higher theoretical resonant frequencies are caused by the simplicity of Eq. 5, which does not take into account the cross-section area change coefficient (due to the use of a nozzle 10×10^{-3} m in diameter at the end of pipe). The directional factor of the empirical resonant frequency characteristics is lower in comparison with the theoretical value (by around 25%). The calculated resonant frequencies are similar to those measured experimentally. Generally, the experimental results are comparable with those of the numerical studies. The differences identified were caused by the simplicity of the 1D model used, based on MOC.

The resonance phenomenon is very often used in internal combustion engines as a dynamic boost intake system (significantly improving filling efficiency) and in the exhaust system (significantly lowering exhaust losses). The research presented here has very important implications for the automotive industry, due to significant influence that the dynamic properties of manifolds with pulsating flows have on the efficiency and environmental performance of internal combustion engines. The resonance phenomenon was also observed closely in automobile intake and exhaust manifolds. Intake and exhaust systems generally operate with various mass flow rates and at different temperatures. During the research, there were audible signs which confirmed the observed resonance phenomenon. The author is planning a synthesis of the measurement methods used in the presented studies with acoustic research, to objectify the acoustic impressions from pipes tested with pulsating flows.

5 Conclusions

Air temperature and mass flow rate have a significant influence on the dynamic properties of pipes supplied with pulsating flows. This paper has presented the results of a quantitative and qualitative investigation into the influence of both the air temperature and the mass flow rate. Numerical modeling and experimental studies were performed in parallel and showed quite close agreement. Understanding changes in the dynamic properties of pipes supplied with pulsating flows is essential for the construction and operation of all kinds of pipelines and compressed air lines, which suffer due to vibrations induced by resonance frequencies. The results presented here are very important for the mathematical modeling, design and control of pipeline systems interacting with mediums such as compressed air in a wide range of pipeline systems, especially compressed air ducts, internal combustion engine inlets and exhaust systems.

References

1. He, S., Jackson, J.: An experimental study of pulsating turbulent flow in a pipe. Eur. J. Mech. B/Fluids **28**, 309–320 (2009)
2. Park, J.-I., Adams, D., Ichikawa, Y., Bayyouk, J.: Frequency response of pressure pulsations and source identification in a suction manifold. J. Sound Vib. **277**, 669–690 (2004)
3. Dowling, J., Peat, K.: An algorithm for the efficient acoustic analysis of silencers of any general geometry. Appl. Acoust. **65**, 211–227 (2003)
4. Samuelson, R.D.: A second order system model for pneumatic instrumentation lines. IEEE Trans. Nucl. Sci. **16**(1), 271–276 (1969)
5. Howel, P.D., et al.: Mathematical analysis of the dynamic flow characteristic in a damping nozzle for a pressure transmitter. J. Phys.: Conf. Ser. **52**, 83 (2006)
6. Vetter, G., Seidl, B.: Pressure pulsation dampening methods for reciprocating pumps. In: Proceedings of the 10th International Pump Users Symposium, Houston, Texas, vol. 19 (1993)
7. Metwally, M.: Review of compressible pulsating flow effects on system performance. In: 13th International Conference on Aerospace Sciences & Aviation Technology, ASAT-13, 26–28 May 2009
8. Cyklis, P., Młynarczyk, P.: The influence of the spatial discretization methods on the nozzle impulse flow simulation results. Procedia Eng. **157**, 396–403 (2016). ISSN 1877-7058. https://doi.org/10.1016/j.proeng.2016.08.382
9. Jungowski, W.: Podstawy dynamiki gazów, pp. 101–105. WPW, Warszawa (1972)
10. Pałczyński, T, Rydlewicz, W.: Hybrid method for researching pulsating flows in pipes exemplified with orifice application. In: Advances in Condition Monitoring of Machinery in Non-Stationary Operations, pp. 309–317. Springer, Cham (2018)
11. Benson, R.S.: One-dimensional transient flow in a pipe with two gases. The Engineer **202**, 687–691 (1956)
12. Pałczyński, T.: A hybrid method of estimating pulsating flow parameters in the space-time domain. Mech. Syst. Signal Process. **89**, 58–66 (2017)
13. Olczyk, A.: Identification of dynamic phenomena in pipes supplied with a pulsating flow of gas. Proc. Inst. Mech. Eng. Part C: J. Mech. Eng. Sci. **223**(8), 1851–1867 (2009)

Model of Kinetic Energy Recuperation System for City Buses

Tomasz Pałczyński and **Jakub Łagodziński**

Abstract Energy consumption is a significant issue for public transport providers, because of the relatively high mass of the vehicles and the huge amounts of energy used to overcome inertial forces. In city buses, the kinetic braking energy is usually transformed into waste heat. In this paper, we propose a system to enable the recovery of braking energy in city buses, using a Kinetic Energy Recuperation System (KERS). The main assumptions of the system were elaborated in a Matlab/Simulink model of city bus dynamics, based on the real driving cycles of buses in Lodz (Poland). The following components were modelled: the flywheel supported in an active magnetic bearing, two reverse electric motors, the high ratio gears and the control system. The main objective of the control system was to balance operation of the braking and drive systems with optimal usage of the flywheel system. The charging and discharging phases of the KERS were analysed, as well as the energy stored. Fuel consumption savings were calculated via a comparison with normal city bus driving cycles without KERS. This model could be a very useful tool for research into city bus dynamics with KERS systems, providing a wide range of operational parameters for city bus powertrains.

Keywords Kinetic Energy Recuperation System · City bus · Matlab Simulink

1 Introduction

Kinetic Energy Recuperation Systems have been used to improve the efficiency of various power systems [1–3], including vehicle powertrains for city transport. The

T. Pałczyński (✉)
Flow Metrology Division, Institute of Turbomachinery, Lodz University
of Technology, 219/223 Wólczańska Street, 90-924 Łódź, Poland
e-mail: tomasz.palczynski@p.lodz.pl

J. Łagodziński
Diagnostic of Turbomachinery Division, Institute of Turbomachinery,
Lodz University of Technology, 219/223 Wólczańska Street, 90-924 Łódź, Poland

303

key advantages of such systems include their relatively long life-cycles, the short time they require to accumulate waste kinetic energy, their high power density and environmental benefits. Moreover, dynamically changing energy demand and supply often requires an additional system such as KERS. Sudden peaks in energy flow result in temporary surpluses or deficits in the total energy balance. Flywheels can store energy for a relatively long time, without significant energy loss. Given the high total vehicle weight of buses (about 22,000 kg) and the sharp changes in vehicle speed according to traffic, schedules and stops, KERS represents a good option for recouping transient energy currently wasted in city buses [4–6]. The main idea behind the presented system is to recoup waste energy in a simple way during the braking process, which is accumulated and stored until the start of the acceleration process. Generally, the global energy that can be recouped (during the braking process) is similar to the energy needed to move the vehicle. The crucial parameter of the system is the short time needed to accumulate braking energy and transmit it to the powertrain during the driving process. The modelled system consists of a reverse electric motor coupled with a high-speed flywheel. The flywheel is designed to work at low pressure to minimize the paddle resistance caused by air viscosity based on [7]. The concept for a KERS for city buses is based on a simplified model in Matlab/Simulink of city bus dynamics presented in [8].

1.1 Concept of City Bus KERS Model

The KERS system is implemented as a component of the city bus power-train. This enables overlay work, meaning that the classical powertrain can work without KERS. The main concept for city bus dynamics was presented in detail in [8]. The Solaris Urbino 18 City Bus was used as the reference vehicle (Fig. 1).
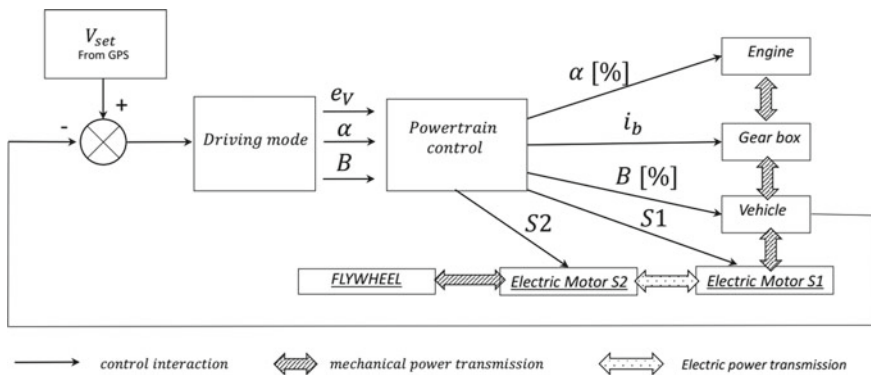
Fig. 1 Main concept of city bus dynamics with KERS model

The main process can be summarized up as follows:

- Downloading measurement data collected via GPS as a V_{set} as a simulation time function;
- Comparison with actual vehicle velocity, estimation of control error;
- Selection of Driving mode on the basis of set acceleration calculated as a derivate of the set velocity. Driving mode is selected between acceleration and braking. The Driving mode block also transports the control error, defined as the difference between the actual and set vehicle velocities $e_V = V_{set} - V_{actual}$;
- The powertrain control block is a control loop feedback mechanism. It consists of three independent feedback loops, dedicated to controlling degrees of engine load and braking. The powertrain control blocks also perform logical shifts, based on shifting lines which switch the required gear ratio i_b;
- The engine block estimates engine torque as a function of the engine load and the angular velocity, including engine inertia. Two mechanisms of energy transmission are shown: mechanical (arrow dashed) and electrical (clear arrow), as well as signal transmission (solid line);
- The Gear box and Vehicle block estimates the influence of automatically-chosen gear ratio and movement resistances (rolling, inertia of the masses in linear and angular movement, aerodynamics).

KERS assumptions:

- The flywheel will be supported on magnetic bearings. The Institute of Turbomachinery at TUL has significant experience in this field. Flywheel revolutions will range from 1500 to 3000 rad/s (15,000 to 30,000 rev/min);
- Two electric motors will be used: S1—connected to the powertrain via the gearbox (MSPW 24/30-6-A1 ALKA, [9]) and S2 connected to S1 and the flywheel (MSPW 20/22-4-C3 ALKA [9]). These electric motors have been chosen for their compatibility with the cooperating system component. For the gear connected to S1, the following efficiency ratios were assumed: $\eta_{S1} = 82\%$ and $\eta_{S2} = 85\%$;
- The drive process will be controlled in such a way as to achieve as complete as possible usage of the energy accumulated by the flywheel during vehicle acceleration and as full as possible participation of KERS during braking.

The Solaris Urbino 18 Bus is equipped with a DAF PR228 engine with maximum power of 231 kW and maximum torque of 1300 Nm available at CAV 115–178 rad/s. The curb weight of the bus is 16,000 kg and GVWR is 28,000 kg (for further calculations, it has been assumed that the maximum mass of the vehicle is 22,000 kg, which accounts for 79% of the maximum weight) [8].

The main gear ratio is 6.2 and gear ratios for subsequent gears of the automatic gearbox are respectively: 3.43; 2.01; 1.42; 1.00; 0.83. Universal engine torque characteristics T_e have been implemented in the model as a 3D map versus engine ω_e (rad/s) and engine load α (%). These are quasi-statistical characteristics and therefore have been extended using a dynamics model of the engine itself, taking account of its inertia. Universal engine torque characteristics were based on the external characteristics of the engine, assuming its linearity for fractional loads.
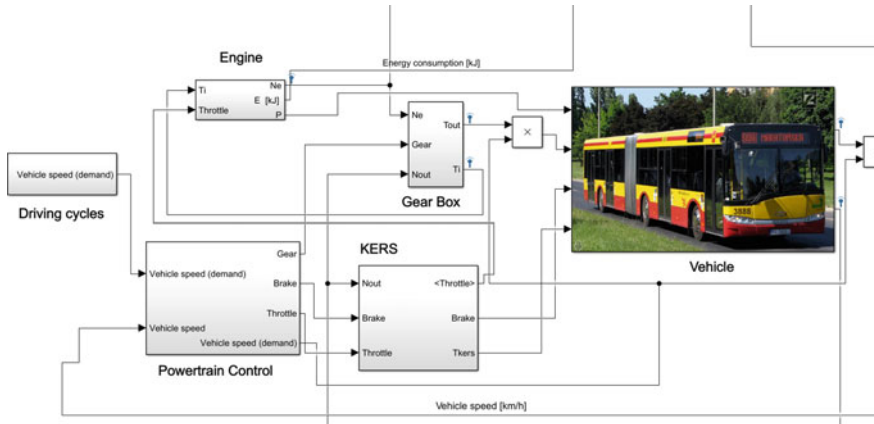
Fig. 2 Simulink model of the city bus with KERS

2 KERS Interaction with City Bus Transmission

The focus of this article is on the model of the KERS system and its interaction with city bus dynamics. As presented in Fig. 2, there is a KERS subsystem which performs the following tasks:

- Identification as true or false of the signal from the Powertrain Control during the driving phase, for "*Brake*" and "*Throttle*" (braking and acceleration).
- Processing of the following decisions and transient values.

  – the power (angular velocity and torque) of the primary S1 and secondary S2 electric motors; the direction of power flow; the work intensity of the S1 motor via producer power characteristics of the used machines.
  – Control (correction) of the engine load—defined as the throttle percentage position. Engine load is corrected according to the additional energy available to KERS.

The latter functions are performed according to the input. For example: *Nout*, *Brake*, *Throtle*, are processed as a new throttle position, braking intensity and KERS system torque through the bus powertrain. The self-matching feature is used.

3 KERS Interaction with City Bus Transmission—Selected Results

In this section, we present selected simulation results for the most important parameters estimated in this project. First, we consider the quality of the simulation results

with respect to the reference work [7]. The total modulo of the deviations sum (quantitative) and the mean value of this (qualitative) were calculated as an indication of the quality of vehicle speed mapping:

$$CMSO = \int\limits_{0}^{t} \left| V_p(t) - V_z(t) \right| dt, \tag{1}$$

where: V—vehicle velocity, p—demanded, z—realized and t—time at simulation domain.

$$\acute{S}MSO = \frac{CMSO}{t}, \tag{2}$$

Simulations were processed for three representative driving cycles, described in detail in [7]. The first is representative of normal traffic without traffic jams. The second represents weekend traffic. The last is representative of work days with traffic jams.

Figure 3 presents simulation results for drive cycle 1, based on real vehicle velocity (Fig. 3a) acquired using GPS technology. Figure 3b shows the total modulo of the deviations (between demanded and realised vehicle speed) versus time. This parameter enabled optimization of the three PID controllers (corrected throttle value) parameters. The first two PID's are implemented at "POWERTRAIN CONTROL" subsystem presented in Fig. 2, which are responsible for control of acceleration and braking process—these regulators replace the driver's work in the modelled system and make it repeatable for various analysed driving cycles. The third one PID controller, implemented at KERS subsystem. Engine load is corrected according to the additional energy available to KERS.

Multi-criteria optimization made it possible to select the inertia of the flywheel as a combination of the main parameters. Figure 3c shows the estimated transient course and angular velocity of the flywheel. As can be seen, the real range of work of this element is between 1500 and 3000 rad/s. The minimum value for the flywheel was determined as the minimum power available to the secondary electric motor. Maximum angular velocity has been limited by the conditions resulting from the maximum allowable tensile stresses (for the assumed material and dimensions of rotating ring) caused by huge (because of relative large radiuses) centrifugal forces. The most interesting results are presented in Fig. 3d, which shows measurable gains from the application of the KERS in the city bus powertrain. Fuel consumption was reduced from 6 to 4 L (about 30% decrease). Assumed efficiency of the primary and secondary electric motor ($\eta_{S1} = 82\%$, $\eta_{S2} = 85\%$) in author opinion covers other power losses and not modelled because of model simplifications (not covered: wadding losses, electromechanical detailed interaction between powertrain and KERS). It is proven e.g. in [10, 11] that braking energy recovery, especially at heavy vehicles like long city buses at intensive accelerating and braking driving cycle condition can give the 25–30% fuel consumption savings.
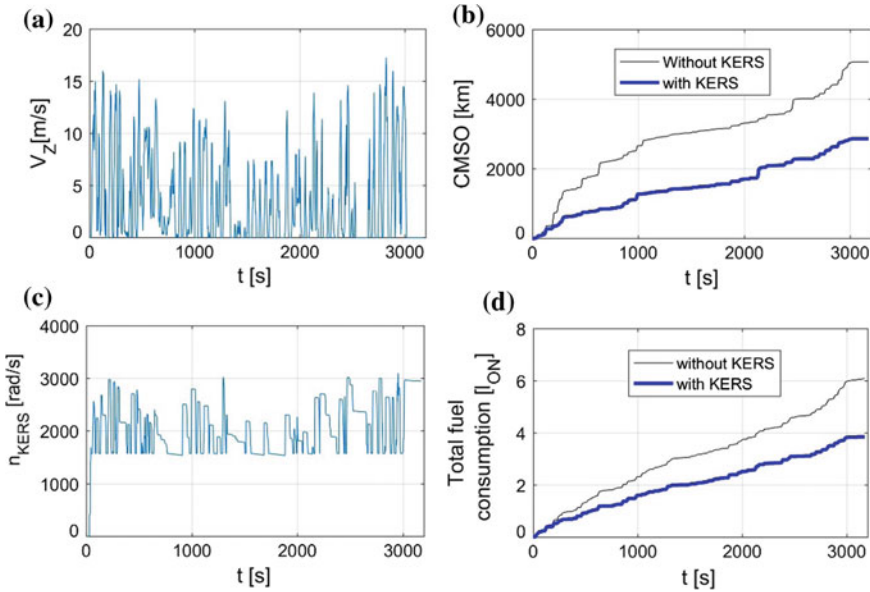
Fig. 3 Simulation result for cycle 1, **a** vehicle speed set, **b** CMSO versus simulation time, **c** flywheel angular velocity, **d** total fuel consumption

Table 1 Fuel consumption in three considered diving cycles

Driving cycle	Fuel consumption w/o KERS (l/100 km)	Fuel consumption with KERS (l/100 km)	Fuel consumption reduction (%)
1st	60.4	39.0	35.4
2nd	57.9	39.4	32.0
3rd	53.2	42.0	21.1

The proportion of KERS transient power in the total power transmitted to the powertrain is significant, as shown in Fig. 4a, b for the braking mode and in Fig. 4c, d for the acceleration mode. Figure 4e, f show significant decreases in total energy demand, due to the use of KERS. Overall, Fig. 4 proves that KERS can reduce the energy usage of IC engines and the heat capacity of vehicle braking systems. Table 1 shows fuel consumption for the three considered driving cycles.

Finally, the weighted average total fuel consumption was estimated, based on repetition of the three driving cycles over a month. Total estimated weighted fuel consumption for 2017 without KERS was 58.4 l/100 km and with KERS only 39.6 l/100 km, representing a 32.2% improvement. The mean price of diesel and the assumed cost of manufacturing and servicing the technology were calculated at 40,000 PLN—providing an estimated net profit of around two million PLN for the 90 buses. This means that implementation of this system in a 90 bus fleet would almost cover the cost of purchasing two new buses over the typical lifetime of the
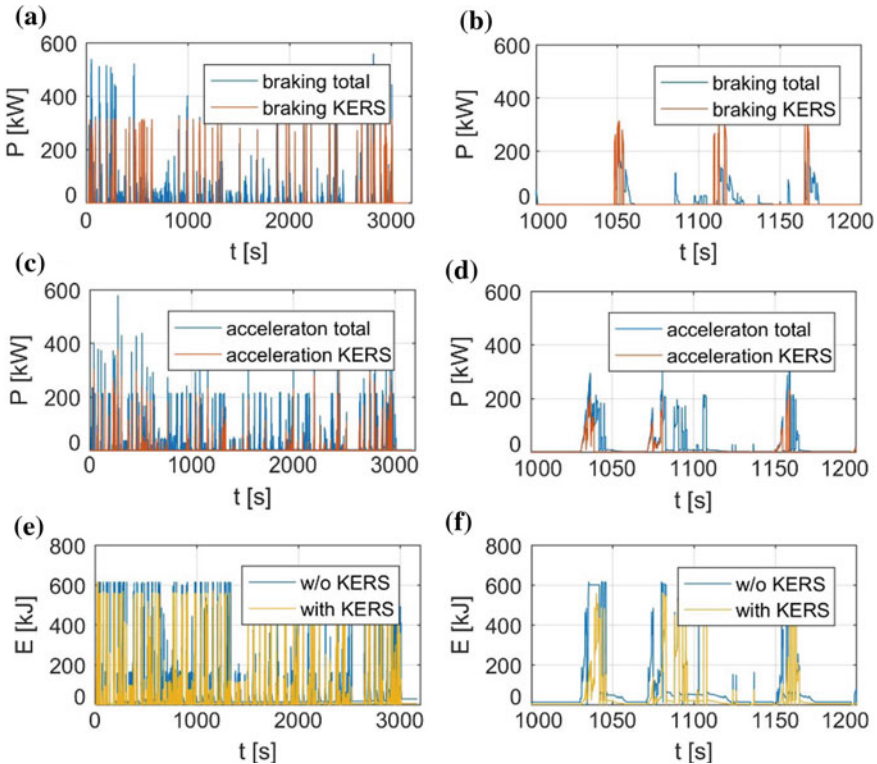
Fig. 4 Simulation results for cycle 1, **a** transient power transition at braking mode—total and KERS in the whole time domain, **b** transient power transition in braking mode—total and KERS in shortened time domain, **c** transient power transition in acceleration mode—total and KERS in the whole time domain, **d** transient power transition in acceleration mode—total and KERS in shortened time domain, **e** total energy demand with and w/o KERS in the whole time domain, **f** total energy demand with and w/o KERS in shortened time domain

fleet of vehicles. These calculations demonstrate the potential economic benefits of the proposed concept.

4 Conclusions

The implementation of a KERS system into city bus powertrains enables improved energy transmission, especially for recuperation of braking energy during driving mode. The presented model could be a very useful tool for research into city bus dynamics with KERS systems, providing a wide range of operational parameters for city bus powertrains. The tool enables easy analysis of a given vehicle's energy consumption, taking into account real-life changes in movement registered with

a simple, readily-available GPS device. The proposed method makes it possible to adjust the model to real-life conditions, thus creating a hybrid model, which combines the advantages of simulation with experimental research. The results presented in this paper show that maximum engine power usage can be reduced in vehicles with KERS, thanks to the input of an additional energy source. By analogous reasoning, the thermal capacity of the braking system can be decreased because of the existence of additional energy storage capacity.

References

1. Medina, P., Bizuayehu, A.W., Catalao, J.P.S., Rodrigues, E.M.G., Contreras, J.: Electrical energy storage systems: technologies' state-of-the-art, techno-economic benefits and applications analysis. In: Proceedings of the 47th Hawaii International Conference on System Sciences, Waikoloa, HI, USA, 6–9 Jan 2014, pp. 2295–2304
2. Chen, H., Cong, T.N., Yang, W., Tan, C., Li, Y., Ding, Y.: Progress in electrical energy storage system: a critical review. Prog. Nat. Sci. **19**, 291–312 (2009)
3. Hadjipaschalis, I., Poullikkas, A., Efthimiou, V.: Overview of current and future energy storage technologies for electric power applications. Renew. Sustain. Energy Rev. **13**, 1513–1522 (2009)
4. Esfahanian, M., et al.: Matlab-based modeling, simulation and design package for Eletric, Hydraulic and Flywheel hybrid powertrains of a city bus. Int. J. Automot. Technol. **15**(6), 1001–1013 (2014)
5. D'Ovidio, G., Masciovecchio, C., Rotondale, N.: City bus powered by hydrogen fuel cell and flywheel energy storage system. In: Electric Vehicle Conference (IEVC), 2014 IEEE International. IEEE (2014)
6. D'Ovidio, G., Masciovecchio, C., Rotondale, A.: Hydrogen fuel cell and kinetic energy recover systems technologies for powering urban bus with zero emission energy cycle. IET Intell. Transp. Syst. **10**(9), 573–578 (2016)
7. Zieliński, P.: Design for Kinetic Energy Recuperation System for city buses. Master Thesis, Supervisor: Ph.D., Eng Jakub Łagodziński, Diploma Thesis defended at 09.2017 at Institute of Turbomachinery, Lodz University of Technology
8. Pałczyński, T.: Simplified model of city bus dynamics as a tool of an energy consumption estimation. In: Dynamical Systems Theory and Applications. Springer, Cham (2015)
9. https://motorscout.eunda.ch/ available at 1.09.2017
10. Soylu, S.: The effects of urban driving conditions on the operating characteristics of conventional and hybrid electric city buses. Appl. Energy **135**, 472–482 (2014)
11. Taymaz, I., Benli, M.: Emissions and fuel economy for a hybrid vehicle. Fuel **115**, 812–817 (2014)

Signal Prediction in Bilateral Teleoperation with Force-Feedback

Mateusz Saków, Krzysztof Marchelek, Arkadiusz Parus, Mirosław Pajor and Karol Miądlicki

Abstract In the paper a sensor-less and self-sensing control scheme for a bilateral teleoperation system with force-feedback based on a prediction of an input of a non-linear inverse model by prediction blocks was presented. As a part of the paper a method of a time constant estimation of the prediction block was also proposed. The prediction method of an input of an inverse model was designed to minimize the effect of the transport delay and the phase shift of sensors, actuators and mechanical objects. The solution is an alternative to complex non-linear models like NARX or artificial neural networks, which requires complex stability analysis, and control systems with high computing powers. The effectiveness of the method has been verified on the hydraulic manipulator's test stand.

Keywords Bilateral teleoperation · Non-linear inverse modeling · Signal prediction

1 Introduction

Nowadays it is hard to find a factory without a device being controlled by a joystick, a keyboard or other type of remote control [14]. From early 60's of the previous century

M. Saków (✉) · K. Marchelek · A. Parus · M. Pajor · K. Miądlicki
Faculty of Mechanical Engineering and Mechatronics, West Pomeranian University
of Technology, Szczecin, 19 Piastów Avenue, 70-310 Szczecin, Poland
e-mail: mateusz.sakow@zut.edu.pl

K. Marchelek
e-mail: krzysztof.marchelek@zut.edu.pl

A. Parus
e-mail: arkadiusz.parus@zut.edu.pl

M. Pajor
e-mail: miroslaw.pajor@zut.edu.pl

K. Miądlicki
e-mail: karol.miadlicki@zut.edu.pl

research is being carried out to obtain remote control [5] or partially autonomous [31] device operation. The breakdown into remotely controlled and autonomous devices was proposed, when scientists discovered the critical value of a delay in the communication channel, which had a crucial impact on a stability of the telemanipulation system [31]. However, the transmission delay is not the only component of an aggregate delay in the teleoperation system. The aggregate delay usually consists a processing time of an analog-digital converter, a time of calculation completion by a controller, a processing time of a digital-analog converter and transition states of dynamic properties of actuators, sensors and mechanical objects [31].

The problem of a stability and a counteract of the effect of the delay in the communication channel are addressed by many scientific papers [5, 10, 29, 34, 36]. At the beginning research was focused on methods maintaining the stability which were the move-and-wait strategy and the deliberate slowdown of operator's motion when the environmental object was approached [5]. Later, sensor based control schemes was redesigned and equipped with a shared compliant control method by Kim [11]. The shared compliant control included flexible bodies in a mechanical structure of a Master manipulator. W. S. Kim also proposed a control scheme of bilateral force control, based on a position error between Master and Slave manipulators which control scheme has improved transparency of a force in the force-feedback communication channel [10]. However, none of these control schemes could guaranteed the stability of a system, when large delays are expected in the communication channel. Only, after the modification of the communication channel based on a wave variables, bilateral teleoperation systems were able to maintain stability regardless to the delay in the communication channel [30]. The wave variables were also extended with the passivity formalism [1]. However, a significant improvement of a force projection was achieved by the four-channel architecture of the communication channel [6, 12]. Finally, the four-channel communication system was equipped with an adaptive controller which estimated control parameters of force and position channels simultaneously [36].

XXI century is a domain of control schemes based on: sliding mode controllers [19], fuzzy logic controllers [4], force-feedback communication channel frequency separation techniques [21], special methods for discretization of a sensor resolution [7], artificial neural networks [34] and adaptive controllers dedicated to variable and asymmetric time delays, which are using adaptive filtering methods [37]. However, it is important to pay attention that bilateral teleoperation systems feature three types of feedback with the operator: vision-feedback [28, 31], force-feedback [5] and combination of vision-feedback and force-feedback [5, 10, 29, 34, 36]. Remotely controlled devices can be controlled by operator's motion scanners [11, 29], which in a special case are exoskeletons for upper limb [24], by gesture control techniques [15, 20] or by voice control methods [32, 33]. And also methods, which are dedicated to real-time monitoring of remote environment [16–18]. Also an important classification of bilateral teleoperation systems with force-feedback are systems, which using force sensor [2, 5, 11, 21], and devices without force sensors also known as a sensor-less or self-sensing techniques in the telemanipulation field [22–27, 29, 34, 35]. The sensor-less teleoperation systems group usually is based on impedance

control methods [8], and the inverse modeling techniques to obtain correct value of force in the force-feedback communication channel [24, 26, 35]. Inverse models are represented frequently by artificial neural networks [34], nonlinear autoregressive model with exogenous inputs (NARX) [24], and by micromanipulators which are using reversal processes that occur in piezo-crystals [22].

The paper addresses the transport delay problem in a sensor-less control scheme based on a dynamic inverse modeling procedure, which allows the system to estimate environmental force affecting the Slave manipulator. The dynamic inverse model used in the control unit was extended with proposed prediction blocks. The single prediction block has been a phase shifter with a specific characteristics. The specific feature of the prediction block is a strongly linear and positive phase diagram in a useful frequency spectrum, which allows the system to predict the manipulator's motion with a close to constant time shift. The gain of the block is close to the a unity, when system is operating also in a useful frequency spectrum. The proposed nonlinear inverse dynamic model structure which nonlinearity included the modified Stribeck friction model was validated on a 1-DOF hydraulic manipulator. The experiment and simulations confirmed the effectiveness of the predictive nonlinear inverse model, by reducing the time shift error between measured and simulated control signals.

2 Problem Statement

The primary issue of inverse models used in a control unit of any device is always present transport delay [31]. Usually, a control scheme based on differential equations will cause a delay between measured and simulated signals. Thus, the delay between signals will result in a noise appearance in the force-feedback channel with an amplitude that may destabilize the system even in free-motion operation—Fig. 1.
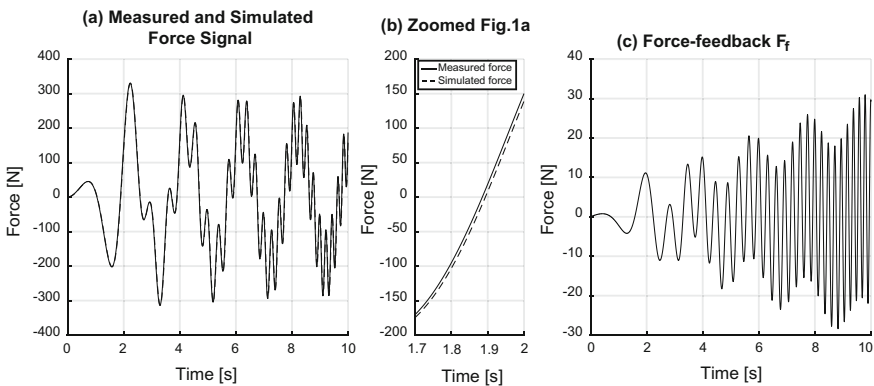
Fig. 1 **a** Measured and simulated force, **b** zoomed (**a**), **c** force-feedback channel

The seemingly unnoticeable delay between two signal in Fig. 1a zoomed in Fig. 1b caused deformation of force and could destabilize the entire bilateral system with a force-feedback communication channel. This difference, which has been calculated from the control signal Fig. 1c is caused by a 10 ms transport delay. The effect of a dangerous noise in the force-feedback channel increases its negative impact on the force transparency. This feature is a one of the primary concerns of the sensor-less control schemes based on inverse modeling techniques, but it is also a motivation of a research presented in the paper.

3   The Prediction Block

This section presents an approach for minimizing the effect of a transport delay in the communication channel and it is based on a prediction of inputs of an inverse model by a simple phase shifter. The prediction block minimizes the transport delay effect of a control unit, an actuator, objects and sensors directly in the control unit of a Slave subsystem. Schematic diagram of the Master-Slave system with force-feedback is presented in Fig. 2a.

The system structure contains 3 specific objects: the operator block which controls the position of the Master subsystem (motion scanner) by affecting it with human force F_h. The Master subsystem transfers its position x_m to the Slave subsystem. The control unit of the Slave subsystem seeks to obtain the position of Master subsystem by the Slave subsystem $x_s = x_m$. By the force-feedback communication channel F_f environmental force influence F_e is being transfer back to the Master subsystem. The second task of the motion scanner is to deliver the force from the force-feedback communication channel back to the operator $F_f = F_e$. Theoretically the value of the force $F_m = F_e$ [24], but for real devices, the F_m force delivered by an actuator of the Master subsystem to the operator strongly depends on the inverse model accuracy. In the case of the considered system, 3 types of feedback with the operator can be used: force-feedback F_m (F_f), vision-feedback of the Master Subsystem position x_m, and the vision-feedback of the Slave subsystem position x_s. The Slave vision-feedback can be useful only, when both subsystems are in close range or when an image is being transmitted online from the cameras around the Slave subsystem placement.

During the analysis of the control schemes based on the NARX model [23, 24] and the first introduction of the prediction techniques [25–27, 29], in the paper a
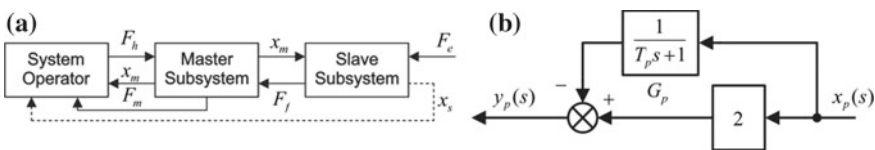
Fig. 2   **a** Master-Slave system analyzed, **b** the prediction block

prediction block with its time constants T_p estimation method is proposed. The prediction block and its structure was developed during the analysis of the Smith prediction control [9]. The proposed structure of the prediction block is presented in the Fig. 2b. The transmittance characterizing the automation structure in the Fig. 2b is described by a ratio of an output signal $y_p(s)$ and an input signal $x_p(s)$ and is given by Eq. (1):

$$y_p(s)/x_p(s) = (2T_ps + 1)/(T_ps + 1) \tag{1}$$

where s is the Laplace operator. Examining the transmittance (1) in the frequency domain it has to be paid attention to the amplitude (Fig. 3a) and phase diagrams (Fig. 3b) of the prediction block presented in the Fig. 3. The prediction block depending on the T_p constant is able to linearly shift a phase of an input signal, resulting in a constant time shift, but only in a useful frequency spectrum—Fig. 3b. Unfortunately, the prediction block like any phase shifter is a cause of a gain of the input signal amplitude, but in the useful frequency range, the gain is close to a unity—Fig. 3a. The useful frequency spectrum is understood to be the achievable for a human motion. Scientific literature gives a limit of a 6 Hz [13] but for the inverse modeling technique it was decided to increase the limit to 10 Hz, to leave a bigger margin of error for the inverse model output signal. The prediction ability was confirmed also in a simulation of the first order transfer function with $T = 0.001$ parameter which response was predicted. Simulations results in time domain are presented in the Fig. 3c.

Both frequency diagrams in Fig. 3a and b, and the step response in Fig. 3c are the proof of a predictive capabilities of the prediction block. But, it is important to note that the prediction block is sensitive to a noise and changes of a signal derivative sign $x_p(t)$. An amplitude of a noise will be increased twice, when using only one prediction block. When using more of the prediction blocks in a serial connection,
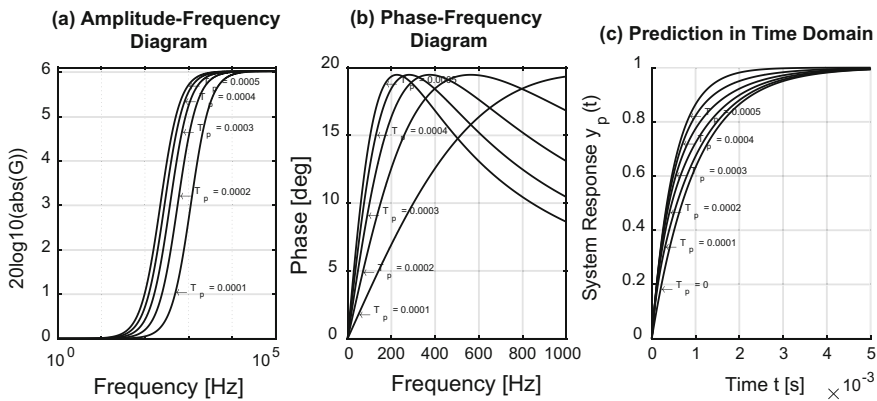
Fig. 3 **a** Amplitude-frequency, **b** Phase-frequency diagrams of the prediction block, **c** Step response prediction of a first order transfer function response

the gain depends on a number of prediction blocks used by 2 to the power of the number of prediction blocks.

4   Inverse Model with Prediction of Input and Output Signals

Theoretical analysis carried out in the previously published papers [23–26] proved that, the ideal response of a sensor-less control scheme in the force-feedback channel is only reachable, when the system is equipped with an ideal inverse model. In practice, obtaining an ideal inverse model of any subsystem is impossible.

In the paper, it was decided to estimate an environmental force based on the control signal, which is well-known. The inverse dynamic model G^{-1} in this case, estimated a control signal which is required for free-motion of a Slave manipulator, and based on the position x_s in a single joint. The estimated control signal was then subtracted from the well-known control signal, which was applied to the object—Figure 4.

The control unit scheme describes the Slave subsystem with a dual channel based communication technique. The Slave subsystem consists of a controller $K_c(s)$, an actuator $G_a(s)$, an object $G_o(s)$ and a sensor $G_s(s)$ transfer functions. The actuator was described by three parameters, a gain K_a, a transport delay T_1^a and a constant parameter of a first order inertia object T_2^a. The object describes the 1-DOF Slave manipulator body and is characterized by two parameters, a mass M_s and a linear viscous damping h_e. The sensor transfer function is similar to the actuator's transfer function and it is described by three parameters, a gain K_s, a transport delay T_s^1 and a constant parameter of a first order inertia object T_s^2. The estimation block consists the inverse model G^{-1}, a low-pass filter $G_f(s)$ with a parameter T_f and a gain K_a, same as in the actuator's transfer function. In the case of a known inverse model, which describes Slave subsystem in the Fig. 4, by the Eq. (2):

$$G^{-1} = e_1^{s(Ta+Ts)}{}_1 \left(T_2^a s + 1\right)\left(T_2^s s + 1\right)(h_e + M_s s)s / \left(K_a K_s \left(T_f s + 1\right)\right), \qquad (2)$$
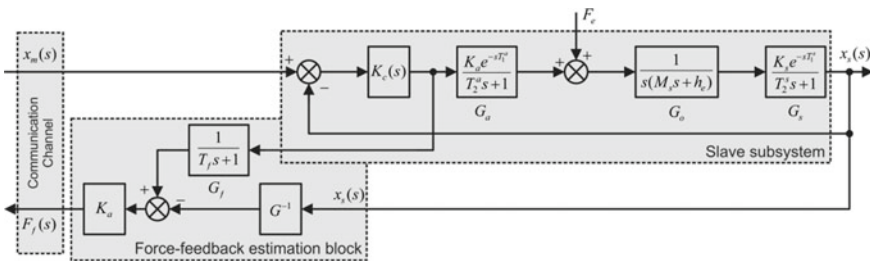
Fig. 4   Control unit scheme of the Slave subsystem with force-feedback estimation block

the difference between the object control signal and the estimated control signal in free-motion, increased by the gain K_a gain describes the force $F_f(s)$ in the force-feedback communication channel, and is equal to the environmental force impact $F_e(s)$ (3):

$$F_f(s) = F_e(s). \tag{3}$$

However, the presence of a positive parameter in the exponential functions makes the G^{-1} model (which describes the process) impossible for physical interpretation and also without a possibility of implementation in a control unit.

To minimize the effect of a transport delay in the force-feedback communication channel, two prediction blocks have been implemented into the structure of the inverse model replacing the exponential function with a positive parameter. Also, prediction blocks replaced first order inertias with parameters T_2^a and T_2^s, to minimize the noise effect of a high order numerical differential calculation. However, to equalize the degree of polynomials in the denominator and the numerator it has been added subsequent first-order inertial block with parameter T_d which has been working as another low-pass filter. The proposed inverse model is described by an Eq. (4):

$$G^{-1} = (h_e + M_s s)s / \left(K_a K_s (T_f s + 1)(T_d s + 1) \right)(2T_p + 1)$$
$$(2T_p + 1) / \left((T_p s + 1)(T_p s + 1) \right). \tag{4}$$

The output signal of the inverse model $K_c^s(s)$ which control unit should apply to the actuator, is a signal $K_c(s)$, when the Slave manipulator performs movement in a space without the environmental influence. In practice, the estimated control signal approximates signal controller K_c described by $K_c^s(s) \cong (x_m(s) - x_s(s))K_c(s)$, which is affected by the transport delay. However, to obtain the parameter T_p, it is required to find a solution of an equation describing the force-feedback estimation block presented in the Fig. 4 under two conditions. First condition concerns situation when environmental force is not applied to the manipulator's body: $F_e(s) = 0$ and second condition when zero value of force in the force-feedback channel is expected: $F_f(s) = 0$. Under these two conditions, equation describing subsystem in the Fig. 4 takes the following form (5):

$$(x_m(s) - x_s(s))K_c(s)G_f(s) + G^{-1}(s, T_p)x_s(s) = 0, \tag{5}$$

where the $G^{-1}(s, T_p)$ is the inverse model (5) as a function of two variables; the Laplace operator and the parameter T_p. Unfortunately, the parameter T_p even for such a simple example as the presented one, is described as a function of the Laplace operator: $T_p = T_p(s)$. During the research carried out with multiply model structures it was discovered that optimal value of T_p has been always obtained for the pulsation value which boundary was tending to zero. After that, it was proposed to calculated the limit of the T_p as a function of Laplace operator s, when s tends to zero—Eq. (6):

(a) Comparison of inverse models resposes with $(x_m(s)-x_s(s))K_cK_a$

(b) Force in the force-feedback channel $F_f(t)$ [N], during free-motion
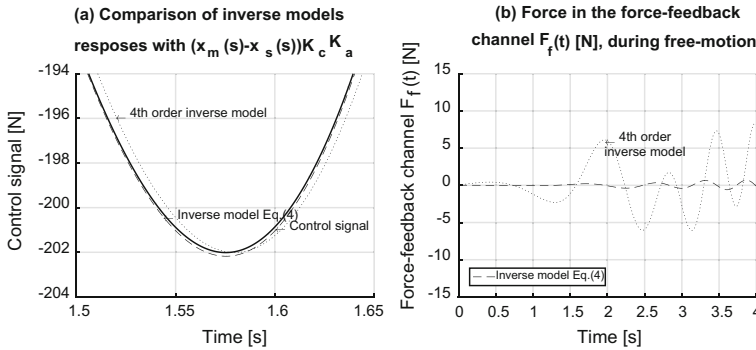
Fig. 5 The Subsystem Slave simulation results **a** force prediction, **b** force-feedback channel

$$T_p = lim_{s \to 0} T_p(s). \tag{6}$$

Currently, Eqs. 5 and 6, is a proposition for the T_p parameter estimation. In a future, it is planned to introduce a proof that will confirm this description, which was given in the paper.

Subsystem in the Fig. 4 was analyzed during multiple simulations. The comparison of the linear model—Eq. (4) and the standard 4th order transfer function with an equal degree of the polynomial in the numerator and the denominator. The simulation research was carried out on the subsystem Slave, and for the following data: $K_c = 100$; $K_a = 1$; $K_s = 1$; $T_1^a = 0.002$; $T_2^a = 0.002$; $M_s = 10$; $h_e = 1$; $T_1^s = 0.002$; $T_2^s = 0.002$; $F_e = 0$; $T_d = 0.0005$; $T_f = 0.0005$ and $x_m(t)$ was a harmonic signal with variable frequency in the range of 0.1–10 Hz. The results are presented in the Fig. 5.

Simulation results confirmed, that the inverse model which structure included prediction blocks was able to predict the control signal with higher accuracy, than the same order model was obtained during standard identification techniques. Two prediction blocks were able to replace two first order inertia parameters like T_1^a and T_1^s, and also minimize the effect of a transport delay present in the system. The results are confirmed by the diagram in the Fig. 5a, where the inverse model with prediction blocks response is much closer to the original control signal, than the standard 4th order inverse model response. This significant difference in identification techniques is especially visible in the force-feedback communication channel—Fig. 5b. The noise in the force-feedback channel $F_f(t)$ is barely visible for the proposed model when the 4th order inverse model obtained in the standard identification technique has caused a significant error of the force estimation.
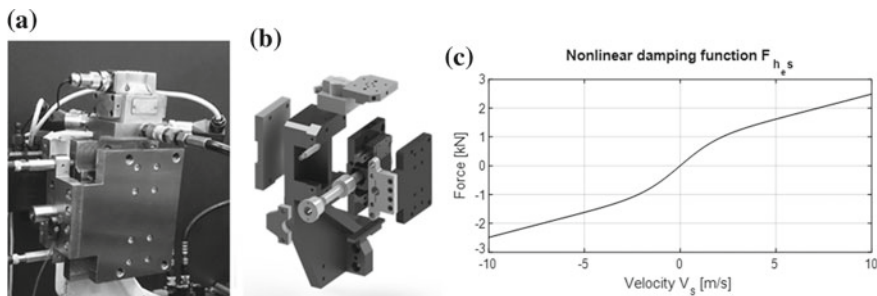
Fig. 6 **a** The experimental test stand **b** exploded CAD view **c** damping function

5 The Experiment

The method based on prediction of an input of an inverse model was validated on a hydraulic 1-DOF linear manipulator presented in the Fig. 6.

The experimental 1-DOF manipulator has been actuated by the 760s MOOG servo-valve. The test stand was equipped with two independent pressure sensors placed in both piston chambers. The position was measured by two inductive sensors. The measured and estimated control signal by the inverse model was the valve current. The inverse model has a structure presented by the Eq. (4) but included a nonlinear component describing the damping force F_{hes}, which is given by the Eq. (7):

$$F_{hes}(t) = \left(\left(1 + e_s^{-v(t)} \right) \right)^{-1} - 0.5 + 0.1 v_s(t) + 0.00045 |v_s(t)| v_s(t)) h_e, \quad (7)$$

where $v_s(t) = dx_s(s)/dt$.

The damping coefficient h_e, was identified at level of a 1.61 kNs/m. The mass was identified at 6.8 kg. The proposed damping function has not been chosen accidently. The noise present in the velocity signal has caused a significant amplitude of disturbance, when standard Stribeck friction model was used [3]. The nonlinear damping function is presented by a diagram in the Fig. 6c.

The identified model was expanded by two prediction blocks and implemented in the control unit. The identification of the T_p coefficient was carried out iteratively. For two prediction blocks, the T_p coefficient was identified at 0.0018. Unfortunately, for the remaining transport delay, responsible was the step change of a friction force described by the Stribeck model, but it is barely visible amid the noise. The implementation of prediction blocks allowed to minimize the current mean absolute error from 0.55 to 0.39 mA when chirp signal response was used as a comparison input signal. This is a significant difference which allowed to reduce the estimation error about 30%. The ability of proposed inverse prediction model is presented in the Fig. 7.

Diagrams presented in the Fig. 7 are the best proof of the proper functioning of the method. The advantage of the method is especially visible for low frequency
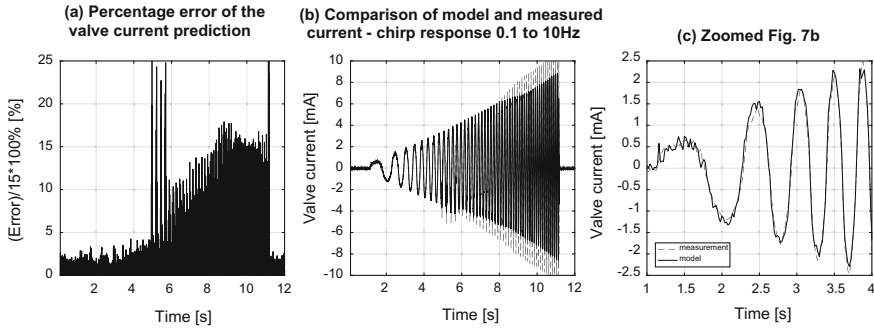
Fig. 7 **a** Percentage absolute error of the valve current prediction, **b** comparison of model and measured current data–chirp response 0.1–10 Hz, **c** Zoomed (**b**)
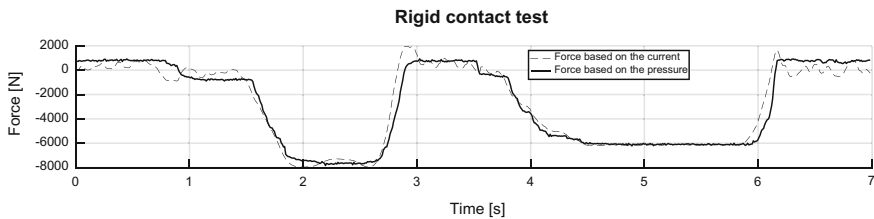
Fig. 8 Force in the force-feedback communication channel during rigid contact test

spectrum, when error is at the level of the noise—below 5% relative to maximum possible valve current—15 mA. The ability of prediction allowed the system to maintain the stability even during a rigid contact situation task by minimizing the aggregate delay of the system in the force-feedback communication channel. The force in the force-feedback communication channel during a rigid contact task is presented in the Fig. 8.

During the rigid contact test, the operator was obliged to move the manipulator body until the piston will reach its maxim possible position. The operator forced twice the remotely controlled manipulator to interact with its movement boundaries, with different force interaction. The method allowed the system to predict the environmental force up to 200 ms faster, than it could be sensed by the pressure sensor during free motion (Fig. 8, time period from 0.5 to 1 s). It is important to note that the force value in the force-feedback channel was reduced a hundred times, because the hydraulic manipulator was able to generate a force of a 20 kN. Also during the identification procedure of the inverse model, it was carried out a standard identification procedure of a 4th order inverse model, not based on the signal prediction technique. Unfortunately, for all collected data, the model remained unstable and the comparison could not be taken into account.

6 Conclusion

The paper presents a novel approach to a control design in bilateral and sensor-less teleoperation systems based on the prediction of an input and an output of an inverse model. The technique was based on prediction blocks which each prediction block was a phase shifter with specific properties. Alike simulations and experiments are the proof of an advantage of the technique over standard identification methods. The method allowed the introduction of significant simplifications of the model while accuracy of the prediction was improved. The inverse model was used in the control unit of the test stand and series of tests were carried out. Experimental results confirmed that the system equipped with the proposed method is able to predict the environmental force impact with higher accuracy then the standard identification technique.

References

1. Arcara, P., Melchiorri, C., Stramigioli, S.: Intrinsically passive control in bilateral teleoperation mimo systems. In: Control Conference (ECC), 2001 European. Porto, Portugal, pp. 1180–1185 (2001)
2. Atashzar, S.F., Polushin, I.G., Patel, R.V.: Projection-based force reflection algorithms for teleoperated rehabilitation therapy. In: 2013 IEEE/RSJ International Conference on Intelligent Robots and Systems, Tokyo, Japan, pp. 477–482 (2013)
3. Awrejcewicz, J., Olejnik, P.: Analysis of dynamic systems with various friction laws. Appl. Mech. Rev. **58**, 389–411 (2005)
4. Chang, M.-K.: An adaptive self-organizing fuzzy sliding mode controller for a 2-DOF rehabilitation robot actuated by pneumatic muscle actuators. Control Eng. Pract. **18**, 13–22 (2010)
5. Ferrell, W.R.: Delayed Force Feedback. Hum. Factors J. Hum. Factors Ergon. Soc. **8**, 449–455 (1966)
6. Hastrudi-Zaad, K., Salcudean, S.E.: On the use of local force feedback for transparent teleoperation. In: Robotics and Automation, 1999. Proceedings. 1999 IEEE International Conference on. Detroit, MI, USA, vol. 1863, pp. 1863–1869 (1999)
7. Hulin, T., Albu-Schäffer, A., Hirzinger, G.: Passivity and stability boundaries for haptic systems with time delay. IEEE Trans. Control Syst. Technol. **22**, 1297–1309 (2014)
8. Hyun Chul, C., Jong Hyeon, P., Kyunghwan, K., et al.: Sliding-mode-based impedance controller for bilateral teleoperation under varying time-delay. In: Proceedings 2001 ICRA. IEEE International Conference on Robotics and Automation, 2001, Seoul, South Korea, vol. 1021, pp. 1025–1030 (2001)
9. Kaya, I.: Obtaining controller parameters for a new PI-PD Smith predictor using autotuning. J. Process Control **13**, 465–472 (2003)
10. Kim, W.S.: Developments of new force reflecting control schemes and an application to a teleoperation training simulator. In: Proceedings 1992 IEEE International Conference on Robotics and Automation, 1992, Nice, France, vol. 1412, pp. 1412–1419 (1992)
11. Kim, W.S., Hannaford, B., Fejczy, A.K.: Force-reflection and shared compliant control in operating telemanipulators with time delay. IEEE Trans. Robot. Autom. **8**, 176–185 (1992)

12. Lawrence, D.A.: Stability and transparency in bilateral teleoperation. IEEE Trans. Robot. Autom. **9**, 624–637 (1993)
13. Lichiardopol, S., Wouw, N.V.D., Nijmeijer, H.: Control scheme for human-robot co-manipulation of uncertain, time-varying loads. In: 2009 American Control Conference, St. Louis, MO, USA, pp. 1485–1490 (2009)
14. Miądlicki, K., Pajor, M.: Overview of user interfaces used in load lifting devices. Int. J. Sci. Eng. Res. **6**, 1215–1220 (2015)
15. Miądlicki, K., Pajor, M.: Real-time gesture control of a CNC machine tool with the use Microsoft Kinect sensor. Int. J. Sci. Eng. Res. **6**, 538–543 (2015)
16. Miadlicki, K., Pajor, M., Sakow, M.: Loader crane working area monitoring system based on LIDAR scanner. In: Advances in Manufacturing, p. 465 (2017)
17. Miądlicki, K., Pajor, M., Saków, M.: Ground plane estimation from sparse LIDAR data for loader crane sensor fusion system. In: 2017 22nd International Conference on Methods and Models in Automation and Robotics (MMAR), pp. 717–722. IEEE, Międzyzdroje, Poland (2017)
18. Miądlicki, K., Pajor, M., Saków, M.: Real-time ground filtration method for a loader crane environment monitoring system using sparse LIDAR data. In: 2017 IEEE International Conference on INnovations in Intelligent SysTems and Applications (INISTA), pp. 207–212. IEEE (2017)
19. Nguyen, T., Leavitt, J., Jabbari, F., et al.: Accurate sliding-mode control of pneumatic systems using low-cost solenoid valves. IEEE/ASME Trans. Mechatron. **12**, 216–219 (2007)
20. Pajor, M., Miądlicki, K., Saków, M.: Kinect sensor implementation in FANUC robot manipulation. Arch. Mech. Technol. Autom. **34**, 35–44 (2014)
21. Polushin, I.G., Takhmar, A., Patel, R.V.: Projection-based force-reflection algorithms with frequency separation for bilateral teleoperation. IEEE/ASME Trans. Mechatron. **20**, 143–154 (2015)
22. Rakotondrabe, M., Ivan, I.A., Khadraoui, S., et al.: Simultaneous displacement/force self-sensing in piezoelectric actuators and applications to robust control. IEEE/ASME Trans. Mechatron. **20**, 519–531 (2015)
23. Saków, M., Miądlicki, K., Parus, A.: Self-sensing teleoperation system based on 1-dof pneumatic manipulator. J. Autom. Mobile Robot. Intell. Syst. **11**, 64–76 (2017)
24. Saków, M., Pajor, M., Parus, A.: Estimation of environmental forces impact on remote control system with force-feedback and upper limb kinematics (in Polish). Modelowanie Inzynierskie **58**, 113–122 (2016)
25. Saków, M., Pajor, M., Parus, A.: Self-sensing control system determining the environmental force influence on the manipulator during the operation of the telemanipulation system (in Polish). In: Projektowanie Mechatroniczne - Zagadnienia Wybrane. Katedra Robotyki i Mechatroniki, Akademia Górniczo-Hutnicza w Krakowie, pp. 139–150 (2016)
26. Saków, M., Parus, A.: Sensorless control scheme for teleoperation with force-feedback, based on a hydraulic servo-mechanism, theory and experiment. Meas. Autom. Monit. **62**, 417–425 (2016)
27. Saków, M., Parus, A., Miądlicki, K.: Predictive method of force determination in the force-feedback communication channel of remotely controlled system (in Polish). Modelowanie Inżynierskie **31**, 88–97 (2017)
28. Sakow, M., Parus, A., Pajor, M., et al.: Unilateral hydraulic telemanipulation system for operation in machining work area. In: Advances in Manufacturing, p. 415 (2017)
29. Saków, M., Parus, A., Pajor, M., et al.: Nonlinear inverse modeling with signal prediction in bilateral teleoperation with force-feedback. In: 2017 22nd International Conference on Methods and Models in Automation and Robotics (MMAR), pp. 141–146. IEEE, Międzyzdroje, Poland (2017)
30. Sheridan, T.B.: Space teleoperation through time delay: review and prognosis. IEEE Trans. Robot. Autom. **9**, 592–606 (1993)
31. Sheridan, T.B., Ferrell, W.R.: Human control of remote computer-manipulators. In: Proceedings of the 1st International Joint Conference on Artificial intelligence, pp. 483–494. Morgan Kaufmann Publishers Inc., Washington, DC (1969)

32. Stuart, K.D., Majewski, M.: Intelligent Opinion Mining and Sentiment Analysis Using Artificial Neural Networks. International Conference on Neural Information Processing, pp. 103–110. Springer, Istanbul, Turkey (2015)
33. Stuart, K.D., Majewski, M., Trelis, A.B.: Intelligent semantic-based system for corpus analysis through hybrid probabilistic neural networks. In: International Symposium on Neural Networks, pp. 83–92. Springer, Berlin (2011)
34. Tadano, K., Kawashima, K.: Development of 4-DOFs forceps with force sensing using pneumatic servo system. In: Proceedings 2006 IEEE International Conference on Robotics and Automation, 2006. ICRA 2006, Orlando, FL, USA, pp. 2250–2255 (2006)
35. Wei Tech, A., Khosla, P.K., Riviere, C.N.: Feedforward controller with inverse rate-dependent model for piezoelectric actuators in trajectory-tracking applications. IEEE/ASME Trans. Mechatron. **12**, 134–142 (2007)
36. Wen-Hong, Z., Salcudean, S.E.: Stability guaranteed teleoperation: an adaptive motion/force control approach. IEEE Trans. Autom. Control **45**, 1951–1969 (2000)
37. Zhai, D.H., Xia, Y.: Adaptive control for teleoperation system with varying time delays and input saturation constraints. IEEE Trans. Industr. Electron. **63**, 6921–6929 (2016)

Method of Direct Separation of Motions Applied to a Non-ideal Electromechanical Pendulum System

Shahram Shahlaei-Far and José Manoel Balthazar

Abstract This paper uses the approach of Vibrational Mechanics (VM) performing the Method of Direct Separation of Motions (MDSM) for the analysis of a non-ideal rotor mechanism with a limited power source. We employ a modification of the method to study the governing equations of a non-ideally excited electromechanical pendulum system consisting of three masses (block, rotating, pendulum) and a DC motor. The mechanism has three degrees of freedom and we derive the main equations of the slow component of motion from the initial governing equations to allow for a derivation of analytical solutions in the stability domain. The paper focuses on a purely analytical approach.

Keywords Method of direct separation of motions · Non-ideal system
Electro-mechanical pendulum

1 Introduction

A mechanical system is said to have an ideal power source when the excitation is not influenced by the motion response of the dynamical system. In this case, an ideal energy source acts on the vibrating system, but does not experience any reciprocal influence from it, i.e. the amplitude and frequency are independent from the motion of the system. Conversely, when the excitations of the system are limited, that is, when the real capacity of a particular energy source defined by its characteristic is considered, or its limitation by the dependence of the motion of the oscillatory system on the motion of the power supply, it is said to be a non-ideal energy source.

Non-ideal mechanical systems are of great interest in many fields of science and engineering since for most practical vibrating systems the power supply of the energy source is generally limited. Although non-ideal problems are far more realistic, they

S. Shahlaei-Far (✉) · J. M. Balthazar
Aeronautics Technological Institute, Marechal Eduardo Gomes Square 50,
São Jose dos Campos, SP 12228-900, Brazil
e-mail: shazzz_85@yahoo.de

have been explored fairly recently and in most cases investigated only by numerical or experimental methods [1–3].

For a purely analytical discussion of a non-ideal dynamical system, the general approach of Vibrational Mechanics (VM) or rather Oscillatory Strobodynamics (OS) (considering specifically oscillating actions on dynamical systems) is proposed using as its main tool the corresponding Method of Direct Separation of Motions (MDSM) [4–6] to study a non-ideally excited electromechanical pendulum system with a limited power source. Previously, Tusset et al. [7] analyzed the nonlinear motion control of this mechanical system using the State Dependent Riccati Equation (SDRE) technique. They applied a perturbation method, known as the method of variations of parameters to obtain analytical solutions, but concluded that these are not feasible due to the complexity of the governing equations.

Here, the MDSM is applied to transform the initial governing equations into vibro-transformed dynamics equations, i.e. equations describing only the main slow component of motion, that comprise the averaged effect of the oscillating action. In other words, the system behavior is perceived under a stroboscopic light by an observer who does not notice "fast forces and fast motions" but needs to add vibrational forces to all slow forces exerted on the system. With this transition, the derivation of analytical solutions will be made feasible, even for such a complex system of differential equations as discussed in this paper. In general, this transition gives way to phenomena that were unprecedented when considering the complete dynamics of processes as the laws of conservation might break down and additional terms may appear or parameter values may be changed.

The method has proved to be an effective tool to study the oscillating action on nonlinear dynamical systems. MDSM succeeded in analyzing many phenomena arising in the field of mechanics such as hysteresis, chaos and the Sommerfeld effect. Sorokin [8] studied the motion of a pendulum with vibrating suspension axis near its inverted equilibrium at low-frequency excitation using a modified version of the MDSM. Shishkina et al. [9] considered the so-called Indian magic rope trick and demonstrated the method's capability to derive explicit analytical solutions, in their case for the vibrational correction to the critical flexural stiffness. Demidov and Sorokin [10] discussed the motions of particles and gas bubbles in a horizontally oscillating vessel filled with viscous fluid and confirmed their analytical results with numerical ones allowing for a physical insight into the problem.

A rigorous mathematical treatment of fast and slow motions in mechanical systems considering high frequency modulation of the dissipation coefficient is given in [11] by Blekhman and Sorokin. It exemplifies how MDSM can be applied to strongly nonlinear differential equations without using small parameters. This has been possible due to recent modifications of the method to account for a broader range of problems which do not require the nonlinearities to be weak or imply restrictions on the spectrum of excitation frequencies [6, 8, 12]. Finally, to prove its worth and versatility the method has been used to study problems from various fields of science beyond mechanics, such as physics, chemistry and biophysics [6, 12].

Fig. 1 Electromechanical pendulum system with limited power source [4]
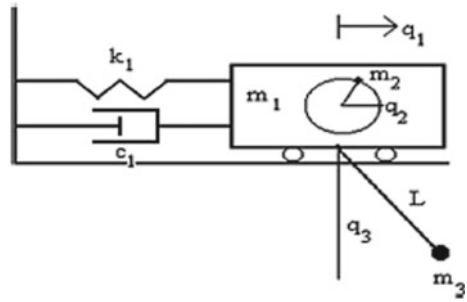
The present paper demonstrates the method's effectiveness to study a complex nonlinear mechanical system with three degrees of freedom and produce analytical derivations of the main slow component of motion for its analysis.

2 Governing Differential Equations

The electromechanical pendulum system with a non-ideal power source (see Fig. 1) was reviewed by Tusset et al. [7]. In that article a full description of the problem was presented in which the governing equations were derived as

$$m_1\ddot{q}_1 - m_2R\big(\ddot{q}_2\sin(q_2) + \dot{q}_2^2\cos(q_2)\big) + m_3l\big(\ddot{q}_3\cos(q_3) - \dot{q}_3^2\sin(q_3)\big) + k_1q_1 = -c_1\dot{q}_1 \tag{1}$$

$$I\ddot{q}_2 - m_2R\ddot{q}_1\sin(q_2) + gm_2R\cos(q_2) = M(\dot{q}_2) \tag{2}$$

$$m_3l^2\ddot{q}_3 + m_3l\ddot{q}_1\cos(q_3) + gm_3l\sin(q_3) = -c_3\dot{q}_3 \tag{3}$$

where m_1, m_2, m_3 are a mass block, a rotating mass at a distance R from the DC motor axis and a pendulum mass, respectively. k_1 and c_1 are the coefficients of the spring and damper, respectively, that connect the mass block to the wall. c_3 is the coefficient of viscous resistance.

The driving torque is given by $M(\dot{q}_2) = a + b\dot{q}_2$ with a describing the voltage across the armature and b a constant. The moment of inertia is $I = m_2R^2 + J$, where J is the rotor moment of inertia. g is the gravitational acceleration.

Here the generalized coordinates q_1, q_2, q_3 are the horizontal displacement of mass m_1, the angle of rotation of the rotor with rotating mass m_2, counted from the horizontal direction and the angle of deviation of the pendulum with mass m_3 from its lower vertical position, respectively.

Using the following relations

$$u = \frac{q_1}{l}, \varphi = \frac{q_2}{Q_2}, \theta = \frac{q_3}{Q_3} \text{ with } Q_2 = 1 \text{ (rad)}, Q_3 = 1\text{(rad)} \tag{4}$$

we transform the differential Eqs. (1)–(3) into

$$\ddot{u} + \mu_1\dot{u} + \omega_1^2 u = p_2\ddot{\varphi}\sin(\varphi) + p_2\dot{\varphi}^2\cos(\varphi) + p_5\ddot{\theta}\cos(\theta) + p_5\dot{\theta}^2\sin(\theta) \quad (5)$$

$$\ddot{\varphi} - a - b\dot{\varphi} = p_3\ddot{u}\sin(\varphi) + gp_4\cos(\varphi) \quad (6)$$

$$\ddot{\theta} + \mu_3\dot{\theta} + \omega_3^2\sin(\theta) = -\ddot{u}\cos(\theta) \quad (7)$$

where $m = m_1 + m_2 + m_3$ is the total mass of the system and $\omega_1^2 = \frac{k_1}{m_1}$, $\omega_3^2 = \frac{g}{l}$, $p_2 = \frac{m_2 R}{m}$, $p_3 = \frac{m_2 Rl}{I}$, $p_4 = \frac{m_2 R}{I}$, $p_5 = \frac{m_3}{m}$, $\mu_1 = \frac{c_1}{m}$, $\mu_3 = \frac{c_3}{m_3 l^2}$.

3   Method of Direct Separation of Motions

Using the method of direct separation of motions the solutions of Eqs. (5)–(7), considering the law of motion of the pendulum under vibration, are assumed to be

$$\dot{\varphi} = \alpha(t) + \psi(t, \omega t), \theta = \beta(t) + \eta(t, \omega t), u = u(t, \omega t) = P\cos(\omega t) \quad (8)$$

where $\alpha(t)$, $\beta(t)$, are the main slow components and $\psi(t, \omega t)$, $\eta(t, \omega t)$ and $u(t, \omega t)$ are the fast 2π-periodic components with respect to $\tau = \omega t$ such that

$$\langle\psi(t, \tau)\rangle = \langle\eta(t, \tau)\rangle = \langle u(t, \tau)\rangle = 0, \psi \ll \alpha, \eta \ll \beta \quad (9)$$

where $\langle\ \rangle$ designates averaging in the period 2π on the fast time variable τ as $\langle f(t, \tau)\rangle = \frac{1}{2\pi}\int_0^{2\pi} f(t, \tau)d\tau$ for a continuous function $f(t, \tau)$.

For the problem at hand, we consider the stiffness force $\omega_1^2 u$, the damping force $\mu_1\dot{u}$, the driving torque $M(\dot{\varphi})$, the moment of viscous damping $\mu_3\dot{\theta}$, the moment of gravitational force $\omega_3^2\sin(\theta)$ to be the slow components, whereas all the other forces are considered as fast components.

Linearizing $M(\dot{\varphi})$ close to $\dot{\varphi} = \dot{\varphi}_0 = \alpha$ we have [4]

$$M(\dot{\varphi}) = M(\alpha) - c(\dot{\varphi} - \alpha), c = c(\alpha) = -dM/\dot{\varphi}|_{\dot{\varphi}=\alpha} > 0, \quad (10)$$

Applying MDSM to the system described in (5)–(7) we obtain equations for the slow and fast motions

$$\dot{\alpha} = M(\alpha) + V_1(\alpha) \quad (11)$$

$$\dot{\psi} = -c\psi + \Psi(\ddot{u}, \varphi) \quad (12)$$

$$\ddot{\beta} = -\mu_3\dot{\beta} - \omega_3^2\sin(\beta) + V_2(\beta) \quad (13)$$

$$\ddot{\eta} = H(\beta, \dot{\eta}, \eta, \tau) \quad (14)$$

$$\ddot{u} + \mu_1\dot{u} + \omega_1^2 u = p_2\ddot{\varphi}\sin(\varphi) + p_2\dot{\varphi}^2\cos(\varphi) + p_5\ddot{\theta}\cos(\theta) + p_5\dot{\theta}^2\sin(\theta) \quad (15)$$

with

$$\Psi(\ddot{u}, \varphi) = p_3 \ddot{u} \sin(\varphi) + g p_4 \cos(\varphi) - \langle p_3 \ddot{u} \sin(\varphi) + g p_4 \cos(\varphi) \rangle \qquad (16)$$

$$H(\beta, \dot{\eta}, \eta, \tau) = - \mu_3 \dot{\eta} - \omega_3^2 (\sin(\beta + \eta) - \langle \sin(\beta + \eta) \rangle)$$
$$- \langle \ddot{u} \cos(\beta + \eta) - \langle \cos(\beta + \eta) \rangle \rangle \qquad (17)$$

$$V_1(\alpha) = \langle p_3 \ddot{u} \sin(\varphi) + g p_4 \cos(\varphi) \rangle \qquad (18)$$

$$V_2(\beta) = \omega_3^2 (\sin(\beta) - \langle \sin(\beta + \eta) \rangle) - \langle \ddot{u} \cos(\beta + \eta) \rangle \qquad (19)$$

The system in Eqs. (11)–(14) is equivalent to the system in Eqs. (6), (7) in the sense that if $\alpha, \beta, \psi, \eta$ are solutions to the former system, then $\varphi = \alpha + \psi, \theta = \beta + \eta$ are solutions to the latter.

Assuming $t, \alpha(t), \dot{\alpha}(t)$ to be constant (the admissibility proved in [4]) and $\Psi(\ddot{u}, \varphi)$ to be small we can write

$$\Psi(\ddot{u}, \varphi) = \rho \Psi_1(\ddot{u}, \varphi) \qquad (20)$$

where $\rho > 0$ is a small parameter.

The first approximation of ψ is $\psi_0 = 0$ satisfying the condition in Eq. (9). Thus, considering Eq. (8), we have $\dot{\varphi}_0 = \alpha(t)$ and can assume

$$\varphi = \varphi_0 = \int_0^t \alpha(t) dt = \alpha(t) t + \gamma(t) \qquad (21)$$

where $\gamma(t)$ is a function of t. Note that according to our assumptions $\ddot{\varphi} = \dot{\alpha}(t) \ll \alpha^2(t) = \dot{\varphi}^2$.

Now, let us make some assumptions about β and η in order to solve Eq. (14). First, we consider β to be constant in the solution process. Secondly, we make the following suppositions about the magnitude of the following parameters:

$$\frac{\omega_3}{\omega} \sim \varepsilon, \frac{A}{l} \sim \varepsilon, \frac{\mu_3}{\omega} \sim \varepsilon \qquad (22)$$

where $\varepsilon \geq 0$ is a small parameter.

Considering the pendulum, as before, we can assume $H(\beta, \dot{\eta}, \eta, \tau)$ to be small and we can rewrite Eq. (14) as

$$\ddot{\eta} = \varepsilon H_1(\beta, \dot{\eta}, \eta, \tau) \qquad (23)$$

with

$$\varepsilon H_1 = H(\beta, \dot{\eta}, \eta, \tau) \qquad (24)$$

The solution of Eq. (23) satisfying the condition in Eq. (9) at $\varepsilon = 0$ is $\eta = \eta_0 = 0$. A first approximation is defined as a periodic solution $\eta = \eta_1$ of the equation

$$\ddot{\eta} = \frac{\ddot{u}\,\cos(\beta)}{l} = -\omega^2 P\,\frac{\cos(\beta)}{l}\,\sin(\omega t) \tag{25}$$

With the condition in Eq. (9), we can easily obtain

$$\eta = \eta_1 = \frac{u\,\cos(\beta)}{l} = \frac{P\,\cos(\beta)\,\sin(\omega t)}{l} \tag{26}$$

Linearizing Eq. (19) we obtain

$$V_2(\beta) = \ddot{u}\,\sin(\beta)\langle \eta\,\sin(\omega t)\rangle \tag{27}$$

Inserting Eq. (26) into Eq. (27) with $\langle \sin^2(\omega t)\rangle = \langle \cos^2(\omega t)\rangle = \frac{1}{2}$, $\langle \sin(\omega t)\cos(\omega t)\rangle = 0$ we have

$$V_2(\beta) = \frac{m_3\omega^2}{4}P^2\sin(2\beta) = \bar{V}\sin(2\beta) \tag{28}$$

where $\bar{V} = \frac{m_3\omega^2}{4}P^2$.

The main equation of vibrational mechanics, namely the equation of slow motions is given by

$$\ddot{\beta} + \mu_3\dot{\beta} + \omega_3^2\sin(\beta) - V_2(\beta) = 0 \tag{29}$$

According to Eq. (29) the positions of the quasi-equilibrium of the pendulum, that is, the positions of equilibrium for the slow component of motion $\beta = \bar{\beta}$, are derived from

$$\omega_3^2\sin(\bar{\beta}) - V_2(\bar{\beta}) = 0 \tag{30}$$

with the definite equilibrium position satisfying the condition

$$\omega_3^2\cos(\bar{\beta}) - \dot{V}_2(\bar{\beta}) > 0 \tag{31}$$

Indeed, in this case Eq. (29) of slow motions of the pendulum near the stable position of equilibrium can be written as

$$\ddot{\beta} + \mu_3\dot{\beta} + (\omega_3^2 + 2\bar{V})\beta = 0 \tag{32}$$

Inserting the solution of Eq. (32) and the expressions for φ in Eq. (21) and θ in Eq. (8), with η from Eq. (26), into Eq. (5), considering the conditions in Eq. (9), we obtain

$$u = u_0(t, \tau) = A \, \cos(\alpha t + \gamma) + B \, \sin(\alpha t + \gamma) + C \, \cos(\beta + \eta) + D \, \sin(\beta + \eta) \tag{33}$$

or

$$u = u_0(t, \tau) = K \, \cos(\alpha t + \gamma + \xi) + N \, \cos(\beta + \eta + \varsigma) \tag{34}$$

with

$$A = \frac{p_2 \alpha^2 k}{k^2 + \lambda} \tag{35}$$

$$B = \frac{p_2 \mu_1 \alpha^3}{k^2 + \lambda} \tag{36}$$

$$C = \frac{p_5(\ddot{\beta} + \ddot{\eta})}{n}\left(1 + \frac{\mu_1}{n - \mu_1}\right) \tag{37}$$

$$D = \frac{p_2(\ddot{\beta} + \ddot{\eta})}{n - \mu_1} \tag{38}$$

with

$$k = \omega_1^2 - \alpha^2, \lambda = \mu_1^2 \alpha^2, n = \omega_1^2 - 1, K = \sqrt{A^2 + B^2}, N = \sqrt{C^2 + D^2}, \xi = \tan^{-1}\left(\frac{B}{A}\right),$$

$$\xi = \tan^{-1}\left(\frac{B}{A}\right), \varsigma = \tan^{-1}\left(\frac{D}{C}\right) \tag{39}$$

Inserting Eqs. (21) and (33) into Eq. (18) we obtain the approximate equation for the vibrational torque by averaging and finally the main equation of vibrational mechanics is achieved to be

$$\dot{\alpha} = M(\alpha) + V_1(\alpha) \tag{40}$$

Equation (40) has half a degree of freedom whereas the initial system in Eqs. (5)–(7) has two degrees of freedom. Moreover, the addition of $V_1(\alpha)$ to the slow forces exerted on the system is due to the transition from the complete dynamical description to the separation of fast and slow forces of motion.

The frequency of rotation of the rotor in stationary regimes is determined by

$$M(\alpha) = V_1(\alpha) \tag{41}$$

Three steady-state solutions α_1, α_2 and α_3 of Eq. (40) correspond to below-resonance, above-resonance and highly above-resonance regimes, respectively. Near the resonance at $\alpha_1 < \omega_1$, the system is captured (Sommerfeld effect) by $M(\alpha_1)$. $M(\alpha_2)$ corresponding to a jump transition from resonance mode α_1 to α_3 makes α_2 an unstable solution. $M(\alpha_3)$ corresponds to a more powerful motor and thus a nominal steady-state is achieved at α_3. Near $\alpha = \omega_1$, $|V_1(\alpha)|$ has a maximum demonstrating

that its dependency on the frequency of rotation is of a resonant character. Thus, the peculiar behavior of the system is explained based on the vital role of the vibrational torque $V_1(\alpha)$.

4   Conclusions

The present paper analyzed a non-ideally excited pendulum system with a limited power supply by means of the direct method of separation of motions. The complex system of three differential equations has been transformed to obtain the main equations of the slow components of motion to allow for an analysis of the solutions in the stability domain and a justification of the peculiar behavior of the dynamical system. The vibrational torque added to the slow forces is the main difference to the regular approach of other analytical methods.

The transition to the equations of the slow components of motions allows for solving the complex system of differential equations as it breaks the system into more, but at the same time treatable, nonlinear differential equations overcoming the unfeasibility to solve the problem by perturbation methods. This demonstrates the simplicity of application and the transparency of the physical interpretation as crucial advantages of the MDSM displayed effectively in this study.

References

1. Balthazar, J.M., Mook, D.T., Weber, H.I., Brasil, R.M.I.R.F., Fenili, A., Beltano, D., Felix, J.L.P.: An overview on non-ideal vibrations. Meccanica **38**(6), 613–621 (2003). https://doi.org/10.1023/A:1025877308510
2. Balthazar, J.M., Brasil, R.M.I.R.F., Weber, H.I., Fenili, A., Beltano, D., Felix, J.L.P., Garzelli, F.J.: A review of new vibration issues due to non-ideal energy sources. In: Udwadia, F.E., Weber, H.I., Leitmann, G. (eds) Dynamical Systems and Control, Stability and Control: Theory, Methods and Applications, pp. 237–258. Chapman & Hall/CRC, Boca Raton (2004)
3. Cveticanin, L.: Dynamics of the non-ideal mechanical systems: a review. J. Serb. Soc. Comput. Mech. **4**(2), 75–86 (2010)
4. Blekhman, I.I.: Vibrational Mechanics. Nonlinear Dynamic Effects, General Approach, Applications. World Scientific, Singapore (2000)
5. Blekhman, I.I.: Oscillatory strobodynamics—a new area in nonlinear oscillations theory, nonlinear dynamics and cybernetical physics. Cybern. Phys. **1**(1), 5–10 (2012)
6. Blekhman, I.I., Sorokin, V.S.: Extension of the method of direct separation of motions for problems of oscillating action on dynamical systems. Procedia IUTAM **19**, 75–82 (2016). https://doi.org/10.1016/j.piutam.2016.03.011
7. Tusset, A., Bueno, A.M., Martins dos Santos, J.P., Tsuchida, M., Balthazar, J.M.: A non-ideally excited pendulum controlled by SDRE technique. J. Braz. Soc. Mech. Sci. Eng. **38**(8), 2459–2472 (2016). https://doi.org/10.1007/s40430-016-0517-7

8. Sorokin, V.S.: Analysis of motion of inverted pendulum with vibrating suspension axis at low-frequency excitation as an illustration of a new approach for solving equations without explicit small parameter. Int. J. Non-Linear Mech. **63**, 1–9 (2014). https://doi.org/10.1016/j.ijnonlinmec.2014.03.003
9. Shishkina, E.V., Blekhman, I.I., Cartmell, M.P.: Application of the method of direct separation of motions to the paframetric stabilization of an elastic wire. Nonlinear Dyn. **54**(4), 313–331 (2008). https://doi.org/10.1007/s11071-008-9331-9
10. Demidov, I.V., Sorokin, V.S.: Motions of deformable inclusions in a horizontally oscillating vessel with a compressible fluid. J. Sound Vib. **383**, 324–338 (2016). 10.106/j.jsv.2016.07.034
11. Blekhman, I.I., Sorokin, V.S.: On the separation of fast and slow motions in mechanical systems with high-frequency modulation of the dissipation coefficient. J. Sound Vib. **329**, 4936–4949 (2010). https://doi.org/10.1016/j.jsv.2010.06.008
12. Blekhman, I.I., Sorokin, V.S.: Effects produced by oscillations applied to nonlinear dynamic systems: a general approach and examples. Nonlinear Dyn. **83**, 2125–2141 (2016). https://doi.org/10.1007/s11071-015-2470-x

Problem of Dynamics of an Elastic Rod with Decreasing Function of Elastic-Plastic External Resistance

Ivan Shatskyi and Vasyl Perepichka

Abstract The wave problem of propagation of shock perturbation in a semi-infinite elastic rod interacting with the medium is investigated using the model of elastic-plastic resistance with decreasing relation between shear stress and jump of displacement on the lateral surface. An exact solution of the initial-boundary problem is obtained using the Laplace transforms. A wave pattern of perturbation including the prefront zone of rest, the area of motion and the domain of stationary residual stresses has been built. The three-dimensional diagrams for nonstationary fields of displacement, velocity and stresses have been constructed too.

Keywords Elastic rod · Elastic-plastic resistance · Dynamics · Shock wave

1 Introduction

The analysis of energy dissipation due to the inelastic interaction of deformable contacting bodies is of the great importance in the research of applied problems of the structural dynamics. In this proceeding we researched the nonstationary dynamics of an elastic rod with inelastic external resistance having decreasing stress-displacement relation under shock loading, This problem can be used for modelling the dynamics of drilling equipment to eliminate the sticking of the tool, the process of the pulling of rods in building or the dynamical damage of fibers in the composite with inelastic matrix. The cases of purely dry friction have been studied earlier using the analytical [1–3] and numerical methods [4, 5]. The dynamical problems for elastic rods with

I. Shatskyi (✉) · V. Perepichka
Department of Modelling of Damping Systems, Ivano-Frankivsk Branch of Pidstryhach-Institute for Applied Problems of Mechanics and Mathematics, NAS of Ukraine, Mykytynetska Str., 3, 76002 Ivano-Frankivsk, Ukraine
e-mail: ipshatsky@gmail.com

V. Perepichka
e-mail: an_w@i.ua

viscoplastic friction modeled by means of the interaction trough the Bingham layer
are investigated in papers [6–9].

2 Formulation of the Problem

We have been considered the propagation of longitudinal shock wave in immersed
into the elastic-plastic medium semi-infinite elastic rod with constant cross section
induced by sudden loading of the end. The classical theory of rods dynamics has
been used. The shear forces on the lateral surface are modeled by Voigt parallel con-
nection of Saint-Venant's and "negative" Hooke's elements (the model of interaction
through a thin rigid-plastic layer with decreasing relation between shear stress and
displacement) (Fig. 1). We study the process of wave attenuation due to action of
this external rigid-plastic resistance with softening.

The initial-boundary-value problem for the partial differential equation of rod
motion is the following:

$$\frac{u''}{L} + \frac{\tau_x}{E} = \frac{\ddot{u}}{L}, \quad x > 0, \quad t > 0; \tag{1}$$

$$\begin{bmatrix} \dot{u} \neq 0 : & \tau_x = -\tau_c \, \text{sgn} \, \dot{u} + ku; \\ \dot{u} = 0 : & |\tau_x - ku| < \tau_c. \end{bmatrix} \tag{2}$$

$$u(x, 0) = \dot{u}(x, 0) = 0, \quad x > 0; \tag{3}$$

$$\frac{u'(0, t)}{L} = -\frac{\sigma_0}{E} H(t), \quad u(\infty, t) = 0, \quad t > 0, \tag{4}$$

where: u is the axial displacement, τ_x is the shear stress, $x = X/L$, $t = cT/L$ are
dimensionless coordinate and time, $L = F/\Pi$ is the characteristic size, F is the
area and Π is the perimeter of cross-section, $c = \sqrt{E/\rho}$ is the wave velocity, E
is Young's modulus and ρ is density of the rod material, $k = E_l/h_l$—module of
softening, τ_c, E_l and h_l—is the threshold friction, secant module of material and

Fig. 1 The rheological
model
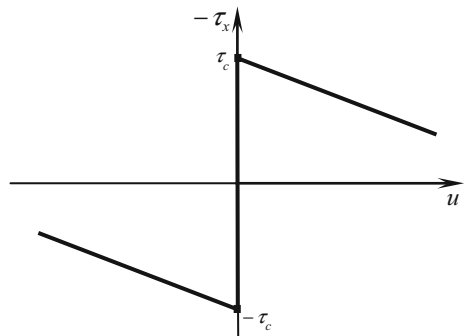
thickness of layer accordingly; σ_0 is the stress at the rod end and $H(t)$ is a Heaviside function.

The primes and the dots denote the partial derivate with respect to the dimensionless coordinate and to the dimensionless time respectively.

3 Analytical Solution

Divining the sign of the velocity, we linearize the nonlinear relations (2) and represent them in motion domain in the form

$$\tau_x = -(\tau_c H(t - x) - ku). \tag{5}$$

The Eq. (1) taking into account the expression (5) converts to tachyon version of linear Klein-Gordon equation with negative stiffness and inhomogeneous right side:

$$\frac{u''}{L} + \lambda^2 \frac{u}{L} = \frac{\ddot{u}}{L} + \frac{\tau_c}{E} H(t - x), \quad x > 0, t > 0, \tag{6}$$

where $\lambda^2 = kL/E = E_l L/(E h_l)$—is a dimensionless parameter of softening.

The analytical solution of problem (6), (3) and (4) is constructed using the Laplace transforms over the time coordinate. The problem of operational calculus equivalent to this problem has the following form

$$\frac{U''}{L} - (s^2 - \lambda^2)\frac{U}{L} = \frac{\tau_c}{E}\frac{e^{-sx}}{s}, \quad x > 0,$$

$$\frac{U'(0)}{L} = -\frac{\sigma_0}{E}\frac{1}{s}, \quad U(\infty) = 0, \tag{7}$$

where $U(x) = \int_0^\infty e^{-st}u(x, t)dt$ and s is the parameter of the Laplace transform.

The solution of the boundary-value problem (7) for the transform is written as

$$\frac{U(x)}{L} = \frac{\sigma_0}{E}\left[\left(\frac{1}{s} - \frac{2}{L_*}\frac{1}{\lambda^2}\right)\frac{e^{-x\sqrt{s^2-\lambda^2}}}{\sqrt{s^2 - \lambda^2}} + \frac{2}{L_*}\frac{1}{\lambda^2}\frac{e^{-sx}}{s}\right], \tag{8}$$

where $L_* = 2\sigma_0/\tau_c$ is the dimensionless length of disturbed part of rod.

In one's turn the solution of the original problem gives the analytical expressions for the axial displacement and its derivations as follow [10]:

$$\frac{u(x,t)}{L} = \frac{\sigma_0}{E}\left[\int_x^t I_0\left(\lambda\sqrt{\tau^2 - x^2}\right)d\tau - \frac{1}{\lambda^2}\frac{2}{L_*}\left\{I_0\left(\lambda\sqrt{t^2 - x^2}\right) - 1\right\}\right]H(t - x),$$

$$\frac{\dot{u}(x,t)}{L} = \frac{\sigma_0}{E}\left[I_0\left(\lambda\sqrt{t^2 - x^2}\right) - \frac{2}{L_*}t\frac{I_1\left(\lambda\sqrt{t^2 - x^2}\right)}{\lambda\sqrt{t^2 - x^2}}\right]H(t - x),$$

$$\frac{u'(x,t)}{L} = -\frac{\sigma_0}{E}\left[1 - \lambda x\int_x^t \frac{I_1\left(\lambda\sqrt{\tau^2 - x^2}\right)}{\sqrt{\tau^2 - x^2}}d\tau - \frac{2}{L_*}x\frac{I_1\left(\lambda\sqrt{t^2 - x^2}\right)}{\lambda\sqrt{t^2 - x^2}}\right]H(t - x), \qquad (9)$$

where $I_0(z)$, $I_1(z)$ are modified cylindrical Bessel functions of the first kind [11].

4 Analysis of the Results

We gave an example of calculations for the parameters values: $\tau_c/\sigma_0 = 1$ and $\lambda^2 = 2/5$. Then $L_* = 2$.

It has been built the wave pattern of nonstationary perturbation in the rod including the prefrontal zone of rest, the area of motion and the domain of stationary residual stresses (Fig. 2).

The three-dimensional diagrams for nonstationary fields of displacement, velocity and stresses in the rod have been constructed in the Figs. 3, 4, 5 and 6 too.

The regions A and B in Fig. 2 are separated by the characteristic $x = t$ which describes the wave front and is a line of strong discontinuity of velocity and axial stress. The curve that separates zones B and C is found numerically from the condition $\dot{u}(x,t) = 0$ and makes the line of weak discontinuity of acceleration, shear stress and axial stress gradient. The solution (9) is valid in area B where the velocity is positive. In domain C the displacement and cessation of the motion is observed at a distance axial the stress do not change with time and have values recorded on line of

Fig. 2 Wave pattern of motion in the rod: A is the prefront zone of rest, B is the area of motion and C is the domain of stationary residual stresses; the dashed lines are the corresponding boundaries for the dry friction [1]
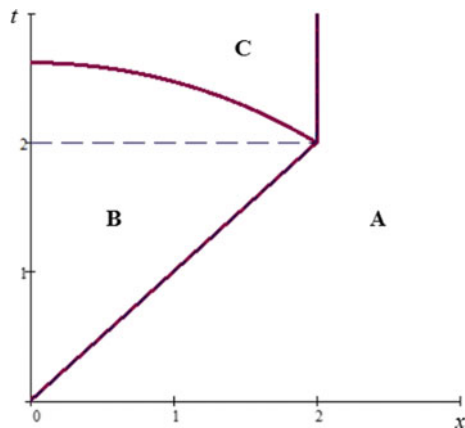
Fig. 3 The field of
displacement in the disturbed
part of rod
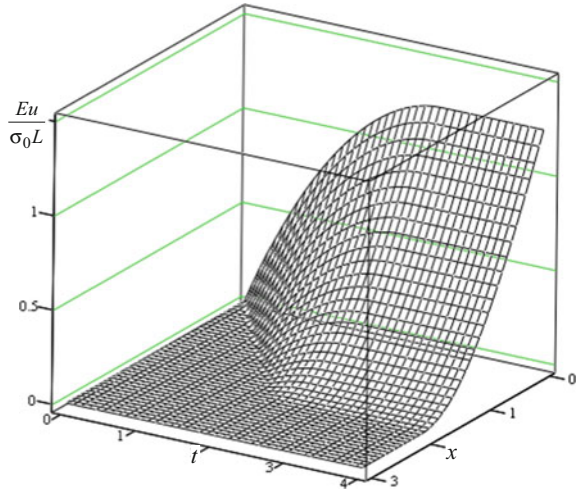
Fig. 4 Distribution of the
velocity in the rod
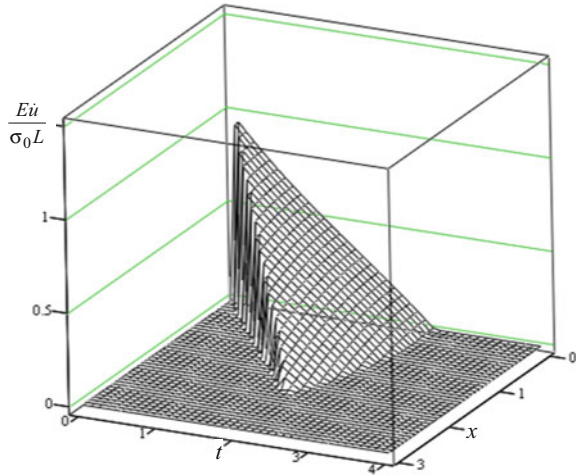
arrest of the motion. The final cessation of the motion is observed at a distance L_*
from the end of the rod.

Intent analysis of results designate the sphere of correctness of solution (9) in
the form of inequality: $\lambda^2 \leq 1/2$. Under such condition the line of cessation of the
motion does not advance the characteristic of reflected wave and the jump of residual
shear stress is smaller than the threshold value. In addition the graph of shear stress
in Fig. 1 does not crossing the abscissa axis.

The asymptotic expansions of results (9) for small values of softening parameter
are obtained as a first approximation:

Fig. 5 Distribution of the
normal stress in the rod
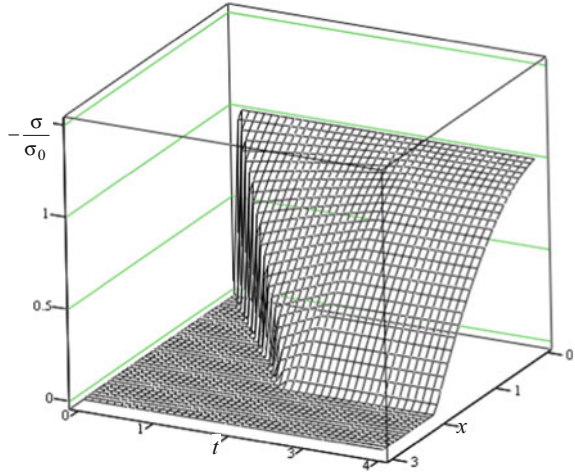
Fig. 6 Distribution of the
shear contact stress in the rod
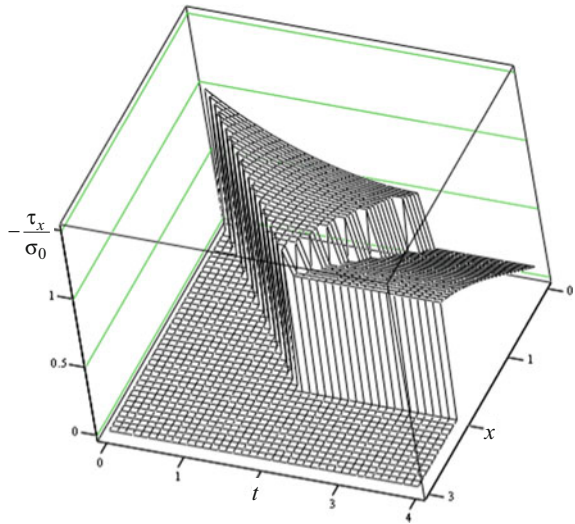
$$\frac{u(x,t)}{L} = \frac{\sigma_0}{E}\left\{(t-x) - \frac{1}{4}\frac{\tau_c}{\sigma_0}(t^2 - x^2)\right.$$

$$\left. + \left[\frac{1}{3}(t^3 - x^3) - x^2(t-x) - \frac{1}{16}\frac{\tau_c}{\sigma_0}(t^2 - x^2)^2\right]\frac{\lambda^2}{4} + O(\lambda^4)\right\}H(t-x),$$

$$\frac{\dot{u}(x,t)}{L} = \frac{\sigma_0}{E}\left\{1 - \frac{1}{2}\frac{\tau_c}{\sigma_0}t + \left(1 - \frac{1}{4}\frac{\tau_c}{\sigma_0}t\right)(t^2 - x^2)\frac{\lambda^2}{4} + O(\lambda^4)\right\}H(t-x),$$

$$\frac{u'(x,t)}{L} = -\frac{\sigma_0}{E}\left\{1 - \frac{1}{2}\frac{\tau_c}{\sigma_0}x - \left[2x(t-x) - \frac{1}{4}\frac{\tau_c}{\sigma_0}x(t^2 - x^2)\right]\frac{\lambda^2}{4}\right.$$

$$\left. + O(\lambda^4)\right\}H(t-x).$$

These expressions are correct in domain of motion which bounded by stop line:

$$t = t_*(x) = \frac{2\sigma_0}{\tau_c}\left[1 + \left(L_*^2 - x^2\right)\frac{\lambda^2}{8} + O\left(\lambda^4\right)\right].$$

Finally, the residual stresses in domain C can be estimated as follow:

$$\sigma^{res}(x) = -\sigma_0\left[1 - \frac{x}{L_*} - x(L_* - x)\left(3 - \frac{x}{L_*}\right)\frac{\lambda^2}{8} + O\left(\lambda^4\right)\right]H(L_* - x),$$

$$\tau_x^{res}(x) = -\frac{\tau_c}{2}\left[1 - \left(3L_*^2 - 8L_*x + 3x^2\right)\frac{\lambda^2}{8} + O\left(\lambda^4\right)\right]H(L_* - x).$$

5 Conclusions

In the presence of elastic-plastic external resistance, the motion of rod cross-sections is similar in nature to the motion in the presence of dry friction ($\lambda = 0$) [1–3], and the negative elasticity effect is less significant. In contrast to the case of rigid-plastic resistance (purely dry friction), where the perturbed part of the rod moves as a perfectly rigid body and the motion stops simultaneously over the entire length from the rod end to the wave front, the presence of the softening component of the resistance is responsible for the motion of the perturbed zone as a deformable region, and the cessation of motion in the area between the wave front and the rod end occurs at a rate exceeding the speed of the perturbation propagation.

References

1. Nikitin, L.V.: Statics and Dynamics of Solids with External Dry Friction. Mosk. Litsei, Moscow (1998)
2. Nikitin, L.V.: Dynamics of elastic rods with external dry friction. Usp. Mekh. **11**(4), 53–106 (1988)
3. Zharkova, N.V., Nikitin, L.V.: Applied problems of plastic rod dynamics. Izv. RAN, Mekh. Tverd. Tela **6**, 80–98 (2006)
4. Aleksandrova, N.I.: Numerical-analytical investigation into impact pipe driving in soil with dry friction. Part 1: nondeformable external medium. J. Min. Sci. **48**(5), 856–869 (2012). https://doi.org/10.1134/s1062739148050103
5. Aleksandrova, N.I.: Numerical-analytical investigation into impact pipe driving in soil with dry friction. Part 2: deformable external medium. J. Min. Sci. **49**(3), 413–425 (2013). https://doi.org/10.1134/s106273914903009x
6. Shatskii, I.P., Perepichka, V.V.: Shock wave propagation in an elastic rod with a viscoplastic external resistance. J. Appl. Mech. Techn. Phys. **54**(6), 1016–1020 (2013). https://doi.org/10.1134/S0021894413060163
7. Shatsky, I.P., Perepichka, V.V.: Non-stationary twisting of an elastic bar with viscoplastic external resistance. Dopov. Nac. akad. nauk Ukraine **10**, 63–69 (2014). https://doi.org/10.15407/dopovidi2014.10.0633

8. Shatskyi, I., Perepichka, V.: Dynamic problem for an elastic rod with decreasing function of viscoplastic friction. In: Proceedings of 22nd International Conference "MECHANIKA 2017" (19 May 2017, Kaunas, Lithuania), pp. 348–350 (2017)
9. Shatskyi, I., Perepichka, V.: Shock wave in a pile immersed into viscoplastic medium. Trans. VŠB—TU Ostrava Civ. Eng. Ser. **17**(2), 115–118 (2017)
10. Bateman, H., Erdélyi, A.: Tables of Integral Transforms, vol. 1. McGraw-Hill, New York (1954)
11. Abramowitz, M., Stigan, I.A. (eds.): Handbook of Mathematical Functions. Dover, New York (1970)

Hysteretic Properties of Shell Dampers

Ivan Shatskyi, Ihor Popadyuk and Andrii Velychkovych

Abstract The achievements of the authors in the analytical modeling of hysteretic energy dissipation in the systems of shells with deformable filler at the expense of dry friction are presented. Four design variants are considered: solid shell with filler, cut shell with filler and the same systems with internal coaxial shell. Based on the one-dimensional models of shells and filler the non-conservative quasi-static problems for the dampers under nonmonotonic loading are formulated and solved. The distribution of the stresses and displacements in contact system has been studied for the processes of active loading, unloading and repeated loading. The loop of structural damping (the force-displacement diagram) is constructed too. The last obtained result describes the effect of maximum energy absorption by a shell damper. Importance of tribology settings of contact system, for which the dissipated energy of the external load reaches the maximum, is revealed.

Keywords Shell-like damper · Filler · Dry friction · Cyclic loading · Hysteresis

1 Introduction

The operation of almost all, without exception, modern machines and mechanisms, is typically connected with vibration processes which lead to undesirable conse-

I. Shatskyi (✉) · I. Popadyuk
Department of Modelling of Damping Systems, Ivano-Frankivsk Branch of Pidstryhach-Institute for Applied Problems in Mechanics and Mathematics, NAS of Ukraine, Mykytynetska Str. 3, Ivano-Frankivsk 76002, Ukraine
e-mail: ipshatsky@gmail.com

I. Popadyuk
e-mail: igorpopadyuk60@gmail.com

A. Velychkovych
Department of Structural Mechanics, Ivano-Frankivsk National Technical University of Oil and Gas, Karpatska Str. 15, Ivano-Frankivsk 76019, Ukraine
e-mail: a_velychkovych@ukr.net

quences. In the vast majority of cases, vibration decreases the strength, reliability and durability of industrial machines, mechanisms and structures, as well as affects health of personnel. Thus, the problem of vibration insulation proves to be quite urgent both in technical and social terms. One of the ways used to solve the formulated problem is connected with the application of vibration protecting devices, such as shock absorbers, dampers, dynamic vibration absorbers, etc. This is why the research and design works and theoretical investigations in the field of development of new means of vibration protection and methods for their numerical analyses are of crucial importance.

The authors have developed advanced design of vibration insulators [1–8], among which the leading place belongs to shell elastic elements with deformable filler. The main feature of these structures is the use of thin-walled elements (shells, plates, and rods) as the main carriers and function elements. By their design these are deformable shell systems with dry friction. A detailed review of publications devoted to the study of dynamic systems with various friction laws is made in the paper [9]. Since the work of the vibration protection system is mainly determined by the stiffness and damping of the elastic element, when formulating the dynamic tasks, it is necessary to have these parameters to include them into the system of the initial equations of motion. To determine the above-mentioned characteristics a quasistatic approach to the analysis of the process of dynamic loading of a shell elastic element was used. It provided for dividing of this process into stages where loading is monotonous. Consequently we get a class of nonlinear non-conservative mixed contact problems of the frictional interaction of thin shells with deformable fillers [7, 8].

Formulations and methods of solving contact problems taking into account dry friction which use continuum models of a continuous medium are known (see, for example, [10–12]). There are two areas of research that correspond to two types of initial assumptions. The first approach represents the contact problem as a mixed problem of the theory of elasticity, and the method of singular integral equations is the main method of research. A fundamental description of this direction is given in the works [10, 11, 13]. The second direction interprets the contact problem as a variational problem with unilateral connections, and the most effective instruments of research are, as a rule, the apparatus of variational inequalities, variational-difference approaches, etc. [14–16]. For engineering studies of the frictional interaction of contacting bodies, approaches that use models and methods of the theory of rods, shells and plates are more suitable.

The aim of the report is to acquaint the scientific audience with the results obtained due to the analytical modeling of hysteretic energy dissipation in the shells with filler at the expense of dry friction. Thus, the latest achievement, i.e. the effect of maximum energy absorption by shell damper, is described.

Fig. 1 Scheme of a shell damper
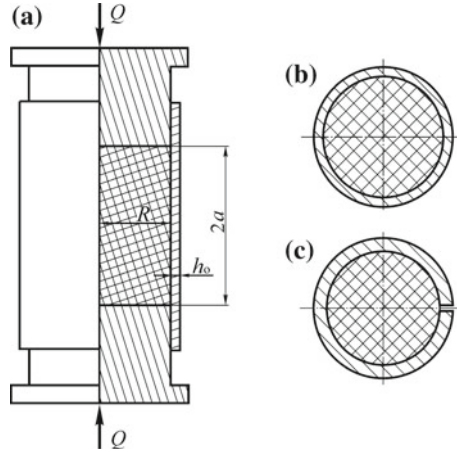
2 Formulation of the Problem

Consider an elastic deformable cylinder (filler) of radius R and length $2a$ placed into a cylindrical shell with thickness h_0 (Fig. 1a).

The filler is compressed on the end faces by perfectly rigid pistons subjected to the action of an external load Q non-monotonic as a function of time. Dry position friction occurs on contact surface of the shell with filler. We need to study the phenomenon of structural damping in the given non-conservative system.

The shell, depending on the conditions of use of the structure, can be of closed (solid—Fig. 1b) or open (cut along a generating line—Fig. 1c) profiles. In the first case (Fig. 1b), the shell works on the tangential stress, and in the second case (Fig. 1c)—on the bending.

Analogical variants of constructions of dampers with internal technological shell are also considered (Fig. 2).

3 Analysis of the Results

Using applied shell and filler models the analytic algorithm of solving nonlinear mixed problem on frictional interaction of elastic filler with a shell at non-monotonic quasi-static loading has been developed. The solution of the problem at the stages of active loading, unloading and repeated loading has been proposed, characteristics of stress-strain state, stiffness and damping ability of the system have been obtained.

An approximate analytical description of the structural hysteresis loop obtained for shells with shear-unresisting slight-compressible filler is provided in the works. Thus, we describe the dependences without displacements of the piston and load-

Fig. 2 Shell damper equipped with an internal shell
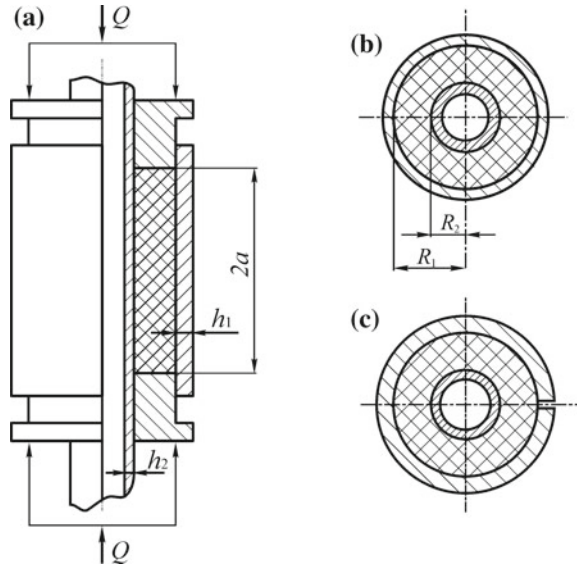
ing with arbitrary asymmetry cycle coefficient $s = Q_{min}/Q_{max} \in [0, 1]$ by the following relations.

For active loading

$$\delta^I = \frac{Q}{c}\left(b + (1-b)\frac{1-e^{-\lambda}}{\lambda}\right), \ 0 \le Q \le Q_{max};$$

for unloading

$$\delta^{II} = \begin{cases} \delta^I_{max} - \frac{1}{c}\left[b(Q_{max} - Q) + (1-b)\frac{(\sqrt{Q_{max}}-\sqrt{Q})^2}{\lambda}\right], & Q_{max} \ge Q \ge s_* Q_{max}; \\ \frac{Q}{c}\left(b - (1-b)\frac{e^{\lambda}-1}{\lambda}\right), & s_* Q_{max} \ge Q \ge 0; \end{cases}$$

for repeated loading

$$\delta^{III} = \begin{cases} \delta^{II}_{min} + \frac{1}{c}\left[b(Q - Q_{min}) + (1-b)\frac{(\sqrt{Q} - \sqrt{Q_{min}})^2}{\lambda}\right], \\[2mm] \qquad Q_{min} \le Q \le \min\left\{\dfrac{Q_{min}}{s_*}, \ Q_{max}\right\}; \\[4mm] \delta^I, \ \ \min\left\{\dfrac{Q_{min}}{s_*}, \ Q_{max}\right\} \le Q \le Q_{max}. \end{cases}$$

Here, $s_* = e^{-2\lambda}$; λ is the index of exponential decay, c is the linear stiffness of the conservative system, and b is the factor of transversal interaction. These values depend on type, size and physical and mechanical characteristics of the shells and filler.

The parameters λ, c and b for one-shell dampers (Fig. 1) are the following: for a solid shell (Fig. 1a, b)

$$\lambda = 2f\frac{a}{R}, \quad c = \frac{\pi R^2 E}{a}\frac{1}{3(1-2v)+2\varepsilon}, \quad b = \frac{v_0\varepsilon}{3(1-2v)+2\varepsilon},$$

and for shell cut along a generating line (Fig. 1a, c)

$$\lambda = 2f\frac{a}{R}\frac{1}{1+36\frac{R^2}{h_0^2}\varepsilon}, \quad c = \frac{\pi R^2 E}{a}\frac{1+36\frac{R^2}{h_0^2}\varepsilon}{36\frac{R^2}{h_0^2}\varepsilon}, \quad b = 0.$$

Here, f is the coefficient of dry friction in the shell–filler pair; $\varepsilon = ER/(E_0 h_0)$; E, v, E_0, v_0 are Young's modulus and Poisson's ratio of the materials of the filler and shell respectively.

In cases of two-shell dampers (Fig. 2) we have those relations: for solid external shell (Fig. 2a, b)

$$\lambda = \frac{2a(f_1 R_1 + f_2 R_2)}{R_1^2 - R_2^2}, \quad c = \frac{\pi\left(R_1^2 - R_2^2\right)E}{a}\frac{1}{3(1-2v)+2\frac{R_1^2\varepsilon_1+R_2^2\varepsilon_2}{R_1^2-R_2^2}},$$

$$b = \frac{f_1 v_1 R_1 \varepsilon_1 - f_2 v_2 R_2 \varepsilon_2}{f_1 R_1 + f_2 R_2}\frac{1}{3(1-2v)+2\frac{R_1^2\varepsilon_1+R_2^2\varepsilon_2}{R_1^2-R_2^2}}$$

and for cut external shell (Fig. 2a, c)

$$\lambda = 2a\frac{f_1 R_1 + f_2 R_2\left(1 - 12\frac{R_1^2}{h_1^2}\varepsilon_1\right)}{R_1^2\left(1 + 36\frac{R_1^2}{h_1^2}\varepsilon_1\right) - R_2^2\left(1 - 12\frac{R_1^2}{h_1^2}\varepsilon_1\right)},$$

$$c = \frac{\pi\left(R_1^2 - R_2^2\right)E}{a}\frac{R_1^2\left(1 + 36\frac{R_1^2}{h_1^2}\varepsilon_1\right) - R_2^2\left(1 - 12\frac{R_1^2}{h_1^2}\varepsilon_1\right)}{R_1^2 36\frac{R_1^2}{h_1^2}\varepsilon_1}, \quad b = 0.$$

Here, f_i are the coefficients of friction on the contact faces $r = R_i$; $\varepsilon_i = ER_i/(E_i h_i)$; E, v, E_i, v_i are Young's modulus and Poisson's ratio of the materials of the filler and shells respectively; $i = 1, 2$.

System "shell–deformable filler" with parameters $h_0/R = 0.1$, $E/E_0 = 0.001$, $v = 0.499$, $v_0 = 0.3$, $a/R = 2$ was chosen as an example. A diagram of cyclic deformation of damper is provided in Fig. 3.

The value of dissipated energy was defined as the area of the hysteresis loop

Fig. 3 The loop of
constructive hysteresis:
active loading (line *OA*),
unloading (line *AO*),
repeated loading (lines *BA*
and *DEA*)
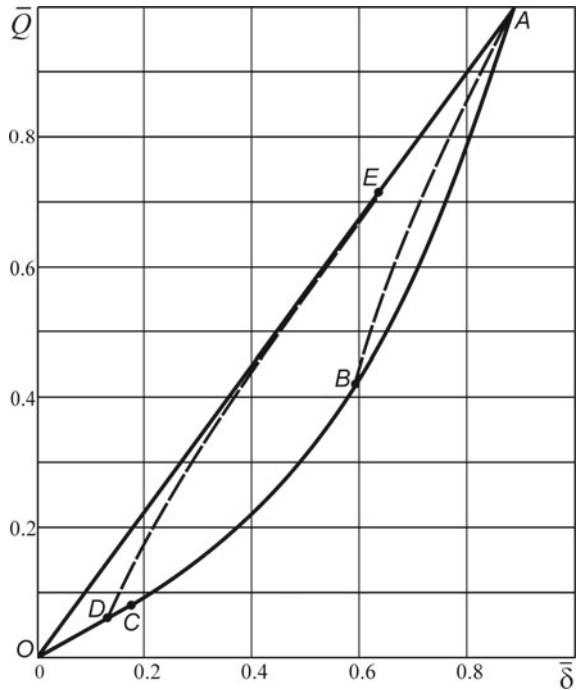
$$\psi = \begin{cases} \frac{Q^2_{\max}(1-b)}{3c\lambda}(1-s)(1-\sqrt{s})^2, \ s_* \le s \le 1; \\ \frac{Q^2_{\max}(1-b)}{6c\lambda}\left[(2+e^{-\lambda})(1-e^{-\lambda})^2 - s^2(e^{\lambda}-1)^2(2+e^{\lambda})\right], \ 0 \le s \le s_*. \end{cases}$$

Figure 4 features a typical dependence of the normalized value of the dissipated energy $\tilde{\psi} = \psi/A$ on the coefficients of dry friction f and asymmetry of the load cycle s. Energy of the elastic deformation of a conservative system was taken as a normalizing factor $A = Q^2_{\max}/(2c)$.

For each value of stress ratio there is a value $\lambda_*(s)$, at which function $\psi(\lambda, s)$ reaches the extreme $\max_{\lambda} \psi(\lambda, s) = \psi(\lambda_*(s), s) = \psi^*(s)$.

Figure 5 features results of such analysis. The global maximum is attained for pulsating cycle at $f \approx 0.253$. Then $\lambda_*(0) = 4f = 1.012$, and $\max_{\lambda,s} \tilde{\psi}(\lambda, s) = \tilde{\psi}(1.012, 0) \approx 0.304$.

Existence of the extreme value is explained by the fact that in systems with dry positional friction distribution of the friction forces depends on the deformations of the contact pair (the filler and shell), and deformations, in turn, depend on the friction forces. Such a close relationship identifies specific, often intuitively unpredictable behaviors of such structures. In this situation, the increase in the coefficient of dry friction f leads to a reduction in the area of mutual slippage of the shell and filler,
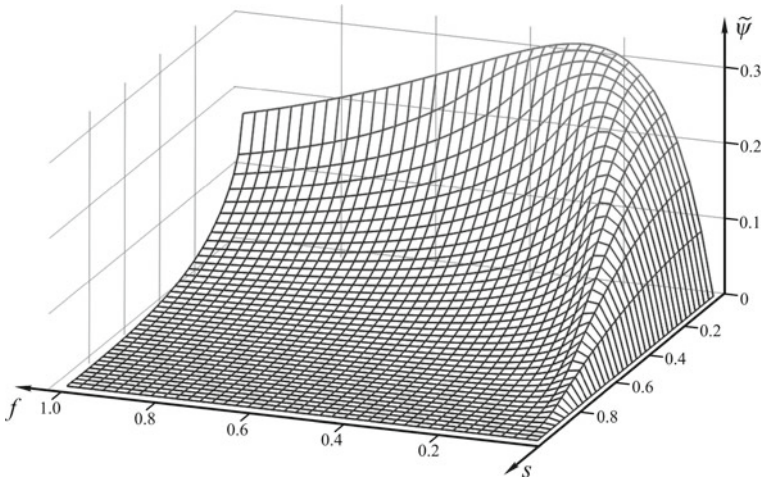
Fig. 4 The value of dissipated energy

Fig. 5 Stationary value λ and the highest values of dissipation, which are achieved for them
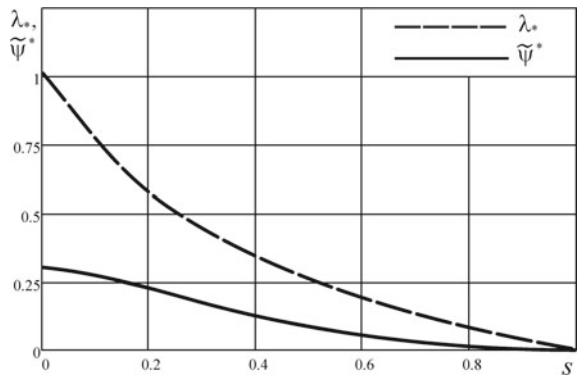
and, consequently, reduction of structural energy dissipation, which occurs only in this area.

4 Conclusions

The article presents the analytical results of the modeling of structural hysteresis at frictional interaction of the systems of solid and cut shells with deformable filler. The hysteresis properties of such systems under dynamic loading are studied in detail. It has been first established that for a fixed ratio of cycle asymmetry with increasing coefficient of friction between the shell and filler, the amount of energy dissipated per cycle grows, reaches an extremum, and then gradually decreases. The maximum

capabilities of the shell damper as for the energy absorption have been determined, and the optimal coefficients of friction have been calculated. Therefore, the idea of optimization of shell vibration protecting devices according to the criterion of maximum energy absorption of external influences by providing the desired tribologic properties of the contacting pairs is declared.

References

1. Shopa, V.M., Shatskii, I.P., Popadyuk, I.I.: Elementary calculation of structural damping in shell springs. Sov. Eng. Res. **9**(3), 42–44 (1989)
2. Velichkovich, S.V., Popadyuk, I.I., Shatskii, I.P., Shopa, V.M.: Structural hysteresis in a shell-type vibration damper with distributed friction. Strength Mater **23**(3), 279–281 (1991). https://doi.org/10.1007/bf01194768
3. Bedzir, A.A., Shatskii, I.P., Shopa, V.M.: Nonideal contact in a composite shell structure with a deformable filler. Int. Appl. Mech. **31**(5), 351–354 (1995). https://doi.org/10.1007/BF00846842
4. Velichkovich, A.S.: Shock absorber for oil-well sucker-rod pumping unit. Chem. Petrol. Eng. **41**(9–10), 544–546 (2005). https://doi.org/10.1007/s10556-006-0015-3
5. Velichkovich, A.S., Popadyuk, I.I., Shopa, V.M.: Experimental study of shell flexible component for drilling vibration damping devices. Chem. Petrol. Eng. **46**(9–10), 518–524 (2011). https://doi.org/10.1007/s10556-011-9370-9
6. Velichkovich, A.S., Dalyak, T.M.: Assessment of stressed state and performance characteristics of jacketed spring with a cut for drill shock absorber. Chem. Petrol. Eng. **51**(3), 188–193 (2015). https://doi.org/10.1007/s10556-015-0022-3
7. Shopa, V.M., Shatskyi, I.P., Bedzir, O.O., Velychkovych, A.S.: Contact Interaction of Cut Shells with Deformable Bodies. IFNTUOG, Ivano-Frankivsk (2015)
8. Popadyuk, I.Y., Shats'kyi, I.P., Shopa, V.M., Velychkovych, A.S.: Frictional interaction of a cylindrical shell with deformable filler under nonmonotonic loading. J. Math. Sci. **215**(2), 243–253 (2016). https://doi.org/10.1007/s10958-016-2834-x
9. Awrejcewicz, J., Olejnik, P.: Analysis of dynamic systems with various friction laws. Appl. Mech. Rev. **58**(6), 389–411 (2005). https://doi.org/10.1115/1.2048687
10. Galin, L.A.: Contact Problems of Theory of Elasticity and Viscoelasticity. Science, Moscow (1980)
11. Johnson, K.L.: Contact Mechanics. University Press, Cambridge (1985)
12. Zmitrowicz, A.: Contact stresses: a review of models and methods of computations. Arch. Appl. Mech. **80**(12), 1407–1428 (2010)
13. Goryacheva, I.G., Martynyak, R.M.: Contact problems for textured surfaces involving frictional effects. Arch. Appl. Mech. **228**(7), 707–716 (2014). https://doi.org/10.1177/1350650114528318
14. Gol'dshteyn, R.V., Zazovskiy, A.F., Spektor, A.A., Fedorenko, R.P.: Decision of spatial contact problems of wobbling a variation method with slipping and tripping. Successes Mech. **5**(3), 6–102 (1982)
15. Telega, Y.: The variation methods in the contact problems of mechanics. Successes Mech. **10**(2), 3–95 (1987)
16. Kravchuk, A.S., Neittaanmäki, P.J.: Variational and Quasi-Variational Inequalities in Mechanics. Springer, Berlin (2007)

Modal Analysis of the Vehicle Model

Martin Svoboda, Václav Schmid, Josef Soukup and Milan Sapieta

Abstract The article deals with the numerical solution of modal analysis of a simple model. It is a system of rigid bodies resiliently mounted and bound. The solution was done in the Ansys simulation program. The article describes how to build the program. Further, some of the results of the actual frequencies and shapes of the symmetrically loaded system are shown. The results served to refine the mathematical model that solves the vertical oscillation of the symmetrically or asymmetrically loaded model with different kinematic excitation. The numerical solution of vehicle model vibration was done in MSC Adams. The results of the vertical vibration measurement of the vehicle model are also given in the article. After adjusting the boundary conditions of the numerical solution, good agreement between experimental and numerical solution (more than 90%) was achieved.

Keywords Vehicle · Experiment · Modal analysis · Vibration

M. Svoboda (✉) · V. Schmid · J. Soukup
Department of Machines and Mechanics, Faculty of Production Technology and Management,
Jan Evangelista Purkyně University in Ústí nad Labem, Na Okraji 1001, 400 01 Ústí nad Labem,
Czech Republic
e-mail: svoboda@fvtm.ujep.cz

V. Schmid
e-mail: schmid@fvtm.ujep.cz

J. Soukup
e-mail: soukup@fvtm.ujep.cz

M. Sapieta
Department of Applied Mechanics, Faculty of Mechanical Engineering, University of Žilina,
Univerzitná 8215/1, 010 26 Žilina, Slovakia
e-mail: milan.sapieta@fstroj.uniza.sk

1 Introduction

Modal analysis is most often performed to determine modal parameters (own frequencies, own shapes or modal damping) without reference to the theoretical model. Finding modal parameters to compare experimentally obtained data with corresponding data obtained using FEM or other theoretical methods. The aim here is to verify the theoretical model, which serves to predict the dynamic behaviour of the model system—the vertical vibration of the vehicle model.

Oscillation is a phenomenon that can be used in many technical applications. However, it can also be an uncomfortable compilation, which can lead to equipment malfunctions as well as environmental degradation. In order to exploit the favorable effects of oscillation and to suppress it adversely, we have to understand the problem of oscillation. It is not easy to master oscillation. Explanation of a number of intuitively unexpected behaviours of oscillating systems often requires relatively demanding mathematical calculations. Some of these are analytically manageable; others require a numerical approach [1, 2].

Solution of oscillation of a spatially resilient housing with consideration of varied influences can be applied in various areas of technical work, e.g. in the elastic storage of machines and machinery [3–5], in the suppression of the influence of unacceptable vibrations and impacts, the transport of special consignments, the oscillation of production machines, Foundations (forming and machine tools, production lines, etc.), in the investigation of oscillation of sprung parts of rail and road vehicles, oscillation of chassis, etc. [3, 6].

The mechanical system consists of elements interconnected. Elements can be carriers of kinetic energy (mass) or potential (springs). These elements have the ability to change mechanical energy in heat (shock absorbers, energy dissipaters). If each element of the system has only one of these functions, we speak of a system of simple (discrete) elements. Otherwise the system may be composed of elements, each of which has simultaneously two or three functions (acts as a mass, a spring and damper). It can be said that real bodies always have all the properties and that simple elements are mere models having the property that is most manifest in the real body [7].

When analyzing the effect of the asymmetry on the vertical oscillation of the body array, it is necessary to distinguish three basic cases of asymmetry with respect to the geometric symmetry axes. These axes are determined by two mutually perpendicular axes of symmetry of the gauge and the wheelbase of the vehicle and intersecting in the geometric centre of the mechanical system

– unbalance of mass distribution with respect to geometric symmetry axes, centre of gravity position, directions of main centre axes of inertia
– the asymmetry of the geometry of the distribution of the elastic and dissipative elements of the joints of the individual bodies of the system and their mechanical properties, the stiffness of the springs, the intensity of the viscous damping, provided the linear bonds of the individual variables and the small displacements and the turning of the parts of the system

– asymmetry of kinematic excitation, for example in road or rail vehicles, the unevenness field of the road surface, Tracks defining kinematic excitation of the system at the wheel-road contact point.

These kinds of asymmetries may exist separately or together. For real objects (such as road or rail vehicles, storage of machines, etc.), the third case occurs most often.

Nowadays simulation programs make it easier for us to work and it is advisable to use them to predict the behavior of mechanical systems or structures when they are loaded. Once the numerical model has been assembled, the results obtained must be verified (e.g. with experiment, modal analysis, etc.) and in the case of nonconformity the numerical model can modify or change the boundary conditions. Almost all commercially-used FEM programs allow fast and reliable analysis of their own frequencies and their own shapes and harmonic and transient analysis with symmetric matrices.

2 Simplified Body Model

The model system (Fig. 1) consists of a steel plate, which is resiliently mounted on four screw springs. To achieve geometric asymmetry, two steel weights were placed on the base plate. These weights were placed in different combinations on the base plate. The investigations are carried out in the case of a symmetrical arrangement (using weights) and for five cases of asymmetrical arrangement (see Table 1). In an unbalanced arrangement of the weight, the centre of gravity of the system is shifted to the point (displacement e_x, e_y), where T is the centre of gravity of the system, C—the geometric centre of the plate. In the case of a symmetrical arrangement ($C = T$).

3 Modal Analysis of Mechanical System in ANSYS Program

Modal analysis was solved using ANSYS. Almost all commercial FEM programs allow fast and reliable analysis of their own frequencies and their own shapes and harmonic and transient analysis with symmetric matrices. In solving modal analysis for multiple types of plate layout, a macro (text file) was created by which the used and modified commands were applied to all types of tasks, changing the positions of individual bodies. The solution process consists of the following steps:

(1) General program settings

– Exiting all previous tasks using FINI commands and deleting all data from the database/CLE so that values are written to an empty value field
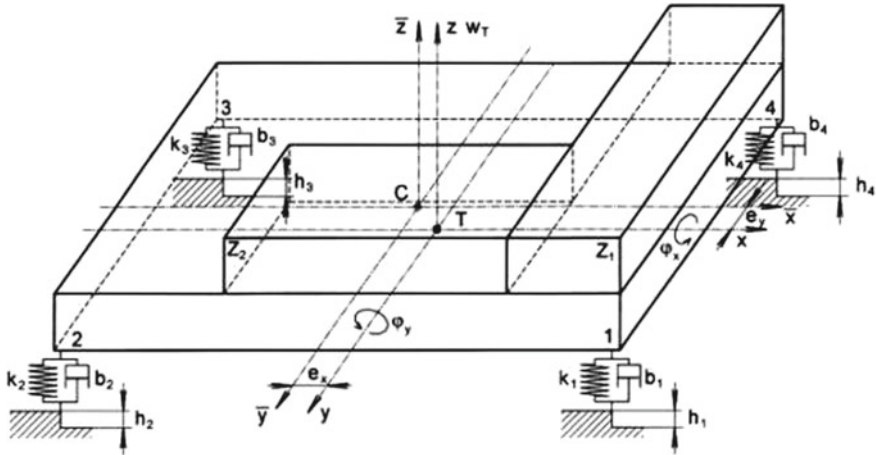
Fig. 1 Scheme of system—asymmetrical arrangement of extra weights

- Entering a file name, command/FILENAME, NAME, 1 and creating output file/OUTPUT, NAME, LOG
- Inputting the analysis type (modal) - ANTYPE, MODAL and setting the modal analysis specification by MODOPT, LANB, 12. This command sets Block Blocking Lanczos' modal analysis and the number of system frequencies we find. You can also set the frequency range to search for frequency, etc. Using the command MXPAND, 12, you set the number of custom shapes that the program renders.
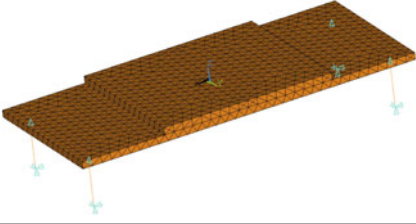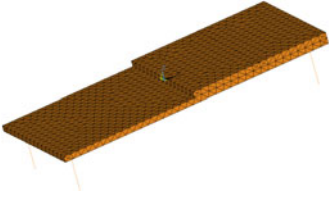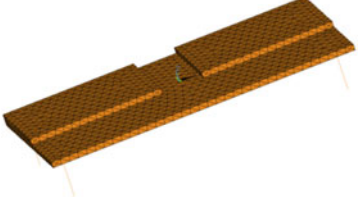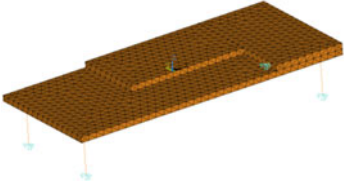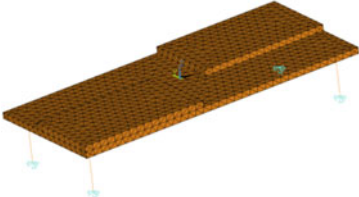
(2) Creating a geometric model

- For simplicity, the input dimensions, density and density constants were initially specified to be easily identified
- Geometry was entered through points K, POINT NUMBERS, X, Y, Z, A, NUMBER OF POINTS and volumes by command VA, NUMBER OF AREAS
- Springs were entered as rod members with a measured stiffness value.

(3) Definition of material properties

- Entry of modulus of elasticity—MP, EX, NUMBER MAT. GROUP, VALUE with a value of 2.1×10^{11} Pa
- Poisson number entry—MP, PRXY, MATERIAL GROUP NUMBER, VALUE (value was entered 0.3)
- Density input—MP, PRXY, MATERIAL GROUP NUMBER, VALUE that has been re-calculated according to the dimensions and weight of the individual plates of the experimental model.

Table 1 Variants of loading model system—ANSYS program

Variant I

Variant II	Variant III

Variant IV	Variant V

(4) Definition of boundary conditions

– The boundary conditions were applied to the spring end attachment using the DK command, POINT NUMBER, REDUCED DEGREE OF CHARACTER, VALUE. All degrees of freedom have been removed, i.e., shift ux, uy, uz and rotation φx, φy, φz at all four points.

(5) Setting network parameters, network generation

– Defining element types. For the boards, the element type SOLID92 was chosen, which is a three dimensional 10-node quadrangle, and the element CONBIN14 as a 3D element (ET, NUMBER ET, ELEMENT TYPE)
– Division of geometric entities - determination of network density. Element size was entered 0.02 m by ESIZE command, 0.020 for volumes. For the springs, the number of ESIZE elements was specified, 1
– Network generation was performed first for volumes (VMESH, 1), and then elements corresponding to the springs (LMESH, NUMBER OF LOT) were

generated. Then, the stiffness of the springs (REAL, NUMBER OF CON-FORMITY SUCCESS) was entered.

(6) Start solving a task

  – The solution was run by the SOLVE command.

(7) Analysis of results

  – The results were evaluated in postprocessing, where the respective own frequencies and shapes were obtained. For each variant of the geometric arrangement of the weights, models of the modal analysis system in ANSYS were compiled—see Table 1.

The results of modal analysis were custom shapes. They contained solid forms of their own, deformed own shapes in a given frequency spectrum, and high own shapes that may contain residual effects [2].

Custom frequencies are positive, but your own frequencies may be zero (or near zero). The zero own frequencies correspond to the self-styled shapes.

The results of the values of the frequencies of the given storage system are shown in Table 2. The first six shapes always match the solid shapes (highlighted in yellow in the table). Other shapes are already own shapes.

The following figures show some instances of custom shapes in a symmetrically arranged system. These shapes can be rendered from ANSYS even for other storage options (Figs. 2, 3, 4, 5).

Table 2 Cases distribution of load on the vehicle and the location of wedges

Variant I		Variant II		Variant III		Variant IV		Variant V	
Set	Time/Freq.	Set	Time/Freq.	Set	Time/Freq.	Set	Time/Freq.	Set	Time/Freq.
1	0.0000	1	0.0000	1	0.0000	1	0.0000	1	0.0000
2	0.0000	2	0.0000	2	0.0000	2	0.0000	2	0.0000
3	0.00014	3	0.000288	3	0.0000	3	0.0000	3	0.000738
4	0.20725	4	0.20167	4	0.19973	4	0.20123	4	0.20741
5	0.26201	5	0.26238	5	0.28770	5	0.26999	5	0.25459
6	0.37564	6	0.34989	6	0.31746	6	0.34360	6	0.34457
7	281.49	7	176.45	7	179.87	7	230.41	7	176.89
8	416.65	8	274.03	8	312.26	8	320.71	8	300.02
9	554.38	9	577.15	9	680.97	9	545.93	9	658.24
10	614.42	10	692.67	10	727.09	10	630.06	10	767.90
11	1001.5	11	936.91	11	1067.0	11	975.73	11	1056.7
12	1001.9	12	1044.4	12	1077.6	12	1131.5	12	1090.2
13	1190.2	13	1049.3	13	1222.2	13	1158.9		
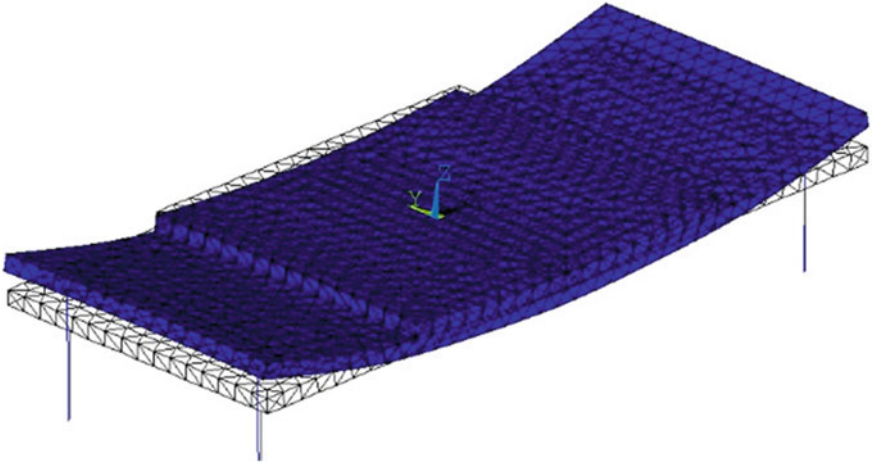
Fig. 2 The first natural modes—long symmetric bending
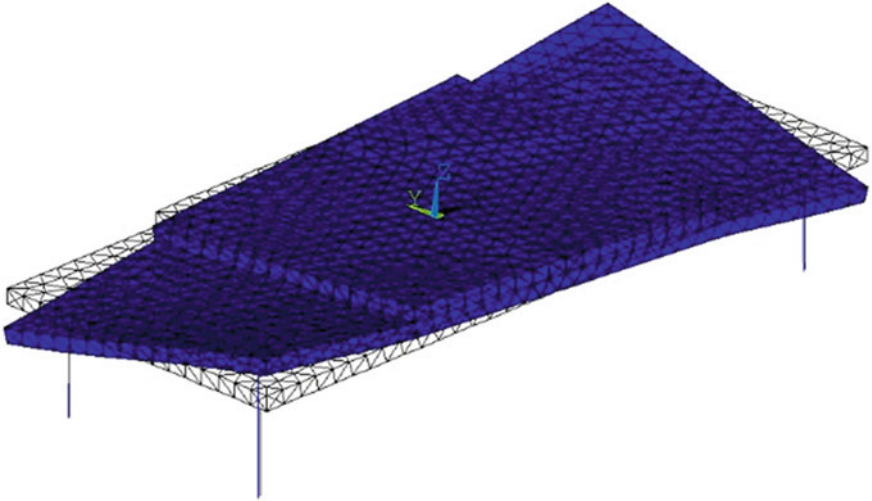
Fig. 3 The second natural modes—torsional

4 Verification of the Numerical Model

The kinematic excitation of the model system was performed by a single jump (Heaviside function) $h = 5$ mm. For our investigation, six variations of jumps (see Table 2), one case of symmetrical excitation (all springs jump at once) and five cases of unsymmetrical excitation were created. For unbalanced excitation (variants A to E), one, two or three springs jump in different combinations. The numbering of the jump
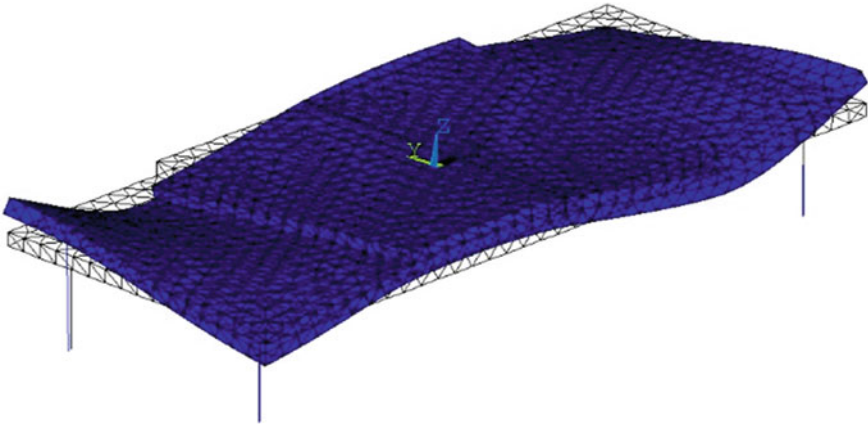
Fig. 4 The fifth natural modes—combinational of to bending and torsion
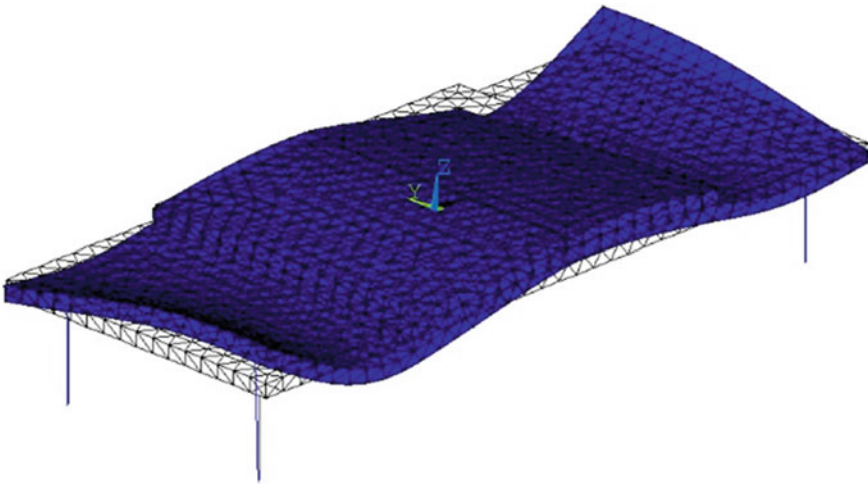
Fig. 5 The sixth natural modes—bending

springs in the Table 3 is used according to the markings that can be observed in Fig. 6.

The oscillation plate or vertical displacements were measured by inductive proximity sensor type Hottinger VA-50-T with the tip with a range of 0–50 mm. On the board, 3 sensors were installed at the mounting points of the springs to the plate. The signal is transmitted to the bridge amplifier.

Amplifiers were stored in DeweRack and the signal was sent to the computer where it was evaluated in LabVIEW.

Table 3 Options of excitation

Variant of generation	Designation of jump springs
A	3
B	2, 4
C	3, 4
D	2, 3
E	2, 3, 4
F	1, 2, 3, 4
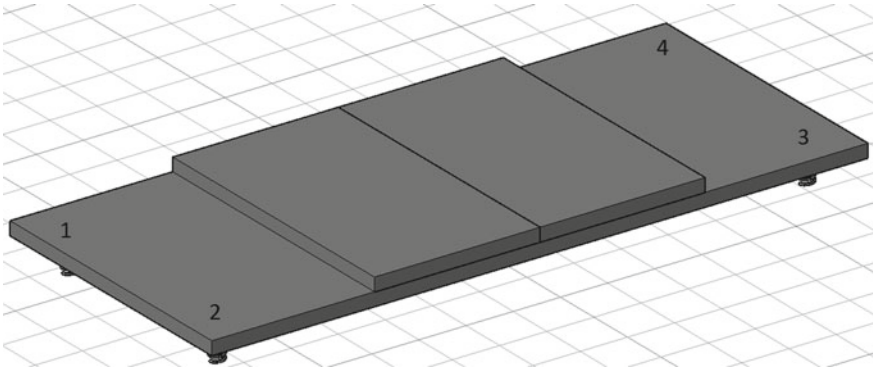
Fig. 6 Marking the springs
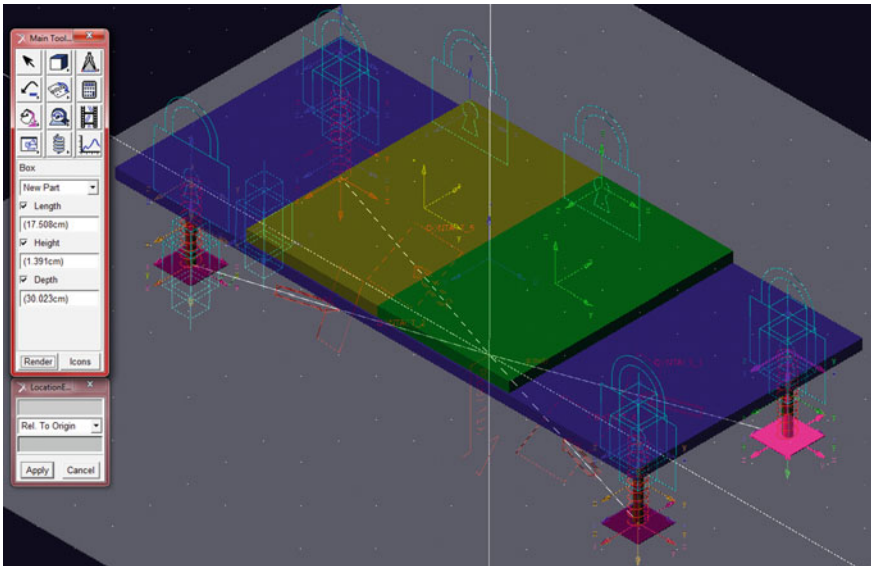
Fig. 7 Model of mechanical system in ADAMS program

The ADAMS simulation program was used to solve the vertical oscillation of the mechanical system. The boundary conditions were verified based on the results of the modal analysis. A vehicle model for a numerical solution is shown in Fig. 7.

The numerical model was verified based on experimental results and with the help of a modal analysis performed in ANSYS program.
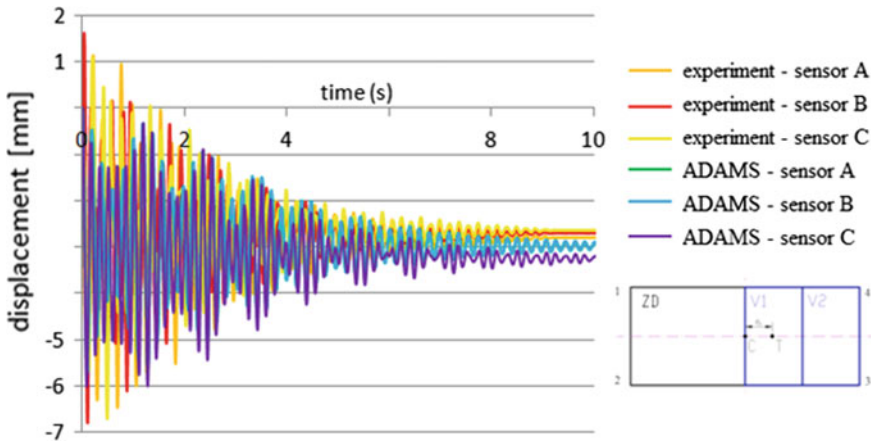
Fig. 8 Comparison of experiments and simulations—Variant II, spring jump 2, 4
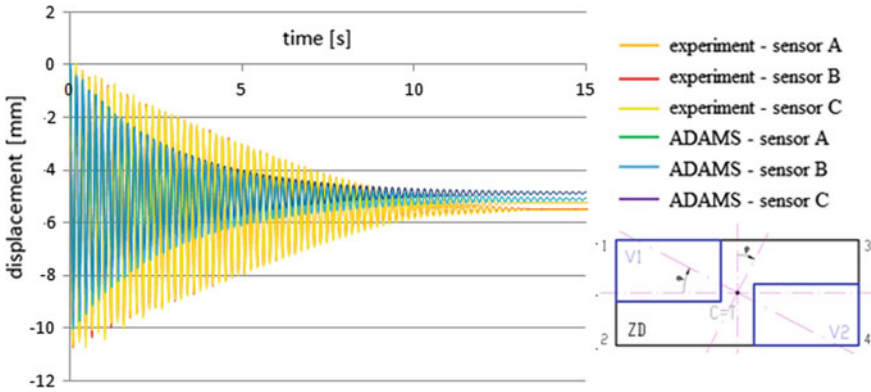
Fig. 9 Comparison of experiments and simulations—Variant V, spring jump 1, 2, 3, 4

5 Results of Numerical and Experimental Solution

The results of the experimental and numerical solution are shown in one graph (Fig. 8), which corresponds to the same asymmetry and the same kinematic excitation. Measured values can be seen in Table 4 (Fig. 9).

Table 4 Comparison of measured values—Variant I, excitation 1, 2, 3, 4

Time (s)	Deflection—experiment (mm)			Deflection–ADAMS (mm)			Deviation (%)		
	Sensor A	Sensor B	Sensor C	Sensor A	Sensor B	Sensor C	Sensor A	Sensor B	Sensor C
0.1	−10.0616	−9.95541	−10.7018	−9.718	−9.718	−9.718	3.417	2.387	9.195
0.2	−0.73339	−0.77808	−0.83246	−0.737	−0.737	−0.737	0.468	5.303	11.489
0.3	−9.0429	−9.37508	−8.98949	−8.631	−8.631	−8.631	4.553	7.935	3.986
0.4	−2.11115	−2.39702	−1.57624	−2.115	−2.115	−2.115	0.160	11.785	34.150
0.5	−7.72173	−7.71211	−8.20076	−7.046	−7.046	−7.046	8.748	8.634	14.078
0.6	−3.29182	−3.43563	−3.70745	−3.782	−3.782	−3.782	14.904	10.094	2.022
0.7	−5.94391	−5.99111	−6.21872	−5.375	−5.375	−5.375	9.566	10.278	13.562
0. 8	−5.62972	−5.74897	−5.19092	−5.404	−5.404	−5.404	4.012	6.003	4.102
0.9	−4.44125	−4.43621	−4.37971	−3.877	−3.877	−3.877	12.708	12.608	11.481
1	−6.83575	−6.74155	−7.1934	−6.721	−6.721	−6.721	1.683	0.309	6.571
1.5	−1.64279	−1.47048	−1.85209	−2.248	−2.248	−2.248	36.863	52.900	21.396
2	−7.13823	−7.11376	−7.47742	−6.015	−6.015	−6.015	15.732	15.442	19.554
2.5	−6.45325	−6.41336	−6.656	−6.067	−6.067	−6.067	5.989	5.404	8.852
3	−2.82345	−2.69319	−2.91667	−3.457	−3.457	−3.457	22.437	28.359	18.524
3.5	−6.46692	−6.37333	−6.69278	−5.497	−5.497	−5.497	14.993	13.744	17.861
4	−6.22883	−6.20924	−6.38423	−5.648	−5.648	−5.648	9.319	9.033	11.527
4.5	−3.81287	−3.74581	−3.87705	−4.135	−4.135	−4.135	8.442	10.384	6.647
5	−5.75266	−5.67293	−5.89792	−5.237	−5.237	−5.237	8.967	7.687	11.209
5.5	−6.02783	−6.00112	−6.11655	−5.388	−5.388	−5.388	10.616	10.218	11.912
6	−4.74764	−4.67235	−4.80064	−4.527	−4.527	−4.527	4.642	3.105	5.694
6.5	−5.23942	−5.17864	−5.32782	−5.107	−5.107	−5.107	2.532	1.388	4.149
7	−5.73315	−5.69894	−5.77531	−5.229	−5.229	−5.229	8.788	8.240	9.454
7.5	−5.27259	−5.23867	−5.32578	−4.734	−4.734	−4.734	10.216	9.634	11.112
8	−5.15746	−5.1086	−5.2277	−5.046	−5.046	−5.046	2.168	1.233	3.483
8.5	−5.4736	−5.43879	−5.52398	−5.136	−5.136	−5.136	6.172	5.572	7.028
9	−5.41505	−5.38676	−5.46677	−4.851	−4.851	−4.851	10.417	9.946	11.264
9.5	−5.30187	−5.24868	−5.34621	−5.016	−5.016	−5.016	5.394	4.435	6.179
10	−5.39749	−5.35074	−5.44838	−5.079	−5.079	−5.079	5.906	5.084	6.785
average							**8.922**	**9.898**	**10.831**

6   Conclusions

The paper describes the numerical solution of the mechanical analysis of the mechanical system in ANSYS simulation program. The result of the modal analysis of the mechanical system was its own shapes. Custom shapes contained gestures of their own shapes, deformed own shapes in a given frequency spectrum, and high own shapes that may contain residual effects. Experimental measurement of the modal analysis was performed on the laboratory model. Experimental results served to verify numerical model data and its further modification, refinement. The numerical vehicle model for measuring vertical oscillation was compiled in ADAMS. This model is used to predict the dynamic behaviour of the model system - the vehicle model. When comparing the results obtained were found good agreement between experimental and numerical solutions. The numerical model of a vehicle can be used to describe and predict the behaviour of a given system for the general case of loading and its kinematic excitation. More than 90% match between numerical and experimental measurements was achieved.

References

1. Stejskal, V., Okrouhlík, M.: Vibration with Matlab. Publishing ČVUT, Prague (2002). ISBN 80-01-02435-0
2. Laurin, J.: New trends in construction and exploitation automobiles. In: International Scientific Conference—Vehicles 2007, Nitra (2007)
3. Blundell, M., Harty, D.: The Multibody Systems Approach to Vehicle Dynamics. Elsevier (2004). ISBN 0750651121
4. Awrejcewicz, J., Kurpa, L., Shmatko, T.: Vibrations of functionally graded shallow shells with complex shape. In: Dynamical Systems—Mathematical and Numerical Approaches, pp. 57–67. Politechnika Lodž, Lodž (2015). ISBN 978-83-7283-706-6
5. Nowak, A., Nowak, P., Awrejcewicz, J.: Influence of position of an anvil beam on vibrations of collecting electrodes. In: Dynamical Systems—Mathematical and Numerical Approaches, pp. 391–402. Politechnika Lodž, Lodž (2015). ISBN 978-83-7283-706-6
6. Brepta, R., Půst, L., Turek, F.: Mechanical Vibration. Technical Guide 71. Sobotáles, Pra gue (1994). ISBN 80-901684-8-5
7. Kožešník, J.: Vibration of Mechanical Systems. Czechoslovak Academy of Sciences, Prague (1979)
8. Svoboda, M.: Analysis of the influence of geometrical and production asymmetry and kinematic excitation on the oscillation of the mechanical system. Dissertation thesis, FVTM UJEP, Ústí nad Labem (2012)

Directional Stability Control of Body Steer Wheeled Articulated Vehicles

Aleksander Skurjat and Andrzej Kosiara

Abstract Demanding higher travel velocities of rigid body articulated wheeled vehicles and maintaining high safety while moving on stiff ground requires finding more accurate methods of adjusting steering angle between rigid frames and using special solutions allowing the driver keeping desired path. In this article, identification of factors affecting directional stability is discussed. A new mathematical algorithm for estimating vehicles directional stability is proposed and tested. Computer simulations of methods counteracting snaking behavior indicates that the speed limit of 50–60 km/h for articulated rigid body vehicles can be exceeded by using new solutions.

Keywords Snaking · Directional stability · Articulated vehicle · Path correction control system

1 Introduction

Higher velocities of wheeled vehicles require more and more modern solutions to ensure the safety of the traffic. Safety systems can be divided into two basic groups: active safety, which includes the structural components of the vehicle so that the driver can comfortably drive the vehicle on a given trajectory and have the ability to perceive the lane and surroundings.

This group also includes driver assistance solutions related to external factors such as the use of ABS braking systems, anti-skid systems (e.g. ESP, DSC, ABC), as well as proper road lighting or tire construction.

A. Skurjat (✉) · A. Kosiara
The Department of Off-Road Machine and Vehicle Engineering, Wrocław University of Science and Technology, ul. Łukasiewicza 7/9, 50-371 Wrocław, Poland
e-mail: aleksander.skurjat@pwr.edu.pl

A. Kosiara
e-mail: andrzej.kosiara@pwr.edu.pl
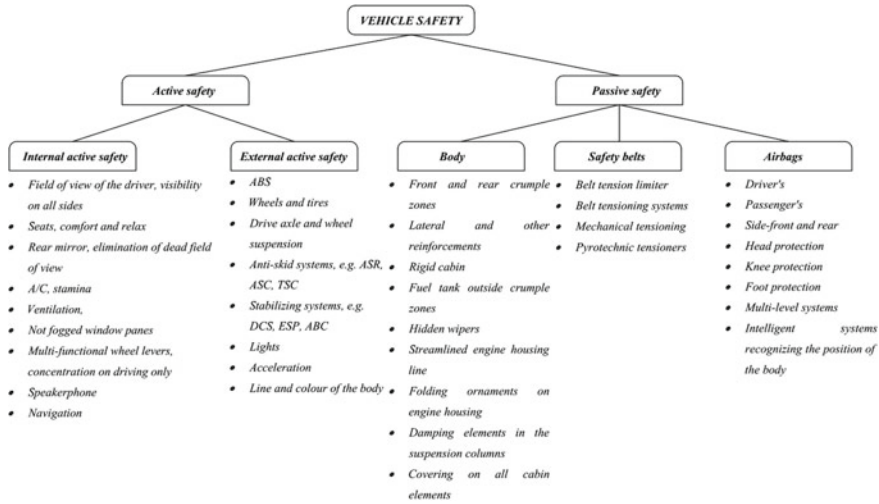
Fig. 1 Diagram showing the division of the safety system in motor vehicles [8]

The second group - passive safety—includes solutions to minimize the effects of a possible road accident. These include, e.g., crumple zones, reinforced door constructions, streamlined shapes, seat belt solutions and airbags.

A diagram showing the breakdown of the safety system in motor vehicles is shown in Fig. 1.

Part of the solutions is used in different types of vehicles. These are generally solutions from the group of passive internal safety. Unfortunately, due to the differences in the construction of particular groups of vehicles, it is not possible to directly map ready-made and well-considered concepts from well-developed automobiles and transfer them directly to the off-road vehicles working typically on construction side, but moves often on public roads. These groups are: articulated wheel loaders, truck and trailer assembly. The basic problems include: differences in the construction of steering systems, the use of tires of different profile height and different diameters, change of height of center of gravity, differences in the construction of the suspension system, the purpose of the wheeled vehicle, etc.

Particularly large differences in construction occur between motor vehicles and articulated vehicles such as wheel loaders. The presence of articulated steering system instead of a front wheel steering makes it impossible to directly apply traction control systems (e.g. ASR, ACS, ESP, etc.) without previous simulation testing and without actual experiments. Undeniably, using such systems will allow to achieve higher speeds and will provide a higher level of safety.

There are many problems faced by articulated vehicle manufacturers. These are, e.g. the presence of articulated steering and a low torsional rigidity hydrostatic system causing deviations from the assumed straight-line direction and snaking behavior of the vehicle [1–3]. No less important reason is obtaining a change in trajectory of

motion as a result of even a slight rotation of the steering wheel. This is due, among other things, to the fact that a slight change in the angle between the articulated vehicle frames significantly affects the resulting turning radius and the pivot point of the body. The use of hydrostatic systems introduces delays in trajectory corrections and elasticity between the front and rear frames, as well as clearance on the steering wheel (with the use of so called "orbitrols"), resulting in the snaking behavior.

In articulated steering system non linear dumping properties can be found. Because of a few degree amplitude continuous oscillations in steering joint we can propose methods presented in [4] for determine a real dumping values. Results obtained in on vehicle experiment is going to present soon.

Tires characteristics are believed to have a great impact on both on and off-road vehicles on directional stability. Results are presented on [5].

Problems encountered in design of articulated vehicles and a three-dimensional multi-body dynamic model is formulated integrating the hydro-mechanical frame steering and hydro-pneumatic suspension, numerical investigations, and tests are shown in [6].

The lack of full trajectory control over the articulated vehicles reduces its maximum speed and is also the reason why the articulated steering systems *do not* comply with EN 12643 + A1: 2009. One of the solutions could be the introduction of systems that automatically minimize the oscillation amplitude between the articulated vehicles frames and will positively affect its trajectory.

2   Simulation Testing of the Anti-oscillation System in Steering System

The experimentally verified model of a wheel articulated loader [1, 2] was used for simulated testing. The testing is conducted simultaneously in the integrated MSC Adams and Matlab/Simulink environments. MBS tests provide information on the loads that occur in kinematic pairs of cooperation, wheel—surface contact, steering angle in the articulation, while Matlab/Simulink complements the model with the driving torque necessary to accelerate the vehicle and maintain the set speed, and also introduces the braking torque values into the MBS model, which are calculated from the Matlab package control system. The vehicle model is shown in Fig. 2.

The principle of operation of the oscillation amplitude reduction system in the steering system is based on the use of the articulated vehicle braking system and thereby the construction of a prototype track stabilizer system. Depending on the design of the motor vehicle, the control algorithm enables the braking of 1, 2 or 3, or all vehicle wheels, and allows the change of the motion trajectory. The proposed system, in its initial phase of operation, reduces the snaking behavior by appropriate braking of the front wheel, which reduces the oscillation amplitude in the articulated joint. The development of the system with the possibility of obtaining a trajectory correction is in the testing phase and will be presented at a later date.
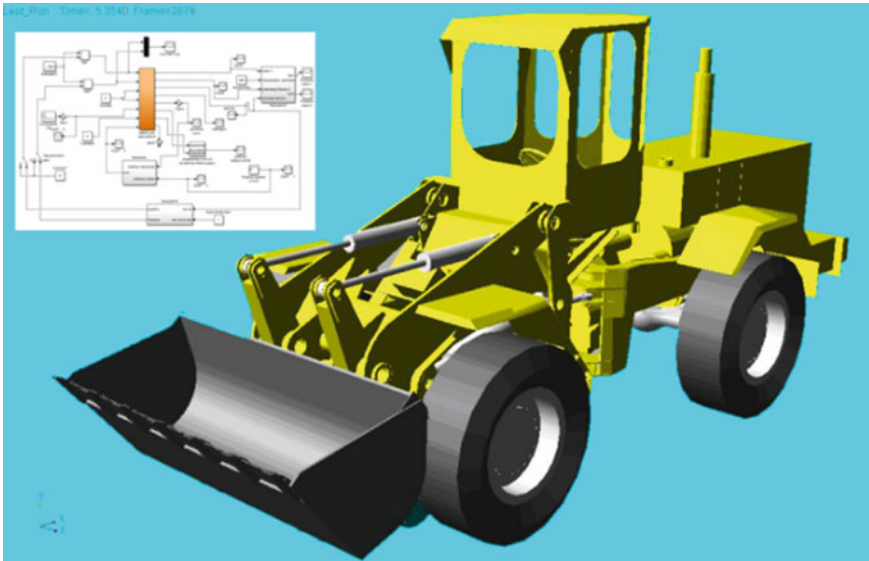
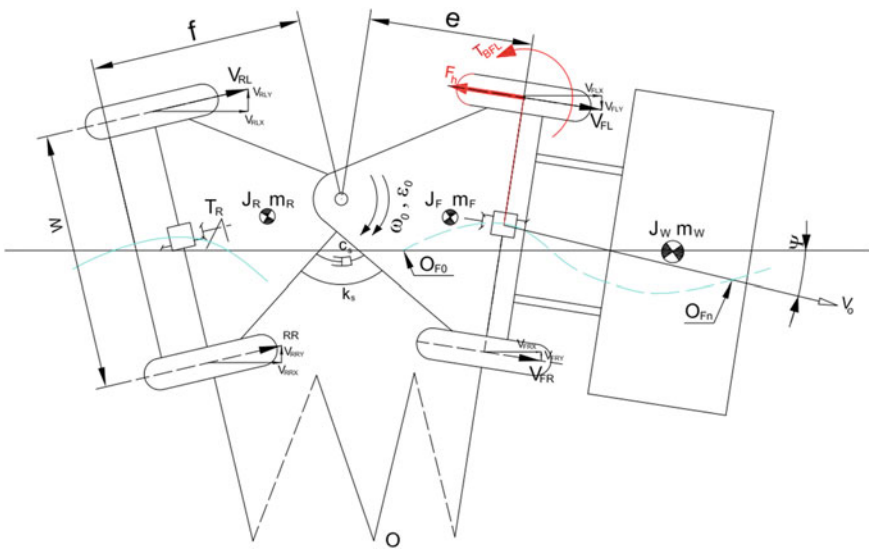**Fig. 2** Model of vehicle involved in simulation testing

Fig. 3 The principle of operation of the system eliminating oscillation in the steering system

The principle of operation of the proposed system is presented in Fig. 3.

The control system calculates the correct braking torque applied to the vehicle's wheel according to the author's dependence:

$$F_h = -k \frac{2\frac{ds}{dt}I}{W\frac{x_z}{V_z}r_k} \tag{1}$$

where

s stroke of the actuator of the steering system [m]
I reduced vehicle moment of inertia [kg m^2]
W vehicle track width [m]
x_z acceptable standard lateral displacement [m]
v_z vehicle velocity [m/s]
r_k wheel dynamic radius [m]
k factor depending on the applied solution [−].

The aim of the simulation testing is to determine the efficiency of the system to eliminate the oscillation in the steering system and to determine the trajectory of the vehicle movement depending on its speed and the value of force in the steering system. Oscillations in the steering system were forced by a short-time torque impulse between the frames with the value of 30 kNm after obtaining the set speed.

Simulation testing using the MBS environment do not allow for the recognition of computational equations and the user only receives the mathematical solution of the problem. This results in difficulties in comparing the results obtained, particularly when the problem under consideration is more complex. For this reason, in order to check the effectiveness of the stabilizing system, W_{SD} performance index has been developed. The dimensionless W_{SD} index combines both the behavior of the steering system, i.e. the amplitudes and duration of the oscillation and the vehicle resulting motion trajectory with side slip on wheels. The value is determined by the formula:

$$W_{SD} = \int_{t0}^{t1} \tan\left|\frac{x}{y}\right| dt \int_{t0}^{t1} \tan|\gamma| dt \tag{2}$$

where

x lateral displacement [m]
y displacement of the vehicle in the direction of travel [m]
γ angle at turn of elements [rad]

The relationship was composed of two products. The first describes the trajectory based on the deviation from the straight line motion of the vehicle. The second defines the amplitude and duration of the oscillation in its turn. A lower value of the W_{SD} determines a solution that has smaller amplitudes and time of oscillation of the angle γ or moves at a smaller angle relative to the assumed track and thus become a more advantageous solution. Because every change in course angle Ψ is the result of angle change in articulated steering γ it is not possible to achieve lower values of W_{SD} only in the case of oscillation γ. However, it is possible to achieve low values of W_{SD} with no oscillation γ. In this situation, the vehicle moves along a straight line running at an angle Ψ in relation to the assumed direction of movement, which is due
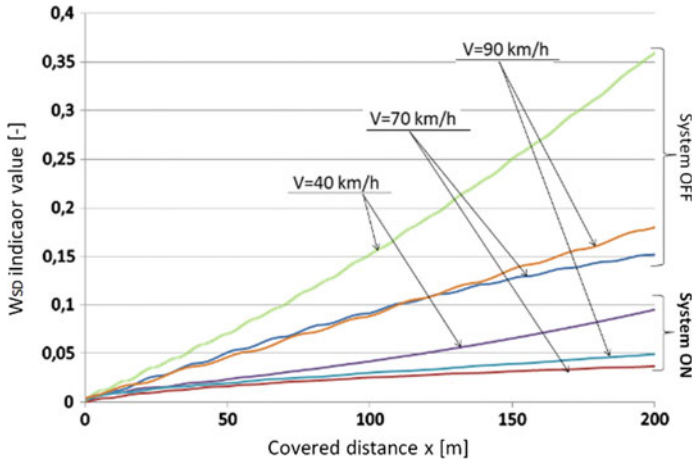
Fig. 4 Effect of the proposed stabilization system depending on the speed of movement

to the wrong placement of the vehicle at the beginning of the simulation or operation of lateral forces and drift. Of course, such a solution, from the point of view of the snaking behavior, is also beneficial, although it requires the driver to adjust the angle at which the vehicle moves. Simulation time t_0–t_1 must be chosen in such a way that the vehicle in each test case covers the same distance x.

Figure 4 presents the comparison and derived W_{SD} values at 40, 70 and 90 km/h when switching on and off the proposed stabilizer. Studies have shown that a system with a running system allows W_{SD} values of 3.5–4 times lower for all speeds. The final W_{SD} values varied widely. For the speed of 40 km/h, the highest and the least favorable values were reached, while at the speeds of 70 and 90 km/h less differences were observed. This is related to the different course angles Ψ of vehicle after the stabilization system has completed its operation and the vehicle moves at a fixed angle with respect to the straight line travel direction. The increase in value is obtained by multiplying the non-zero (and constant after the oscillation of the angle) value of the second product of the W_{SD} by the first product, which has the value related to the fact that the vehicle moves at a course angle Ψ (relative to the x-axis). The result is shown in Fig. 5.

This is related to the different course angles Ψ of vehicle after the stabilization system has completed its operation and the vehicle moves at a fixed angle with respect to the straight line travel direction. The increase in value is obtained by multiplying the non-zero (and constant after the oscillation of the angle) value of the second product of the W_{SD} by the first product, which has the value related to the fact that the vehicle moves at a course angle Ψ (relative to the x-axis). The result is shown in Fig. 5.

Course angle Ψ reached the highest values for the speed of 40 km/h. The arrows in Fig. 5 indicate the moment of action of the short-time impulse of the torque acting on the steering to stimulate and observe the snaking behavior. Section x of the value
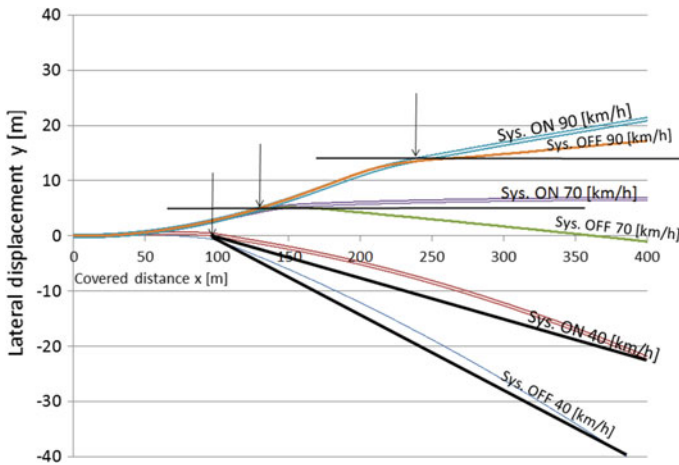
Fig. 5 The obtained angle of the vehicle's course depending on the stabilizer system depending on the speed of movement
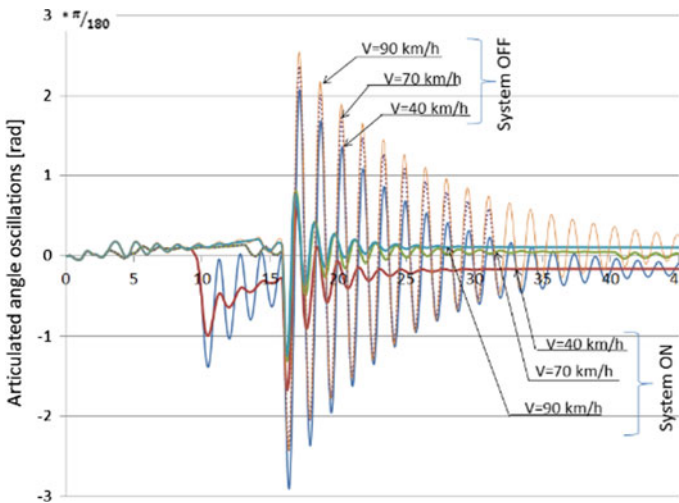
Fig. 6 Steering angle of the system with the stabilizer on and off for different speeds

from 0 to the point indicated by the arrow indicates the vehicle's run up to obtain the set speed. It can also be noted that depending on the value of the driving torque, the vehicle's accelerating phase is not uniform. The vehicle tends to "deviate" from a given trajectory of motion under the influence of the applied driving torque of the rear wheels.

Figure 6 shows the course of the steering angle oscillation depending on the speed of movement and for the stabilization system on and off.

The research showed that the stabilization system is characterized by rapid reaction. It did not allow for higher angular values in the articulation than 1.2°, which reduced the maximum amplitude of the oscillation two-fold. It should be noted that the control system algorithm requires that the range of acceptable angles is correct. This prevents the brake system from constant turning on when there is a small amount of oscillation that occurs while the vehicle is moving.

The above solution was reported to the patent office [7].

3   Conclusion

The research showed the possibility of using a proposed trajectory movement stabilizer to reduce oscillation amplitudes by up to 250% and to shorten their duration by several times. It also has a positive effect on the trajectory of the movement.

W_{SD} appears to be correctly comparing the behavior of different solutions. Its lower values indicate solutions in which the vehicle moves with comparatively lower course angles Ψ and lower angular amplitude values in the articulation. W_{SD} indicator allows to compare different behaviors of wheeled vehicles and it is especially valuable when MBS environment don't show the user a real equations used in numerical calculations.

The braking system takes into account in the operation algorithm simultaneous braking of only one of the front wheels. Control algorithm is calculating braking torque applied to one wheel, but to do that braking time is important too. Simulations assumed fixed time braking impulse. The further studies should consider solutions in which the algorithm will also take into account the use of rear wheel brakes. A very first stage calculations show that braking wheels at a cross of vehicle promising even better results as presented in this paper.

The economic aspect of the system used and defining the typical time of braking of wheels on a typical road are also important. The increased fuel consumption and wear when using this system should also be considered.

References

1. Skurjat, A., Serwatka K.: Badanie możliwości eliminacji zjawiska wężykowania pojazdów przegubowych poprzez przyhamowanie kół, nr 5, s. 1363–1370. Logistyka (2015)
2. Dudziński, P., Skurjat, A.: Badania eksperymentalne i symulacje wężykowania przegubowych pojazdów przemysłowych na podwoziu kołowym, R.71, nr 11, s. 29–32. Cz. 2, Badania symulacyjne, Przegląd Mechaniczny (2012)
3. Dudziński, P., Skurjat, A.: Badania eksperymentalne i symulacje wężykowania przegubowych pojazdów przemysłowych na podwoziu kołowym, R. 71, nr 10, s. 31–35. Cz. 1, Badania eksperymentalne, Przegląd Mechaniczny (2012)
4. Azad, N.L., Mcphee, J., Khajepour, A.: The effects of front and rear tires characteristics on the snaking behavior of articulated steer vehicles. In: Vehicle Power and Propulsion, 2005 IEEE Conference

5. Yin, Y., Rakheja, S., Boileau, P.-E.: Multi-performance analyses and design optimisation of hydro-pneumatic suspension system for an articulated frame-steered vehicle. Veh. Syst. Dyn. (2018)
6. Olejnik, P., Awrejcewicz, J.: Coupled oscillators in identification of nonlinear damping of a real parametric pendulum. Mech. Syst. Sig. Process. **98**, 91–107 (2018)
7. Dudziński, P., Skurjat, A., Dacko, P.: Sposób aktywnej poprawy stateczności kierunkowej pojazdu z wieloczłonowym układem podwoziowym. Patent pending P421682 (2016)
8. Rokosch, U.: Poduszki gazowe i napinacze pasów. Wydawnictwo WKŁ, Warszawa (2003)

Influence of the Mechanical Properties of Pantograph Structural Parts on Its Interaction with a Catenary

Paweł Zdziebko, Adam Martowicz and Tadeusz Uhl

Abstract The paper addresses dynamic interaction in the pantograph–catenary system present in a rail vehicle. The contact force, which is measured between pantograph and catenary, may significantly fluctuate during ride due to nonlinear properties of the entire system. This may cause unexpected drops of the current flow efficiency and further power decreases. Following the relevant significance of the addressed issue, the authors performed an analysis of the influence of suspension properties of the critical pantograph's passive components on the improvement of electric current collection on a train. The analysis was performed based on a co-simulation model for the pantograph–catenary interaction elaborated by the authors. The Finite Element catenary model assumes nonlinear droppers, large displacements and contact with the pantograph slider. To overcome limits of widely used lumped parameters model of the pantograph, the relatively more realistic Multibody model was considered. Reported in other works, the use of Multibody models, in which all properties of pantograph keep physical sense, provide wide range of design improvements for better current collection. By using the adapted model, the ability of implementation additional dampers in a pantograph structure for improvement of contact quality was investigated. Utilized pantograph model takes into account friction forces, suspension springs and aerodynamic effects. Presented results proof the ability to effectively improve current collection merely by adjusting pantograph's passive components.

Keywords Pantograph · Catenary · Dynamic interaction · Contact force
Mechanical properties

P. Zdziebko (✉) · A. Martowicz · T. Uhl
Department of Robotics and Mechatronics, AGH University of Science
and Technology, Al. A. Mickiewicza 30, 30-059 Krakow, Poland
e-mail: zdziebko@agh.edu.pl

A. Martowicz
e-mail: adam.martowicz@agh.edu.pl

T. Uhl
e-mail: tuhl@agh.edu.pl

1 Introduction

Nowadays, high speed of travel in passengers railways becomes a standard. It should be noticed, that increasing of operational speed of trains may have a negative effect on the performance of its components, because working conditions become more challenging. One of the subsystems which limits the maximum speed is a pantograph—catenary interface. A railway catenary, also called overhead line (OL), as shown in Fig. 1, is a flexible structure constructed along rails, which is responsible for conducting the electric energy to a train form a traction current converter plant. On the other hand, a pantograph is involved in current transmission to a locomotive or electric multiple unit (EMU) from an overhead lines. A necessary condition of proper current collection in high speed electrified railways is a continues contact between pantograph and contact wire. In reality, the contact is disturbed by many external sources of interruption. The authors have already presented in [16], that fluctuations of the contact force have many sources, including (but not limiting to): wave propagation in catenary, nonlinear characteristic of droppers and external forces acting on a pantograph. A pantograph is mounted on the roof of train, therefore accelerations exerted by a rail vehicle on a pantograph are also an important factor [5–7]. Rail vehicle dynamics was deeply investigated by Zboiński and Dusza [14].

Unfavorable phenomenon of contact force oscillation is usually investigated by numerical analysis, which have become a powerful tool in studying pantograph–catenary dynamic interaction. The most recent numerical models usually consider Finite Element (FE) model of a catenary [17] (which is able to handle the phenomenon like wave propagation) and lumped parameters [12] or Multibody (MB) pantograph model [11, 13].

The present research aims at studying the mechanical properties (stiffness and damping) of a pantograph collector head suspension, and to check how much they influence the contact force course. This could help to improve the interaction between pantograph and OL solely by tuning the suspension characteristic. This subject was previously analyzed by several authors [1, 8, 10, 18] and the results were promising.

Fig. 1 Pantograph–catenary system
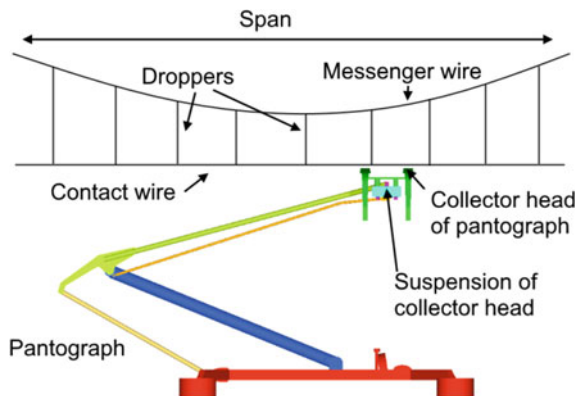
To extend the state of the art, the authors have performed similar analysis presented in this paper, employing proposed multi-domain co-simulation approach including very realistic MB model of the pantograph, which corresponds to the one used in European railways. The utilized simulation approach considers multi-domain phenomena and was introduced by the authors in their previous papers [15, 16]. The algorithm assumes the co-simulation between FE code (for catenary) and MB rail vehicle–pantograph model. All necessary phenomena, which disturb pantograph—OL interaction are present in the simulation procedure. It addresses the issues related to: wave propagation in a catenary, slackening of droppers, nonlinear pantograph, which is subjected to aerodynamic forces and vibration from a rail vehicle. Moreover, realistic variants of suspension springs were investigated.

The paper is organized as follows. After short introductory Sect. 1, the following Sect. 2 describes the elements of pantograph head suspension, the object of the investigation. Next, Sect. 3 describes contributing models employed in the co-simulation of pantograph–catenary interaction. Subsequently, the results are presented and discussed in Sect. 4 and, finally, Sect. 5 concludes the paper.

2 Case Study

The goal of the presented analysis is to investigate, how the stiffness (K) and damping (C) properties of the pantograph collector suspension affect the contact force variation. The pantograph model employed in the simulation represents the one which is commonly used in Europe, 160ECT (produced by EC Engineering). Basic kinematic diagram of this mechanism is presented in Fig. 2.

Revolute joints which are present in the structure are shown in the scheme by black circles (rotational axis is perpendicular to the ZX plane). Triangular symbols represents mounting points at the frame. Kinematic joints in the pantograph are listed in Table 1. The original suspension of the collector head is composed of four

Fig. 2 Kinematic diagram of pantograph (frame is not visible)
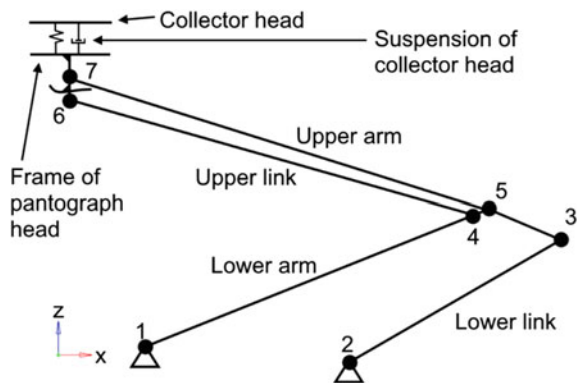
Table 1 Revolute joints in the model

No.	First body	Second body
1	Frame	Lower arm
2	Frame	Lower link
3	Lower link	Upper arm
4	Lower arm	Upper link
5	Lower arm	Upper arm
6	Upper link	Frame of pantograph head
7	Upper arm	Frame of pantograph head

Table 2 Properties of analyzed spring-damper elements

	Unit	Spring 1	Spring 2	Nominal spring	Spring 3	Spring 4
G	[MPa]	80,000	80,000	80,000	80,000	80,000
d	[mm]	2.5	2.5	2.5	3	2.9
D	[mm]	32.5	27.5	25	30	25
n		11	10	9	8	10
K	[N/m]	1030	1880	2780	3750	4530
	Relative change of K	−63%	−33%	0%	35%	63%
C	[Ns/m]	4.7	8.5	12.5	16.9	20.4

independent spring-damper elements. Each of them is characterized by stiffness and damping coefficient—those values are denoted as nominal ones.

To be close to the reality, alternative stiffness and damping coefficients should correspond to real-life elements. Considering deviations of nominal values, four alternative springs are investigated in the paper, see Table 2. Calculations of the stiffness coefficient of springs were performed in terms of geometrical and material properties, according to the formula (1).

$$k = \frac{Gd^4}{8nD^3} \tag{1}$$

where: k—stiffness coefficient of a spring, G—modulus of rigidity of spring material (Kirchhoff's modulus), d—wire diameter, n—number of active turns, D—mean coil diameter.

The damping coefficient of each spring (resulting from the material properties) represents 0.45% of the stiffness coefficient particular one. This ratio was chosen on the basis of data provided by the manufacturer for similar pantograph. In fact, this proportion may vary from 0.24 (as found e.g. in [3]) up to 0.64 [2]. Therefore, the value assumed presently (0.45%) is reliable. Subsequently, presence of additional dashpots was investigated, by increasing the resultant damping coefficient respec-

tively with additional amount of 33, 66, 100, 133, 166 and 200% of the damping coefficient of nominal spring. To sum up, 35 combinations of damping and stiffness coefficients were investigated.

3   Multi-domain Simulation

The model, which is utilized in the work is based on the multi-domain co-simulation approach presented in extended form by the authors in [16]. The main algorithm is presented Fig. 3.

The calculations are performed within the following computational framework. At the beginning, two separate models are constituted in the analysis:

1. Initial FE model of a catenary, used to build a final catenary model with allowable pre-sag (considering gravity force and tension in cables), elements were modeled in the Altair Hyper Mesh program.
2. Fluid structure interaction (FSI) model of a pantograph. Calculated aerodynamic forces acting on it are then passed into the MB model.

Next, when a proper shape of a catenary is achieved (10 spans are modeled, each of them is 60 m long) and aerodynamic forces are computed, the MB coupled track-rail vehicle–pantograph model is set. Finally, pantograph–catenary interaction is being calculated with given time step dt over defined time period t in the co-simulation between FEM and MB models. The algorithm assumes that MB code is run first [9], and passes the position of the collector head (considering train speed and vibrations of a rail vehicle) into FEM catenary model. Subsequently, FEM code computes
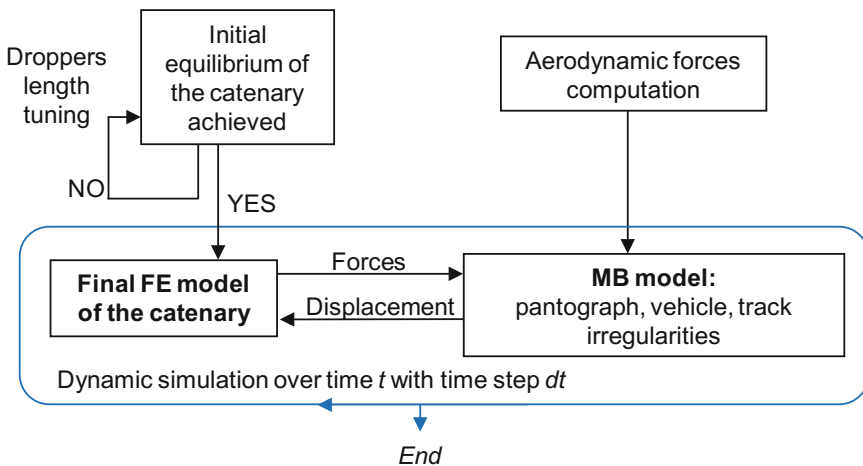
Fig. 3 Co-simulation procedure

dynamic solution (employing MSC.Marc solver) of a catenary under actual position of collector head and passes reaction forces acting on it into MB code, where the MB model is computed again, considering contact force delivered by catenary FEM model. The algorithm is iterated within a loop to cover the total simulation time. The obtained results are shown in the following and, then, briefly discussed. The proposed multi–domain co-simulation produces reliable results, the method of simulation was validated according to the first step of validation process presented in the European Standard 50318 [3].

4 Results

In this chapter, results of pantograph–catenary interaction are presented. The total number of 35 combinations of K and C was analyzed using the multi-domain co-simulation introduced in Sect. 3. According to [3], it is advised to filter the actual contact force with low–pass filter with cutoff frequency of 20 Hz and to analyze the results only for two central spans (to omit negative influence of boundary conditions—ends of the catenary structure). An exemplary course of the contact force, which is measured between collector head and catenary, is presented in Fig. 4.

Usually, statistical parameters of the contact force are used to make the results comparison more clear. In this work, for each combination of K and C, the following statistical parameters were determined: mean, standard deviation, minimum, maximum and peak-to-peak of contact force. In Figs. 5, 6, 7, 8 and 9 these statistical parameters are presented for stiffness and damping combination (as previously mentioned, 35 combinations in total).

Notice, that for some of the presented figures different perspectives were used for better presentation. Accurate results were computed only for dark blue points, while approximate shape of the surfaces (outspread between them to cover the entire input parameters domain) are shown for more convenient way of results presentation.

Fig. 4 Contact force between pantograph and OL for nominal K and C configuration
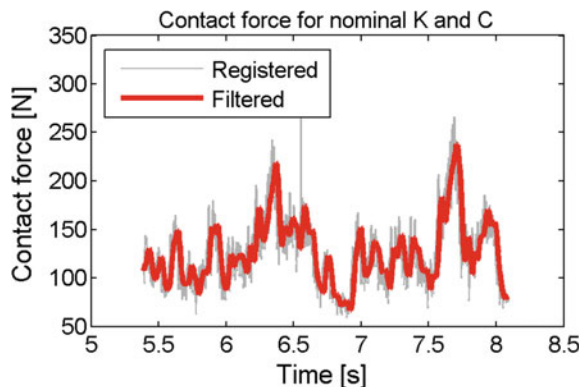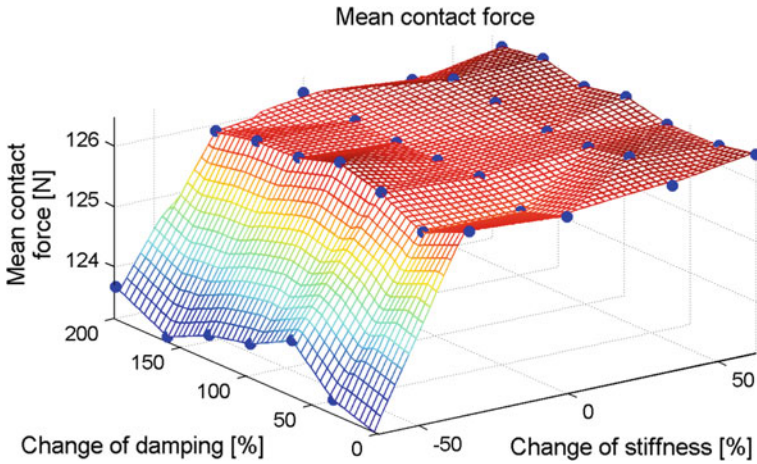
Fig. 5 Mean contact force versus stiffness and damping coefficients
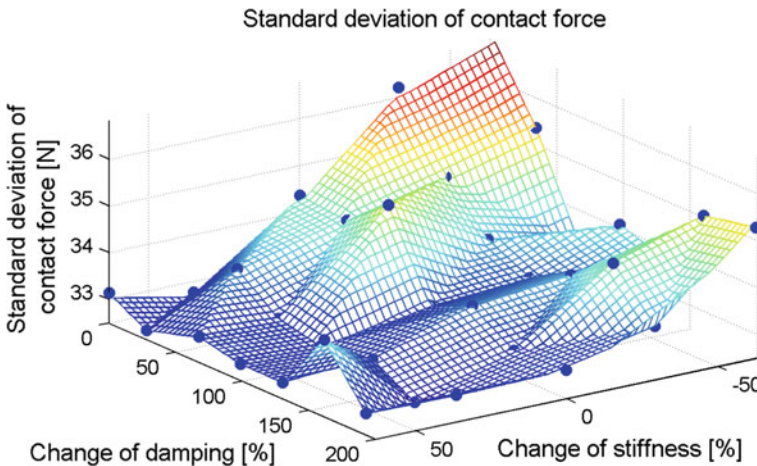
Fig. 6 Standard deviation of contact force versus stiffness and damping coefficients

Percentage factors were used to describe the stiffness and damping change in relation to the nominal values.

It can be observed (Fig. 5), that only for the most flexible spring (change of the stiffness by −63%), the mean contact force is slightly different comparing to the other cases. Nonetheless, according to the European Standard [4], for 3 kV DC catenary system (commonly used in Poland) the contact force should be in the range ~108–135 N (for speed 160 km/h), therefore that parameter is not crucial. Hence, it can be assumed that the mean contact force is not significantly influenced by any of the analysed suspension characteristic, because in all cases the mean contact force is found to be within the above mentioned limits.
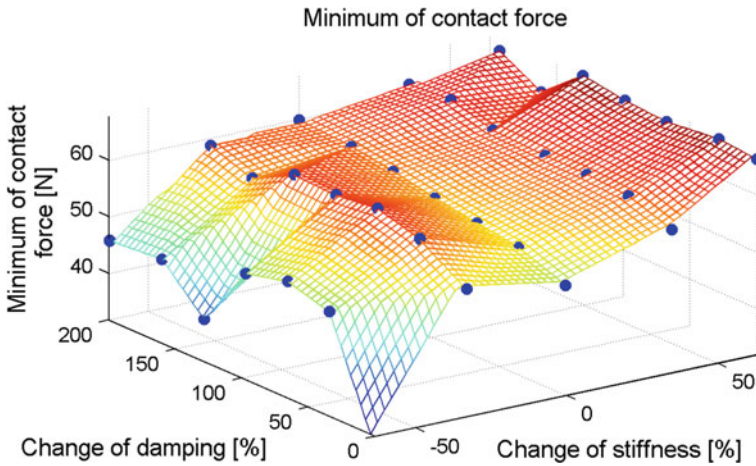
Fig. 7 Minimum of contact force versus stiffness and damping coefficients
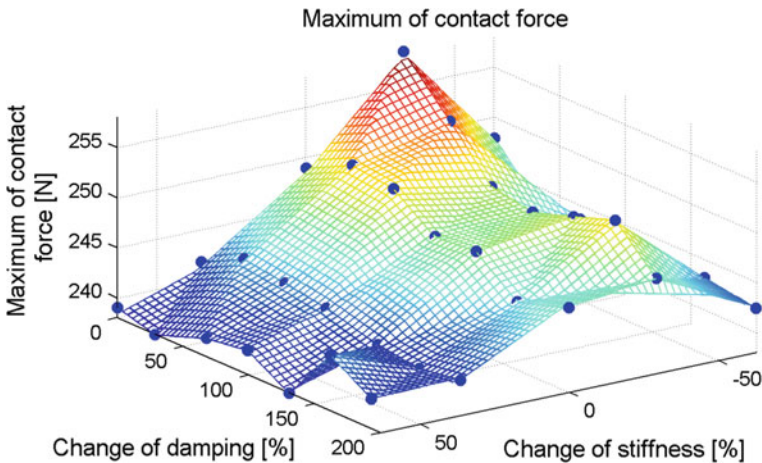
Fig. 8 Maximum of contact force versus stiffness and damping coefficients

Even though, the standard deviation of contact force in within the acceptance ranges presented in [4] for all of analyzed cases, it is considered that for better pantograph–catenary interaction, the standard deviation and maximum of contact force should be minimised—to provide smoother contact and to decrease wear of contact slider, while minimum of contact force should be maximized, to reduce the risk of detachment between pantograph carbon slider and contact wire. Based on Fig. 6 it can be observed that the standard deviation highly depends on particular combination of K and C. Higher stiffness in collector head suspension provides generally lower standard deviation. The exception was noted only in a combination with damping increase by 166%. For the nominal stiffness, additional damping also provides
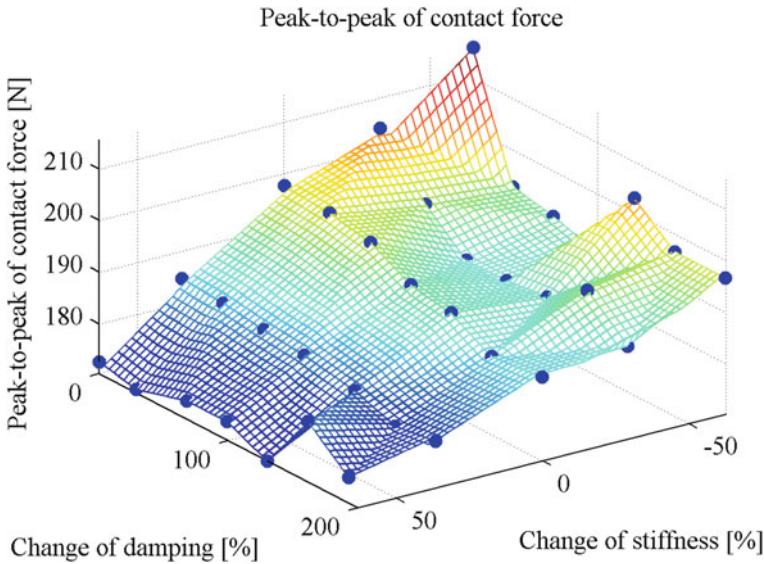
Fig. 9 Peak-to-peak of contact force versus stiffness and damping coefficients

decrease of the standard deviation. What is very important for pantograph–catenary performance, the minimum of contact force can be significantly increased while stiffer springs are used (comparing to the nominal case). The most flexible springs exhibit lowering of minimum contact force.

Cases with +35% and +63% change of stiffness, regardless of damping change, exhibit higher minimum and lower maximum and peak-to-peak of contact force comparing to the nominal stiffness. Cases exhibiting −63% change of stiffness, irrespective of change of damping, produce lower maximum, but also lower minimum of the contact force.

The standard deviation, minimum and maximum of contact force were assumed by the authors as the most crucial parameters for proper current conduction to a train. Therefore, the best and worst cases are presented in Table 3. The lowest standard deviation and maximum of contact force was observed for the same case (no. 1). Concurrently, for the same case the highest minimum of contact force is noted (good performance), hence the Case no. 1 is assumed to be the best one. The lowest minimum was observed in case no. 2, while the greatest maximum in case no. 3.

The comparison of statistical parameters change for contact force is presented in Fig. 10. The most undesired performance is noted for −63% change of stiffness and nominal damping—the minimum contact force is 41.5% lower than for the nominal case (see Fig. 10), which increases the risk of detachment.

The best investigated combination of K and C (case 1) decreases the standard deviation, maximum, peak–to–peak and increases minimum of contact force by −4.8,

Table 3 Comparison of contact force (CF) results regarding pantograph–catenary performance for the selected cases

	Case nominal	Case 1 (best)	Case 2	Case 3
Change of stiffness	0%	+63%	−63%	−33%
Change of damping	0%	+33%	0%	0%
Mean CF [N]	126.1	126.3	123.1	126.2
Standard deviation of CF [N]	34.4	32.7	37.0	36.2
Minimum of CF [N]	51.3	67.0	30.0	54.3
MAX [N]	249.0	238.0	248.0	258.5
PEAK–PEAK CF [N]	197.7	171.0	218.0	204.3
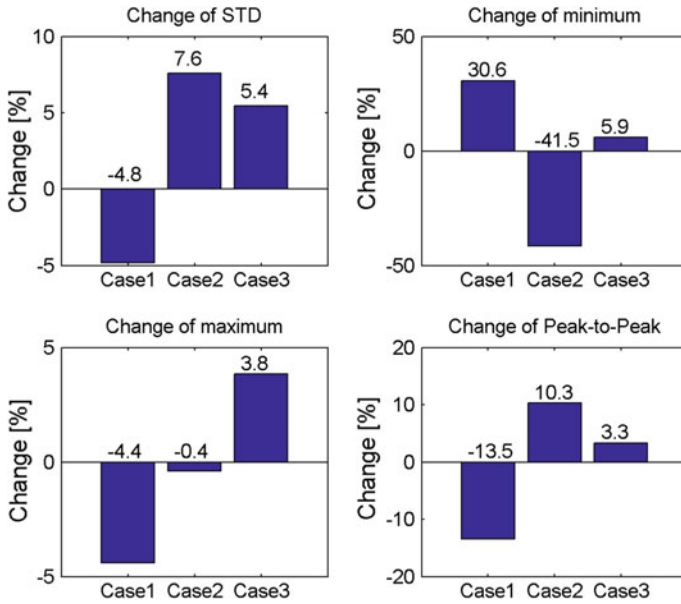
Fig. 10 Change of statistical parameters of contact force for selected cases

−4.4, −13.5 and 30.6% respectively, which is demanded in the modeled system and may be assumed as a significant design improvement.

5   Conclusions

The main conclusions resulting from the paper are as follows:

1. Multi-domain co-simulation is a powerful tool for analyzing the pantograph—catenary dynamic interaction since various physical phenomena are consider for more realistic computations.
2. Using the proposed co-simulation model, the influence of suspension characteristic of collector head on the resulting contact force between pantograph slider and contact wire can be determined.
3. Stiffness and damping properties of the collector head suspension significantly influence the performance of pantograph–catenary contact, which is crucial when addressing effective current delivery to a train.
4. Generally speaking higher stiffness provides better contact (lower standard deviation and maximum and higher minimum of contact force).
5. The influence of damping on contact performance highly depends on the concomitant stiffness value (based on the properties of the mounted spring).
6. The best performance of contact quality was noted for the spring with increased stiffness (+65%) and additional damping (+33%). Simultaneously, the lowest standard deviation, maximum and peak-to-peak and the greatest minimum of contact force was observed in that case.
7. The present study confirms that further investigation is needed for optimization of collector head suspension characteristic (also preferably in wider domain) due to shown non-trivial relationships between design and operational properties of the system under study.

References

1. Ambrosio, J., Pombo J., Pereira, M.: Optimization of high-speed railway pantographs for improving pantograph–catenary contact. Theor. Appl. Mech. Lett. **3**, 1–7 (2013). https://doi.org/10.1063/2.1301306
2. Bruni, S., Ambrosio, J., Carnicero, A., Cho, Y.H., Finner, L., Ikeda, M., Kwon, S.Y., Massat, J.-P., Stichel, S., Tur, M., Zhang, W.: The results of the pantograph–catenary interaction benchmark. Veh. Syst. Dyn. **53**(3), 412–435 (2015)
3. CENELEC: European Standard EN 50318:2002
4. CENELEC: European Standard EN 50367:2012
5. Kurowski, P., Martowicz, A., Uhl, T., Lasko, G.: Analysis of the rail roughness influence on vehicle dynamic behavior by means of multibody simulation. Arch. Transp. **23**(1), 23–35 (2011)

6. Martowicz, A., Kurowski, P., Uhl, T., Lasko, G.: Design optimization of multibody model of rail vehicle supported by Response Surface Method. In: Proceedings of the 2nd International Conference on Engineering Optimization (EngOpt), Instituto Superior Técnico, Lisbon, 6–9 Sept 2010

7. Martowicz, A., Kurowski, P., Uhl, T., Lasko, G.: An application of response surface method to design optimization of a model of rail vehicle considering uncertainties. Mech. Control **30**(2), 85–95 (2011)

8. Massat, J.-P., Laurent, C., Bianchi, J. P., Balmes, E.: Pantograph catenary dynamic optimization based on advanced multibody and finite element co-simulation tools. Veh. Syst. Dyn. **52**, 338–354 (2014). https://doi.org/10.1080/00423114.2014.898780

9. MSC Software, Adams Co-Simulation Interface (ACSI): https://simcompanion.mscsoftware.com/infocenter/index?page=content&id=DOC11064&cat=2016_DOCS&actp=LIST (2017). Accessed 31 Oct 2017

10. Pombo, J., Ambrosio, J.: Influence of pantograph suspension characteristics on the contact quality with the catenary for high speed trains. Comput. Struct. **110–111**, 32–42 (2012)

11. Pombo, J., Ambrosio, J.: Environmental and track perturbations on multiple pantograph interaction with catenaries in high-speed trains. Comput. Struct. **124**, 88–101 (2013)

12. Song, Y., Liu, Z., Wang, H., Lu, X., Zhang, J.: Nonlinear modeling of high-speed catenary based on analytical expressions of cable and truss elements. Veh. Syst. Dyn. **53**(10), 1455–1479 (2015)

13. Song, Y., Ouyang, H., Liu, Z., Mei, G., Wang, H., Lu, X.: Active control of contact force for high–speed railway pantograph–catenary based on multi–body pantograph model. Mech. Mach. Theory **115**, 35–59 (2017)

14. Zboiński, K., Dusza, M.: Bifurcation analysis of 4-axle rail vehicle models in a curved track. Nonlinear Dyn. **89**, 863–885 (2017)

15. Zdziebko, P., Martowicz, A., Uhl, T.: Model hybrydowy do symulacji interakcji pantografu i sieci trakcyjnej. In: Mańka, M. (ed.) Projektowanie mechatroniczne: zagadnienia wybrane. AGH University of Science and Technology, Kraków (2017) (in press)

16. Zdziebko, P., Martowicz, A., Uhl, T.: Multi-domain simulation for a pantograph–catenary system investigation. In: Proceedings of the 2nd International Conference of Computational Methods in Engineering Science, Lublin University of Technology, Lublin, 23–25 Nov 2017 (in press)

17. Zdziebko, P., Uhl, T.: Finite element analysis of pantograph–catenary dynamic interaction. Arch. Transp. **39**(3), 77–85 (2016)

18. Zhou, N., Zhang, W.: Investigation on dynamic performance and parameter optimization design of pantograph and catenary system. Finite Elem. Anal. Des. **47**, 288–295 (2011)

Modelling Water Hammer with Quasi-Steady and Unsteady Friction in Viscoelastic Pipelines

Kamil Urbanowicz and Mateusz Firkowski

Abstract The model of water hammer in viscoelastic pipelines was considered. Additional term describing the retarded deformation of the pipe wall was added to continuity equation. System of partial differential equations describing this type of flow was analyzed using the method of characteristics and finite difference method. To determine the unsteady wall shear stress, a new effective method of solution which corresponds to Zielke (laminar flow) and Vardy-Brown (turbulent flow) models were used. The convolution integral of local pressure history and derivative from the material creep function is found similarly to the efficient Zielke convolution solution presented by Schohl. The research was carried out with the assumption of a quasi-steady and unsteady character of resistance. The comparison of numerical simulation and experimental results was presented.

Keywords Water hammer · Unsteady friction · Viscoelastic · Method of characteristics

1 Introduction

An appropriate modelling of a physical phenomenon which occurs in the hydraulic transients is important for safety of a pipeline system. Well-chosen parameters of the system like pipe material, wall thickness or surge protection device can protect system from unpleasant consequences. The first common danger in hydraulic transients is associated with water hammer, which takes place after sudden valve closure. It caused unsteady flow, fast pressure and velocity pulsations, which can destroy components

K. Urbanowicz · M. Firkowski (✉)
Department of Mechanical Engineering and Mechatronics,
West Pomeranian University of Technology Szczecin,
Piastów 19, Szczecin 70-310, Poland
e-mail: mateusz.firkowski@zut.edu.pl

K. Urbanowicz
e-mail: kamil.urbanowicz@zut.edu.pl

of the system. Polymer pipes exhibit a viscoelastic rheological behavior, that is why a prolonged delay in the mechanical response of the material is noticed during transient flow.

The study of the influence of the viscoelasticity of the conduit walls on the flow began in the 1960s. Hardung [12] described the physical phenomena which come into play in the arterial system as a consequence of heart action. He made a thorough study of the influence of internal wall friction and liquid viscosity on damping of pressure wave velocity. Also discussed were the limits of electric transmission line analogy to propagation of pulse waves in pipe systems. From the linearized dynamic equations of viscous incompressible fluid flow in visco-elastic tubes Martin [21] calculated frequency response of specific tube flow system. He concluded that realized calculations agree well with experiments made from Latex tubes. In 1970, Kokoshvili [20] derived the analytical solution for a system with low density polyethylene pipe, air chamber (as shock absorber) and a pump (designed to give an established flow rate). The milestone to modern modelling was deriving general equations of the transient flow in the viscoelastic properties by Rieutord and Blanchard [27]. Watters et al. [40] conducted water hammer experiments in PVC and PERMASTRAN (fiberglass-reinforced) plastic pipes. Their tests included buried and unburied pipes. Buried test pipes were more rigid, it lead to higher pressure wave velocities. For buried PER-MASTRAN pipe measured pressure increment were 15–20% higher than calculated from Joukowski formula. Sadly, in this paper no pressure runs were presented. Fortunately, the results of the study can be found in the earlier report [39] written in Utah Water Research Laboratory which were commissioned by Johns-Manville Corporation (manufacturer of PVC pipes). Meissner [22] incorporated the complex creep compliance into the unsteady momentum and continuity equations then derived the wavespeed and damping factor for an oscillating pressure wave propagating in a thin-walled viscoelastic pipe. Rieutord and Blanchard [28] presented a theoretical study of the effect of viscoelastic properties of pipe wall material on transients. Gally et al. [9] compared the calculated (using finite difference method) pressure runs, with waterhammer laboratory test data in polyethylene pipes, showing a good agreement between numerical and experimental results. Güney [11] later proposed a modified model that took into account the effects of time-varying: diameter, pipe thickness, parameter representing pipe constraints. Also, Güneys model simulated cavitation effects and used Zielke frequency-dependent friction (valid only for laminar flow). Hirschmann [13] studied the resonating conditions in viscoelastic pipes with a modified impedance method, later Franke and Seyler [8] utilized an impulse response method to calculate water hammer. This method was later further extended and modified by Sou and Wylie [32, 33]. Horlacher [14] presented pressure transients results from real HDPE water supply pipes (1625 and 2314 m long) buried in ground near Halle and Oschatz (Germany).

Waterhammer in viscoelastic pipes has been experimentally investigated at the beginning of XXI century by Covas et al. [4, 5], who conducted tests on a 277 m high density polyethylene (HDPE) pipeline which where a part of test stand build in Imperial College London. In this work, the authors presented also the new simplified model that allowed a fast calculation of pressure runs in viscoelastic

conduit. Weinerowska-Bords [41] concluded that application of a viscoelastic model is connected with many problems of different natures, of which very important is parameter estimation. Soares et al. [31] and Duan et al. [6] argued that the combination of unsteady friction and pipe wall viscoelasticity have similar effects on the transient pressures and that this two mechanisms must contribute to an accurate calculation of the damping of pressure waves. Brunone and Berni [3] studied the significance of the unsteady pipe friction effect and its interaction with viscoelasticity. Bergant et al. [1] investigated transients accompanying waterhammer experiments in a large-scale pipeline apparatus made of polyvinyl chloride (PVC). The authors of [2] conclude that the incorporation of both unsteady skin friction and viscoelastic pipe wall behaviour in the hydraulic transient model contributed to a more favourable fitting between numerical results and observed data. Keramat et al. [17] investigated cavitated flows in viscoelastic pipes using method of characteristics, and concluded that column separation can hardly result in pressures higher than the Joukowsky pressure (even for fast closure of an upstream valve). Another conclusion was that the simplest model (DVCM) of column separation provided acceptable results for cavitating flow in viscoelastic pipes. Later [18] these authors have extended their model so it could simulate the FSI (fluid structure interaction) effects. In conclusion to their paper they state that damping in transient flow may come from (unsteady) friction, (unsteady) valve resistance, small amounts of air, wall viscoelasticity, fluid structure interaction, rubbing, ratcheting and other non-elastic behaviour of supports, radiation to surrounding soil and water, pipe lining, etc. (many of these effects are unknown). When these effects are not (properly) included in the transient solver, the Kelvin-Voigt model will not only represent viscoelasticity, but all the rest too. In 2013 Keramat [16] proposed to use a time-dependent Poisson's ratio in standard Covas viscoelastic model, next year in a collaboration with Haghighi [15] showed a straightforward transient-based approach for the creep function determination.

Recently many authors [7, 23, 42] concluded that one element Kelvin-Voigt model is sufficiently good to obtain the satisfactory solution. Kodura [19] showed that, the characteristic of butterfly valve closure has a significant influence on water hammer in PE pipes for closure times higher than 25% of the return time of the reflected pressure wave. For shorter closures the maximum pressure could be calculated with Joukowsky's formula. Ferrante and Capponi [7] introduced generalized viscoelastic Maxwell model, based on fractional derivatives. After several water hammer tests for HDPE and PVC-O they conclude that this model performs slightly better than the well-known generalized Kelvin-Voigt model. The optimization function for this new model seems to improve the calibration reliability and speed.

The goal of this paper is to determine the influence of unsteady wall shear stress on velocity and pressure pulsation. Unsteady wall shear stress plays an important role in modelling transients in pipes made from elastic materials (e.g. brass or steel) [37, 44]. The question is: what is the role of unsteady wall shear stress in modelling transients in viscoelastic pipes? The answer is not clear at this moment. The preliminary Matlab simulations showed that in particular cases quasi-steady friction gives satisfactory results.

2   Modelling Liquid Flow in a Viscoelastic Pipe

2.1   Modified Solution

Polymer pipeline do not respond according to Hook law when subjected to a certain instantaneous stress. Strain can be decomposed into a sum of instantaneous elastic strain ε_e and a retarded strain ε_r [5, 11, 36]:

$$\varepsilon(t) = \varepsilon_e + \varepsilon_r(t). \tag{1}$$

The continuity equation is very similar to the one used in elastic pipeline, but does include an additional term:

$$\frac{1}{\rho c^2} \frac{\partial p}{\partial t} + \frac{\partial v}{\partial x} + 2 \frac{\partial \varepsilon_r}{\partial t} = 0, \tag{2}$$

where: p – pressure [Pa], t – time [s], v – mean velocity in pipe cross section [m/s], ρ – density of the fluid [kg/m³], c – pressure wave speed [m/s].

The retarded strain is a convolution integral of pressure and derivative of the creep function J which describes viscoelastic behavior of the pipe material:

$$\varepsilon_r(t) = \int_0^t \frac{\alpha D}{2e} \left(p(t-u) - p(0) \right) \frac{\partial J(u)}{\partial u} du, \tag{3}$$

where: D – pipe inside diameter [m], e – pipe wall thickness [m], α – pipe wall constraint coefficient [−], $J(u)$ – polymer creep function $[Pa^{-1}]$.

The creep function in generalized Kelvin-Voigt model is time dependent

$$J(t) = J_0 + \sum_{i=1}^{k} J_i \left(1 - e^{-\frac{t}{T_i}} \right), \tag{4}$$

where: J_0 – creep compliance equal to the inverse modulus of elasticity ($J_0 = 1/E_0$), T_i – the retardation time of the dashpot of i-element.

This function should be determined experimentally for polymer pipelines in independent mechanical tests. Because this function consists of at least a few terms

$$\varepsilon_r(t) = \sum_{i=1}^{k} \varepsilon_{ri}(t) \text{ and } \frac{\partial \varepsilon_r(t)}{\partial t} = \sum_{i=1}^{k} \frac{\partial \varepsilon_{ri}(t)}{\partial t}. \tag{5}$$

The derivative of the creep function is

$$\frac{\partial J(t)}{\partial u} = \frac{\partial}{\partial t} \left(J_0 + \sum_{i=1}^{k} J_i \left(1 - e^{-\frac{t}{T_i}} \right) \right) = \sum_{i=1}^{k} \frac{J_i}{T_i} e^{-\frac{t}{T_i}}. \tag{6}$$

So, Eq. (3) becomes

$$\varepsilon_r(t) = \int_0^t \frac{\alpha D}{2e} \left(p(t - u) - p(0)\right) \cdot \left(\sum_{i=1}^{k} \frac{J_i}{T_i} e^{-\frac{u}{T_i}}\right) du \tag{7}$$

and its partial derivative with respect to time t:

$$\frac{\partial \varepsilon_r(t)}{\partial t} = \frac{\alpha D}{2e} \int_0^t \frac{\partial}{\partial t} \left(p(t - u) - p(0)\right) \cdot \left(\sum_{i=1}^{k} \frac{J_i}{T_i} e^{-\frac{u}{T_i}}\right) du. \tag{8}$$

By analogy with the modeling of hydraulic resistance, where $\sum_{i=1}^{k} m_i e^{-n_i \frac{v}{R^2} u} = w(u)$, we obtain

$$\sum_{i=1}^{k} \frac{J_i}{T_i} e^{-\frac{u}{T_i}} = w_J(u) \tag{9}$$

and as

$$\frac{\partial}{\partial t} \left(p(t - u) - p(0)\right) = \frac{\partial}{\partial t} p(t - u) - \frac{\partial}{\partial t} p(0) = \frac{\partial}{\partial t} p(t - u) - 0, \tag{10}$$

one obtains

$$\frac{\partial \varepsilon_r(t)}{\partial t} = \frac{\alpha D}{2e} \int_0^t \frac{\partial p(u)}{\partial t} \cdot w_J(t - u) du. \tag{11}$$

An efficient numerical solution of this integral is presented by Schohl [30]:

$$\frac{\partial \varepsilon_r}{\partial t}(t + \Delta t) \approx \frac{\alpha D}{2e} \sum_{i=1}^{k} \underbrace{\left(x_i(t) \cdot e^{-\frac{\Delta t}{T_i}} + \frac{J_i}{\Delta t} \left[1 - e^{-\frac{\Delta t}{T_i}}\right] (p(t + \Delta t) - p(t))\right)}_{x_i(t + \Delta t)},$$

$$\tag{12}$$

where: Δt – in method of characteristics a constant time step [s]. Writing constant as

$$A_i = \frac{J_i}{\Delta t} \left[1 - e^{-\frac{\Delta t}{T_i}}\right] \text{ and } B_i = e^{-\frac{\Delta t}{T_i}}, \tag{13}$$

one has

$$\frac{\partial \varepsilon_r}{\partial t}(t + \Delta t) = \frac{\alpha D}{2e} \sum_{i=1}^{k} \underbrace{(x_i(t) \cdot B_i + A_i \cdot p(t + \Delta t) - A_i \cdot p(t))}_{x_i(t + \Delta t)} \tag{14}$$

$$= \frac{\alpha D}{2e} \sum_{i=1}^{k} A_i \cdot p(t + \Delta t) - \frac{\alpha D}{2e} \sum_{i=1}^{k} (A_i \cdot p(t) - x_i(t) \cdot B_i) \tag{15}$$

$$= p(t + \Delta t) \frac{\alpha D}{2e} \sum_{i=1}^{k} A_i - \frac{\alpha D}{2e} \sum_{i=1}^{k} (A_i \cdot p(t) - x_i(t) \cdot B_i) \quad (16)$$

Now assuming additional constants we obtain

$$F = \frac{\alpha D}{2e} \sum_{i=1}^{k} A_i \text{ and } G = \frac{\alpha D}{2e} \sum_{i=1}^{k} (A_i \cdot p(t) - x_i(t) \cdot B_i), \quad (17)$$

the final simplified equation that describe the derivative of retarded strain has the form

$$\frac{\partial \varepsilon_r}{\partial t}(t + \Delta t) = p(t + \Delta t) \cdot F - G. \quad (18)$$

The presented solution simplifies the calculation process to analyze the transients in engineering polymer pipes.

2.2 General Final Equations

For laminar flow where Darcy-Weisbach friction factor is $\lambda = 64/Re$ the complete set of equations describing this type of flow (continuity and motion) have following form:

$$\begin{cases} \frac{1}{\rho c^2} \frac{\partial p}{\partial t} + \frac{\partial v}{\partial x} + \alpha \frac{D}{e} \int_0^t \frac{\partial p(u)}{\partial t} \cdot w_J(t - u) du = 0, \\ \rho \frac{\partial v}{\partial t} + \frac{\partial p}{\partial x} + \frac{32\mu}{D^2} v + \frac{16\mu}{D^2} \int_0^t \frac{\partial v(u)}{\partial t} \cdot w(t - u) du = 0, \end{cases} \quad (19)$$

where: μ – dynamic viscosity of fluid [Pa · s].

There is no known analytical solution for this system of hyperbolic partial differential equations (also for a more complicated turbulent case). The initial condition is that on the length of the pipe from $x = 0$ to $x = L$ the mean velocity is constant $v_0 = const$, and that the linear pressure decrease in the direction of flow occurs on the pipe length. The reservoir pressure can be assumed as constant not only for the steady initial state, but also for the transient state that occurs after quick closing of the valve. On the walls of the pipe the no slip condition is generally assumed so the velocities on the walls is set to zero. At starting time $t = 0$ an instantaneous valve closure is assumed on one pipe boundary (with valve) which means that the velocity changes there instantly from v_0 to 0. Next, the pressure oscillation of fluid occurs until the final full suppression. The final pressure on the pipe length from $x = 0$ to $x = L$ is then equal to the constant reservoir pressure $p = p_R$ and the mean velocity is $v = 0$ through the entire length L of pipe. The $w(t - u)$ is a weighting function with fixed shape, and the $w_J(t - u)$ function does also have a fixed shape and it describes the mechanical material properties of the pipe.

Until analytical solution is found for above formulated system, calculations must be performed using numerical methods. In this work a method of characteristics is used with classic constant rectangular grids, to avoid problems with interpolation.

3 Simulations

3.1 Experimental Setup Details

The experimental setup was composed of three main parts [9–11]: a constant pressure reservoir, a horizontal low density polyethylene test pipe (LDPE – with Poisson's ratio $v_P = 0.38$) and a quick-closing piston valve at the downstream end of the $L = 43.1$ m long pipe as shown in Fig. 1. The pipe has an inside diameter $D = 0.0416$ m and a wall thickness $e = 0.0042$ m. Initial steady-state flow was determined by measuring volumes of water collected in a fixed time. The experimental uncertainty was estimated to within ± 3 kPa for pressure and $\pm 1\%$ for the initial flow velocity. Several transient tests were run for varied initial flow velocity and water temperature. Temperature strongly influences the mechanical behaviour of the pipe-wall material. The number of tests were conducted at various temperatures to determine the reliability of the values of creep function (Fig. 2) coefficient presented in Table 1. In all cases the closure time of the valve was $T_c = 0.012$ s.

It is not clear, as the authors of the experimental setup do not mention it [9–11], but according to the experimental setup schematic diagram it looks like that in all cases the liquid flow into the atmosphere. Güney in his Ph.D. work [10] presented the tank pressures values as a total dynamic heads h. The absolute reservoir pressure can be derived from the following formula:

$$p_R = p_{atm.} + hg\rho, \tag{20}$$
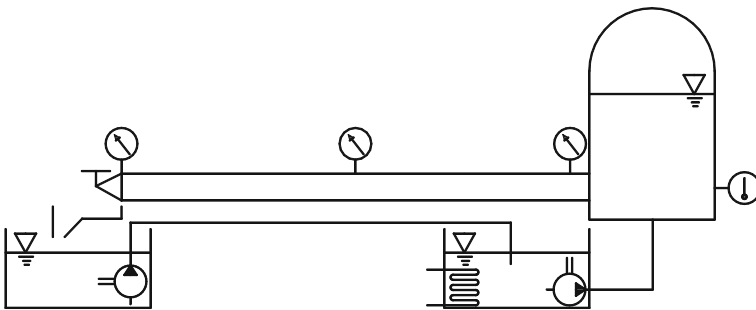
where: g – acceleration due to gravity $\left[\text{m/s}^2\right]$.

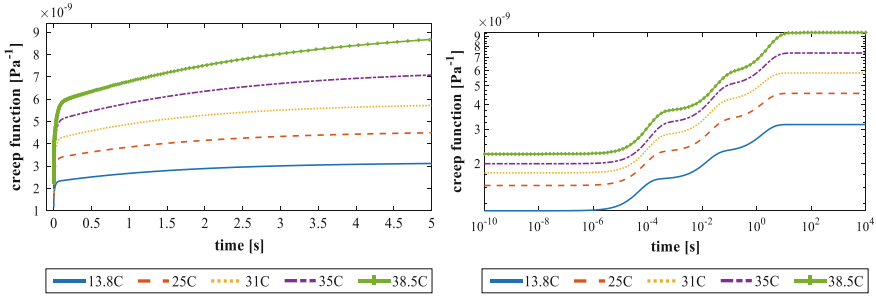**Fig. 1** Schematic diagram of Güney's experimental setup

Fig. 2 Creep compliance $J(t)$ of LDPE at different temperatures: lin-lin space (left), log-log space (right)

Table 1 Creep function coefficients (estimated by Güney)

Temp. (°C)	J_0 (Pa^{-1})	J_1 (Pa^{-1})	J_2 (Pa^{-1})	J_3 (Pa^{-1})	τ_1 (s)	τ_2 (s)	τ_3 (s)
13.8	1.144×10^{-9}	0.516×10^{-9}	0.637×10^{-9}	0.871×10^{-9}	0.56×10^{-4}	0.0166	1.747
25	1.542×10^{-9}	0.754×10^{-9}	1.046×10^{-9}	1.237×10^{-9}	0.89×10^{-4}	0.0222	1.864
31	1.791×10^{-9}	1.009×10^{-9}	1.397×10^{-9}	1.628×10^{-9}	1.15×10^{-4}	0.0221	1.822
35	1.995×10^{-9}	1.235×10^{-9}	1.797×10^{-9}	2.349×10^{-9}	1.38×10^{-4}	0.0265	2.392
38.5	2.239×10^{-9}	1.479×10^{-9}	2.097×10^{-9}	3.570×10^{-9}	1.24×10^{-4}	0.0347	3.077

Calculated values of reservoir pressures p_R, and all other important parameters needed for numerical simulation are presented in Table 2.

In Güney's works [9–11] there is no details about pressure wave speed values. In Table 2 the data were calculated for theoretical values of water density, bulk modulus, viscosity and using Young modulus $E_0 = 1/J_0$. Unfortunately, preliminary simulations have shown that the simulated results with such values of c (and with creep function coefficients from Table 1) significantly deviated from the experimental results. The values for presented simulations where therefore calibrated accordingly (Case 1 and 4 – 425 m/s; Case 2 – 375 m/s; Case 3 and 6 – 390 m/s; Case 5 – 400 m/s). In all numerical simulations, the pipeline was divided into 64 equally long elements ($N = 64$ [−], $\Delta x \approx 0.67$ [m]). With use of Poisson's ratio, one can determine the pipe-wall constraint coefficient $\alpha = 0.97$. As in some simulations the unsteady friction were calculated, in this work a new simplified method [34, 35], and a scaling procedure [38] were needed to get proper values of weighting functions coefficients. A characteristic roughness size $k_s = 1.5 \times 10^{-6}$ were assumed for LDPE pipes.

Table 2 Case details

Case	Temp. (°C)	Reservoir pressure (Pa)	Water density (kg/m^3)	Water kinematic viscosity (m^2/s)	Pressure wave speed (m/s)	Initial velocity (m/s)	Initial Reynolds number [−]	Water Bulk modulus (Pa)	Vapour pressure (kPa)
1	13.8	1.0593×10^5	999.3	1.17×10^{-6}	295.5	0.49	17422	2.14×10^9	1.57
2	25	1.0661×10^5	997.1	0.892×10^{-6}	256.3	0.55	25650	2.24×10^9	3.16
3	31	1.0670×10^5	995.3	0.784×10^{-6}	238.6	0.57	30245	2.27×10^9	4.48
4	35	1.0649×10^5	994.1	0.723×10^{-6}	226.5	0.55	31646	2.285×10^9	5.61
5	38.5	1.0649×10^5	992.6	0.675×10^{-6}	214.2	0.56	34513	2.295×10^9	6.79
6	38.5	1.1204×10^5	992.6	0.675×10^{-6}	214.2	0.82	50536	2.295×10^9	6.79

3.2   Results of Simulations

Figure 3 provides detailed comparisons between measured and calculated results corresponding to the proposed mathematical model (where: unsteady friction – **UF**, quasi-steady friction – **no UF** and no friction at all – **no F**), which included the viscoelastic behavior of the pipe wall material. A comparative study of these pressure runs disclosed the following:

1. the temperature and associated change in properties representing the conduit and liquid affect the amount of pressure amplitudes that appear in the analyzed first four second of water hammer. The smaller the temperature, the more frequent the pressure pulsation. For approximately the same initials velocities $v_0 \approx 0.55$ m/s (Case 2–Case 5), in Case 2 there are five visible pressure amplitudes and in the Case 5 there is only four;
2. low pressures (runway valleys) was more accurately simulated with use of unsteady-friction model, while high (amplitude peaks) using a quasi-steady friction model;
3. surprisingly good results were obtained with complete absence of hydraulic resistance;
4. the most important factor in the modelling of non-stationary flows in polymeric pipes looks to be the selection of the weight function w_J, which is a derivative of the creep function.

3.3   Short Discussion

As it was noticed from completed simulations (Fig. 3), the maximal pressure in viscoelastic pipes occurs not directly after valve closing but after two time steps (Fig. 4). A formula for pressure increase can be derived using the characteristic method. According to Fig. 5 presenting the method of characteristics grid near the valve boundary the maximum pressure will occur in point M, and the final equations are:

$$p_{max} = \frac{p_S - c\rho v_0 + \frac{c\rho\Delta t v_0|v_0|\lambda_0}{2D} + 2c^2\rho\Delta t G_D}{1 + 2c^2\rho\Delta t F}, \tag{21}$$

where:

$$G_D = p_D(F - H) + p_A H, \tag{22}$$

$$H = \frac{\alpha D}{2e} \sum_{i=1}^{k} A_i \cdot B_i. \tag{23}$$

In Eq. (22) p_D is calculated from the same formula as (21) but G_D need to be replaced by the product of initial pressure and constant F ($p_A F$).
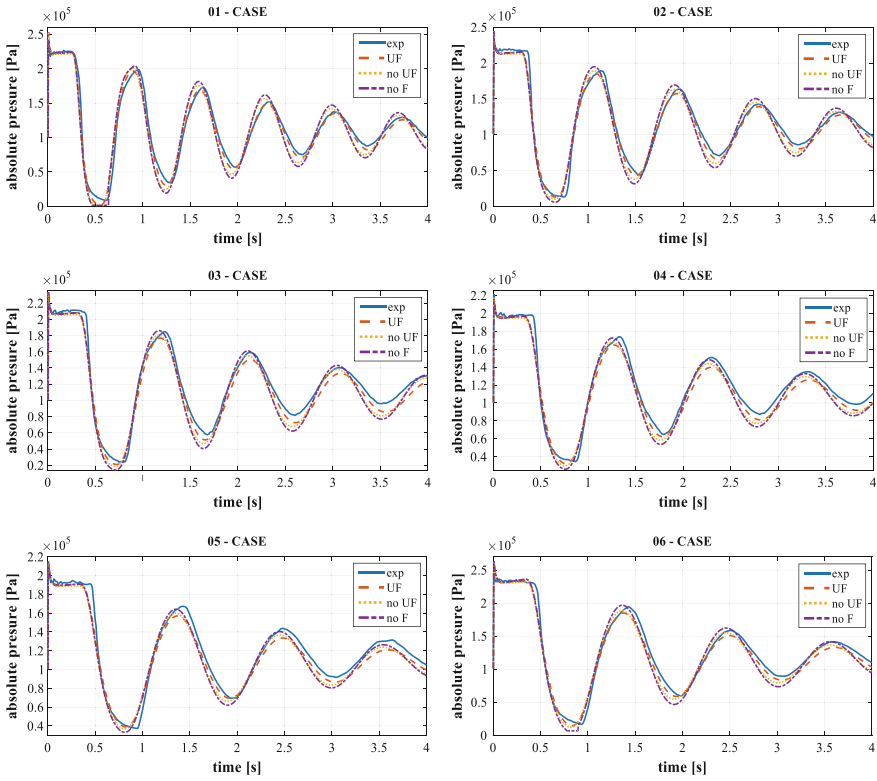
Fig. 3 Comparison of computed and measured transient pressures at the downstream end of the pipe
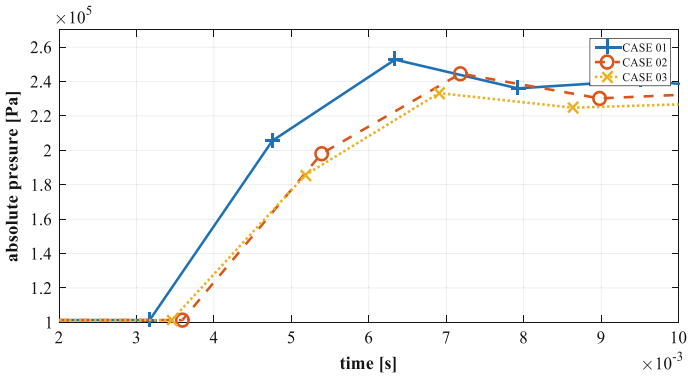

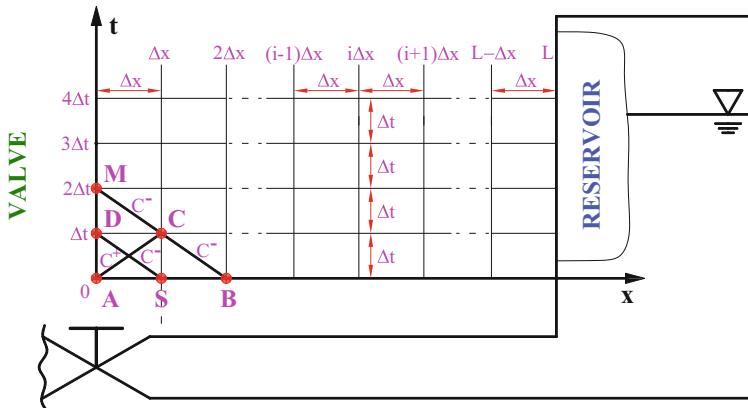**Fig. 4** Example of maximum pressures on second time steps

Fig. 5 Calculation of maximum pressures on first amplitude

From Eq. (21) one can see that the unsteady friction does not have any effect on the maximum pressure rise on the first amplitude, the opposite role fulfills the shape of assumed viscoelasticity creep function described by the generalized Kelvin-Voigt model. Also, this formula shows the weak side of the analyses fluid flow model in viscoelastic pipes. Detailed results obtained with the assumption of various time steps will be presented and discussed in an extended version of this work and during the presentation at the conference.

In the opinion of many researchers for a given temperature, the creep function depends on the stress time-history and pipe constraints, and it cannot be obtained by means of mechanical tests on pipe samples [4, 26]. So, the only way to predict the Kelvin-Voigt parameters is when transient tests can be executed on an existing pipe and evaluated as the unknowns of an inverse transient analysis (ITA) [5, 15, 31, 42, 43]. Pezzinga [25] found a decrease in the modulus of elasticity over time, and a correlation of the retardation time with the oscillation period. Moreover, some authors pointed out that the wave velocity in plastic pipes may be calculated as a function of the length of the pipeline. As an example, Mitosek with Chorzelski noticed the velocity increase when the length of the MDPE pipe decrease [24]. In a family of polyethylene pipes, one can distinguish HDPE, MDPE, LDPE, HPPE and for each type the producers give the range of the values that Young's modulus can take [41]. If the values are taken from handbooks of polymers the range of values can also differ slightly: the modulus of elasticity for MDPE takes the values 0.6–0.8 GPa, while for HDPE one can find the values of Young's modulus of a range 0.7–1.0 GPa [4] or even 0.6–1.4 GPa [29]. In consequence, the values of pressure wave speed calculated theoretically may differ significantly from the observed ones. However, in the perception of the authors of this paper what mainly affects the results of the simulation, is the shape of the creep function, and in particular its derivative, which occurs in the convolutional integral in the continuity equation. By changing the coefficients of the exponential terms describing this function one can "control"

significantly simulated pressure run (increase-decrease the value of the successive pulsation and pressure amplitudes).

4   Conclusions

The main purpose of the presented research was to determine the influence of the applied friction model on the obtained simulation results. Studies have shown that unsteady friction affects the frequency of emerging pressure amplitudes. Omission of unsteady friction on the modeling stage increases the frequency and values of the peak pressures on following amplitudes. It follows that unsteady friction are closely related to the velocity of the pressure wave propagation.

However, to thoroughly analyze the impact of the applied friction models, new experimental studies are needed. They should be made for small Reynolds numbers ($Re < 6000$) in a simple horizontal pipeline. The length of the conduit should be at least 150 m so as to minimize the effect of local resistance on the discharge from the pressure reservoir. There should be no elbows in this system that distort simulated results by introducing additional local resistance (unknown for unsteady flows).

The sub-objective goal was to study the flow model itself. The research done outlined some of the problems associated with the experimental creep function that will be solved and shown in the extended version of this work.

References

1. Bergant, A., Hou, Q., Keramat, A., Tijsseling, A.S.: Experimental and numerical analysis of waterhammer in a large-scale PVC pipeline apparatus. In: Proceedings of 4th International Meeting on Cavitation and Dynamic Problems in Hydraulic Machinery and Systems, pp. 27–36. Belgrade, Serbia (2011)
2. Bergant, A., Hou, Q., Keramat, A., Tijsseling, A.S.: Waterhammer tests in a long PVC pipeline with short steel end sections. J. Hydraul. Struct. **1**(1), 23–34 (2013)
3. Brunone, B., Berni, A.: Wall shear stress in transient turbulent pipe flow by local velocity measurement. J. Hydraul. Eng. **136**(10), 716–726 (2010)
4. Covas, D., Stoianov, I., Ramos, H., Graham, N., Maksimovic, C.: The dynamic effect of pipe-wall viscoelasticity in hydraulic transients. Part I - experimental analysis and creep characterization. J. Hydraul. Res. **42**(5), 517–531 (2004)
5. Covas, D., Stoianov, I., Ramos, H., Graham, N., Maksimovic, C.: The dynamic effect of pipe-wall viscoelasticity in hydraulic transients. Part II - model development, calibration and verification. J. Hydraul. Res. **43**(1), 56–70 (2005)
6. Duan, H.F., Ghidaoui, M., Lee, P.J., Tung, Y.K.: Unsteady friction and visco-elasticity in pipe fluid transients. J. Hydraul. Res. **48**(3), 354–362 (2010)
7. Ferrante, M., Capponi, C.: Viscoelastic models for the simulation of transients in polymeric pipes. J. Hydraul. Res. **55**(5), 1–14 (2017)
8. Franke, P.G., Seyler, F.: Computation of unsteady pipe flow with respect to visco-elastic material properties. J. Hydraul. Res. **21**(5), 345–353 (1983)
9. Gally, M., Güney, M.S., Rieutord, E.: An investigation of pressure transients in viscoelastic pipes. J. Fluids Eng. **101**(4), 495–499 (1979)

10. Güney, M.S.: Contribution à l'étude du phénomène de coup de bélier en conduite viscoélastique. Ph.D. thesis, Université de Lyon I (1977)
11. Güney, M.S.: Waterhammer in viscoelastic pipes where cross-section parameters are time dependent. In: Proceedings of the 4th International Conference on Pressure Surges, pp. 189–204. BHRA Fluids Engineering, Bath, UK (1983)
12. Hardung, V.: Propagation of pulse waves in visco-elastic tubings. In: Handbook of Physiology. American Physiological Society, chap. 7, pp. 107–135 (1962)
13. Hirschmann, P.: Resonanz in visko-elastischen Druckleitungen. 29. Lehrstuhl für Hydraulik u. Gewässerkunde, Technical University of München (1979)
14. Horlacher, H.: Transient behavior of HDPE pipes due to pressure fluctuations. In: Proceedings of 3rd International Conference on Hydro-Science and Engineering, vol. 3. Brandenburg University of Technology at Cottbus, Cottbus/Berlin, Germany (1998)
15. Keramat, A., Haghighi, A.: Straightforward transient-based approach for the creep function determination in viscoelastic pipes. J. Hydraul. Eng. **140**(12), 04014058 (2014)
16. Keramat, A., Kolahi, A.G., Ahmadi, A.: Water hammer modelling of viscoelastic pipes with a time-dependent Poisson's ratio. J. Fluids Struct. **43**, 164–178 (2013)
17. Keramat, A., Tijsseling, A.S., Ahmadi, A.: Investigation of transient cavitating flow in viscoelastic pipes. In: IOP Conference Series: Earth and Environmental Sciencs, vol. 12, No. 1, p. 012081 (2010)
18. Keramat, A., Tijsseling, A.S., Hou, Q., Ahmadi, A.: Fluid-structure interaction with pipe-wall viscoelasticity during waterhammer. J. Fluids Struct. **28**, 434–455 (2012)
19. Kodura, A.: An analysis of the impact of valve closure time on the course of water hammer. Arch. Hydro-Eng. Environ. Mech. **63**(1), 35–45 (2016)
20. Kokoshvili, S.M.: Water hammer in a viscoelastic pipe. Polym. Mech. **6**(5), 786–788 (1970) (Translated from Mekhanika Polimerov **5**, 908–912)
21. Martin, T.: Pulsierende strömung in visko-elastischen leitungssystemen. Ingenieur-Archiv **37**(5), 315–325 (1969) (in German)
22. Meissner, E.: Berechnung instationärer strömungsvorgänge in kunststoffleitungen. 19. Lehrstuhl für Hydraulik u. Gewässerkunde. Technical University of München (1976)
23. Meniconi, S., Brunone, B., Ferrante, M., Massari, C.: Energy dissipation and pressure decay during transients in viscoelastic pipes with an in-line valve. J. Fluids Struct. **45**, 235–249 (2014)
24. Mitosek, M., Chorzelski, M.: Influence of visco-elasticity on pressure wave velocity in polyethylene MDPE pipe. Arch. Hydro-Eng. Environ. Mech. **50**(2), 127–140 (2003)
25. Pezzinga, G., Brunone, B., Cannizzaro, D., Ferrante, M., Meniconi, S., Berni, A.: Two-dimensional features of viscoelastic models of pipe transients. J. Hydraul. Eng. **140**(8), 04014036 (2014)
26. Pezzinga, G., Brunone, B., Meniconi, S.: Relevance of pipe period on Kelvin-Voigt viscoelastic parameters: 1D and 2D inverse transient analysis. J. Hydraul. Eng. **142**(12), 04016063 (2016)
27. Rieutord, E., Blanchard, A.: Influence d'un comportement viscoélastique de la conduite dans le phénomène du coup de bélier. C. R. Acad. Sci. Paris **274**, 1963–1966 (1972)
28. Rieutord, E., Blanchard, A.: Pulsating viscoelastic pipe flow–water-hammer. J. Hydraul. Res. **17**(3), 217–229 (1979)
29. Saechtling, H.: International Plastics Handbook, 3rd edn. Hanser Pub, Munich (1995)
30. Schohl, G.: Improved approximate method for simulating frequency-dependent friction in transient laminar flow. J. Fluids Eng. **115**, 420–424 (1993)
31. Soares, A.K., et al.: Analysis of PVC pipe-wall viscoelasticity during waterhammer. J. Hydraul. Eng. **134**(9), 1389–1394 (2008)
32. Suo, L., Wylie, E.B.: Impulse response method for frequency-dependent pipeline transients. J. Fluids Eng. **111**(4), 478–483 (1989)
33. Suo, L., Wylie, E.B.: Complex wavespeed and hydraulic transients in viscoelastic pipes. J. Fluids Eng. **112**(4), 496–500 (1990)
34. Urbanowicz, K.: Simple modelling of unsteady friction factor. In: Proceedings of the 12th International Conference on Pressure Surges, pp. 113–130. BHR Group, Dublin, Ireland (2015)

35. Urbanowicz, K.: Analytical expressions for effective weighting functions used during simulations of water hammer. J. Theor. App. Mech.-Pol. **55**(3), 1029–1040 (2017)
36. Urbanowicz, K., Firkowski, M., Zarzycki, Z.: Modelling water hammer in viscoelastic pipelines: short brief. J. Phys.: Conf. Ser. **760**(1), 012037 (2016)
37. Urbanowicz, K., Zarzycki, Z.: Improved lumping friction model for liquid pipe flow. J. Theor. App. Mech.-Pol. **53**(2), 295–305 (2015)
38. Urbanowicz, K., Zarzycki, Z., Kudźma, S.: Universal weighting function in modeling transient cavitating pipe flow. J. Theor. App. Mech.-Pol. **50**(4), 889–902 (2012)
39. Watters, G.Z.: The behavior of PVC pipe under the action of water hammer pressure waves. Reports (Paper 20) (1971)
40. Watters, G.Z., Flammer, G.H., Jeppson, R.W.: Water hammer in PVC and reinforced plastic pipe. J. Hydraul. Div. **102**(7), 831–843 (1976)
41. Weinerowska-Bords, K.: Viscoelastic model of waterhammer in single pipeline–problems and questions. Arch. Hydro-Eng. Environ. Mech. **53**(4), 331–351 (2006)
42. Weinerowska-Bords, K.: Alternative approach to convolution term of viscoelasticity in equations of unsteady pipe flow. J. Fluids Eng. **137**(5), 054501 (2015)
43. Yao, E., Kember, G., Hansen, D.: Water hammer analysis and parameter estimation in polymer pipes with weak strain-rate feedback. J. Eng. Mech. **142**(8), 04016063 (2016)
44. Zarzycki, Z., Kudźma, S., Urbanowicz, K.: Improved method for simulating transients of turbulent pipe flow. J. Theor. App. Mech.-Pol. **49**(1), 135–158 (2011)

The Concept of Autonomous Damper in Vehicle Suspension

Jan Warczek, Rafał Burdzik and Łukasz Konieczny

Abstract The vibration of a vehicle treated as an object can be varied in two basic ways. Parametric or structural modifications can be made. Applying parametric modifications is not always possible. Examples are the suspension of motor vehicles. Changing the elasticity factor is limited by the allowable deflection arrow for different loads. Structural modifications are used for vibration isolation or vibration elimination. Vibro-isolation tasks are somewhat contradictory and practically impossible to achieve in passive systems. The alternative is to use in the suspension system elements with adjustable characteristics. On the vibrations object of the specified mass acts on the control signal. The control signal has a force dimension. This force is produced by a vibration isolator for which vibration parameters are input signals. The control force is the weighted sum of the forces of elasticity and damping. These components of the control force are proportional to relative displacement and relative velocity, respectively. In the developed concept of autonomous vibration damper, a control algorithm is applied which deactivating damper if the damping force influences the increase acceleration of the object's vibration.

Keywords Vibration control · Semi active shock absorber · Dissipation of vibration energy

1 Introduction

The work of all machines and equipment, both very simple as well as complex, is closely related to the vibroacoustic processes occurring in themselves or their

J. Warczek · R. Burdzik · Ł. Konieczny (✉)
Faculty of Transport, Silesian University of Technology, Krasińskiego 8, 40-019
Katowice, Poland
e-mail: lukasz.konieczny@polsl.pl

J. Warczek
e-mail: jan.warczek@polsl.pl

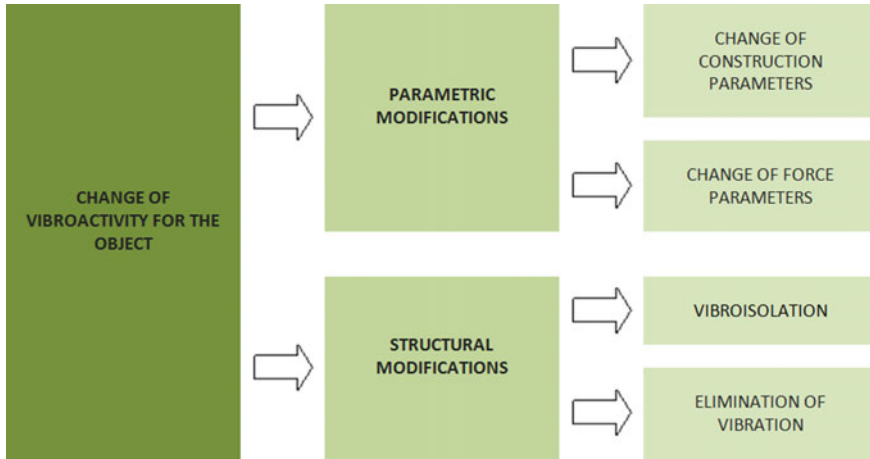R. Burdzik
e-mail: rafal.burdzik@polsl.pl

Fig. 1 Ways of changing vibration of an object

surroundings. Vibration processes are most commonly undesirable. Ensuring the reliability and durability of machines and equipment, and above all, protection of people and the environment from the harmful effects of vibration generated, requires effective ways and means to counter the emergence or spread. The vibroactivity of a machine (device) treated as an object can be changed in two basic ways by introducing parametric or structural modifications [3, 5, 6].

Parametric modifications consist in changing the construction parameters of the object or the parameters of the forces acting on the object. Most often, they relate to structural parameters such as inertia and stiffness of components and dampening in motion connections. Applying parametric modifications is not always possible or intentional. Examples may be automobile suspension where the change in suspension coefficient is limited by the allowable deflection arrow at load changes [8]. We apply structural modifications, whose generalized scheme is shown in Fig. 1.

The change of vibroactivity through structural modifications can be realized in two ways. The first involves attaching to an object mounted on the substrate additional EL elements (dynamic vibration eliminators). These are power generating devices applied to a specific point of the vibration isolation facility and having a fixed operating line. They reduce the motion parameters of the object's vibration (e.g., reduce displacement) in the direction of force. The second method of structural modification is to introduce between the object and the substrate an additional element called the vibration isolator. If kinematic constraints affect the substrate, the vibration isolation of the object is called displacement one. If force exertions affect an object, then vibration isolation is called strength one. Practical calculations of the vibration isolation system rely on the choice of the vibration isolator so that the vibration frequency of the object-vibro-isolator system is different from that of the external force spectrum.

2   Research Problem

In linear systems, a vibration transfer coefficient is used to evaluate the quality of vibration isolation. It is defined as the ratio of the amplitude of the object's vibration to the amplitude of the extortion force (Fig. 2).

The vibration isolation evaluation is based on the transfer function $T(\omega)$. For the selected extortion frequency, the values of this function can be determined as:

- for kinematic extortion $T = |z_1/z|$,
- for force extortion $T = |F/P|$.

where: z_1—amplitude of object vibration, z—vibration amplitude of the substrate, F—force transferred to the ground, P—extortion force.

If $T \leq 1$, vibration isolation is effective. Changes in vibration isolation properties are achieved by varying the frequency of system vibration. The range of vibration isolation is the wider the lower the frequency of the system's vibration. The introduction of vibration-limiting resonance damping reduces the vibration isolation properties of the vibration isolation. This is a major disadvantage of passive vibration isolation systems. And it is not the only one. For example, for a vibration isolation system, the system should meet the following conditions:

- relative displacement $\Delta = z_1 - z$ from the vibration isolation facility should be less than the permissible values (due to static deflection), i.e., the rigid system,
- object should be insulated from the kinematic excitations (minimum acceleration, velocity or displacement) i.e., the soft system.

The formulated tasks that the vibration isolation system should perform are contradictory and practically impossible to achieve in passive systems. New possibilities create active vibration reduction systems. The beginning of active vibration reduction methods is the last decade of the nineteenth century. Methods of active reduction of vibration of means of communication, machines and devices have their origins

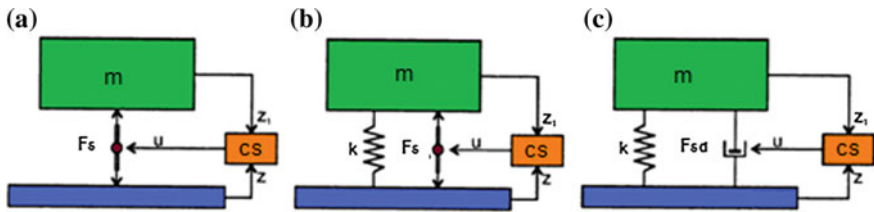**Fig. 2** Classical vibration isolation system of one-way system
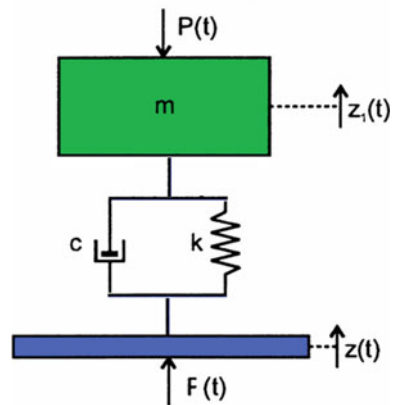
Fig. 3 Schemes of active vibration isolation systems, **a** active, **b** hybrid, **c** semi-active

in 1892 [2, 4]. In practical applications, active systems are reduced to structural or parametric vibration modifications using an additional energy source. The controller includes measuring transducer (of displacement, speed, acceleration, force, etc.) an amplifier and the actuator (hydraulic, pneumatic, electric). Control is carried out in very different ways. The actuator can produce a force that compensates for vibration inducing forces and can also actively change the system parameters.

There are three essential elements in the vibration and control systems: the object, the regulator and the connection between them. On the vibration isolation object with mass m of, affects a control signal which has the dimension of force (control force). Object mass m of the vibration isolation affects a control signal which has the dimension of force (control force) F_s.

This force is produced by a vibration isolator for which the vibration parameters of the substrate and vibration isolation are input signals. Control force is the sum of the weight of the elastic force and damping force. These components of the control force are proportional to relative displacement and relative velocity, respectively. Proportional coefficients are the coefficients of elasticity and damping of the vibration isolator, respectively.

The task of improving the quality of vibration isolation (e.g. minimizing vibration acceleration of the object) for the required force is to optimize the choice of elasticity and damping factors to obtain the desired vibration transfer coefficient. The operation of the active vibration isolator is to generate additional dynamic extortion forces that provide the required vibration parameters of the vibration isolation object. Depending on the use of additional power source, vibration reduction systems (vibration isolators and vibration eliminators) can be divided into active, hybrid and semi-active systems (Fig. 3).

In active systems, additional force or displacement is generated, applied directly to the insulated object to compensate for force and kinematic forces that are considered as interference. They require the use of high power sources (BOSE solution). Semi-active systems (semi-active) include passive, elastic and damping elements, but the spring and damping forces can be altered (adjustable), e.g., an adjustable energy dissipation element. They require an external source of low power (at the signal level). Examples are MR shock absorbers with magneto-rheological liquid. Hybrid systems combine the properties of active and passive systems (e.g. the ABC solution in Mercedes cars).

Fig. 4 Diagram of suspension model with vibration damper control. m_2—sprung mass, m_1—unsprung mass, k_1—stiffness of wheel, k_2—stiffness of suspension, c_2—damping of suspension, c_1—damping of wheel, h—excitation, z_2—vertical displacement of sprung mass, z_1—vertical displacement of wheel, p_1, p_2—velocity sensor, cs—controller
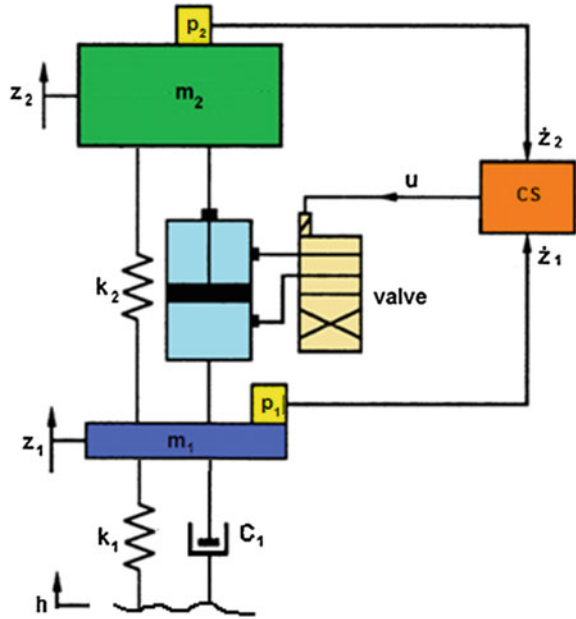
In semi-active systems, vibration isolation characteristics vary depending on changes in interference induced by changes in elasticity or damping at low power output. Damping parameters can be changed quickly and at low power consumption, e.g. with electrohydraulic valves. In the case of changes in spring elasticity the situation is more difficult. The spring stores energy, so changing the coefficient of elasticity when it is under load requires the supply or absorption of energy. Realization of rapid changes in elasticity requires the use of a high power source (so the active or hybrid system). With slow changes in elasticity, low power is required and one of the ways to achieve these changes is the use of a pneumatic spring (Citroen Hydro-active Suspension Solution).

3 Vibration Damper Proposal

The diagram of the tested vehicle suspension model together with the control system is shown in Fig. 4. It contains a semi-active system with continuous damping control F_{sd}.

The accepted assumptions of the developed concept of autonomous vibration damper are as follows:

1. developed element will be able to be used interchangeably with passive shock absorbers,
2. all components of the system will be included in one package,

3. due to the minimization of energy demand, the developed damper will be a semi-active system

A damper generates a control force associated with the relative velocity of the sprung and not sprung masses. Damping power modifications can be implemented by the control system according to any feedback function from the state variables. In the hydraulic system the adjustment can be done by servo valve. The fulfilment of the condition of the vibration damper's ability to operate as a passive element forced the use of a discontinuous control algorithm [6, 7].

In the classic passive suspension system, the shock absorber can only draw energy from the system (converts mechanical vibration to heat) [1]. However, if the speed of the not sprung mass is greater than the speed of the sprung mass (in the indicated direction), then the damping force is the accelerating force of the vehicle. The concept of discontinuous control consists in switching off a damper if there are conditions where the damping force affects the acceleration of the vibration object—the sprung mass.

$$If\ \dot{z}_2\ and\ \dot{z}_1\ are\ opposing\ sings,\ then\ F_{sd} = F_d \quad (1)$$

$$If\ \dot{z}_2\ and\ \dot{z}_1\ the\ sigs\ are\ the\ same,\ then:$$
$$if\ |\dot{z}_1| > |\dot{z}_2|\ then\ F_{sd} = 0, \quad (2)$$
$$if\ |\dot{z}_1| < |\dot{z}_2|\ then\ F_{sd} = F_d.$$

where: F_{sd}—corrected damping force, F_d—damping force of a damper.

In order to avoid jitter shifting the damping force should take place at a time when the relative speed is zero. In practice, this means that the ground (input) and vibration isolation motions must be continually monitored and processed logically in order to decide if a damper is to be turned on or off. This type of control is a semi-active ON-OFF dual-stack control. The jump parameter change is realized by disconnecting and restoring the constraints, i.e. by changing the structure of the system, so it is a semi-active vibration system with variable structure.

4   Simulation Verification of Vibration Damper Model Assumptions

A half-active vibration damper with discontinuous control was designed in the dual-mode suspension of the vehicle [10, 12]. The model was implemented in MATLAB's SIMULINK environment. In the case of operation when the control is off, the shock absorber characteristics are nonlinear and asymmetrical [2, 9, 11, 13]. This is a classic example of damping behaviour of passive dampers (Fig. 5).

Deterministic and random determinants were used in the study. Stochastic extortion correspond to road roughness profiles specified in ISO standards. The vibration of the sprung mass of m_2 was used to assess the performance of the shock absorber
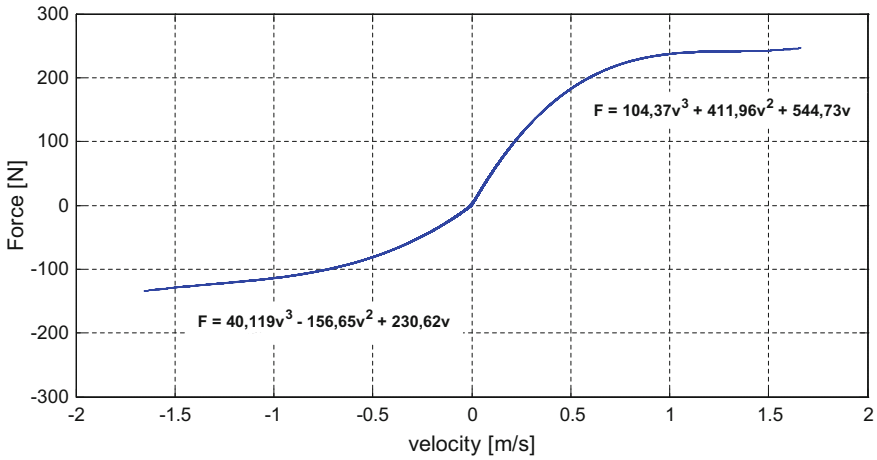
Fig. 5 Damping characteristics used in the studies

Fig. 6 Comparison of sprung mass displacement, for extortion of chirp type (blue—the controller switched off, black—damping characteristic regulator switched on)

with variable characteristics (temporarily deactivated by the control system). Two parameters of motion of this mass, displacement and acceleration were analysed. Figures 6, 7 and 8 show a comparison of vibration displacement results obtained for different types of extortion. Analogous results obtained for acceleration of vibrations of the sprung mass are shown in Figs. 9, 10 and 11.

The presented results confirm the effectiveness of the damper with adjustable characteristics. For the practical implementation of the control, the signal of the relative suspension deflection shall be used, supplemented by signals of acceleration of the sprung and not sprung masses. The mounting points for the sensors are identical to the shock absorber mountings for the suspension and the bodywork.

Fig. 7 Comparison of displacement of sprung mass for stroke extortion (blue—the controller switched off, black—damping characteristic regulator switched on)
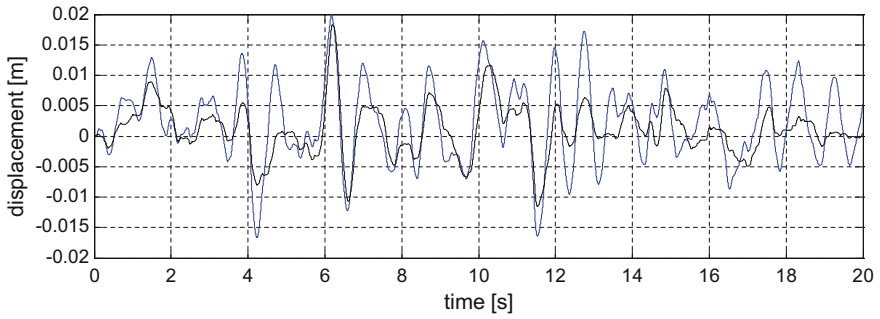
Fig. 8 Comparison of displacement of sprung mass for random extortion (blue—the controller switched off, black—damping characteristic regulator switched on)

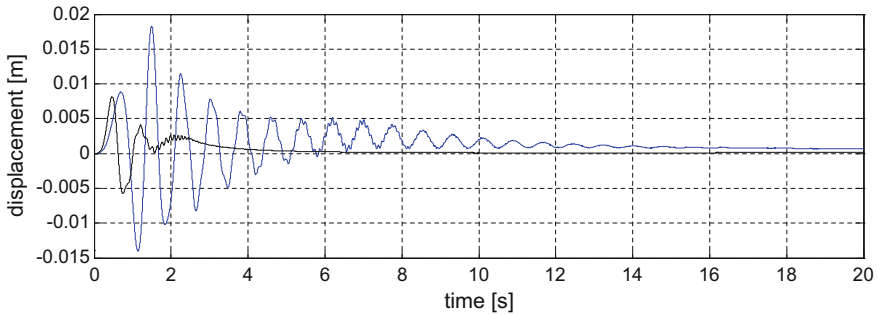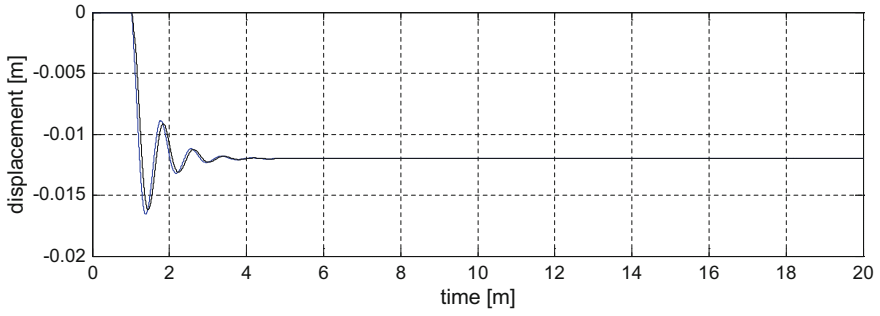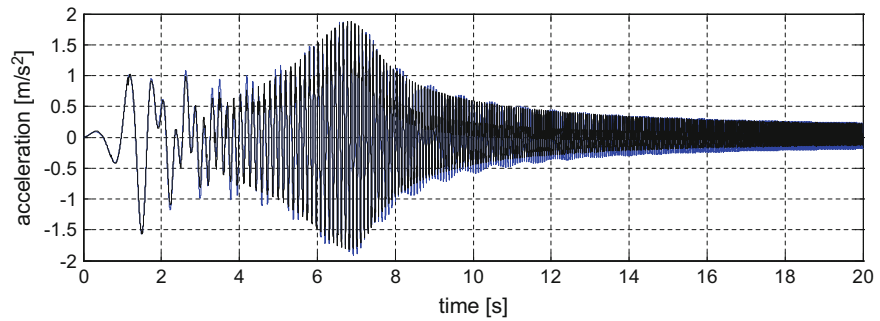**Fig. 9** Comparison of acceleration of sprung mass for extortion of chirp type (blue—the controller switched off, black—damping characteristic regulator switched on)
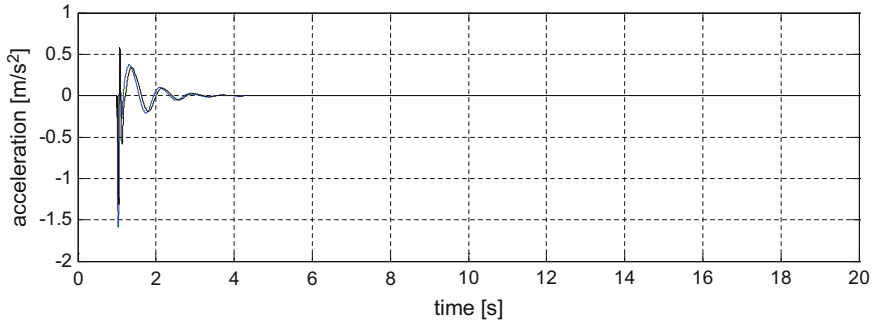
Fig. 10 Comparison of acceleration of sprung mass for extortion of stroke type (blue—the controller switched off, black—damping characteristic regulator switched on)
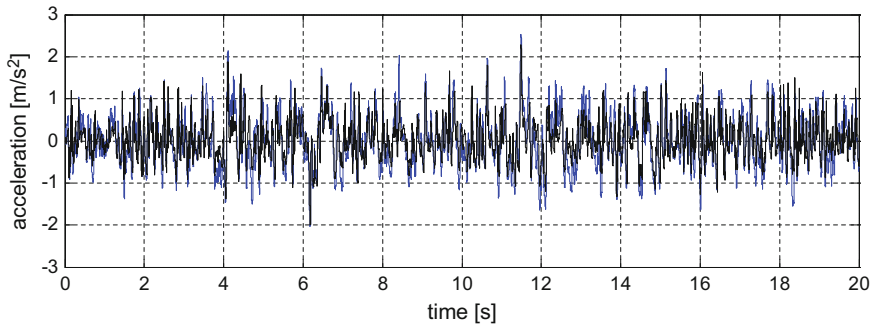
Fig. 11 Comparison of sprung mass acceleration for extortion of random type (blue—the controller switched off, black—damping characteristic regulator switched on)

5 Summary

The developed vibration damper will be a discontinuous damper that will function as a standalone interchangeable element in passive suspension systems. In practical implementation, the assumption of such a system can be a linear current generator, whose load influences the value of the generated control force. The use of a linear generator provides the ability to quickly change the characteristics needed for the correct operation of the proposed solution.

References

1. Alonso, M., Comas, Á.: Thermal model of a twin-tube cavitating shock absorber. Proc. Inst. Mech. Eng. Part D: J. Autom. Eng. **222**(11), 1771–1780 (2008)
2. Dixon, C.J.: The Schock Absorber Handbook. Wiley, West Sussex (2007)

3. Gardulski, J., Warczek, J.: Active suspension research in the aspect of travel safety. Telematics and transport safety. In: TiBT'06, vol. 2: Safety of Transport (2006)
4. Giorgetti, N., Bemporad, A., Tseng, H.E., Hrovat, D.: Hybrid model predictive control application towards optimal semi-active suspension. Int. J. Control **79**(5), 521–533 (2006)
5. Karnopp, D., Crosby, M.J., Harwood, R.: Vibration control using semi-active force generators. J. Eng. Ind. **96**, 619 (1974)
6. Rakheja, S., Sankar, S.: Vibration and shock isolation performance of a semi-active "on-off" damper. J. Vib. Acoust. Stress Reliab. Des. **107**, 398–403 (1985)
7. Shida, N., Ye, Z., Yong, W., Konghui, G.: Velocity and displacement-dependent damper: a novel passive shock absorber inspired by the semi-active control. Mech. Syst. Sig. Process. **99**(15), 730–746 (2018)
8. Tseng, H.E., Hrovat, D.: State of the art survey: active and semi-active suspension control. Veh. Syst. Dyn. **53**(7), 1034–1062 (2015)
9. Warczek, J.: Application of time shift for nonlinear damping characteristic identification. In: Transport Problems, vol. 4, issue 3, part 2. Gliwice, Poland (2009)
10. Warczek, J., Burdzik, R.: Visco-elastic model of dynamic of hydraulic damper as a basis for determining the measurement condition. In: Scientific Papers of Transport, issue 66. Silesian University of Technology (2010)
11. Warczek, J., Burdzik, R., Peruń G.: The method for identification of damping coefficient of the trucks suspension. Smart diagnostics V. In: Uhl T. (ed.) Selected, Peer Reviewed Papers from the 5th International Congress of Technical Diagnostics, Krakow, Poland, 3–5 Sept 2012, pp. 281–289. Trans Tech Publications, Stafa-Zurich (2014); Key Engineering Materials; vol. 588, pp. 1662–9795
12. Warczek, J., Młyńczak, J., Celiński, I.: Simulation studies of a shock absorber model proposed under conditions of different kinematic input functions. Vibroengineering Procedia **6**, 248–253 (2015)
13. Olejnik, P., Awrejcewicz, J.: Coupled oscillators in identification of nonlinear damping of a real parametric pendulum. Mech. Syst. Sig. Process. **98**, 91–107 (2018)

Validation of the Numerical Model of Impuls I Electric Multiple Unit Driver's Cab

Paweł Wątroba, Mariusz Pawlak and Damian Gąsiorek

Abstract The article presents the validation of a numerical model of the electric multiple unit (EMU) driver's cab. The subject of the study was the cab of the driver of the Impuls I rail vehicle of Newag S.A. The numerical model was developed in the LS-Dyna environment based on the documentation received from the manufacturer. The driver's cab was modelled as shell elements, the additional parts required for the crash test were modelled as solid elements. Experimental research was carried out on the order of Newag S.A. on the experimental track of the Railway Institute in Węglewo near Zmigrod according to PN-EN 15227. The collision was recorded by 3 cameras used for fast changing phenomena. Additionally, acceleration sensors were placed at specific locations of the construction. The article presents results from experimental research and their comparison with the results of numerical simulation.

1 Introduction

The requirements for structural integrity of rail vehicles in Europe come mainly from the International Union of Railways (UIC) and normative documents such as the PN-EN 15227 standard describing the requirements for calculations, experimental studies and validation of rail vehicle collisions. The requirements included in the standard

P. Wątroba · M. Pawlak (✉) · D. Gąsiorek
Faculty of Mechanical Engineering, Silesian University of Technology, ul.
Konarskiego 18A, 44-100 Gliwice, Poland
e-mail: mariusz.pawlak@polsl.pl

P. Wątroba
e-mail: pawel.watroba@polsl.pl

D. Gąsiorek
e-mail: damian.gasiorek@polsl.pl

411

do not cover all possible accident scenarios but provide some degree of resistance to damage that will provide an adequate degree of protection in most cases where active safety measures are insufficient. It is required to provide a level of protection consistent with the probable threat of collision and this can be achieved by simulating the most common types of collisions causing injury and death [1–4].

Validating a numerical model is a very important modeling process. It involves comparing the results of numerical simulations with experimental results. The purpose of this process is to quantify the errors resulting from the assumptions made in the model, which has been solved numerically. For a model to be considered as correct it must meet the following criteria [2, 5, 6]:

- sequences in crash are the same,
- there are similar deformations,
- the difference of dissipated energy cannot be greater than 10% of the initial energy from the test,
- the simulation produces a global force curve, which exhibits the same general characteristics as measured in the test.

If collision energy is absorbed by many different mechanisms or progressive stages, the following comparison criteria should be applied:

- The permissible difference in displacement is 10% compared to the test value,
- The average force value read out from the force-displacement graph should be 10% of the test value.

The high compatibility of the numerical model with real tests depends mainly on the quality of the numerical model and kinematic imaging. Material properties used in crushing zones should be empirically determined, while nominal values may be used in other parts of the model. Ideally, only the mass and speed should be matched to the results of the calibration test [2].

Simulations of reference scenarios (based on which the validation is done) must be carried out using numerical models that faithfully reflect construction geometry and energy absorbing devices. On the other hand, the numerical calculations of complete vehicles must be based on the same modeling techniques and degree of detail as the simulations of real tests [2].

Poland is one of the few countries in the world that have rolling stock and infrastructure to conduct experimental research (currently there are 8 in the world), which is situated in Węglewo near Żmigród. Using the available infrastructure, in this study we analysed the driver's cab of the Impuls I rail vehicle of Newag S.A.

2 Experimental Tests

Experimental tests were carried out at the Test Track of the Railway Research Institute in Żmigród on the order of Newag S.A. Two crash tests were carried out, the first including the side absorbers and the second without the absorbers. The purpose of the first test was to determine how the vehicle would behave while absorbing energy

Fig. 1 Driver's cab with and without the side absorbers [7]

Fig. 2 Method of fixing
EMU driver's cab to the
coach wall with highlighted
crash zone [7]

from the side absorbers, while the second was to test the impact of the crush zone in the rear of the driver's cab. In this paper, we consider only the second test [7] (see Fig. 1).

Experimental research required special preparation of the driver's cab and the coach during the collision. The front wall behind the driver's cab was modified in such a way that it could be bolted to the coach wall by force sensors [7] (see Fig. 2).

Additionally, for the second test, anti-climbing plates were installed in place of the absorbers (see Fig. 3). The same plates were on the second coach wall. The crash zone in the vehicle Impuls I is located behind the driver's seating position [7] (see Fig. 2).

Fig. 3 Anti-climbing plates
instead of side absorbers [7]

Table 1 List of masses

	Coach C [t]	Coach A [t]
Coach frame	10	10
Bogie	5	5
Back wall	3.66	–
Front wall	3.2	3.5
Additional frame	3	5.94
Load box 1	14.25	–
Load box 2	3.71	–
Load box 3	3.6	–
Load box 4	3.79	–
Summary	55.21	29.44

The cab and coaches are fitted with quadrant symmetry markers that allow analyzing the sequence of collisions and obtaining additional parameters from the crash test. Looking from the side, there were 13 markers, two on the front wall, while looking upwards, two markers in the seat, 6 markers on the crossbar connecting the side walls of the cab and one on the front wall. Two markers were located on the frame of Coach A [7].

The mass of the wagon with the cab mounted was added to steel boxes filled with concrete to achieve the most even pressure on the wheels. The total weight of the wagon C with the installed cab was 55.21t (Coach C), while the standing wagon was 29.44t (Coach A). The list of masses of an individual coach is shown in Table 1 [7].

The collision was carried out in accordance with the diagram shown in Fig. 4. The coach C with the driver's cab, was accelerated by a locomotive up to 34 km/h,
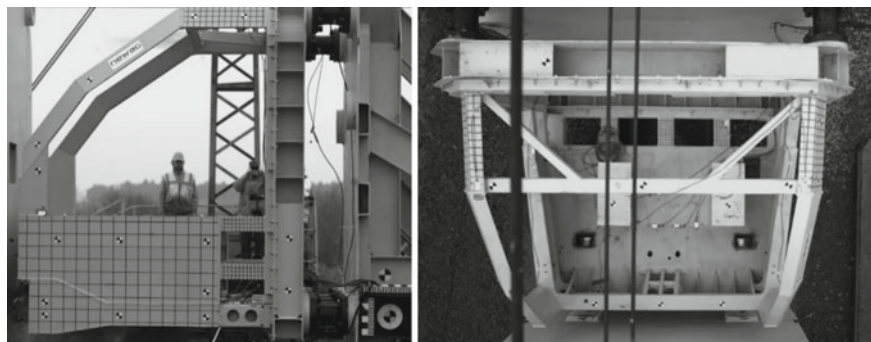
Fig. 4 Location of quadrant symmetry markers [7]
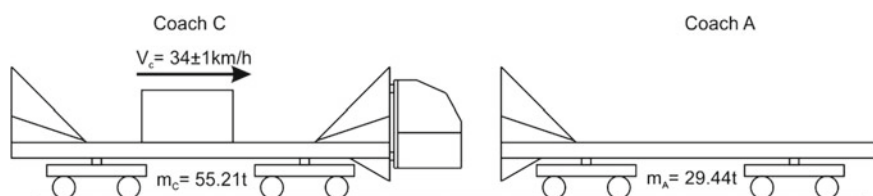
Fig. 5 Scheme of crash test

and just before the collision a coach was disengaged, and impacted on the unbraked coach A [7] (Fig. 5).

The crash test proceeded well, the velocity of the coach measured just before the impact reached 34.2 km/h. The greatest deformations occurred in the crumbling zone, thus absorbing the greatest part of the energy. Figure 6 shows the driver's cab just after the collision [7].

3 Numerical Model

The numerical model was based on the documentation received from the vehicle's manufacturer Newag S.A. The driver's cab model was simplified to a surface model. Surface model was prepared in SpaceClaim environment [8] (Fig. 7).

The prepared surface model was imported into the LS PrePost environment and then a finite element mesh was created. On the coach, a coarse mesh of finite elements was created. A high-quality mesh was created on the driver's cab [9–13] (Fig. 8).

The exact numerical model has created many finite elements, 450,000 nodes and above 600,000 elements, so it was decided to simplify the model in order to reduce the calculations time. Reduction of time is very important for optimization, which will be carried out later. The geometry of the coach was replaced by a lumped mass with a moment of inertia. The m1 represents the mass of coach C without wheelsets,

Fig. 6 Driver's cab after crash test [7]
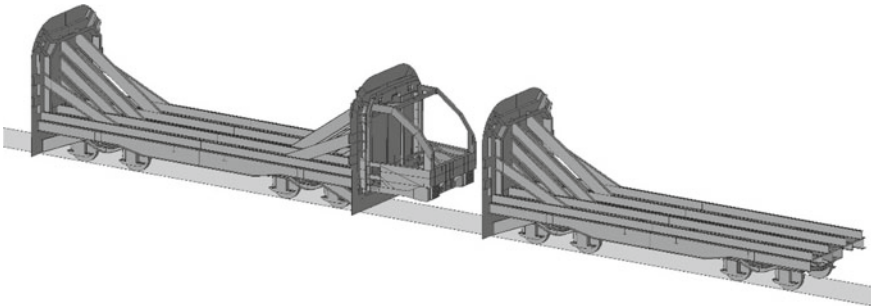
Fig. 7 Surface model from SpaceClaim environment

m1 equals 51,048 kg. The m2 is 25,193 kg and corresponds to the weight of coach A without wheelsets. The m3 weight is 1050 kg and corresponds to the weight of half of two wheelsets. Primary suspension spring was reduced to equivalent stiffness. The k_{eq} is equal 5.28 [kN/mm] (Fig. 9).

The moment of inertia was appointed from full model and shown in Table 2.

The simplified model is shown in Fig. 10. The numerical model has about 300,000 nodes and 300,000 elements. Accelerometers were modeled in LS Dyna by *ELE-MENT_SEATBELT_ACCELEROMETER in locations similar to markers in real

Fig. 8 Finite element mesh for the full model
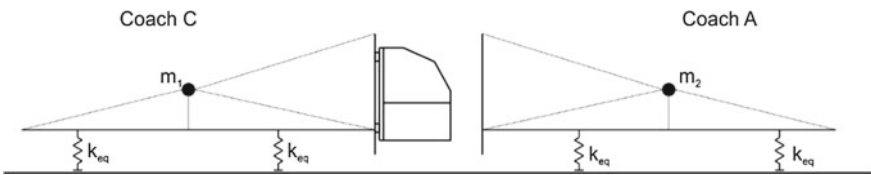
Fig. 9 Scheme of simplification model

Table 2 List of moment of inertia

	Coach C (kg/mm^2)	Coach A (kg/mm^2)
I_{xx}	3.42e+10	1.56e+10
I_{yy}	5.46e+11	2.21e+11
I_{zz}	5.42e+11	2.21e+11
I_{xy}	2.75e+8	6.86e+7
I_{yz}	6.84e+7	−3.03e+7
I_{xz}	−8.99e+9	1.88e+10

tests. This approach is popular in the automotive industry to measure the safety of passengers during crash tests [14–16].

The material properties were defined based on the experimental results obtained from the NEWAG company. True stress versus true plastic strain was shown in Fig. 11 [17].

4   Validation of the Numerical Model

The scheme of crash test presented in Fig. 5 was also applied in the numerical model. Time of crash simulation was set to 100 ms and as a result of the collision and crash
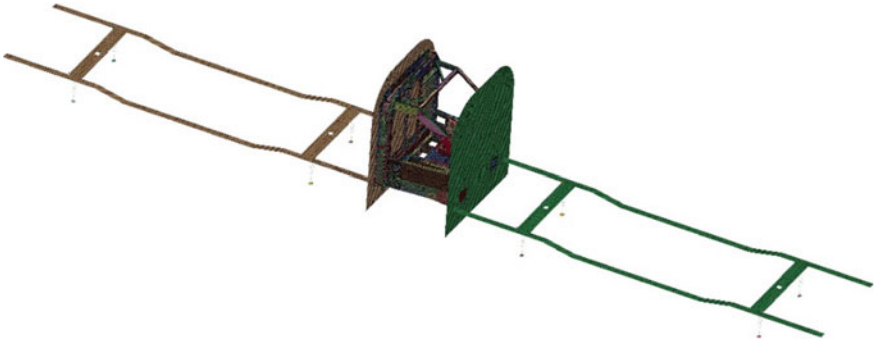
Fig. 10 Simplified model in LS-PrePost
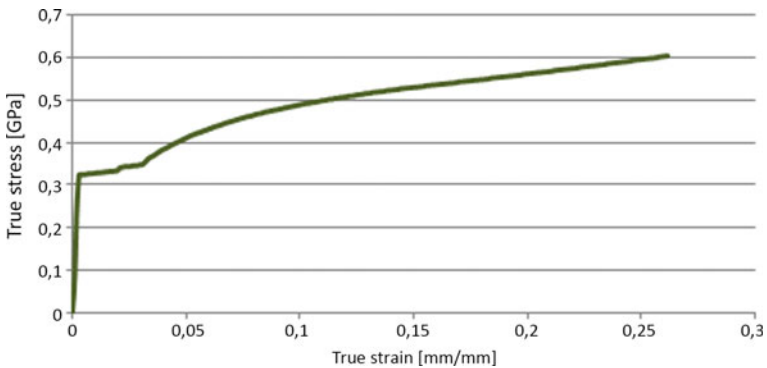
Fig. 11 True stress versus true strain

sequence and deformation character in the crash zone was the same as on the real test. In Fig. 12 a comparison between crash test and simulation has been shown [18–20].

The velocity was measured on the rigid bodies coaches in center of mass. The comparison velocity has been shown in Fig. 13.

In figure, velocity characteristics are similar. At the beginning, the velocity measured on the high-speed camera is clearly distorted. The difference in results between test and simulation in 100 ms was 7% for coach C and 10% for coach A. The energy characteristic has been shown in Fig. 14.

Dissipated energy in the real test was equal to 804 kJ. In numerical model, total dissipation energy was close to the real test. The total dissipation energy in the simulation was equal to 850 kJ. The difference of dissipated energy was equal to 2% of initial energy from real test.

The total deformation in the crash zone was measured between two markers. First was located on the front wall, second on the driver's cab (Fig. 15).

In figure, the deformation in the crush zone is very similar to the real test, with the difference in deformation less than 6%. There is a good correlation between deformation of the real object and simplified model, what gives the ability to make
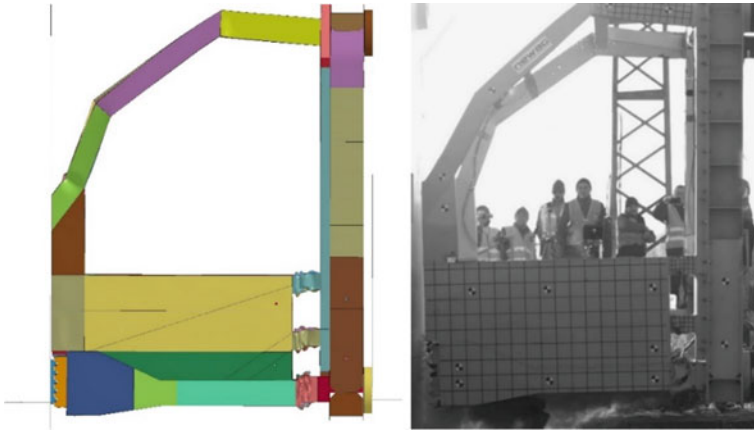
Fig. 12 Comparison of geometry after the collision of a numerical model with the test
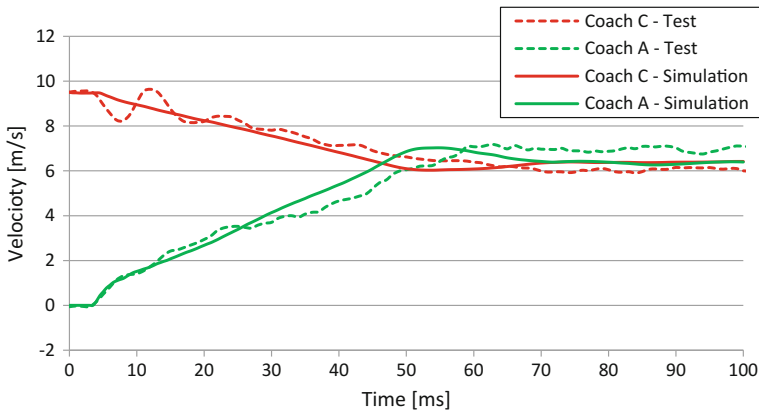
Fig. 13 Comparison of velocity between numerical model and crash test

sensitivity analysis of cab for optimization purposes in a similar way as in literature [21, 22].

The acceleration was measured at the driving position in the cab. The characteristics of acceleration were shown in Fig. 16.

In figure, it is noticeable that the acceleration curve from the simulation is different from the actual test. This is likely due to the simplification of the model and the sizing of the finite element mesh. To receive better acceleration characteristics much better mesh quality model must be applied. This issue will be the subject of further work.
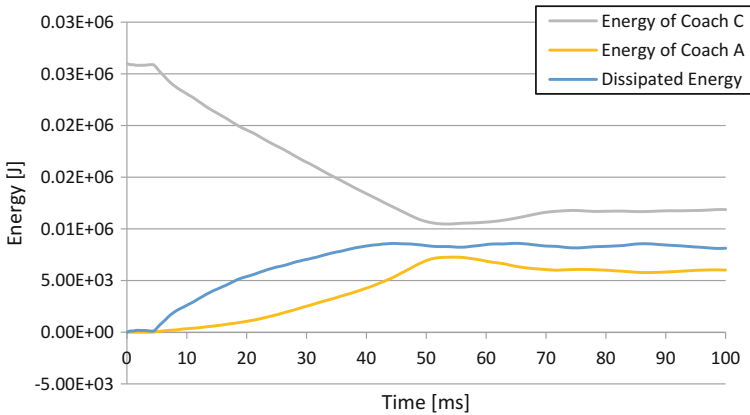
Fig. 14 Energy characteristics of simulation
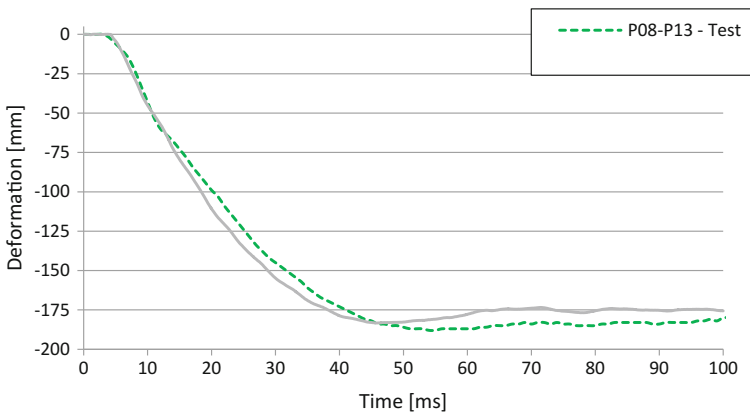
Fig. 15 Comparison of deformation in crash zone

5   Conclusions

The work has shown that there is a convergence between velocities and energy of coaches the from the test and the simulation. The difference in absorbed energy is only 2% of the initial energy. The velocity and displacements fall within the error limits of 10%. The exception is in the acceleration, for which convergence has not been achieved. The conclusion is that to analyze acceleration a more detailed model is required and finer mesh must be applied. Simplification of the numerical model has significantly reduced computational time, which is very importance for optimization purposes. Further work must be done to fully validate the numerical model with the acceleration characteristics. The obtained numerical model will be used to solve shape optimization problem of deformation tubes.
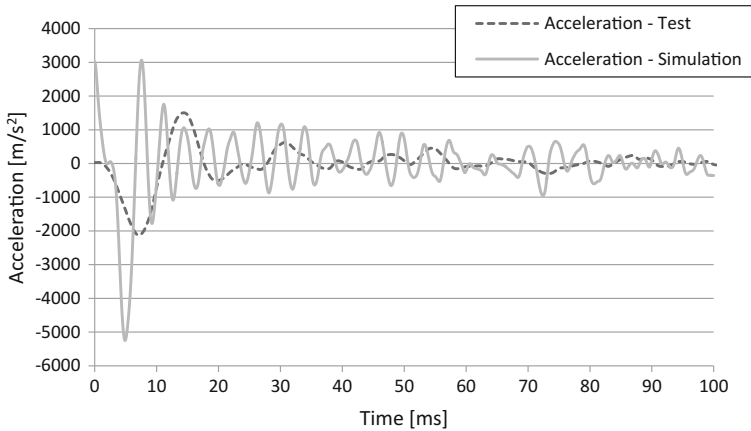
Fig. 16 Comparison of acceleration at the driving position

References

1. SAFETRAIN: Train crashworthiness for Europe, sub-task 1.1 collision risk analysis. Final report
2. EN 15227:2008: Railway applications. Crashworthiness requirements for railway vehicle bodies
3. Pereira, M.: Structural crashworthiness of railway vehicles. In: 7th World Congress of Rail Research (2006)
4. UIC 518: Testing and approval of railway vehicles from the point of view of their dynamic behaviour—Safety—Track fatigue—Running behavior (2009)
5. Milho, J.F., Ambrósio, J.A.C., Pereira, M.F.O.S.: Validated multibody model for train crash analysis. Int. J. Crashworthiness **8**(4), 339–352 (2003)
6. Polach, O., Evans, J.: Simulations of running dynamics for vehicle acceptance: application and validation. Int. J. Railway Technol. **2**(4), 59–84 (2013)
7. Sprawozdanie nr LW/69.01/14 z testu zderzeniowego kabiny elektrycznego zespołu trakcyjnego IMPULS produkcji Newag S.A. Instytut Kolejnictwa, Warszawa, 30 Dec 2014
8. Priante, M., Tyrell, D., Perlman, B.: A collision dynamics model of a multi-level train. In: Proceedings of IMECE2006—ASME International Mechanical Engineering Congress and Exposition, Chicago, Illinois, USA, 5–10, Nov 2006
9. Belytschko, T., Liu, W.K., Moran, B.: Nonlinear Finite Elements for Continua and Structures. Wiley, New York (2001)
10. Danek, W., Gąsiorek, D.: Symulacja numeryczna zderzenia pojazdu z aluminiowym, wykopywanym słupem oświetleniowym. Paper presented at the 56. Sympozjon Modelowanie w Mechanice, Ustroń, 25 Feb–1 Mar 2017

11. Fasanella, E.L., Jackson, K.E., Kellas S.: Soft soil impact testing and simulation of aerospace structures. Paper presented at the 10th LS-DYNA users conference, Dearborn, 8–10 June 2008

12. Gao, G.J., Tian, H.Q.: Train's crashworthiness design and collision analysis. Int. J. Crashworthiness **12**(1), 21–28 (2007)

13. Kirkpatrick, S., Schroeder, M., Simons, J.: Evaluation of passenger rail vehicle crashworthiness. Int. J. Crashworthiness **6**(1), 95–106 (2001)

14. Hallquist, J.O.: LS-DYNA Keyword User's Manual; Version 971. Livermore Software Technology Company, Livermore, CA (2006)

15. Hallquist, J.O.: Recent developments in LS-DYNA. Paper presented at the German LS-DYNA Forum, Bamberg, 13 Oct 2011

16. Pawlak, M.: The Acceleration severity index in the impact of a vehicle against permanent road equipment support structures. Mech. Res. Commun. **77**, 21–28 (2016)

17. Sprawozdanie z badań Nr M/800/2014/E. Laboratorium materiałowe Glinik, 30 Sept 2014

18. Hiermaier, S.J.: A Structures Under Crash and Impact, Continuum Mechanics Discretization and Experimental Characterization. Springer, New York (2008)

19. Kosaka, I.: Improvement of energy absorption for the side member using topography optimization. Paper presented at the 11th international LS-DYNA users conference, Dearborn, 6–8 June 2010

20. Xue, X., Schmid, F.: Modelling study to validate finite element simulation of railway vehicle behaviour in collisions. In: Proceedings of 5th European LS-DYNA Users Conference

21. Duda, S., Gembalczyk, G., Ławniczek, R., Trawiński, T.: Comparison of dynamic interactions in the drive system of electric locomotive EU07 before and after the modernization drive unit. In: 20th International conference on Engineering Mechanics, Book of full text, pp. 140–143. Svratka, Czech Republic, 12–15 May 2014

22. Mężyk, A., Klein, W., Pawlak, M., Kania, J.: The identification of the vibration control system parameters designed for continuous miner machines. Int. J. Non-Linear Mech. 1–8 (2017) (in press)

Approach for Determination of Functioning of Lower Limb Muscles

Wiktoria Wojnicz, Bartłomiej Zagrodny, Michał Ludwicki, Małgorzata Syczewska, Jerzy Mrozowski and Jan Awrejcewicz

Abstract The purpose of the study is elaboration of approach for determination of functioning of chosen muscles that are essential for gait performance (Tibialis Anterior, Rectus Femoris, Gastrocnemius Medialis, Biceps Femoris). The scope of the study involves the analysis of the symmetric planar motion performing in the sagittal plane of the body by applying planar multibody model and electromyography signals (EMG) registered over normal gait performance. The analysis is performed by applying two types of multibody model: six degree of freedom system and seven degree of freedom system. Inverse dynamics task was used to calculated joint moments influenced ankle joints, knee joints and hip joints. Applied model also described single support phase and double support phase by taking into consideration the model of interaction between the ground and the contact foot. The activity states of considered muscles are determined on the base of their average activations and sequences in time.

W. Wojnicz (✉)
Mechanical Engineering Faculty, Gdansk University of Technology,
G. Narutowicza 11/12 Street, 80-233 Gdansk, Poland
e-mail: wiktoria.wojnicz@pg.edu.pl

B. Zagrodny · M. Ludwicki · J. Mrozowski · J. Awrejcewicz
Mechanical Engineering Faculty, Lodz University of Technology,
Stefanowskiego 1/15 Street, 90-924 Lodz, Poland
e-mail: bartlomiej.zagrodny@p.lodz.pl

M. Ludwicki
e-mail: michal.ludwicki@p.lodz.pl

J. Mrozowski
e-mail: jerzy.mrozowski@p.lodz.pl

J. Awrejcewicz
e-mail: jan.awrejcewicz@p.lodz.pl

M. Syczewska
The Children's Memorial Health Institute, Dzieci Polskich 20 Avenue, 04-730
Warsaw, Poland
e-mail: M.Syczewska@ipczd.pl

1   Introduction

The gait is a complex performance, which is induced by nervous system function (due to reflexes), muscle system action, skeletal system and external load configuration including gravitational field influence. Brain induces muscle activation that provide to gait performance (physical activity of a person) and muscle activation depends on descending and reflex inputs [7].

To estimate activity of muscles inducing a motion the electromyography (EMG) system is used [14] and muscle excitation timing can be estimated [8, 9]. To analyze EMG data there are applied processing algorithms, e.g. rectifying, smoothing, filtering, normalization [4]. Furthermore, one should consider the action of muscle by taking into account the path of this muscle and skeletal system configuration. It is worth noticing that the function of one-joint muscle is different from the function of two-joint muscle (or multi-joint muscle) [19].

To improve and stabilize movement activity a muscle co-contraction mechanism can occur [11]. During the prolonged action of this mechanism the metabolic transformation is growing up and this may increase the risk of damage of muscles causing this co-contraction action.

The aim of this study was to elaborate an approach for determination of functioning (activity) of the chosen lower limb muscles, which are essential for human gait performance. The scope of the study involves the analysis of the symmetric planar motion performing in the sagittal plane of the body by applying planar multibody model and EMG signals registered over normal gait performance.

2   Method

In the scope of this study it was investigated an influence of four muscles of lower limb: Tibialis Anterior (1), Rectus Femoris (2), Gastrocnemius Medialis (3), Biceps Femoris (4) (Fig. 1). These muscles were chosen due to the fact that they are superficial muscles that have a high priority in gait performance (the number of chosen muscles was caused by the limited possibility of EMG system used in experiments). The Tibialis Anterior is a one-joint muscle that performs dorsiflexion of the foot and slight inversion at the ankle joint [10]. The Rectus Femoris is a two-joint muscle that conducts flexion of the hip joint and extension of the knee joint. The Gastrocnemius Medialis is a two-joint muscle that performs plantar flexion of the foot at the ankle and flexion of the knee joint. The Biceps Femoris is a two-joint muscle that conducts: flexion and lateral rotation of the knee joint; extension and lateral rotation of the hip joint.

Fig. 1 Muscle system
examined: Tibialis Anterior
(1), Rectus Femoris (2),
Gastrocnemius Medialis (3),
Biceps Femoris (4)
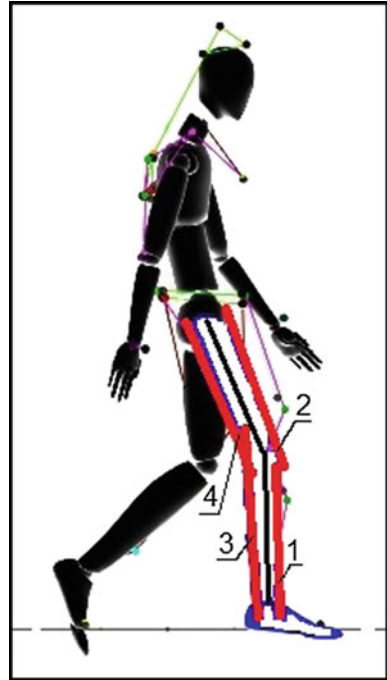
To determine functioning of chosen muscles of lower limb over given gait phase the following inference method was developed. According to this method, one should first determine the condition of the joint examined [i.e. it is stiffened (blocked) or released (unblocked)]. After that one should consider whether a co-contraction of muscles acting on this joint is observed. To apply proposed inference method, one should obtain the following data:

(1) kinematic data (relative angular displacements, relative angular velocities and relative angular accelerations of lower limb segments);
(2) kinetic data (net joint moments (joint moments));
(3) EMG data (measured and processed EMG).

In order to determine whether considered joint is stabilized or is released, one should analyze kinematic data by considering the influence of gravitational force and skeletal system configuration (in what way skeletal components interact with each other). To consider a muscle co-contraction one should analyze muscle influence by taking into account the motor function of muscles. It was assumed that functioning (activity) of each considered muscle is determined by average activation and its sequence in time.

To perform a kinetic (dynamic) analysis of normal human gait in the single support and the double support phase, two biomechanical models were used [17]. There were developed by applying the Newton-Euler approach [1] and the method of seg-
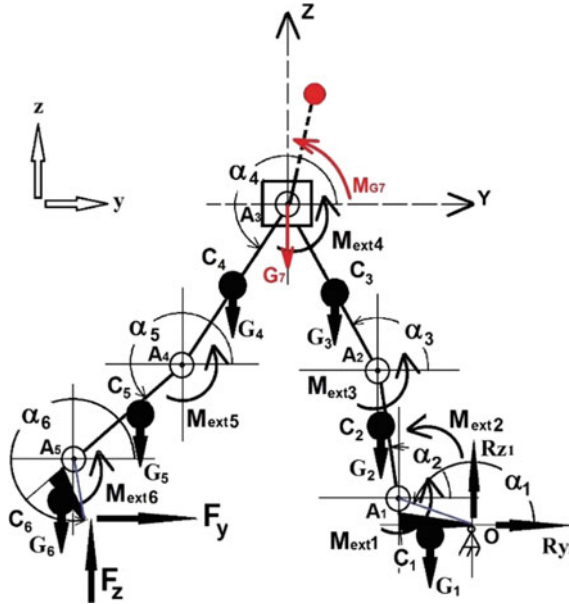
Fig. 2 The 6DOF model (*O*—the point between the support foot and the ground; A_1—the ankle joint of stance leg; A_2—the knee joint of stance leg; A_3—the hip joint; A_4—the knee joint of swing leg; A_5—the hip joint of swing leg; α_i—the angle of the *i*-th segment (each angle is measured as an absolute coordinate); G_i—the gravity force of the *i*-th segment that acts at its centre of gravity C_i; M_{exti}—the external moment acting on the *i*-th segment; F_y and F_z—the *y*-th component and *z*-th component of the reaction force influenced by the ground; R_{y1}—the *y*-th component of stance leg reaction force; R_{z1}—the *z*-th component of the stance leg reaction force; *y*—the sagittal axis; *z*—the vertical axis) [17]

mentation described in [2]. The first biomechanical model is the 6DOF model that treats a human body as a structure composed of six segments serially linked by hinge joints (Fig. 2). The second biomechanical model is the 7DOF model that treats a body as a dendritical structure composed of seven segments linked by hinge joints (Fig. 3). Over each phase of the gait the 6DOF or 7DOF model is connected to the ground at the joint O. During the single support phase two interaction forces acting at the sixth segment are equal to zero ($\underline{F_y} = 0$ and $F_z = 0$), whereas over the double support phase these two forces have some defined values ($\underline{F_y} \neq 0$ and $F_z \neq 0$). These values can be measured by applying a force plate (an external device used to measure interaction forces between the foot and the ground).

The 6DOF model assumes that a load of the upper part of the body (a force G_7 and the moment of this force M_{G7}) influences the stance leg. The mathematical form of the 6DOF model is a non-linear system of six equations:

Fig. 3 The 7DOF model (symbols are described in the Fig. 2) [17]
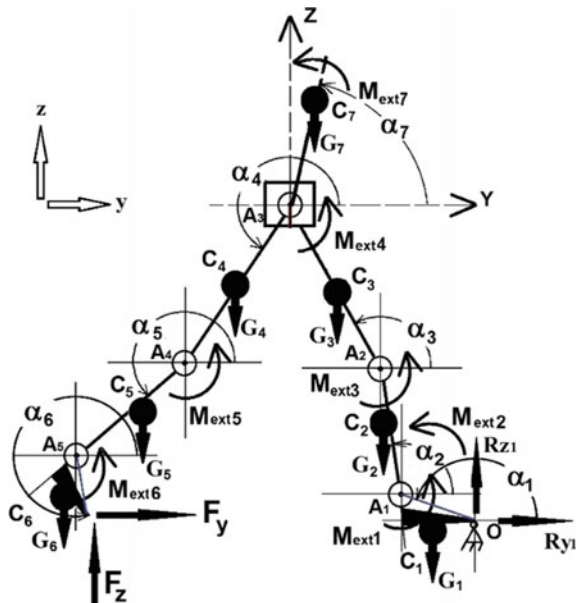
$$
\begin{bmatrix}
A'_{11} & A'_{12} & A'_{13} & A'_{14} & A'_{15} & A'_{16} \\
A'_{21} & A'_{22} & A'_{23} & A'_{24} & A'_{25} & A'_{26} \\
A'_{31} & A'_{32} & A'_{33} & A'_{34} & A'_{35} & A'_{36} \\
A'_{41} & A'_{42} & A'_{43} & A'_{44} & A'_{45} & A'_{46} \\
A'_{51} & A'_{52} & A'_{53} & A'_{54} & A'_{55} & A'_{57} \\
A'_{61} & A'_{62} & A'_{63} & A'_{64} & A'_{65} & A'_{67}
\end{bmatrix}
\cdot
\begin{bmatrix}
\ddot{\alpha}_1 \\
\ddot{\alpha}_2 \\
\ddot{\alpha}_3 \\
\ddot{\alpha}_4 \\
\ddot{\alpha}_5 \\
\ddot{\alpha}_6
\end{bmatrix}
=
\begin{bmatrix}
M'_1(\alpha_1, F_y, F_z) \\
M'_2(\alpha_2, F_y, F_z) \\
M'_3(\alpha_3, F_y, F_z) \\
M'_4(\alpha_4, F_y, F_z) \\
M'_5(\alpha_5, F_y, F_z) \\
M'_6(\alpha_6, F_y, F_z)
\end{bmatrix},
\tag{1}
$$

where: α_i—the i-th angular displacement of the i-th segment (the i-th joint angle); $\ddot{\alpha}_i$—the i-th angular acceleration of the i-th segment; $M'_i(\alpha_i, F_y, F_z)$—the i-th segment moment of the 6DOF model; A'_{ij}—non-linear functional coefficient of the 6DOF model that depends on the segment mass, segment length, segment radius of gyration, segment moment of inertia and segment angular displacements.

The 7DOF model assumes that the upper part of the body is modelled as one segment (the seventh segment). The mathematical form of the 7DOF model is a non-linear system of seven equations:

$$
\begin{bmatrix}
A''_{11} & A''_{12} & A''_{13} & A''_{14} & A''_{15} & A''_{16} & A''_{17} \\
A''_{21} & A''_{22} & A''_{23} & A''_{24} & A''_{25} & A''_{26} & A''_{27} \\
A''_{31} & A''_{32} & A''_{33} & A''_{34} & A''_{35} & A''_{36} & A''_{37} \\
A''_{41} & A''_{42} & A''_{43} & A''_{44} & A''_{45} & A''_{46} & A''_{47} \\
A''_{51} & A''_{52} & A''_{53} & A''_{54} & A''_{55} & A''_{56} & A''_{57} \\
A''_{61} & A''_{62} & A''_{63} & A''_{64} & A''_{65} & A''_{66} & A''_{67} \\
A''_{71} & A''_{72} & A''_{73} & A''_{74} & A''_{75} & A''_{76} & A''_{77}
\end{bmatrix}
\cdot
\begin{bmatrix}
\ddot{\alpha}_1 \\
\ddot{\alpha}_2 \\
\ddot{\alpha}_3 \\
\ddot{\alpha}_4 \\
\ddot{\alpha}_5 \\
\ddot{\alpha}_6 \\
\ddot{\alpha}_7
\end{bmatrix}
=
\begin{bmatrix}
M''_1(\alpha_1, F_y, F_z) \\
M''_2(\alpha_2, F_y, F_z) \\
M''_3(\alpha_3, F_y, F_z) \\
M''_4(\alpha_4, F_y, F_z) \\
M''_5(\alpha_5, F_y, F_z) \\
M''_6(\alpha_6, F_y, F_z) \\
M''_7(\alpha_7)
\end{bmatrix},
\qquad (2)
$$

where: $M''_i(\alpha_i, F_y, F_z)$—the i-th segment moment of the 7DOF model; A''_{ij}—non-linear functional coefficient of the 7DOF model that depends on the segment mass, segment length, segment radius of gyration, segment moment of inertia and segment angular displacements.

It is worth emphasizing that the i-th segment moment ($M'_i(\alpha_i, F_y, F_z)$ of the 6DOF model and $M''_i(\alpha_i, F_y, F_z)$ of the 7DOF model) depends on the joint moment M_{ij} generated between the i-th segment and j-th segment ($M_{ij} = M_{ji}$).

3 Application

Proposed inference method was applied to study the right lower limb having four EMG electrodes fixed according to the SENIAM requirement. Investigation was performed over one single support phase (that occurs after the toe-off of the left limb, i.e. from the 10% of stride) and following one double support phase to 58% stride period. To perform a normal gait analysis an experimental testing was conducted on one male health person [70.2 kg body mass, 183 cm body height, moments of inertia (Table 1)] that did five full steps (a middle step was taken into consideration). To obtain kinematic data a motion capture system OptiTrack Flex 13 with dedicated software was used. To measure interaction forces the Steinbichler force plate was applied. To measure surface EMG signals the Noraxon Myotrace 400 with MyoResearch XP Clinical Edition software was used (four channels system). The barefoot person walked with preferred speed in vision-on mode. It was assumed that all tests were done in a homogenic gravity field (with constant gravity acceleration).

Kinematic data were calculated by applying method presented in [15] and methods of signal processing (filtering, interpolating and differentiating): relative angular displacements are presented in Fig. 4; relative angular velocities are given in Fig. 5; relative angular accelerations are shown in Fig. 6.

Kinetic data (joint moments) were estimated by solving an inverse dynamics task and applying two biomechanical models (the 6DOF model and the 7DOF model). For this, kinematic data and measured interaction forces were used as input data. Kinetic

Table 1 Moments of inertia

Moment of inertia	6DOF model (kg m^2)	7DOF model (kg m^2)	Comment
J_1	0.0060	0.0060	The moment is calculated with respect to the p. O
J_2	0.2223	0.2223	The moment is calculated with respect to the p. A_1
J_3	1.1859	1.1859	The moment is calculated with respect to the p. A_2
J_4	0.6877	0.6877	The moment is calculated with respect to the p. A_3
J_5	0.1538	0.1538	The moment is calculated with respect to the p. A_4
J_6	0.0054	0.0054	The moment is calculated with respect to the p. A_5
J_7	–	3.5719	The moment is calculated with respect to the p. A_3

data calculated for 6DOF are presented in Fig. 7, whereas kinetic data calculated for 7DOF are shown in Fig. 8a, b.

In order to analyze EMG data measured there were rectified and normalized (to the maximum values) and processed by applying Root Mean Square algorithm (RMS) with the 10 ms frame (Fig. 9) and 50 ms frame (Fig. 10). The threshold of EMG was assumed to be equal 0.2 of the normalized RMS value.

To estimate the phases of joint stiffness it was taken into consideration that the threshold range of relative angular acceleration should be equal ± 1 rad/s^2 (Fig. 11).

4 Discussion

Considering kinematic data (Figs. 4, 5 and 6) and joint stiffness phases, (Fig. 11) it was defined that over the [10; 58]% of stride the right leg, which is the stance leg during the single support phase, was stabilized: (1) at the ankle joint over [22.5; 25.8]% of stride (stage IA) and [27.5; 38]% of stride (stage IB); (2) at the knee joint over [23; 33]% of stride (stage II); (3) at the hip joint over [24; 29] % of stride (stage III). It is worth noticing that given results are consistent with data described in [14]. Based on obtained results it was concluded that over the single support phase the
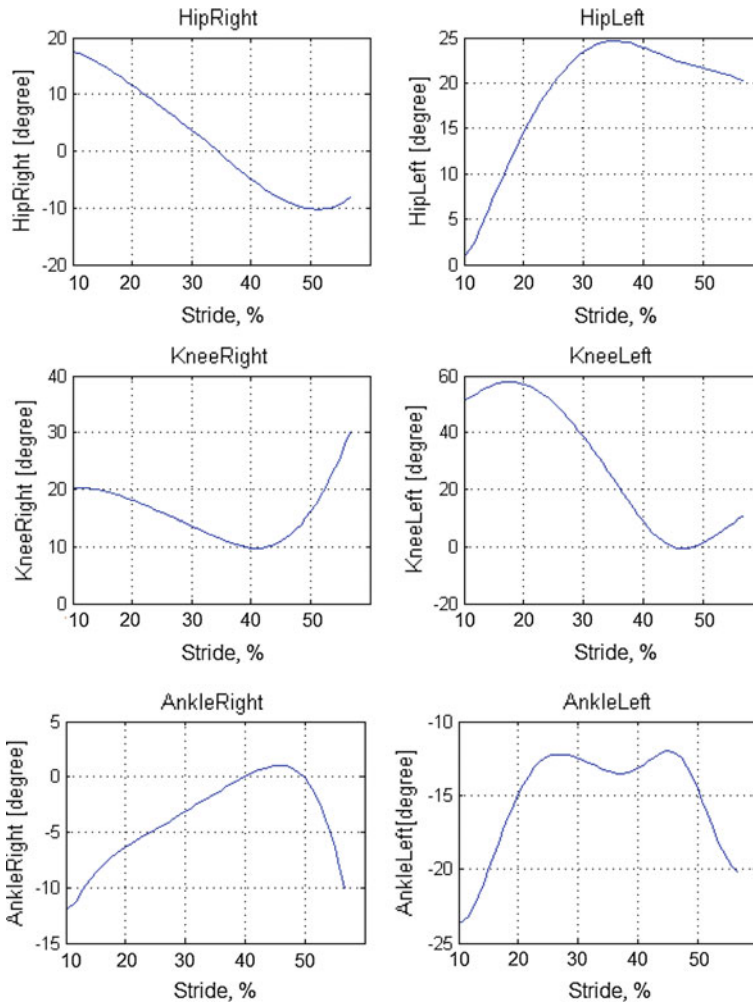
Fig. 4 Kinematic data: relative angular displacements

ankle joint of the stance leg should be stabilized as the first joint, the knee joint of this leg should be stabilized as the second joint and the hip joint of this leg should be stabilized as the third joint. After this the releasing of these joints should be performed in the reverse sequence: the hip joint should be released as the first joint, the knee joint should be released as the second joint and the ankle joint should be released as the third joint.

Analyzing kinetic data (joint moments) and joint stiffness phases (Fig. 11), it was noticed that: (1) over the stage IA and stage IB a joint moment calculated at the ankle joint ($M_{jointA1}$) is an increasing function (for the 6DOF model) or a wavy increasing function (for the 7DOF model); (2) over the stage II a joint moment calculated at
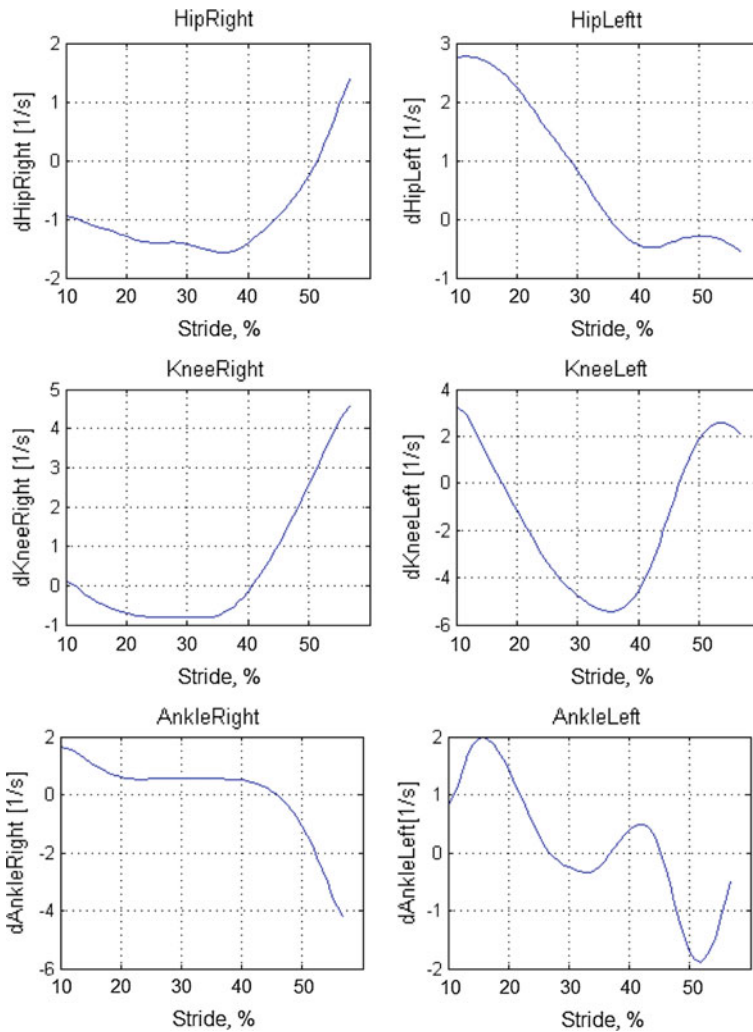
Fig. 5 Kinematic data: relative angular velocities

the knee joint ($M_{jointA2}$) is an increasing function (for the 6DOF model) or wavy function that changes its sign (for the 7DOF model); (3) over the stage III a joint moment calculated at the hip joint ($M_{jointA3}$) is equal to zero (for the 6DOF model and 7DOF model). It is worth emphasizing that calculated kinetic data only give us information whether the considered joint is loaded or unloaded. These data do not allow us to conclude whether the load at the joint is transmitted through antagonistic muscle pairs (muscle co-contraction), passive tissues or joint interaction (contact phenomena).
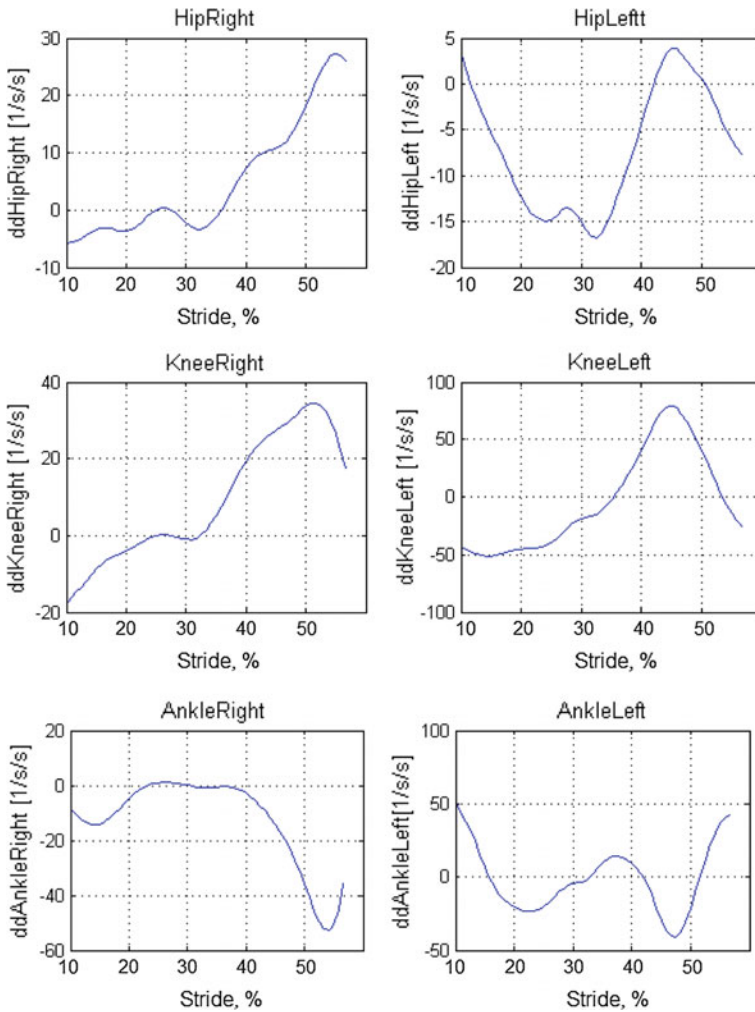
Fig. 6 Kinematic data: relative angular accelerations

Considering EMG data, muscle activity state of each examined muscle was determined. This state is described by the average activation time and its sequence in time. Analyzing normalized RMS EMG data (Figs. 9 and 10), average activation times were calculated:

(1) for the 10 ms frame RMS the activation times are equal 0.648 ms for the first (1), 0.293 ms for the second (2), 0.511 ms for the third (3) and 0.498 ms for the four muscles (4), respectively;
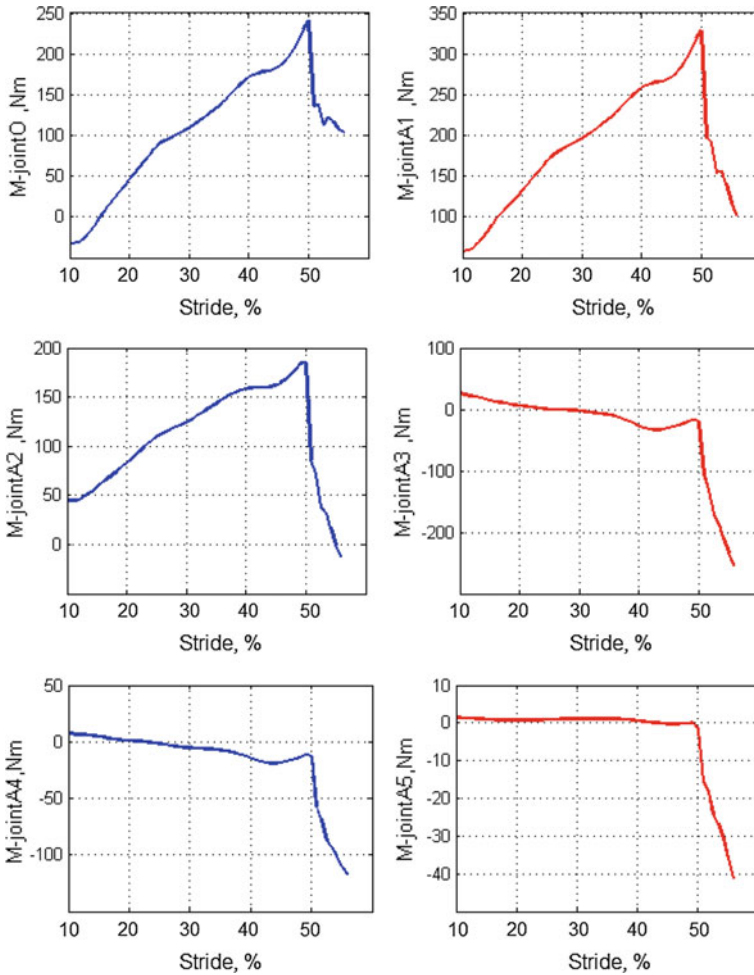
Fig. 7 Numerical results of 6DOF model: joint moments

(2) for the 50 ms frame RMS the activation times are equal 0.924 ms for the first
(1), 0.526 ms for the second (2), 0.891 ms for the third (3) and 0.765 ms for the
four muscles (4), respectively.

It is worth noticing that due to the fact that the processing algorithm has a huge
impact on the data obtained (the 10 ms RMS method gives smaller values that the
50 ms RMS method) one should select a time frame on the base of the type of
physical activity. In this study, we used the 50 ms RMS method because an examined
walking performance can be treated as a moderate physical activity. Analyzing EMG
processed data (Fig. 10) and joint stiffness phases (Fig. 11) it was observed that:
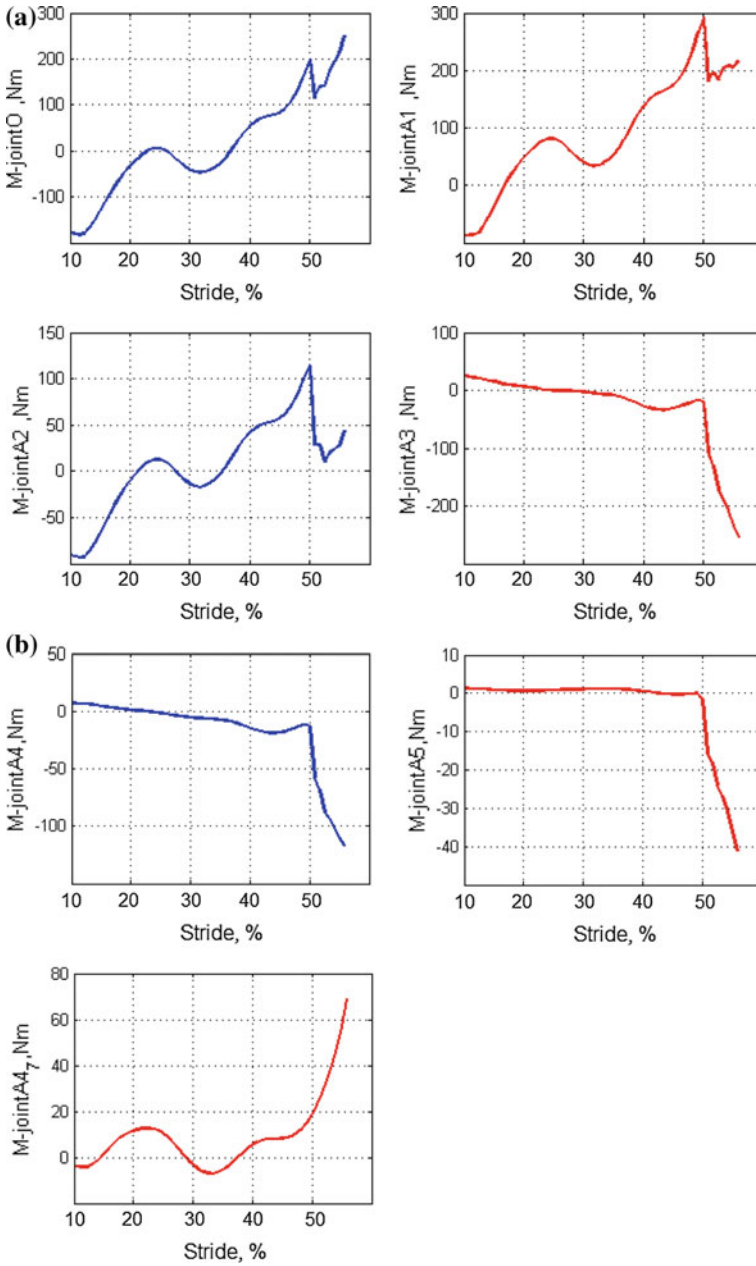
Fig. 8 A. Numerical results of 7DOF model: joint moments, B. Numerical results of 7DOF model: joint moments
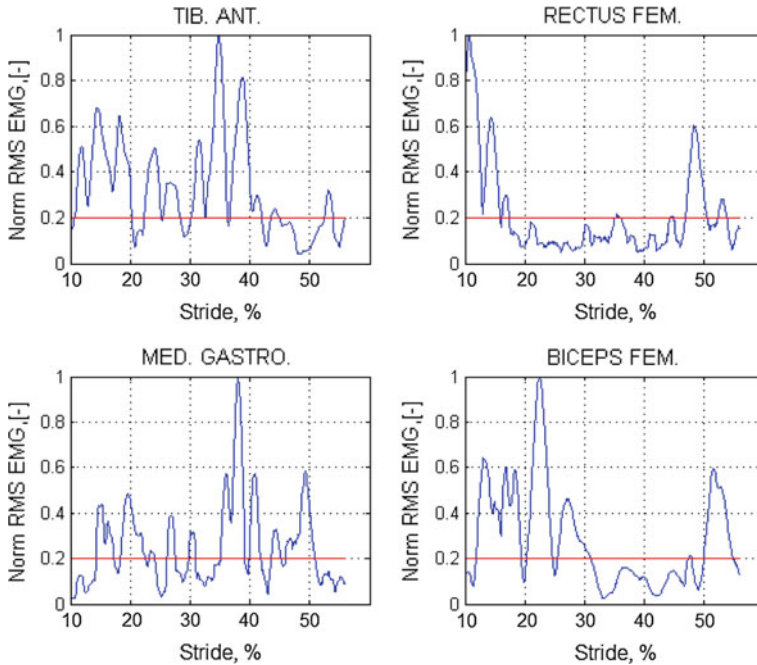
Fig. 9 Normalized RMS EMG signal (10 ms RMS)

(1) the antagonistic muscles acting on the ankle joint (the dorsiflexor muscle (1) and plantarflexor muscle (3)) showed similar activities over the stage IA and stage IB; moreover, over the second part of the stage IB it was noticed an occurrence of muscle co-contraction;

(2) the three muscles acting at the knee joint (the extensor muscle (2), the flexor muscle (3) and the flexor muscle (4)) presented different activities without any muscle co-contraction;

(3) the antagonistic muscles acting on the hip joint (the flexor muscle (2) and extensor muscle (3)) showed different activities over the stage III without any muscle co-contraction.

Considering the sequence of each muscle activity, it was noticed that obtained results are consistent with results presented in [14].

5 Conclusions

The aim of this study was elaborating an approach (inference method) that can be applied to determine functioning (activity) of lower limb muscles that are essential for gait performance over single support phase and double support phase by assuming
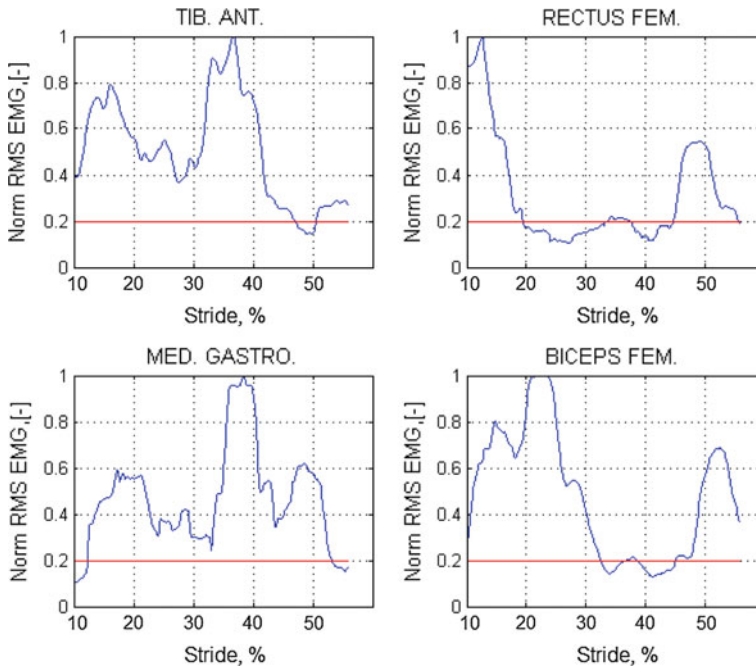
Fig. 10 Normalized RMS EMG signal (50 ms RMS)

the model of interaction between the ground and the contact foot. The scope of the study involved the analysis of the symmetric planar motion performing in the sagittal plane of the body by measuring kinematic, kinetic (force plate) and EMG data over normal gait performance. The kinetic (dynamic) analysis was performed by applying two multibody models (the 6DOF model and the 7DOF model) and solving an inverse dynamics task. It was assumed that activity state of each considered muscle is determined by average activation time and its sequence in time.

According to the presented approach, the conditions of the joint examined (stiffened or released) should be determined on the base of kinematic data by taking into consideration the influence of gravitational field and skeletal system configuration. After this one could consider processed EMG data and functions of examined muscles to conclude whether a muscle co-contraction was occurred. It is worth noticing that the method of EMG data processing has a huge impact on the result of muscle co-contraction investigation.

One should keep in mind that an inverse dynamics approach does not allow predicting an occurrence of muscle co-contraction [3]. The reason of this is the fact that during a co-contraction phase the agonist group and antagonist group produce moments that stabilize a joint at the same time. That is why calculated joint moment (net joint moment) does not give us any information what is the share of agonist group, what is the share of antagonist group, what is the share of passive tissues
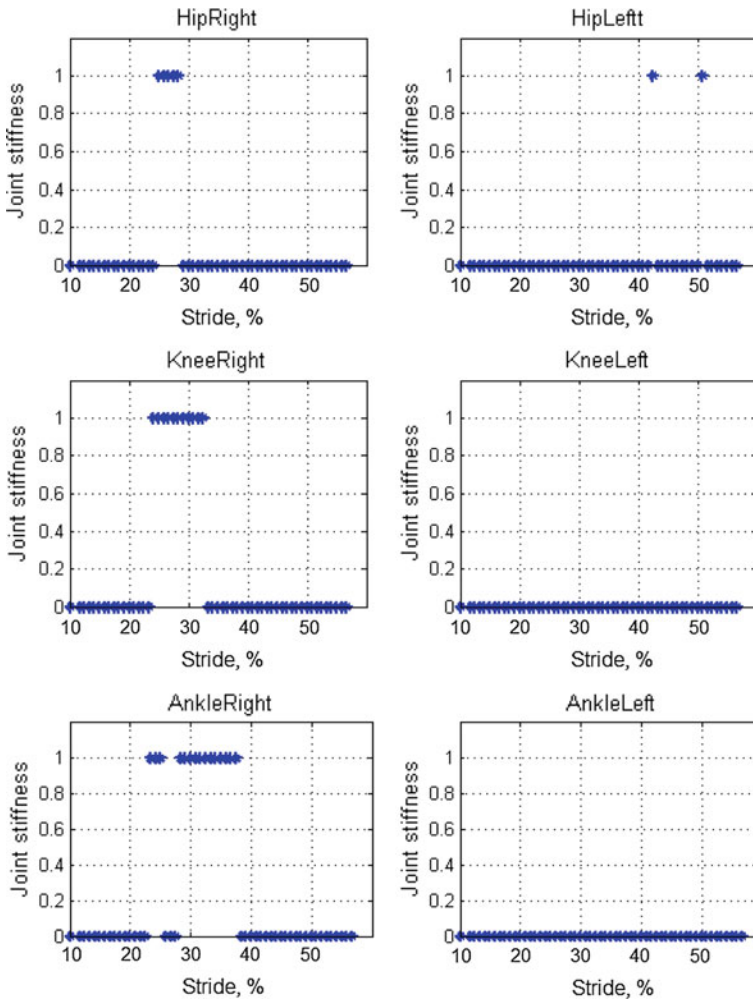
Fig. 11 Joint stiffness phases

influencing this joint and what is the share of contact forces acting at the joint. To detect a muscle co-contraction, one should measure and analyze EMG data of the muscles acting on the examined joint and consider kinematic data. It is worth emphasizing that information about an occurrence of muscle co-contraction is very important for clinical gait analysis and development of external device that helps to produce gait (e.g. exoskeleton for lower limb rehabilitation).

The future development of approach presented in this study involves: (1) analyzing influence of all superficial muscles that are essential for gait performance and can be measured by using surface EMG system (due to the fact that only non-invasive method can be used in the scope of presented study); (2) analyzing clinical gait

performance on the base of an index quantifying deviation from normal gait [12, 13]; (3) considering muscle biomechanics [16, 18] and estimation of muscle synergy indices [5] to elaborate a method for solving the problem of redundancy [6].

References

1. Awrejcewicz, J.: Classical Mechanics. Dynamics. Springer, Berlin (2012)
2. De Leva, P.: Adjustments to Zatsiorsky-Seluyanov's segment inertia parameters. J. Biomech. **29**(9), 1223–1230 (1996)
3. Farley, C.T., Ferris, D.P.: Biomechanics of walking and running: center of mass movements to muscle action. Exerc. Sport Sci. Rev. **26**, 253–285 (1998)
4. Krishnamoorthy, V., Scholz, J.P., Latash, M.L.: The use of flexible arm muscle synergies to perform in isometric stabilization task. Clin. Neurophysiol. **118**, 525–537 (2007)
5. Latash, M.: Fundamentals of Motor Control. Elsevier, New York (2012)
6. Latash, M.L.: Biological movement and laws of physics. Mot. Control **21**, 327–344 (2017)
7. Latash, M.L.: Towards physics of neural processes and behavior. Neurosci. Biobehav. Rev. **69**, 136–146 (2016)
8. Neptune, R.R., Kautz, S.A., Zajac, F.E.: Contributions of the individual ankle plantar flexors to support, forward progression and swing initiation during walking. J. Biomech. **34**, 1387–1398 (2001)
9. Neptune, R.R., Zajac, F.E., Kautz, S.: Muscle force redistributes segmental power for body progression during walking. Gait Posture **19**, 194–205 (2004)
10. Platzer, W.: The Handbook Atlas of Man's Anatomy: The Locomotor Aparatus, vol. 2 (in Polish). Słotwiński Verlag, Brema (1997)
11. Souissi, H., Zory, R., Bredin, J., Gerus, P.: Comparison of methodologies to assess muscle co-contraction during gait. J. Biomech. **24**(57), 141–145 (2017)
12. Syczewska, M., Dembowska-Bagińska, B., Perek-Polnik, M., Kalinowska, M., Perek, D.: Gait pathology assed with Gillette Gait Index in patients after CNS tumour treatment. Gait Posture **32**, 358–362 (2010)
13. Schutte, L.M., Narayanan, U., Stout, J.L., Selber, P., Gage, J.R., Schwartz, M.H.: An index for quantifying deviations from normal gait. Gait Posture **11**, 25–31 (2000)
14. Vaughan, C.L., Davis, B.L., O'Connor, J.C.: Dynamics of Human Gait. 2nd Edition, Kiboho Publishers, Cape Town, South Africa (1999)
15. Winter, D.A.: The biomechanics and motor control of human gait. University of Waterloo Press, Canada (1987)
16. Wojnicz, W., Wittbrodt, E.: Application of muscle model to the musculoskeletal modeling. Acta Bioeng. Biomech. **14**, 29–39 (2012)
17. Wojnicz, W.: Biomechaniczne modele układu mięśniowo-szkieletowego człowieka (Biomechanical Models of the Human Musculoskeletal System), pp. 1–209. Wydawnictwo Politechniki Gdanskiej, Gdansk, Poland (2018)
18. Wojnicz, W., Zagrodny, B., Ludwicki, M., Mrozowski, J., Awrejcewicz, J., Wittbrodt, E.: A two-dimensional approach for modelling of pennate muscle behavior. Biocybern. Biomed. Eng. **37**, 302–315 (2017)
19. Zajac, F.E., Neptune, R.R., Kautz, S.A.: Biomechanics and muscle coordination of human walking. Part I: Introduction to concepts, power transfer, dynamics and simulations. Gait Posture **16**(2002), 215–232 (2002)

Modeling and Control of Motion Systems for an Electro-Hydraulic Tripod Manipulator

Piotr Wos and Ryszard Dindorf

Abstract The paper presents the results of theoretical considerations, experimental studies and control of electro-hydraulic servo control of manipulator. The structure of the device together with an analysis of its kinematic structure is described. The structure of dynamic manipulator model is derived from each axis dynamic model. The issue that has been discussed, focused on providing robust of electro-hydraulic servo controller to change the dynamic properties. The results of simulation and experimental tests data are presented and analyzed.

Keywords Electro-hydraulic parallel manipulator · Kinematics · Dynamic model · Control system

1 Introduction

The development of automation and robotization causes a growing interest in multi-axis hydraulic drives in manipulators and robots with the perpendicular kinematic structures. This kind of structure is defined as a combination of a working platform with a base using active elements being closed kinematic chains. Platforms based on various flat or spatial parallel mechanisms are used, among others, in manipulators, robots, machine tools, telescopes, measuring machines and car suspension systems [9]. Parallel manipulators are mechanisms with structures of closed kinematic chains. The passive element (effector) is connected to a stationary base using parallel intermediary elements called branches. The effector of such a parallel spatial mechanism has two to six degrees of freedom (6-DoF) [6, 7]. Parallel manipulators have been used wherever high accuracy of positioning and orientation of high-mass

P. Wos (✉) · R. Dindorf
Kielce University of Technology, 25-314 Kielce al. Tysiaclecia Panstwa
Polskiego 7, Kielce, Poland
e-mail: wos@tu.kielce

R. Dindorf
e-mail: dindorf@tu.kielce

objects is required. As pioneers in the field of manipulators with a parallel structure are considered three people, including Eric Gough, Klaus Cappel and D. Stewart [3, 12]. Their interest in this field had a significant impact on the development of new software or inventions which are accompanied by parallel mechanisms. The main advantage of the parallel manipulator structure is the extremely favorable load-to-weight ratio of the mechanism due to the uniform distribution of load of the passive element on the base by independent kinematic chains (branches). Less drive power is required than the power in serial manipulators, as the individual branches are less loaded. They have good dynamic properties thanks to the small mass of the elements which allows for higher speeds and acceleration of the effector. The good stiffness of the structure allows for high accuracy of the effector positioning. Considering the kinematic analysis, it is important to note that the advantage of parallel manipulators is the easy and unequivocal solution to the inverse kinematics problem and solving the forward dynamics problem. The main disadvantage of these manipulators is primarily the small working area (as compared to open-type manipulators), dependent on the kinematic chains connecting the effector to the base and the occurrence of peculiar configurations within the working area, i.e. those in which the impact on the movement parameters of the effector is impeded or even impossible. Platforms based on different flat or spatial parallel mechanisms are used, among others, in manipulators, robots, machine tools, telescopes, measuring machines and car suspension systems.

2   Test Stand Construction

The prototype of a three-axis electro-hydraulic parallel manipulator is shown in Fig. 1.

In this manipulator, electro-hydraulic servo-drive of integrated design are used for active drives. Each of the three servo-drive consists of a hydraulic cylinder (1), a proportional control valve 4/3 (2) and a magnetostrictive piston rod displacement transducer (6). The whole structure of the manipulator rests on the base (5) in the shape of an equilateral triangle. The articulated mechanisms (4) enable the manipulator base to be connected to the drives while providing them with adequate mobility. The mobile platform (3) is mounted on the main articulated joint (7).

The manipulator control system directly controls servo-drive mounted in the joints. The effector trajectory is performed by minimising the difference of the current and predetermined position of the individual joint. Signals from actuator sensors are processed through *real-time* software. Direct and continuous position control with the ability to smoothly adjust the speed of movements to a large extent improves the dynamic properties of the drive when used for automating fast-changing technological processes. The computer system enables data acquisition. On the other hand, large computational capabilities allow the use of adaptive control or artificial intelligence elements in the control process. At the same time, the use of discrete control increases the area of application of hydraulic axes as it serves to solve complex problems with
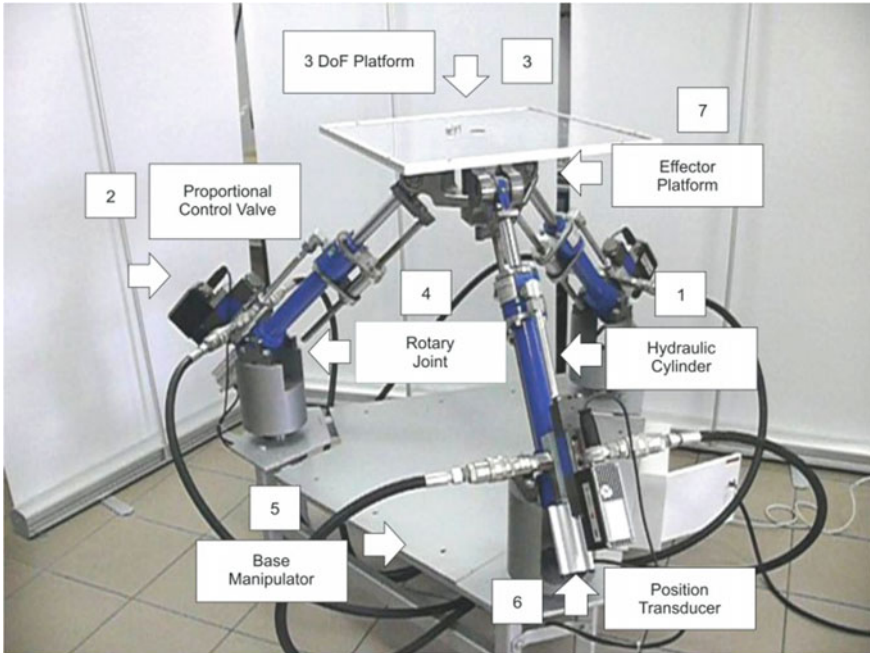
Fig. 1 The manipulator prototype: 1—hydraulic cylinder with a linear mechanism, 2—proportional control valve, 3—platform, 4—joint connecting the actuator with the base, 5—base, 6—position transducer, 7—effector platform

difficulties in defining rules of conduct which are computationally complicated and require rapid responses, e.g. during parametric identification. The distributed system was used for rapid prototyping of fluid power servo-drives in RT. On PC computes Matlab/Simulink and *xPC Target* were installed. In Matlab/Simulink package it is possible to create processing procedures for both conventional and artificial intelligence controllers and to execute own control and visualization applications. PC has the card of analog input/output and *Real-Time xPC Target* system which is used for measurement data acquisition and fluid power drives control. Target PC can simulate the flow of control and measurement signals in real time by means of HIL (*Hardware-in-the-Loop*) method [11].

3 Kinematic Model of the Manipulator

In a parallel manipulator, each arm can take infinitely many positions at a given ejection of its drive. The position of the centre of the platform is at the point of intersection of the lines defining the available positions of the ends of the individual arms at the drive ejections. The basic problem of kinematic structure analysis is the correct
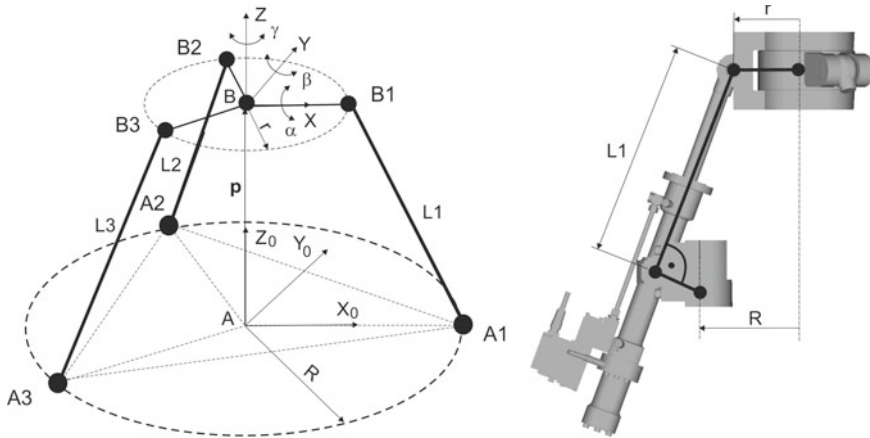
Fig. 2 Model and kinematic diagram of the manipulator

planning of the trajectory of the manipulator. This task is treated as the designation of the transition path between the start and end points of the effector motion. It is also necessary to identify movements, speeds, and acceleration for movement connections. When arm drives impact directly on the platform, the dependence between the robot tip movement and the drive extension is the distance between the start and end attachment points of the drive. This situation occurs in the kinematics of the examined manipulator (Fig. 2), where three identical arms directly impact on the platform using the linear drives on them. Each of the arms forms a kinematic chain whose origin is associated with the accepted base, and the end connection has a direct influence on the position of the platform. The solutions of the forward and inverse kinematics problems are necessary in the positioning and control of the manipulator along a given curve in the Cartesian space [8].

Figure 2 shows the kinematic diagram of the manipulator. The actuator elements consist of three electro-hydraulic servo-drive. Dimensions L_i, $i = 1, 2, 3$ are the lengths of the ejections of the individual actuators. The servomechanisms attachment locations are marked as A_i, $i = 1, 2, 3$. Individual manipulator arms form a closed kinematic chain. Simultaneous control of the L_i actuators in the form of three identical servomechanisms enables moving the platform anchored in points B_i, $i = 1, 2, 3$.

Three identical integrated hydraulic axes from Bosch Rexroth are included in the spatial parallel manipulator. The single integrated electrohydraulic axle consists of CS hydraulic cylinder (with an internal magnetostrictive positioning system—Novostrictive) coupled to 4/3 proportional valve (Bosch–Rexroth). Parameters of CS hydraulic cylinders are as follows: piston diameter $D = 40$ mm, piston rod diameter $d = 28$ mm, stroke $h = 220$ mm, nominal pressure $p = 160$ bar. The lengths of the electrohydraulic axes (hydraulic cylinders, including their fixing in joints) as the active elements (actuators) of the manipulator are:

$$L_i = L_{si} + h_i, \quad i = 1, 2, 3 \tag{1}$$

where: L_{si}—the length of the actuators in the initial state at the extreme position of the piston, taking into account the clamping length of the piston rod in the rotary joint ($L_{si} = 425$ mm), h_i—the cylinder stroke ($h_i = 250$ mm).

The amount of extraction of individual servo-drives can be determined in a vector form $\mathbf{L}_i$.

$$\mathbf{L}_i = \mathbf{p} + \mathbf{R}_B^A \cdot \mathbf{r}_i - \mathbf{R}_i \tag{2}$$

where: $\mathbf{p} = \overleftarrow{AB}$, $\mathbf{p} = [x_p \ \ y_p \ \ z_p]^T$—vector of the end (center) B point of the platform against point A based on, $\mathbf{R}_B^A$—rotation matrix of the reference system to the base system, $\mathbf{r}_i$—the coordinates of the $\mathbf{B}_i^B$ vector in the base space (B, X, Y, Z), and are:

$\mathbf{R}_i$—the coordinates of the $\mathbf{A}_i^A$ vector in the reference space (A, X_0, Y_0, Z_0):
$\mathbf{R}_i$ and $\mathbf{r}_i$ vectors are described respectively by (2):

$$\mathbf{R}_i = [R \cdot \cos \varphi_i, \ R \cdot \sin \varphi_i, \ 0]^T$$
$$\mathbf{r}_i = [r \cdot \cos \varphi_i, \ r \cdot \sin \varphi_i, \ 0], \quad i = 1, 2, 3 \tag{3}$$

The position angles of the individual joints in the base and platform are: $\phi_1 = 0°$, $\phi_2 = 120°$, $\phi_3 = 240°$.

$\mathbf{R}_B^A$ rotation matrix is written as follows:

$$\mathbf{R}_B^A = R_{Bx}(\alpha) \cdot R_{By}(\beta) \cdot R_{BZ}(\gamma) \tag{4}$$

where:

$$\mathbf{R}_{Bx}(\alpha) = \begin{bmatrix} 1 & 0 & 0 \\ 0 & \cos\alpha & -\sin\alpha \\ 0 & \sin\alpha & \cos\alpha \end{bmatrix}, \mathbf{R}_{By}(\beta)$$

$$= \begin{bmatrix} \cos\beta & 0 & \sin\beta \\ 0 & 1 & 0 \\ -\sin\beta & 0 & \cos\beta \end{bmatrix}, \mathbf{R}_{Bz}(\beta)$$

$$= \begin{bmatrix} \cos\gamma & -\sin\gamma & 0 \\ \sin\gamma & \cos\gamma & 0 \\ 0 & 0 & 1 \end{bmatrix}$$

Angles: α, β, γ (RPY—*roll-pitch-yaw*) denote respectively the rotations of the reference system: XYZ around the axis: transverse X (rolling), longitudinal Y (pitching), vertical Z (yawing).

Derivation of the Eq. (2) over time and the use of the rotation derivative properties leads to the dependence:

$$\dot{\mathbf{L}}_i = \dot{\mathbf{p}} + \dot{\mathbf{R}}_B^A \cdot \mathbf{r}_i = \mathbf{v} + \boldsymbol{\omega} \times \mathbf{R}_B^A \cdot \mathbf{r}_i \tag{5}$$

where $\mathbf{v}$, $\boldsymbol{\omega}$ are linear and angular velocities vectors, respectively:

$$\mathbf{v} = \begin{bmatrix} v_x, v_y, v_z \end{bmatrix}^T$$
$$\boldsymbol{\omega} = \begin{bmatrix} \omega_x, \omega_y, \omega_z \end{bmatrix}^T$$

The mechanism of parallel structure is a closed mechanism, so the restriction of the mechanism movement can be defined: $f(\mathbf{L}, \mathbf{q}) = 0$.

The inverse kinematics problem can be written as:

$$d\mathbf{L} = \mathbf{J} \cdot d\mathbf{q} \tag{6}$$

where:

$\mathbf{L} = [L_1 \quad L_2 \quad L_3]^T$—translation vector of hydraulic drive axes,
$\mathbf{q} = \begin{bmatrix} x_p & y_p & z_p & \alpha & \beta & \gamma \end{bmatrix}^T$—position and rotation vector of the mobile manipulator platform,
$\mathbf{J} = -\mathbf{J}_L^{-1} \cdot \mathbf{J}_q$—*Jacobian* matrix.

The resulting position and orientation error in the forward kinematics system can be written as follows:

$$\delta q = \mathbf{J}^{-1} \cdot \delta \mathbf{L} \tag{7}$$

where: $\delta \mathbf{q} = [\Delta x_p \ \Delta y_p \ \Delta z_p \ \Delta \alpha \ \Delta \beta \ \Delta \gamma]$, $\delta \mathbf{L} = [\Delta L_1 \ \Delta L_2 \ \Delta L_3]$

A simulation experiment was conducted to determine the space in the *Matlab/Simulink* environment by observing the *P* point of the working platform. The figure shows the trajectory of motion in the form of a closed curve and the set of the resultant points of the manipulator working area (Fig. 3).

4 Dynamic Model of the Manipulator

Finding equations describing the dynamics of a designed robot is a much more complicated task. The robot has three arms, each of which rotates around two axes and performs the translation movement resulting from the drives work. The arms are connected by a common joint whose construction determines the position of the robot gripper. Attempting to formulate equations describing the dynamics of such constructions is a difficult task and often superfluous to be used in the project. In a parallel robot, there are many elements that affect its dynamics. For each element,
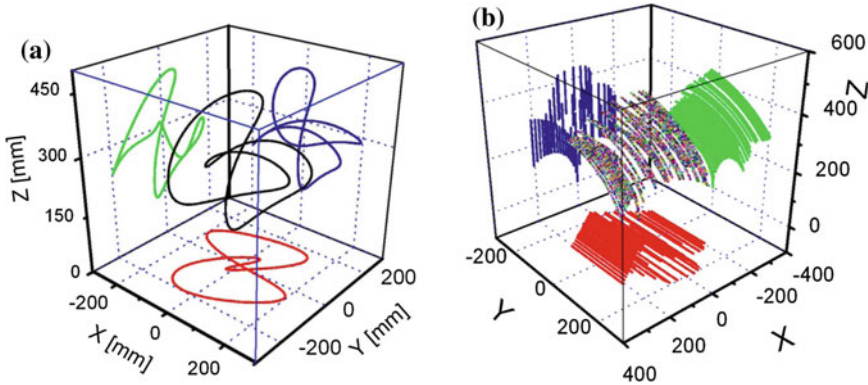
Fig. 3 Simulation charts: **a** trajectory in the form of a closed curve in the Cartesian space, **b** the working area of the manipulator

it would be necessary to determine its temporary position and acceleration related to its dynamics. Searching for acceleration involves assigning derivatives of functions derived from transformations of equations contained in the forward and inverse kinematics problems. It is natural that the form of such equations will be greatly expanded. Even if you manage to find all the dependencies then you will encounter a problem with their verification resulting from numerical errors. The sense in looking for accurate equations describing the dynamics can be undermined by the limitations of the computing power of the control system that will use such equations. In addition, it is important to note that often when performing robot movements, the range of position changes in many components is small. This means that their influence on dynamics can be also negligibly small. For example, in the described robot, the simulations made using *Sim-Mechanics* [10] showed that the range of angular swings in many rotary joints was not more than several degrees, and that the forces values required for motion were lower by an order of magnitude than the forces needed to compensate for the gravity force.

Using the orthogonal complement method, the dynamics of 3-DoF parallel manipulator can be described as a second-order differential Eq. (8),

$$\mathbf{M}(\mathbf{x})\ddot{\mathbf{X}} + \mathbf{G}(\mathbf{x}) = \mathbf{J}_f^T \mathbf{F}_p \tag{8}$$

where: $\mathbf{X} \in \mathbf{R}^3$ is a vector of the generalized coordinates, $\mathbf{M} \in \mathbf{R}^{3 \times 3}$ is the manipulator mass matrix, $\mathbf{G} \in \mathbf{R}^3$ is the vector of gravitation effects, $\mathbf{J}_f \in \mathbf{R}^{3 \times 3}$ is the force Jacobian matrix and $\mathbf{F}_p \in \mathbf{R}^3$ is the vector of the applied force of the actuators given by,

$$\mathbf{F}_p = (F_{p1}, F_{p2}, F_{p3}) \tag{9}$$

Fig. 4 Scheme of the
hydraulic servo model
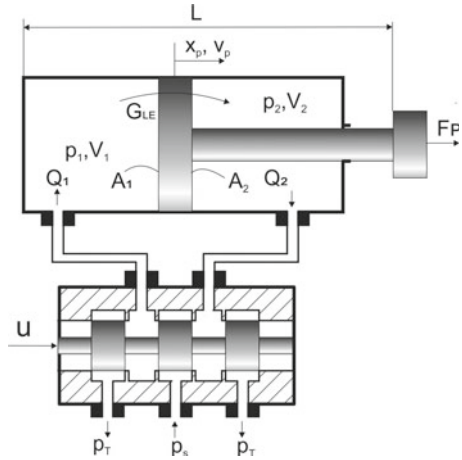
where F_{pi}, $i = 1, 2, 3$ are individual hydraulic forces acting on the manipulator
platform.

The end-effector position (x_p, y_p, z_p) of the moving platform could be obtained by
substituting the elongation L_i of every linear hydraulic axis into the forward motion
equation.

Using the differential kinematics mechanism were: $\mathbf{L} = \mathbf{J(x)} \cdot \mathbf{x}$, we can write
(10),

$$\mathbf{M^+(x)\ddot{L}} + \mathbf{G^+(x)} = \mathbf{F}_p \tag{10}$$

where: $\mathbf{L} = [L_1 \ L_2 \ L_3]^T$—translation vector of hydraulic drive axes,
$\mathbf{M^+(x)} = [\mathbf{J(x)}^T]^{-1}\mathbf{M(x)J(x)}^{-1}$—positive definite mass matrix and $\mathbf{G^+(x)} = [\mathbf{J(x)}^T]^{-1}\mathbf{G(x)}$—gravity forces vector.

4.1 Dynamic Model of the Hydraulic Servo System

Calculation diagram of the hydraulic servo drive model, consisting of the double-
acting cylinder with one-sided piston rod and directional control valve is presented
in the Fig. 4.

The equations relating mechanical to hydraulic variables [1, 2, 4] are described
by,

$$\begin{aligned}
F_{pi} &= A_{1i} p_{1i} - A_{2i} p_{2i} \\
Q_{1i} &= A_{1i} \dot{L}_i + C_1 \dot{p}_{1i} + G_{le}(p1 - p2), \quad i = 1, 2, 3, \\
Q_{2i} &= A_{2i} \dot{L}_i - C_2 \dot{p}_{2i} + G_{le}(p1 - p2)
\end{aligned} \tag{11}$$
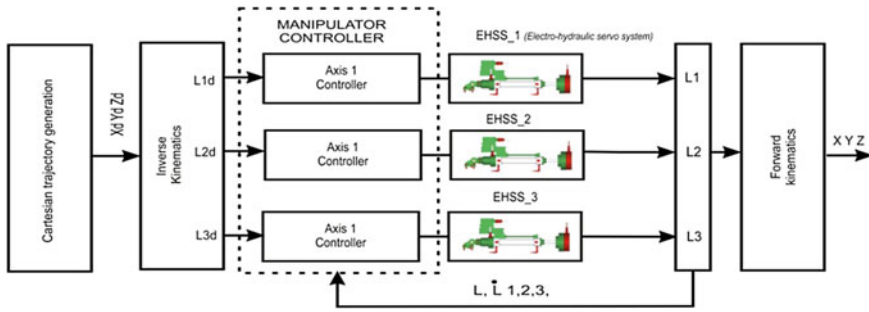
Fig. 5 The controller block diagram of the 3-DoF electro-hydraulic manipulator

where: Q_{1i}—volumetric flow rate, C_1, C_2—fluid capacitances in the cylinder chambers G_{le}—coefficients of leakages in the cylinder.

Substituting (11) in the system equation of motion (10), the following equations of motion are derived,

$$\mathbf{M}^+(\mathbf{x})\ddot{\mathbf{L}} + \mathbf{G}^+(\mathbf{x}) = \begin{bmatrix} A_{11} \cdot p_{11} - A_{21} \cdot p_{21} \\ A_{12} \cdot p_{12} - A_{22} \cdot p_{22} \\ A_{13} \cdot p_{13} - A_{23} \cdot p_{23} \end{bmatrix} \tag{12}$$

The hydraulic forces developed by the actuators are given by,

$$[p_{1i} \cdot A_{1i} - p_{2i} \cdot A_{2i}] = \left[A_{1i} \cdot p_s - A_{2i} \cdot p_T - \frac{A_{1i}^3 + A_{2i}^3}{(K_1 \cdot u + K_{0.1})^2} \cdot \dot{L}_i^2 \right], \quad i = 1, 2, 3 \tag{13}$$

where: u—control input, K_1, $K_{0.1}$—constants factors, which correspond to the main and leakage valve flow paths.

5 Control Design

Design of the control system for the tested manipulator was carried out in the following stages: selection of control laws, virtual prototyping of the control system, simulations of the controller in real time, and implementation on the target manipulator (Fig. 5).

The control analysis is based on the system dynamic and hydraulic model (10).

$$\mathbf{F}_p = \mathbf{M}^+(\mathbf{x})\left[\ddot{\mathbf{L}}_d + \mathbf{K}_p(\mathbf{L}_d - \mathbf{L}) + \mathbf{K}_v(\dot{\mathbf{L}}_d - \dot{\mathbf{L}})\right] + \mathbf{G}^+(\mathbf{x}) \tag{14}$$
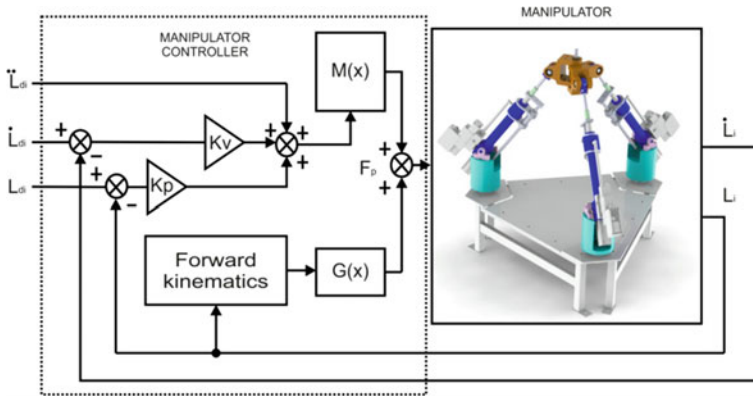
Fig. 6 The block diagram of closed loop control

where: $\mathbf{K}_p$, $\mathbf{K}_v$—diagonal matrices, which represent the control gains of the system, $\mathbf{L}_d$—desired cylinder displacement vector.

Initial axis controller settings were chosen in an experimental way in the process of virtual prototyping. Axis controller gain coefficients $\mathbf{K}_p$, $\mathbf{K}_v$ were chosen in such a way so that the position error of the movement trajectory would be minimized. Only after determining the correct coefficient values for the virtual control system, it was possible to proceed to the phase of rapid prototyping [5] (Fig. 6).

6 Experimental Results

In order to show the accuracy of the control system, an experiment on a real object was conducted. In order to obtain wider information about the control quality, different trajectories of movement were studied. Based on distributed measurement and control system a test stand for rapid prototyping controller of the electro-hydraulic servo-drive was set up [10]. Figure 7 presents results of the control process for references signals (Xd, Yd, Zd) in Cartesian coordinates.

Figure 8 presents the change effects in movement frequency of hydraulic axis on the quality control.

For practical applications such as high positioning accuracy, the control algorithm gives satisfactory results for the regulation of frequencies 0.8 Hz (5 rad/s).

7 Conclusions

This paper presents the prototype of a spatial 3-DoF hydraulic parallel manipulator consisting of a stationary base and a mobile platform that are connected to joints hav-
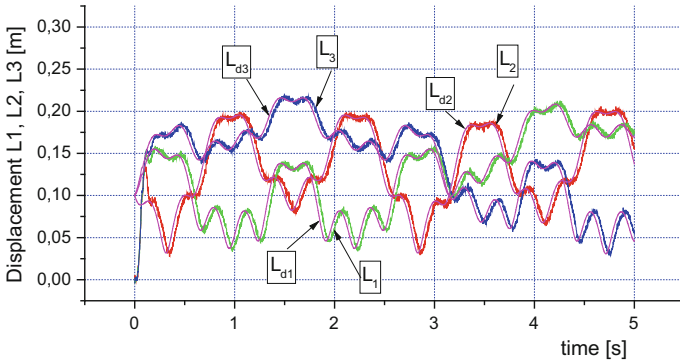
Fig. 7 Displacement of the manipulator arms for control algorithm, according to the sinusoidal reference trajectory in Cartesian coordinates

Fig. 8 Absolute follow-up error of position signal δL
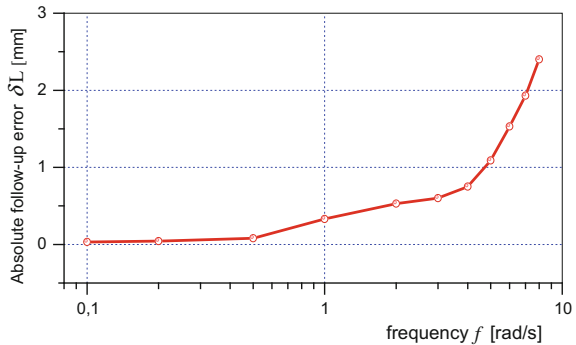
ing three integrated electro-hydraulic axes. A general kinematic model and a dynamic model of a parallel 6-DoF manipulator are presented but they can be simplified by describing the researched spatial 3-DoF hydraulic manipulator. The adjustment system adapting dynamic changes of the forces impacting on the manipulator, ensuring smoothness and uniformity as well as the most accurate reproduction of the trajectory of motion, was the subject of research. The benefits of improving the dynamics of mechanisms and the ability to automate control and regulation processes using proportional technologies cause the increased use of these technologies in electro-hydraulic drives.

References

1. Awrejcewicz, J., Lewandowski, D., Olejnik, P.: Modeling of Electrohydraulic Servomechanisms. Dynamics of Mechatronics Systems, pp. 169–194 (2016). https://doi.org/10.1142/978 9813146556_0006

2. Ahmadnezhad, M., Soltanpour, M.: Tracking performance evaluation of robust back-stepping control design for a nonlinear electrohydraulic servo system. World Aacad. Sci. Eng. Technol. Int. J. Mech. Aerosp. Ind. Mechatron. Manuf. Eng. **9**(7) (2015)
3. Dindorf, R., Wos, P.: Contour error of the 3-DoF hydraulic translational parallel manipulator. Adv. Mater. Res. **874**, 57–62 (2014)
4. Jelali, M., Kroll, A.: Hydraulic Servosystems: Modelling, Identification and Control. Springer, London (2003)
5. Kheowree, T., Kuntanapreeda, S.: Adaptive dynamic surface control of an electrohydraulic actuator with friction compensation. Asian J. Control **17**, 855–867 (2015)
6. Kim, H.S., Cho, Y.M., Lee, K.I.: Robust nonlinear task space control for 6DOF parallel manipulator. Automatica **41**(9), 1591–1600 (2005)
7. Laski, P.A., Takosoglu, J.E., Blasiak, S.: Design of a 3-DOF tripod electro-pneumatic parallel manipulator. Robot. Auton. Syst. **72**, 59–70 (2015)
8. Merlet, J.-P.: Parallel Robots, Solid Mechanics and its Applications. Springer, New York (2006)
9. Tsai, L.W.: Robot Analysis: The Mechanics of Serial and Parallel Manipulators. Wiley, New York (1999)
10. Wos, P., Dindorf, R.: Adaptive control of a parallel manipulator driven by electro-hydraulic cylinders. Int. J. Appl. Mech. Eng. **17**(3), 1061–1071 (2012)
11. Wos, P., Dindorf, R.: Adaptive control of the electro-hydraulic servo-system with external disturbances. Asian J. Control **15**, 1065–1080 (2013)
12. Zhao, D., Li, S., Gao, F.: Fully Adaptive feedforward feedback synchronized tracking control for stewart platform systems. Int. J. Control Autom. Syst. **6**(5), 689–701 (2008)

Support Reaction in the Brachistochrone Problem in a Resistant Medium

Alena Zarodnyuk and Oleg Cherkasov

Abstract The horizontal coordinate's maximization problem as well as related the brachistochrone problem are considered. The particle is moving in the vertical plane under influence of gravity, viscous drag that proportional to n-th degree of the velocity. The reaction of the basement is considered as a control. The optimal control problem is reduced to the boundary value problem for the system of two nonlinear equations. It was established that the reaction force of the basement could change its sign no more than one time, moreover, it changes only from the negative value to the positive value. The qualitative features of the optimal control allows to elaborate the results obtained in other studies.

Keywords Brachistochrone problem · Viscous drag · Optimal control

1 Introduction

A mass-point's motion in the vertical plane is considered. The point moves in a homogeneous field of the gravity and in a uniform resisting medium. The problem is to determine the qualitative features of the base-curve reaction that maximizes the horizontal coordinate of the point during its motion from the given point for the fixed time interval. The range maximization problem is interrelated with the modified brachistochrone problem – the choice of the minimum-time curve from the given initial point to the given final vertical line [11].

A. Zarodnyuk · O. Cherkasov (✉)
Moscow State Iniversity, Leninskie gori 1, Moscow, Russia
e-mail: oyuche@yandex.ru

A. Zarodnyuk
e-mail: alenaz_90@inbox.ru

Various generalizations of the brachistochrone problem are included in universities' lectures and practices on the control theory and have not only of methodical interest. Minimum-time and maximum-range problems may be of interest for an aircrafts trajectory optimization, if the lifting force is controlled without the change of the resisting force; for designing a profile rail marshaling yards, escape ladders form, and attractions of roller-coaster-type as well. The known shape of the trajectory will allow us to calculate the acceleration when driving on them for subsequent simulation of these processes on a dynamic simulator. The conception of optimal trajectories is important for constructing the programmed paths which applied in developing the software for flight simulators. These simulators are used for training and testing of pilots and operators that control the various moving objects, in particular, aircraft. One of the pilot's tasks is to control the moving object on the desired trajectory. Once found the program trajectory, the characteristic overload acting on the pilot during aircraft movement on the programmed trajectory should be determined. These overloads as a time-functions should be reproduced in the simulator dynamic motion simulation. With the active participation of the pilot who operates the object, the computer simulator using the information from the actuator integrates the equations of motion of the object and obtains the program trajectory. According to the parameters of the trajectory the control signals for the actuators of simulator are generated.

The brachistochrone problems with the dry friction with support reaction considered as a control were studied in detail. In [8] it was assumed that vertical component of the reaction force along the trajectory is of constant sign and directed opposite to the gravity force, and extremals are presumed to be concave. For the nonzero initial velocity it was shown that the motion should starts with the zero reaction force, and then it switched on the positive definite time-function. The same conclusions about non-negativity of the reaction force are reflected in [3] for a peculiar class of extremals, i.e., the optimal trajectory between the initial point and the terminal point was taken such that the time needed to reach each internal point is minimal for this point.

Present paper is dedicated to an analytical research of the sign of the reaction force of base-curve along an extremal for range-maximization problem and the brachistochrone one for the nonzero initial velocity and non-linear viscous drag.

2   Problem Formulation

The motion of a particle of the mass m in the vertical plane in a uniform gravitational field under the influence of a resisting force is considered. The resisting force is supposed to be proportional to real n-th power of the velocity, $n > 0$.

The equations of the motion for dimensionless variables are as follows [7]:

$$\begin{cases} \dot{x} = v\cos\theta, \\ \dot{y} = v\sin\theta, \\ \dot{v} = -v^n - \sin\theta, \\ \dot{\theta} = u - \frac{\cos\theta}{v}. \end{cases} \tag{1}$$

Here x, y are the horizontal and vertical coordinates of the particle, correspondingly, v is the absolute value of the velocity (let $v > 0$), θ is the slope angle, $u = \frac{N}{mv}$ is a control, linked with a normal component of the reaction force of the curve N. The control is supposed to has no constraints. The dot denotes the differentiation with the respect to the dimensionless time τ.

The initial and final conditions for the system (1) are as follows:

$$\begin{aligned} &x(0) = x_0, \ y(0) = y_0, \ v(0) = V_0, \\ &\theta(0), \theta(T), y(T), v(T) - \ \text{are free,} \end{aligned} \tag{2}$$

where V_0 - the absolute value of the initial velocity, (x_0, y_0) - the initial coordinates of the particle.

The goal function is

$$J = -x(T) \to \min_{u \in U}, \tag{3}$$

where U is the set of piecewise continuous functions. In other words, it is the same as to maximize the horizontal distance, while the duration T of the process is fixed.

The problem (1)–(3) is a singular optimal control problem [4], for which necessary optimal conditions in the form of the Maximum Principle satisfied trivially. One of the common approaches of research of such problems is replacement of the degenerate irregular problems to a regular problem that includes all the elements for the subsequent construction of the desired solution [6].

Note that only the last equation of the system (1) has an explicit form of u. Thus, this equation of the system might be omitted and the system (1) could be reduced to the system of the third-order:

$$\begin{cases} \dot{x} = v\cos\theta, \\ \dot{y} = v\sin\theta, \\ \dot{v} = -v^n - \sin\theta. \end{cases} \tag{4}$$

The goal function (3) could be rewritten as follows:

$$J = -x(T) \to \min_{\theta \in U}, \tag{5}$$

where θ – new control variable.

The problem (2), (4), (5) is regular and could be analyzed due to Maximum Principle. When this problem is solved the extremal control u could be calculated from the fourth equation of the system (1).

3   The Study of the Reaction's Sign

Application of Pontryagin's maximum principle to the optimal control problem (2), (4), (5) allows us to reduced it to the following boundary-value problem for the system of two nonlinear differential equations [11]:

$$
\begin{cases}
\dot{v} = -v^n - \sin\theta, & v(0) = V_0, \\
\dot{\theta} = \frac{\cos\theta}{v}\left(1 + (n+1)v^n \sin\theta\right), & \theta(T) = 0,
\end{cases}
\tag{6}
$$

with an additional condition $\cos\theta > 0$. A similar approach that allows to reduce the optimal problem with nonlinear control to a boundary-value problem for the system of differential equations in the original variables and controls, was used in [1, 2] for optimal navigation problems analysis.

The control related with the support reaction of the curve considering the fourth equation of the the system (1) has a form:

$$
u = \dot{\theta} + \frac{\cos\theta}{v},
$$

Substituted to this formula the expression for $\dot{\theta}$ from the system (6) we obtain the expression for the control with the respect to v and θ:

$$
u(v, \theta) = \frac{\cos\theta}{v}\left(2 + (n+1)v^n \sin\theta\right).
$$

While Pontryagin's function is constant $H = C$ on the optimal control then the first integral of the system (6) is

$$
H = \frac{v}{\cos\theta}\left(1 + v^n \sin\theta\right) = C.
$$

The phase portrait of the system (6) for $n = 1$ (see Fig. 1). For $n \neq 1$ phase portrait becomes topologically equivalent to the one showed. The darkened area on the picture (see Fig. 1) is the area of various possible initial conditions of the system (6) that satisfy to boundary conditions of the problem considered.

Different values of the constant C correspond to various trajectories in the plane of (v, θ). Moreover, there is a bijection between trajectories and corresponding them values of C in the the area of valid initial conditions on v and θ. Thus, choosing the value of C, in fact, we choose the specific trajectory. Note, that for all possible trajectories the boundary condition $C = v(T) > 0$ is fulfilled.

Let us investigate the type of the reaction normal component's sign changing. As much as there is existing explicit link between N and the control u which is given as $u = \frac{N}{mv}$, then to explore the sign changing of N it is needed to keep track of control's u sign changing. To find the quantity of intersections of the integral curve of the
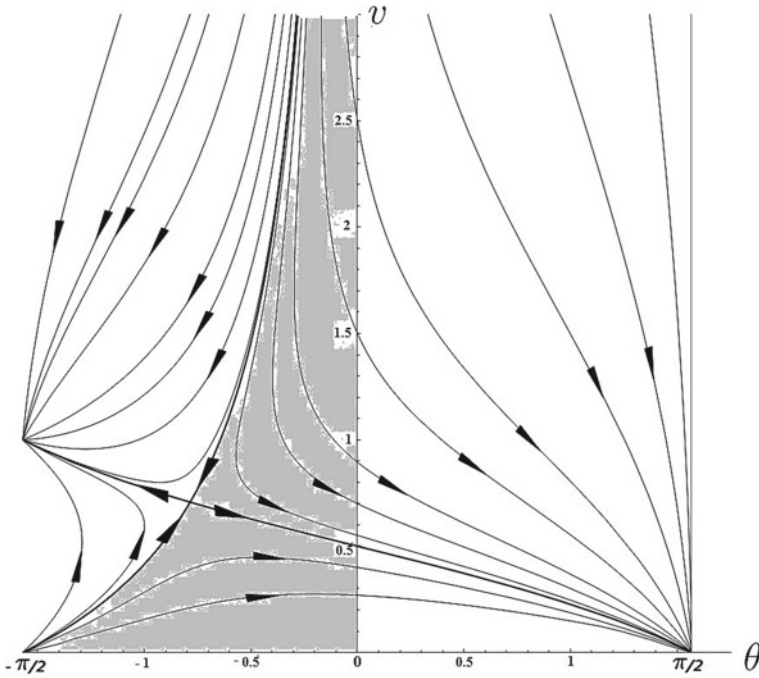
Fig. 1 The phase portrait of the system (6) for $n = 1$

system (6) with boundary of the constant sign area of the control function $u(v, \theta)$ it is needed to find the quantity of solutions of the system

$$\begin{cases} u = \frac{\cos \theta}{v}\left(2 + (n + 1)v^n \sin \theta\right) = 0, \\ H = \frac{v}{\cos \theta}\left(1 + v^n \sin \theta\right) = C, \end{cases} \tag{7}$$

$$\cos \theta > 0, \quad v > 0,$$

with the dependence on C.

Let $n \neq 1$. Extracting $\sin \theta$ from the first equation of the system and substituting to the second one we obtain the following equation:

$$P(v) = (n - 1)^2 v^{2n+2} - C^2(n + 1)^2 v^{2n} + 4C^2, \quad n \neq 1.$$

Taking into account the constrain $|\sin \theta| < 1$ we could obtain that $P(v)$ could be considered for value $v \geq \hat{v}$, where $\hat{v} = \sqrt[n]{\frac{2}{n+1}}$.

Let us estimate the quantity of roots of the polynomial $P(v)$. Investigate the monotonic of function $P(v)$. Critical points of $P(v)$ could be found from the equation

$$P'(v) = 2(n+1)v^{2n-1}\left((n-1)^2 v^2 - (n+1)nC^2\right) = 0.$$

Solution of this equation is

$$v_1 = C\sqrt{\frac{n(n+1)}{(n-1)^2}}.$$

Then the function $P(v)$ decreases if $v \in (0; v_1)$ and $P(v)$ increases if $v \in (v_1; +\infty)$. Thus, $\mathrm{argmin}(P(v)) = v_1$. To understand if these intervals have the roots of the $P(v)$ let us consider the value of $P(v)$ in the minimum point and in the infinity:

$$P(+\infty) = +\infty > 0,$$

$$P(\hat{v}) = (n-1)^2 (\frac{2}{n+1})^{(2n+2)/n} > 0, \quad n \neq 1,$$

$$P(v_1) = C^2\left(4 - (n+1)\left(C\sqrt{\frac{n(n+1)}{(n-1)^2}}\right)^{2n}\right).$$

It was obtained that if $v_1 \leq \hat{v}$ then $P(v)$ is strictly positive therefore no change of sign may be occur. If $v_1 > \hat{v}$ then there are three cases could be:

1. $P(v_1) > 0$. Then $P(v) \neq 0$ for $v \in (\hat{v}, +\infty)$, no roots exist, consequently, no switch of sign of the control along the trajectory;
2. $P(v_1) = 0$. Then only one root exists;
   Here it should be cleared that for the specific value of constant C in phase plane two trajectories correspond that situated on the opposite sides of separatrix and the saddle-point but the only one curve of each pair satisfies the boundary condition of the problem (6). Due to mutual position of these trajectories and the curve $u = 0$ it is possible to ascertain that if the intersection exists and is unique then it is located out of the domain considered, consequently, in this case there are no switches of the control function along the extremal trajectory (see Fig. 2).
3. $P(v_1) < 0$. Then $P(v) = 0$ at two points, which means two roots exist;
   In this case there is the intersection with the second trajectory corresponded to the constant C, it means that the control changes its sign during the motion along the extremal trajectory, and besides, only ones during the whole time. Since in the final moment the control $u(T) = \frac{2}{C} > 0$, where $C = v(T)$, it might be obtained that the change of the sign could be only from minus to plus.

The constant C for which $P(v_1) = 0$ is denoted by $\widetilde{C}$, that is

$$\widetilde{C} = \sqrt{\frac{4^{1/n}(n-1)^2}{n(n+1)^{1+1/n}}}.$$
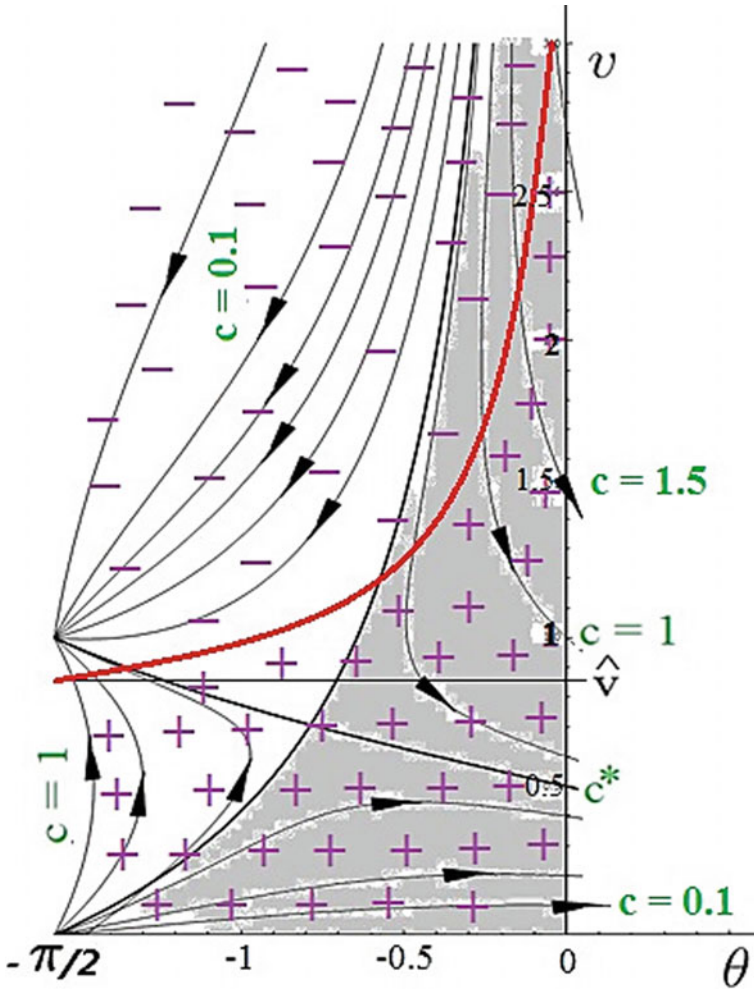
Fig. 2 The sign of the reaction

It was obtained that for all values of $C \leq \tilde{C}$ inequality $P(v_1) \geq 0$ satisfies and there are no switches of the control, and no more than one switching for $C > \tilde{C}$. The constant that corresponds to separatrix is denoted by the C^*:

$$C^* = \sqrt{\frac{n}{(n+1)^{1+1/n}}}.$$

The following equality is evident:

$$\widetilde{C} = C^* \sqrt{\frac{4^{1/n}(n-1)^2}{n^2}}.$$

To define the mutual location of the separatrix and the trajectory corresponded to the C^*, it is necessary to compare the values of $\widetilde{C}$ and C^*, or, that is the same

$$\sqrt{\frac{4^{1/n}(n-1)^2}{n^2}} \quad \vee \quad 1 \quad \Longleftrightarrow \quad \left(1 - \frac{1}{n}\right)^2 \quad \vee \quad 4^{-\frac{1}{n}}.$$

Denote the left part of inequality as $l(n)$, $l(n) \to +\infty$ for $n \to +0$ and $l(1) = 0$. Then $l'(n) = 2(1 - \frac{1}{n})\frac{1}{n^2}$. The derivation is equal to zero only if $n = 1$, that is why the function $l(n)$ decreases for $n \in (0, 1)$ and increases for all $n > 1$.

Let us study the right-hand of the function $r(n) = 4^{-\frac{1}{n}}$. It is obviously that $r(n) \to 0$ for $n \to +0$ and $r(1) = 0.25$. As $r'(n) = \frac{\ln 4}{\sqrt[n]{4n^2}} > 0$ for all $n > 0$, so the function $r(n)$ increases for all $n > 0$. Since the function $l(n)$ decreases on the interval $n \in (0, 1)$, and the function $r(n)$ increases on the same set, the unique value of $n = n^*$ exists such that $l(n^*) = r(n^*)$, and $l(n) > r(n)$ for $n < n^*$ and $l(n) < r(n)$ for $n^* < n < 1$. So it is obtained that $\widetilde{C} > C^*$ for $n < n^*$ and $\widetilde{C} < C^*$ for all $n^* < n < 1$.

The case of $n > 1$, where both functions monotonically increases requires a consideration. To clarify it let us power $l(n)$ and $r(n)$ to the $\frac{n}{2}$-th degree:

$$(1 - \frac{1}{n})^n \quad \vee \quad \frac{1}{2},$$

further it might be transformed to the form

$$2 \quad \vee \quad (1 + \frac{1}{n-1})^n.$$

The generalization of the Bernoulli's inequality is used for the right-hand expression

$$(1 + \frac{1}{n-1})^n \geq 1 + \frac{n}{n-1} = 2 + \frac{1}{n-1} > 2.$$

It is obtained that $\widetilde{C} > C^*$ for all $n > 1$.

Finally, it was obtained that for $n < n^*$ there is no switch of sign of the control for each phase trajectories laying under the separatrix entered to the saddle-point, and there is no more than one switching from the minus to plus on those which laying above. In the case of $n \in (n^*, 1) \cup (1, +\infty)$ it was derived that there is no switching of sign of the control for each phase trajectories located under the trajectory that corresponded to the constant $\widetilde{C}$, and for those that above - no more than once and from minus to plus.

Note that at the point θ^*, corresponded to the abscissa of the saddle-point, the curve $u = 0$ is above the saddle-point for every n. Rewriting the condition $u(v, \theta) = 0$ as $v(\theta) = \left(\frac{-2}{(n+1)\sin\theta}\right)^{1/n}$ (along the solutions of the boundary value problem (6) the
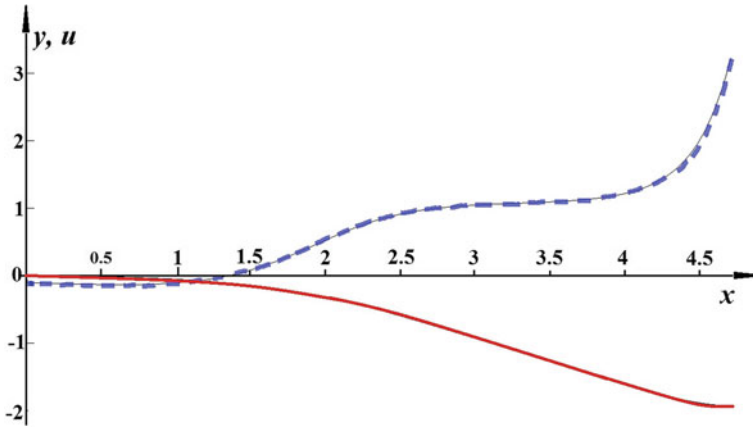
Fig. 3 Trajectory of the motion in the vertical plane (solid line) and the control along it (dashed line)

relation $\sin\theta < 0$ is fulfilled). Since the function $v(\theta)$ increases monotonically and at the point $\theta = -\pi/2$ takes the value of $v = \hat{v}$, then the motion of the phase-point on any of the paths located below the line $V_0 = \hat{v}$ in the considerable area has no switching of control and the sign of reaction is positive.

Let us consider the case $n = 1$. Then the polynomial $P(v)$ has a form:

$$P(v) = 4C^2(1 - v^4).$$

The permitted area for function $P(v)$, the ray $[\hat{v}, +\infty)$, is converted to the $[1, +\infty)$ and $P(1) = 0$. It is obtained that in the considered area $P(v) \geq 0$ is satisfied, consequently, there is no change of the control's and reaction's sign along the extremal trajectory.

The results of computer simulating are presented in Fig. 3 for $v(0) = 0.5$ and $T = 5$. The punctured line is the chart of function $u(v, \theta)$ along the extremal trajectory, and the solid line is the extremal trajectory of the motion in the vertical plane (x, y).

4 Conclusions

It was derived that in the case of linear viscous drag the sign of the reaction force along the extremal trajectory is positive. In the case of nonlinear viscous drag that proportional to n-th power of the velocity, the threshold exists. This threshold is such that the reaction's sign is positive if the initial velocity is less than the threshold. If the velocity is more than the limit value than the change of sign is possible no more than once, and the switching could be only from the negative value to the positive

one. The conclusions obtained are in agreement with results of computer simulation presented in [11], [5], where the range maximization and minimal-time problems for a nonzero initial velocity were studied, as well as results of [3], [9], where the initial velocity was supposed to be zero. The behavior of the sign in the case of simultaneous action of dry and viscous friction [10] is difficult problem, that required additional study.

References

1. Bryson, A., Ho, Y.: Applied Optimal Control. Blaisdell Publishing Company, Waltham, Massachusetts (1968)
2. Cherkasov, O., Yakushev, A.: Singular arcs in the optimal evasion against a proportional navigation vehicle. JOTA **113**, 211–226 (2002)
3. Golubev, Y.: Brachistochrone with friction. J. Comput. Syst. Sci. Int. **5**, 41–52 (2010)
4. Gurman, V., Kang, N.M.: Degenerate problems of optimal control. I. Autom. Remote Control **72**, 497–511 (2011)
5. Jeremic, O., Salinic, S., Obradovic, A., Mitrovic, Z.: On the brachistochrone of a variable mass particle in general force fields. Math. Comput. Model. **54**, 2900–2912 (2011)
6. Kelley, H.: A transformation approach to singular subarcs in optimal trajectory and control problems. SIAM J. Control **2**, 234–240 (1964)
7. Lokshin, B., Cherkasov O.: On the structure of optimal trajectories of a rotating rigid body in resistant medium. Vest. Mosk. Univ. Ser. 1 Matem. Mekh. **2**, 63–67 (1990)
8. Salinic, S.: Contribution to the brachistochrone problem with coulomb friction. Acta Mech. **208**, 97–115 (2009)
9. Vratanar, B., Saje, M.: On the analytical solution of the brachistochrone problem in a nonconservative field. Int. J. Non-Linear Mech. **33**, 489–505 (1998)
10. Zarodnyuk, A., Cherkasov, O.: Brachistochrone problem with coulomb friction and viscous drag: qualitative analysis. IFAC-PapersOnLine **48**, 1018–1023 (2015)
11. Zarodnyuk, A., Cherkasov, O.: Qualitative analysis of optimal trajectories of the point mass motion in a resisting medium and the brachistochrone problem. J. Compt. Syst. Sci. Int. **54**, 39–47 (2015)

Free Vibration of Cantilever Bars Having a Shape of Solid and Hollow Curvilinear Truncated Cone

Olga Szlachetka, Jacek Jaworski and Marek Chalecki

Abstract In calculations of first natural frequency of transversal vibrations of clamped-free bars with variable cross section, one can use an energetic method. The aim of this paper is an analysis of vibrations of solid and hollow slender posts having the shape of solid of revolution with the generatrix described by an exponential curve. The authors used the Rayleigh's method with the assumption that the shape of the post axis deflected during vibration is the same as a shape of the axis of a beam deflected by a uniform continuous static load. It was also assumed that the bars are made of an elastic and continuously distributed material what required numerous integrations of complicated expressions, therefore the calculations were carried out using the MATHEMATICA environment. Apart of the elastic energy of the bar, the authors considered also the potential energy connected to changes of location of the gravity center of elementary material slices during the post axis deflection. It was considered both the kinetic energy resulting from the replacement of the material slices perpendicular to the post axis as well as the energy connected to their rotation. The obtained results are very close to those obtained in FEM.

Keywords First natural frequency · Cantilever bar · Variable cross section

1 Introduction

For many cantilever constructions (posts, towers, chimneys) it is necessary to check the construction susceptibility to dynamic influences of wind gusts. Thus, it is useful

O. Szlachetka (✉) · J. Jaworski · M. Chalecki
Faculty of Civil and Environmental Engineering,
Warsaw University of Life Sciences—SGGW, Nowoursynowska 166, 02-787 Warsaw, Poland
e-mail: olga_szlachetka@sggw.pl

J. Jaworski
e-mail: jacek_jaworski@sggw.pl

M. Chalecki
e-mail: marek_chalecki@sggw.pl

to have a possibility of calculation of an approximated value of the first natural frequency of transverse vibrations of variably shaped bar elements with non-uniform cross-sections. To achieve this, various methods are used—one of them is an integration of the differential equation of Bernoulli-Euler's beam. Exact solutions are known here only for special cases. One of them is the benchmark solution for a wedge bar and truncated cone bar [4] obtained in the form of Bessel functions, replaced for the numerical calculations by polynomial equivalents. Caruntu [3] presented the solution for a curvilinear solid of revolution with sharp free end and parabolic generatrices. Other authors (e.g. [1, 5, 12, 13]) also analyzed the truncated cone bar problem using various methods. Some investigations concerned bars with rectangular cross-section where one of the cross-section dimensions is constant and the second one changed linearly [6], parabolically [2] or exponentially [7].

However, similar solutions for non-prismatic bars having the shape of conical pipes (solids of revolution with the recti- or curvilinear generatrices of the internal and external cone) are very hard to obtain. There are several papers concerning hollow truncated cones—solids of revolution with recti- or curvilinear generatrices—and their authors consider only selected, special geometrical cases of hollow bars (cf. e.g. [11, 15]). Two cases of "exponential" posts having very special shapes for which the integrated expressions fundamentally reduce themselves, are presented and solved in [14].

The authors of this paper have applied the Rayleigh's method consisting in comparison of the kinetic and potential energies with the assumption that the shape of the bar axis deflected during vibration is the same as a shape of the axis of a beam deflected by a uniform continuous static load. Such approach turned out to be useful to determine the first natural frequency of transversal vibrations both of solid and hollow truncated cone bars having various shapes of generatrix: rectilinear [9] and parabolic where the parabola is concave [8] or convex [10] in relation to the longitudinal cone axis.

In this paper, the authors have analyzed cantilever bars having the shape of solid of revolution with the generatrix described by an exponential curve. It has been assumed that the vibration amplitude is small, the material is homogeneous, isotropic and ideally elastic, the bars are slender, their mass is distributed continuously. In aim to carry out calculations, the Mathematica environment was used. As the authors did not find exact solutions for the "exponential" post in the literature, the obtained results have been compared to those obtained using Finite Element Method (in ANSYS).

2 Cantilever Bar Having the Shape of Solid of Revolution with the Generatrix Described by an Exponential Curve

Consider a post—cantilever bar with the shape of a curvilinear solid truncated cone as in Fig. 1 whose generatrices are described by an exponential function according

Fig. 1 Uniformly loaded
"exponential" post
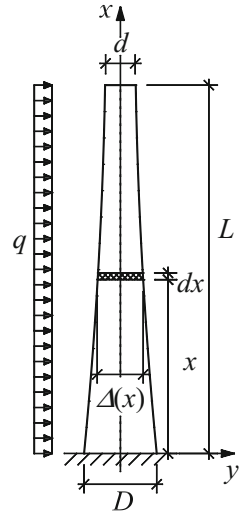
Form. (1). This formula is a dependence of a bar diameter Δ in any cross-section on a coordinate x of localization of this cross-section:

$$\Delta(x) = D\eta^{-\frac{x}{L}} = De^{bx} \tag{1}$$

where L—post height; D, d—bar diameters at the clamp and at the free end, respectively; η—the quotient of the diameters describing a convergence ratio of external walls of the solid. Following denotations have been introduced:

$$\eta = \frac{D}{d}, \tag{2}$$

$$b = -\frac{\ln \eta}{L}. \tag{3}$$

The cross-section area and second area moment equal, respectively:

$$A(x) = \frac{\pi \Delta^2(x)}{4} = \frac{\pi}{4} D^2 e^{2bx}, \tag{4}$$

$$J(x) = \frac{\pi \Delta^4(x)}{64} = \frac{\pi}{64} D^4 e^{4bx}. \tag{5}$$

The bar deflection by a uniform continuous static load q has been calculated through the integration of the differential equation of bar elastic deflection curve:

$$E J(x) \frac{d^2 u(x)}{dx^2} = \frac{q}{2}(x^2 - 2Lx + L^2),$$

$$\frac{\pi E D^4}{32q} \frac{d^2 u(x)}{dx^2} = \left(x^2 - 2Lx + L^2\right)e^{ax} \tag{6}$$

where $u(x)$—deflection, E—the longitudinal modulus of elasticity.

It has been denoted:

$$a = -4b = 4\frac{\ln \eta}{L}. \tag{7}$$

After the first and second integration of Eq. (6) it has been obtained, respectively:

$$\frac{\pi E D^4}{32q} \frac{du(x)}{dx} = P(x), \tag{8}$$

$$\frac{\pi E D^4}{32q} u(x) = R(x). \tag{9}$$

The integration constants have been determined from the boundary conditions for clamped-free bar and the expressions denoted as $P(x)$ and $R(x)$ equal, respectively:

$$P(x) = -\frac{L^2 a^2 + 2La + 2}{a^3}$$
$$+ \frac{e^{ax}}{a}\left[x^2 - 2x\left(L + \frac{1}{a}\right) + \frac{L^2 a^2 + 2La + 2}{a^2}\right], \tag{10}$$

$$R(x) = -\frac{L^2 a^2 + 2La + 2}{a^3}x - \frac{L^2 a^2 + 4La + 6}{a^4}$$
$$+ \frac{e^{ax}}{a^2}\left[x^2 - 2x\left(L + \frac{2}{a}\right) + \frac{L^2 a^2 + 4La + 6}{a^2}\right] \tag{11}$$

Then, the elastic potential energy in a deflected position and the kinetic energy connected to the velocity of passing of each slice through the position of equilibrium can be calculated. The potential energy equals:

$$E_p = \int_0^L \frac{1}{2} q u(x) dx = \frac{1}{2}\frac{32q^2}{\pi E D^4}\int_0^L R(x) dx. \tag{12}$$

If the mass of a material slice with a thickness dx is denoted as $m(x)$, i.e.:

$$dm(x) = \frac{\rho \pi}{4}\Delta^2(x)\, dx = \frac{\rho \pi}{4}D^2 e^{2bx} dx \tag{13}$$

then the kinetic energy is determined as:

$$E_k = \int_0^L \frac{1}{2} dm(x)\omega^2 u^2(x) = \frac{1}{2}\frac{\rho\pi}{4}D^2\omega^2\left(\frac{32q}{\pi E D^4}\right)^2\int_0^L e^{2bx} R^2(x) dx \tag{14}$$

where ρ is the mass density and ω is the vibration frequency.

The energy comparison enables to determine the vibration frequency ω and period T:

$$\omega^2 = \frac{D^2}{8} \frac{E}{\rho} \frac{\int_0^L R(x)dx}{\int_0^L e^{2bx} R^2(x)dx}, \tag{15}$$

$$T = \frac{2\pi}{\omega} = \frac{4\pi}{D} \sqrt{\frac{2\rho}{E}} \sqrt{\frac{\int_0^L e^{2bx} R^2(x)dx}{\int_0^L R(x)dx}}. \tag{16}$$

Additionally, a possibility of consideration of two corrections in the energy balance is presented below. The potential energy connected to the changes of height of the gravity center of elementary material slices during the post axis deflection has been calculated with use of Fig. 2a. If one assumes the approximation of $\cos \varphi$ by two first terms of the MacLaurin series, then an elementary segment, having the length dx and subjected to the deflection angle φ, changes its height over the post base by a quantity Δl which can be expressed as:

$$\Delta l = [1 - \cos \varphi(x)]dx = \frac{1}{2}\varphi^2(x)dx. \tag{17}$$

To calculate the sought component of the potential energy, one must count the sum of the changes Δl of height coordinate of all elementary segments of the post—here denoted as ΔL. It can be achieved using Forms. (8) and (10):

$$\Delta L(x) = \int_0^x \frac{1}{2}\varphi^2(\xi)d\xi = \frac{1}{2}\left(\frac{32q}{\pi E D^4}\right)^2 \int_0^x P^2(\xi)d\xi. \tag{18}$$

The component of the potential energy being calculated can be expressed as:

Fig. 2 **a** Scheme to determine the changes of location of the gravity center of an elementary material slice as the effect of the post axis deflection. **b** Scheme to determine a trajectory of the point A during deflection of the post axis
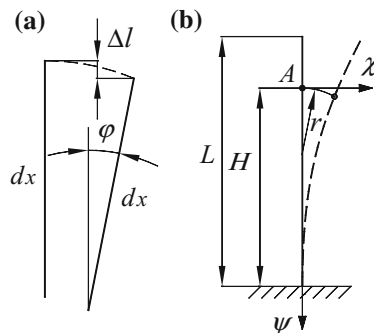
$$E_p^{\Delta h} = \int\limits_0^L \rho\, g\, A(x)\Delta L(x)dx = \frac{\pi D^2}{4}\rho g \int\limits_0^L e^{2bx}\Delta L(x)dx \qquad (19)$$

where g—the gravitational acceleration.

The kinetic energy, connected to the rotation of the material slices during deflection of the post axis has been calculated as follows: After the deformation of the post axis, a point A, placed in the distance H from the clamp (Fig. 2b), changes its position. The trajectory of this point can be described in a new coordination system χ, ψ. The coordinates of the point A in its certain new position are—according to the Forms. (9) and (18)—respectively:

$$\chi = \frac{32q}{\pi E D^4}R(x), \qquad (20)$$

$$\psi = \frac{1}{2}\left(\frac{32q}{\pi E D^4}\right)^2 \int\limits_0^x P^2(\xi)d\xi. \qquad (21)$$

Calculation of the load q from the Form. (20) and its substitution into Form. (21) yields in the trajectory equation:

$$\psi = \frac{1}{2}\frac{\int_0^x P^2(\xi)d\xi}{R^2(x)}\chi^2. \qquad (22)$$

The curvature radius r of this trajectory in the non-deflected position of the bar is described as:

$$r = \frac{\left(1+\psi_0'^2\right)^{3/2}}{\left|\psi_0''\right|} = \frac{\left(1+0^2\right)^{3/2}R^2(x)}{\int_0^x P^2(\xi)d\xi} = \frac{R^2(x)}{\int_0^x P^2(\xi)d\xi}. \qquad (23)$$

The velocity of the point A in this position can be expressed as:

$$\Omega = \omega\frac{y(x)}{r(x)}, \qquad (24)$$

thus the kinetic energy connected to the rotation of an elementary material slice is:

$$\Delta E_k^{rot} = \frac{1}{2}J(x)\Omega^2\rho dx. \qquad (25)$$

Using Forms. (5) and (7) it can be expressed as:

$$\Delta E_k^{rot} = \frac{1}{2}\frac{\pi D^4}{64}e^{-ax}\rho\omega^2\left(\frac{y(x)}{r(x)}\right)^2 dx. \qquad (26)$$

After the integration of the Form. (26) along the whole bar and considering that

$$\frac{y(x)}{r(x)} = \frac{32q}{\pi E D^4} \frac{\int_0^x P^2(\xi)d\xi}{R(x)} \tag{27}$$

one obtains the formula for the kinetic energy connected to the rotation of the material slices during deflection of the post axis:

$$E_k^{rot} = \frac{1}{2}\rho \frac{16}{\pi D^4} \frac{q^2}{E^2}\omega^2 \int\limits_0^L e^{-ax} \left(\frac{\int_0^x P^2(\xi)d\xi}{R(x)}\right)^2 dx. \tag{28}$$

Both corrections (19) and (28) have very small value in comparison with the elastic potential energy expressed by (12) and the kinetic energy expressed by (14).

3 Computational Examples, Accuracy and Comparison of Results

Figure 3 presents the results obtained with use of the Rayleigh's method—the vibration period, calculated from Form. (16) and corresponding to the first natural frequency of transversal vibrations for a steel curvilinear truncated cone post with the generatrix described by an exponential curve. The vibration period for the analyzed post has been compared to the periods of posts with rectilinear and parabolic generatrices—using the results printed in [8, 9]. The following data have been assumed: $E = 205$ GPa, $\rho = 7850$ kg m^{-3}, post height $L = 6$ m, diameter in the base $D = 0.2$ m. Various values of the parameter η have been considered, what corresponds to various values of diameters by the post top. One can notice that even small shape differences between the "parabolic" and "exponential" posts evoke significant differences in vibration periods, especially for $\eta > 8$.

The results obtained in this paper have been compared to those achieved in FEM (ANSYS). High conformity has been stated—the differences between the vibration periods for $\eta \le 4$ do not exceed 0.35%, whereas within the range $\eta \ge 8$ the differences between the vibration periods do not exceed 3% in average for the three examined cases.

The calculations in FEM for the hollow curvilinear cones were carried out in the following way: Firstly, the height was divided into 12 equal sections and the post diameters in 13 points were calculated according to the curve equation. Each pair of the adjacent points was joined with one straight segment and 12 such segments made a generatrix which in turn made a solid of revolution. Then, using 3D solids, a regular mesh was created in such way that 5 elements were distributed in the height of one section and 40 elements—on the circumference. There were ca. 30,000 elements in total and 60 elements along the post's height.

The paper [8] contains the comparison of results obtained from the method applied by the authors and results of FEM calculations to the results of exact solutions of a Bernoulli-Euler's beam for a truncated cone bar presented in [12] and obtained in the
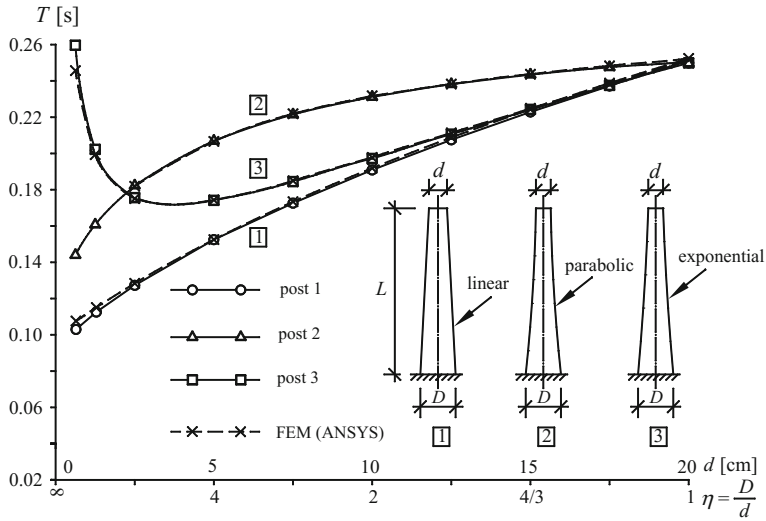
Fig. 3 Vibration periods for solid posts with different shapes of generatrix. Comparison of the own results to those obtained in FEM

form of Bessel functions (as in [4]). For the analyzed truncated cone, the vibration period calculated in FEM (ANSYS) was by 0.2% higher in average and the vibration period obtained by the authors was by 0.4% lower in average than in [12]. It can be concluded that the method applied by the authors allows to obtain results with accuracy sufficient for practical calculations.

Table 1 presents the percentage increase of the vibration period resulting from considering the two corrections: $E_p^{\Delta h}$—connected to the changes of height of the gravity center of elementary material slices during the post axis deflection and E_k^{rot}—connected to the rotation of the material slices.

The solid "exponential" posts of two types are compared—made of steel ($\rho = 7850\,\text{kg}\,\text{m}^{-3}$, $\sqrt{\rho/E} = 1.95685 \times 10^{-4}\,\text{s}\,\text{m}^{-1}$) and of ferroconcrete ($\rho = 2400\,\text{kg}\,\text{m}^{-3}$, $\sqrt{\rho/E} = 3.5 \times 10^{-4}\,\text{s}\,\text{m}^{-1}$)—having the diameter by the base $D = 1\,\text{m}$, various convergence ratios of the external walls ($\eta = 1, 4/3, 2, 4$) corresponding to the diameters by the top $d = 1, 0.75, 0.5, 0.25\,\text{m}$ as well as various slendernesses $\lambda = 2, 4, 8, 16, 32$ corresponding to the heights $L = 2, 4, 8, 16, 32\,\text{m}$. The slenderness is defined here as the quotient of the height and greater diameter $\lambda = L/D$.

As one can see from the data presented in Table 1, these both corrections increase the vibration period but their influence for the posts with medium slenderness is small. The influence of the correction connected to the rotation of the material slices is important for the posts with very small slenderness, whereas the influence of the correction connected to the changes of height of the gravity center of material slices—for the posts with high slenderness. It is visible that the quantity of the

Table 1 Influence of the corrections on the post vibration period

		Steel				Ferroconcrete			
		$\eta=1$	$\eta=4/3$	$\eta=2$	$\eta=4$	$\eta=1$	$\eta=4/3$	$\eta=2$	$\eta=4$
$\lambda=2$	T [s]	0.005573	0.004986	0.004383	0.003870	0.009967	0.008917	0.007840	0.006922
	$T^{\Delta h+rot}$ [s]	0.005690	0.005644	0.004431	0.003892	0.010177	0.009058	0.007925	0.006961
	$\Delta T^{\Delta h}$ [%]	0.000359	0.000301	0.000228	0.000258	0.00100	0.000841	0.000765	0.000578
	ΔT^{rot} [%]	2.101	1.580	1.083	0.570	2.101	1.580	1.083	0.570
$\lambda=4$	T [s]	0.022291	0.019924	0.017533	0.015480	0.039870	0.035636	0.031360	0.027687
	$T^{\Delta h+rot}$ [s]	0.022410	0.020004	0.017581	0.015502	0.040084	0.035780	0.031447	0.027728
	$\Delta T^{\Delta h}$ [%]	0.00269	0.00201	0.00171	0.00129	0.00778	0.00645	0.00510	0.00506
	ΔT^{rot} [%]	0.529	0.397	0.272	0.143	0.529	0.397	0.272	0.143
$\lambda=8$	T [s]	0.089165	0.079696	0.070133	0.061920	0.159478	0.142544	0.125439	0.110748
	$T^{\Delta h+rot}$ [s]	0.089300	0.079788	0.070190	0.061949	0.159788	0.142759	0.125578	0.110831
	$\Delta T^{\Delta h}$ [%]	0.0192	0.0161	0.0134	0.0123	0.0621	0.0512	0.0430	0.0397
	ΔT^{rot} [%]	0.133	0.0993	0.0682	0.0357	0.133	0.0989	0.0686	0.0361
$\lambda=16$	T [s]	0.356658	0.318786	0.280533	0.247678	0.637914	0.570176	0.501758	0.442994
	$T^{\Delta h+rot}$ [s]	0.357326	0.319275	0.280881	0.247943	0.641290	0.572677	0.503569	0.444425
	$\Delta T^{\Delta h}$ [%]	0.154	0.129	0.108	0.0981	0.496	0.414	0.344	0.314
	ΔT^{rot} [%]	0.0331	0.0248	0.0171	0.00888	0.0331	0.0249	0.0169	0.00880
$\lambda=32$	T [s]	1.42663	1.27514	1.12213	0.990712	2.55166	2.28070	2.00703	1.77198
	$T^{\Delta h+rot}$ [s]	1.44464	1.28854	1.13191	0.998573	2.65871	2.35978	2.06442	1.81808
	$\Delta T^{\Delta h}$ [%]	1.254	1.045	0.867	0.791	4.187	3.461	2.855	2.599
	ΔT^{rot} [%]	0.00841	0.00627	0.00446	0.00232	0.00823	0.00658	0.00448	0.00226

correction E_k^{rot} does not depend on material properties whereas the quantity of the correction $E_p^{\Delta h}$ depends on the material parameters ρ and E.

The method presented in the paper can be also applied for variously shaped hollow solids of revolution. It is illustrated by another example where ferroconcrete towers have been analyzed, having the shape of a hollow truncated cone, of which external generatrix is an exponential function. The tower parameters are: $\sqrt{\rho/E} = 3.5 \times 10^{-4}\,\mathrm{s\,m^{-1}}$, height $L = 18\,\mathrm{m}$, external diameter by the base $D = 3\,\mathrm{m}$, various external diameters by the top changing from $d = 0.9\,\mathrm{m}$ to $d = 3\,\mathrm{m}$, what corresponds to the values of the parameter η shown in Fig. 4. As it concerns medium slenderness bars, the corrections E_k^{rot} and $E_p^{\Delta h}$ have not been considered in the calculations.

The curves 1–5 in Fig. 4 show the vibration periods of the towers in which the wall thickness (horizontally measured) is equal to $t_2 = 0.2\,\mathrm{m}$ by the base and $t_1 = 0.1\,\mathrm{m}$ by the top and their internal surfaces are variously shaped. For $d = 3\,\mathrm{m}$ what corresponds to $\eta = 1$, the external generatrix, described by an exponential function, becomes a straight line and the internal diameter by the post top is equal $d = 2.8\,\mathrm{m}$, so it is greater than the diameter by the post base equal $2.6\,\mathrm{m}$. The differences between the vibration periods for the tower with the exponential internal generatrix (curve 3) and for the tower with the wall thickness changing linearly (curve 4) are lower than 0.3%—the curves practically cover each other.

The curves 6 and 7, marked with dashed lines, consist the vibration periods of the towers of a similar type—with the wall having a constant thickness (measured
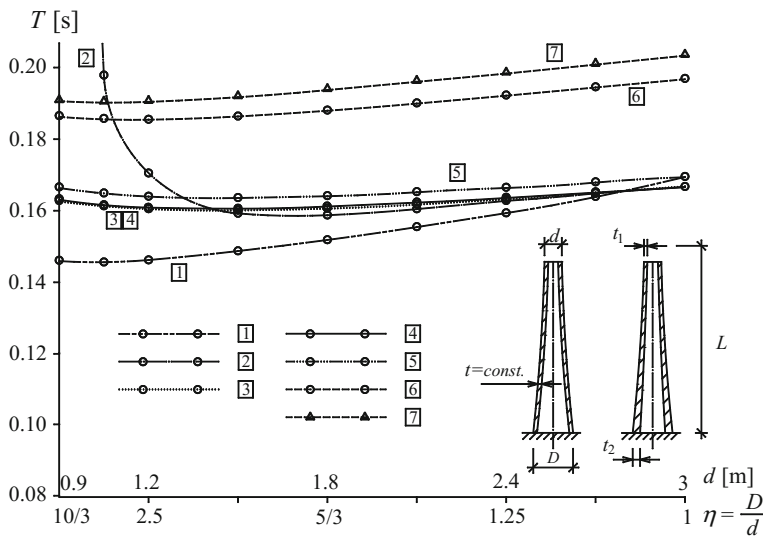
Fig. 4 Vibration period for variously shaped hollow "exponential" ferroconcrete towers: 1—the internal generatrix is a parabola, 2—the internal generatrix is a straight line, 3—the internal generatrix is an exponential curve, 4—the wall thickness changes linearly from t_2 to t_1, 5—the wall thickness changes parabolically from t_2 to t_1, 6—the wall thickness is constant $t = 0.1\,\mathrm{m}$, 7—the wall thickness is constant $t = 0.2\,\mathrm{m}$

horizontally): $t = 0.1\,\text{m}$ and $t = 0.2\,\text{m}$. The above-mentioned example proves that the method applied by the authors allows to calculate the first frequency / period of transverse vibrations of slender shell constructions having the shape of solid of revolution—curvilinear hollow truncated cones.

4 Summary and Conclusions

The Rayleigh's method can be effectively applied for calculations of first natural frequency of (transversal) free vibrations of non-prismatic cantilever bars with solid and hollow (tubular) cross-section, providing sufficient accuracy for practical engineering applications. However, the condition must be fulfilled that the external (and internal, if necessary) diameter of a hollow bar being a solid of revolution is describable by a continuous and smooth function of a coordinate x and the functions describing vibration period T are integrable. In some cases one obtains a solution in form of elementary functions, in others the numerical integration is inevitable. The complication degree of such calculations causes that it is necessary to apply a professional computer program. It can be stated that it is possible to use a computational program (like e.g. Mathematica, Maple) instead of FEM environments to count the first natural frequency of a post.

For posts of very small and high slenderness, the accuracy of solutions described by Form. (16) can be increased by introduction of appropriate corrections connected to certain additional energy components, while for medium slenderness posts the influence of these corrections is insignificant.

References

1. Abdelghany, S.M., Ewis, K.M., Mahmoud, A.A., Nassar, M.M.: Vibration of a circular beam with variable cross sections using differential transformation method. Beni-Suef Univ. J. Basic Appl. Sci. **4**(3), 185–191 (2015)
2. Caruntu, D.I.: Classical Jacobi polynomials, closed-form solutions for transverse vibrations. J. Sound Vib. **306**(3), 467–494 (2007)
3. Caruntu, D.I.: Dynamic modal characteristics of transverse vibrations of cantilevers of parabolic thickness. Mech. Res. Commun. **36**(3), 391–404 (2009)
4. Conway, H.D., Dubil, J.F.: Vibration frequencies of truncated-cone and wedge beams. J. App. Mech. **32**(4), 932–934 (1965)
5. Coşkun, S.B., Atay, M.T., Öztürk, B.: Transverse Vibration Analysis of Euler-Bernoulli Beams Using Analytical Approximate Techniques. INTECH Open Access Publisher (2011)
6. Datta, A.K., Sil, S.N.: An analysis of free undamped vibration of beams of varying cross-section. Comput. Struct. **59**(3), 479–483 (1996)
7. Ece, M.C., Aydogdu, M., Taskin, V.: Vibration of variable cross-section beam. Mech. Res. Commun. **34**(1), 78–84 (2007)

8. Jaworski, J., Szlachetka, O.: Free vibrations of cantilever bars with linear and nonlinear variable cross-section. Discontinuity Nonlinearity Complex. **6**(4), 489–501 (2017)
9. Jaworski, J., Szlachetka, O., Aguilera-Cortés, L.A.: Application of Rayleigh's method to calculation of the first natural frequency of cantilever columns with variable cross-section (in Polish). JCEEA **62**(3/II), 185–194 (2015)
10. Jaworski, J., Szlachetka, O., Chalecki, M.: Analysis of free vibrations of cantilever bars with parabolically variable cross sections using the Rayleigh's method. Acta Sci. Pol. Arch. **16**(4), 5–14 (2017)
11. Kang, J.H., Leissa, A.W.: Three-dimensional vibrations of solid cones with and without an axial circular cylindrical hole. Int. J. Solids Struct. **41**(14), 3735–3746 (2004)
12. Lau, J.H.: Vibration frequencies for a non-uniform beam with end mass. J. Sound Vib. **97**(3), 513–521 (1984)
13. Naguleswaran, S.: A direct solution for the transverse vibration of Euler- Bernoulli wedge and cone beams. J. Sound Vib. **172**(3), 289–304 (1994)
14. Suppiger, E.W., Taleb, N.J.: Free lateral vibration of beams of variable cross section. Z. Angew. Math. Phys (ZAMP) **7**(6), 501–520 (1956)
15. Wu, J.S., Chiang, L.K.: Free vibrations of solid and hollow wedge beams with rectangular or circular cross-sections and carrying any number of point masses. Int. J. Numer. Meth. Eng. **60**(3), 695–718 (2004)

Four-Bar Mechanism Substitution for Balance Board Experiments: A Parametric Study

Ambrus Zelei, Csenge A. Molnár and Tamás Insperger

Abstract Our research aims the study of balancing on a rolling balance board with respect to dynamic properties such as stability and stabilizability. The goal is to identify the parameter regions where human subjects are able to keep themselves stable in the upright position for at least 60 s. The radius of the balance board and the height of the foot platform are adjusted for each individual test, which is a time demanding process. We give a preliminary design of a substituting four-bar mechanism in order to speed up the balance board experiments and to extend the limits of the parameter study. The mechanism is tunable quickly in order to imitate the motion of the balance board with different radii and platform heights; whilst the agreement of the kinematic behaviour is almost perfect for tilt angles within the region of $\pm 30°$. The dynamic behaviour of the mechanism and the balance board are compared based on theoretically derived stability diagrams associated with the underlying mechanical models. The balancing process is modelled by a proportional-derivative delayed feedback controller in order to account with the reaction time delay of the subject. We show that the stable parameter regions of the balance board and the mechanism are in good agreement, therefore the mechanism can be used as a substituting device for balance board.

Keywords Human balancing · Rolling balance board · Four-bar mechanism
Time-delay systems · Parameter optimization

A. Zelei (✉)
MTA-BME Research Group on Dynamics of Machines and Vehicles
and MTA-BME Lendület Human Balancing Research Group,
Muegyetem rkp 3-5, Budapest H-1111, Hungary
e-mail: zelei@mm.bme.hu

C. A. Molnár · T. Insperger
Department of Applied Mechanics, Budapest University of Technology
and Economics and MTA-BME Lendület Human Balancing Research Group,
Budapest, Hungary
e-mail: csenge.molnar@mm.bme.hu

T. Insperger
e-mail: insperger@mm.bme.hu

1   Introduction

Understanding the mechanism of keeping balance during everyday activities is an important task for physiologists and neuroscientists. Balance disorders often leads to falls, which may result in fatal injuries, especially in the elderly, therefore the development of techniques and biomechanical devices to prevent falling is of high importance [14, 15]. A key element of human balance research is to find an appropriate mechanical model with some adjustable characteristic parameters, which reflects balancing abilities of human subjects. For example, in stick balancing on the fingertip, the mechanical model is an inverted pendulum and the characteristic parameter is the smallest length of the stick that a subject is able to balance for certain time [2, 5, 6, 10, 18]. Typically, human subjects cannot balance stick of shorter than 30 cm [11]. For quiet standing, the mechanical model is again an inverted pendulum [7, 16], however, the length of the pendulum, i.e., the height of the subject, is fixed and cannot be considered as an adjustable parameter. The advantage of the controlled inverted pendulum model is its publicity in the literature, e.g. [1, 4]. Balancing on a balance board is a generalized version of quiet standing, where some parameters of the balance board (e.g., the geometry or the mass) can be adjusted [3, 12]. Signals of balancing trials with different balance board geometry can be analyzed and quantified using the method of stabilometry [13, 17]. This way the ability of balancing in standing position can be analyzed as a function of some well defined parameters [12]. A drawback of such analysis is that the configuration of the balance board should be modified before each balancing trial, which, in case of systematic series of measurements, may be time-consuming. This motivates the idea of creating a simply adjustable mechanism, which provides the same motion as the balance board.

The concept of a four-bar mechanism substitution of a rolling balance board is proposed, which can speed up the balance board laboratory measurement process. The adjustment of the parameters of the balance board for different balancing trials takes considerable time. Especially the interchange of the arcs is time consuming, because in this case the balance board have to be completely disassembled (see Fig. 1c). In addition to the quick adjustment, another advantage of the substituting mechanism is that the parameters can be adjusted continuously. The first goal of this work is to find the four-bar mechanism for which any point of the coupler link has the same trajectory as the corresponding point of the balance board. This ensures the same kinematic behavior. Secondly, it is shown that the dynamic behavior of the balance board and the mechanism under delayed feedback control is similar.

2   Kinematic Analysis

The main criteria to the mechanism is that the ankle joint position of the balance board (see point A in Fig. 1d) and the ankle joint position of the substituting mechanism (see point E in Fig. 2) must have the same trajectory when the tilt angle ϑ is varied. This results the same rigid body motion for the balance board and the coupler link of the mechanism.

Fig. 1 Balance board experiment set-up (**a**), simplified mechanical model (**b**), balance board with interchangeable arcs (**c**), geometry (**d**)

Fig. 2 Substituting four-bar mechanism

2.1 Balance Board

A rolling balance board shown in Fig. 1 is tilted by angle ϑ with respect to the horizontal line. The subject's feet are placed on the balance board. The geometric parameters of the balance board are the radius R, the sole depth v and the parallel shift e. The location of the foot is given by e, which is a fix parameter for each subject, while R and v are tuned during balance experiments. Note that R and v can

be adjusted to discrete values only. The human body is modeled by a rigid body of which the tilt angle φ is measured from the vertical.

Figure 1d introduces a global frame of reference denoted by 0 and a local frame B that is fixed to the balance board. The following position vector and rotation matrix provides the transformation between frames 0 and B:

$$
{}^0\mathbf{p}_B = \begin{bmatrix} -R\vartheta \\ R \\ 0 \end{bmatrix}, \qquad {}^0\mathbf{R}_B = \begin{bmatrix} c_\vartheta & -s_\vartheta & 0 \\ s_\vartheta & c_\vartheta & 0 \\ 0 & 0 & 1 \end{bmatrix}. \tag{1}
$$

The position of the ankle joint A in the local and global system with the simplified notations $s_\vartheta = \sin \vartheta$ and $c_\vartheta = \cos \vartheta$ are given by:

$$
{}^B\mathbf{r}_A = \begin{bmatrix} -e \\ -v \\ 0 \end{bmatrix}, \qquad {}^0\mathbf{r}_A = {}^0\mathbf{R}_B\,{}^B\mathbf{r}_A + {}^0\mathbf{p}_B = \begin{bmatrix} -R\vartheta + v\,s_\vartheta - e\,c_\vartheta \\ R - v\,c_\vartheta - e\,s_\vartheta \\ 0 \end{bmatrix}. \tag{2}
$$

2.2 Substituting Mechanism

The geometric parameters of the four-bar mechanism shown in Fig. 2 are the distance d and the depth a of the pivot points, the crank lengths l, the coupler length c and the horizontal shift e of ankle joint E. The coupler link is tilted by angle ϑ, which angle corresponds to the tilt angle of the balance board. The foot is kept parallel to the coupler bar such that the elevation of the ankle joint is h.

2.2.1 Closed Form Solution for the Crank Angles

In order to express the ankle joint position, we need to determine the crank angles α_1 and α_2. The goal is to find α_1 and α_2 as functions of tilt angle ϑ such that the following vector-loop equations satisfy:

$$
c_1 + c_2 = \frac{d}{l} + \frac{c}{l} c_\vartheta \tag{3}
$$

$$
s_1 - s_2 = \frac{c}{l} s_\vartheta, \tag{4}
$$

where $s_1 = \sin \alpha_1, c_1 = \cos \alpha_1, s_2 = \sin \alpha_2$ and $c_2 = \cos \alpha_2$. The following identities are applied to reorganize the vector-loop equations:

$$
c_1 + c_2 = 2c_p c_m \quad \text{and} \quad s_1 - s_2 = 2s_m c_p, \tag{5}
$$

where $s_p = \sin \gamma_p, c_p = \cos \gamma_p, s_m = \sin \gamma_m, c_m = \cos \gamma_m$ and the new variables

$$\gamma_p = \frac{\alpha_1 + \alpha_2}{2}, \quad \text{and} \quad \gamma_m = \frac{\alpha_1 - \alpha_2}{2}. \tag{6}$$

Applying the identities (5) and the newly introduced variables (6), the vector-loop equations (3) and (4) can be reformulated again in the form

$$2c_p c_m = \frac{d}{l} + \frac{c}{l} c_\vartheta, \tag{7}$$

$$2s_m c_p = \frac{c}{l} s_\vartheta. \tag{8}$$

By dividing (8) and (7) the solution for γ_m and γ_p can be expressed as

$$\gamma_p = \arccos\left(\frac{c}{2l} \frac{s_\vartheta}{s_m}\right) \quad \text{and} \quad \gamma_m = \arctan\left(\frac{c\, s_\vartheta}{d + c\, c_\vartheta}\right). \tag{9}$$

Finally, the crank angles are expressed using Eq. (6) as direct functions of the tilt angle ϑ:

$$\alpha_1 = \gamma_p + \gamma_m \quad \text{and} \quad \alpha_2 = \gamma_p - \gamma_m. \tag{10}$$

2.2.2 Position of the Ankle Joint in the Global Frame of Reference

The position vector of the local frame of reference M can be written based on Fig. 2. Since the origin is in the middle of the coupler bar, the average of the endpoint positions of the cranks are used.

$$^0\mathbf{p}_M = \begin{bmatrix} ^0 x_M \\ ^0 y_M \\ 0 \end{bmatrix} = \begin{bmatrix} \frac{1}{2}(-d + l\,c_1) + \frac{1}{2}(d - l\,c_2) \\ -a + \frac{1}{2}l\,s_1 + \frac{1}{2}l\,s_2 \\ 0 \end{bmatrix} = \begin{bmatrix} \frac{l}{2}(c_1 - c_2) \\ -a + \frac{l}{2}(s_1 + s_2) \\ 0 \end{bmatrix}. \tag{11}$$

The fully expanded expressions for the position of the origin of frame M as functions of ϑ are

$$^0 x_M = -\frac{cA\, s_\vartheta}{2(d + c\, c_\vartheta)B}, \quad \text{and} \quad ^0 y_M = -a + \frac{A}{2B}, \tag{12}$$

where

$$A = \sqrt{4l^2 - c^2 - d^2 - 2cd\, c_\vartheta} \quad \text{and} \quad B = \sqrt{1 + \frac{c^2\, s_\vartheta^2}{(d + c\, c_\vartheta)^2}}. \tag{13}$$

Since the tilt angle ϑ are the same, the rotation matrix of reference frames 0 and M is the same as in the case of the balance board:

$$^0\mathbf{R}_M =\ ^0\mathbf{R}_B\ . \tag{14}$$

Finally, the ankle joint E position in the local and the global frames are expressed as

$$^M\mathbf{r}_E = \begin{bmatrix} -e \\ h \\ 0 \end{bmatrix}, \qquad ^0\mathbf{r}_E =\ ^0\mathbf{R}_M\ ^M\mathbf{r}_E +\ ^0\mathbf{p}_M = \begin{bmatrix} ^0x_M - h\,s_\vartheta - e\,c_\vartheta \\ ^0y_M + h\,c_\vartheta - e\,s_\vartheta \\ 0 \end{bmatrix}. \tag{15}$$

2.3   Optimization of the Substituting Mechanism

The cost function below expresses the integral of the error between the balance board and the substituting mechanism ankle positions, which have to be minimized:

$$\int_{-\vartheta_{max}}^{\vartheta_{max}} \left|\, ^0\mathbf{r}_E -\ ^0\mathbf{r}_A \right|^2 \mathrm{d}\vartheta = \min! \tag{16}$$

The set of parameters $\{c,\ d,\ a,\ l,\ h\}$ of the substituting mechanism has to be found for which the cost function (16) is minimal in case of a certain set of parameters $\{R,\ v\}$ of the balance board. The number of unknown parameters is reduced by considering $\vartheta = 0$ horizontal position. Based on Eqs. (2), (12), (13) and (15), expression $^0y_E =\ ^0y_A$ reads:

$$R - v\,c_\vartheta - e\,s_\vartheta = -a + \frac{A}{2B} + h\,c_\vartheta - e\,s_\vartheta, \tag{17}$$

which simplifies after canceling the term $e\,s_\vartheta$ and substituting $\vartheta = 0$. Substituting expressions $B(\vartheta = 0) = 1$ and $A(\vartheta = 0) = A_0$ we obtain an expression for a:

$$a = v + \frac{A_0}{2} + h - R, \quad \text{with}\quad A_0 = \sqrt{4l^2 - c^2 - d^2 - 2cd}\ . \tag{18}$$

Parameter c can be fixed too by setting its value in a certain region found by trial-and-error method. Out of this region there is no solution that results close to zero cost function (16). We set $c = 1.4R$.

After fixing parameters a and c, the remaining unknown parameters are d, l and h. The minimum cost function have to be found in the three dimensional parameter space (d, l, h). By means of a well chosen initial guess and a local minimum search algorithm we construct generally applicable formulae for the substituting mechanism geometric parameters:

$$c = 1.4R; \quad d = 2.956R; \quad a = 0.8786R; \quad l = 2.530R; \quad h = 0.5896R - v. \tag{19}$$

Table 1 Some examples for optimal parameters of the substituting mechanism (the parameter values used in the dynamic analysis in Sect. 3 are indicated by boldface)

Balance board radius	$R = 0.1$ m	$R = \textbf{0.25}$ m
Parameter set for any v value		
Coupler length	$c = 0.14$ m	$c = \textbf{0.35}$ m
Pivot points distance	$d = 0.2956$ m	$d = \textbf{0.739}$ m
(Pivot points depth)	($a = 0.08786$ m)	($a = \textbf{0.21965}$ m)
Crank length	$l = 0.253$ m	$l = \textbf{0.6325}$ m
Sole elevation for $v = \textbf{−0.1}$ m	$h = 0.15896$ m	$h = \textbf{0.2474}$ m
Sole elevation for $v = 0$ m	$h = 0.05896$ m	$h = 0.1474$ m
Sole elevation for $v = 0.1$ m	$h = −0.04104$ m	$h = 0.0474$ m
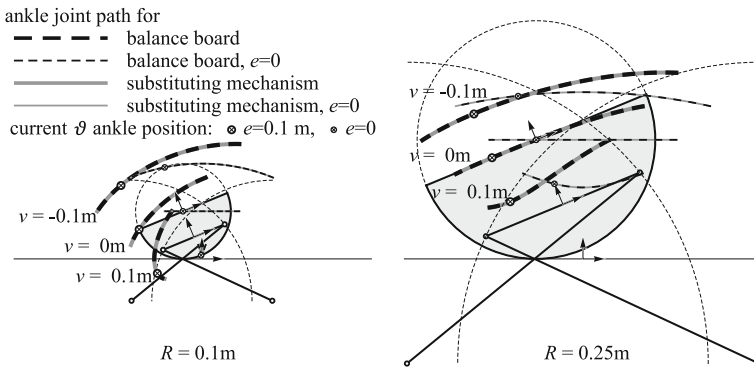
Fig. 3 Balance board and four bar mechanism together with parameters $R = 0.1$ m, $R = 0.25$ m and $v = −0.1$ m, $v = 0$ m, $v = 0.1$ m

The above parameters of the substituting mechanism can be set according to the desired R and v values of the equivalent balance board. A few examples are collected in Table 1 and in Fig. 3. Note that parameter a does not play any role in a real application, because it induces a shift only of the ankle joint path and hence neither the gradient of the potential function nor the stability properties change. Figure 3 shows that the ankle joint paths for the balance board and the mechanism overlap each other with a difference smaller than 1 mm.

3   Dynamic Analysis

We construct the dynamic model both for the balance board and the mechanism. The dynamic behaviour is compared via the mass and stiffness matrices and the stability properties. Since the kinematics (i.e. the motion of the ankle joint as the function of

the tilt angle) are the same in case of both equipments, it is obvious that the dynamic behaviour is the same when the inertial parameters of the equipments are neglected (see Sect. 3.5). We observed that when considering the inertial parameters of the equipments, the mass and stiffness matrix and the stability behavior are still similar.

3.1 Dynamic Model of a Human Standing on the Balance Board

The mechanical model depicted in Fig. 1a is applied. We consider undeformable bodies and ground, therefore rolling resistance does not appear in the model. This is an acceptable simplification, since the balance board is placed on hard surface and the wooden made balance board itself is also stiff.

We apply the Lagrange equation of motion for which the kinetic energy T, the potential function U and the generalized force $\mathbf{Q}$ of the ankle control torque M are expressed as:

$$T = \frac{1}{2}m_H \, |\dot{\mathbf{r}}_{C_H}|^2 + \frac{1}{2}m_B \, |\dot{\mathbf{r}}_{C_B}|^2 + \frac{1}{2}J_H \dot{\varphi}^2 + \frac{1}{2}J_B \dot{\vartheta}^2 \,, \tag{20}$$

$$U = m_H \, g \, y_{C_H} + m_B \, g \, y_{C_B} + \frac{1}{2}k_A \, (\vartheta - \varphi + \varphi_0)^2 \,, \tag{21}$$

$$\mathbf{Q} = [-M, \, M]^T \,, \tag{22}$$

where m_H and m_B are the mass and J_H and J_B are the mass moment inertia of the human body and the balance board respectively, k_A is the stiffness of the ankle and $\varphi_0 = \arcsin(e/l_H)$ is the equilibrium angle of the human (Fig. 1a shows the tilted human body near equilibrium). The human body and balance board centre of mass positions are simply given by $\mathbf{r}_{C_H} = \mathbf{r}_A + l_H \left[-s_\varphi, \, c_\varphi, \, 0\right]^T$ and $\mathbf{r}_{C_B} = \mathbf{p}_B - c_B \left[-s_\vartheta, \, c_\vartheta, \, 0\right]^T$ respectively.

Using the generalized coordinates $\mathbf{q} = [\varphi(t), \, \vartheta(t)]$, the following form of the Lagrange equation of motion is used:

$$\frac{\mathrm{d}}{\mathrm{d}t} \frac{\partial T}{\partial \dot{q}_i} - \frac{\partial T}{\partial q_i} + \frac{\partial U}{\partial q_i} = Q_i \,; \quad i = 1, \, 2 \,. \tag{23}$$

3.2 Dynamic Model of a Human Standing on the Substituting Mechanism

The mechanical model in Fig. 2 is applied with frictionless joints and undeformable bodies. The kinetic energy and potential function of the substituting mechanism reads

$$T = \frac{1}{2}m_{\mathrm{H}}\,|\dot{\mathbf{r}}_{C_{\mathrm{H}}}|^2 + \frac{1}{2}m_{\mathrm{c}}|\dot{\mathbf{p}}_{\mathrm{M}}|^2 + \frac{1}{2}J_{\mathrm{H}}\dot{\varphi}^2 + \frac{1}{2}J_{\mathrm{c}}\dot{\vartheta}^2 + \frac{1}{2}J_l\dot{\alpha}_1^2 + \frac{1}{2}J_l\dot{\alpha}_2^2, \quad (24)$$

$$U = m_{\mathrm{H}}\,g\,y_{C_{\mathrm{H}}} + m_l\,g\frac{l}{2}s_1 + m_l\,g\frac{l}{2}s_2 + m_{\mathrm{c}}g y_{\mathrm{M}} + \frac{1}{2}k_{\mathrm{A}}\,(\vartheta - \varphi + \varphi_0)^2, \quad (25)$$

where m_{c} is the mass and J_{c} is the mass moment of inertia with respect to the centre of mass of the coupler link. The crank mass is m_l and J_l is the mass moment of inertia of one crank with respect to the pivot point. The centre of mass of the human body is $\mathbf{r}_{C_{\mathrm{H}}} = \mathbf{r}_{\mathrm{E}} + l_{\mathrm{H}}\left[-s_\varphi,\ c_\varphi,\ 0\right]^{\mathrm{T}}$. The generalized force vector $\mathbf{Q}$ is the same as in (22).

3.3 Computation of Ankle Torques During Human Balancing

During the balancing process the brain collects information from the environment via the sensory organs and after processing sends signals to the muscles. This process takes a certain time, which is modeled as a delay in the feedback loop. Here, we assume a delayed linear feedback controller [16]. The ankle torque is calculated based on the deviation from the equilibrium state $\mathbf{q}_0 = [\varphi_0,\ 0]$ as follows

$$M = P_\varphi\,(\varphi(t-\tau) - \varphi_0) + P_\vartheta\,\vartheta\,(t-\tau) + D_\varphi\,\dot{\varphi}(t-\tau) + D_\vartheta\,\dot{\vartheta}\,(t-\tau). \quad (26)$$

3.4 Stability Diagrams

The linearized equation of motion reads:

$$\mathbf{M}\ddot{\mathbf{q}}(t) + \mathbf{K}\dot{\mathbf{q}}(t) + \mathbf{S}\mathbf{q}(t) = \mathbf{P}\mathbf{q}(t-\tau) + \mathbf{D}\dot{\mathbf{q}}(t-\tau). \quad (27)$$

The stability of (27) can be determined by the semidiscretisation method [8]. The stability of the system is represented in the space of the four control gains P_φ, D_φ, P_ϑ and D_ϑ. A projection of the stability diagrams to a fixed pair of P_φ and D_φ is shown in Fig. 4.

3.5 Comparison of Stability Properties in an Illustrative Example

The coefficient matrices and the stable region are compared in four cases:

- case **BB0**: balance board dynamic model, b. board inertia neglected ($m_{\mathrm{B}} = 0$, $J_{\mathrm{B}} = 0$)

- case **Me0**: mechanism dynamic model, mechanism inertia neglected ($m_c = 0$, $m_l = 0$),
- case **BB**: complete balance board dynamic model,
- case **Me**: complete substituting mechanism dynamic model.

It is important to note, that the dynamic models are still not singular, even in the case when we neglect the inertia of the balancing equipments. If the balance board kinematics were imitated by the mechanism exactly, cases **BB0** and **Me0** would provide exactly the same dynamic behaviour. When the inertia of the balancing equipment is also considered, then a slightly modified dynamic behaviour is expected, which is detailed in this section.

The balance board parameters were set to $R = 0.25$ m and $v = -0.1$ m and the corresponding geometric parameters of the substituting mechanism are collected in Table 1. The horizontal shift of the ankle joint is $e = 0.1$ m. The inertial parameters of the balance board are: $m_B = 3.42$ kg and $J_B = 0.0298$ kg/m^2. The centre of mass position is given by $c_B = 0.136$ m. The inertial parameters of the substituting mechanism are: $m_c = 2$ kg, $m_l = 1.5$ kg and the mass moments of inertia J_c and J_l are calculated by considering homogeneous and prismatic bars. The parameters of the bar that represents the human body are body mass $m_H = 65$ kg, centre of mass distance from the ankle $l_H = 1$ m, estimated mass moment of inertia with respect to the centre of mass $J_H \approx 1/12\, m_H\, n^2 = 16.21$ kg m^2, where $n = 1.73$ m is the height of the subject. Ankle stiffness is $k_A \approx 0.91\, m_H\, g\, n/2 = 501.9$ Nm/rad [9]. The damping matrix and the coefficient matrices of the delayed terms are the same in all cases:

$$\mathbf{K} = \begin{bmatrix} 0 & 0 \\ 0 & 0 \end{bmatrix}; \quad \mathbf{P} = \begin{bmatrix} -P_\varphi & -P_\vartheta \\ P_\varphi & P_\vartheta \end{bmatrix}; \quad \mathbf{D} = \begin{bmatrix} -D_\varphi & -D_\vartheta \\ D_\varphi & D_\vartheta \end{bmatrix}. \tag{28}$$

The mass and stiffness matrices in cases **BB0** and **Me0** respectively are:

$$\mathbf{M} = \begin{bmatrix} 81.211 & 21.986 \\ 21.986 & 8.6125 \end{bmatrix} \text{kg m}^2; \quad \mathbf{S} = \begin{bmatrix} -132.53 & -501.93 \\ -501.93 & 438.16 \end{bmatrix} \text{Nm/rad}. \tag{29}$$

$$\mathbf{M} = \begin{bmatrix} 81.211 & 22.040 \\ 22.040 & 8.6506 \end{bmatrix} \text{kg m}^2; \quad \mathbf{S} = \begin{bmatrix} -132.53 & -501.93 \\ -501.93 & 451.09 \end{bmatrix} \text{Nm/rad}. \tag{30}$$

In cases **BB0** and **Me0**, the difference between the elements of the mass matrices of are less than 0.5% and less than 3% for the stiffness matrices. This difference is because the mechanism can not imitate exactly the balance board motion. The mass and stiffness matrices in cases **BB** and **Me** respectively are:
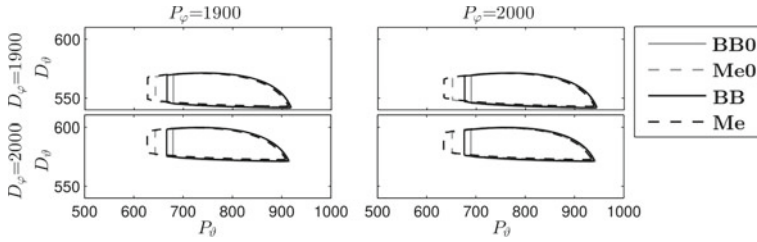
Fig. 4 Stability maps for the balance board and the substituting mechanism with and without neglecting the inertia of the balancing equipments (cases **BB0**, **Me0**, **BB** and **Me**)

$$\mathbf{M} = \begin{bmatrix} 81.211 & 21.986 \\ 21.986 & 8.6870 \end{bmatrix} \text{kg m}^2 ; \quad \mathbf{S} = \begin{bmatrix} -132.53 & -501.93 \\ -501.93 & 442.71 \end{bmatrix} \text{Nm/rad} . \quad (31)$$

$$\mathbf{M} = \begin{bmatrix} 81.211 & 22.040 \\ 22.040 & 8.7337 \end{bmatrix} \text{kg m}^2 ; \quad \mathbf{S} = \begin{bmatrix} -132.53 & -501.93 \\ -501.93 & 456.85 \end{bmatrix} \text{Nm/rad} . \quad (32)$$

Comparing cases **BB0** and **BB** one can notice that M_{22} and S_{22} changes only with $\Delta M_{22}^{\text{B}} = 0.0745 \text{ kg m}^2$ and $\Delta S_{22}^{\text{B}} = 4.55 \text{ Nm/rad}$. Comparing cases **Me0** and **Me** one can notice that M_{22} and S_{22} changes only with $\Delta M_{22}^{\text{M}} = 0.0831 \text{ kg m}^2$ and $\Delta S_{22}^{\text{M}} = 5.76 \text{ Nm/rad}$. Since $\Delta M_{22}^{\text{B}} \approx \Delta M_{22}^{\text{M}}$ and $\Delta S_{22}^{\text{B}} \approx \Delta S_{22}^{\text{M}}$, we can conclude that adding the inertia of the balancing equipments changes the dynamic behaviour similarly. Therefore the mechanism is suitable for the substitution of the original balance board.

Figure 4 shows the stability maps generated by the method explained in Sect. 3.4 for cases **BB0**, **Me0**, **BB** and **Me**. The stability maps differ slightly which leads to the conclusion again that the substituting mechanism can be used in laboratory experiments instead of the balance board.

4 Conclusions

We proposed the idea of a substituting mechanism that makes the balance board laboratory experiments faster and easier. The mechanism avoids the reassemble of the balance board in each measurement point regarding different parameter setting, like arc radius. Furthermore, the substitution mechanism can imitate the feeling of other balancing experimental equipments.

We have presented the geometric parameters of the mechanism that results the approximately the same kinematic behaviour as the balance board in the relevant tilt angle region. We showed that the dynamic properties of the balance board and the substituting mechanism are very close to each other so that the measurement result are not affected. The coefficients in the linearised equation of motion and the stable region of a controlled dynamic model were compared considering realistic inertial properties. We conclude that the application of a substituting mechanism is feasible.

References

1. Awrejcewicz, J., Wasilewski, G., Kudra, G., Reshmin, S.A.: An experiment with swinging up a double pendulum using feedback control. J. Comput. Syst. Sci. Int. **51**(2), 176–182 (2012)
2. Cabrera, J., Milton, J.: Human stick balancing: tuning lévy flights to improve balance control. CHAOS **14**(3), 691698 (2004)
3. Chagdes, J., Rietdyk, S., Jeffrey, M., Howard, N., Raman, A.: Dynamic stability of a human standing on a balance board. J. Biomech. **46**(15), 2593–2602 (2013)
4. Enikov, E., Stépán, G.: Stabilizing an inverted pendulum—alternatives and limitations. Periodica Polytech.—Mech. Eng. **38**, 379–382 (1994)
5. Gawthrop, P., Loram, I., Gollee, H., Lakie, M.: Intermittent control models of human standing: similarities and differences **108**(2), 159–168 (2014)
6. Insperger, T., Milton, J.: Sensory uncertainty and stick balancing at the fingertip. Biol. Cybern. **108**(1), 85–101 (2014)
7. Insperger, T., Milton, J., Stepan, G.: Acceleration feedback improves balancing against reflex delay. J. R. Soc. Interface **10**(79), Article No. 20120, 763 (2013)
8. Insperger, T., Stepan, G.: Semi-discretization for Time-Delay Systems. Stability and Engineering Applications. Springer, New York (2011)
9. Loram, I., Lakie, M.: Direct measurement of human ankle stiffness during quiet standing: the intrinsic mechanical stiffness is insufficient for stability. J. Physiol. **545**, 1041–1053 (2002)
10. Mehta, B., Schaal, S.: Forward models in visuomotor control. J. Neurophysiol. **88**, 942953 (2002)
11. Milton, J., Meyer, R., Zhvanetsky, M., Ridge, S., Insperger, T.: Control at stability's edge minimizes energetic costs: expert stick balancing. J. Royal Soc. Interface **13**, 20160,212 (2016)
12. Molnar, C.A., Zelei, A., Insperger, T.: Estimation of human reaction time delay during balancing on balance board. In: Proceedings of International Conference on Biomedical Engineering (BioMed 2017), pp. 195–199. IASTED-ACTA Press (2017)
13. Nagymáté, G., R.M., K.: Stabilometry as a diagnostic tool in clinical medicine. Periodica Polytech. Mech. Eng. **60**(4), 238–246 (2016)
14. Priplata, A., Niemi, J., Harry, J.D., Lipsitz, L.A., Collins, J.J.: Vibrating insoles and balance control in elderly people. Lancet **362**, 11231124 (2003)
15. Robinovitch, S., Feldman, F., Yang, Y., Leung, P., Schonnop, R., Sarraf, T., Sims-Gould, J., Loughin, M.: Video capture of the circumstances of falls in elderly people residing in long-term care: an observational study. Lancet **381**, 47–54 (2013)
16. Stepan, G.: Delay effects in the human sensory system during balancing. Trans. R. Soc. A **367**(1981), 1195–1212 (2009)
17. Terekhov, Y.: Stabilometry as a diagnostic tool in clinical medicine. Can. Med. Assoc. J. **115**(7), 631–633 (1976)
18. Yoshikawa, N., Suzuki, Y., Kiyono, K., Nomura, T.: Intermittent feedback-control strategy for stabilizing inverted pendulum on manually controlled cart as analogy to human stick balancing. Front. Computat. Neurosci. **10**, 34 pages (2016)

Numerical and Experimental Modal Analysis of Laminated Glass Beams

**Alena Zemanová , Tomáš Plachý, Jaroslav Schmidt, Tomáš Janda,
Jan Zeman and Michal Šejnoha**

Abstract This paper presents a numerical and experimental modal analysis of laminated glass beams, i.e. a multilayer composite structure made of glass panes bonded to an interlayer foil. These polymer foils provide shear coupling of glass layers, damping of vibrations, and play a key role in post-breakage performance. In this contribution, three-layer beams with ethylene-vinyl acetate interlayer are investigated. Using a finite element discretization and the Newton method, we solve numerically a complex eigenvalue problem which is nonlinear due to the frequency/temperature-sensitive viscoelastic behavior of the interlayer. In our experimental investigations, a roving hammer test was carried out to identify the mode shapes, natural frequencies, and modal damping. The validation shows that there is a good agreement between the numerical predictions and experimental data in natural frequencies. However, the errors in loss factors can be high, because these values are very sensitive to the material properties of polymer, frequency, temperature, and boundary conditions. These effects are discussed in the concluding part of our study.

Keywords Laminated glass · Ethylen-vinyl acetate · Generalized Maxwell
model · Complex shear modulus · Modal analysis · Natural frequency · Loss factor

1 Introduction

Laminated glass is widely used for transparent load-bearing, fail-safe structures. The glass layers are connected with plastic interlayers, which provide shear coupling of glass layers, damping of noise and vibrations, hold the broken glass layer together, and can have also other functions such as UV control or aesthetics. Therefore, these foils improve the behavior of brittle glass elements, but also complicate the simulation of their response because of the viscoelastic nature of polymers [2].

A. Zemanová (✉) · T. Plachý · J. Schmidt · T. Janda · J. Zeman · M. Šejnoha
Faculty of Civil Engineering, Czech Technical University in Prague,
Thákurova 7/2077, 166 29 Prague 6, Czech Republic
e-mail: alena.zemanova@fsv.cvut.cz

The overview of approaches to static and dynamic analyses of multi-layer beams can be found, e.g., in [1, 3, 6, 8]. In this study, we focus on numerical and experimental modal analysis of laminated glass beams. The geometrical and material parameters of laminated glass specimens are introduced in Sect. 2. In Sect. 3, the Newton-method-based finite element solver for free vibration analysis of laminated glass beams is proposed and the results in terms of natural frequencies and loss factors are derived from the complex-valued eigenvalues. In Sect. 4, we describe the experimental setup and report the measured values of natural frequencies and damping ratios. The numerical model is validated against the experiment and the errors are compared and discussed in Sect. 5. The main findings are finally summarized in Sect. 6.

2 Properties of Laminated Glass Specimens

Two samples of three-layer laminated glass beams with two different types of glass were tested and analyzed, see Table 1.

The dimensions of all samples were as follows (see Fig. 1): the length $l = 1.1$ m, the width $b = 0.36$ m, and the thicknesses $h_1/h_2/h_3 = 10/0.76/10$ mm.

For both types of glass, the physical and mechanical properties for the description of the linear elastic behavior are listed in Table 2. These values stay unaffected by the tempering process. The Young modulus was measured by indentation using T750

Table 1 The material composition of the layers in the tested specimens

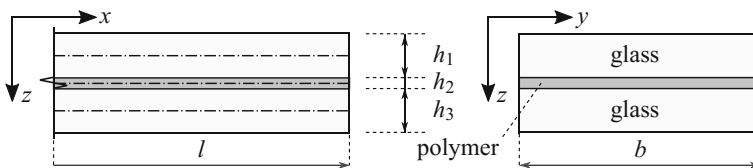| Name	Interlayer	Glass
EVA-HS	Ethylen-vinyl acetate (EVA)	Heat strengthened glass
EVA-AN	Ethylen-vinyl acetate (EVA)	Annealed glass

Fig. 1 The geometry of a three-layer laminated glass sample

Table 2 Material parameters for the description of elastic behavior of glass (the same values for the annealed and heat strengthened glass)

Glass			
Density	$\rho_1 = \rho_3$	2500	$kg\,m^{-3}$
Young's modulus of elasticity	$E_1 = E_3$	76.6	GPa
Poisson's ratio	$\nu_1 = \nu_3$	0.22	–

Hysitron TriboIndenter in the Centre of Excellence Telč, and the other values were set according to the data provided in the draft prEN 16612 standard [4].

The polymer behavior shows frequency and temperature sensitivity. To capture this fact, we use a generalized Maxwell model for the description of viscoelastic response of polymer behavior, yielding the frequency-dependent complex-valued shear modulus in the form

$$G_2(\omega) = G_{2,0} + G_{2,\omega}(\omega), \tag{1}$$

where the initial shear modulus $G_{2,0} = G_{2,\infty} + \sum_{p=1}^{P} G_{2,p}$ is a real constant corresponding to the sum of a long-term modulus $G_{2,\infty}$ and all moduli of individual Maxwell cells $G_{2,p}$. On the other hand, the second part,

$$G_{2,\omega}(\omega) = -\sum_p G_{2,p} \frac{1}{\omega^2\theta_p^2 + 1} + \mathrm{i} \sum_p G_{2,p} \frac{\omega\theta_p}{\omega^2\theta_p^2 + 1}, \tag{2}$$

is complex-valued and depends on an angular frequency ω. The relaxation times θ_p are related to the viscosity of each unit. To capture also the temperature-dependency, these times are shifted using the factor a_T from the Williams-Landel-Ferry equation [11]

$$\log a_T = -\frac{C_1(T - T_0)}{C_2 + T - T_0}, \tag{3}$$

where T and T_0 are the given and reference temperatures, respectively, and the parameters C_1 and C_2 are to be determined from the experimental data.

The frequency/temperature characteristics of polymer interlayers were obtained by dynamic torsion tests in the HAAKE MARS rheometer with the frequency range up to 100 Hz. More details about the experimental measurement and the subsequent
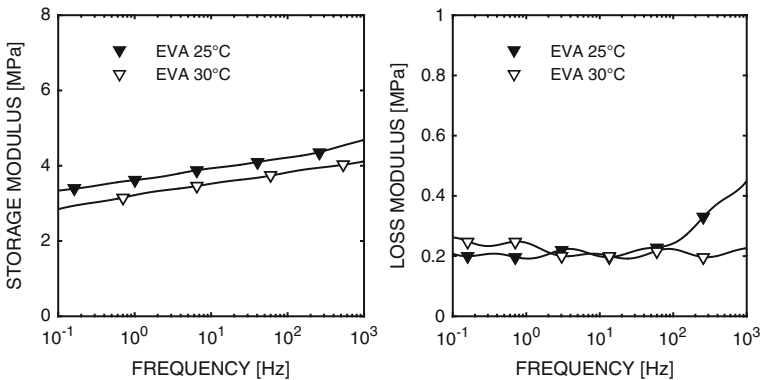

Fig. 2 The frequency/temperature-dependence of the real and imaginary part (storage and loss moduli) of the complex-valued shear modulus $G_2(\omega)$ for the EVA interlayer according to Table 3

Table 3 Material parameters for the description of linear viscoelastic behavior of ethylen-vinyl acetate (EVA) interlayer

Polymer		EVA	
Density	ρ_2	950	$\mathrm{kg\,m^{-3}}$
Long-term shear modulus	$G_{2,\infty}$	1009	kPa
Poisson's ratio	ν_2	0.49	–
Reference temperature	T_0	20	°C
Parameters	C_1	113	–
	C_2	404	°C

Table 4 Prony series for spring-dashpot Maxwell elements of ethylen-vinyl acetate (EVA) interlayer

p	θ_p (s)	$G_{2,p}$ (kPa)	p	θ_p (s)	$G_{2,p}$ (kPa)
1	10^{-3}	1177	8	10^4	126
2	10^{-2}	447	9	10^5	425
3	10^{-1}	265	10	10^6	203
4	10^0	323	11	10^7	224
5	10^1	267	12	10^8	206
6	10^2	350	13	10^9	133
7	10^3	411	14	10^{10}	278

determination of the parameters for the generalized Maxwell model can be found in [10] or [7]. The data were measured in the frequency range 0.001–100 Hz and temperatures 20–60 °C. However, the measurements of the storage and loss moduli for the frequencies over 50 Hz exhibited high scatter. In addition an unreliable rapid decrease in the storage modulus was observed. The data beyond 50 Hz were therefore excluded from further consideration. The complex shear modulus of EVA foil is shown for two temperatures in Fig. 2, and the corresponding parameters are summarized in Tables 3 and 4. The data for higher frequencies were obtained by shifting values for lower temperatures according to Eq. 3.

3 Finite Element Solver for Complex-Eigenvalue Analysis

In our numerical simulation, we rely on the finite element method and use refined beam elements with 9 unknowns per cross-section related to bending, shear and membrane effects in each layer. Due to the perfect bond of polymer and glass on inter-layer surfaces, only 5 unknowns are independent, see Fig. 3.

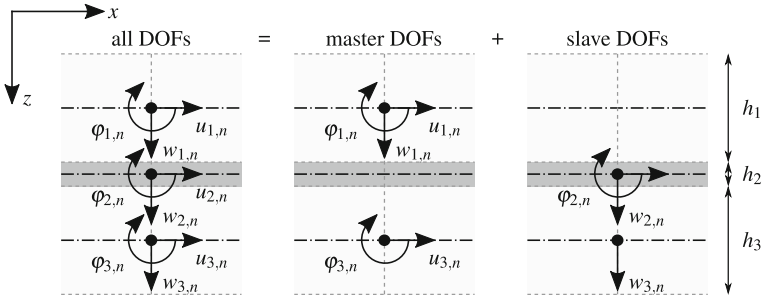After discretization, we solve a problem described by the system of equations [6],

Fig. 3 The refined beam element and its degrees of freedom for the cross-section related to the n-th node

$$\left(\mathbf{K}(\omega) - \omega^2 \mathbf{M}\right) \mathbf{U} = \mathbf{0},$$
$$\mathbf{U}_0{}^\mathsf{T}(\mathbf{U} - \mathbf{U}_0) = 0, \tag{4}$$

with the unknown natural angular frequencies ω, the corresponding mode shapes $\mathbf{U}$, the stiffness matrix $\mathbf{K}(\omega)$, the mass matrix $\mathbf{M}$, and an initial value of mode shapes $\mathbf{U}_0$. The first equation is a classical eigenvalue problem which is complex and nonlinear due to the frequency-dependency complex-valued stiffness matrix $\mathbf{K}$. The second equation corresponds to a normalization condition to obtain a well-posed problem.

The stiffness matrix can be decomposed into a constant and a frequency-dependent part

$$\mathbf{K}(\omega) = \mathbf{K}_0 + G_{2,\omega}(\omega)\mathbf{K}_c, \tag{5}$$

where the constant component $\mathbf{K}_0$ contains the stiffnesses of glass layers and the part of the interlayer stiffness matrix corresponding to the initial shear modulus $G_{2,0}$,[1] and the frequency-dependent member $G_{2,\omega}(\omega)\mathbf{K}_c$, where the frequency-dependent shear modulus $G_{2,\omega}(\omega)$ is extracted from the matrix, recall Eq. 1.

In the numerical analysis, we use the following linearization of the unknowns

$$^{k+1}\omega = {}^k\omega + \delta\omega,$$
$$^{k+1}\mathbf{U} = {}^k\mathbf{U} + \delta\mathbf{U}, \tag{6}$$

where the quantities for the $(k+1)$-th step are computed from the previous ones for the k-th iteration and their increments. Using the Newton method, the nonlinear system Eq. 4 is converted to the linear system

$$\begin{bmatrix} \mathbf{K}({}^k\omega) - {}^k\omega^2\mathbf{M} & \left(\dfrac{\partial G_{2,\omega}}{\partial\omega}({}^k\omega)\mathbf{K}_c - {}^k\omega 2\mathbf{M}\right){}^k\mathbf{U} \\ \mathbf{U}_0{}^\mathsf{T} & \mathbf{0} \end{bmatrix} \begin{bmatrix} {}^{k+1}\mathbf{U} \\ \delta\omega \end{bmatrix} = \begin{bmatrix} \mathbf{0} \\ \mathbf{U}_0{}^\mathsf{T}\mathbf{U}_0 \end{bmatrix}. \tag{7}$$

---

[1] The initial shear modulus $G_{2,0}$ was selected as a starting point of a solver, because its value is always nonzero, unlike the long-term modulus $G_{2,\infty}$.

Then, the algorithm based on the Newton method is schematically summarized in Algorithm 1. At the beginning, we solve only the eigenvalue problem from Eq. 4 with the constant stiffness matrix $\mathbf{K}_0$ to obtain the initial values of frequencies and mode shapes, ω_0 and $\mathbf{U}_0$. The complex-valued natural angular frequency ω is obtained by the iterative procedure for each searched mode independently. Finally, the real-valued natural frequency f_{Hz} and the loss factor η are extracted according to

$$\omega^2 = (2\pi f_{Hz})^2 (1 + i\eta),$$ (8)

which corresponds to the last two lines of Algorithm 1.

Algorithm 1: Newton method-based eigenvalue solver

Data and initial values:
set tolerance ϵ_{tol}
assemble $\mathbf{K}_0$, $\mathbf{K}_c$, and $\mathbf{M}$
get ω_0, $\mathbf{U}_0$ solving $\left(\mathbf{K}_0 - \omega_0^2\mathbf{M}\right)\mathbf{U}_0 = \mathbf{0}$
for *GIVEN MODE* **do**

    initialization: $k \leftarrow 0$, $^0\omega = \omega_0$, $^0\mathbf{U} = \mathbf{U}_0$, $^0\epsilon_{res} = 10\epsilon_{tol}$
    while $^k\epsilon_{res} > \epsilon_{tol}$ **do**

        evaluate $G_{2,\omega}(^k\omega)$, $\dfrac{\partial G_{2,\omega}}{\partial \omega}(^k\omega)$
        get $\delta\omega$, $^{k+1}\mathbf{U}$ solving system Eq. 7
        update $^{k+1}\omega \leftarrow {}^k\omega + \delta\omega$
        residual $^{k+1}\epsilon_{res} = \dfrac{\|(\mathbf{K}(^{k+1}\omega) - {}^{k+1}\omega^2\mathbf{M})^{k+1}\mathbf{U}\|}{\|^{k+1}\mathbf{U}\|}$
        $k \leftarrow k + 1$

    $\omega \leftarrow {}^{k+1}\omega$, $\mathbf{U} \leftarrow {}^{k+1}\mathbf{U}$
    ▷ natural frequency $f_{Hz} = \dfrac{\sqrt{\mathrm{Re}[\omega^2]}}{2\pi}$
    ▷ loss factor $\eta = \dfrac{\mathrm{Im}[\omega^2]}{\mathrm{Re}[\omega^2]}$

In Table 5, the values obtained by the proposed solver, Algorithm 1, are summarized in terms of natural frequencies and loss factors derived from Eq. 8. Let us note

Table 5 Numerical predictions of natural frequencies and loss factors for samples with ethylen-vinyl acetate interlayer (EVA) and analytically obtained natural frequencies for free-free beams made of monolithic glass (MG) for first three bending modes [5]

Mode	Natural frequency (Hz)			Loss factor (%)
	EVA 26 °C	MG 20.76 mm	MG 10 mm	EVA 26 °C
1st bending	82.26	97.62	47.02	1.40
2nd bending	182.37	269.10	129.62	1.99
3rd bending	317.05	527.58	254.13	1.92

that the modes related to the rigid body motion of a free-free beam were excluded from our consideration. To gain an insight into the level of shear coupling provided by the interlayers, we show also the natural frequencies of the monolithic glass beam with the thickness of 20.76 mm (the whole thickness of laminated glass beam) and the natural frequency of one independent glass layer (10 mm thick) in the third and fourth column in Table 5. It is obvious that this range is quite wide. The values corresponding to no shear interaction in the interlayer are one half of those corresponding to the perfect bond in the interlayer.

4   Experimental Testing

In our experiment, two samples of laminated glass beams, recall Table 1 and Fig. 1, were analyzed. Each beam was suspended in such a way as to simulate free-free boundary conditions. We tested two options: first, the glass pane was mounted on soft pads made of a flexible sponge substrate, and second, the specimen was suspended on a pair of soft strings as shown in Fig. 4. The data presented here correspond to the second experimental setup as it delivered smaller values of damping and therefore it better represents the unsuspended (free-free) beam.

Experimental modal parameters (in our case the natural frequencies, damping in terms of damping ratios, and mode shapes) were obtained from a set of frequency response function measurements with a frequency step of 1 Hz. We used a measuring device (Brüel and Kjaer) consisting of a data acquisition unit type 3560-B-120, an impact hammer type 8206, and a miniature piezoelectric accelerometer type 4519-003 placed at a corner of a laminated glass plate. The sample was impacted at 27 points in a 3 × 9 grid to define the mode shapes of the structure. The software Pulse (Brüel and Kjaer) was used for the signal acquisition and processing. Then the obtained frequency response functions were exported to a post-processing software MEscopeVES (Vibrant Technology) where the modal parameters were extracted. The ambient temperature during the experiment was 26 °C.
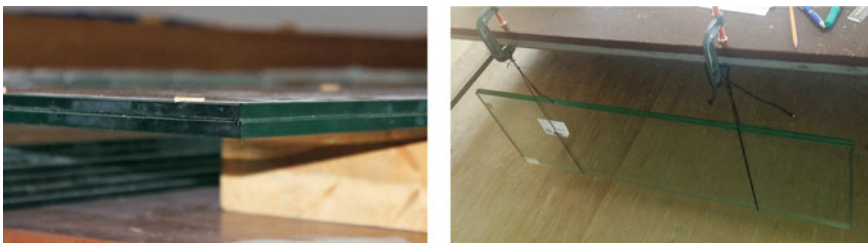

Fig. 4 A tested sample of a three-layer laminated glass beam (left) and the experimental setup for the simulation of free-free boundary conditions in the modal analysis of a laminated glass beam (right)

Table 6 Experimentally determined natural frequencies and damping ratios for both tested samples for first three bending and torsional mode shapes

Mode	Frequency (Hz)		Damping ratio (%)	
	EVA-HS	EVA-AN	EVA-HS	EVA-AN
1st bending	80.32	81.08	1.298	1.286
1st torsional	120.8	122.0	2.016	1.957
2nd bending	182.4	183.8	2.298	2.252
2nd torsional	241.1	243.2	2.157	2.106
3rd bending	318.0	320.3	2.302	2.218
3rd torsional	365.2	368.4	2.238	2.195

The natural frequencies and damping ratios from our experimental modal analysis are summarized for the first three bending and torsional modes in Table 6. It is obvious that the response is almost the same for both the heat strengthened and annealed glasses owing to the same Young modulus and density, recall Table 2.

5 Validation and Discussion

In this section, we validate our numerical predictions of natural frequencies and loss factors against the experimental data and discuss the results and errors.

5.1 Natural Frequencies

Let us start with the comparison of the numerical predictions and experimental values of the first three natural frequencies. Figure 5 (left) shows quantile-quantile plots for these values. There are two plots in each graph: the numerical prediction against the experimental data for heat strengthened or annealed glass. However, they overlap, and only a very small difference can be seen for the samples with different glasses. The dashed line indicates a perfect match with the experiment.

The corresponding errors can be found in Fig. 5 (right). For the EVA foil, we predicted the values of the first three natural frequencies with errors below 2.5%.

5.2 Loss Factors

Until now we have used two parameters characterizing damping: the loss factor in our numerical simulations and the damping ratio from experimental measurement. Therefore, the essential step is to specify a formula for the transfer of these two
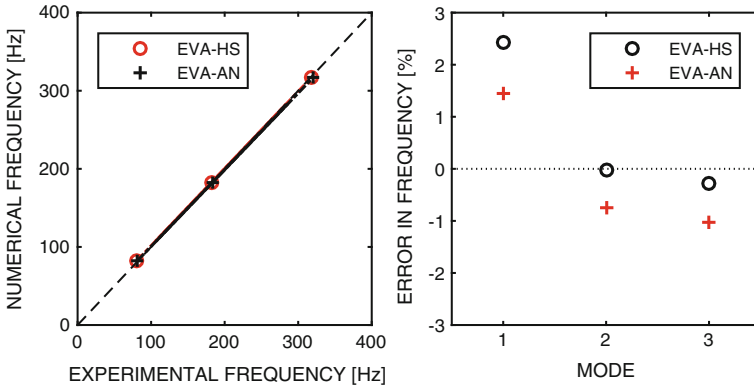
Fig. 5 Comparison of numerical and experimental natural frequencies for first three modes expressed by quantile-quantile plot (left) and errors of numerical predictions against experimental data (right)
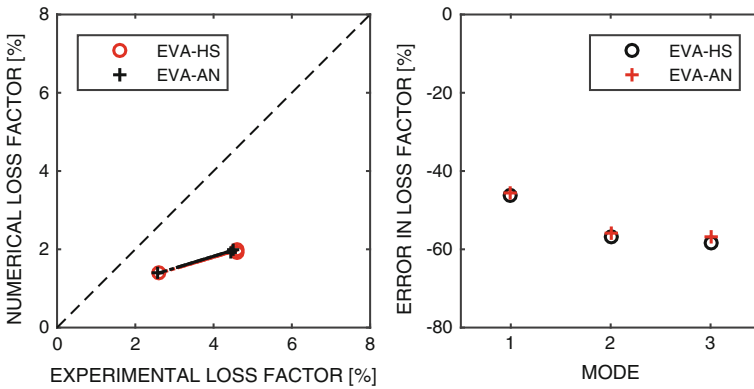

Fig. 6 Comparison of numerical and experimental loss factors for first three modes expressed by quantile-quantile plot (left) and errors of numerical predictions against experimental data (right)

quantities. Because the damping ratios are small, up to 3% for EVA, we use the approximation [1]

$$\eta \approx 2\zeta, \tag{9}$$

where ζ is the measured damping ratio and η is the numerically evaluated loss factor. This formula is accurate within the error of 0.2% for damping ratios $\zeta < 5\%$ (which is our case). A more accurate relation is available in [9].

The validation of the loss factors from our numerical simulation against the corresponding properties from the experimental measurements is shown in Fig. 6 representing again the quantile-quantile plot of the numerical and experimental loss factors (left) and the errors of our numerical predictions against the experimental data (right). It is obvious that the agreement of the numerical prediction of the loss
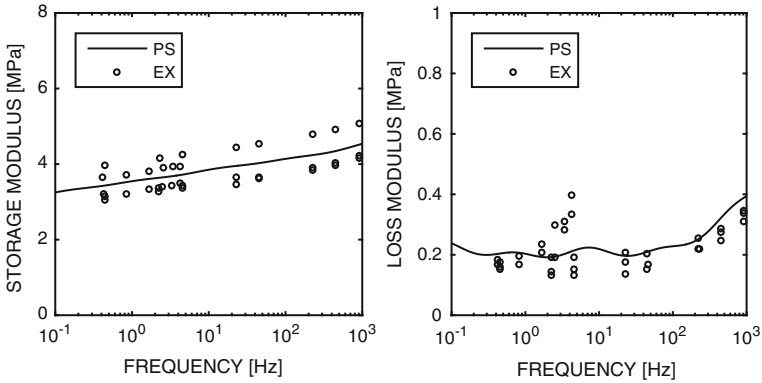
Fig. 7 Storage and loss moduli for EVA interlayer at 26 °C: fitted curve according to Prony series (PS) in Table 3 and measured values from rheometer shifted to given temperature (EX)

factor with the experimental data is substantially worse than for natural frequencies. In particular, the predicted damping is underestimated in all cases.

The errors in loss factors are about 45% for the loss factor related to the first mode shape, 55% for the second mode, and up to 58% for the third mode. The reasons for these high errors can be divided into two categories: (i) a non-optimal fit of the loss modulus for this frequency range or (ii) some additional damping which is omitted in our model. To gain an insight into the level of damping of glass layers, air damping, or the influence of the soft wires, we also plan to perform the experimental modal analysis of a single monolithic glass plate under the same boundary conditions. In our discussion, we will focus on the possible effect of the loss modulus on the errors, because the validation of the fitted Prony series for the two interlayers was the main aim of this study.

It can be seen from Eq. 8 and Algorithm 1 that the loss factor η is the ratio of the imaginary and real part of the second power of the complex-valued natural angular frequency. Therefore, it is strongly influenced by the imaginary and real part of the complex-valued shear modulus of the interlayer.

In Fig. 7, the comparison of the measured data from the rheometer (EX) and the fitted curve (PS) according to Table 3 is shown for both moduli. The fitted curve was plotted for the ambient temperature 26 °C and the frequency up to 50 Hz (due to the frequency limit of the rheometer) and shifted using the factor from Eq. 3 for the measurements at 20 and 30 °C. In case of the loss modulus, there is an increase in measured values. However, this increase is not reflected in the fitted curve.

This corresponds to the fact that our prediction of loss factors always underestimated the measured values. Moreover, the damping of laminated glass members in this study is quite small – the values of the loss factors are under 5%, and they are strongly sensitive to temperature and boundary conditions.

6 Conclusions

We performed a numerical and experimental modal analysis of laminated glass beams. The aim of this study was to verify and validate the material data for the EVA interlayer, which were obtained by fitting from the dynamic torsion tests in the HAAKE MARS rheometer. It follows from our analysis that we can predict the natural frequencies of laminated glass elements very well using the fitted material parameters of the generalized Maxwell model. On the other hand, the estimation of damping in the laminated glass structures is only rough. One of the reasons can be non-optimal fit of the loss modulus for the EVA interlayer. On the basis of this study, we plan to develop an approach based on an inverse finite element analysis, which could solve this issue.

References

1. Aenlle, M., Pelayo, F.: Frequency response of laminated glass elements: analytical modeling and effective thickness. Appl. Mech. Rev. **65**(2), 020802 (2013)
2. Andreozzi, L., Bati, S.B., Fagone, M., Ranocchiai, G., Zulli, F.: Dynamic torsion tests to characterize the thermo-viscoelastic properties of polymeric interlayers for laminated glass. Constr. Build. Mater. **65**, 1–13 (2014). https://doi.org/10.1016/j.conbuildmat.2014.04.003
3. Awrejcewicz, J., Krysko, V., Zhigalov, M., Krysko, A.: Mathematical model of a three-layer micro-and nano-beams based on the hypotheses of the Grigolyuk-Chulkov and the modified couple stress theory. Int. J. Solids Struct. **117**, 39–50 (2017)
4. CEN/TC 129: Draft prEN 16612: glass in building—determination of the load resistance of glass panes by calculation and testing. Technical report (2013)
5. Clough, R.W., Penzien, J.: Dynamics of structures. Comput. Struct. Inc. (2003)
6. Daya, E.M., Potier-Ferry, M.: A numerical method for nonlinear eigenvalue problems application to vibrations of viscoelastic structures. Comput. Struct. **79**(5), 533–541 (2001). https://doi.org/10.1016/S0045-7949(00)00151-6. http://www.sciencedirect.com/science/article/pii/S0045794900001516
7. Janda, T., Zemanová, A., Zeman, J., Šejnoha, M.: Finite element models for laminated glass units with viscoelastic interlayer for dynamic analysis. In: High Performance and Optimum Design of Structures and Materials II, vol. 166, pp. 245–254. WIT Press (2016)
8. Krysko, A., Awrejcewicz, J., Saltykova, O., Zhigalov, M., Krysko, V.: Investigations of chaotic dynamics of multi-layer beams taking into account rotational inertial effects. Commun. Nonlinear Sci. Numer. Simul. **19**(8), 2568–2589 (2014)
9. Liu, W.: Experimental and analytical estimation of damping in beams and plates with damping treatments. Ph.D. thesis, University of Kansas (2008)
10. Schmidt, J., Janda, T., Šejnoha, M., Valentin, J.: Experimental determination of visco-elastic properties of laminated glass interlayer. Proc. Eng. Mech. **2017**, 850–853 (2017). ISBN :978-80-214-5497-2
11. Williams, M., Landel, R., Ferry, J.: The temperature dependence ofrelaxation mechanisms in amorphous polymers and other glass-forming liquids. J. Am. Chem. Soc. **77**(14), 3701–3707 (1955). https://doi.org/10.1021/ja01619a008

Methods of Simulation Investigations of Non-linear Vibrations in the Steering System of a Motorcycle

Dariusz Żardecki and Andrzej Dębowski

Abstract The paper presents special methods of modeling and simulation based sensitivity analysis of torsional vibrations in the motorcycle steering system. The vibrations generated in the motorcycle steering system in the presence of freeplay and friction phenomena have a strong non-linear nature because of stick-slip processes. Due to the threshold character of these nonlinearities and the variability of the model structure, simulation-type investigations of such vibrations are difficult and still require extensive research. For solution these difficult problems, special methods of modeling and special methods of simulation analysis have been applied. The luz(…) and tar(…) projections with their original mathematical apparatus give new facilities for modeling and analysis strong non-linear vibrations. Among other, they can be used for synthesis substitutive formulas expressing time lag phenomena in such systems, they are very useful also when the model of the system is reduced parametrically. Application of Lissajou portraits and Poincare maps seems to be attractive methods not only for visualization of the non-linear vibrations, but also effective methods for analysis these spectacular signals what has been done in a simulation software.

Keywords Systems with freeplay and friction · Simulation of vibrations · Sensitivity analysis · Computational procedures · Matlab-Simulink

1 Introduction

Torsional vibrations observed in motorcycle steering systems are a significant problem for the handling quality and active safety as well as for the comfort of riders.

D. Żardecki · A. Dębowski (✉)
Military University of Technology (WUT)/Institute of Mechanical Vehicle and Transport,
ul. gen. Sylwestra Kaliskiego 2, 00-908 Warsaw, Poland
e-mail: andrzej.debowski@wat.edu.pl

D. Żardecki
e-mail: dariusz.zardecki@wat.edu.pl

These vibrations are especially evident in motorcycles operated at high dynamic loads and high speeds. The physical nature of the vibrations can be different and very complicated. Two groups of reasons are visible: the first one—direct excitations (by wheel's unbalance, road surface's unevents), and the second one—structural dynamical effects even instabilities (caused by improper design of the vehicle and wear of steering mechanism and suspension) [1, 2]. Note, that vibrations generated in the motorcycle steering system in the presence of mechanical backlash and friction may have a strong non-linear nature because of stick-slip processes and other strange dynamical effects [3]. It is well known, that due to the threshold character of these nonlinearities and the variability of the model structure, simulation investigations of such vibrations are especially difficult and still require extensive research [4–6].

For solution these difficult problems, special methods of modeling (based on piecewise linear luz(…) and tar(…) projections) and special methods of simulation-based sensitivity analysis (with phase-type and Lissajou plots, Poincare maps) have been elaborated and applied [7, 8]. In this paper this methods are briefly described and illustrated by several examples of investigations. The reported study is related to Dębowski's doctoral thesis on automatic damping of vibrations in motorcycle steering system.

The paper is organized as follows. In Sect. 2 the main information on the mathematical model and on the luz(…) and tar(…) mathematical apparatus is given. Section 3 presents information on the simulation software and method of analysis. Section 4 presents examples of simulation investigations for several sets of the model data. Section 5 contains recapitulation and conclusion.

2 Modeling of Torsional Vibrations with Using Luz(…) and Tar(…) Projections

Elaboration of simulation-based methods of analysis of nonlinear vibrations in motorcycle steering systems requires rather simple mathematical models which express only main attributes of the system's nonlinear dynamics and main attributes of external excitations. Such a model should express dynamic effects of inertia, damping (with friction) and elasticity (with freeplay). For testing simulation-based methods of analysis nonlinear vibrations in the steering system, its substitute physical structure can be simplified to the one-mass system (Fig. 1).

This physical model corresponds with a situation where the motorcycle's handlebar is fixed and torsional vibrations of the wheel may be caused by the application of a variable external torque (e.g. due to wheel unbalance) or by twisting the system to move the wheel out of its angular position of equilibrium and then releasing it free. This equivalent of the steering system is actually a torsional pendulum where a twisted rigid inert element (the motorcycle's wheel) is coupled with a weightless elastic shaft (linear elasticity) mounted with a freeplay in a housing [9]. The shaft of the inert element is placed in a housing bearing. The bearing acts on the twisting motion

Fig. 1 Idea of physical substitute model for testing methods of simulation investigations of nonlinear vibrations in the motorcycle steering system
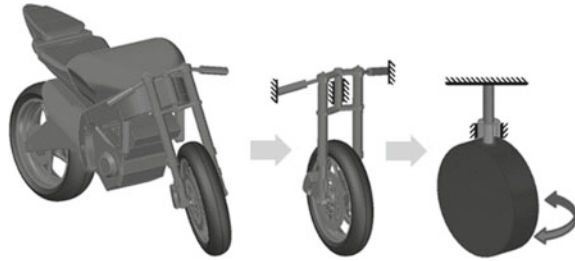
through viscous friction forces (linear damping) and dry friction forces (dry kinetic and dry static friction, which causes the stick-slip phenomenon). Such a single-mass object reflects the most important attributes of the steering system dynamics and simultaneously makes it possible to analyse torsional vibrations in the presence of "sharp" non-linearities arising from the freeplay and friction actions. Note, that the aspect of tyre-road interaction is disregarded here. Otherwise, the model would be more complicated unnecessarily (without any impact on the analysis method).

The mathematical model that describes torsional vibrations of the wheel (nonlinear because of the freeplay and friction effects) is given by the second-order differential equation with a variable structure [6]:

$$J\ddot{\alpha}(t) = \begin{cases} M_w(t) - k \cdot luz(\alpha(t), \alpha_0) - \mu \cdot tar\left(\dot{\alpha}(t), \frac{M_{TK0}}{\mu}\right), & if\, \dot{\alpha}(t) \neq 0 \\ luz(M_w(t) - k \cdot luz(\alpha(t), \alpha_0), M_{TS0}), & if\, \dot{\alpha}(t) = 0 \end{cases} \quad (1)$$

Notation:

J—moment of inertia; μ—damping coefficient (for viscous friction); M_{TK0}—moment of dry kinetic friction force; M_{TS0}—maximum value of the moment of dry static friction force; k—stiffness coefficient; α_0—angular freeplay ("dead zone") parameter; α—angle of torsion; M_w—moment of the external input force; t—time.

The luz(…) and tar(…) are piecewise-linear mutually inverse projections (Fig. 2) and have analytical description:

$$luz(x, a_1) = x + \frac{|x - a_1| - |x + a_1|}{2} \quad (2)$$

$$tar(x, a_2) = x + a_2 s^*, \quad where\, s^* \in [-1, 1], a_2 > 0 \quad (3)$$

Two different structures of the model (1) for the conditions $\dot{\alpha}(t) \neq 0 / \dot{\alpha}(t) = 0$ express a dry friction action for dynamic and static states. In this model, the tar(…) is used to describe the classic Coulomb function expressing the kinetic friction force, and the luz(…)—to describe the stiffness force with the freeplay (backlash), as well us to express action of the static dry friction force when the mass has a speed equal zero. Note, that in the state $\dot{\alpha}(t) = 0$ when $|M_W(t) - k \cdot luz(\alpha(t), \alpha_0)| \leq M_{TS0}$, one obtains

Fig. 2 Topological
interpretation of luz(…) and
tar(…) projections
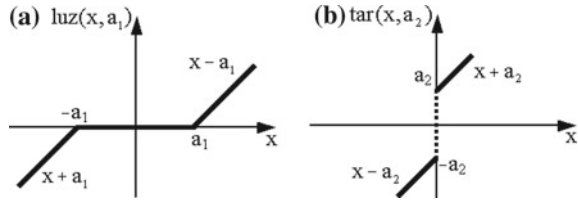
also the zeroing of the second derivative of the $\alpha(t)$ and finally the stiction. This
state is finished when $|M_W(t) - k \cdot luz(\alpha(t), \alpha_0)| > M_{TS0}$. In numerical calculations, the
controlling of variability of the model structure is operated by adopting the conditions
$|\dot{\alpha}(t)| > \varepsilon$ and $|\dot{\alpha}(t)| \leq \varepsilon$, where ε is a "small parameter" (as in the Karnopp model of
stick-slip [10]).

The luz(…) and tar(…) projections with their original simple mathematical appa-
ratus (developed in Żardecki's papers [6, 11, 12]) give new facilities for modeling
and analysis vibrations in such strongly non-linear systems. This is because luz(…)
and tar(…) have surprisingly simple properties. Example analytical formulas (here
for tar(…) and non-negative parameters) are presented below:

$$k \cdot tar(x, a) = tar(k \cdot x, k \cdot a) \tag{4}$$

$$k_1 \cdot tar(x, a_1) + k_2 \cdot tar(x, a_2) = (k_1 + k_2) \cdot tar\left(x, \frac{k_1 \cdot a_1 + k_2 \cdot a_2}{k_1 + k_2}\right) \tag{5}$$

$$tar(\ldots) = luz(\ldots)^{-1} \tag{6}$$

Because of inversity (6), luz(…) and tar(…) are very useful to unravel degenerated
Eq. (1), when the model is reduced parametrically by zeroing of the small inertia
parameter. Finally, in such case when $J \to 0$ the model reduces to the first order
differential equation [6].

In the absence of freeplay ($\alpha_0 = 0$) and dry friction ($M_{TK0} = M_{TS0} = 0$), the
non-linear Eq. (1) reduces to the well known linear form:

$$J\ddot{\alpha}(t) + \mu\dot{\alpha}(t) + k\alpha(t) = M_w(t) \tag{7}$$

This linear differential equation can be presented in the Laplace or Fourier operator
form which are very useful in the classic frequency analysis of the vibrations. At
zero initial conditions, the Laplace operator Eq. (8) with the transfer function (9) is
obtained:

$$\tilde{\alpha}(s) = G(s)\widetilde{M}_w(s) \tag{8}$$

$$G(s) = \frac{G_0}{\left(\frac{s}{\omega_0}\right)^2 + 2\xi\frac{s}{\omega_0} + 1} \tag{9}$$

where the transmittance parameters are:

$$G_0 = \frac{1}{k} \quad \text{system gain factor} \tag{10}$$

$$\omega_0 = \sqrt{\frac{k}{J}} \quad \text{characteristic frequency of the}$$

$$\text{breakpoint in the spectral-response curve} \tag{11}$$

$$\xi = 0.5 \frac{\mu}{\sqrt{Jk}} \quad \text{system damping coefficient}$$

$$(\text{when } \xi \geq 1, \text{ the system does not oscillate}) \tag{12}$$

The transmittance parameters makes easier the scaling of Eq. (1) in a simulation program.

3 Research Software for the Simulation and Analyses of Non-linear Vibrations

The luz(…) and tar(…) mathematical apparatus has been applied in simulation programs written in Matlab-Simulink environment. Details about this software and its testing with using different numerical algorithms (difficult problems of simulation of stick-slip processes in the neighbourhood of zero velocity) are shown in articles [7, 8]. The presented paper supplements and develops previous authors publications on simulation of torsional vibrations.

The first part of the software is an M-file prepared in the Matlab language and the second one is a simulation model defined in the form of block diagrams implemented in the Simulink graphic environment. The M-file organizes the simulation calculations and their visualization; moreover, the variables and parameters are also defined in it. The model may be downloaded from the Internet [13].

The general structure of simulation model in the Simulink is presented in Fig. 3. The macro-block includes a detailed schematic diagram of the simulation model. The other blocks represent virtual oscilloscope, clock unit, generator block (also for nonlinearly modified input excitations), and blocks of the "To-Workspace" type, making it possible to export the computation results to the M-file level. The extended simulation model also includes generators of disturbances (white noise) of signals.

The schematic diagrams in Figs. 4 and 5 depict the essence of functioning of the computational model. This model has so called "hard zeroing mechanism". For the whole reset signal duration time, the integrator remains in its initial state. The reset signal is generated by the detector block in a closed loop system, based on the velocity state output signal. This signal becomes available earlier than the signal at the integrator output, thanks to which an algebraic loop is avoided. The control condition ($\dot{\alpha}(t) \neq 0/\dot{\alpha}(t) = 0$ or $|\dot{\alpha}(t)| > \varepsilon$ and $|\dot{\alpha}(t)| \leq \varepsilon$) is defined in the detector.

The visualization of simulation results contains standard presentation of waveforms $M_w(t)$, $\alpha(t)$, phase portraits $\dot{\alpha}(\alpha)$, Lissajou figures $\alpha(M_w)$, stroboscopic
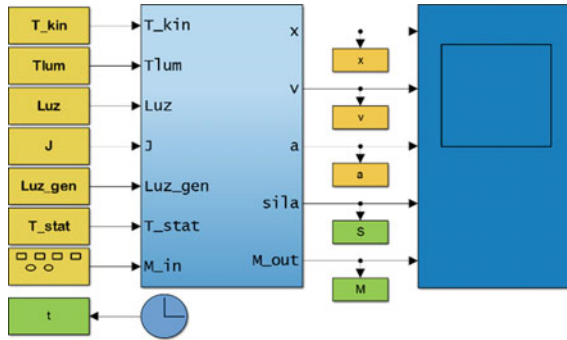
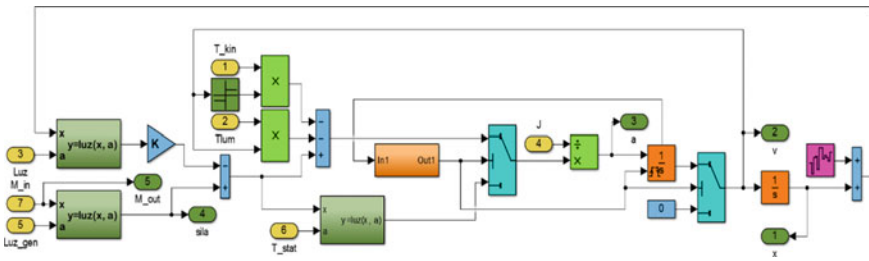**Fig. 3** Schematic diagram of the basic model structure

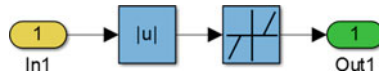**Fig. 4** Simulation model with a "hard zeroing mechanism"

Fig. 5 Singular state detector model

Poincare maps. Two representative examples for the system with freeplay and dry friction are in Fig. 6 [8].

The latest version of the software (used in this paper) introduces new visualization procedures that facilitate the sensitivity analysis. They enable 3D presentation for changed values of the selected parameters.

4 Example Results of Simulation Tests and Vibration Analyses

The simulation investigations described in this paper present the essence of sensitivity methods. These studies are an extension of the research described in the paper [8]. Because of editorial limitations, the presented results (Fig. 7) are limited only to the new 3D visualization procedures.
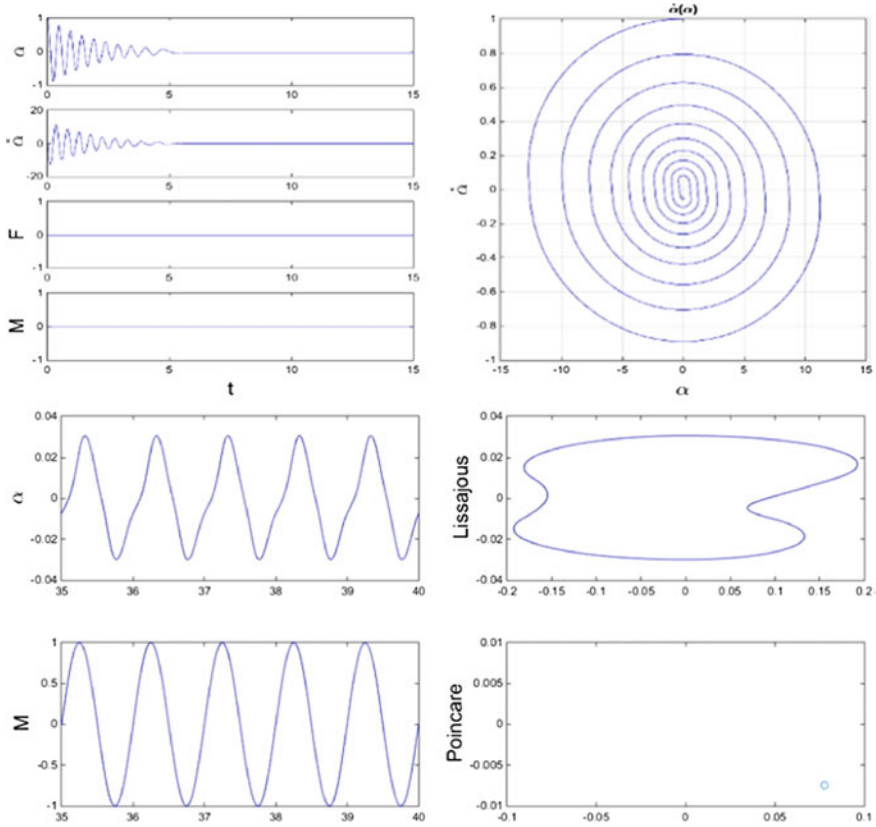
Fig. 6 Results of testing free and induced vibrations

The research concept of the presented studies is as follows:

- The initial conditions of variables are zero, and the input signal has a form $M_w(t) = M_{w0}\sin(\omega t)$.
- The assumed values of the model parameters concern a scaled model, previously used at the testing of numerical and graphical procedures [7, 8]. They are given in the Table 1.

The computations are carried out for data sets, with variations of compliance-type parameters

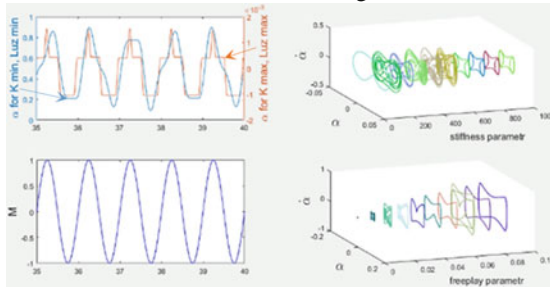$$(K = 100, 200, \ldots 1000, Luz = 0, 0.01, \ldots 0.1)$$

- Variant 1: Linear model (Luz_0 = 0, T_kin = 0, T_stat = 0). Here, only K is changed;
- Variant 2: Non-linear model, with freeplay but without dry friction (T_kin = 0, T_stat = 0);

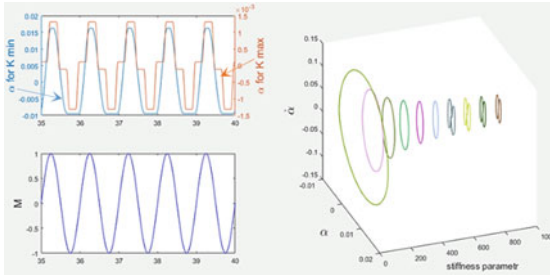Variant 1: linear model (with neither freeplay nor dry friction). K is changed
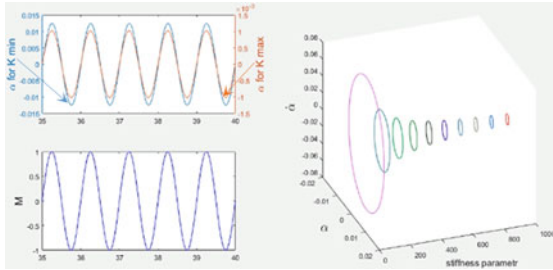
Variant 2: non-linear model (with freeplay but without dry friction).

K and Luz are changed

Variant 3: non-linear model (without freeplay but with dry friction). K is changed

Variant 4: non-linear model (with freeplay and dry friction). K and Luz are changed
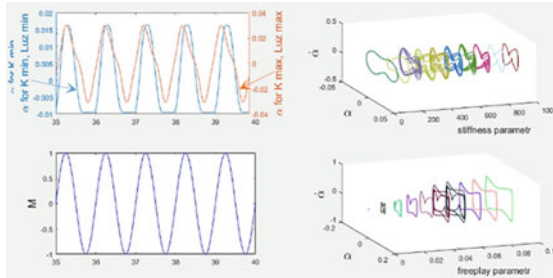

Fig. 7 Results of testing forced vibration in the absence of measurement disturbances

Table 1 List of parameters of the simulation model

Notation used	Value	Description
Alfa	0	Initial angle of torsion of the torsional pendulum
Ampl	1	Amplitude of the input signal
Omega	1	Angular frequency of the input signal
K	100–1000	Stiffness parameter
T_stat	0.2	Maximum moment of static friction forces
T_kin	0.2	Moment of dry kinetic friction forces
J	0.5	Moment of inertia
Tlum	0.5	Damping coefficient (for viscous friction)
Luz	0–0.1	Angular freeplay parameter
Luz_gen	0	Freeplay parameter of the external input generator
e	0.0001	"Hard zeroing" parameter
np	0	Amplitude parameter of the measurement noise

Their values are in SI system

- Variant 3: Non-linear model without freeplay but with dry friction ($Luz\_0 = 0$). Here only K is changed;
- Variant 4: Non-linear model, with freeplay and dry friction.

- Calculation of sensitivity curves is performed for fixed vibration conditions (when $t > 35$ s).

5 Conclusions

This paper has presented the methods of simulation-based sensitivity investigations of non-linear torsional vibrations in the steering system of a motorcycle. The examples of the studies have been based on the substitute one-mass model (torsional pendulum) taking into consideration non-smooth non-linearities—the freeplay and dry friction with stiction. The vibrations analyzed in the paper were caused by external sinusoidal excitations. Simulation processes have been executed with using special numerical procedures in Matlab-Simulink environment. Visualization of the results has been done not only in standard way but also with using 3D charts of Lissajou figures.

The presented methods of investigations are based solely on time-domain simulations and do not require frequency analysis, which is known to be unreliable in the case of dynamic studies of strongly nonlinear systems.

Of course, the use of these methods in the analysis of torsional vibrations in the motorcycle steering systems requires multiple simulations to be carried out on a model having a more complicated structure with respecting road-wheel interactions. But the methodology of this research will be the same.

References

1. Cossalter, V.: Motorcycle Dynamics. United Kingdom (2006)
2. Pacejka, H.B.: Tyre and Vehicle Dynamics. Elsevier, Oxford (2012)
3. Olejnik, P., Awrejcewicz, J., Fečkan, M.: Friction Laws in Modeling of Dynamical Systems, Modeling. Anal. Control Dyn. Syst. **92**
4. Awrejcewicz, J., Lamarque, C.H.: Bifurcation and Chaos in Nonsmooth. Mechanical Systems. World Scientific, Singapore (2003)
5. Brogliatto, B., Dam, A.A.T., Paoli, L., Genot, F., Abadie, M.: Numerical simulation of finite dimensional multibody nonsmooth mechanical systems. Appl. Mech. Rev. **55**(2), 107–150 (2002)
6. Żardecki, D.: *Modelowanie luzu i tarcia oparte na odwzorowaniach luz(…) i tar(…) – podstawy teoretyczne i zastosowanie w symulacji drgań nieliniowych w układach kierowniczych samochodów (Freeplay and friction modelling based on the luz(…) and tar(…) representations – theoretical grounds and application in the simulation of nonlinear vibrations in motor vehicle steering systems)*. Postdoctoral dissertation, Wydawnictwo WAT (Publishing House of the Military University of Technology), Warszawa (2007)
7. Żardecki, D., Dębowski, A.: Examination of computational procedures from the point of view of their applications in the simulation of torsional vibration in the motorcycle steering system, with freeplay and friction being taken into account. Arch. Automot. Eng. **64**(2), 179–195 (2014)
8. Żardecki, D., Dębowski, A.: Method of analysing torsional vibrations in the motorcycle steering system in the phase plane. Arch. Automot. Eng. **76**(2), 137–154 (2017)
9. Czerwiński, E., Olejnik, P., Awrejcewicz, J.: Modeling and parameter identification of vibrations of a double torsion pendulum with friction. Acta Mech. et Automatica **9**(4), 204–212. ISSN (Online) pp. 2300–5319
10. Armstrong-Helouvry, B., Dupont, P., Canudas de Wit, C.: A survey of models, analysis tools and compensation methods for the control of machines with friction. Automatica **30**(7), 1083–1138 (1994)
11. Żardecki, D.: Piecewise linear luz(…) and tar(…) projections. Part 1—theoretical background. J. Theor. Appl. Mech. **44**(1), 163–184 (2006)
12. Żardecki, D.: Piecewise linear luz(…) and tar(…) projections. Part 2—application in modeling of dynamic systems with freeplay and friction. J. Theor. Appl. Mech. **44**(1), 185–202 (2006)
13. http://andrzejdebowski.wat.edu.pl/Publikacje.html#about6